Lecture Notes in Civil Engineering

Scott Walbridge · Mazdak Nik-Bakht · Kelvin Tsun Wai Ng · Manas Shome · M. Shahria Alam · Ashraf el Damatty · Gordon Lovegrove *Editors*

Proceedings of the Canadian Society of Civil Engineering Annual Conference 2021

CSCE21 Structures Track Volume 2

Springer

Lecture Notes in Civil Engineering

Volume 244

Lecture Notes in Civil Engineering (LNCE) publishes the latest developments in Civil Engineering - quickly, informally and in top quality. Though original research reported in proceedings and post-proceedings represents the core of LNCE, edited volumes of exceptionally high quality and interest may also be considered for publication. Volumes published in LNCE embrace all aspects and subfields of, as well as new challenges in, Civil Engineering. Topics in the series include:

- Construction and Structural Mechanics
- Building Materials
- Concrete, Steel and Timber Structures
- Geotechnical Engineering
- Earthquake Engineering
- Coastal Engineering
- Ocean and Offshore Engineering; Ships and Floating Structures
- Hydraulics, Hydrology and Water Resources Engineering
- Environmental Engineering and Sustainability
- Structural Health and Monitoring
- Surveying and Geographical Information Systems
- Indoor Environments
- Transportation and Traffic
- Risk Analysis
- Safety and Security

To submit a proposal or request further information, please contact the appropriate Springer Editor:

- Pierpaolo Riva at pierpaolo.riva@springer.com (Europe and Americas);
- Swati Meherishi at swati.meherishi@springer.com (Asia - except China, and Australia, New Zealand);
- Wayne Hu at wayne.hu@springer.com (China).

All books in the series now indexed by Scopus and EI Compendex database!

More information about this series at https://link.springer.com/bookseries/15087

Scott Walbridge · Mazdak Nik-Bakht ·
Kelvin Tsun Wai Ng · Manas Shome ·
M. Shahria Alam · Ashraf el Damatty ·
Gordon Lovegrove
Editors

Proceedings of the Canadian Society of Civil Engineering Annual Conference 2021

CSCE21 Structures Track Volume 2

Springer

Editors
Scott Walbridge
University of Waterloo
Waterloo, ON, Canada

Kelvin Tsun Wai Ng
University of Regina
Regina, SK, Canada

M. Shahria Alam
University of British Columbia - Okanagan Campus
Kelowna, BC, Canada

Gordon Lovegrove
University of British Columbia - Okanagan Campus
Kelowna, BC, Canada

Mazdak Nik-Bakht
Concordia University
Montreal, QC, Canada

Manas Shome
Matrix Solutions Inc.
Edmonton, AB, Canada

Ashraf el Damatty
University of Western Ontario
London, ON, Canada

ISSN 2366-2557 ISSN 2366-2565 (electronic)
Lecture Notes in Civil Engineering
ISBN 978-981-19-0655-8 ISBN 978-981-19-0656-5 (eBook)
https://doi.org/10.1007/978-981-19-0656-5

This Springer imprint is published by the registered company Springer Nature Singapore Pte Ltd.
The registered company address is: 152 Beach Road, #21-01/04 Gateway East, Singapore 189721, Singapore

Contents

About the Editors

Dr. Scott Walbridge, Ph.D., P.Eng. (Alberta) is a Professor at the University of Waterloo, where he has worked since completing his Ph.D. at the EPFL in Lausanne, Switzerland, in 2005/6. Dr. Walbridge currently serves as Technical Committee (TC) Vice-Chair for the CSA S157 Design Code (Strength Design of Aluminum Structures) and TSC Chair for CSA S6 (Canadian Highway Bridge Design Code) Section 17 (Aluminum Structures). He is also a member of CSA W59 and W59.2 (Canadian structural steel and aluminum welding codes). In addition to his work on various structural design codes, he also currently serves as the Program Director for the University of Waterloo's new undergraduate program in Architectural Engineering. His research has investigated topics in various areas including: fatigue of steel and aluminum welded connections, performance of steel and aluminum mechanical connections, vibration of aluminum pedestrian bridges, and stability of aluminum structures. He was awarded an Alexander von Humboldt Fellowship related to his research on metal fatigue in 2016–2017.

Dr. Mazdak Nik-Bakht is an Associate Professor of Construction Engineering & Management in the Department of Building, Civil and Environmental Engineering at Concordia University, Montreal. He is the director of Compleccity Lab and a co-director of Centre for Innovation in Construction and Infrastructure Engineering & Management (CICIEM) at Gina Cody School of Engineering & Computer Science. He has a Ph.D. in Construction Engineering & Management from the University of Toronto (2015), as well as a Ph.D. in Structural Engineering from Iran University of Science and Technology (2011). Dr. Nik-Bakht is a licensed Professional Engineer with Professional Engineers Ontario and has years of professional experience as a structural designer, structural engineering division head, and project manager in structural & infrastructure rehabilitation projects. A new course called 'Big Data Analytics for Smart City Infrastructure' to train the next generation of construction and infrastructure engineering professionals was developed by him in 2019 and has been delivered annually ever since.

Dr. Kelvin Tsun Wai Ng is Professor of Environmental Systems Engineering at University of Regina, Canada. His major fields of interest are in waste management and environmental sustainability, particularly in development of (i) sustainable waste management system, (ii) evidence-based waste policy, and (iii) data-driven waste collection and disposal methods. His projects have been funded by a number of provincial and federal agencies, including NSERC, Mitacs, Communities of Tomorrow, Innovation Saskatchewan, Ministry of Environment, and City of Regina, etc. Dr. Ng is a Professional Engineer with Permission to Consult in Saskatchewan, Canada. He is also the instructor for a number of popular courses at the Faculty of Engineering and has received the 2017 President's Award for Teaching Excellence.

Manas Shome, Ph.D., P.Eng. is a Principal Engineer at Matrix Solutions, a Calgary-based environmental engineering consulting firm. Based in Edmonton, he provides technical leadership on water resources engineering projects. He obtained a B.Sc. and M.Sc. in Civil Engineering at the Bangladesh University of Engineering and Technology and earned his Ph.D. in Civil Engineering from the University of Alberta in 1995. His professional experience includes more than 30 years in sustainable water resources management, river engineering, computational modeling of rivers and drainage systems, design of hydraulic structures, and environmental impact assessment studies. An expert in the field of hydrology and hydraulic engineering, he frequently serves as an expert witness at regulatory hearings. Outside his consulting practice, Manas enjoys research, teaching, and watching sports. His research outcomes have been published in prestigious peer-reviewed journals and in conference proceedings. He is a co-recipient of the 2010 Keefer Medal award and recipient of the 2015 Excellence in Teaching award from the University of Alberta's Faculty of Extension. He has been elected to the grade of Fellow by the CSCE in 2019. Manas has been involved with CSCE since 2000 serving on the Edmonton section in various roles including Chair, and on the organizing committee of the 2012 Annual Conference in Edmonton, Alberta.

Dr. M. Shahria Alam is a Professor of Civil Engineering at the University of British Columbia (UBC)'s Okanagan Campus and the Director of Green Construction Research & Training Center (GCRTC) at UBC. He is currently serving as the Chair of the Engineering Mechanics & Materials (EMM) division of the Canadian Society for Civil Engineering (CSCE). His research interests include applications of smart materials like shape memory alloys and sustainable construction materials, performance-based design, repair/retrofit of structures, and self-centering structures. Dr. Alam is the Director of the Applied Laboratory for Advanced Materials & Structures (ALAMS) at UBC. He has authored over 250 peer-reviewed articles and holds several patents. He is the recipient of several national and international awards including CSCE's Pratley Award. He is also an active member of several ACI and ASCE code committees.

Dr. Ashraf el Damatty, Professor and Chair of the Department of Civil and Environmental Engineering at the University of Western Ontario, London, Ontario, Canada. He is a Fellow of the Canadian Society of Civil Engineering and Fellow of the Engineering Institute of Canada. He is a Research Director at the WindEEE Research Institute. He holds the title of High-End Expert at Tongji University and Sichuan Universities, China. He obtained a BSc. and M.Sc. from Cairo University in 1986 and 1991, Ph.D. in Structural Engineering from McMaster University, Canada, in 1995, and an MBA in 2016 in Higher Education Management from University College, London, UK. He is the founder of the Canadian Society of Civil Engineering (CSCE) Steel Structures Committee and serves currently as the Chair of the CSCE Structures Division. Dr. El Damatty has consulted on many projects in North America and the Middle East. He has written about 250 publications, supervised more than 30 Ph.D. and 20 M.Sc. students, and has been invited as keynote speaker in many countries around the globe. He received several awards including the Alan Yorkdale Award by ASTM, Honorable Mention in 2014 Casimir Gzowski Medal Competition, 2015 CSCE Whitman Wright Award, 2016 CSCE Horst Leipholz Medal and Western University Faculty Scholar Award, and the 2018 professional Engineers of Ontario Engineering Medal of Research of Development. His research work has influenced the international codes and engineering practice worldwide.

Dr. Gordon Lovegrove is an MBA/Civil Engineer with over 30 years of experience in smarter growth, housing, sustainable transportation, safety, economics, and project management. Dr. Lovegrove was the point man that got the award-winning Universal Transportation Pass (U-Pass) for UBC that tripled transit use at both campuses. His current research focus is on zero-emission, hydrogen-powered rail (hydrail), including several industry partnerships to develop Canada's first hydrail switcher locomotive. Dr. Lovegrove is founding partner of the SMARTer Growth Partnership (smartergrowthpartnership.ca), an Associate Professor/founding member of UBCO's School of Engineering (ok.ubc.ca), VP Technical Programs for the Canadian Society of Civil Engineering (csce.ca); and co-author of several best practice guides on sustainable development, health, and safety. He brings 20 years of practical industry development experience plus 14 years of engineering research and design expertise. His research team includes electrical, mechanical, and civil engineering graduate students, plus computer science coders and research assistants.

Soil Structure Interaction (SSI) Analysis of Shear Wall Buildings with a Below-Ground Parkade

N. Porchelvam, J. L. Humar, S. Sivathayalan, and P. Mortazavi

1 Introduction

Despite advances in the understanding of seismicity and the response of soils and structures to earthquake loading, structural failure due to earthquake shaking is still not uncommon. One of the reasons for this outcome is the lack of appropriate consideration of the potential changes in both the seismic demand and the capacity due to the interaction of the structure with the subsoil. The soil-structure interaction (SSI) effects have been researched for many years, but as noted by NIST (2012) the literature does not provide sufficient clarity nor guidance to practicing engineers for dealing with specific building configurations. It is often presumed that SSI is beneficial and ignoring SSI would lead to a conservative design. Neglecting SSI effects in routine design facilitates a simpler design process, but this practice may lead to unsafe designs under some circumstances, depending on the properties of the soils and the characteristics of the structure. Observations during previous earthquakes as well as research studies have shown that the interaction between the soil and structure does influence the response of the structure and the damage caused to it [5]. The selective structural damage witnessed during the 1985 Mexico City earthquake highlights the influence of local geology and subsoil conditions on earthquake hazard.

Often buildings have large below grade structures in which case SSI may have a major influence on their response to earthquakes. The SSI effect on the seismic response of a structure depends on both the interaction between the soil and foundation, and that between the soil and sidewalls. It requires careful evaluation to determine whether SSI has a significant effect on the forces produced in the structure.

N. Porchelvam (✉) · J. L. Humar · S. Sivathayalan
Department of Civil and Envronmental Engineering, Carleton University, Ottawa, Canada
e-mail: NanthineePorchelvam@cmail.carleton.ca

P. Mortazavi
Department of Civil and Mineral Engineering, University of Toronto, Toronto, Canada

S. Walbridge et al. (eds.), *Proceedings of the Canadian Society of Civil Engineering Annual Conference 2021*, Lecture Notes in Civil Engineering 244,
https://doi.org/10.1007/978-981-19-0656-5_1

There are not many recommendations in the building codes concerning the seismic response of buildings that have several underground storeys. Engineers usually crop the building at the ground level and analyze it assuming that it has a fixed base at that level. The lateral earth pressure on the basement walls is later accounted for by using the Mononobe-Okabe formulation [3, 7]. Many earlier studies have focused on the effect of soil structure interaction on buildings at the soil/foundation interface, limited studies exist on the effect of interaction between the foundation of the structure and the soil, along with the interaction between the soil and the basement walls.

The provisions in the newer generation design codes (NBCC 2005 and later) imply higher earthquake loads on foundations and structures. While significant attention has been paid to the effects of this increased demand within the context of structural design, there has been little research on the effects of this on soil structure interaction. Further, the Mononobe-Okabe (MO) method relies on the values of the pseudo-static coefficients (k_h & k_v) which are deemed to be functions of the peak ground acceleration, and are estimated based on past experience. It is unknown whether the formulations to estimate k_h & k_v values are applicable under the current regime of shaking intensity. These concerns highlight the need to conduct further studies to assess the response of structures under earthquake loads prescribed by the current building codes, and the implications of using MO as in current practice.

Tall buildings with multiple levels of underground parking space are common in many parts of Canada, including Vancouver and the Lower mainland. This region is subject to high seismic hazard due to the Cascadia subduction zone. Better understanding of the seismic demand on such buildings with a below ground parkade can lead to safer designs. A comprehensive analytical study is carried out to determine the seismic response of a shear wall building (assumed to be located in Vancouver) using a model that incorporates the structure, the underground parkade, the foundation and the surrounding soil. The analysis considers the interaction between both the side-walls and foundation of the structure and the soil. The research focuses on providing an indication of when a designer should take SSI into account. Programs SAP2000 and OpenSees are used to create finite element models for analysis. The OpenSees analysis models the entire building (tower & underground parkade), its foundation and the surrounding soil. The far ends of the soil layers are attached to absorbing boundaries to represent infinite extent of the layers. A number of ground motions that are compatible with the uniform hazard spectra for Vancouver [6] are used in the analysis. The response of the structure including SSI effect is compared to that of a model of tower and parkade alone analyzed with a fixed base. The following two cases are considered.

1) Building founded on rock (“BOR”).
2) Building founded on soil overlying rock (“BOSR”).

For the BOR case, earthquake motions are directly transmitted to the structure from the bedrock, and the presence of soil is limited to the soils surrounding the parkade. The BOSR case includes soil surrounding and underlying the parkade. The bedrock motions in this case propagate through the soil to reach the rigid mat foundation

placed on the soil to support the structure. For both cases, a parametric study is carried out considering buildings with towers of different heights (4, 8, 12, 16 and 20 storeys) above the ground with a five level below grade parkade. The response of each building model is assessed for a range of subsoil conditions that represent different site classes, or different stiffnesses within the same site class, as defined in NBCC 2015.

2 Building Founded on Rock

The models analyzed consist of five different building configurations differentiated by the height of their tower above the ground, namely 4, 8, 12, 16, and 20 storeys. The tower sits on a deep below grade parkade surrounded by a large block of soil. In this case of the study, the foundation of the building is assumed to be resting on a rigid bedrock. Each storey is 3 m high and the plan dimensions of the tower are 30 m × 30 m, and of the parkade 40 m × 70 m as shown in Fig. 1. The buildings are referred to as 9-storey, 13-storey, 17-storey, 21-storey, and 25-storey based on the total number of storeys inclusive of the parkade. Different site conditions are simulated by changing the properties of the soil surrounding the parkade. Any variations observed with changing soil type in the BOR cases represent the influence of the dynamic forces on the parkade walls.

2.1 Analytical Model

The analysis is 2-D with earthquake motion applied in the X-direction. Walls lying in the X-Y plane constitute the Seismic Force Resisting System (SFRS), Walls that are in the Y-Z plane are assumed to provide negligible resistance, but deliver to the SFRS the forces imposed by interaction with the surrounding soil. It is assumed that the walls deform within their elastic limit, while recognizing that in practice one can

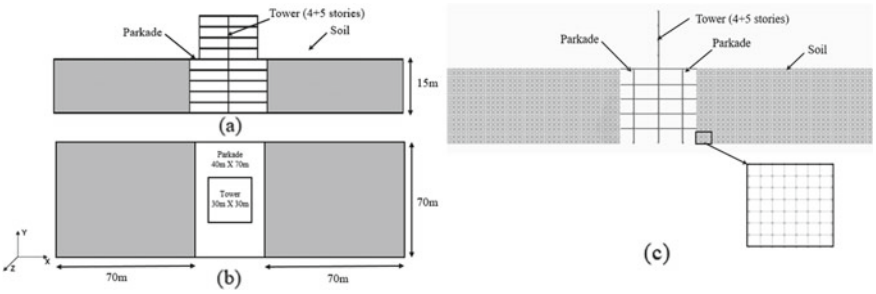

Fig. 1 **a** Elevation **b** Plan of the 9-storey building **c** Analytical model

expect a shear wall to crack at a drift of 0.5% and to start yielding when the drift reaches 2.5%. The tower and parkade are modelled as stick elements with masses lumped at their storey levels. The tower and parkade floors are formed by concrete slabs and may be considered as rigid diaphragms [4].

The tower, parkade, and soil are rigidly connected so that they move together. To incorporate the effect of cracking in tower and parkade, the cracked shear stiffness is taken as 10% of the uncracked shear stiffness, which is modelled by applying a modifier to the shear area of the tower and parkade. The elements are fixed at the base. Thus, the analytical model considered in this section ignores kinematic interaction effect between the soil and the structure. Rayleigh damping of 5% is used in the analysis.

The analysis is carried out using OpenSees which provides for easy modelling of both the structure and soil together. In OpenSees, the structure is modelled using elastic Timoshenko beam-column elements and the soil is modelled using four node quadrilateral elements with plane strain behavior. To represent the stress-strain relationship of the soil elements, an NDmaterial object of type elastic isotropic is used. The shear modulus (G) of the soil is obtained from the known shear wave velocity, V_s (m/s) of the soil profile using $G = \rho {V_s}^2$, where ρ, the density of the soil, is taken as 1920 kg/m^3. The soil behaviour is approximated as linear elastic, and pore water pressure effects are not considered in the analysis.

The standard viscous boundary (SVB) of Lysmer and Kuhlemeyer [2] type, is used to provide absorbing boundary conditions at the sides to ensure the transmission of incident waves without any reflection from the boundary. The efficiency of the SVB boundary is evaluated under free-field response. The results of the free-field analysis (i.e., the response at the top surface of the soil deposit) should almost be the same at all nodes. Based on this many trial analyses are carried out to determine the extent of soil deposit (70 m) on either side of the building, such that, with boundary conditions employed, the response of the free-field analysis seems reasonable. The nodes along the bottom boundary of the analytical model are fixed in OpenSees to permit the application of the seismic shaking along the bottom boundary, assuming that the entire soil structure system rests on a rigid rock. The lateral boundaries are SVB simulated using dashpots that are attached along horizontal and vertical directions to absorb shear and compression waves, respectively. The horizontal and vertical dashpots with coefficients $C_s = V_s A\rho$ and $C_p = V_p A\rho$ are modelled in OpenSees using a uniaxial viscous material command. The primary wave velocity V_p, is obtained from V_s and Poisson ratio μ using the equation $V_p = V_s\sqrt{(2-2\mu)/(1-2\mu)}$. The Poisson's ratio is assumed to be 0.20. Direct integration time history analysis that provides the response at discrete intervals of time is carried out in OpenSees. A set of 11 ground motion records that are considered representative of the seismicity of the region are downloaded from PEER website and scaled to match the Vancouver site B spectrum according to NBCC 2015 (Commentary J). Further, an Eigen analysis is carried out to determine the vibration periods of the building.

2.2 Validation of OPENSEES Model

To validate the numerical model in OpenSees, a similar model is created in SAP2000. Both models are analyzed for the same earthquake input motion, and the results obtained are compared. In SAP2000, the tower and the parkade are modelled as frame elements, and the soil region is modelled using shell elements. To simplify the analysis employed in this comparison study, the lateral soil boundaries are modelled as free boundaries. The analysis is direct integration time history analysis and the base shears obtained from the SAP2000 and OpenSees are compared. The percentage difference observed between the two is approximately 3.3%, which could be attributed to the difference in the formulation of soil elements since the elements are shell elements in SAP2000 and quad elements in OpenSees.

2.3 Parametric Study

A parametric study is conducted to characterize the response of a wide range of buildings founded in different subsoil conditions. Five different buildings with 4, 8, 12, 16, and 20 storey towers, all situated above an underground parkade of 5 storeys are analysed. Different soil types are simulated by varying the shear wave velocities of the soil surrounding the parkade. A range of shear wave velocities ranging from 100 m/s to 1000 m/s is considered. This covers the range of soil types that are expected in the region, from very soft clays soils to dense sands.

2.4 Analysis of Results

The storey shears, storey moments, displacements, drifts, and the accelerations are recorded for each building height and for varying soil properties for all 11 earthquake inputs. In most cases the response in the storey just above the junction of the tower and the parkade, referred to as the base storey, is critical. The effect of the interaction on such response is presented in the form of magnification of the response of the structure in presence of the soil when compared with the response of the structure alone. The magnification factors observed in the base storey of the tower are observed to quantify the effect of soil structure interaction on the seismic response of the structures.

2.4.1 Magnification Factor

The magnification factor is defined herein as the ratio of the mean of the peak response of the building with soil to that of the building alone. Magnification factors are

observed for shear, moment, drift, displacement, and acceleration in the base storey for 4, 8, 12, 16, and 20 storey towers with varying soil properties. From the results, it is observed that the magnification factor is, in general, higher than 1 when the soil has shear wave velocities of 100 m/s (site class E), 150 m/s (site class E), 200 m/s (near the lower borderline of site class D), 300 m/s (near the upper borderline of site class D) or 450 m/s (middle of site class C). The magnification factors also show that in a few cases, stiff soils having shear wave velocity higher than 450 m/s cause significant magnification in acceleration response. It is apparent that there is magnification in structural response when soil structure interaction is considered in this type of buildings.

2.4.2 Effect of Soil Type on Seismic Response

To observe the effect of soil type on the seismic response of the buildings, the magnifications in shear at the base of the tower for different heights of tower analyzed with varying conditions of soil are plotted in Fig. 2. From the plot it is clear that for different tower heights soils having different shear wave velocities ranging from100 m/s (site class E), to 300 m/s (near the upper borderline of site class D) cause significant magnification. For sites with class C soil (450 m/s and 600 m/s), there is magnification in shear at the tower base, its value being different for different heights of the building. Effect of SSI with soils belonging to site class B (850 m/s and 1000 m/s) is reduction in base shear. The reduced SSI effect for site class B is attributed to the high stiffness of the soil. In general, a reduction in soil stiffness leads to an increase in the base shear.

It is sometime reasoned that nonlinearity in the soil response would reduce the effect of soil-structure interaction. In the present study, it is assumed that the soil

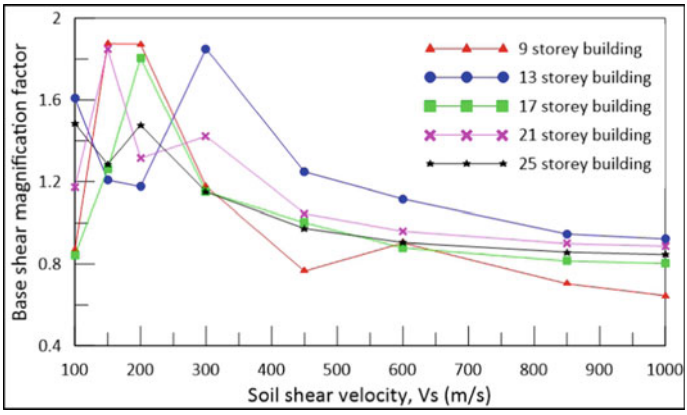

Fig. 2 Shear magnification factors for different tower heights and varying soil properties

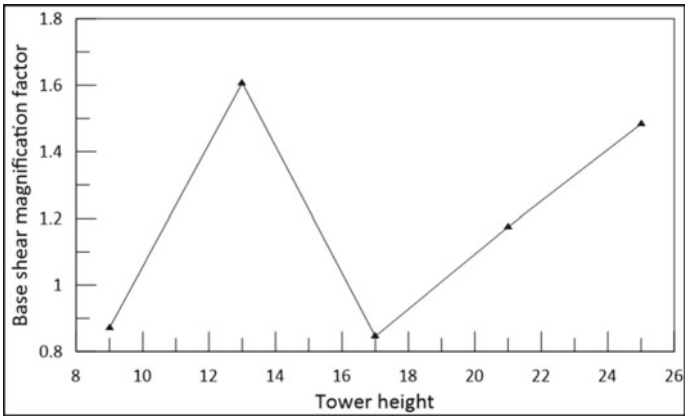

Fig. 3 Shear magnification factors for different tower heights with a 100 m/s shear wave velocity soil

remains elastic during its response to an earthquake and hence the effect of nonlinearity is not directly considered. However, the effect of nonlinearity would lead to a reduction in the shear wave velocity and hence in the modulus of rigidity for the soil. Thus, the assumption that with nonlinearity the SSI effect will reduce were to be true a softer soil should reduce the magnification in response. The results show that this is not true. In fact, the softer soils tend to increase the impact of SSI.

2.4.3 Effect of Number of Above Ground Stories on Seismic Response

For the same local site conditions, the height of the tower above ground influences the seismic response. The magnifications in base shear of buildings with varying tower heights but all founded in a site with class E soil (100 m/s) are shown in Fig. 3. It is apparent that although the height of the structure above ground influences the seismic response, no direct relationship exists between the tower height and the magnification. Similar response was noted in other soil types as well.

2.4.4 Effect of Earthquake Characteristics on Seismic Response

Figure 4 compares the effect of earthquake characteristics on the storey shears in the soil structure system for a 9-storey building. The variation in storey shear forces is dependent on the type of the soil. The figure shows two illustrative examples for the cases with soil having shear wave velocity of 100 m/s and 600 m/s. The variation of the storey shear for each of the 11 earthquake inputs (all scaled to match the Vancouver site B spectrum) are shown in Fig. 4. It is seen that the storey shears are affected by the characteristics of the earthquake input; but the differences in the upper storeys are less significant when compared to those on the lower storeys for the case

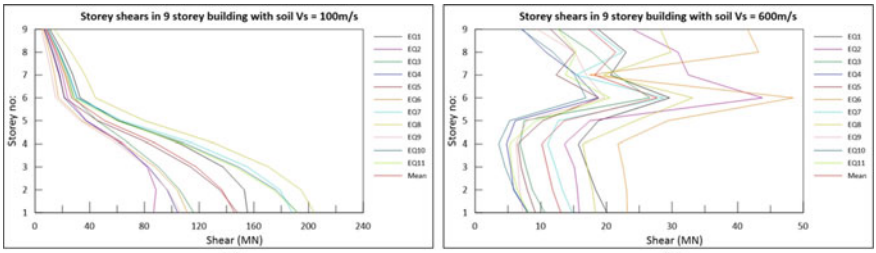

Fig. 4 Storey shears in 9-storey building with soil shear wave velocity, Vs = 100 m/s and 600 m/s for 11 different earthquake inputs

of soft, class E, soil sites (Fig. 4a). However, the variation of the story shears is of the same order across the height in a building founded on the relatively competent, Class C, soil.

2.4.5 Effect of Resonance on Seismic Response

An issue that has been discussed by some is whether the magnification of base shear occurs when there is resonance between the predominant periods of the structure and the soil. To examine this issue, the shear magnification factors for the base storey of the tower, the period of the soil for its first mode, which has a modal participation factor of 75%, and the periods for the first and second modes of the structure, which dominate the response are compared and it is observed that no correlation exists between the fundamental period and the magnification [9]. This indicates that the observed magnification in base shear cannot be attributed to resonance.

3 Building Founded on Soil Overlying Rock

In many instances, the foundations of the buildings are placed on soil overlying the bedrock. The seismic response of buildings in such cases will depend on interaction between the side walls and the surrounding soil, and between the foundation and the underlying soil. Both the inertial and kinematic soil-structure interactions come into play in this case. The buildings analysed herein are assumed to be supported on a thick mat foundation that moves as a rigid body and rests on soil that overlies the bedrock. As previously noted, the buildings are identified by the total number of storeys inclusive of the parkade, and the same building configurations, with tower heights varying from 4 to 20 storeys are considered in the analysis. The parkade is surrounded by a large block of soil, having a plan dimension of 70 m by 70 m. The soil deposit under the tower is 180 m by 70 m in size and 30 m in depth. A 30 m thick soil deposit below the foundation is employed to characterize the soil based on $V_{s,30}$

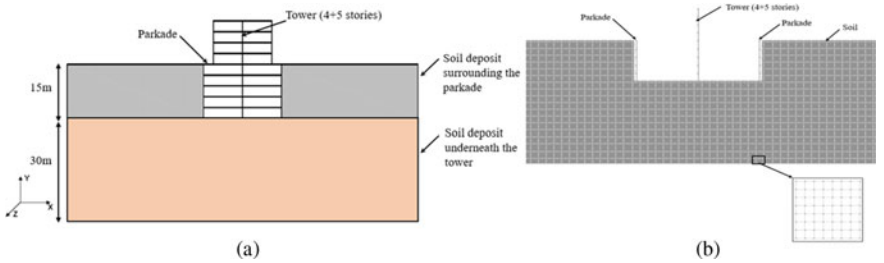

Fig. 5 **a** Elevation of the 9-storey building **b** Analytical model

as per the NBCC site classification. The plan view is similar for all the buildings and is as shown in Fig. 1(a) The elevation view and the numerical model of the 9-storey building are illustrated in Fig. 5.

3.1 Analytical Model

The details of the tower structure, including the supporting structure below the ground level, and parkade model are the same as previously presented in Sect. 2.1. The soil profile is assumed to consist of two soil layers, one below the foundation level, and another surrounding the parkade. The mat foundation is modelled using a series of elastic beam-column elements of 0.5 m length (selected to be equal to the dimension of the soil element). Very large values are specified for the modulus of elasticity E so that both the flexural rigidity EI and axial rigidity EA are large and the foundation is essentially rigid. The foundation nodes are connected to the soil nodes using equalDOF command in OpenSees in both X and Y directions.

The buildings are assumed to be located on a rock site in Vancouver, conforming to site class A, as defined in NBCC 2015, so the 11 selected ground motion are scaled to be compatible with the corresponding uniform hazard spectrum. However, only one earthquake record, which closely matches the UHS for Vancouver, selected from the scaled 11 records, is used in the analysis. The primary focus here is on the variation of the base shear of the building.

3.2 Parametric Study

Three different foundation soils types are considered for each tower height. The shear wave velocity of the soil deposit underneath the building is chosen to represent Site Class B and C, and a borderline case between B & C. For each foundation soil, three different types of top soil layer (soil surrounding the parkade) are considered. The shear wave velocity of the top soil layer is equal to or lower than that of the

Table 1 Subsoil conditions considered in the parametric study

	Shear wave velocity, V_s m/s	
	Bottom layer: foundation soil	Top layer: surrounding soil (Relative stiffness, $G_{SurroundingSoil}/G_{FoundationSoil}$)
Class B (Middle)	1000 m/s	Case 1: 200 m/s (Very soft ≈ 5%) Case 2: 750 m/s (Soft, ≈ 55%) Case 3: 1000 m/s (Same stiffness, 100%))
Borderline: Class B/C	750 m/s	Case 1: 200 m/s (Very soft ≈ 7%) Case 2: 550 m/s (Soft, ≈ 55%) Case 3: 750 m/s (Same stiffness,100%)
Class C (Middle)	450 m/s	Case 1: 200 m/s (Very soft ≈ 20%) Case 2: 300 m/s (Soft, ≈ 45%) Case 3: 450 m/s (Same stiffness, 100%))

foundation soil. The cases studied are intended to represent typically encountered site conditions, (a) a uniform soil layer throughout, or a top soil layer that is (b) somewhat softer, or (c) much softer than the bottom layer. The different subsoil conditions considered for each tower height are summarized in Table 1.

A ground response analysis of a model comprising just the soil block below the foundation without the building and surrounding soil is carried out to determine its response to the excitation produced by the application of the selected ground motion at the rock below the foundation block of soil. The time history of the horizontal motion at the top surface of the block is determined. This motion is referred to as the propagated motion or free field motion.

To observe the structural demand when the soil structure interaction is ignored, the building consisting of the tower and parkade but without the surrounding soil is analysed for its response to the propagated motion applied at the foundation level. The storey shears, moments, deflections, and accelerations are determined. Next a model comprising the tower, the parkade and the surrounding soil is analysed for its response to the propagated motion. Finally, the complete system comprising the building the surrounding soil and the soil below the foundation is analysed for the same ground motion (Vancouver site Class A motion) applied at the rock level.

3.3 Analysis of Results

The structural response is determined by (1) a fully coupled SSI analysis (the building, the soil surrounding the parkade and the soil under the foundation) with Site class A compatible earthquake motion as input at bedrock, (2) an analysis of the building and the soil surrounding the parkade for free-field motion (BOR case), and (3) an analysis of the building alone for free-field motion to establish a reference “typical design” response.

3.3.1 Magnification Factor

The intent of the analysis is to delineate the cases where the typical practice would lead to unsafe designs, and to identify which combinations of soil properties lead to the highest structural demand. For all cases detailed in the previous section on parametric study, magnification factors are computed for shear, moment, drift, displacement, and acceleration at the base storey of the tower. The analysis covers typical cases anticipated in the Vancouver region. The results indicate that the BOR analysis, which ignores the kinematic interaction computes higher base shear, moment, drift etc., or higher magnification factor when compared to the BOSR analysis, the magnifications being measured with respect to the baseline case (case of the building alone subjected to the propagated motion).

A representative comparison between the results of BOSR case and BOR case is presented in Fig. 6, which shows the magnification factors observed for 9-storey building with subsoil conditions belonging to middle of site class C (450 m/s). The abscissa in Fig. 6 represents the case numbers as detailed in Table 1, cases 1, 2 and 3 correspond to BOSR analysis and cases 4, 5 and 6 correspond to BOR analysis, respectively. The BOSR case consistently yields lower demand compared to BOR. In fact, in many cases demand is seen to be lower than in the baseline analysis [9]. BOSR configuration considers both inertial interaction and kinematic interactions and demonstrates that simplified models which ignore kinematic interaction may lead to conservative estimates of the structural demand. It is also noted that higher contrast between the soil surrounding the parkade and the soil underneath the base of the tower (case 4) leads to an increase in magnification.

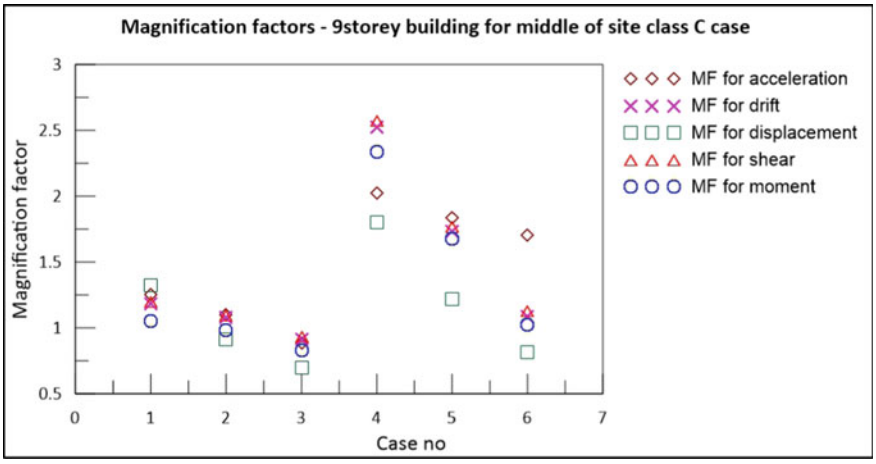

Fig. 6 Magnification factors for 9 storey building, Shear wave velocity of underlying soil 450 m/s

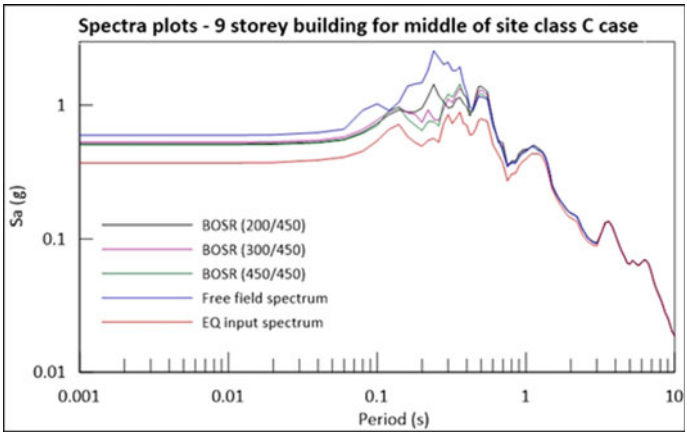

Fig. 7 Spectra plots for 9 storey building, middle of site class C (450 m/s) case

3.3.2 Base Slab Averaging Effect

The presence of stiff foundation elements causes the motion to deviate from the free field motion. The impact of this effect is a function of the relative values of the wave length and foundation width. From the results of analysis presented in this section it is observed that there is a reduction in seismic demand when the structure is analyzed with a rigid foundation resting on a soil deposit overlying rock (BOSR). Analyses are carried out for varying tower heights for various BOSR cases and the horizontal ground accelerations are recorded at the base of the structure for each BOSR case.

Figure 7 shows the spectra plots of the recorded ground motions for 9-storey building with middle of site class C (450 m/s) shear wave velocity soil. For identification, a backslash (/) is used to separate the shear wave velocity of the soil deposit surrounding the parkade and the shear wave velocity of the soil deposit underneath the tower. Similar plots for all the cases analyzed can be plotted. For comparison, the free field spectra of the horizontal acceleration recorded at the top of the soil deposit when the structure and side soil are absent are included in the plots. The spectrum of the earthquake input motion for Site Class A applied at the base of the underlying soil is also plotted. It is observed that the spectra of accelerations recorded at the base of the structure are de-amplified when compared with the free field spectra for the same site condition. Hence, there is a reduction in seismic demand on the structures owing to the base slab averaging effect.

3.3.3 Foundation Rotation

The foundation rigidity combined with flexibility of the soil under the foundation causes the base slab to rotate in addition to being displaced in the horizontal direction. Such rotation causes an increase in the displacements of the upper storeys and a

lengthening of the period. Because the spectral accelerations generally decrease with increasing period, lengthening of the period results in a reduction in the seismic demand on the structure. To illustrate the extent of base slab rotation, the vertical displacements and the rotations at the two end and at the mid-point of the base slab are recorded. These records confirm the rotation of base slab. The demand for structures with mat foundation resting on a soil deposit is found to be lower than in the case when the structure is assumed to be resting on a rock (when no rotation in foundation is allowed) due to the combined effect of base slab averaging and foundation flexibility.

4 Conclusions

The primary objective of this research is to better understand whether the seismic demands considered in the design of structures with a relatively tall underground parkade, within the Canadian context, are appropriate. Analytical studies presented here are limited to the expected ground motions in the Vancouver region given its high seismic hazard compared to other Canadian locales, and to structural configurations that are typical in Vancouver. The results are however valid irrespective of the level of hazard. The results indicate that the practice of analyzing structures ignoring the effect of soil structure interaction could lead to unsafe designs depending on the subsoil conditions.

Analyses of buildings with different tower heights show no distinctive relationship between the building heights and the response magnification. The analyses confirm that SSI depends on the properties of the soil at the site and softer soils have greater impact on the response. For BOSR cases, a high magnification in response is observed when the structure is surrounded by very soft soil and is underlain by a very stiff soil, i.e., when there is a significant difference in shear wave velocities of the soil surrounding the parkade and the soil under the base of the tower. Both, the rotation of the foundation and filtering of the motion at the foundation due to base slab averaging, contribute to reduction in the demand. As a result, the seismic responses in the BOR cases are higher than in the corresponding BOSR cases. This highlights the effects of kinematic interaction which is absent when the structure is founded on rock, and significant when the structure is founded and/or surrounded by soft soils.

References

1. CSI (2019) Analysis reference manual
2. Lysmer J, Kuhlemeyer RL (1969) Finite dynamic model for infinite media. J Eng Mech Div 95:859–878
3. Mononobe N, Matsuo M (1929) On the determination of earth pressures during earthquakes. In: Proceedings, world engineering congress 9:179–187

4. Mortazavi P, Humar J (2016) Consideration of diaphragm flexibility in the seismic design of one-story buildings. Eng Struct 127:748–758
5. Mylonakis G, Syngros C, Gazetas G, Tazoh T (2006) The role of soil in the collapse of 18 piers of Hanshin expressway in the Kobe earthquake. Earthquake Eng Struct Dynam 35(5):547–575
6. NRCC (2015) National Building Code of Canada 2015 (NBCC 2015). Canadian Commission on Building and Fire Code, National Research Council of Canada, Ottawa
7. Okabe S (1926) General theory of earth pressure. J Jpn Soc. Civ. Eng. 12(1)
8. OpenSees (2014) Open system for earthquake engineering simulation. Pacific earthquake engineering research center (PEER). (http://opensees.berkeley.edu)
9. Porchelvam N (2020) Soil structure interaction (SSI) analysis of shear wall buildings with a below-ground parkade, MASc thesis, Carleton University, 348p

Probabilistic Analysis of Brittle Fracture Design Code Provisions for Steel Bridges

M. Y. X. Chien, S. Walbridge, and B. Kühn

1 Introduction

Historical collapses of steel bridges caused by brittle fracture, such as the Duplessis Bridge in Trois-Rivières, Québec (failed in 1951), the Silver Bridge in Point pleasant, West Virginia (1967), and the Mianus River Bridge on I-95 in Cos Cob, Connecticut (1983), have motivated code writers around the world to create regulations for designing against brittle fracture since the 1970s and 1980s.

Brittle fracture design rules can vary significantly between regions. In Canada, the Canadian Highway Bridge Design Code, CSA S6-19, provides Table 10.12 and Table 10.13, which specify toughness requirements solely based on the minimum service temperature of the geographic location, split into two temperature zones [4].

However, it is known that temperature is not the only factor that plays a role in the fracture behaviour of steels. The American code, AASHTO LRFD Part 6, provides a slightly more sophisticated table, which has three temperature zones and takes into account the steel plate thickness [1].

In Europe, significant advances have been made in recent decades in the sophistication of the tools available for modelling and understanding brittle fracture in new and existing structures. The Eurocode (EN 1993-1-10) provides the most detailed approach for brittle fracture design, which takes into consideration numerous factors such as plate thickness, yield strength of the material, stresses on the component, radiation losses, member shape and dimensions, safety allowances, strain rate, and degree of cold forming if applicable [6]. While adaption of similar approaches in North America to assess these special situations may be of interest, it is worth noting that in no part of the world has a rigorous probabilistic assessment been performed to

M. Y. X. Chien (✉) · S. Walbridge
University of Waterloo, Waterloo, Canada
e-mail: michelle.chien@uwaterloo.ca

B. Kühn
Technische Hochschule Mittelhessen, Giessen, Germany

S. Walbridge et al. (eds.), *Proceedings of the Canadian Society of Civil Engineering Annual Conference 2021*, Lecture Notes in Civil Engineering 244,
https://doi.org/10.1007/978-981-19-0656-5_2

assess the reliability levels being achieved using the various existing brittle fracture design methods. For example, although probabilistic considerations have been incorporated in the calibration of the Eurocode provisions, it seems this has been done only to ensure a high probability that ultimate failure will be governed by ductile, rather than brittle, fracture.

Although the Eurocode takes more factors into consideration, it is uncertain how the results compare with the current Canadian provisions, and whether this increase complexity is justified. To answer these questions, a basic analysis was previously done to compare the brittle fracture provisions in EN 1993-1-10 with CSA S6-19. The example bridge used was from the CISC's "Straight Plate Girder Bridge Design Example 1", where the loads, dimensions and boundary conditions were obtained. This analysis found that the toughness requirements of CSA S6 are more conservative than EN 1993-1-10 for thinner plates, that the design provisions in both codes result in the same toughness requirement in the middle range of plate thicknesses, and EN 1993-1-10 is generally more conservative for thicker plates.

2 Literature Review on Eurocode Methods

The Eurocode contains two methods of assessing brittle fracture, a simplified method using design tables, and a fracture mechanics method. The latter is described briefly in the following section, as it is the method that is modified and applied in the subsequent probabilistic analysis.

2.1 Eurocode Fracture Mechanics: K-factor Based Method

The first form of the fracture mechanics method is presented in a stress intensity factor framework and is based the toughness of the material ($K_{Mat,d}$, which is a function of a reference temperature, T_{Ed}) being greater than the applied effects (expressed as the stress intensity factor, $K_{appl,d}$). This is shown in Eq. 1, in terms of K-values, or plain strain stress intensity factor [12]. The original master curve, which forms the basis of this method was developed in [15].

$$K^*_{appl,d} = \frac{K_{appl,d}}{k_{R6} - \rho} \leq 20 + \left[70 \left\{ \mathrm{EXP}\left(\frac{T_{Ed} - [T_{27J} - 18\,^{\circ}\mathrm{C}] + \Delta T_R}{52} \right) \right\} + 10 \right] \cdot \left(\frac{25}{b_{eff}} \right)^{\frac{1}{4}} \quad (1)$$

The left-hand side of the equation is calculated using Eq. 2.

$$K^*_{appl,d} = \frac{K_{appl,d}}{k_{R6} - \rho} = \frac{\sigma_{Ed}\sqrt{\pi \cdot a_d} \cdot Y \cdot M_k}{k_{R6} - \rho} \left[\mathrm{MPa}\sqrt{\mathrm{m}} \right] \quad (2)$$

where
σ_{Ed} is the stress from external loads [MPa],
a_d is the design size of the crack [m],
Y is the is the correction function for various crack positions and shapes [-] [11],
M_k is the correction function for various attachments with semi-elliptical crack shapes [-],
k_{R6} is the plasticity correction factor from the R6-Failure Assessment Diagram (FAD) [-], and
ρ is a correction factor for local residual stresses, which may be taken $\rho = 0$ for non welded details [-].

On the right-hand side of Eq. 1, the term T_{Ed} is expanded using Eq. 3.

$$T_{Ed} = T_{md} + \Delta T_r + \Delta T_\sigma + \Delta T_{\dot{\varepsilon}} + \Delta T_{cf}\ [^\circ\mathrm{C}] \tag{3}$$

T_{md} is the lowest daily air temperature of the location of interest, with a 50-year return period.

ΔT_r is an adjustment for radiation loss, which depends on the topography, latitude, albedo, etc., of the location of interest. Currently, research has been done in Germany to establish an average value of –5 °K radiation loss for the entire country. Other European countries often adopt the –5 °K radiation loss from Germany. However, this parameter has not yet been established in Canada.

ΔT_σ *is* the temperature shift due to the applied stress.

$\Delta T_{\dot{\varepsilon}}$ is the adjustment for strain rates other than the reference rate of $\varepsilon_0 = 10^{-4}$/sec, based on Eq. 4.

$$\Delta T_{\dot{\varepsilon}} = -\left(1440 - f_y(t)/550\right) \cdot (\mathrm{LN}(\dot{\varepsilon}/\dot{\varepsilon_0}))^{1.5}\ [^\circ\mathrm{C}]$$

$\Delta T_{\varepsilon cf}$ is the adjustment for the degree of cold forming ε_{cf}, calculated using Eq. 5.

$$\Delta T_{\varepsilon_{cf}} = -3 \cdot \varepsilon_{cf}\ [^\circ\mathrm{C}] \tag{5}$$

In Eq. 1, the term $(T_{27J} - 18)\ [^\circ\mathrm{C}]$ represents the temperature correlation between the CVN test temperature corresponding to a notch toughness of 27 J and the fracture mechanics transition temperature, T_{100}, which is the temperature corresponding to a fracture toughness of 100 MPa$\sqrt{\mathrm{m}}$.

It is also worth noting that in Eq. 1, ΔT_R is a safety allowance, if required, to reflect different reliability levels for different applications, and b_{eff} is a measure of the effective crack front length. It is dependent on the crack shape (e.g. surface crack, edge crack, double edge crack, or through-thickness central crack), crack size (in the case of a surface crack), and plate thickness, and takes on one of the values given in Tables 2–7 of the Eurocode background document EUR 23,010 EN [7].

3 Probabilistic Analysis

Following the preliminary code comparison published previously and briefly described in the introduction, a probabilistic analysis was performed to observe the sensitivity of the probability of failure, P_f, to changes in each of the input parameters of the Eurocode fracture mechanics method. The equations and tables of the method were programmed using Visual Basic. Statistical distributions for the key input parameters were identified and probability of failure was determined by Monte Carlo Simulation (MCS).

By simulating a large number of trials, the sensitivity of the P_f to changes in each input parameter can be determined, along with limits on each parameter based on the target P_f or reliability index. The loads, dimensions, and boundary conditions were again obtained from the CISC Straight Plate Girder Bridge Design Example 1 for the probabilistic brittle fracture analysis. A sketch of the dimensions (in mm) and girder layout are presented in Fig. 1.

This bridge has four three-span continuous girders (43 m / 53 m / 43 m) with flange and web plate thicknesses varying along the span. A 350 W steel grade ($f_y =$ 350 MPa) is assumed. However, as no North American equivalent currently exists, a generic European "master curve" relating CVN notch toughness to fracture toughness is assumed to also apply to North American steels. In order to study the effect of the extreme cold temperature on the probability of brittle fracture, the fictitious bridge was "placed" in three locations: Fort McMurray, AB, Vancouver, BC, and Waterloo, ON.

3.1 Target Reliability Index (Beta) and Probability of Failure

For brittle fracture, a suitable target reliability index of $\beta = 4.0$ can be identified based on CSA S6 Chapter 14 [5] for brittle element behaviour in a structural system

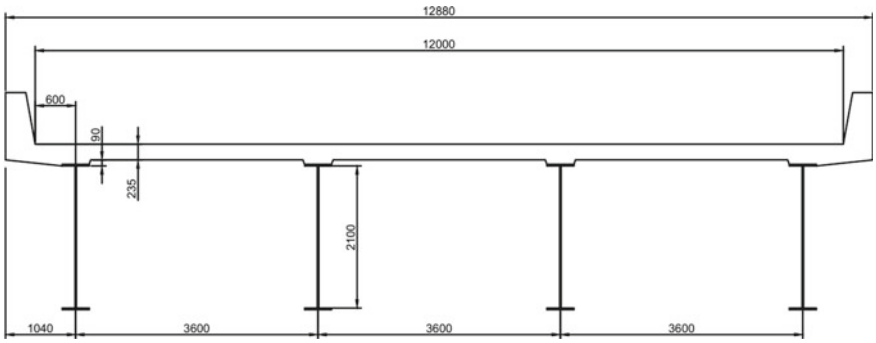

Fig. 1 Straight plate girder bridge

with no redundancy and limited inspectability under normal traffic. The question of system behaviour for multi-girder bridges is one that is still currently being pondered by code writers and researchers. If the highest level of redundancy can be assumed (meaning the brittle fracture of one girder does not result in structure collapse), then the target value of the reliability index can decrease to as low as 3.5. The corresponding probabilities of failure are $3.17 \cdot 10^{-5}$ and $2.33 \cdot 10^{-4}$ for $\beta = 4.0$ and 3.5 respectively, where:

$$P_f = \Phi(-\beta) \tag{6}$$

and $\Phi()$ is the standard normal cumulative density function.

3.2 Distribution Types and Statistical Parameters

In the probabilistic implementation of the Eurocode fracture mechanics method, bias factors are applied to the deterministic model parameters, typically in the form of "multipliers", which are defined to account for the various sources of uncertainty associated with each parameter. Table 1 summarizes the deterministic values assumed for each input parameter. Sources for these parameters are given where appropriate. In this table, t and B are the girder flange thickness and width, flange stresses at the location of interest are denoted with a σ, and H_w and W_w are the weld height and width associated with the critical detail. The weld parameters are used to calculate the local stress intensity factor using equations not shown here for reasons of brevity. To apply these equations, a weld detail geometry must be assumed. In the calibration of the Eurocode simplified method, a longitudinal plate attachment detail was assumed, due to its relative severity. Thus a similar detail is conservatively assumed in the current analysis.

Table 2 summarizes the bias factors assumed in the probabilistic analysis. Sources used to establish the distribution type, mean, and COV for each bias factor are given in this table where appropriate. Concerning parameters in Tables 1 and 2, the following additional information is noteworthy:

- The COV of the extreme minimum temperature was calculated following a procedure described in the CAN/CSA-S6 Calibration Report [2].
- For the base case, a 2.2 mm crack size constant is assumed, as was done for the Eurocode simplified method calibration [7]. This parameter is varied subsequently in a parametric study. The COV of the crack size was taken as 0.2 from [14].
- The bias factor for the dead load stress was obtained from [4] with type D1 (factory-produced components) assumed for the entire dead load. In reality, if the concrete deck were cast-in-place and covered with an asphalt wearing surface, a larger COV would be appropriate, or separate bias factors should be used for each dead load source. Uncertainties in the brittle fracture resistance can be captured using bias factors, Z9 and Z10, to consider uncertainties associated with the brittle

fracture "master curve" formula and the notch to fracture toughness conversion, based on raw test data in EUR 23,510 EN [12]. Steel grades S355, S460, S690, and S890 were tested (and are reported in this reference) and the lower shelf of the master curve was fitted. Since the master curve was fitted to the average of the data, Z9 is a multiplicative factor to model the scatter of test data for the fitting, which has been assigned a mean of 1.0 and standard deviation of 25%. Using this value, a close replication of the 50%, 95%, and 5% failure probability curves for the raw test data from Figs. 2–7 in EUR 23,510 EN [12] could be produced. Note that the 20 MPa$\sqrt{\text{m}}$ term is not multiplied by Z9 because $K = 20$ MPa$\sqrt{\text{m}}$ represents the lower bound for cleavage fracture in steels, and therefore the stress intensity factor cannot be lower than that value [16].

- Z10 is an additive factor to model the scatter in test data correlating the fracture mechanics transition temperature, T100, to the Charpy test temperature, T27J. which has been assigned a mean of 0 and standard deviation of 0.13 (the transition temperature standard deviation is 13 °C), based on the raw data from Fig. 2–8 in EUR 23,510 EN [12].

The modified limit state function is presented as Eqs. 7–9:

$$K^*_{appl} = \frac{K_{appl}}{k_{R6} - \rho} \leq 20 + \text{Z}_9\left[70\left\{\text{EXP}\left(\frac{T_{Ed} - T_{27J} + 18\,^\circ\text{C} + \text{Z}_{10} + \Delta T_R}{52}\right)\right\} + 10\right] \cdot \left(\frac{25}{b_{eff}}\right)^{\frac{1}{4}} \tag{7}$$

$$K^*_{appl} = \frac{K_{appl}}{k_{R6} - \rho} = \frac{(\sigma_{D1} \cdot Z_5 + \sigma_L \cdot Z_6) \cdot \sqrt{\pi \cdot a \cdot Z_4} \cdot Y \cdot M_k}{k_{R6} - \rho} \left[\text{MPa}\sqrt{\text{m}}\right] \tag{8}$$

$$T_{Ed} = T_{md} \cdot Z_3 + \Delta T_r + \Delta T_\sigma + \Delta T_{\dot{\varepsilon}} + \Delta T_{cf}\ [^\circ\text{C}] \tag{9}$$

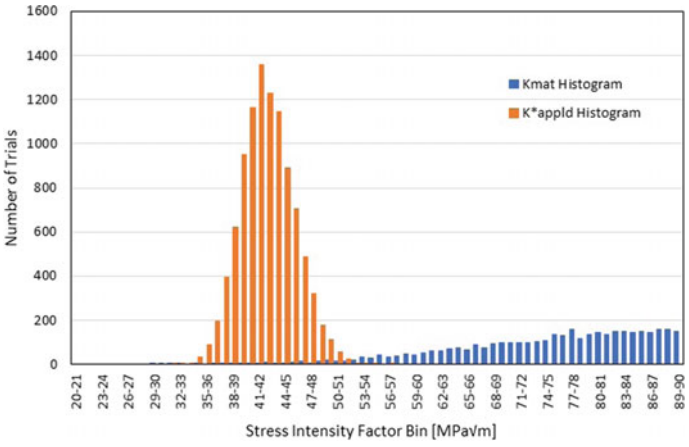

Fig. 2 Sample output for base case (Ft. McMurray, 50-year service period, $T_{27J} = -30$ °C)

Table 1 Deterministic parameters model parameters

Parameter	Units	Value	Source
F_y	MPa	350	(CSA 2019)
t	mm	25	(CISC 2002)
B	mm	375	(CISC 2002)
T_{md}	°C	Location-dependent	–
ΔT_r	°C	−5.0	[12]
ΔT_σ	°C	0.0	–
ΔT_R	°C	0.0	–
ΔT_ε	°C	0.0	–
ΔT_{ecf}	°C	0.0	–
T_{27J}	°C	−20 or −30	(CSA 2019)
a	m	0.0022	[12]
σ_{DLbc}	MPa	102.99	(CISC 2002)
σ_{DLac}	MPa	21.43	(CISC 2002)
σ_{LL}	MPa	64.78	(CISC 2002)
H_w	mm	10	–
W_w	mm	10	–

Table 2 Statistical variables for base case analysis (Ft. McMurray)

Z	Modifies	$\overline{Z}$	V_Z (σ_Z)	Distribution	Source
Z1	F_y	1.101	0.0915	Lognormal	[9]
Z2	t	1.02	0.012	Lognormal	[10]
Z3	T_{md}	1.0	0.0574	Normal	50-year service period, calculated based on [2]
Z4	a	1.0	0.20	Lognormal	[14]
Z5	σ_{D1}	1.03	0.08	Lognormal	[2]
Z6	σ_{LL}	1.5228	0.0304	Lognormal	50-year service period, calculated based on [2]
Z7	H_w	1.0	0.16	Lognormal	[8]
Z8	W_w	1.0	0.16	Lognormal	[8]
Z9	Master Curve	1.0	0.25	Lognormal	[12]
Z10	CVN to SIF Conversion	0.0	(13 °C)	Normal	[12]

3.3 Results: Base Case Analysis

Figure 2 shows sample output for MCS with 10,000 trials for one of the base case simulations, which assumed the bridge was located in Ft. McMurray, AB, and fabricated with steel having notch toughness, $T_{27J} = -30$ °C. On this basis of this simulation, a probability of failure of $p_f = 0.0054$ is calculated ($\beta = 2.55$), which is below the target reliability index range of 3.5–4.0. The following should be noted:

- The basis for this probability of failure calculation is a 50-year service period, which is used to calculate the extreme live load and the extreme cold temperature. It is then very conservatively assumed that these two events occur at exactly the same time.
- It should not be surprising that such a low probability of failure is obtained with such a highly conservative assumption implicitly made in the analysis. Clearly, in order to estimate the probability of failure more reasonably, a time-dependent reliability framework is needed, where the live load and temperature are allowed to fluctuate realistically over time or the effect of this realistic fluctuation is captured using an appropriate approximation. This is the next step in this research project, and not a possibility that is considered further in the current paper.
- For the purpose of assessing the implications of the assumed analysis period, in the sensitivity studies presented in the following sections, two service periods are considered: the 50-year service period employed in the base case analysis and a 1-year service period, the latter yielding "annual probability of failure" results, which still employ the overly conservative assumption that the extreme live load and temperature occur at the same time within the service period. In order to do this, the statistical approaches in [2] were employed with the raw traffic statistical data for the province of Ontario for midspan moment of a simply supported 40 m girder. (In future analyses, more recent raw data for Ontario, BC, and Alberta could be used where appropriate. However, for this study, the bridge "location" only affected the extreme temperature statistics.)

3.4 Results: Variation of Crack Size

A semi-elliptical crack shape was assumed, with "size" referring to the crack depth. The mean crack size was varied between 2 and 20 mm, and as expected, the probability of failure increases with increasing crack size. The results are presented in Fig. 3. Looking at this figure, it can be seen that the annual probability of failure curves are—as expected—lower than the 50-year service period curves.

Note that in order to present curves with only two variables changing at a time (location, which affects extreme temperature nominal and bias factor values, and mean crack size), the fracture toughness of the steel was held fixed at $T_{27J} = -20$ °C, even though (CSA 2019) would require a lower value of −30 °C for the coldest (Ft. McMurray) location. Looking at these curves, it can be seen that as the climate

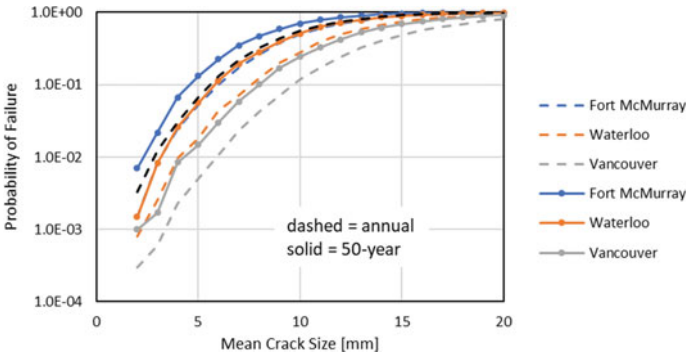

Fig. 3 P_f vs. crack size ($T_{27J} = -20$ °C)

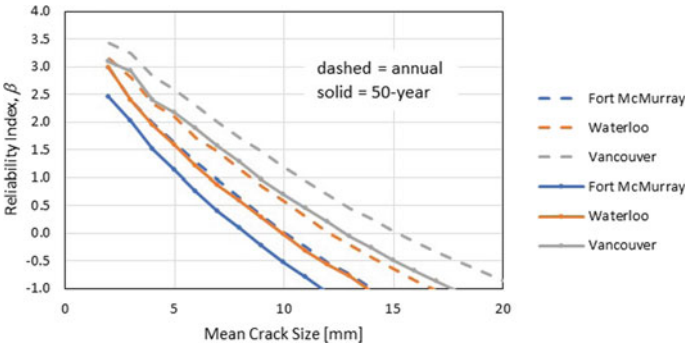

Fig. 4 β vs. crack size ($T_{27J} = -20$ °C)

becomes more severe, the probability of failure curve shifts upwards, as expected. Figure 4 presents the corresponding set of reliability index vs. mean crack size curves, based on Eq. 6.

3.5 Results: Variation of Load

In the next sensitivity study, the maximum nominal applied stress at the detail was varied to investigate the effect of this parameter. The dead-to-live load ratio was maintained all analyses. As can be seen in Fig. 5, the results show an expected increase in the probability of failure with an increase in the maximum nominal applied stress. It should be noted that the higher stress levels in this analysis exceed the nominal yield strength of the steel. This raises broader questions regarding the competing ductile and brittle fracture failure modes, which warrant further study. Questions such as: should the probability of failure for each failure mode be kept

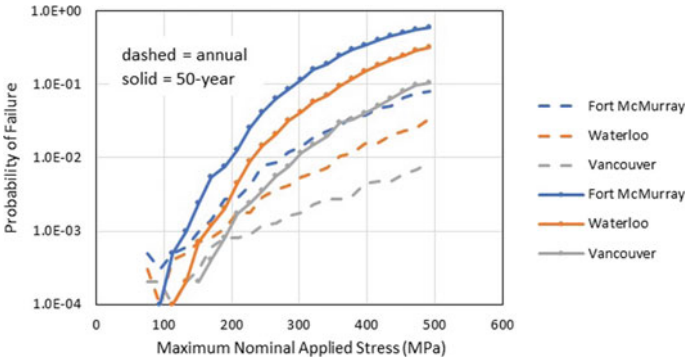

Fig. 5 P_f vs. maximum nominal applied stress ($T_{27J} = -20$ °C)

below a target threshold or should the probability of failure considering both failure modes simultaneously be kept below a threshold could be considered in this study.

3.6 Results: Variation of Plate Thickness

The simulation results from a flange plate thickness variation study interestingly showed a local minimum point in the p_f vs. flange plate thickness output, in contrast with the monotonically increasing curves obtained in the first two studies. Initially, the failure probability is high, as the crack takes up a significantly large proportion of the overall plate depth, making it a point of weakness as there is an insufficient amount of uncracked flange area to prevent failure. In the first portion of the graph, p_f decreases when the thickness increases, as gradually the crack is taking up less of the cross section. At a point near 50 mm thickness, the local minimum is reached. Beyond the optimum point, the p_f increases again as the increased thickness causes a reduction in ductility. The graph for the 8 mm crack is shown in Fig. 6.

Plate thickness variation was simulated for four different mean initial crack sizes ranging from 6 to 12 mm. The results for the 12 mm crack are shown in Fig. 7. In general, the trends were seen to be similar. However, as the mean crack size increases, the flange plate thickness for which the probability of failure by brittle fracture is a minimum also increases. Also, as expected, the probabilities of failure increase for all cases with an increase in the mean initial crack size or severity of the local climate.

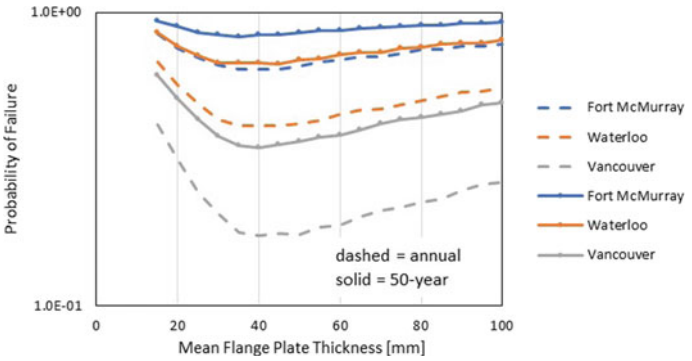

Fig. 6 P_f vs. plate thickness (8 mm mean initial crack size, $T_{27J} = -20$ °C)

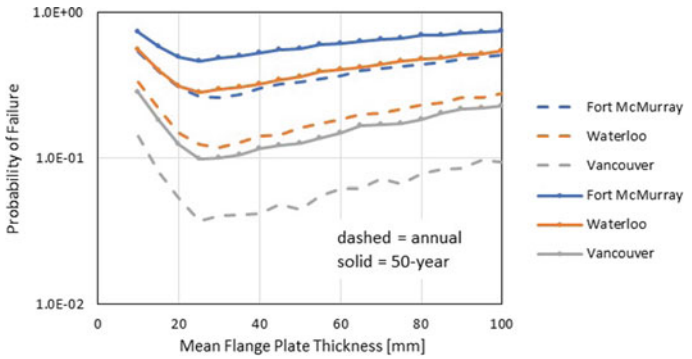

Fig. 7 P_f vs. plate thickness (12 mm mean initial crack size, $T_{27J} = -20$ °C)

4 Conclusions and Future Work

This paper describes a probabilistic analysis of brittle fracture risk in Canadian steel bridge girders, using the Eurocode fracture mechanics method, applied in a simple probabilistic framework. It is observed that the probability of failure by brittle fracture is affected by the crack size, load level, and plate thickness. Currently, on the resistance side of the limit state function, the research only considers bias factors for variability in the master curve and temperature correction. There remains work to be done to consider other sources of uncertainty, e.g. in the thickness correction, plasticity correction, etc. Further literature review and new experimental work may be needed to better characterize the statistical variables for the North American steels, traffic loading, etc. It must also be acknowledged that the treatment of the traffic load and extreme cold temperature in this analysis is highly simplistic and an area where future work is needed. An important next step of this work will be to cast the problem as a time-dependent reliability problem, with the extreme traffic and temperature loads fluctuating realistically over time.

A final recommended improvement to the presented methodology would be to consider the competing mechanisms of ductile and brittle fracture in a more sophisticated way, such as considering the two failure mechanisms simultaneously for each trial in an appropriate system reliability model.

Acknowledgements Financial support of this research project is generously provided by the Canadian Institute of Steel Construction (CISC), the Natural Sciences and Engineering Research Council (NSERC), and the Ontario Graduate Scholarship (OGS) Program.

References

1. AASHTO (2017) AASHTO LRFD bridge design specifications. Washington D.C.
2. Agarwal AC et al (2007) Calibration report for CAN/CSA-S6-06 Canadian highway bridge design code
3. Canadian Institute of Steel Construction (2002) Straight plate girder bridge design example 1
4. Canadian Standards Association (2019) Canadian highway bridge design code. CAN/CSA-S6-19
5. Canadian Standards Association (2019) Commentary on CSA S6-14, Canadian highway bridge design code. CSA-S6.1-19
6. European Commission (2006) Eurocode 3: design of steel structures. EN 1993
7. Feldmann M et al (2012) Choice of steel material to avoid brittle fracture for hollow section structures: background documents in support to the implementation, harmonization and further development of the Eurocodes. Joint Research Centre (JRC)
8. Kala Z, Melcher J, Puklický L (2009) Material and geometrical characteristics of structural steels based on statistical analysis of metallurgical products. J Civ Eng Manag 15(3):299–307
9. Kennedy DJL, Baker KA (1984) Resistance factors for steel highway bridges. Can J Civ Eng 11:324–334
10. Kennedy DJL, Gad Aly M (1980) Limit states design of steel structures - performance factors. Can J Civ Eng 7:45–77
11. Newman JC, Raju IS (1981) An empirical stress intensity equation for the surface crack. Eng Fract Mech 185–192
12. Sedlacek G, Feldmann M, Kühn B, Tschickardt D, Höhler S, Müller C, Hensen W, et al (2008) EUR 23510 EN: commentary and worked examples to EN 1993-1-10 “material toughness and through thickness properties” and other toughness oriented rules in EN 1993. Joint Report, European Commission Joint Research Centre, Luxembourg. European Communities
13. Simões da Silva L, Rebelo C, Nethercot D, Marques L, Simões R, Vila Real PMM (2008) Statistical evaluation of the lateral–torsional buckling resistance of steel I-beams, Part 2: variability of steel properties. J Constr Steel Res 65:832–849
14. Vojdani A, Farrahia GH, Mehmanparast A, Wang B (2018) Probabilistic assessment of creep-fatigue crack propagation in austenitic stainless steel cracked plates. Eng Fract Mech 200:50–63
15. Wallin K (1998) Master curve analysis of ductile to brittle transition region fracture toughness round robin data: the “EURO” fracture toughness curve. Technical Research Centre of Finland (VTT)
16. Wallin K (1992) Guidelines for deriving fracture toughness estimates from normal and miniature size Charpy-V specimen data. Rakenteiden Mekaniikka (J Struct Mech). Finnish Association for Structural Mechanics 25:24–40

Geocell-Reinforced Lateral Support for Anchoring Structural Foundations

Arghya K. Chatterjee, Sanat K. Pokharel, and Marc Breault

1 Introduction

Light weight structures are either attached to heavier structural members or directly to the ground, eventually relying on a foundation that completes the load transfer path. Portable light weight structures like floating fence needs anchor rods to hold them against dynamic loads such as wind load. These anchor rods are similar to micro-piles and are often designed shallow where competent soil conditions exist.

With seasonal variation in temperature leading to freeze-thaw in cold climatic region, growth of vegetation over time and other natural and human interventions, topsoil tends to lose the strength with time. Particularly, where the seasonal frost line extends beyond two meters, chances are that the weak topsoil covers almost the entire depth of anchoring rods. Alternative design would demand either a greater number of anchor points or longer rods and at times both. Despite it being the most common conventional solution, it is neither economical nor environment friendly strategy. Another solution could be removing the entire weak soil and replacing it with competent engineered fill which may also be impractical in most of the situations.

Over past couple of decades there has been a significant advancement on soil reinforcement technology. High strength, creep resistant and high modulus polymeric geocell have been used to design the lateral foundation support to for light structure successfully. Geocell made from novel polymeric alloy (NPA) material provides ductility like HDPE and elastic behavior like thermoplastic [2]. Pokharel et al. [12, 14] had identified lateral and vertical confinement, beam (slab) effect and wider load distribution as the major reinforcement mechanism provided by geocell reinforcement. [3] showed that geocell with higher stiffness provides higher rigidity

A. K. Chatterjee (✉) · S. K. Pokharel · M. Breault
Stratum Logics Inc., Acheson, Canada
e-mail: arghya.chatterjee@stratumlogics.com

S. Walbridge et al. (eds.), *Proceedings of the Canadian Society of Civil Engineering Annual Conference 2021*, Lecture Notes in Civil Engineering 244,
https://doi.org/10.1007/978-981-19-0656-5_3

of the reinforced. A comprehensive study done by Pokharel [12] and [4] explained the mechanism of load transfer and subgrade modulus improvements. Pokharel [12] reported a modulus ratio of up to 7.6 by geocell reinforcement, that is, the modulus improvement over the modulus of the underlaying soil layer. The geocell-reinforced soil also provides improved bending resistance, tensile strength, and shear strength [13]. [3] showed that geocell with higher stiffness provides higher rigidity of subgrade. The three-dimensional confinement of polymeric geocell can improve soil modulus by at least 2.5 times [1] and [10]. This performance improvement for higher soil stiffness has been verified by multiple field level practical design implementations [5, 11]. There has not been a noticeable amount of research in structural engineering field that considers the recent developments in soil reinforcement technology. Reinforcing soil with naturally occurring infill material can be a sustainable solution to many structural foundation designs.

This paper is one of the initial attempts to take advantages of improved elastic properties of soil using three-dimensional geocell reinforcement while considering anchor rod and pile designs. A bare minimum thickness of reinforced natural material laid on top of existing top weak layers can reduce effective member size and increase design life. Thus, leading to a more sustainable design. Primarily two cases have been observed to compare the effect of a reinforced top layer with unreinforced layers. Since geocell reinforced soil provides resistance even on load reversal, it is expected to add enhanced performance on screw pile pull out strengths [9]. However, the scope for this paper is limited to lateral loads only.

First case discussed in this paper involves the comparison of reinforced verses unreinforced soil in design of anchoring rods for light weight structure like floating fence. In the second case, the study has been extended to heavier hypothetical structure with deep plies and pile cap. In both cases a weak top organic layer resting above weathered crust has been assumed. All analysis has been done with Finite Element Method (FEM) using Autodesk Robot Structural Analysis (ARSA) program.

2 Methodology

Objective of this study is to observe and compare the improvement of factor for piles or anchor rods when subject to lateral loads. Theoretical background study has been performed on how improved subgrade modulus with reinforcement can lead to more lateral stability of buried structures. Linear elastic model has been developed through analytical calculations to characterize the initial spring stiffness of soil.

Two hypothetical cases have been independently treated with similar soil conditions to obtain member design forces and design deflections. The purpose of both the studies is to observe the influence on foundation design with addition of a layer with geocell reinforcement on top of soft organic layers.

NPA geocell with yield strength exceeding 22 kN/m, dynamic (elastic stiffness) modulus more than 650 MPa at 60 °C, cumulative long term plastic deformation less than 3% at 65 °C, provides a beam effect [12] that can be used to add lateral stiffness

to foundation structures. Fill inside geocell is naturally occurring granular material compacted to defined minimum thickness. Since the infill layer is assumed to be on top of a soft organic layer prone to high water content, it may not be possible to achieve a defined compaction on the granular infill material. Achieving maximum possible compaction is assumed to be enough for developing lateral stiffness. Influence of rutting, settlement, frost-heaving are neglected for the study on lateral stability of foundations. So, to study the lateral influence of reinforced layer, those parameters are neglected.

Finally, an attempt has been made to relate reinforced soil lateral stiffness parameter to structural member section dimensions that can be used for future designs.

3 Modeling Elastic Soil Stiffness

Currently, there is no available data how to calculate the lateral stiffness of reinforced soil. However, there are several studies on subgrade modulus improvements [1] and [10]. Typically, a study in soil subgrade modulus involves study only in the vertical direction. An attempt has been made to relate the vertical stiffness to horizontal stiffness using an idealized linear elastic model with no damping.

Subgrade modulus at specific depth (K_s) was first introduced by [6].

$$K_s = \frac{\text{stress}}{\text{deflection}} \tag{1}$$

Since, linear elastic model has been assumed, a unit cube of soil can be replaced by horizontal and vertical springs (Fig. 1a). Force 'P' is applied independently, once in horizontal direction and then in vertical direction against respective spring stiffness K_H (initial horizontal spring stiffness) and K_V (initial vertical spring stiffness). Thus, for the purpose of this study volumetric change, superposition of load and poisson's

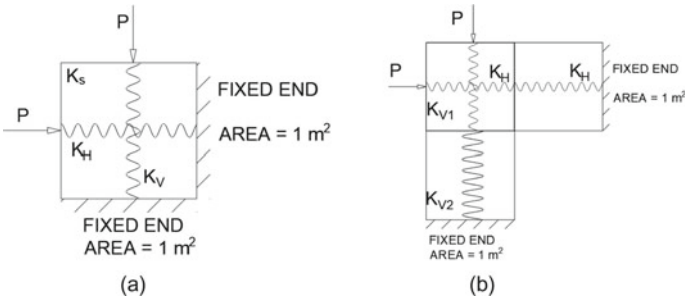

Fig. 1 **a** Single block representation and **b** 3-block representation of soil stiffness

ratio can be neglected. Since the model assumes end boundary conditions as rigid (Fig. 1a) deflection is basically the deformation in springs.

Thus, along vertical direction,

$$K_s = \frac{P/A_V}{\delta_V} \tag{2}$$

And, for a linear elastic model,

$$P = K_V * \delta_V \tag{3}$$

Combining (2) and (3)

$$K_s = \frac{K_V}{A_V} \tag{4}$$

Similarly, for horizontal case,

$$K_{sH} = \frac{K_H}{A_H} \tag{5}$$

where, A_H and A_V are respective horizontal and lateral areas and d_H and d_V are respective horizontal and vertical deformations.

When load is transferred from a circular pile to surrounding soil, effective areas are (as shown in Fig. 2)

$$A_V = \text{Lateral area} = \pi * D * t \tag{6}$$

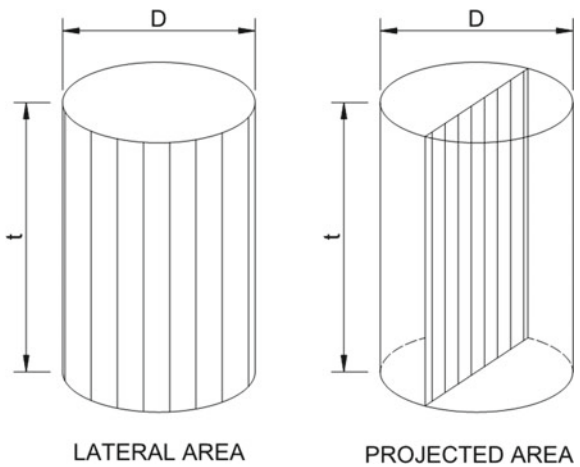

Fig. 2 Effective area for circular structure

$$A_V = \text{Projected area} = D * t \tag{7}$$

Consider, α is a constant representing the ratio of initial spring stiffness. When α > 1 the effective horizontal stiffness of soil is more and thus, more load is transferred horizontally than vertically.

$$\alpha = K_H / K_V \tag{8}$$

In reality, each block is significantly smaller and is supported by multiple blocks around it. Figure 1b represents a three-block scenario. Horizontally, since the same stratum continues to the connected blocks, they have identical stiffness (Fig. 1b). However, vertically as we get deeper natural soil tends to get stiffer. Assuming, connected linear blocks, linear stiffness can act as springs connected in series. Thus,

$$\frac{1}{K_{eH}} = \frac{1}{K_H} + \frac{1}{K_H}$$
$$\frac{1}{K_{eV}} = \frac{1}{K_{V1}} + \frac{1}{K_{V2}} \tag{10}$$

Considering an example where top one meter is organics (say, K_{V1} = a kN/m) and the next meter silty clay having twice the stiffness (K_{V2} = 2 * a kN/m). For cubes of unit areas, the effective area is one square meter.

$$\frac{K_{eH}}{K_{eV}} = \frac{3}{4} * \alpha$$

Equation 11 can be interpreted as the effective horizontal stiffness is 75% of the vertical stiffness.

Now, for the same three block system consider the effect of reinforcement. The top one meter is reinforced, and another one meter below is organic. Horizontal stiffness relations stay the same (Eq. 9). However, in the vertical direction the layer reinforced with geocell is at least 2.5 times stiffer than an unreinforced soil [1] and [10]. The top granular material can be couple of times stiffer than organic below thus scaling up the effective layer stiffness ratio. However, for this calculation conservative number 2.5 is used. Thus, K_{sV} = 2.5 * a kN/m^3 and K_{sV2} = a kN/m^3 yields Eq. 12.

$$\frac{K_{eH}}{K_{eV}} = 1.75 * \alpha \tag{12}$$

So, horizontal stiffness is 75% higher leading to more load transfer horizontally and less lateral deformations. Where lateral deflection is a dictating parameter for design, reinforced top layer can play a significant role. If an un-reinforced layer is added on top of soft organic soil, the increased lateral stiffness may not be enough to contribute to design material savings because unreinforced layers lack the required

modulus improvement. It must be noted that not all variety of reinforcing material may have the same reinforcing effect. The stiffer the geocell material the more effective contribution it shall hold. The three-dimensional confinement effect of geocell is another important parameter for uniform interaction between structure and confining soil.

The load P gets dissipated as it transfers from one elastic block to another in Fig. 1b. Thus, the magnitude of P, plays a major role to determine how many linked blocks will affect the effective stiffness in both horizontal and vertical direction. More number of blocks involved imply lesser equivalent stiffness. So, for detailed design, individual P-d (load-deformation) curves are recommended to be used, with reinforced top layer, to determine the effective lateral stiffness.

4 CASE 1 – Light Anchoring Rods

Figures 3a and b show anchor rods supporting floating fence. The fence is assumed to be in Blainville, Quebec. This is one of those areas in Canada where wind load is high and ground conditions are weak. Thick layer of organic soil (peat) is very common. A weathered clay crust supports the organic layers. This crust is the main load bearing layer and is sufficiently thin for load bearing structures. Layer below the weather crust is sensitive clay. Typical construction in these areas involves deep piles, reduction of loading mass with lighter fills or alternate geosynthetics designs such as reinforcing soil with geocells.

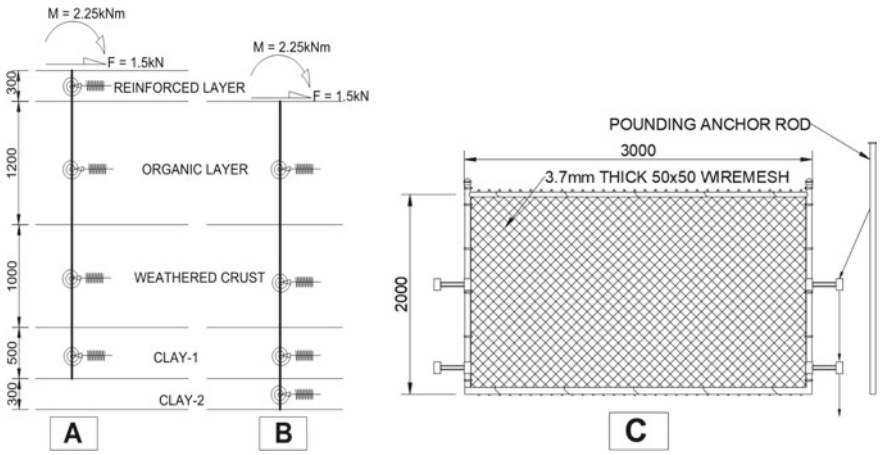

Fig. 3 **a** Reinforced stratum for anchoring rod, **b** Unreinforced & **c** Single panel of floating fence

4.1 Fence description

Each panel of fence is 2.0 m height and 3.0 m wide. 3.7 mm thick wire mesh with opening size of 50 mm × 50 mm. Based on National Building Code of Canada 2015 and Quebec Construction Code 2015, velocity of wind for Blainville area can be safely assumed as 56 m/s. After adjusting for importance factor and all relevant pressure coefficients the applicable design pressure is 0.82 kPa. With simplified structural analysis, effective load on the pounding road at the embedment surface comes out to be 1.5 kN lateral load and 2.25 kNm bending moment. The rod is assumed to be a 350 MPa steel with 38 mm solid diameter and 3 m long.

The reinforcement effect is studied using two sub cases. Once, when the top 300 mm of soil is reinforced and the rod is pounded inside (Fig. 3a) and second when it is dipped directly into natural soil (Fig. 3b). The anchor rod is modeled as frame member in Autodesk Robot Structural FE package. Initial elastic spring stiffness (as per Table 1) at the center of each layer are added as boundary condition for both two horizontal (k_H) and one vertical (k_V) directions. Linear elastic analysis is performed on the model.

4.2 Soil Stratum

Using the homogeneous elastic model, as discussed above, the equivalent horizontal and vertical spring constants are derived. For simplicity, on this study and for conservative results, rocking stiffness or rotational stiffness of soil has been neglected.

From [7, 8] it has be assumed that for silty-clay type soil typical value of K_{sV1} is 10,000 kN/m^3. Also, for every 1 m depth the value increases by 10,000 kN/m^3. For compacted reinforced layer assume typical California Bearing Ratio (CBR) of 50% and polymeric geocell modulus improvement factor 2.5 [1].

Thus, from American Concrete Institute PRC-360-10 Clause 4.4.3, Resilient Modulus, $M_R = 2.5 * 1500 * CBR$ lb.in and, Subgrade modulus, $K_s = M_R/19.4$ lb/in^3 = 874,507 kN/m^3.

Horizontal component of stiffness is assumed as 80% of the vertical. Detailed calculation of α has been neglected to reduce the number of variables in parametric observations. Since the diameter of the rod is just 38 mm, end bearing strength is neglected. The supporting soil being very soft, rotational stiffness of soil is neglected throughout the study.

Table 1 Horizontal and vertical spring constants for the anchor rod

Layers	Thickness (m)	Depth (m)	K_{sV} (kN/m^3)	K_V (kN/m)	K_H (kN/m)
Reinforced (factor 2.5)	0.3		874,507	24,726	6296
Organic	1.2	1.5	5000	565	144
Weathered crust	1	2.5	100,000	9425	2400
Clay - 1	0.5	3	10,000	471	120
Clay - 2	0.3	3.3	13,000	368	94

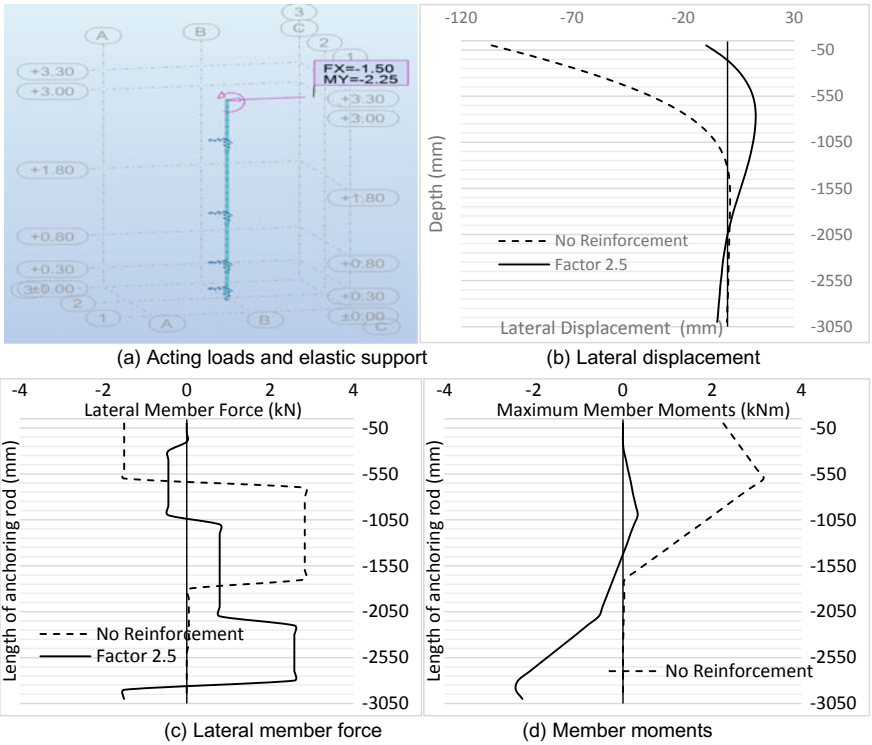

(a) Acting loads and elastic support (b) Lateral displacement

(c) Lateral member force (d) Member moments

Fig. 4 Member forces and displacement comparison between reinforced and unreinforced cases

4.3 Results

Finite element analysis with Autodesk Robot Structural Analysis, shows that without the 300 mm thick reinforcing layer, the 38 mm diameter anchoring rod fails miserably in deflection (Fig. 4b), demanding larger and deeper anchor system. For a light structure like the anchoring rod, the effect of soil reinforcement on member's design forces is almost insignificant (Fig. 4c, d). However, where deflection dictates the

design, structure can be economized significantly using natural fill material and geocell type reinforcements.

The character response of the anchoring rod under later load for the given natural soil condition is like a cantilever beam. Whereas, with the addition of a reinforced layer, the characteristic changes to propped cantilever. Thus, increasing indeterminacy and reducing deflections. Even the member forces are reduced to almost zero. Whether pile caps can create similar effect as reinforcing layer's lateral stiffness, has been independently studied thorough CASE-2.

5 CASE 2 – Pile with Pile Cap

Since the presence of cap action is not captured by single anchoring rods, so CASE-2 (Fig. 5) with heavier isolated structural unit has been studied to comment on the influence of soil reinforcement. While based on the previous case study, it is expected that there will be influence on deflection, but an attempt has been made to observe

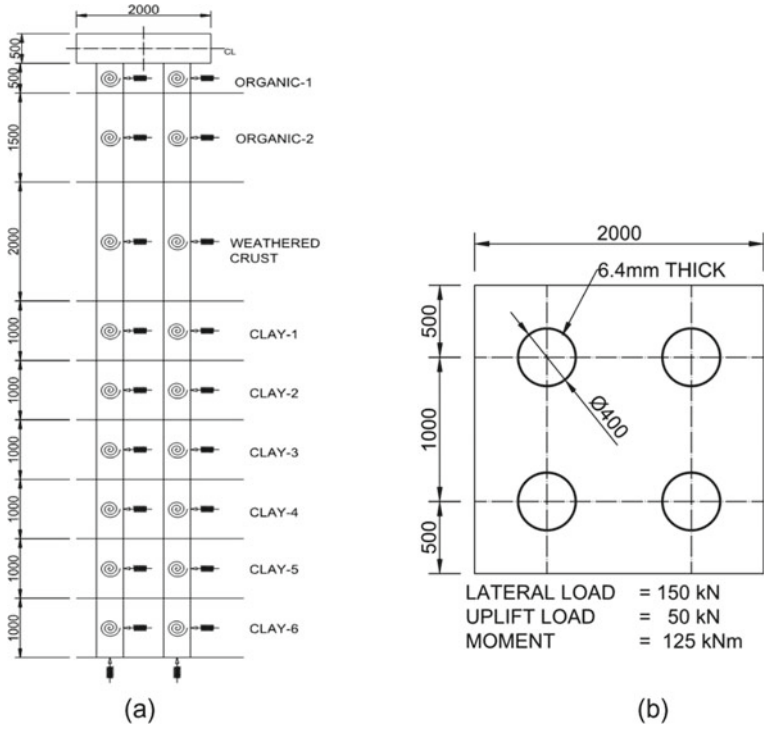

Fig. 5 **a** Soil Stratum for 4 pile structure **b** Pile cap geometry and applied loads d

Table 2 Horizontal and vertical spring constants for the piles

Layers	Thickness (m)	Depth (m)	K_{sV} (kN/m^3)	K_V (kN/m)	K_H (kN/m)
Reinforced (factor 2.5)	0.5	0.5	874,507	549,469	139,921
Organic	1.5	2	5000	9425	2400
Weathered crust	2	4	100,000	251,327	64,000
Clay - 1	1	5	10,000	12,566	3200
Clay - 2	1	6	13,000	16,336	4160
Clay - 3	1	7	20,000	25,133	6400
Clay - 4	1	8	30,000	37,699	9600
Clay - 5	1	9	40,000	50,265	12,800
Clay - 6	1	10	50,000	62,832	16,000
Clay - 7	1	11	60,000	75,398	19,200
End bearing				82,938	

whether that influence increases or decreases when the inertia of primary structure is significantly higher.

Figure 5 shows the geometry of the structure under observation. Steel pipe of yield strength 350 MPa has been considered for piles and 500 mm thick concrete pile cap with 28 days strength of 35 MPa. Loads are applied at the center of the pile cap. In Autodesk Robot Structural, pile cap has been modelled as shell element and 10 m long piles are modeled as frame elements. The two directional horizontal stiffness and vertical stiffness are applied at the center of each layer for boundary conditions. Two conditions were checked, first where Organic-1 (Fig. 5a) is naturally occurring organic-peat and second where that 500 mm thick layer is replaced by polymeric geocell that has modulus improvement factor of 2.5.

5.1 Soil Stratum

Using identical soil methodology as described in CASE-1, the spring constant for the soil has been derived (Table 2). $K_{rotation}$ has been assumed zero.

5.2 Results

Results of analysis show that a significant addition on overall integrated structural stiffness is achieved with reinforcement. Deflection is almost zero with reinforced layer as compared to 8.2 mm in unreinforced layer. In lieu of higher indeterminacy and better distribution of external forces, member forces were reduced (Fig. 6b, c).

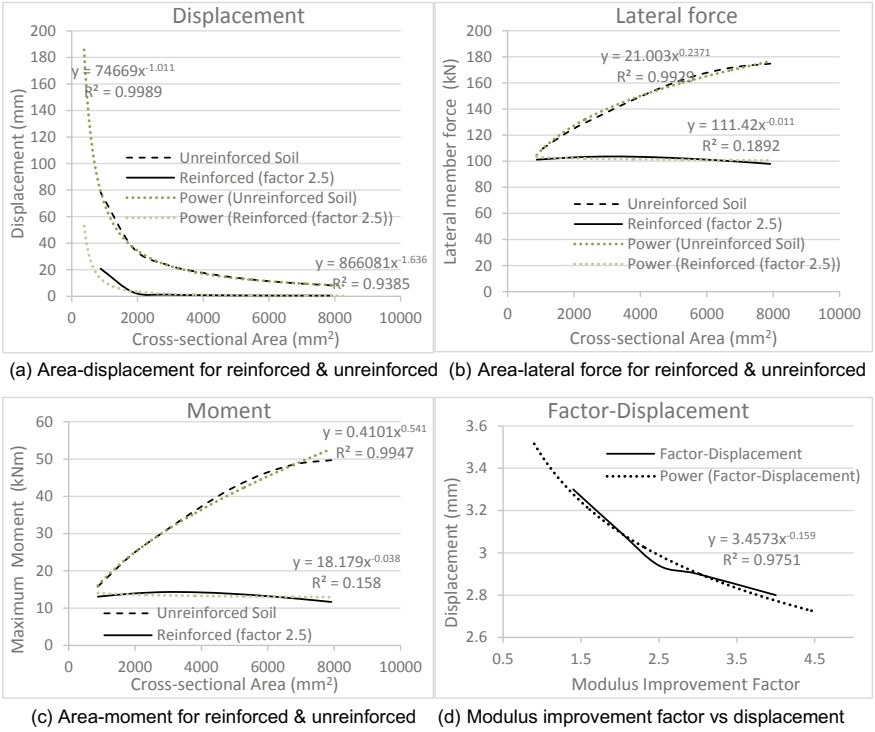

(a) Area-displacement for reinforced & unreinforced (b) Area-lateral force for reinforced & unreinforced

(c) Area-moment for reinforced & unreinforced (d) Modulus improvement factor vs displacement

Fig. 6 Relation of varying member forces with structural stiffness for reinforced & unreinforced cases

Thus, it is possible to design a lighter pile structure with addition of bare minimum top geocell reinforced structure. Keeping all other parameters constant, the diameter of piles has been varied to observe the effect of structural inertia on reinforced topsoil addition. With soil reinforcement, member forces remain almost steady. However, when compared with unreinforced soil, the gap between the demands widens (Fig. 6b, c).

Focusing just on deflection (Fig. 6a), it can be stated that for reinforced topsoil 100 mm diameter pile (area = 1881mm^2) is more conservative design than 200 mm diameter pile (area = 3892mm^2) without reinforcement. Both having 6.4 mm thick wall thickness. Lateral member force is reduced by 25% and moments by 40%. Thus, reducing the overall structure by at least 25%.

Figure 6d has been developed by varying the stiffness of top reinforced layer for 100 mm diameter piles. Variation in topsoil lateral stiffness can happen for multiple reasons, like use of different reinforcement or not achieving certain compaction. Modulus Improvement Factor hold a power relation with displacement. Thus, it is necessary to achieve a minimum amount of reinforced stiffness with modulus improvement factor to take advantage of this top reinforced layer. However, increasing the stiffness (either by increasing the thickness or reinforced

layer or compaction or different reinforcing material) may not necessarily show visible advantage. Rather, having an almost rigid top layer and very soft intermediate layers increase the risk of member bucking. A balance must be developed to optimize the depth of reinforced layer, with use of case specific load-displacement curves.

With typical compacted clay on $K_s = 20{,}000 kN/m^3$ the displacement of the pile system increases to 15.6 mm. This is almost 50% reduction from just having organics on top. However, the entre study is on initial spring stiffness. If unreinforced fill is used to reduce design section, the compaction loss for lateral displacement is significant as compacted to the three-dimensional confining effect of geocell. Additionally, without reinforcement, achieving decent compaction on top of soft organic is another challenge. Further study is required to observe the effect of fill thickness verses reinforced thickness to comment on how much of regular fill can be an alternative of reinforced fill, if at all that is possible.

6 Conclusion

Through this study, the following observations has been made.

- Adding high strength polymeric geocell reinforced soil at the top provides significant advantage on design buried structures, particularly where deflection dictates the design. For the observed cases, structures could be reduced by a minimum 25%. With lighter structures and using naturally available soil as reinforcing material, less manufactured material like steel and quarrying virgin aggregate is required on site. Thus, less raw material exploitation for steel production, less manufacturing and reduced number of trucks on road. Overall, contributing significantly to reduced carbon footprint.
- With reinforced soil layer, member forces are reduced as compacted to unreinforced structure, particularly when the structure is heavy. However, increasing soil stiffness does not affect member forces after a certain limit. So, case specific design optimization is necessary.
- Through the CASE-2 study, it can be stated that the effect of reinforced soil stiffness is observed not just applicable to light foundations but also deep foundations with higher inertia.
- Increasing soil reinforcing stiffness has positive power relation with lateral deflection. So, with minimum thickness of reinforcement maximum effect can be achieved, if the reinforcing material is stiffer. High strength NPA geocell used as reinforcing material for this study, does show excellent lateral stiffness performance.

This paper is mostly a theoretical background opening opportunity for further study on artificially adjusting soil stiffness to reduce foundation structures. Further study is necessary to determine the influential parameters once beyond the initial spring stiffness. Also, the elastic model used to derive lateral stiffness for this study needs

to be verified experimentally. Effect of three-dimensional confinement or planar reinforcing or interlocking behaviours of filling material need to be independently studied, particularly under the influence of dynamic loads.

References

1. Kief O, Schary Y, Pokharel SK (2014) High-modulus geocells for sustainable highway infrastructure. Indian Geotech J 45:389–400
2. Kief O, Rajagopal K, Veeraragavan A, Chandramouli S (2011) Modulus improvement factor for geocell-reinforced bases. In: Proceedings of geosynthetics India 2011, Chennai, India, 22–23
3. Rajagopal K, Veeraragavan A, Chandramouli S (2012) Studies on geocell reinforced road pavement structures. In: Geosynthetics Asia - 5th Asian regional conference on geosynthetics: geosynthetics for sustainable adaptation to climate change, pp 497–502
4. Emersleben A (2013) Analysis of geocell load transfer mechanism using a new radial load test. In: GeoCongress, San Diego, pp 345–357
5. Pokharel SK, Martin I, Breault M (2013) Causeway design with neoweb geocells. In: Ling H, Gottardi G, Cazzuffi D, Han J, Tatsuoka F (eds) Proceedings of design and practice of geosynthetic-reinforced soil structures, Bologna, Italy, pp 351–358
6. Winkler E (1867) Die Lehre von der Elastizitat and Festigkeit (on elasticity and fixity), Verlag, Prague, p 182
7. Uzodimma UO, Nwaiwu CMO, Mezie E (2020) Effect of soil compressibility on the structural response of box culverts using finite element approach. Niger J Technol 39(1):42–51
8. Bohnhoff DR (2014) Modeling soil behavior with simple springs, Part 1. Frame building news, pp 49–54
9. Abbas HO (2017) Pullout capacity of screw piles in sandy soil. J Geotech Eng 4(1):8–12
10. Pokharel SK, Han J, Parsons RL, Qian Y, Leshchinsky D, Halahmi I (2009). Experimental study on bearing capacity of geocell-reinforced bases. In: Tutumluer, Al-Qadi (eds) Bearing capacity of roads, railways and airfields. Taylor & Francis Group, London. ISBN 978-0-415-87199-0
11. Pokharel SK, Martin I, Norouzi M, Breault M (2015). Validation of geocell design for unpaved roads. In: Geosynthetics conference, Portland, OR, USA, pp 711–719
12. Pokharel S, Han J, Leshchinsky D, Parsons RL, Halahmi I (2010) Investigation of factors influencing behavior of single geocell-reinforced bases under static loading. Geotext Geomembr 28:570–578
13. Zhou H, Wen X (2008) Model studies on geogrid- or geocell-reinforced sand cushion on soft Soil. Geotext Geomembr 26(3):231–238
14. Pokharel S, Han J, Manandhar C, Yang X, Leshchinsky D, Halahmi I, Parsons RL (2011) Accelerated pavement testing of geocell-reinforced unpaved roads over weak subgrade. Transp Res Rec J Transp Res Board (2204):67–75

Analysis of Full-Scale Plate-Based Tensegrity Structure Using Dynamic Relaxation

H. Gathman and A. C. Sychterz

1 Introduction

Modular and lightweight structures have increasingly become an area of interest to researchers and engineers due to the reduction in construction times and flexibility for future modification or relocation. This has led to the continued development of innovative structural designs and the utilization of nonstandard construction materials. Among these innovative designs are tensegrity structures, which first began as an art form until engineers realized their unique structural properties [11, 16, 20]. Tensegrity structures are made of discrete bars in pure compression held together by prestressed cables in pure tension and are stabilized by self-stress. They have a high strength-to-weight ratio, can be adjusted after the structure is loaded, and are well-suited for deployable and modular structures [19, 22].

The utilization of aluminum in the civil engineering profession offers appreciable advantages over steel and concrete due to its lightweight, low maintenance costs, extrudability, and infinite recyclability [5, 18]. The structure simulated in this study is made primarily of aluminum.

Tensegrity structures have applications in civil engineering including bridges [13, 17], towers [12], and grid shell structures [1, 14]. However, these studies have not included surface elements such as bridge decks or roof coverings incorporated into the tensegrity structure. The classic definition of tensegrity structures includes bar and cable elements held together in a state of self-stress. The introduction of a plate as a third element type allows the concept of tensegrity to be extended to roof and shell structures.

H. Gathman (✉) · A. C. Sychterz
Civil and Environmental Engineering, University of Illinois at Urbana-Champaign, Champaign, USA
e-mail: hfg2@illinois.edu

S. Walbridge et al. (eds.), *Proceedings of the Canadian Society of Civil Engineering Annual Conference 2021*, Lecture Notes in Civil Engineering 244,
https://doi.org/10.1007/978-981-19-0656-5_4

Fig. 1 Proposed unit topology for plate tensegrity structures using square plate with idealized jo dints inspired by [6]

A topology for a plate-based tensegrity structure has been presented [6, 7, 9] as a hypothetical roof over a Swedish equestrian hall using timber plates. The base tensegrity module is composed of a strut passing through the center of polygonal plates which are connected along the plate edges and by cables at the strut ends (Fig. 1). The cables function to stabilize the plate in its plane and hold the strut in compression. This topology would further the range of applications for which the benefit of tensegrity can be realized. However, few analysis methods have been proposed that can account for geometrical nonlinearity. The force density method [16] has been applied to a single plate module and a plane ten-plate system [8], but there has been no analysis of a full-scale or curved structure.

Dynamic relaxation (DR) is a nonlinear numerical method of form finding and static analysis often used for tension structures. The DR method is a pseudo-dynamic method that involves iteratively solving the equations of dynamic equilibrium and kinetically damping the structure until it reaches static equilibrium [3]. DR has been used for a variety of structure types including trusses [15], grid shells [2], and tensegrity structures [17, 24]. It is regarded as a powerful and reliable method for analyzing a variety of engineering problems. The value of using DR for tensegrity structures is that it is able to account for changes in geometry and stiffness during the analysis.

Since many studies focused on the analysis of tensegrity structures are based on simulation only, the challenge of joint design has not been tackled by many researchers. Through the simulation and construction of a deployable hollow-rope footbridge at École polytechnique fédérale de Lausanne (EPFL), it was found that the actual behavior of the deployable tensegrity structure deviated significantly from the predicted behavior due to joint eccentricities and friction during deployment [17, 21]. A modifed dynamic relaxation method has been formulated to account for joint friction during deployment by [21] and has accurately captured the behavoir of continuous cables sliding over joints, though joint eccentricities and unwanted internal movements still remain an issue in accurately modeling and building joints for large scale tensegrity structures. A preliminary joint design idea and proportioning is presented in addition to the DR simulation.

In this paper, a method of static analysis and form-finding for curved plate-tensegrity structures using dynamic relaxation is proposed. Aluminum as a building material is also further explored through the simulation of a full-scale aluminum plate-tensegrity curved roof structure.

2 Analytical Study

2.1 Plate Tensegrity Structure

The simulated structure is an aluminum plate tensegrity structure which will be built as a bike parking shelter south of Newmark Civil Engineering Laboratory on the University of Illinois at Urbana-Champaign's (UIUC) campus. The topology proposed by [6] is adopted. Modules are connected via intermodular cables at the strut ends. The construction of the bike shelter on campus not only will serve as a protected space to store bikes but aims to encourage sustainability on campus and provide important educational and research insights into larger-scale applications of similar structures.

The primarily axial forces and short compression members found in tensegrity structures enable a more optimal use of material and cross section, presenting opportunities to explore underutilized construction materials. Aluminum was chosen as the primary material for the bike shelter due to its lightweight and durability. Plates and struts are modeled as 6061 aluminum and cables are stainless steel. The square plates are 12 gauge (0.081 in thick) 1 ft $\times$ 1 ft plates, and the vertical struts are of 2 ft length with a circular cross section of 1 in outer diameter and ¼ in wall thickness. Cables are stainless steel with 1/16 in diameter. The full-scale roof structure is 4 plates $\times$ 6 plates with curvature resulting in a 6 in change in elevation. Initial member sizes were chosen based on construction feasibility. Figure 2 a) shows a preliminary rendering of the full-scale structure labeled with dimensions. Figure 2 b) shows a rendering of the bike shelter in its proposed location. Joints have been idealized in Fig. 2 and for the analysis described in this paper. The corners of the roof are supported by square HSS aluminum columns.

2.2 Simulated Tensegrity Structure Using Dynamic Relaxation

DR is chosen to analyze the proposed structure since it can account for geometric nonlinearities and is computationally efficient as it does not require matrix inversion. The computation procedure has been implemented in MATLAB.

In order to use DR, the structure must be discretized into a series of bars and cables connected at nodes. A technique which has been used for simplifying finite element

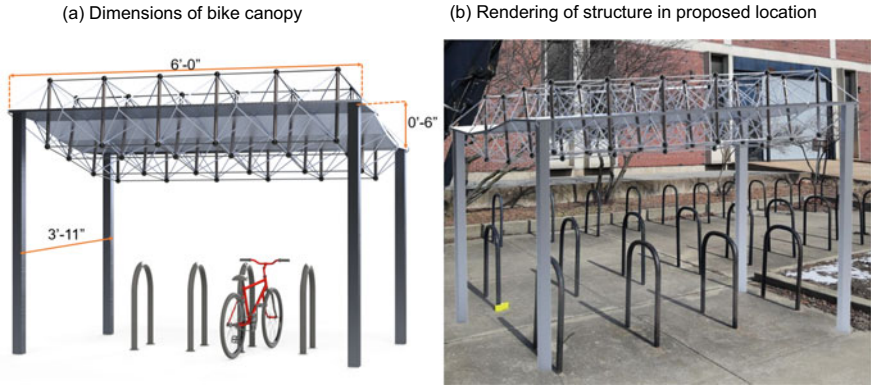

Fig. 2 Preliminary rendering of aluminum plate tensegrity structure (NTS) (a) over rendered bike rack with dimensions (b) next to Newmark Civil Engineering Building

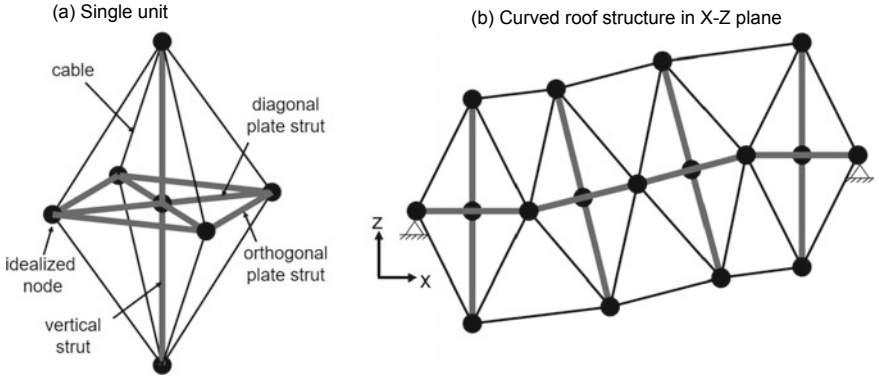

Fig. 3 (a) one plate tensegrity module with equivalent plate struts (b) curved roof structure in X–Z plane with pinned supports in place of columns

models of folded plate structures is to use equivalent framework models. Through this technique, thin panels are modeled as an assembly of bar elements connected to nodes [10, 23]. The bars have adjusted areas to preserve the stiffness and in-plane behavior of a continuous panel. This method is adopted for modeling the plate of the plate tensegrity structure presented in this work. The plate is converted into a plane with 5 nodes and 8 bars (Fig. 3a). The vertical strut is split into two bars meeting at a node in the center of the plate. Figure 3b shows the curved 4 × 6 module roof in the X–Z plane with pinned support conditions in place of the columns. All cables are modeled as discontinuous at nodes.

The American Society of Civil Engineers' ASCE 7-16 Minimum Design Loads and Associated Criteria for Buildings and Other Structures is being used to determine the loads on the structure, load factors, and load combinations. The service snow load

Table 1 Properties of elements in dynamic relaxation model

Element type	Material	Density (kip/in^3)	Young's Modulus (ksi)	Poisson's ratio	Area (in^2)
Cable	Stainless steel	0.284e−3	29,000	–	0.003
Vertical strut	Al 6061	0.098e−3	10,000	–	0.589
Diagonal plate strut	Al 6061	0.098e−3	10,000	0.33	0.509
Orthogonal plate strut	Al 6061	0.098e−3	10,000	0.33	0.365

for central Illinois, USA is applied to plate nodes. The snow load for this type of structure is determined from ASCE 7-16 as 12.1 psf. The dead load is calculated for each member and is applied to the two nodes of the respective member. All loads are applied in the global (-z) direction.

The area of the struts which make up the plate have been calculated to preserve the in-plane behavior of a continuous isotropic plate. Finite element models of the plate under the applied load showed negligible bending stress and therefore stiffness has been adjusted to preserve in-plane stretching and shear behavior [10].

The material properties and resulting area for each element type are summarized in Table 1.

Member forces and the deflected shape are obtained from the DR algorithm. Loads are factored according to the Load and Resistance Factor Design (LRFD) load combinations. In accordance with engineering practice, the unfactored snow load is used to find deflections and factored snow load is applied to find the member forces. The equivalent areas used for plate struts resulted in a dead load self-calculated by the algorithm to be slightly greater than the LFRD factored dead load would be if continuous plates were used and has been conservatively left as such for both deflection and member force calculations.

3 Results

Deflection and member stresses are found due to snow and dead loads. The deflected shape is shown in Fig. 4 and has been exaggerated by a scale factor of 40. Figure 4 shows the deformed structure in the X–Z plane superimposed onto the undeformed shape. The maximum deflection occurs at midspan and is 0.09 in, satisfying the L/360 deflection criteria of 0.20 in. The maximum displacement in the X and Y directions is 0.04 in and 0.04 in, respectively.

By bracing the vertical strut in the center of the plate, the relative displacement of the top and bottom segment of the vertical strut is useful to give an indication of bending stresses which could develop. This phenomenon is observed mostly at the units near the supports which do not have as much support from the cables at

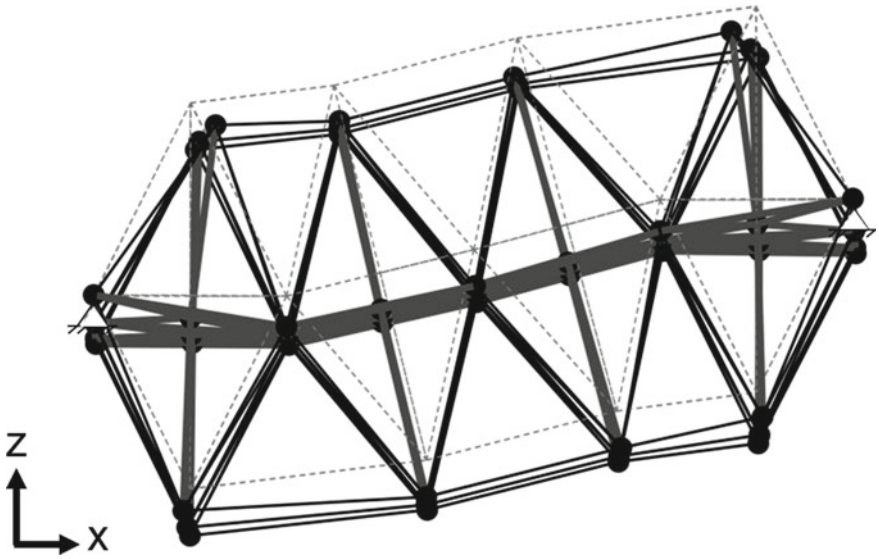

Fig. 4 Deformed configuration view in X–Z plane superimposed over undeformed shape, deformation exaggerated by a factor of 40

adjacent modules. The plates further from the supports primarily undergo rigid body motion with little out of plane deformation at the center node.

Figure 5 shows the normalized axial stress in each member which was found by dividing the member force by its equivalent area. Figure 5a) shows the view in the X–Z plane. Figure 5b) shows the stress in the structure in the 3D view. Since the structure and all conditions are symmetric, one symmetric half of the structure is shown in Fig. 5b) for greater clarity. Blue indicates compressive stress while red indicates tensile stress. Both gradients are normalized to the maximum value of tensile or compressive stress respectively. It can be seen that most of the tensile stress is concentrated near the supports with the maximum occuring at the cable connecting the vertical strut of the corner module to the support. Tension is also observed in the bottom intermodular cables while the top intermodular cables go slack due to the global bending action of the roof. Some tension occurs in the plates, but a majority of the tensile stress in the structure is carried by the cables.

The maximum compressive stress of 1.07 ksi is found in the orthogonal plate struts near the structure's line of symmetry. This is attributed to these struts taking the compressive force produced by the global bending action. The other plate struts carry both tension and compression primarily distributed along the diagonals. The vertical struts carry only compressive stress, with higher stresses near the supports.

The maxiumum stress in the cables is 57.2 ksi which is below the strength of many available stainless steel cable assemblies. The vertical strut has a maximum compressive stress of 0.226 ksi or a force of 0.134 kips. This is well below Euler's critical buckling load of 7.88 kips. Plates have maximum tensile and compressive

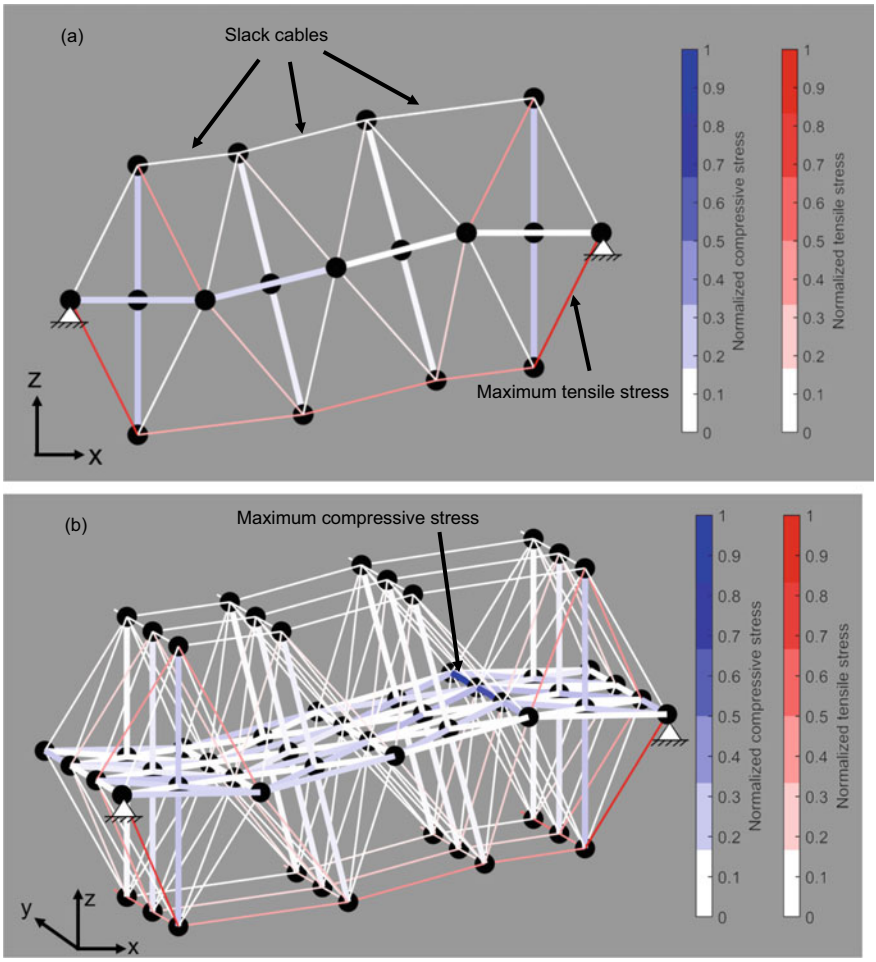

Fig. 5 Stress distribution (a) view in X–Z plane with legend (b) 3D section cut along line of symmetry with legend

stresses of 0.886 ksi and 1.07 ksi, respectively, which is much smaller than 6061 aluminum's yield strength of 35 ksi. Table 2 summarizes the stresses in each element type, where tension is positive and compression is negative.

Table 2 Summary of element stresses; tension (+), compression (−)

Element type	Maximum stress (psi)	Minimum stress (psi)	Average stress (psi)	Standard deviation
Cable	57,200	0.00	5,060	9,630
Vertical strut	−10.7	−226	−70.0	68.9
Diagonal plate strut	226	−278	−20.2	159
Orthogonal plate strut	886	−1,070	−6.69	354

4 Discussion

4.1 Simulation Results

Both deflection and strength requirements are satisfied for the applied snow and dead loads. The deflection was closer to exceeding the design criteria than strength, and suggests if the load requirements or unsupported span were larger, additional supports would be required. Member stresses for the struts and plates are well below the critical buckling load and material yield strength, while the maximum stress in the cables is acceptable but would likely be the limiting member if the load requirements were higher.

One of the most valuable features of tensegrity structures is that they are extremely strong for their weight. The proposed topology paired with a lightweight material such as aluminum results in stresses well below the yield strength of the material and each module weighs just 1.5 lbs excluding joints. The entire roof excluding joints weighs 37.3 lbs. In comparison, if the structure were made of steel, it would weigh over 100 lbs. Lightweight construction materials not only decrease the dead load demand on the structure, but improve the energy efficiency of construction and material transport.

The ability of the square plates and many other polygonal shapes to form tessellations in combination with the lightweight make this structure ideal for modular construction. The individual square units can be pre-assembled offsite, connected by the intermodular cables, and hoisted into place when the bike shelter is ready for construction. The broader impacts of developing analysis methods for lightweight modular structures such as that desribed in this paper can improve the design of similar temporary pop-up structures useful for emergency housing, military applications, or disaster recovery sites.

4.2 Preliminary Joint Design

An issue that has not been well-addressed in the design of large-scale tensegrity structures is joint design. Most analysis methods of tensegrity structures, including the dynamic relaxation method described herein, idealize the joints as perfectly pinned connected. In order to accurately predict the behavoir of the structure simulated in this work, the actual joint must behave as a pin connection and eliminate eccentricities and internal movements. At the same time, the joint must allow for easy assembly and fine adjustment of the cables. [8] have presented a conceptual idea for the cable-strut connection which takes inspiration from a turnbuckle. The design involves threading the inside of the vertical strut and fitting in a male threaded piece which has "wings" for the clevis pins on the end of the cable assemblies to attach (Fig. 6). After the structure is assembled and and tightened, the joint can be locked in place with a jam nut.

The limit state that will govern the design of the wings is tearout and block shear. For preliminary calculations and proportioning, the upper wing is assumed to have dimensions $1'' \times 1'' \times 5/32''$ with a $1/4''$ diameter hole meeting The Aluminum Association's Aluminum Design Manual 2005 requirements for end and edge distances. The allowable tearout force, P_{sr}, is calculated using Eq. 1 from the Aluminum Design Manual for the case where the tension is applied on the upper wing perpendicular to vertical strut.

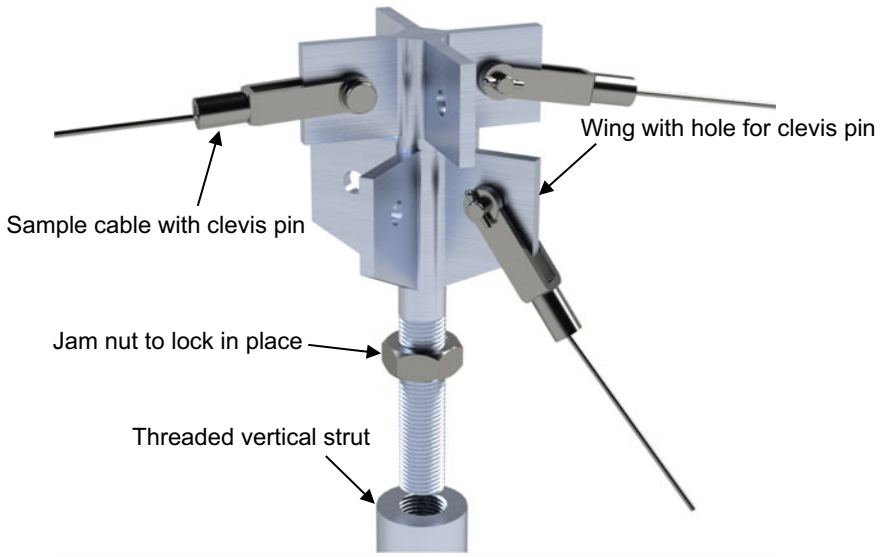

Fig. 6 Rendering of strut-cable connection idea for plate tensegrity module

$$P_{sr} = \left(\frac{F_{ty}}{\sqrt{3}} A_{gv} + F_{tu} A_{nt} \right) / n_u \quad (1)$$

where Psr is the allowable tear out force, n_u is a safety factor of 1.95, F_{ty} is the material yield strength taken as 35 ksi, F_{tu} is the ultimate tensile strength taken as 38 ksi, A_{gv} is the gross area in shear calculated as 0.0781 in.^{2}, and A_{nt} is the net area in tension calculated as 0.0586 in^2. The resulting allowable tearout force is 1.95 kips, exceeding the maximum force in the cable of 55.9 lbs. From a strength perspective, this joint idea and proportioning are feasible.

5 Conclusions and Future Work

Dynamic relaxation has shown to be a fast and useful tool, yielding results which indicate the proposed structure is able to meet current civil engineering criteria for strength and serviceability. The use of aluminum also proves to be a feasible construction material for this type of structure. To enable the use of tensegrity structures in structural engineering practice, is it necessary to develop analysis methods which are capable of modeling the behavior of full-scale systems. Plate tensegrity structures offer an enhancement to the definition of tensegrity which may have more practical uses in civil engineering. The findings presented in this paper show that through the adoption of an equivalent axial-member model, computationally expensive finite element models for static solutions can be avoided, and other methods may be used for the analysis of plate tensegrity structures.

Future work will include analysis of other load cases such as lateral loads and the design of robust joints for strut-cable, plate-plate, and cable-plate connections.

Acknowledgements The authors gratefully acknowledge support from the Institute for Sustainability, Energy, and Environment (iSEE) at the University of Illinois Urbana-Champaign.

References

1. Adriaenssens SML, Barnes MR (2001) Tensegrity spline beam and grid shell structures. Eng Struct 23(1):29–36. https://doi.org/10.1016/S0141-0296(00)00019-5
2. Adriaenssens S, Barnes MR, Harris R, Williams C (2014) Shell Structures for Architecture: Form Finding and Optimization, vol 9781315849. https://doi.org/10.4324/9781315849270
3. Barnes MR (1999) Form finding and analysis of tension structures by dynamic relaxation. Int J Space Struct 14(2):89–104. https://doi.org/10.1260/0266351991494722
4. Nizar BHA, Sychterz AC, Smith IFC (2017) A dynamic-relaxation formulation for analysis of cable structures with sliding-induced friction. Int J. Solids Struct 126–127:240–51. https://doi.org/10.1016/j.ijsolstr.2017.08.008
5. Dey P, Sychterz A, Narasimhan S, Walbridge S (2016) Performance of pedestrian-load models through experimental studies on lightweight aluminum bridges. J Bridg Eng 21(8):1–12. https://doi.org/10.1061/(ASCE)BE.1943-5592.0000824

6. Falk A (2004) Timber-plates in tensile structures. In: IASS annual symposium: shell and spatial structures: from models to realization. Montpellier. https://doi.org/10.13140/2.1.1883.3284
7. Falk A (2006) Architectural and structural development of plate tensegrity. In: IASS annual symposium: new olympics, new shells and spatial structures. Beijing. https://doi.org/10.13140/2.1.1227.9682
8. Falk A, Gunnar T (2005) Plate based tensegrity structures. In: IASS annual symposium: theory, technique, valuation, maintenance, pp 611–18. Bucharest. https://doi.org/10.13140/2.1.2931.9049
9. Falk A, Kirkegaard PH (2012) Pre-stressing timber-based plate tensegrity structures. In: IASS-APCS annual symposium: spatial structures to space structures. Seoul
10. Filipov ET, Liu K, Tachi T, Schenk M, Paulino GH (2017) Bar and hinge models for scalable analysis of origami. Int J Solids Struct 124:26–45. https://doi.org/10.1016/j.ijsolstr.2017.05.028
11. Gantes, CJ (2001) Deployable structures: analysis and design. WIT Press
12. Klimke H, Stephan S, Essrich R (2004) The making of a tensegrity tower. Stahlbau 73(2):74–79. https://doi.org/10.1002/stab.200490054
13. Motro R, Maurin B, Silvestri C (2006) Tensegrity rings and the hollow rope. In: IASS annual symposium: new olympics, new shells and spatial structures, Beijing
14. Olejníková T (2014) Geometry of prismatic tensegrity constructions composed of three and four-strut cells. Sel Sci Papers J Civil Eng 9(2):47–56. https://doi.org/10.2478/sspjce-2014-0015
15. Pajand MR, Taghavian Hakkak M (2006) Nonlinear analysis of truss structures using dynamic relaxation. Int J Eng Trans B 19(1):11–22
16. Pellegrino S (2001). Deployable Structures, vol 53. Springer, Wien. https://doi.org/10.1017/CBO9781107415324.004
17. Rhode-Barbarigos, L (2012) An active deployable tensegrity structure. École Polytechnique Fédérale de Lausanne
18. Davor S, Boko I, Torić N (2015) Aluminium as a material for modern structures. Gradjevinar 67(11):1075–85. https://doi.org/10.14256/JCE.1395.2015
19. Skelton RE, Adhikari R, Pinaud JP, Chan W, Helton WJ (2001) An introduction to the mechanics of tensegrity structures. In: The mechanical systems design handbook: modeling, measurement, and control, February 2001, pp 316–88. https://doi.org/10.1201/9781420036749
20. Snelson K (2012) The art of tensegrity. Int J Space Struct 27(2–3):71–80. https://doi.org/10.1260/0266-3511.27.2-3.71
21. Sychterz AC, Smith IFC (2017) Joint friction during deployment of a near-full-scale tensegrity footbridge. J Struct Eng (United States) 143(9):1–9. https://doi.org/10.1061/(ASCE)ST.1943-541X.0001817
22. Sychterz AC, Smith IFC (2018) Deployment and shape change of a tensegrity structure using path-planning and feedback control. Frontiers Built Environ 4(August):1–17. https://doi.org/10.3389/fbuil.2018.00045
23. Woodruff SR, Filipov ET (2020) A bar and hinge model formulation for structural analysis of curved-crease origami. Int J Solids Struct 204–205:114–127. https://doi.org/10.1016/j.ijsolstr.2020.08.010
24. Zhang J, Ohsaki M (2016) Form-finding of complex tensegrity structures by dynamic relaxation method. J Struct Constr Eng 81(719):71–77. https://doi.org/10.3130/aijs.81.71

Numerical Study of Standard and Extended Shear Tab Connections in Steel I-Beam

Pronob K. Ghosh and Anjan K. Bhowmick

1 Introduction

Shear tab connection is often used in steel construction due to its simplicity in terms of fabrication and erection. Shear tab connection, which is used to transfer shear from beams to the supporting columns or girders, can be two types: conventional and extended shear tab connections. In the conventional shear tab connection, typically The distance between the weld line and the single vertical bolt line should be less than or equal to 89 mm (3.5 in.). Also, the number of bolts in the CST connection should be between 2 and 12. As the bolt eccentricity from the weld line is small, the end moment that develops in the connection is also small. On the other hand, when it is needed to connect the supported beam with the web of the wide flange supporting column or girder, with the CST connection coping of flanges of the beam is necessary. In order to avoid the coping of the beam, the shear tab needs to be extended beyond 89 mm, and this connection is called the extended shear tab connection (EST). Extended shear tab connection could also have multiple vertical bolt lines. The current Canadian steel design standard, CSA S16-19, provides a design table for conventional shear tabs with a single vertical line of two to seven bolts and a 75 mm distance between the weld and bolt line. The design table in S16 is based on the research of Astaneh et al. [4] on CST connections and can not be applied for commonly used shear tab connections with multiple vertical bolt lines. While in the AISC construction manual, design provisions for extended shear tab connections are currently available, no design provisions for EST connections are currently available

P. K. Ghosh
Concordia University, Montreal, Canada

A. K. Bhowmick (✉)
Department of Building Civil and Environmental Engineering, Concordia University, Montreal, Canada
e-mail: anjan.bhowmick@concordia.ca

S. Walbridge et al. (eds.), *Proceedings of the Canadian Society of Civil Engineering Annual Conference 2021*, Lecture Notes in Civil Engineering 244,
https://doi.org/10.1007/978-981-19-0656-5_5

in the Canadian steel design standard. This is mainly because of the lack of adequate research on EST connections.

The present research investigates the behavior and strength of CST and EST connections in I-shaped beams. For this reason, a three-dimensional (3D) finite element model is developed using the commercial finite element software, ABAQUS. The developed FE model is validated for an unstiffened EST connection test done by Sherman-Ghorbanpoor [9]. After that, a parametric study is conducted on both CST and EST connections by varying the length, depth, and thickness of the shear tabs. The selected I-beams are considered to have simply supported boundary conditions and have concentrated loads at their spans. From the parametric study, the variation of shear force, shear displacement, and twist for both CST and EST connections are estimated.

2 Selected Previous Research on Shear Tab Connections

Several studies have investigated both behavior and strength of conventional and extended shear tabs experimentally and numerically. Astaneh et al. [4] experimented five full-scale beam-to-column conventional shear tab connections and proposed a design procedure. This design procedure of shear tab was adopted by the Canadian steel design standard S16. It was concluded that the strength of the shear tab was dependent on the stiffness of the supporting member. Based on the experimental results, Astaneh et al. [4] proposed the following equations for bolt eccentricities (e_b), which were found to be related to the number of bolts (n) and weld to bolt distance (a). For rotationally rigid support:

$$e_b = [(n-1) \times 25 - a]\,\text{mm} \tag{1}$$

and for rotationally flexible support:

$$e_b = [(n-1) \times 25 - a] \geq a\,\text{mm} \tag{2}$$

Sherman and Ghorbanpoor [9] experimented 31 full-scale EST connections under stiffened and unstiffened conditions. Among them, a total of eight tests had unstiffened shear tabs and twenty-three tests had stiffened shear tabs. The varying parameters in the tests were thickness and length of the tab, the number of bolts, bolt-hole type, weld to bolt distance, bracing and different beam, column, and girder section. They proposed a design provision of EST connection ensuring sufficient strength and end rotation. Based on their research, the design section of the extended shear tab connection in the AISC manual was formed. Following equations were recommended for the bolt eccentricity (e_b) for EST connections:

$$e_b = n \leq a\,\text{inch} \quad \text{where } n \leq 6 \tag{3}$$

$$e_b = 3 + \frac{n}{2} \leq a \text{ inch} \quad \text{where } n > 8 \tag{4}$$

In their research, for the unstiffened EST connections, Sherman and Ghorbanpoor [9] identified two new limit states: a) column web mechanism and b) plate twisting. On the other hand, for some of the stiffened ones, the primary failure mode was due to twisting. It was also observed that when EST connections become deeper, it was more prone to twisting failure. Sherman and Ghorbanpoor [9] proposed Eq. 5 to determine the capacity of twisting of shear failure (V_p) of EST as a function of shear tab depth (d_p), the yield stress of shear tab (f_y), and thickness of shear tab (t_p).

$$V_p = 0.3 d_p t_p f_y \tag{5}$$

Rahman et al. [8] developed three-dimensional models to predict the strengths and failure mechanism of unstiffened and stiffened EST connections. Marosi [6] conducted tests on a set of sixteen full-scale beams having shear tab connections with one, two, or three vertical rows of bolts. It was observed that shear yielding extended throughout the shear tab depth for one vertical row of bolt. For connections with two or three vertical rows of bolts, shear yielding was observed in the inner rows of bolts, near the column face.

3 Non Linear Finite Element Modeling of Shear Tabs

3.1 Selection of Element

A non-linear 3D finite element model (FEM), as shown in Fig. 1, was developed using ABAQUS. In the FEM, both material and geometric nonlinearities were considered. ABAQUS contains different types of elements such as solid, shell, and beam elements. For all components of the FE model, 3D solid eight-node brick element

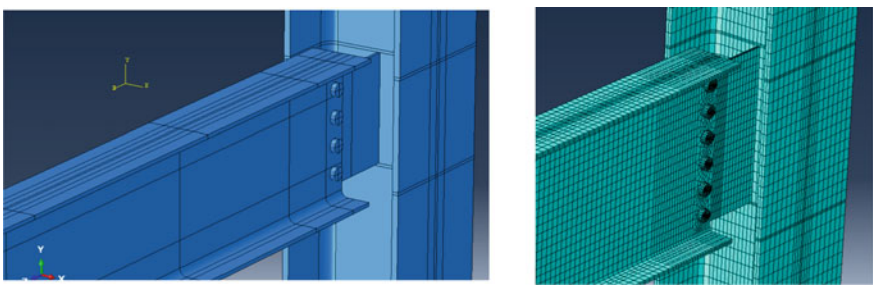

Fig. 1 3D FEM shown (Left) and a FE mesh in EST connection (Right)

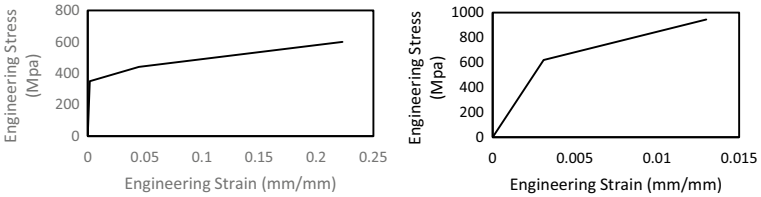

Fig. 2 Stress–strain curves: 350 W steel-left [3]; A325 bolt-right [7]

with reduced integration (C3D8R in ABAQUS library) hourglass controlled element was selected.

3.2 Material Properties

To consider material non-linearity, elastic–plastic with linear hardening relation was implemented for bolt, plate, beam, column, and girder. To validate the experimental test [4, 9], yield stress and ultimate stress were considered as specified in the test report. For all FE models, modulus of elasticity and Poisson's ratio were considered as 200 GPa and 0.3, respectively. The stress–strain curve considered for the A325 bolt, as shown in Fig. 2, was adopted from Rahman et al. [7], For all other steel components stress–strain curve by Ashakul et al. [3] for 350 W steel, as shown in Fig. 2, was considered.

3.3 Contact Properties

Surface to surface interaction with hard contact and a friction coefficient of 0.3 was used to connect the bolt with a bolt hole, beam web, and plate in ABAQUS. To simulate surface-to-surface interaction properly, the bolt head, bolt-shank, and nut were used as master surface (red) since bolt material is stiffer than steel material. On the other hand, beam web, plate, and bolt hole were used as slave surface (pink), as shown in Fig. 3. To connect the shear tab with the supporting column web, tie constraint was used. In this.

constraint, column web was considered as master surface and the shear tab was considered as slave surface.

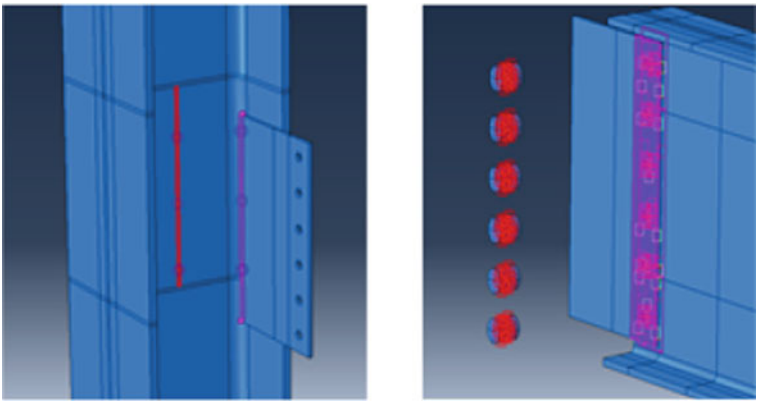

Fig. 3 Interaction used in ABAQUS: master surface (red) and slave surface (pink)

3.4 Boundary Condition

To validate the developed FEM for CST and EST connections, boundary conditions were applied as the experimental setup [4, 9]. In order to prevent lateral- torsional buckling, the top flange of the beam was restrained in the experimental test and this was followed in the FEM as well. For the parametric study, simply supported beam condition was considered for all FE models. The supporting column had pin support condition, translational DOFs about X, Y and Z were restrained ($U_1 = U_2 = U_3 = 0$) at both column ends. The far end of the supported beam had a roller support condition. To obtain roller support condition at the far end, the center of the cross-sectional nodes was restrained vertically ($U_2 = 0$) and all the web nodes were restrained in the lateral direction ($U_1 = 0$). To ensure "plane section remains plane after bending", rotational degrees of freedom ($UR_3 = 0$) was also restrained.

3.5 Analysis Type

First, an eigenvalue analysis was performed through linear perturbation buckling analysis. Corresponding eigenmodes were extracted from each analysis. In each model, five eigenmodes were requested and obtained. From the eigenvalue analysis, a suitable pattern of imperfection was obtained and incorporated into the non-linear analysis. Then, nonlinear buckling analysis was performed using the static RIKS method in ABAQUS. Static RIKS method is suitable in capturing collapse and post-buckling behavior. This method is based on the Arc-length method, a form of the Newton–Raphson iteration method, which uses arc length and load proportionality factor.

3.6 Load Application

In this research, a total of two types of loading, bolt pretension, a concentrated load, were applied. As recommended for ¾ in. A325 bolt in the CISC handbook, a minimum pretension force of 125 kN was applied in each bolt. Secondly, a concentrated load was applied on the top flange of each beam. The concentrated load was applied as a distributed pressure to avoid any local failure of the flange.

3.7 Geometric Imperfection

Geometric imperfection was applied to all FE models. An imperfection value of the length of beam/1000 was applied in all FE models. As the lowest eigenvalue represents critical buckling load and initiates buckling in the FE model, geometric imperfection was applied to this critical buckling mode [10].

3.8 Residual Stress

Residual stress exists in hot-rolled steel members due to a non-uniform cooling system during manufacturing. Early yielding can be initiated by this stress and can affect the overall stiffness and strength of the beam. Therefore, it is essential to consider the residual stress in finite element analysis. In this research, a standard pattern of residual stress was followed which was recommended by ECCS Technical Committee 8 (1984), as presented in Fig. 4.

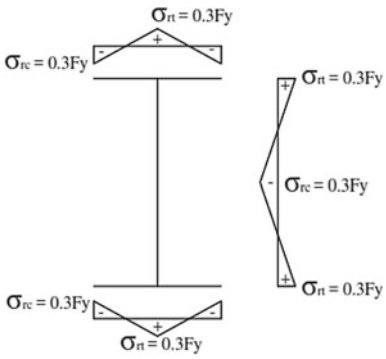

Fig. 4 Residual stress pattern recommended by ECCS (1984)

Table 1 Details of validated finite element model

Reference	Test name	Bolt	Shear tab			Supporting member		Weld to bolt distance
			Length	Thickness	Depth	Section	Span	
			mm	mm	mm		mm	mm
Sherman and Ghorbanpoor [9]	4-U	5	293.1	12.7	381	W18 × 71	6096	255

* 4-U ~ Group 4, Unstiffened Connection

4 Model Validation

4.1 Details of the Validated Specimens

The developed finite element model was validated and compared with the experimental results from the extended shear tab connection tested by Sherman-Ghorbanpoor [9]. Table 1 presents details of the experimental test. In the FE model, the A325 bolt having ¾ in. diameter was used in the connection. A36 material was considered for the shear tab in the experimental tests and ASTM Grade 50 was taken for the beam section.

4.2 Validation of the Finite Element Model

For the finite element model validation, the shear-displacement curve from the FE model was compared against the experiment data. As shown in Fig. 5, a good agreement was observed between experimental results and the FE analysis results. Though the use of tie constraint instead of welding between extended shear tab and web of the

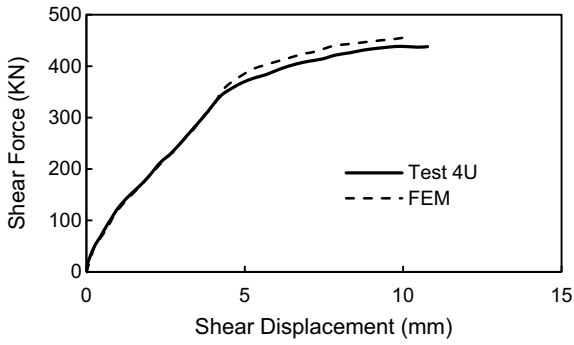

Fig. 5 Comparison of analysis with test results of Sherman and Ghorbanpoor [9]

Table 2 Comparison of results between experiment and FE analysis

Reference	Test	Ultimate load			Shear displacement			Failure mode	
		Test	FEM	Difference	Test	FEM	Difference	Test	FEM
		kN	kN	%	mm	mm	%		
Sherman and Ghorbanpoor [9]	4-U	437.9	455.9	4.11	10.77	10.07	6.49	Twist	Twist

* 4-U ~ Group 4 Unstiffened in experiment

beam was time-efficient, it excluded the effect of welding residual stress in the developed FE model. In addition, bolt material was assumed as linear hardening, and material for other steel members was assumed as tri-linear hardening after yield stress. This assumption in the material stress–strain relationship may be different from the actual stress–strain relation and might be a reason for the small difference between experiment and FEM results; however, the difference remains within an acceptable range, less than 10%. The failure mode of FEM was observed and compared with the experimental failure mode. Table 2 presents a comparison between the experimental and FE analysis results.

5 Parametric Study on Shear Tab Connection

5.1 Parametric Test Details

An extensive parametric study was carried out to find out the effect of shear tab length and thickness on the shear force, shear displacement, and out-of-plane twist. The top flange of the supported beam was braced along the whole length. This was to prevent lateral-torsional buckling of the beam. The far ends of the analysed beams had simply supported conditions. Also, a concentrated load was applied at a one-meter distance away from the single vertical line of bolts. For this study, only one single vertical line of bolt configuration was considered. A total of six different types of bolt configurations, as presented in Table 3, were considered in this study. For all FE models, the shear tabs had 3-in. pitch and 1.5-in. end and edge distances. Both conventional and extended shear tabs were made from A36 steel and all beams and columns were from ASTM Grade 50 steel.

5.2 Variation of Shear Force with Shear Tab Length

The variation of shear force with the distance from weld to first vertical bolt line (a) is plotted in Figs. 6, 7, and 8 for three different shear tab thicknesses. Total six

Table 3 The details of shear tab dimension in the FEM

Beam section	Number of bolt	Dimension of shear tab			Distance from weld to bolt, a
		Depth, d_p	Thickness, t_p	Length, l_p	
		mm	mm	mm	mm
W16 × 36	4	304.8	8 10 12	114.3 190.5 266.7	76.2 152.4 228.6
W18 × 40	5	381.0			
W21 × 44	6	457.2			
W27 × 84	7	533.4			
W30 × 90	8	609.6			
W33 × 118	9	685.8			

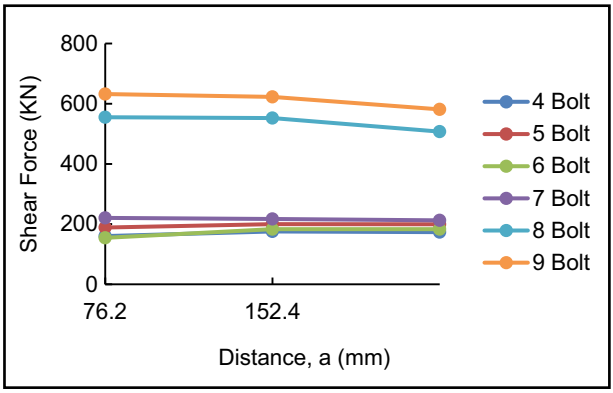

Fig. 6 Variation of shear force with shear tab length (for 8 mm thick shear tab)

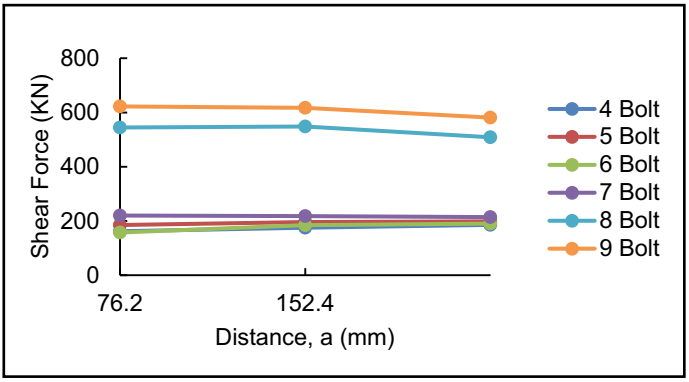

Fig. 7 Variation of shear force with shear tab length (for 10 mm thick shear tab)

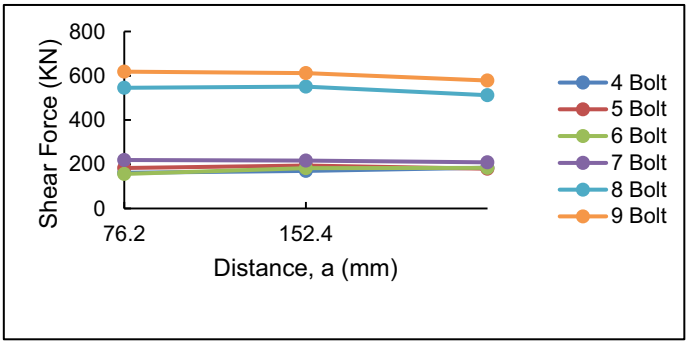

Fig. 8 Variation of shear force with shear tab length (for 12 mm thick shear tab)

types of bolt configurations were considered with an end distance of 38.1 mm and the center to center bolt spacing of 76.2 mm. For all three shear tab thickness, higher shear capacity was observed only for eight and nine bolt configurations. However, the capacity decreased gradually as the shear tab length increased.

5.3 Variation of Twist with the Shear Tab Length

When subjected to gravity loading, CST and EST connections experience in-plane and out-of-plane displacements. Twisting failure mode was noticed as the length and depth of the shear tab increased. The amount of torsion was insignificant when the conventional shear tab was used. But, when the shear tab length was 228.6 mm (extended shear tab) and the number of bolts was four and five, the amount of twist was quite significant. Figure 9 shows the variation of shear force and twist in the

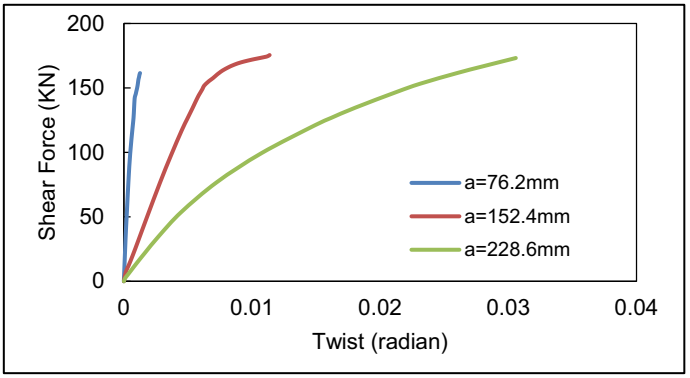

Fig. 9 Variation of shear force with twist (for 4 bolts and 8 mm thick shear tab)

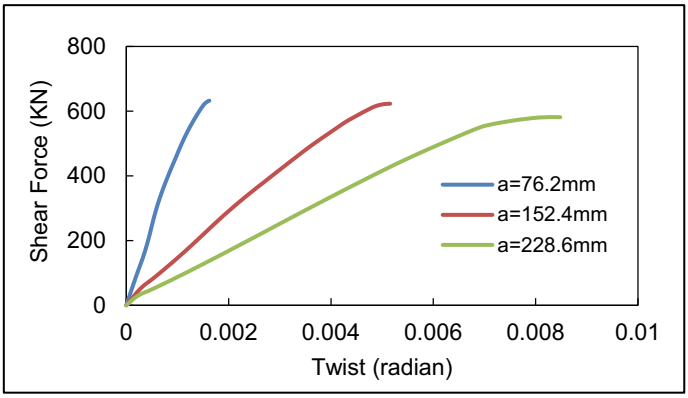

Fig. 10 Variation of shear force with twist (for 9 bolts and 8 mm thick shear tab)

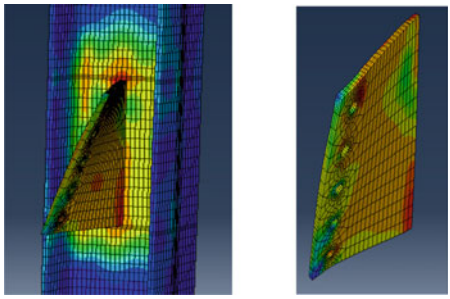

Fig. 11 Twisting failure mode of EST connected with column web (left) and EST itself (right)

shear tab for 4 bolts and shear tabs with 8 mm thickness. Figure 10 shows the shear force versus twist relation for different shear tabs with 9 bolts. It is observed from Fig. 10 that the twist is smaller for all shear tabs when they are connected with the beam with 9 bolts. Twist (φ) was obtained from the following Eq. 6. The twisting failure mode of the shear tab in the EST connection is presented in Fig. 11.

$$\phi = \frac{u_t - u_b}{d_p} \tag{6}$$

where U_t is the lateral displacement at the top of the shear tab, U_b is the lateral displacement at the bottom of the shear tab, and d_p is the depth of the shear tab.

5.4 Connection Shear Force-Shear Displacement Curves

The connection shear force-shear displacement curves were obtained from FE analyses for all bolt configurations. Total six types of bolt configurations, as shown in

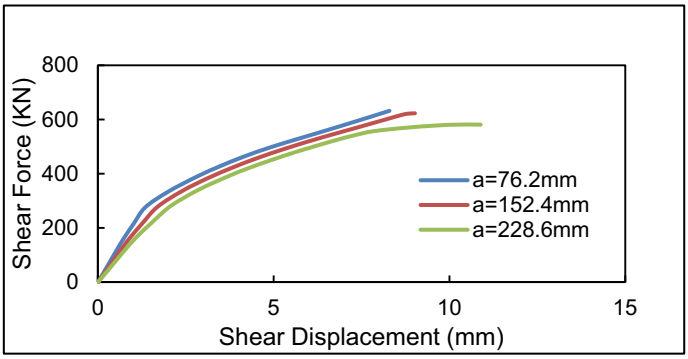

Fig. 12 Shear force versus shear displacement (for 9 bolts and 8 mm thick shear tab)

Table 3, were considered with an end distance of 38.1 mm and the center to center bolt spacing of 76.2 mm. Figure 12 presents the connection's shear force-shear displacement curves for 8 mm thick shear tab connected with the column web with 9 bolts. It is observed from Fig. 12 that the shear displacement for longer shear tab (266.7 mm) is slightly higher than that for the conventional shear tab with a length of 114.3 mm; however, the difference is small when the shear tab connection has 9 bolts.

6 Conclusions

A detailed three-dimensional FE model was developed to study the behaviour of conventional and extended shear tab connections. When compared against experimental results, the developed FE model was able to provide excellent predictions of behaviour of the extended shear tab connections. With the validated FE model, a detailed parametric study was conducted. It was observed that the thickness of the shear tab can increase the shear capacity slightly; however, the higher shear tab thickness can decrease the out-of-plane displacement of the shear tab connection. Also, the length of the shear tab for the EST connection has a great influence on the shear displacement and twist of the shear tab connection. Another important finding from this research was that the shear capacity was high when the shear tab had a higher depth. Thus, shear tab connections with eight and nine bolts showed higher shear strength in comparison to other bolt configurations with smaller shear tab depth. Also, a twisting mode of failure was observed for the EST connections. The amount of torsion was insignificant when the conventional shear tab was used. In the conventional shear tab connection, the failure was initiated by bolt fracture, plate bearing, and bolt bearing. Twisting in shear tabs should be prevented in design so that the supported beam can reach its flexural capacity before any twisting failure occurs in the shear tab connections. Research is currently in progress to investigate effective means of preventing the twisting failure of extender shear tab connections.

Acknowledgements Funding for this research project is provided by the Gina Cody School of Engineering and Computer Science, Concordia University, Montreal, Canada and the Natural Sciences and Engineering Research Council of Canada.

References

1. ABAQUS (2014) ABAQUS standard user's manual, 6.14. Dassault Systems
2. American Institute of Steel Construction (AISC) (2011) Steel construction manual, 14th edn., Chicago
3. Ashakul A (2004) Finite element analysis of single plate shear connections, Doctor of philosophy dissertation, Virginia Polytechnic Institute and State University, Blacksburg, Virginia, USA
4. Astaneh A, Call SM, McMullin KM (1989) Design of single plate shear connections. Eng J Am Inst Steel Constr 26(1):21–32
5. Canadian Institute of Steel Construction (CISC) (2016) Handbook of steel constructions, 11th edn., Toronto, Ontario, Canada
6. Marosi M (2011) Behaviour of single and double row bolted shear tab connections and weld retrofits. MEng thesis, Dept. of Civil Engineering, McGill University, Montreal, Quebec
7. Rahman A, Mahamid M, Amro A, Ghorbanpoor A (2003) 3D FE model of extended shear tab connections. In: 16th engineering mechanics conference. ASCE, Seattle
8. Rahman A, Mahamid M, Amro A, Ghorbanpoor A (2007) The analyses of extended shear tab steel connections, part I: the unstiffened connections. Eng J Am Inst Steel Constr 44(2):117–132
9. Sherman DR, Ghorbanpoor A (2002) Design of extended shear tabs. Research report RR3095, American Institute of Steel Construction, Inc., Chicago, IL, USA
10. Trahair NS (1993) Flexural-Torsional buckling of structures. CRC Press, Boca Raton

Behavior of Steel I-Beams Reinforced While Under Load

Masoud Mohammadzadeh and Anjan Bhowmick

1 Introduction

Reinforcing existing steel beams is often unavoidable due to the change of the primary function of the structure or additional applied loads. Replacement of the beams is more expensive and time-consuming which can be avoided by reinforcing and increasing their capacity. On the other hand, beams that require strengthening often are in service and complete relieving of their loads is not either possible or not economical. Thus, steel beams may need to be reinforced while under load. The main objective of reinforcing a steel beam is to increase stiffness and strength of the reinforced beam or to change the structural behavior and failure mode of the reinforced beam. When the bottom flange of the steel I-beam is easily accessible, the most economical option is to weld a cover plate to the bottom flange. The design procedure generally involves selecting a cover-plate that can resist the additional factored moment applied in the beam. While the current practice is simple, it is not clear how the reinforced beam will behave if locked-in stresses due to service loads are present during the reinforcement. Very limited research is currently available on behaviour of steel beam reinforced while there are subjected to load.

Research on steel beams reinforced with welded steel plates while under load is very limited. Liu and Gannon [9] first studied the behavior of the steel beams reinforced under load by conducting tests on steel I-beams reinforced with welded cover plates. Two different reinforcing patterns, one where a plate was welded to the bottom flange of the beam section along its length (pattern A) and the other where two plates were welded against tips of the flanges of the beam section along its length (pattern B), were considered and the specimens were tested for different

M. Mohammadzadeh · A. Bhowmick (✉)
Department of Building, Civil and Environmental Engineering, Concordia University, Montreal, QC, Canada
e-mail: anjan.bhowmick@concordia.ca

M. Mohammadzadeh
e-mail: masoud.mohammadzadeh@concordia.ca

S. Walbridge et al. (eds.), *Proceedings of the Canadian Society of Civil Engineering Annual Conference 2021*, Lecture Notes in Civil Engineering 244,
https://doi.org/10.1007/978-981-19-0656-5_6

preload levels. It was observed that increasing the preload resulted in a decrease in lateral-torsional buckling strength for beams with pattern A reinforcement (plate welded to the bottom flange) than the same specimen strengthened under no preload.

It was also reported that the variation of the preload level has an insignificant effect on the ultimate resistance of beams with flexural yielding failure. Furthermore, Liu and Gannon [9] continued their investigation by conducting parametric studies on the effects of the preload magnitude, initial imperfection, length of cover-plate, the span of the beam and lateral restraint on the reinforcement of the steel beams. Similar to the experimental results, in their numerical study, a reduction of resistance of beams with lateral-torsional buckling failure by increasing preload was indicated for beams with type A reinforcement. [12] conducted a detailed experimental investigation on the I-steel beams reinforced while under load by welding cover-plates on the top and bottom flanges. In their research, the procedures of reinforcement, preloading and welding of reinforcing plate and its effects were studied. Three reinforced I-beams with the preload level 0, 37% and 74% of the unreinforced beam capacity were investigated. It was reported that for the beam with the 37% preload level, the failure was lateral-torsional buckling and the ultimate capacity reduced comparing with the capacity of the reinforced beam without preloading. However, for the reinforced beam with the 74% preloading level, the ultimate capacity increased. The failure mode for this beam was flange local buckling. Thus, no clear and definable relationship was obtained between the preload and strength of reinforced beam from the study of [12].

Often there is a difference between the steel grades of the existing beam and the reinforcing cover-plate. Beams in many existing structures are often of lower grade steel than the modern steel used for reinforcement. To the best of authors' knowledge, no study is currently available on steel beam reinforced with cover plate of different grade. Also, effect of different welding residual stress on the strength and behaviour of beam reinforced under load is currently not available. In this paper, behaviour of simply supported steel I-beams reinforced with a welded cover-plate at the bottom flange is studied. In addition, effects of preloading, initial and welding residual stress and steel grades of the reinforcing plate are studied.

2 Finite Element Analysis of Reinforced Steel I-Beams

A finite element model of a reinforced I-section steel beam was developed using the commercial finite element software Abaqus. Reinforcing was done by adding a cover plate to the bottom flange of a simply supported I-beam.

2.1 Development of Finite Element Model

The developed finite element model consists of four different parts: a base beam that is a build-up I-section, a reinforcing cover-plate, a duplicate of reinforcing plate with

zero stiffness and a rigid beam connector. The base beam, reinforcing plate and its duplicate were constructed using shell element S4R. S4R is a 4-node doubly curved general-purpose shell element with reduced integration, finite membrane strains and 6 active degrees of freedom. Two-node rigid beam connectors were used to model the welding joints between the base beam and the duplicate of the reinforcing plate. One end of each connecter connected to the beam at the bottom flange tip weld location and the other one was connected to the duplicate of the reinforcing plate. The incorporated rigid beam connector element has 6 active degrees of freedom for each node and imposes kinematic constraints between the nodes. Usually, beam is reinforced when there is some preloading in the beam. Therefore, the reinforcing plate will be active after the preload is applied in the FEM. Since the cover plate can not be modeled within the analysis step, a similar effect can be obtained by creating its elements in the definition of the model, removing them in the first loading step and reactivating them, subsequently. However, during the reactivation, because of the preloading and related displacements, the new configuration of the beam will be different from the original one specified in the definition of the model. For the nodes of reinforcing plates to be in the correct position while reactivation, these nodes shared with the nodes of the reinforcing plate duplicate using tie interaction. The duplicate of the reinforcing plate was not removed during the analysis and its material property and thickness were assigned in a way that did not affect the solution of the reinforced beam, as well as did not cause numerical problems. Surface to surface contact, hard contact in normal direction and penalty in the tangential direction, was incorporated between the bottom flange and duplicate of the reinforcing plate.

The finite element model for the I-section had 40 elements for the depth of the web and 12 elements for the width of the flanges. The mesh size in the longitudinal direction of the beam was based on keeping the aspect ratio of shell elements smaller than 2.0. In this investigation, isotropic steel material with a multi-linear stress–strain curve for the base beam and reinforcing plate was used. The tangent stiffness in the yield plateau region was 0.001E up to $\varepsilon_{sh} = 10\varepsilon_y$, where ε_{sh} is the strain-hardening strain and ε_y is the yield strain of the material, respectively. From this strain up to the strength of strain hardening, a constant strain-hardening modulus equal to 2% E is used [8]. The modulus of elasticity and poison ratio were assumed as 200,000 MPa and 0.3, respectively.

Initial residual stresses of the beam section were applied in the form of initial stress in Abaqus. These residual stresses were introduced as uniform stresses on each element of the beam section in the first step of the analysis. Initial residual stresses of reinforcing cover plate along with residual stresses induced from welding cover plate to the beam section were introduced by applying longitudinal temperature gradient. The initial temperature field of the structure was taken as zero and expansion coefficient in the longitudinal direction for steel material was considered as $1.17 \times 10^{-5}/°C$. This coefficient was taken as zero in transverse and through the thickness direction. Desired residual stresses were introduced by changing the temperature on each node using "Eq. 1".

$$\sigma = -E.\alpha.\Delta T \tag{1}$$

In this equation, σ is longitudinal residual stress, E is the elastic modulus of elasticity, α is expansion coefficient and ΔT is the temperature gradient.

In this study, straight I- beam was subjected to four-point loading. Concentrated loads were applied at one- third of the beam length. Also, transverse stiffeners were attached at the bearing and concentrated load locations. The considered failures were flexural yielding of flange, elastic and nonlinear lateral-torsional buckling. The beam was simply supported in-plane and out-out-plane, while lateral braces were provided in the load locations at the top and bottom flanges for the flexural yielding failure. To impose the simply supported boundary conditions, transverse and vertical displacements were restrained at both ends while longitudinal displacement was restrained at just one end of the beam. In addition, transverse displacement was restrained along both sides of transverse stiffeners tips at the support locations. For this study, the considered cross-section of the beam was a compact section. Therefore, just flange sweep was considered as the initial geometrical imperfection. Web out-of-flatness and flange tilt were not incorporated in this study. For the beams reinforced while under load, there are three sources of imperfections: (1) imperfection from the fabrication and erection of the base beam (δi), (2) weld shrinkage deformation, induced from welding of reinforcing plate under load (δw), and (3) the last one is $P - \delta$ deformations induced from the preloading of the base beam (δI). Based on the American Welding Society [2] limitation/tolerance for the repairing of existing structures, $\delta i + \delta w$ should be smaller than $L_b/1000$ regardless of the welding process and preloading level, in which L_b is the unbraced length of the beam. Therefore, as the geometrical imperfection magnitude, $L_b/1000$ was used and applied at the mid-point of unbraced length at the compression flange in the first step of the loading. In order to analyze the unreinforced beam, initial residual stresses of the beam along with the geometrical imperfection were applied at the first loading step. Then, the concentrated loads were applied through modified Riks analysis to follow the equilibrium path of the beam. To analyze the reinforced beams, the following steps were considered:

1. All components of the beam and reinforcing plates were modeled. In order to avoid interaction between the base beam and the reinforcing plate while applying initial residual stresses of the beam and preloading, all elements of the reinforcing plate were deactivated. Initial residual stresses of the beam along with the initial geometrical imperfection were incorporated into the beam.
2. For the beams reinforced while under-load, four preloading levels, 0%, 20%, 40% and 60% of unreinforced beam strength, were considered in this study.
3. All elements of the reinforcing plate were reactivated in the strain-free mode.
4. Initial residual stresses of the reinforcing plate were applied using temperature gradient.
5. Residual stresses induced from welding the reinforcing plate to the beam were introduced by changing the temperature at the tips of the bottom flange and corresponding locations of the reinforcing plate. The temperature in these locations

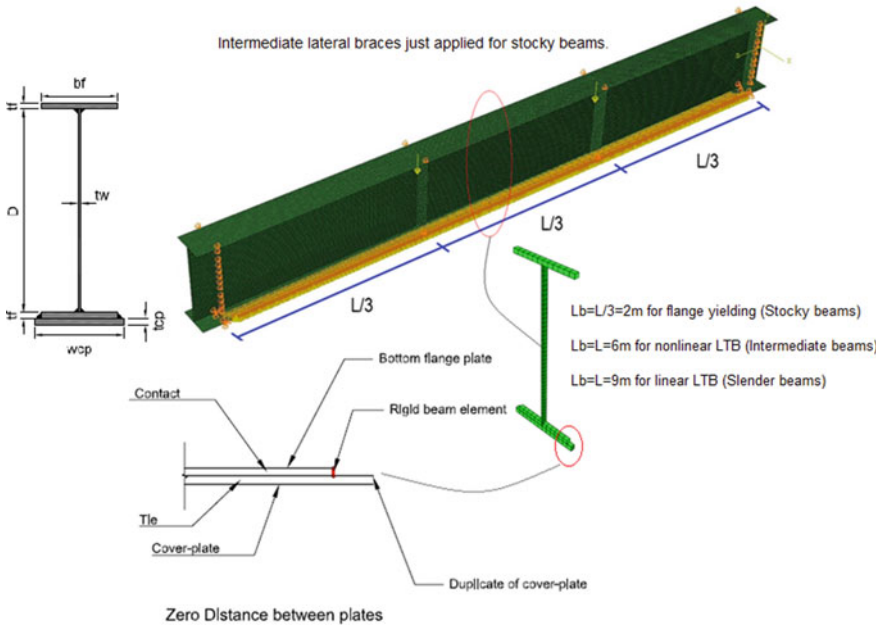

Fig. 1 Details of developed finite element model and schematic view of the reinforced I-beam

was changed to reach 70% or 100% material yield strain and a self-equilibrating residual stress pattern was developed in the reinforced beam.

6. The reinforced beam was further loaded until it reached failure.

Nonlinear static analysis was carried out for all steps from 1 to 5. For the loading step 6, the modified Riks method was incorporated. Details of developed FEM along with the schematic view of the reinforced I-beam are presented in Fig. 1.

2.2 Validation of Finite Element Model

Liu and Gannon [9] conducted a 4-point bending test on simply supported beam reinforced by welding a reinforcing plate at the bottom flange of the beam. The beam cross-section was W310 × 28 with an unbraced length of 2.4 m and the nominal dimension of the reinforcing plate was PL 2304 × 137 × 9.5. Three preload levels with magnitudes of 0 (without preload), 50 kN and 100 kN were considered and named as A1, A2, and A3 in their study. The yield stress, Fy, for steel beam and the reinforcing plate was 374 MPa and 346 MPa, respectively. Initial residual stress distributions for the beam and combined residual stresses of hot rolling and welding for reinforced beams and reinforcing plate were experimentally determined [9]. In their experimental work, the initial imperfection of the unreinforced beams

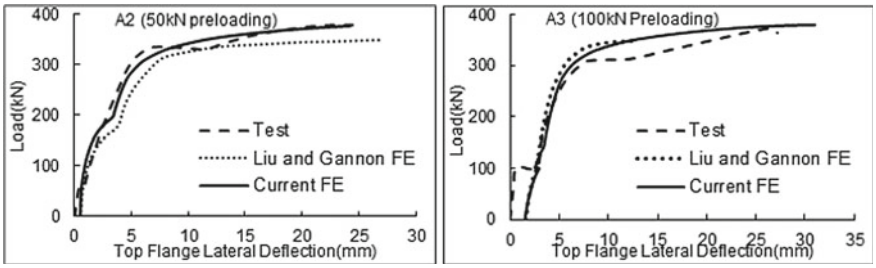

Fig. 2 Validation of FEM for specimens tested by Liu and Gannon [9]

was not reported. Liu and Gannon [9] also developed a FE model and verified their tests. In their numerical study, it was stated that predicting the imperfection of the beams after welding the reinforcement is complicated since it is a function of various uncontrolled factors. Therefore, the initial imperfection in the numerical model was adjusted such a way that top flange deflections after applying preload and welding reinforcement became approximately equal to the experimentally measured imperfection after reinforcement. In this paper, to verify the overall simulating procedures, samples A2, with 50kN preloading, and A3, with 100kN preloading, were modeled and load-lateral deflection of top flange midpoint at the mid-span of these tests are compared with the experimental and finite element results of the Liu and Gannon [9] which is shown in Fig. 2. In the modeling, experimentally measured values for the residual stresses were used. Also, to apply the geometrical imperfection, a procedure similar to the FE model of Liu and Gannon [9] was used. It can be observed from Fig. 2 that the current FE is capable of predicting the overall behavior, buckling and ultimate capacities of the reinforced beams while under load. Furthermore, failure modes of the current FE models were nonlinear lateral torsion buckling, as observed during the tests.

Currently in the literature, no specific welding residual stress pattern is available for steel beams reinforced with a welded cover-plate at the bottom flange. In this study, as an alternative, welding residual stresses were achieved by applying 70% or 100% yielding strength of steel at the bottom flange tips and the corresponding location of the reinforcing plate. This is consistent with the study by [3] on steel column reinforced with welded cover plate. The resulting residual stress pattern would be the combination of initial and welding residual stresses. To validate the accuracy of this method, it was incorporated into numerical modeling of residual stresses of the sample A1, reinforced beam without preloading, and obtained residual stresses from this approach were compared with the experimentally measured ones. Figure 3 shows that the magnitude and distribution of the achieved residual stresses correlates very well with the experimentally measured pattern and can be used in the numerical modeling.

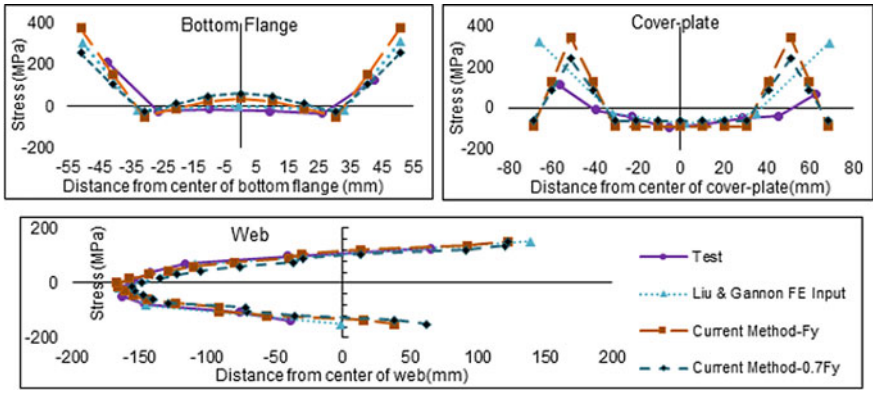

Fig. 3 Validation of welding residual stress application in FEM [9]

3 Parametric Studies

The validated FE model was used to conduct a parametric study to investigate the effects of important parameters such as initial residual stress distributions and magnitudes, welding residual stress, preloading level and material grade difference between the I-beam and the reinforcing plate on the strength and behaviour of I-beam reinforced with a cover plate at the bottom flange. The flange size of the beam cross-section was 300 mm × 20 mm ($b_f \times t_f$), with the web size of 760 mm × 11 mm ($D \times t_w$). Also, a plate with the size of 350 mm × 25 mm ($w_{cp} \times t_{cp}$) was used to reinforce the cross-section. Based on the Canadian steel design standard (CAN/CSA S16-14), the flange is class 1 and the web is class 2 for this section. The parametric studies conducted for the beams with three different unbraced lengths 2 m (Stocky), 6 m (Intermediate) and 9 m (Slender) with the expected failure modes; cross-section yielding, inelastic LTB and elastic LTB, respectively (Fig. 1).

3.1 Effect of Preload Magnitude

In order to study the effect of preloading on the behavior of beams reinforced while under-load, four levels of preloading; 0% (CP-NPL), 20% (CP-20% Preload), 40% (CP-40% Preload), 60% (CP-60% Preload), of the unreinforced beam capacity were considered. Moment-lateral deflection diagrams for top flange at the mid-span of the beams are depicted in Fig. 4 for different preloading levels. These diagrams are for stocky, intermediate and slender beams with the Best-Fit initial residual stress (Shown in Fig. 5) and 100% yielding strength as welding residual stress.

As shown in Fig. 4, adding a cover-plate to the bottom flange increases the stiffness and ultimate capacities of I-beams regardless of preloading level. Furthermore, it can be seen that preloading does not have a significant effect on the behavior and ultimate

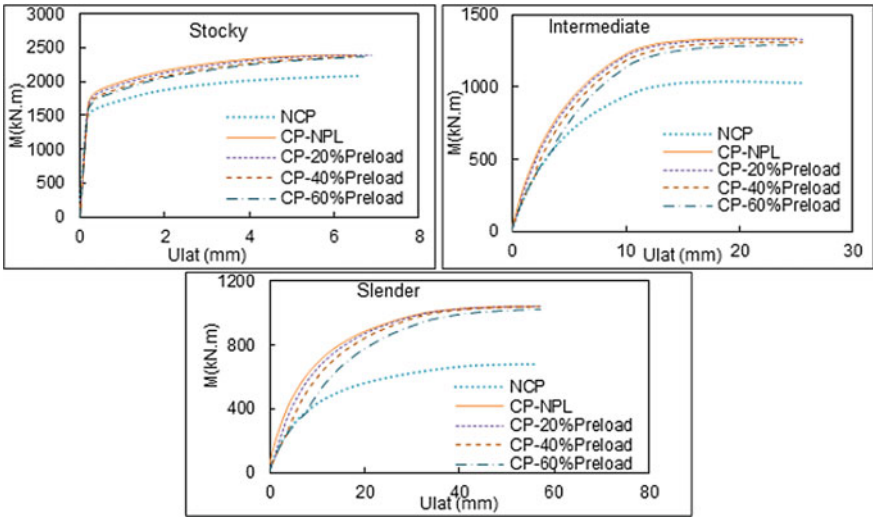

Fig. 4 Moment- top flange lateral deflection at the mid span under various preload level

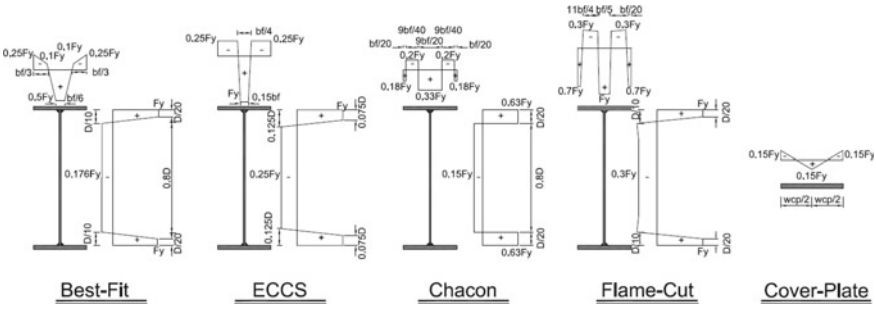

Fig. 5 Initial residual stress patterns for I-beam and cover plate

capacity of beams with yielding failure mode. However, the presence of preloading changes the behavior of the beams with elastic and nonlinear LTB failure modes. For the nonlinear LTB, the buckling and ultimate capacities decrease with an increase in the preload magnitude. For the beams with elastic LTB, the presence of preloading has a significant effect on the buckling behavior of the reinforced beam and reduces the buckling capacity. However, post-buckling capacity compensates the reduction; and the beam with preloading reaches its full capacity but in a very large deflection.

3.2 *Effect of Initial Residual Stress*

In order to study the effects of initial residual stress on the beams reinforced under load, four commonly used patterns for the welded I-sections, Best-Fit Prawel [8], ECCS [7], Chacon [5], and Flame-Cut (Chernenko and Kennedy 1991) and one pattern for the reinforcing cover plate (Wu and Grondin 2002) were considered. The selected residual stresses and shown in Fig. 5.

Table 1 presents ultimate capacities of beams with different initial residual stress patterns. Based on the results in Table 1, reinforcing by adding cover-plate increases the ultimate capacities. The average capacity increase is 12.44%, 29.3%, and 53.7% for stocky, intermediate and slender beams, respectively. In the stocky beams, the maximum amount of capacity increase is 14.31%, which happens in the beam with Chacon initial residual stress. Furthermore, the minimum amount of capacity increase, 10.4%, in these beams happens for the 'ECCS' initial residual stress. For intermediate beams, the maximum capacity increase is 30.85% which happens for the flame cut initial residual stress. In addition, for intermediate beams the minimum capacity increase is 27.5%, happens in Chacon initial residual stress. For the longer span, the capacity increase for all types of the initial residual stress is very close.

The effect of initial residual stress pattern on the strength and behaviour of the beams reinforced while under load is presented in Fig. 6. In this Figure, parameter β is the ratio of beam ultimate capacity under considered preloading level to the beam ultimate capacity without preloading. For the selected beams, the welding residual stress at the welding location was 100% yielding strength (Fy) and the varying parameters were the initial residual stress patterns and preloading level. As observed from Fig. 6, initial residual stress plays a negligible role in the capacity reduction of

Table 1 Ultimate capacities of reinforced beams for different initial residual stresses (with no preloading)

I-Beams	Patterns	Capacity (kN.m)		Capacity increase (%)
		Unreinforced	Reinforced	
Stocky (2 m unbraced beam)	Best Fit, Fy	2112.66	2393.46	13.3
	Flame Cut, Fy	2137.5	2372.94	11.01
	ECCS, Fy	2100.42	2318.76	10.4
	Chacon, Fy	2125.31	2429.46	14.31
Intermediate (6 m unbraced beam)	Best Fit, Fy	1035.44	1338.32	29.29
	Flame Cut, Fy	1085	1419.74	30.85
	ECCS, Fy	991.44	1288.04	29.61
	Chacon, Fy	1075.5	1371.24	27.5
Slender (9 m unbraced beam)	Best Fit, Fy	675.95	1042.57	54.24
	Flame Cut, Fy	715.64	1070.55	49.6
	ECCS, Fy	670	1031.06	53.9
	Chacon, Fy	694.31	1065.12	53.41

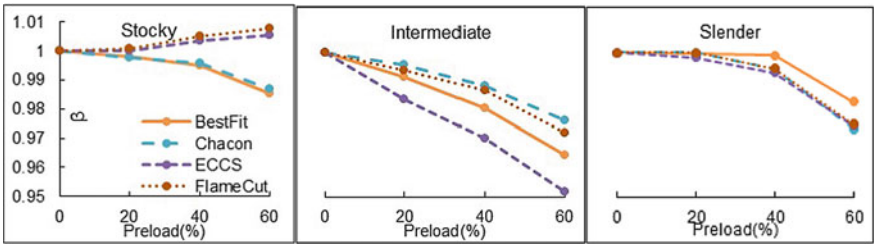

Fig. 6 Effect of the initial residual stress on the capacity reduction of beams reinforced under load

stocky and slender beams since the reduction of capacity is negligible or equal for the considered patterns. However, in the intermediate beams, the capacity reduction is different for the patterns and increases by increasing the preload level but with a different rate. In these beams, the capacity is reduced up to 5% for the beams with 60% of preloading. It is also observed that the minimum capacity reduction is for 'Chacon' initial residual stress pattern and the maximum capacity reduction is for the 'ECCS' initial residual stress pattern.

3.3 Effect of Welding Residual Stress

Welding residual stress of two different magnitudes, 100% and 70% of yielding strength of steel material, at the location of welding were considered to study the effects of residual stresses induced from welding the cover-plate to the bottom flange of I-beams. When investigating the effect of welding residual stress, the initial residual stress was Best-Fit residual stress. It was observed that the differences in the capacities for the two different welding residual stresses are negligibly small. Ultimate capacities of the intermediate beams for different welding residual stresses and with no preloading are presented in Table 2.

Also, for the two selected welding residual stresses, the capacity reduction for the beams is approximately equal when the preload is applied. The effect of welding residual stress on the capacity reduction of the intermediate beams reinforced while under load is presented in Fig. 7. Therefore, welding residual stress does not a have significant effect on the capacity reduction of the reinforced beams while under load.

Table 2 Effect of welding residual stress on capacity of intermediate reinforced beams (with no preload)

Beams	Patterns	Flexural capacity (kN·m)		Capacity increase (%)
		Unreinforced	Reinforced	
Intermediate (6 m unbraced beam)	Best Fit, Fy	1035.44	1338.32	29.29
	Best Fit, 0.7Fy	1035.44	1338.12	29.23

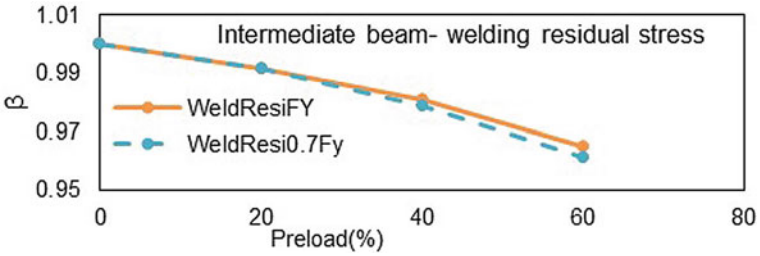

Fig. 7 Effect of the welding residual stress on the capacity reduction of intermediate beams reinforced while under load

3.4 Effect of Difference in Steel Grade Between I-Beam and Cover Plate (Hybrid Material)

To study the effect of difference in steel grade between I-beam and cover plate on the behavior of beams reinforced with welded cover plates, a different steel material, A36, with a yield strength (F_y) of 250 MPa and ultimate strength (F_u) of 400 MPa for the I-beams was considered. Also, for the reinforcing plate, F_y and F_u were 345 MPa and 450 MPa, respectively. The initial residual stress was Best-Fit and welding residual stress magnitude was 100% of the yield strength. Based on the results, it was observed that the overall behavior of hybrid and non-hybrid beams reinforced while under load were similar. Table 3 compares the capacities of hybrid and non-hybrid intermediate reinforced beams with no preloading. It should be noted that for both cases the yield strength for the cover-plate was 345 MPa.

The capacity increase for the hybrid and non-hybrid stocky beams is 18.5% and 13.3%, respectively. Also, the increase in capacity for hybrid and non-hybrid intermediate beams is 31.8% and 29.25%, respectively. Furthermore, for hybrid slender beams, the capacity increase is 53.13%, while for non-hybrid slender beams, it is 54.24%. It can be concluded that using higher strength material for cover-plate will

Table 3 Capacities of hybrid and non-hybrid intermediate reinforced beams with no preloading

Beams	Fy; base I-beam		Fy; cover-plate	Capacity unreinforced	Capacity reinforced	Increase (%)
Stocky	Hybrid	250	345	1552.66	1839.97	18.5
	Non-Hybrid	345	345	2112.66	2393.46	13.3
Intermediate	Hybrid	250	345	860.87	1134.62	31.8
	Non-Hybrid	345	345	1035.44	1338.32	29.25
Slender	Hybrid	250	345	605.84	927.73	53.13
	Non-Hybrid	345	345	675.95	1042.57	54.24

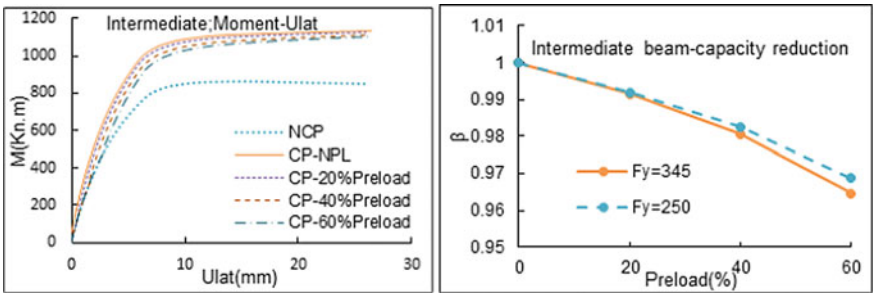

Fig. 8 a) Moment-lateral deflection; b) Reduction of capacity for intermediate hybrid beams.

not have a significant effect on the capacity increase for the slender and intermediate beams. The capacity increase is more in the stocky beams reinforced with high strength cover-plate.

The selected hybrid and non-hybrid sections were analysed for 0%, 20%, 40%. and 60% preloading levels. It was observed that the decrease in flexural capacity for the hybrid and non-hybrid stocky and slender steel beams was insignificant under various preloading levers, less than 2% reduction of capacity for 60% preloading level. Figure 8 presents moment-lateral deflection curves for the top flange of the intermediate hybrid beams for different preloading conditions. No significant difference was observed between different preload levels. Figure 8 also shows that for the intermediate beams the reduction of the ultimate capacity is close for both hybrid and non-hybrid steel beams and the capacity reduction is under 5%.

4 Conclusion

A numerical study was conducted to investigate the effects of preloading, initial and welding residual stresses and steel grade on the behavior of steel I-beams reinforced by welding a cover plate to the bottom flange. The following results are drawn from this investigation:

– Preloading did not have a significant effect on the behavior and ultimate capacity of beams with flexural yielding failure mode. However, preloading had some effect on the behavior of beams with linear and nonlinear LTB failure modes. For the nonlinear LTB, the buckling and ultimate capacities decreased when the preload magnitude was increased. Reduction of the buckling capacity was more than the ultimate capacity reduction. The reduction of ultimate capacities was smaller than 5% for a preload of up to 60% strength of the unreinforced beam. For slender beams, the presence of preloading changed the buckling behavior of the reinforced beams and reduced the buckling capacity.

– Initial residual stress played a negligible role in the capacity reduction of I-beams with flexural yielding and linear LTB failures. However, the capacity reduction was different for different initial residual stress patterns and the difference increased with an increase in the preload level in the I-beams with nonlinear LTB failure.
– Variation of the maximum welding residual stress from 70% up to 100% yielding strength of the material did not change the capacity and behavior of I-beams reinforced while under load.
– Using higher strength material for welded cover-plate did not have a significant effect on the capacity increase for the beams with linear and nonlinear LTB failures. For the beams with flexural yielding failure, using a cover-plate with higher strength, the capacity increase was more in comparision to the case when both the base beam and the cover-plate were of same steel grade. Also, steel grade did not have any signifcant effect on the capacity reduction of the beams reinforced while under load.

Acknowledgements Funding for this research project is provided by the Gina Cody School of Engineering and Computer Science, Concordia University, Montreal, Canada.

References

1. Abaqus (2019) Simulia, Inc., Providence, RI
2. AWS (2020) Structural welding code–steel, AWS D1 .1 /D1 .1 M: 2020, 24th edn. American Welding Society (AWS) D1 Committee on Structural Welding
3. Bhowmick AK, Grondin GY (2016) Limit state design of steel columns reinforced with welded steel plates. Eng Struct 114:48–60
4. CAN/CSA S16-14 (2014) Handbook of steel construction. Mississauga (Ontario, Canada): Canadian Institute of Steel Construction
5. Chacon R, Serrat M, Real E (2012) The influence of structural imperfections on the resistance of plate girders to patch loading. Thin-Walled Struct 53:15–25
6. Chernenko DE, Laurie Kennedy DJ (1991) An analysis of the performance of welded wide flange columns. Can J Civ Eng 180(4):537–555
7. ECCS (2000) New Lateral Torsional Buckling Curves kLT - Numerical Simulations and Design Formulae, European Convention for Constructional Steelwork Technical Committee No. 8
8. Kim YD (2010) Behavior and design of metal building frames using general prismatic and web- tapered steel I-section members. Doctoral dissertation, School of Civil and Environmental Engineering, Georgia Institute of Technology
9. Liu Y, Gannon L (2009) Experimental behavior and strength of steel beams strengthened while under load. J Constr Steel Res 65:1346–1354
10. Liu Y, Gannon L (2009) Finite element study of steel beams reinforced while under load. Eng Struct 31(11):2630–2642
11. Wu Z, Grondin GY (2002) Behaviour of steel columns reinforced with welded steel plates. Structural Engineering Report 250, Department of Civil & Environmental Engineering, University of Alberta
12. Wang Y-Q, Zong L, Zhu R-X, Liu X-Y, Shi, Y-J (2015) Behavior of I-section steel beam welding reinforced while under load. J Constr Steel Res 106:278–288

Origami Enabled Pill-Bug Inspired Tuned-Mass Dampers

A. C. Baruah and A. C. Sychterz

1 Introduction

Adaptive structures can alter their form, configuration, and properties based on environmental conditions. Deployability of such structures has found application in the field of civil engineering for bridges, roof systems [1], and emergency infrastructure [28]. Deployable structures provide an appealing solution for aerospace [29] and extra-terrestrial [23, 26] applications. Dynamic characterization of structures [22] presents computational challenges due to large changes in shape, and therefore geometric compatibility requirements result in non-linear behavior [15]. This limits the application of classical finite element approaches.

Origami, the ancient art of paper folding, has inspired engineering devices and structures over the past few decades. Applications include deployable solar panels [24, 39], sandwich panel cores [3, 30], self-deployable stent-grafts [20], and configurable metamaterials [32]. The concepts of origami have been applied for the development of different self-folding structures [27], that can fold and/or unfold without any external manipulation. Significant contributions by Tachi and Miura towards cellular origami have led to the development of fold patterns named after them. The theory behind flat-foldable origami [16] has extended towards understanding the geometry of rigid-foldable origami [38] and the kinematics of folded metamaterials [31]. Kinematic analysis of origami by modeling the creases as hinges and panels as rigid links were successful in providing insight into the rigid foldability of crease patterns [21]. A similar approach using bar and hinge models was studied by [11–13] and [23] for the analysis of scalable origami structures. However, the fabrication,

A. C. Baruah (✉) · A. C. Sychterz
Civil and Environmental Engineering, University of Illinois at Urbana-Champaign, Champaign, IL, USA
e-mail: abaruah2@illinois.edu

S. Walbridge et al. (eds.), *Proceedings of the Canadian Society of Civil Engineering Annual Conference 2021*, Lecture Notes in Civil Engineering 244,
https://doi.org/10.1007/978-981-19-0656-5_7

testing, and analysis of adaptive deployable origami for civil infrastructure are yet to be achieved.

Tuned-mass dampers (TMDs) are oscillators mounted on a structure to reduce the dynamic response of the structure by absorbing kinetic energy from the system. The concept of multiple TMDs, with natural frequencies distributed over a frequency range, is used to analyze their vibration control capabilities for structures subjected to wide-band input [17]. Recent work includes studies conducted on the control of structural response under seismic loading [2], including active and semi-active vibration control methods [14]. The large mass of conventional TMDs limits its application for lightweight structures and systems with compliant members.

Biomimetics is the study and development of synthetic mechanisms that mimic the structure or functionality of biological organisms. The adaptation of natural conformations to engineering applications is leading to profound changes in the design of structural systems. Enabled by origami techniques for deformability, biomimetic structures can provide novel solutions to practical engineering challenges in terms of sustainability.

Dynamic relaxation method proposed by Otter [25] and Day [8], provides a suitable approach for form-finding and analysis of structures with a high degree of structural non-linearity [7]. It is a vector-based pseudo-dynamic analysis that does not require matrix inversion and results in a static solution. [4, 5] modified the method to include kinetic damping and to improve convergence. This method has also been used to simulate the behavior of adaptive structures [9, 10, 18, 19, 34]. However, the geometry of the origami-enabled pill-bug tuned-mass damper (OPB-TMD) introduces novel challenges to the dynamic relaxation method because of complex kinematic degrees of freedom at its different stages of curling.

The paper provides a comparison of the DR model with the finite element model in addition to experimental data for the OPB-TMD. A program called SOFiSTiK is used to develop the finite element model for dynamic analysis of the OPB-TMD structure. A 3D-printed model comprising of hard polymer panels and flexible rubber hinges is used for the experimental study of the cable-actuated structure. The research focuses on a differential stiffness mechanism for the adaptive TMD capable of altering its shape in response to seismic loads. An overview of the simulated origami structure is provided and is followed by the results of the preliminary experimental study. This is used to validate the results from the DR model for dynamic characterization of the OPB-TMD and its behavior at different configurations.

2 Structural Description

Origami-enabled Pill-Bug Tuned Mass Damper (OPB-TMD) is inspired by the morphological characteristics of the pill-bug (Armadillidiidae), a species of woodlice. The pill-bug rolls its body into a ball shape, a process called conglobation, when triggered by stimuli as shown in Fig. 1. This ability to roll into a ball serves as the basis for the design of the adaptive OPB-TMD structure.

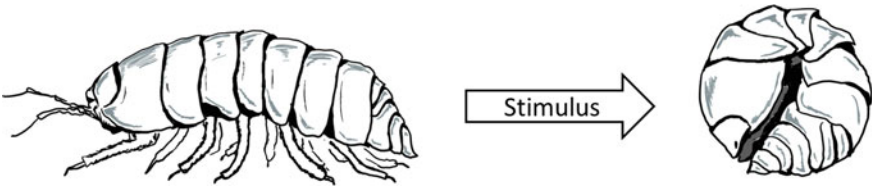

Fig. 1 Rolling of a pill-bug (*Armadillidiidae*) in response to external stimulus

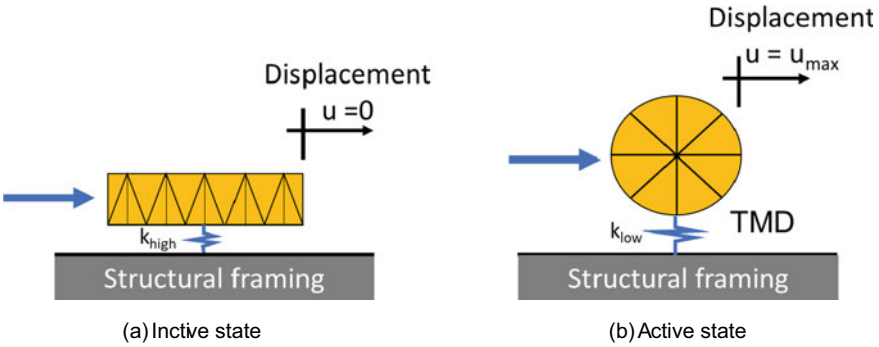

Fig. 2 OPB-TMD structure in active and inactive state

The OPB-TMD will initially be in an inactive unrolled state as shown in Fig. 2(a). The spring stiffness in this configuration is high (k_{high}) and the system behaves as a rigid body with the base structure. In the curled state as shown in Fig. 2(b), the spring stiffness value is low (k_{low}). Thus, the OPB-TMD reacts to the inertial response in the base structure and provides attenuation for vibrations.

3 Simulation of Origami Pill-Bug Tuned-Mass Damper Structure

A module of the OPB-TMD structure is shown in Fig. 3 depicting different element and fold types. Fold lines are categorized into mountain, valley, side, and ridge fold. Four-node five-bar, N4B5, model is used for each rectangular panel of the OPB-TMD structure. Panels are modeled with a diagonal element to allow for panel bending and non-rigid foldability [31].

The structure shown in Fig. 4(a) is a five-module OPB-TMD topology. A partially folded configuration of the structure is used as the base model with an overall width of 15.0 cm and length of 16.2 cm. The OPB-TMD structure is laterally restrained in the x, y, and z-direction at Node 1 and Node 16 as shown in Fig. 4(b). Nodes 2–7, 9, 11, 13, 15, 17–22, 24, 26, 28 & 30 are restrained in the y-direction to facilitate

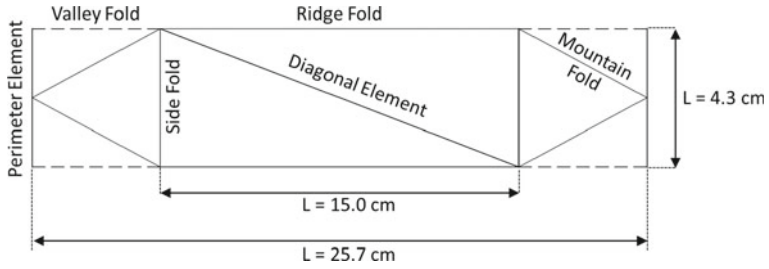

Fig. 3 A module of the OPB-TMD structure showing different element and fold types. N4B5 bar and hinge model is used for the rectangular panels

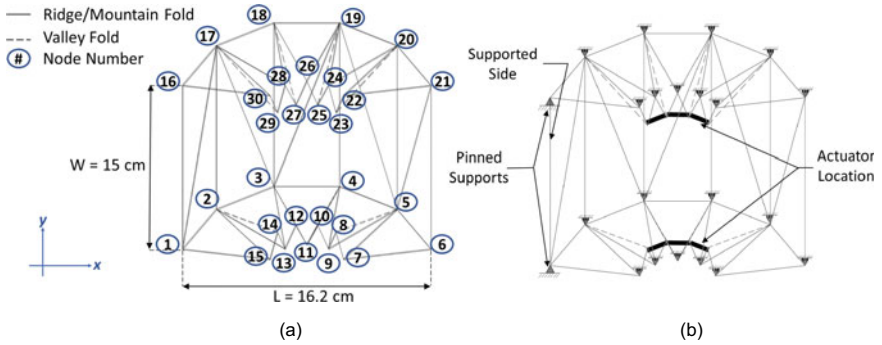

Fig. 4 Five-OPB-TMD structure in partially folded configuration detailing (a) fold-lines and node numbers, (b) support conditions and actuator locations

the target folding pattern. Actuators are located at the base of each valley fold as shown in Fig. 4(b) with thick black lines, connecting Nodes 8 through 14 and Nodes 23 through 29. The structure is actuated in the x-direction as shown in Fig. 4. Nodal displacement at Node 6 and 21 are further used for comparison.

The structure is actuated using continuous cables [37] and the degree of curing of the OPB-TMD can be controlled by varying the length of these actuation cables. The actuation is carried out at a slow and constant rate where the inertial effects due to actuation are negligible. Simulation of the structure is assumed to have reach static equilibrium at each step of the deployment process. A dynamic relaxation formulation is used for quasi-static analysis, and a finite element model is used for the dynamic analysis of the OPB-TMD structure.

3.1 Simulation Using Dynamic Relaxation Method

A new module within the dynamic relaxation (DR) method developed for the actuated Miura-Ori origami structure successfully characterizes origami hinge stiffness and

is suitable for application in iterative actuation algorithms for large structures [35]. It is a pseudo-dynamic analysis that includes fictitious inertia and damping terms. An augmented equation of motion is used to determine a new static equilibrium of the artificially damped structure. The DR module is capable of handling cable friction in the structure [6]. Characterization of folding and bending stiffness in origami within the dynamic relaxation methods is applied to the origami pill-bug.

Preliminary study to determine the folding stiffness (K_F) and bending stiffness (K_B) has been conducted for the OPB-TMD structure [11] as shown in Table 1. To simplify the design, the folding stiffness (K_F) for the valley and mountain folds as shown in Fig. 3, were assigned to be equal. Since the model is restrained at 11 nodes at each side of the model, the desired folding pattern could be achieved by using the same folding stiffness for the side folds. A stiffness ratio of $K_F/K_B = 0.1$ [31] was found to be suitable for the study [35]. The partially folded five-module N4B5 model serves as the base model for simulation. Material properties and stiffness values for the OPB-TMD model are listed in Table 1.

Figure 5 shows the OPB-TMD structure at its initial unrolled and final rolled configuration from the modified DR method. The blue dashed line corresponds to the unfolded state, and the solid black line represents the rolled state of the OPB-TMD. The dimensions of the reference axis in global x, y and z direction are given in cm. The nodal position of Node 6 and Node 21 is used to determine the length of the structure. As shown in Fig. 5, the length of the structure changes from 18.9 cm for the unrolled (inactive) configuration to 12.5 cm for the rolled (active) configuration. Thus, the length of the structure decreases by 6.4 cm (33.9%) between these two configurations. Curling and/or flattening of the model is achieved by controlling the length of the actuator cable.

3.2 *Simulation Using Finite Element Method*

A finite-element (FE) program called [33] is used to model the elements of the OPB-TMD structure. To account for folding and bending stiffnesses in the FE model, rotational springs are assigned at the nodes of the structure. The in-plane stretching

Table 1 Properties for the OPB-TMD model and associated values

Properties		
Thickness, t	0.39	*(mm)*
Young's Modulus, E	11	*(GPa)*
Density, γ	1201	*(kg/m^3)*
Poisson's Ratio, ν	0.2	–-
Bending Stiffness, K_B	94.4	*(N/mm)*
Folding Stiffness, K_F	9.4	*(N/mm)*

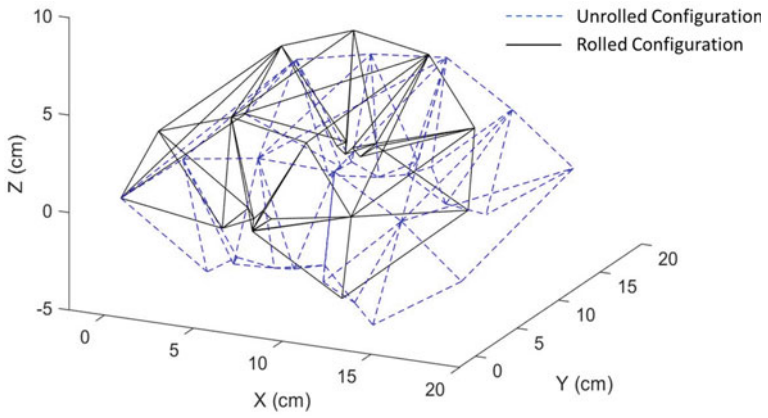

Fig. 5 Initial unrolled (dashed blue line) and final rolled configuration (solid black line) of the OPB-TMD structure from DR method

and shearing of the rectangular panels are approximated with a series of rotational springs at the end nodes of the diagonal elements.

Rotational spring with stiffness $K_F/2$ acting about the local y-axis of the element is assigned at end nodes of each valley and mountain fold. Torsional moment about the local x-axis is released. Moment about the local z-axis is also released at both the end nodes. To approximate the effect of panel bending, rotational stiffness is provided at the end nodes of the diagonal elements. The effective stiffness towards bending of the panel face is calculated as K_B, [11]. Springs with rotational stiffness of $K_B/2$, acting about the local y-axis, are assigned at the nodes. Torsion about the local x-axis is neglected and rotational moment is released about the local z-direction of the diagonal element. This model is used to validate the unrolled and rolled configuration of the OPB-TMD structure obtained from DR method.

The first 6 frequencies represents the free kinematic modes, allowing for rigid-foldability of the structure [11]. The four subsequent frequencies correspond to the structural modes for the OPB-TMD and are tabulated in Table 2.

Table 2 Structural modes and corresponding frequencies for the OPB-TMD model

Structural mode	Frequency (Hz)
1	3.99
2	5.08
3	7.56
4	13.45

4 Experimental Study

This section describes the experimental structure and setup for the study. A bar is fixed to the base table and the model is attached to the bar at one side as shown in Fig. 6. The actuator cables pass over a pulley mounted on a clamp. These are secured to the base table using a T-slotted rail and two corner brackets. For measurement, a black and white checkerboard with one-inch squares was used. This is to measure the structural displacement due to actuation as well as for future image detection algorithms for precise measurements.

As shown in Fig. 6, the preliminary model for the experimental study is made from a dense poster board material with a thickness of 0.39 mm. The material properties for the OPB-TMD model are listed in Table 1. The folding stiffness at the side folds is increased by reinforcing them with cellophane tape to attain the target folding pattern.

Figure 7 shows a 3D model of the OPB-TMD was printed using the Stratasys Object500 3D printer for better experimental results. The 3D model consists of hard polymer material called VeroYellow-V with a yield strength of 65 MPa to represent the rectangular panels and their panel-bending stiffness. To represent the fold lines, the flexible rubber hinges are printed using Agilus, which has a yield strength of 2.5 MPa. The thickness of the rubber hinges governs the stiffness of the fold and accounts for variable stiffness in the model.

The experimental model is actuated by suspending weights on a bar. For uniform actuation on either side, both actuating cables are connected to the same bar. Weights are incrementally applied in steps from 10 to 100 g. Actuation is carried out at a slow and steady rate to avoid inertial effects. The test results are recorded by using a camera, mounted on top of the experimental setup for minimal image and/or video distortion and accurate measurements.

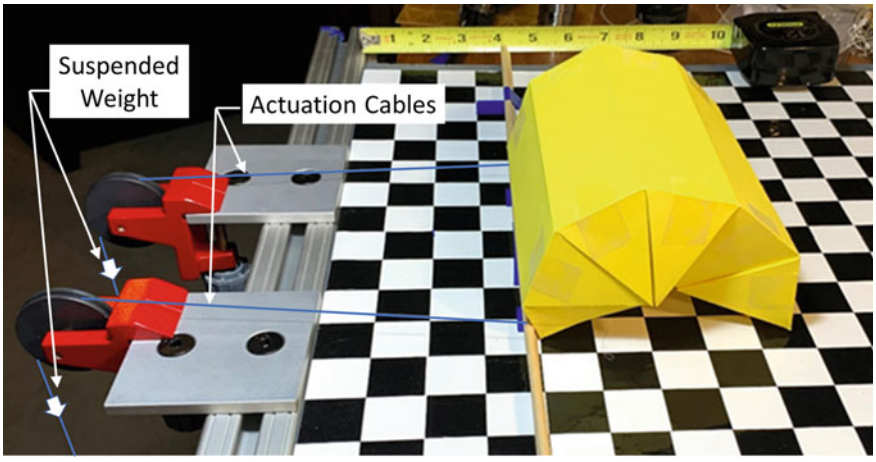

Fig. 6 Setup for experimental study of the five-module OPB-TMD structure

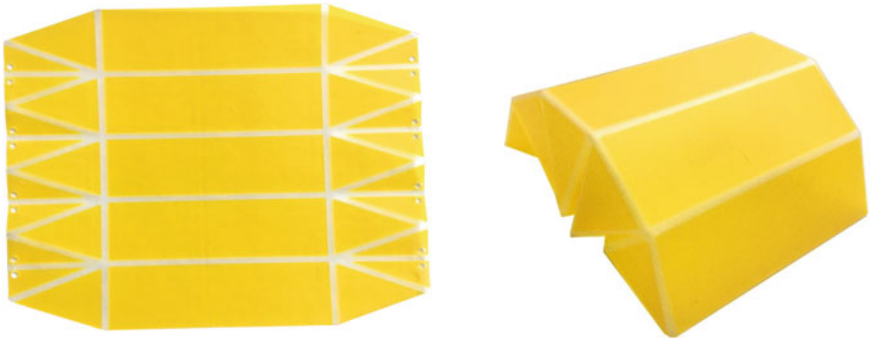

Fig. 7. 3D printed model of the five-module OPB-TMD structure for experimental study

5 Results and Comparison

Validation of the new module in DR was completed using FE simulation. To account for folding and bending, equivalent rotational spring definitions are compared between DR and FE simulation in the static domain. A comparison between the simulation results from DR and the experimental data is also presented for the OPB-TMD. The actuation of the structure in the longitudinal direction is mostly linear and does not show any significant pitch. The change in length of the structure is hence calculated as the average displacement of Node 6 and 21 between the initial uncurled and the final curled configuration of the five-module OPB-TMD model.

As shown in Table 3, the results from the DR simulation and the experimental model are compared. The difference in the initial unrolled length and the final rolled length for the two models is calculated to be 2.1% and 1.6% respectively. The percentage change in the length of the structure for the simulated and experimental results vary by only 0.4%. The effects of joint and cable friction are not significant considering the size of the model. The panels remain mostly planar during the curling process and limit non-rigid folding effects on the structure. Therefore, the form-finding model using the modified DR method gives satisfactory results for characterizing the behavior of the five-module OPB-TMD model.

Table 3 Comparison of the percentage change in structural length for simulated and experimental results

		Simulated (dynamic relaxation)	Experimental	Difference (%)
Initial unrolled length	*(cm)*	18.9	18.5	2.1
Final rolled length	*(cm)*	12.5	12.3	1.6
Change in structural length	*(%)*	33.9	33.5	

6 Conclusion

The dynamic relaxation with the new module for origami joint stiffness is a successful method to solve for quasi-static form-finding of the origami pill-bug tuned-mass damper (OPB-TMD). The variable stiffness model provides an accurate representation of the actual structure and achieves the target folding pattern. A comparison between the simulated and experimental results provides a useful starting point for characterizing the dynamic behavior and kinematic properties of the OPB-TMD. However, further research is required towards understanding the origami mechanics, actuation, and control techniques of the adaptive structure along with comprehensive study in the area of robotic tuned-mass dampers. The uncertainties due to friction on large and mid-scale structures also needs to be explored. A spatial grid of such OPB-TMDs also has the potential to provide information regarding the dynamic response of irregularly shaped and large-span roof structures for structural health monitoring applications.

References

1. Akgün Y, Gantes CJ, Sobek W, Korkmaz K, Kalochairetis K (2011) A novel adaptive spatial scissor-hinge structural mechanism for convertible roofs. Eng Struct 33(4):1365–1376. https://doi.org/10.1016/j.engstruct.2011.01.014
2. Aldemir U, Yanik A, Bakioglu M (2012) Control of structural response under earthquake excitation. Comput Aided Civil Infrastruct Eng 27(8):620–638. https://doi.org/10.1111/j.1467-8667.2012.00776.x
3. Ballard ZC, Thrall AP, Smith BJ (2016) Behavior of folding sandwich panel structures: impact of ground conditions, anchorage, and panel warping. Constr Build Mater 112(June):1110–1122. https://doi.org/10.1016/j.conbuildmat.2016.03.035
4. Barnes MR (1999) form finding and analysis of tension structures by dynamic relaxation. Int J Space Struct 14(2):89–104. https://doi.org/10.1260/0266351991494722
5. Barnes MR, Adriaenssens S, Krupka M (2013) A novel torsion/bending element for dynamic relaxation modeling. Comput Struct 119:60–67. https://doi.org/10.1016/j.compstruc.2012.12.027
6. Nizar BHA, Sychterz AC, Smith IFC (2017) A dynamic-relaxation formulation for analysis of cable structures with sliding-induced friction. Int J Solids Struct. 126–127:240–51.https://doi.org/10.1016/j.ijsolstr.2017.08.008
7. Cassell AC, Hobbs RE (1976) Numerical stability of dynamic relaxation analysis of non-linear structures. Int J Numer Meth Eng 10(6):1407–1410. https://doi.org/10.1002/nme.1620100620
8. Day AS (1965) An introduction to dynamic relaxation. Engineer 219:218–222
9. Domer B, Smith IFC (2005) An active structure that learns. J Comput Civ Eng 19(1):16–24. https://doi.org/10.1061/(asce)0887-3801(2005)19:1(16)
10. Fest E, Shea K, Smith IFC (2004) Active tensegrity structure. J Struct Eng 130(10):1454–1465. https://doi.org/10.1061/(asce)0733-9445(2004)130:10(1454)
11. Filipov ET, Liu K, Tachi T, Schenk M, Paulino GH (2017) Bar and hinge models for scalable analysis of origami. Int J Solids Struct 124:26–45. https://doi.org/10.1016/j.ijsolstr.2017.05.028
12. Filipov ET, Chun J, Paulino GH, Song J (2016) Polygonal multiresolution topology optimization (PolyMTOP) for structural dynamics. Struct Multidiscip Optim 53(4):673–694. https://doi.org/10.1007/s00158-015-1309-x

13. Filipov ET, Tachi T, Paulino GH, Weitz DA (2015) Origami tubes assembled into stiff, yet reconfigurable structures and metamaterials. Proc Natl Acad Sci USA 112(40):12321–12326. https://doi.org/10.1073/pnas.1509465112
14. Fisco NR, Adeli H (2011) Smart structures: Part I - active and semi-active control. Scientia Iranica. Sharif University of Technology. https://doi.org/10.1016/j.scient.2011.05.034
15. Gantes CJ, Connor JJ, Logcher RD, Rosenfeld Y (1989) Structural analysis and design of deployable structures. Comput Struct 32(3–4):661–669. https://doi.org/10.1016/0045-7949(89)90354-4
16. Hull T (1995) On the Mathematics of Flat Origamis. https://www.researchgate.net/publication/2357716.
17. Igusa T, Xu K (1994) Vibration control using multiple tuned mass dampers. J Sound Vib 175(4):491–503. https://doi.org/10.1006/jsvi.1994.1341
18. Kmet S, Platko P, Mojdis M (2012) Analysis of adaptive light-weight structures. Procedia Eng 40:199–204. https://doi.org/10.1016/j.proeng.2012.07.080
19. Korkmaz S (2011) A review of active structural control: challenges for engineering informatics. Comput Struct 89(23–24):2113–2132. https://doi.org/10.1016/j.compstruc.2011.07.010
20. Kuribayashi K, Tsuchiya K, You Z, Tomus D, Umemoto M, Ito T, Sasaki M (2006) Self-deployable origami stent grafts as a biomedical application of Ni-Rich TiNi shape memory alloy foil. Mater Sci Eng, A 419(1–2):131–137. https://doi.org/10.1016/j.msea.2005.12.016
21. Lang RJ, Wang-Iverson P, Yim M (2016) Origami 5: fifth international meeting of origami science, mathematics, and education. https://doi.org/10.5860/choice.47-5704
22. Li T, Guo J, Cao Y (2011) Dynamic characteristics analysis of deployable space structures considering joint clearance. Acta Astronaut 68(7–8):974–983. https://doi.org/10.1016/j.actaastro.2010.08.039
23. Liu, K, Paulino GH (2017) Nonlinear mechanics of non-rigid origami: an efficient computational approach. Proc Roy Soc A Math Phys Eng Sci 473(2206). https://doi.org/10.1098/rspa.2017.0348
24. Miura K, Furuya H, Suzuki K (1985) Variable geometry truss and its application to deployable truss and space crane arm. Acta Astronaut 12(7–8):599–607. https://doi.org/10.1016/0094-5765(85)90131-6
25. Otter JRH (1965) Computations for prestressed concrete reactor pressure vessels using dynamic relaxation. Nucl Struct Eng 1(1):61–75. https://doi.org/10.1016/0369-5816(65)90097-9
26. Pellegrino S (1995) Large retractable appendages in spacecraft. J Spacecr Rocket 32(6):1006–1014. https://doi.org/10.2514/3.26722
27. Peraza-Hernandez EA, Hartl DJ, Malak RJ, Lagoudas DC (2014) Origami-inspired active structures: a synthesis and review. Smart Mater. Struct 23. https://doi.org/10.1088/0964-1726/23/9/094001
28. Pérez-Valcárcel J, Suárez-Riestra F, Muñoz-Vidal M, López-César I, Freire-Tellado MJ (2020) A new reciprocal linkage for expandable emergency structures. Structures 28:2023–2033. https://doi.org/10.1016/j.istruc.2020.10.008
29. Puig L, Barton A, Rando N (2010) A review on large deployable structures for astrophysics missions. Acta Astronaut 67(1–2):12–26. https://doi.org/10.1016/j.actaastro.2010.02.021
30. Sab K, Lebée A (2010) Transverse shear stiffness of a chevron folded core used in sandwich construction. Int J Solids Struct 47(18–19):2620–2629. https://doi.org/10.1016/j.ijsolstr.2010.05.024
31. Schenk M, Guest SD (2013) Geometry of miura-folded metamaterials. Proc Natl Acad Sci USA 110(9):3276–3281. https://doi.org/10.1073/pnas.1217998110
32. Silverberg JL, Evans AA, McLeod L, Hayward RC, Hull T, Santangelo CD, Cohen I (2014) Using origami design principles to fold reprogrammable mechanical metamaterials. Science 345(6197):647–650. https://doi.org/10.1126/science.1252876
33. SOFiSTiK (2020) SOFiSTiK AG
34. Sultan C, Skelton R (2003) Deployment of tensegrity structures. Int J Solids Struct 40(18):4637–4657. https://doi.org/10.1016/S0020-7683(03)00267-1

35. Sychterz AC (2019) Actuator optimization for adaptive origami structures. In: SES-2019 Conference, St. Louis
36. Sychterz AC, Smith IFC (2017) Joint friction during deployment of a near-full-scale tensegrity footbridge. J Struct Eng 143(9):04017081. https://doi.org/10.1061/(asce)st.1943-541x.0001817
37. Sychterz AC, Smith IFC (2018) Deployment and shape change of a tensegrity structure using path-planning and feedback control. Frontiers Built Environ 4(August):45. https://doi.org/10.3389/fbuil.2018.00045
38. Tachi T (2016) Designing rigidly foldable horns using bricard's octahedron. J Mech Rob 8(3). https://doi.org/10.1115/1.4031717
39. Zirbel SA et al (2013) Accommodating thickness in origami-based deployable arrays. In: Proceedings of the ASME design engineering technical conference, vol 6 B. https://doi.org/10.1115/DETC2013-12348

Flexural Cyclic Testing of Precast Concrete Tunnel Segments Reinforced with GFRP Bars

B. Ibrahim, S. Mousa, H. M. Mohamed, and B. Benmokrane

1 Introduction

The use of precast concrete tunnel lining systems in tunneling construction projects has been rising over the conventional in-site lining technique, because of its economic efficiency [13]. Where the fabrication of Precast concrete tunnel lining includes repetitive steps of batching and casting of concrete, which ultimately results in wastage reduction compared to the traditional in-site concrete lining. Moreover, precast concrete tunnel lining speeds the construction process along with ensuring highest quality due to enhanced control during precast segment fabrication in precast plants [8].

For durable and serviceable construction solution, the steel reinforcement in the conventional concrete structure is initially coated and protected against corrosion by the concrete alkalinity. However, for structures subjected to aggressive environmental conditions, such as exposed to de-icing salts, combinations of moisture, temperature and chlorides reduce the concrete alkalinity, and result in the steel reinforcing corrosion. Fiber-reinforced polymers (FRP) could be used as an alternative for the steel in the reinforced concrete (RC) structures, to avoid the structures' deterioration and loss of serviceability due to corrosion. Besides, the problem of the electromagnetic interference and steel corrosion can be avoided, as the FRP are nonmagnetic and noncorrosive materials. Moreover, FRP materials exhibit several advantages, such as high tensile strength, that make them suitable for the use as concrete structural reinforcement [2, 3, 10–12, 14, 15, 19, 20]. Because of the structural effects of the FRP materials' bond behavior [9, 21], this type of reinforcement is not apposite for all applications. However, it appears appropriate for the reinforcement of the tunnel segments, both for the temporary and permanent elements [16].

B. Ibrahim (✉) · S. Mousa · H. M. Mohamed · B. Benmokrane
Université de Sherbrooke, Sherbrooke, Quebec, Canada
e-mail: basil.Ibrahim@Usherbrooke.ca

S. Walbridge et al. (eds.), *Proceedings of the Canadian Society of Civil Engineering Annual Conference 2021*, Lecture Notes in Civil Engineering 244,
https://doi.org/10.1007/978-981-19-0656-5_8

Current design provisions of CSA S806 [5], CSA S6 [4] and ACI 440.1R [1] are not applicable to precast segmental tunnel linings reinforced internally with FRP bars. Recently, few studies investigated the possibility of using the glass FRP (GFRP) reinforcement in the precast concrete tunnel lining segments [6, 7, 16–18]. In order to examine the feasibility and efficiency of using GFRP instead of steel as flexural, shear, and compression reinforcements for precast segmental tunnel linings, this study investigates the behavior of precast concrete tunnel segments reinforced with GFRP bars under cyclic flexural loading.

2 Experimental Work

The experimental program of the current study is focusing on studying the efficiency of using GFRP bars as internal reinforcement for precast concrete tunnel segments as an alternative to the conventional steel reinforcement. A full-scale precast concrete tunnel lining segment reinforced with GFRP bars was tested and compared with another control specimen reinforced with conventional steel bars.

2.1 Materials Properties

Both precast concrete tunnel segments were cast using normal-weight concrete with a targeted compressive strength (f'_c) of 35 MPa after 28 days according to ASTM C39. The concrete mix design is shown in Table 1.

The used steel bars for the control specimen are steel bars 15M for the longitudinal reinforcement and steel bars 10M for the transverse reinforcement. For the GFRP reinforced specimen, GFRP bars used in this study were manufactured and developed by Pultrall Inc., Quebec, Canada. The bars have a sand-coated surface to enhance bond and force transfer between bars and concrete. GFRP V-Rod bars No. 5 and No. 4 were used for longitudinal and transverse reinforcement of the segments, respectively. Table 2 presents the mechanical properties for the used steel and GFRP bars as provided by the manufacturer.

Table 1 Concrete mix design

Type of concrete	Cement (kg/m^3)	Sand (kg/m^3)	Limestone 5/10 (kg/m^3)	Superplasticizer (ml/m^3)	Air entrainment (ml/m^3)	Water (L/m^3)	Fiber (kg/m^3)
NSC	450	615	1015	4500	140	170	–

Table 2 Mechanical properties of the GFRP and steel reinforcement

	Bar size	Diameter (mm)	Area (mm^2)	Elastic tensile modulus (GPa)	Tensile strength (MPa)	Tensile strain (%)
GFRP bars	#4	13	127	46	$f_f = 1000$	2.17
	#5	15	198	46	$f_f = 1000$	2.17
Steel bars	10M	11	100	200	$f_y = 480$	0.24
	15M	16	200	200	$f_y = 460$	0.23

Table 3 Test matrix and specimen details

Specimen ID	f_c' (MPa)	Bar and stirrup type	Flexural reinforcement		Shear reinforcement	
			Bottom	Top	Bar size	Spacing mm
GFRP	35	GFRP	7 No.5	7 No.5	#4	200
Steel	35	Steel	7 bars 15M	7 bars 15M	10M	200

2.2 Test Specimens

The experimental program involved two full-scale reinforced precast concrete tunnel segments tested under flexural cyclic loads. The GFRP specimen reinforced longitudinally with 7 GFRP bars No. 5 and transversely with No. 4 GFRP ties placed at a spacing of 200 mm. The steel specimen reinforced longitudinally with 7 steel bars 15M and transversely with 10M steel ties placed at a spacing of 200 mm. Table 3 below summarizes the test matrix and specimens' details for this experimental study.

The length and width of segments are 3100 and 1500 mm, respectively, while the thickness is 250 mm. Figure 1 shows the reinforcement details of the GFRP specimen.

2.3 Test Setup and Instrumentation

Quasi-static compressive loading has been applied in terms of percentage of calculated maximum displacement. Two cycles of loading and unloading were conducted for 1.25%, 2.5%, 5%, 10%, 25%, 50%, and 75% of maximum estimated displacement. Subsequently, one cycle of loading up to failure was conducted.

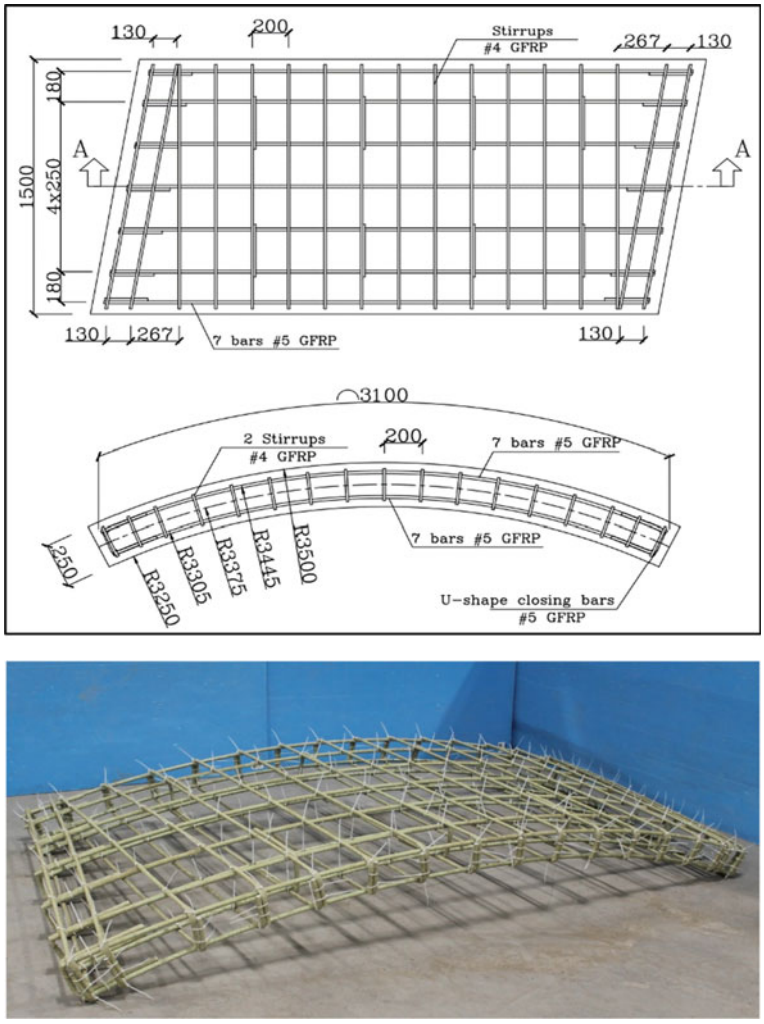

Fig. 1 Details of the GFRP specimen

The test setup was designed and fabricated at the University of Sherbrooke's CFI structural laboratory, as shown in Fig. 2. The specimens were loaded with three-point bending load using 11,000 kN capacity MTS universal testing machine attached to a spreader beam. The load was applied at a displacement-controlled rate of 0.8 mm/min. The mid- and quarter-span deflections were measured using linear potentiometers (POTs). An automatic data-acquisition system monitored by a computer was used to record the readings.

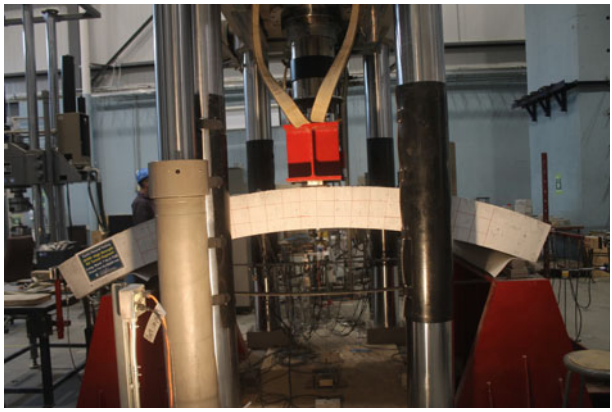

Fig. 2 Test setup

Table 4 Experimental test results

Specimen ID	Load at failure, (kN)	Type of failure	Ultimate load, (kN)	Deflection at ultimate load (mm)	Ultimate deflection (mm)
GFRP	271	Concrete crushing	271	52.8	52.8
Steal	140	Yielding	252	56.3	92.3

3 Experimental Results and Discussion

3.1 Failure Modes and Load Capacity

Table 4 provides flexural capacity and mode of failure for the tested specimens. The failure of the GFRP specimen occurred by concrete crushing in the compression zone. On the other hand, the steel specimen failed due to steel yielding, followed by concrete crushing. Figure 3 provides the cracking patterns at failure for both specimens. The first vertical flexural crack in the GFRP specimen initiated in the tension zone under the point of loading at a load level of 60 kN in the first 5% of the maximum displacement cycle. Beyond the first cracking load, additional flexural cracks developed in the tension zone of the GFRP specimen in the 10% and 25% of the maximum displacement cycles. With further loading, in the 50% of the maximum displacement cycle, the flexural cracks became wider and propagated upward, while some new cracks started to develop in the shear span. Before failure occurred in the GFRP specimen, the cracks along the shear span started to incline towards the loading point. The peak load recorded at the concrete crushing was 271 kN for the GFRP specimen. In contrast, the yielding of the tension bars in the steel specimen resulted in wider concentrated cracks at the tension zone. Yielding of the longitudinal

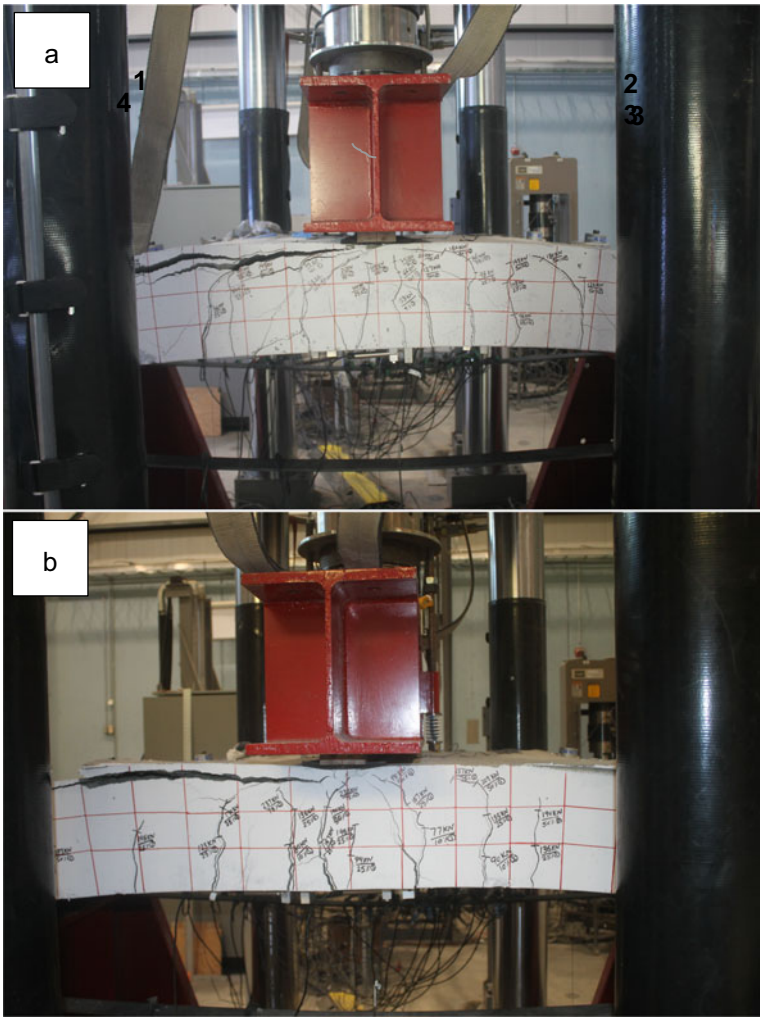

Fig. 3 Failure mode: (a) GFRP specimen, (b) steel specimen

reinforcement at the tension zone occurred at a load level of 140 kN in the first 50% of the maximum displacement cycle, followed by a reduction in the specimen's stiffness. Furthermore, by reaching a load level of about 252 kN in, the concrete crushed in the compression zone.

3.2 Load-Deflection Behaviour

Figure 4 shows the load deflection response of GFRP and steel specimens. Before cracking, an identical linear load-deflection behavior was observed for the GFRP and steel specimens. After cracking, the stiffness of the GFRP specimen reduced with almost linear load-deflection behavior up to the initiation of concrete crushing at the compression zone. After that, a sudden load drop occurred, indicating the concrete crushing failure had transpired at a load level of 271 kN. Interestingly, the specimen did not lose its load carrying capacity after the concrete crushing. Instead, it continued to sustain additional loads. This behavior can be attributed to the contribution of the compression bars that enhanced the specimen ductility and strength. The steel specimen has also initial linear load deflection behavior corresponding to the uncracked condition of the specimen. However, the specimen's stiffness has reduced, by the yielding of the longitudinal reinforcement in the tension zone at a load level of 140 kN, followed by a gradual decrease in overall stiffness. Figure 4 shows that, in the first 50% of the maximum displacement cycle, the steel specimen experienced significant degradation in strength up to the concrete crushing. The steel specimen reached a load level of 252 kN by the time the concrete crushed at the compression zone. Moreover, the GFRP specimen recovered most of their deflection during the unloading of the 50% and 75% of the maximum displacement cycles. While a permanent deflection was recorded in the unloading of the steel specimen by reaching the 50% of the maximum displacement cycle, due to the yielding of the steel bars in the tension zone.

Figure 5 shows the envelope load-deflection curves for the GFRP and steel specimens. After concrete crushing at peak load level of 271 kN, the GFRP specimen continued to carry loads until a second drop in the loading occurred. The GFRP specimen load at the maximum displacement was 263 kN. On the other hand, the yielding

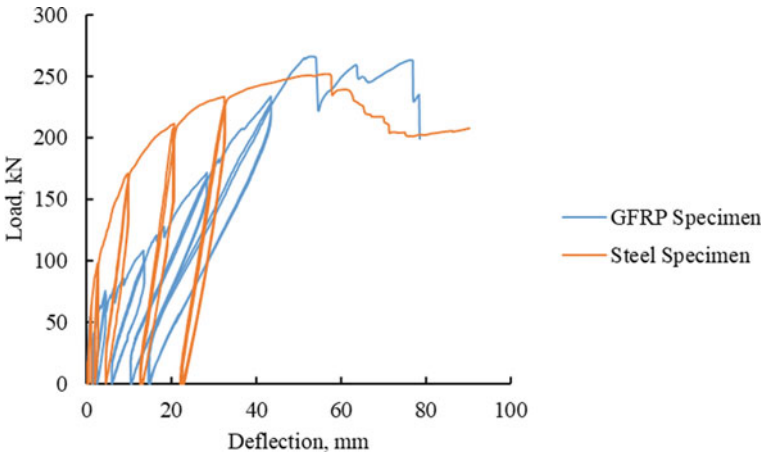

Fig. 4 Load-deflection behavior for both specimens

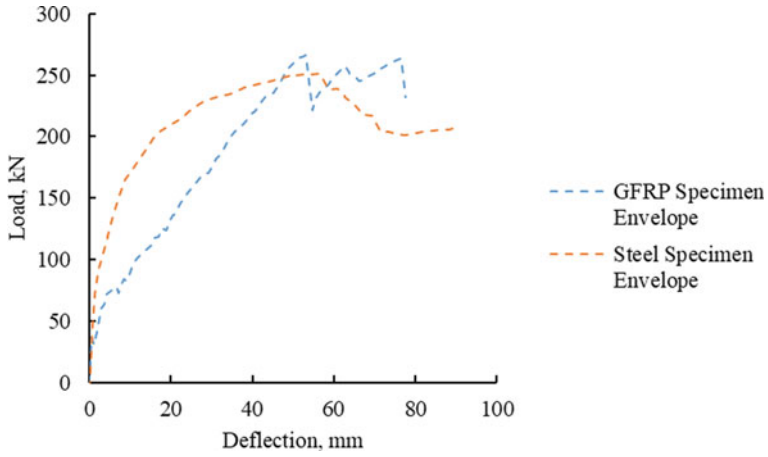

Fig. 5 Envelope behavior for both specimens

and peak loads for the steel specimen were 140 and 252 kN respectively. Overall, the flexural strength at concrete crushing of the GFRP specimen was almost 1.8 times greater than that of the steel specimen at steel yielding with similar reinforcement.

4 Conclusions

A full-scale precast concrete tunnel lining segment reinforced with GFRP bars was tested and compared with another control specimen reinforced with the conventional steel bars. Based on test results, the following conclusions were drawn:

- The GFRP specimen behaved linearly until cracking and almost linearly between cracking and concrete crushing, with reduced stiffness. Interestingly, the specimen did not lose its load-carrying capacity immediately after concrete crushing. Instead, it continued to sustain additional loads. This behavior can be attributed to the contribution of the compression bars that enhanced the specimen ductility and strength.
- The failure of the GFRP specimen occurred by concrete crushing, while the steel specimen failure due to steel yielding followed by concrete crushing.
- The flexural strength at concrete crushing of the GFRP specimen was almost 1.8 times greater than that of the steel specimen at steel yielding with similar reinforcement.
- The results of the current study show the efficiency of using GFRP bars as internal reinforcement for precast concrete segmental tunnel linings under cyclic flexural loading as an alternative to the conventional steel reinforcement.

Acknowledgements This research was conducted with funding from the Natural Sciences and Engineering Research Council of Canada (NSERC), Mathematics of Information Technology and Complex Systems (MITACS), the Fonds de recherche du Québec en nature et technologies (FRQ-NT), The Pole de Recherche et d'innovation en Materiaux Avances au quebéc (PRIMA Quebéc) and the Tier-1 Canada Research Chair in Advanced Composite Materials for Civil Structures. The authors are grateful to the precast company (Sym-Tech Béton Préfabriqué, Sainte-Hyacinthe, QC, Canada) and to the GFRP bar manufacturer (Pultrall Inc., Thetford Mines, QC, Canada) for their effective involvement in this project, and to the technical staff of the structural lab in the Department of Civil Engineering at the University of Sherbrooke.

References

1. ACI (American Concrete Institute) (2015) Guide for the Design and Construction of Structural Concrete Reinforced with Fiber-Reinforced Polymer (FRP) Bars. ACI 440, Farmington Hills, MI
2. Benmokrane B, Rahman H (1998) Durability of Fiber Reinforced Polymer (FRP) composites for construction. In: Proceedings of the first international conference (CDCC 1998), Sherbrooke, Quebec, Canada
3. Burgoyne C (2001) Non-metallic reinforcement for concrete structures—FRPRCS-5. In: Proceedings of international conference, Cambridge, UK
4. Canadian Standards Association (2019) Canadian highway bridge design code. CAN/CSA-S6-19
5. Canadian Standards Association (2012) Design and construction of building structures with fibre-reinforced polymers. CAN/CSA-S806-12
6. Caratelli A, Meda A, Rinaldi Z, Spagnuolo S (2016) Precast tunnel segments with GFRP reinforcement. Tunn Undergr Space Technol 60:10–20
7. Caratelli A, Meda A, Rinaldi Z, Spagnuolo S, Maddaluno G (2017) Optimization of GFRP reinforcement in precast segments for metro tunnel lining. Compos Struct 181:336–346
8. Cheong YW, Kwan HP, Hariyanto AD (2005) Quality control in precast production, a case study on Tunnel Segment Manufacture. J Archit Built Environ 33(2):153–164
9. Coccia S, Meda A, Rinaldi Z, Spagnuolo S (2017) Influence of GFRP skin reinforcement on the crack evolution in RC ties. Compos B Eng 119:90–100
10. Cosenza E, Manfredi G, Nanni A (2001) Composites in construction: a reality. VA, 277
11. Dolan CW, Rizkalla SH, Nanni A (1999) Fourth international symposium on fiber reinforced polymer reinforcement for reinforced concrete structures. American Concrete Institute
12. El-Badry M (1996) Advanced composite materials in bridge and structures. In: Proceedings of the Second International Conference ACMBS-II, Montreal, Canada
13. Elliott KS (2019) Precast concrete structures. Butterworth-Heinemann, Oxford
14. Humar JL, Razaqpur AG (2000) Advanced composite materials in bridges and structures. Canadian Society for Civil Engineering
15. Iyer SL, Sen R (1991) Advanced composites materials in civil engineering structures. ASCE
16. Meda A, Rinaldi Z, Spagnuolo S, De Rivaz B, Giamundo N (2019) Hybrid precast tunnel segments in fiber reinforced concrete with glass fiber reinforced bars. Tunn Undergr Space Technol 86:100–112
17. Spagnuolo S, Meda A, Rinaldi Z, Nanni A (2017) Precast concrete tunnel segments with GFRP reinforcement. J Compos Constr 21(5):04017020
18. Spagnuolo S, Meda A, Rinaldi Z, Nanni A (2018) Curvilinear GFRP bars for tunnel segments applications. Compos B Eng 141:137–147
19. Teng JG (2001) FRP composites in civil engineering. In: Proceedings of the international conference on FRP composites in civil engineering, Hong Kong, China, vol 1

20. White TD (1992) Composite materials and structural plastics in civil engineering construction. In: Proceedings of the American society of civil engineers, pp 532–718. ASCE, New York
21. Yoo DY, Kwon KY, Park JJ, Yoon YS (2015) Local bond-slip response of GFRP rebar in ultra-high-performance fiber-reinforced concrete. Compos Struct 120:53–64

Efficiency of Precast Concrete Tunnel Lining Segments Reinforced with GFRP Bars Under Bending Load

S. M. Hosseini, S. Mousa, H. M. Mohamed, and B. Benmokrane

1 Introduction

In mechanical excavated tunnels in soft ground precast concrete tunnel lining (PCTL) segments are placed to support tunnel boring machine (TBM) during advancement. As a result of applied load during construction and service stage, PCTL segments are subjected to bending moment, axial load and shear forces. Tunnels are among the structures with a high service life demand. However, corrosion of conventional steel reinforcement is one of the major causes of damage in steel-reinforced PCTL segments [3]. To deal with the corrosion problem in conventional steel-reinforced concrete elements, replacement of steel reinforcement with glass fiber-reinforced polymer (GFRP) bars is an effective solution [5, 10, 12]. GFRP bars have numerous advantages such as corrosion resistance, chemical resistance, electromagnetic neutrality, high strength-to-weight ratio, high tensile strength, competitive life cycle cost, and fatigue resistance [2, 11]. In addition to the mention advantages, application of GFRP bars in tunnels offer such distinct advantages as reduction in concrete cover, suitability for parts of the tunnel that eventually should be demolished and possibility to create dielectric joints [2, 8]. Possibility of adopting GFRP reinforcement in PCTL segments was investigated by Caratelli et al. [8]. They compared the behavior of a steel-reinforced with a GFRP-reinforced segment under bending and thrust loads. They concluded that the flexural behavior of GFRP-reinforced and steel-reinforced PCTL segments did not have significant difference. However, they observed bar rupture failure mode which is unfavorable for a GFRP-reinforced flexural element according to design standards [2, 7]. In addition, the reported crack width at service stage was higher than allowable crack width in CAN/CSA S6-19. It can be attributed to using smooth GFRP bars in the segments as their bond behavior is weaker than the other surface conditions [2]. Spagnuolo et al. [13] performed a

S. M. Hosseini (✉) · S. Mousa · H. M. Mohamed · B. Benmokrane
Department of Civil and Building Engineering, Université de Sherbrooke, Sherbrooke, QC, Canada
e-mail: Seyed.mohammad.hosseini@usherbrooke.ca

S. Walbridge et al. (eds.), *Proceedings of the Canadian Society of Civil Engineering Annual Conference 2021*, Lecture Notes in Civil Engineering 244,
https://doi.org/10.1007/978-981-19-0656-5_9

simplified check analysis on the specimens tested by Caratelli et al. [8] according to ACI 440.1R-15 and concluded that the simplified check method is suitable to predict the capacity of a tunnel segments reinforced with GFRP bars. The effect of using different prototypes for manufacturing of curvilinear GFRP bars on the behavior of GFRP-reinforced PCTL segments investigated by Caratelli et al. [9]. The proposed prototypes were closed "Ring Reinforcement", "Lattice Reinforcement" and "Wirenet Reinforcement. In addition, they compared the performance of sand-coated GFRP bars with smooth bars. They experienced bar rupture failure mode in all the specimens. They concluded that closed-ring reinforcement yielded the best results among all the tested prototypes. Furthermore, they reported that using sand-coated GFRP bars reduced the maximum crack width at service load by 70% compared to smooth bars.

There are limited studies in the literature regarding to GFRP-reinforced PCTL segments [8, 9, 13, 14]. The observed failure mode in the literature was tension-bar rupture failure mode which is unfavorable for design purposes. Also, the cracking behavior did not satisfy the requirement of design standards. Furthermore, smooth square GFRP bars were used in majority of tested specimens in the literature which is not among the recommended bar surface conditions in ACI 440.1R-15. Therefore, the efficiency of such structural elements needs further investigation before major application tunnelling projects. In this study, the behavior of a GFRP-reinforced PCTL segment was compared with a steel-reinforced one with identical geometry and details. The GFRP-reinforced segment was designed to experience favorable compression failure mode. Also, the utilized GFRP curvilinear bars are sand-coated and produced with a new manufacturing process with improved properties.

2 Experimental Work

2.1 Materials Properties

The specimens in this study were cast using normal strength concrete with 28-days target compressive strength of 40 MPa. Curvilinear sand-coated bars No. 5 (15 mm) with a radius of 3305 and 3445 mm for bottom and top meshes were used as longitudinal reinforcement in GFRP-reinforced specimen, respectively. Curvilinear bars produced with the specified radius using an innovative manufacturing process. To provide end-anchorage for longitudinal bars, sand-coated U-shape bars #5 were used. Transverse reinforcement was provided using sand-coated GFRP closed ties No. 4 (13 mm). Tensile strength, modulus of elasticity, and ultimate strain of the utilized GFRP curvilinear bars were determined by performing tensile test according to ASTM D7205 [4] on the curvilinear bars with the radius of 3305 mm. For steel-reinforced specimen, deformed 15 and 10M steel bars were used as longitudinal and transverse reinforcement. Table 1 reports the mechanical properties of GFRP and steel reinforcement. Figure 1 shows the assembled GFRP cage before casting.

Table 1 Mechanical properties of GFRP and steel reinforcement

Reinforcement type	Bar size	Bar diameter (mm)	Nominal cross-sectional area (mm^2)	Modulus of elasticity (GPa)	Tensile strength (MPa)	Ultimate tensile strain (%)
GFRP curvilinear bars	#5	15	199	53.4	976	1.8
GFRP U-shaped bars[a]	#5	15	199	53.5	1283	2.4
GFRP closed ties[a]	#4	13	127	55.6	1248	2.2
Steel[b]	10M	11.3	100	200	480	0.24
	15M	16	200	200	480	0.24

[a]The reported mechanical properties of GFRP closed ties and U-shaped bars obtained by testing of straight bars manufactured with the same manufacturing process as the bent bars
[b]The reported tensile strength and ultimate tensile strain of steel bars are related to yield point

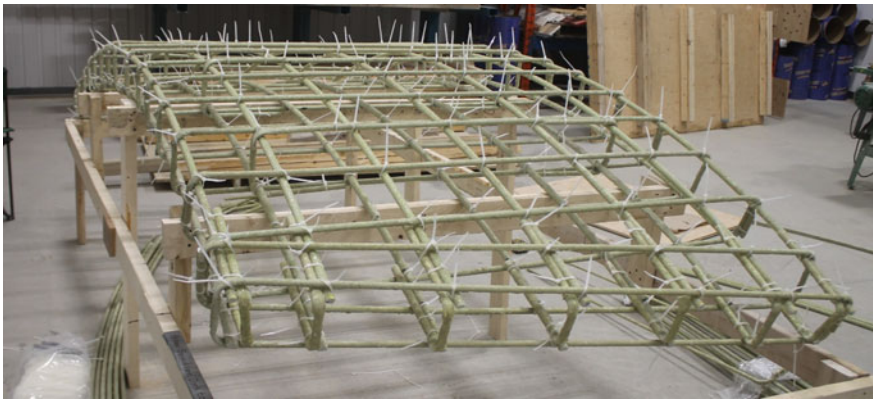

Fig. 1 Assembled GFRP-reinforced PCTL segment cage

2.2 Test Specimens

Two full-scale PCTL segments including one GFRP-reinforced and one steel-reinforced were constructed and tested under bending load. Figure 2 shows the GFRP cage before and during casting. The original tunnel considered in this study was a metro tunnel lining with internal diameter of 6500 mm and external diameter of 7000 mm. A full ring of the considered tunnel constitutes from seven segments with different shapes of rectangular, trapezius, and parallelogram. After consulting with the tunnel design Engineers, the parallelogram shape selected for the specimens in this study. The specimens measured 3100 mm in length (arc length), 1500 mm in width and 250 mm in thickness with an internal and external radius of 3250 and 3500 mm, respectively. The concrete cover was kept constant at 40 mm.

Fig. 2 Casting of the test specimens

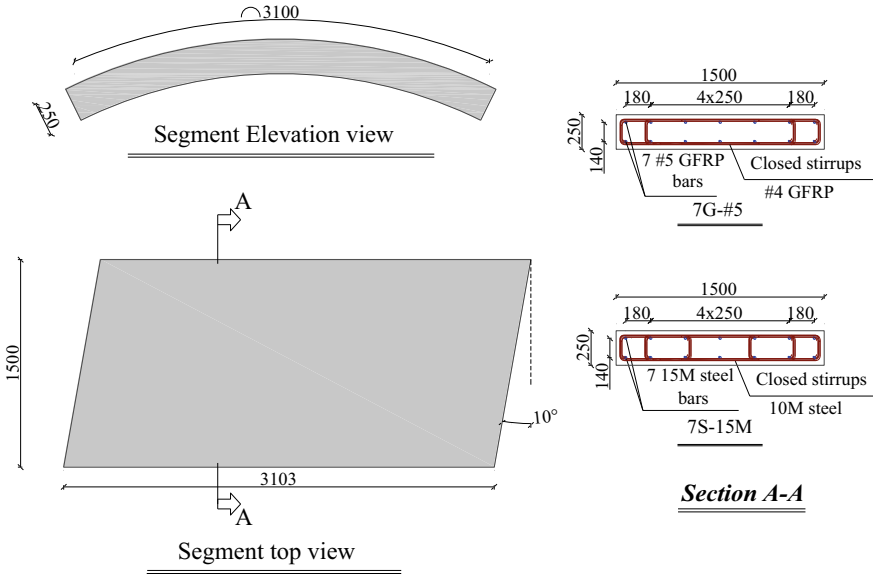

Fig. 3 Specimen details

Figure 3 presents the dimensions and reinforcement details of the specimens. Each specimen comprises from longitudinal reinforcement, transverse ties and end-anchorage U-shape bars. The test matrix and reinforcement details of the tested specimens in this study are presented in Table 2. The two tested specimens had almost identical geometry and reinforcement details to provide possibility of net comparison between GFRP and steel bars in the performance of PCTL segments. To identify the specimens, the first number indicates the number of longitudinal bars. The specimens with steel and GFRP reinforcement are identified with S and G

Table 2 Test matrix and specimen details

Specimen ID	Type of reinforcement	Longitudinal reinforcement	ρ_l (%)	Transverse reinforcement
7G-#5	Glass FRP bars	7 bars #5	0.50	#4 @ 200 mm
7S-15M	Steel	7 bars M15	0.50	10M @ 200 mm

letters, respectively. Finally, the identified number after hyphen provides the size of longitudinal bars. According to the analytical calculations based on ACI 318-19 and ACI 440.1R-15, the flexural strength of the specimen 7G-#5 is 33% greater than 7S-15M with considering all the reduction factors equal to 1.0. However, the specimens have almost the same flexural strength by considering the reduction factors according to the mentioned standards.

2.3 Test Setup and Instrumentation

The bending tests were performed using three-point load test setup with a clear span of 2400 mm (Fig. 4). The supports were cylindrical in shape and the specimens could rotate and move on the supports. Furthermore, in order to minimize the friction, Teflon sheets were placed between the supports and specimens. In the three-point load test setup, investigating the cracking behavior is more accurate than four-point test

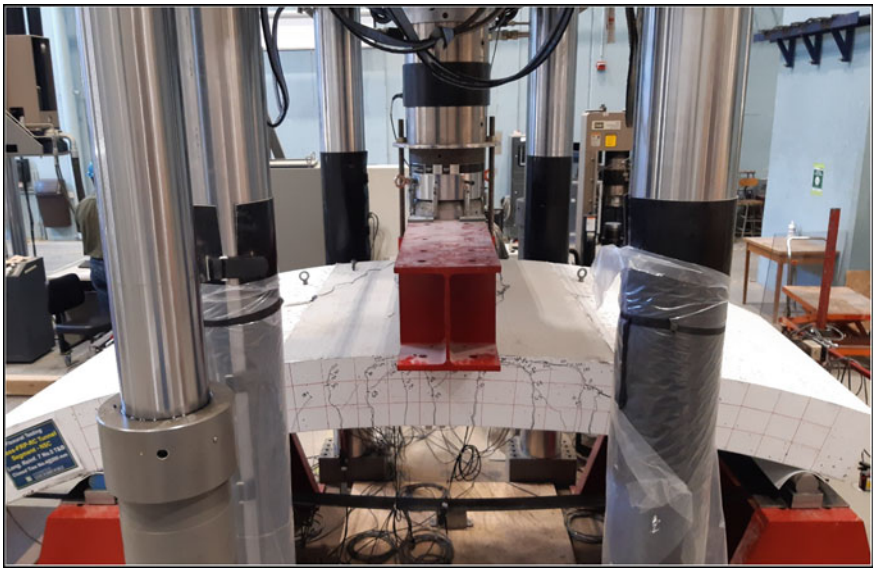

Fig. 4 Test setup

setup since the maximum bending moment and concentration of the flexural cracks occurs in one section rather than a length of the flexural elements [15]. Also, the designed test setup system is statically determinate so that the relationship between the reaction of the supports, axial load and bending moment in the segment can be easily obtained. The test setup was designed and constructed at Canada Foundation for Innovation (CFI) laboratory located at the University of Sherbrooke. A 11,400 kN MTS testing machine was used to apply a load at a displacement-control rate of 0.8 mm/min. Mid-span deflection was measured using three linear potentiometers (LPOTs) distributed along the width of the specimen center.

3 Experimental Results and Discussion

3.1 Failure Modes and Load Capacity

Table 3 lists cracking load, peak load and mode of failure. Moreover, failure modes of all the specimens are shown in Fig. 5. At initial stage of loading, crack propagation in the specimens followed a typical pattern of flexural cracks in a simply supported member subjected to three-point bending load. By increasing the load, the number and width of flexural cracks increased. The steel-reinforced specimen failed

Table 3 Experimental test results

Specimen ID	Cracking load (kN)	Ultimate load (kN)	Failure mode	Deflection at ultimate load (mm)
7G-#5	57	315	Compression-controlled flexural failure	66
7S-15M	68	236	Tension-controlled flexural failure	44

(a) 7S-15M (b) 7G-#5

Fig. 5 Failure mode of the tested specimens

by concrete crushing after yielding of steel reinforcement which denotes tension-controlled flexural failure. The specimen 7G-#5 also failed due to concrete crushing. With using identical reinforcement configuration, the ultimate load carrying capacity of 7G-#5 was 33% higher than that of 7S-15M. Also, 7G-#5 experienced 50% higher deflection at ultimate load that shows its greater deformability.

3.2 Load-Deflection Behaviour

Figure 6 shows the load versus mid-span deflection of the tested specimens. In pre-cracking stage, all the specimens behaved linearly with almost the same stiffness. After the first crack, the specimens experienced a temporary reduction in load. In post-cracking stage, the flexural stiffness of the specimens decreased compared to uncracked section due to transition from gross section to effective section. The post-cracking stiffness of 7S-15M specimen was 2.7 times greater than the 7G-#5. GFRP-reinforced specimen behaved almost linearly up to the failure which can be attributed to linear elastic behavior of GFRP reinforcement. The steel-reinforced specimen experienced nearly linear load-deflection until yielding point. After yielding, it followed a typical steel stress-strain plateau up to failure with a reduced stiffness. However, the ultimate load increased around 58% relative to yield load which can be attributed to strain hardening of steel rebars and increasing the bending moment arm in the section. As concrete crushing in 7S-15M and 7G-#5 specimens was gradual,

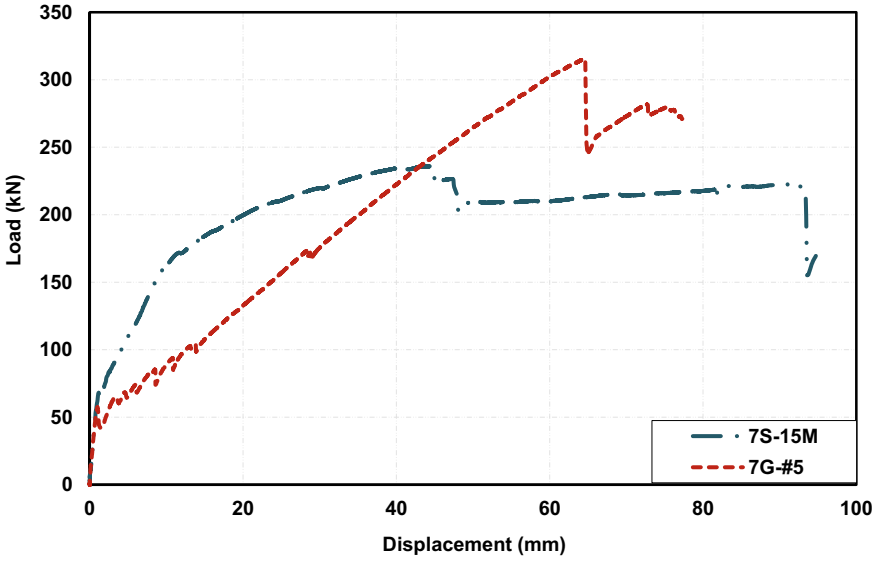

Fig. 6 Load-deflection behavior of the tested specimens

they could carry the load to some extent after the first drop. However, as the confinement did not provide for the compression block, the concrete crushing led to a full spalling which led to a reduction in the load.

4 Conclusions

In this study, the structural performance of a GFRP-reinforced precast concrete tunnel lining segment under bending load was compared with the steel-reinforced one in terms of failure mode and load-deflection behavior. The following conclusions may be drawn:

1. Failure in GFRP-reinforced segment governed by concrete crushing. The steel-reinforced specimen experienced a tension-controlled flexural failure. The ultimate load carrying capacity of GFRP-reinforced specimen was 33% higher than that of steel-reinforced one while the reinforcement detail in these two specimens was almost the same.
2. Steel-reinforced specimen experienced a typical load-deflection plateau which had three stages of cracking, yielding and failure. GFRP-reinforced specimen showed a linear elastic behavior after cracking until failure. While the axial stiffness of steel-reinforced specimen was 3.9 times greater than GFRP-reinforced specimen, it experienced 2.7 times greater axial stiffness.
3. Application of GFRP reinforcement in PCTL segments is an effective approach to deal with the corrosion problem and take advantage from the unique features of GFRP bars in tunnels. GFRP-reinforced PCTL segment showed a satisfactory structural performance under bending loading regarding to failure mechanism, ultimate load and deflection, service cracking and deflection.

Acknowledgements This research was conducted with funding from the Natural Sciences and Engineering Research Council of Canada (NSERC), Mathematics of Information Technology and Complex Systems (MITACS), the Fonds de recherche du Québec en nature et technologies (FRQ-NT), The Pole de Recherche et d'innovation en Materiaux Avances au quebéc (PRIMA Quebéc) and the Tier-1 Canada Research Chair in Advanced Composite Materials for Civil Structures. The authors are grateful to the precast company (Sym-Tech Béton Préfabriqué, Sainte-Hyacinthe, QC, Canada) and to the GFRP bar manufacturer (Pultrall Inc., Thetford Mines, QC, Canada) for their effective involvement in this project, and to the technical staff of the structural lab in the Department of Civil Engineering at the University of Sherbrooke.

References

1. ACI Committee 318 (2019) Building code requirements for structural concrete (ACI 318-19) and commentary (ACI 318R-19). American Concrete Institute, Farmington Hills

2. ACI Committee 440 (2015) Guide for the design and construction of structural concrete reinforced with fiber-reinforced polymer bars (ACI 440.1R-15). American Concrete Institute, Farmington Hills
3. ACI Committee 533 (2020) Guide for precast concrete tunnel segments (ACI 533.5R-20). American Concrete Institute, Farmington Hills
4. ASTM D7205/D7205M-06 (2016) Tandard test method for tensile properties of fiber reinforced polymer matrix composite bars. ASTM International, West Conshohocken
5. Benmokrane B, Wang P, Ton-That TM, Rahman H, Robert J-F (2002) Durability of glass fiber-reinforced polymer reinforcing bars in concrete environment. J Compos Constr 6(3):143–153
6. Canadian Standards Association (CSA) (2019) Canadian highway bridge design code (CAN/CSA S6-19). CSA Group, Mississauga
7. Canadian Standards Association (CSA) (2012) Design and construction of building components with fiber reinforced polymers (CAN/CSA S806-12). CSA Group, Mississauga
8. Caratelli A, Meda A, Rinaldi Z, Spagnuolo S (2016) Precast tunnel segments with GFRP reinforcement. Tunn Undergr Space Technol 60:10–20
9. Caratelli A, Meda A, Rinaldi Z, Spagnuolo S, Maddaluno G (2017) Optimization of GFRP reinforcement in precast segments for metro tunnel lining. Compos Struct 181:336–346
10. Nkurunziza G, Benmokrane B, Debaiky AS, Masmoudi R (2005) Effect of sustained load and environment on long-term tensile properties of glass fiber-reinforced polymer reinforcing bars. ACI Struct J 102(4):615–621
11. Robert M, Benmokrane B (2013) Combined effects of saline solution and moist concrete on long-term durability of GFRP reinforcing bars. Constr Build Mater 38:274–284
12. Robert M, Cousin P, Benmokrane B (2009) Durability of GFRP Reinforcing bars embedded in moist concrete. J Compos Constr 13(2):66–73
13. Spagnuolo S, Meda A, Rinaldi Z, Nanni A (2017) Precast concrete tunnel segments with GFRP reinforcement. J Compos Constr 21(5):04017020
14. Spagnuolo S, Meda A, Rinaldi Z, Nanni A (2018) Curvilinear GFRP bars for tunnel segments applications. Compos B Eng 141:137–147
15. Tengilimoğlu O (2019) An experimental study to investigate the possibility of using macro-synthetic fibers in precast tunnel segments. Ph.D. dissertation, Middle East Technical University, Ankara, Turkey

Axial Capacity of Circular Concrete Hollow Columns Reinforced with GFRP Bars and Spirals

Mohammed Gamal Gouda, Hamdy M. Mohamed, Allan C. Manalo, and Brahim Benmokrane

1 Introduction

Hollow reinforced concrete columns have been used in the past in place of their solid counterparts in the construction of bridges (columns, piles, and bridge pier). These hollow columns have several benefits over solid columns including higher structural performance than solid concrete columns in terms of stiffness-to-weight and strength-to-weight ratios [13]. In addition, hollow concrete columns (HCCs) can be the solution to maximize strength–mass and stiffness–mass ratios and to reduce the mass contribution of the column to the seismic response and demand on foundations. Such members are usually reinforced with conventional steel bars and spirals or ties. Steel reinforcement has a limited-service life and entails high maintenance costs due to corrosion when used in aggressive and/or harsh marine environments. This high cost has spurred interest in alternative noncorrosive reinforcing materials such as fiber-reinforced-polymer (FRP) bars. FRP bars offer many advantages over conventional steel bars, including a density of one-quarter to one-fifth that of steel, greater

M. G. Gouda (✉) · H. M. Mohamed · B. Benmokrane
Department of Civil and Building Engineering, University of Sherbrooke, Sherbrooke, QC, Canada
e-mail: Mohammed.Gamal.Gouda.Hassaan@usherbrooke.ca

H. M. Mohamed
e-mail: Hamdy.Mohamed@usherbrooke.ca

B. Benmokrane
e-mail: Brahim.Benmokrane@usherbrooke.ca

A. C. Manalo
School of Civil Engineering and Surveying, University of Southern Queensland, Toowoomba, Australia
e-mail: Allan.Manalo@usq.edu.au

S. Walbridge et al. (eds.), *Proceedings of the Canadian Society of Civil Engineering Annual Conference 2021*, Lecture Notes in Civil Engineering 244,
https://doi.org/10.1007/978-981-19-0656-5_10

tensile strength than steel, and no corrosion even in harsh chemical environments [8, 14].

The experimental work conducted on concentrically loaded circular and rectangular GFRP RC columns demonstrated that their behavior was very similar to that of conventional steel RC columns, and no appreciable difference has been observed in terms of peak capacity [1, 2, 9, 16]. Afifi et al. [1, 2] concluded that the average load carried by the longitudinal GFRP bars in circular GFRP RC columns ranged between 5 and 10% of the maximum load. Testing GFRP RC columns of rectangular section indicated that the GFRP bars contributed 10% of column capacity [16]. In tests on full-scale rectangular GFRP RC columns, the contribution of the GFRP bars to the column capacity, however, was less than 5% of the peak load [9]. Based on these studies, it has been concluded that the contribution of GFRP bars in compression may be ignored when assessing the nominal capacity of an axially loaded RC column. On the other hand, using GFRP ties, spirals, and hoops was found to be efficient in confining the concrete core, delaying initiation and propagation of unstable cracks, and preventing the buckling of GFRP longitudinal bars at peak load [1, 2, 12, 15]. Limited research work has been conducted on hollow concrete columns reinforced with GFRP reinforcements. AlAjarmeh et al. [3] investigated the axial compression behavior of hollow concrete columns with different ratios of longitudinal GFRP reinforcement. It was found that the structural behavior and failure mechanism of HCCs were strongly affected by the amount of longitudinal reinforcement or the reinforcement ratio. The objective of this study was to obtain experimental data and to better understand the behavior and failure mechanics of full-scale hollow concrete columns reinforced with GFRP bars and spirals tested under axial load. The effect of reinforcement ratio was investigated. The experimental data provide the evidence required to include design provisions in the forthcoming ACI 440 code for the use of GFRP bars and spirals as internal reinforcement in concentrically loaded hollow concrete compression members.

2 Experimental Program

2.1 Design of Test Specimens

Five full-scale circular reinforced-hollow concrete columns were prepared and tested to investigate the influence of the longitudinal reinforcement ratio ρ_l (represented by the number of bars) under pure axial loading. Three columns were reinforced with GFRP bars and spirals with ratios of ρ_l at 1.89%, 2.53%, and 3.79%. One control specimen was reinforced with only GFRP bars, and one plain concrete column was introduced as a reference. All columns were designed with a hollow circular cross-section where the outside diameter of the columns was 305 mm, the inner diameter was 113 mm ($D_{in.}/D_{out.} = 0.37$), and the height was 1500 mm. Concrete cover for all tested columns was set at 27.50 mm. All the GFRP RC columns were

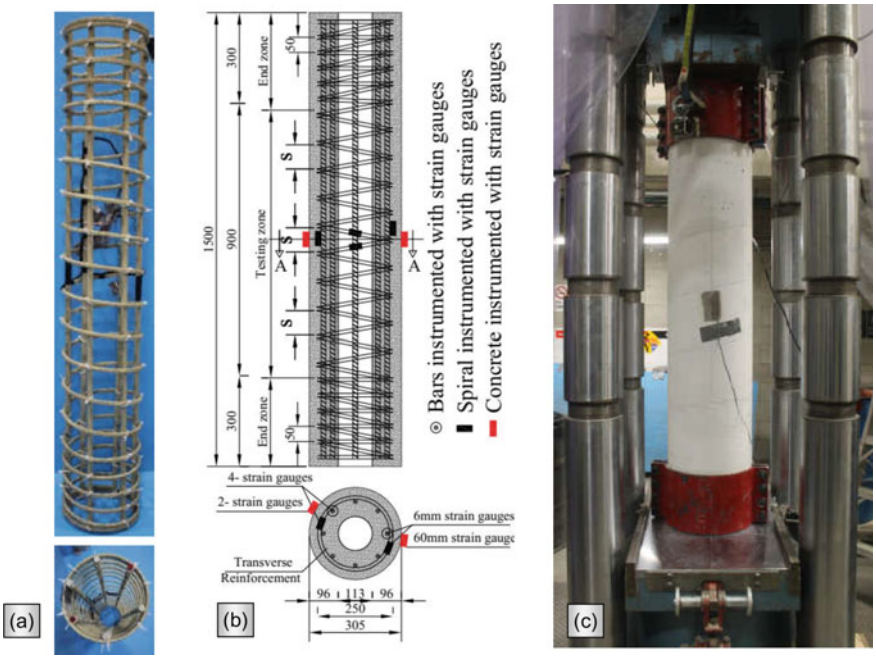

Fig. 1 Experimental program layout: **a** GFRP reinforcement cage; **b** specimen's details and instrumentations; and **c** FORNEY machine "final installation of the specimen"

designed according to CSA/CAN S806-12, clause (8.4.3.6-15) code requirements for longitudinal and transverse reinforcement. Where, clause (8.4.3.10) recommends that the minimum number of longitudinal reinforcing bars in compression members enclosed by spirals shall be six for bars and the minimum FRP bar size for longitudinal FRP bars shall be not less than 15 mm in diameter. Figure 1 displays the GFRP-reinforcement cage, specimen's details, and the final installation of the column-specimen on the FORNEY machine. Table 1 lists the test matrix and the reinforcement details for all tested columns.

2.2 Materials Characterization

All columns were cast with a single batch of nominal 34.70 MPa ready-mix normal-weight concrete with a maximum aggregate size of 10 mm. During casting, the concrete was compacted to ensure adequate consistency of the concrete paste. The average compressive strength of concrete was computed in terms of the characteristic compressive strength of ten 100 × 200 mm cylinders samples cured under the same conditions as the column specimens and examined after 28-days mandated by ASTM C39/C39M 2012. No. 5 and Grade II sand-coated GFRP bars with an average fiber

Table 1 Test matrix and specimen details

Column ID	f'_c (MPa)	Longitudinal reinforcement				Transverse reinforcement			
		Bar type	No. of bars	Bar	ρ_l (%)	Type	d_b^* mm	S mm	ρ_T (%)
HC-6G-80	34.70	GFRP	6	#5	1.89	GFRP spiral	9.50	80	1.11
HC-8G-80			8	#5	2.53	GFRP spiral			
HC-12G-80			12	#5	3.79	GFRP spiral			
HC-8G-W			8	#5	2.53	—	—	—	—
HC-P		—	—	—	—	—	—	—	—

Table 2 Mechanical properties of the GFRP reinforcement

Reinforcement type	Bar size	Diameter (mm)	Nominal area (mm^2)	Elastic tensile modulus (GPa)	Tensile strength (MPa)	Tensile strain (%)
GFRP	# 3	9.5	71	52.5 ± 2.5	$f_{fu} = 1328$	2.30
	# 5	15.9	199	54.9 ± 2.5	$f_{fu} = 1289$	2.40

content of 83.8% and No. 3 Grade II sand-coated GFRP spirals with an average fiber content of 78.9% were used to reinforce all the GFRP-reinforced specimens. Table 2 reports the material properties of the GFRP, as provided by the manufacturer.

2.3 Instrumentation and Testing

During the cage's preparation stage, four strain gauges with a length of 6 mm were mounted on the bars and spirals at mid-height of the cage to monitor the column responses, (see Fig. 1a and b). Before testing, two concrete strain gauges with a 60 mm in length were fixed on the exterior surface at the column and almost parallel to the bars and spirals strains. Finally, the applied axial load and the axial displacement were measured, respectively, with the machine's internal load cells and linear variable differential transformers (LVDTs). All instruments were connected to a data-acquisition system for continuous recording of results.

All the columns were tested under concentric loading with a 6,000 kN capacity FORNEY machine in the Construction Facilities Laboratory of the Department of

Civil Engineering at the University of Sherbrooke, as displayed in Fig. 1(c). Prior to testing, a 20-mm self-leveling cementitious grout was utilized to level the top and bottom ends of each column. Two rigid steel collars were fastened and clamped at the ends of the column to prevent any undesired local failure at these stress-concentration zones. Lastly, the column was placed in the middle of the Forney machine and the test was conducted with a load-controlled technique at a rate of 1.50 kN/s up to failure.

3 Test Results and Discussion

3.1 Failure Modes

The GFRP-RC hollow columns exhibited a compression failure in terms of concrete-cover spalling, accompanied by a drop in the column capacity. Figure 2 shows the failure modes of all tested columns. The failure started by hairline cracks that propagated along the column height as the applied load increased. Spalling of the concrete cover was then observed, followed by rupturing of the longitudinal bars. The GFRP

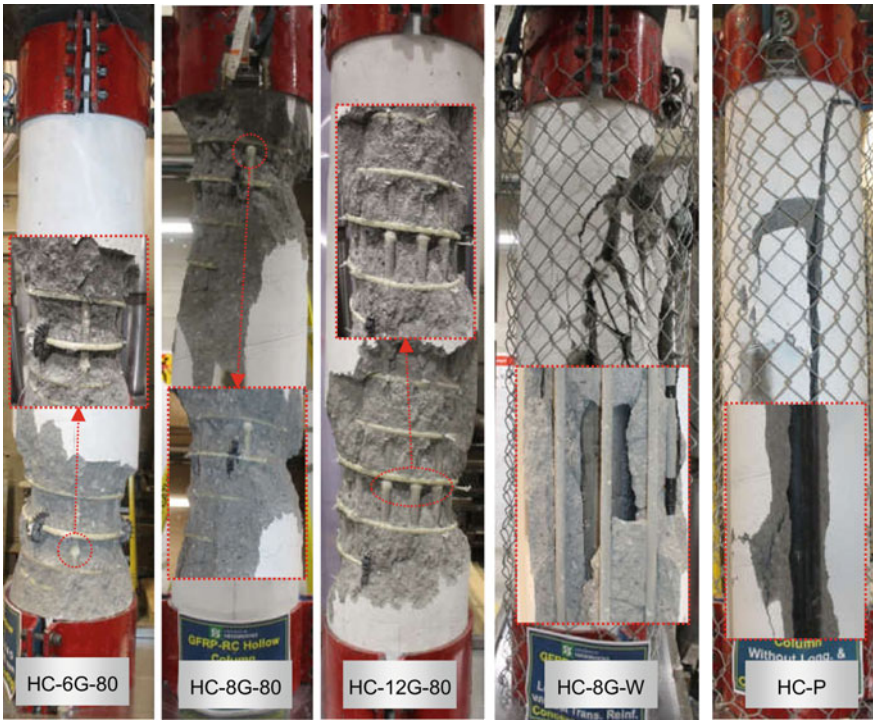

Fig. 2 Failure modes

spirals were not damaged for all tested columns. Table 3 summarizes the failure propagation in the tested hollow concrete columns.

3.2 Load Deformation Behavior

Figure 3 illustrates the relationship between the axial load versus the axial deformation of the tested hollow columns. Prior to cover spalling phase, the column specimens HC-12G-80, HC-8G-80, HC-6G-80, HC-8G-W, and HC-P behaved linearly until the initiation of the hairline cracks at 1810 (73%), 1805 (76%), 1800 (79%), 1795 (85%), and 1790 (90%) kN, with a corresponding axial deformation 3.30, 3.75, 3.90, 3.50, and 3.20 mm, respectively. A gradual loss of initial stiffness after these cracks propagated providing a nonlinear ascending branch up to the peak loads of 2492, 2381, 2271, 2120, and 2000 kN, and the counterparts axial displacement at 7.50, 6.63, 5.79, 7.13, and 5.51 mm, respectively. The tested columns sustained an axial load exceeded the design load (P_o) allowed in CAN/CSA S806-12 with subtracting the area of FRP bars. Ignoring the contribution of GFRP bars in the CAN/CSA S806-12 design equation underestimated the maximum capacity of the tested columns. The difference between the experimental and nominal ultimate capacity based on the CAN/CSA S806-12 limit for the column specimens HC-12G-80, HC-8G-80, HC-6G-80, HC-8G-W, and HC-P, $[\left(\left(P_{exp.} - P_{o,S806}\right)/P_{o,S806}\right)]$, was 39, 31, 25, 17, and 8%, respectively, on average 24%. Due to the concrete cover spalling, a sudden load drop reached to 2000, 1900, 1400, and 1000 kN at corresponding axial deformation of 8.60, 7.10, 6.95, and 10.50 mm, respectively, for the columns HC-12G-80, HC-8G-80, HC-6G-80, and HC-8G-W was observed. Afterward, the applied load was transferred to the inner core, because of the GFRP spirals lateral confinement and contribution of the longitudinal bars in carrying the load, the load curve raised again until the second peak of 2200, 1600, and 1400 kN for the columns HC-12G-80, HC-8G-80, and HC-6G-80. The columns, lastly, failed due to bar or more rupture, as depicted in Fig. 2. Regarding the impact of the longitudinal reinforcement ratio, increasing the number of bars increases the peak axial-load capacity. Therefore, HC-12G-80 ($\rho = 3.79\%$) had 4.70% and 9.70% higher peak strength than HC-8G-80 ($\rho = 2.53\%$) and HC-6G-80 ($\rho = 1.89\%$). Table 3 summarizes the experimental test results.

3.3 GFRP-Bars and Concrete Strains

Figure 4 depicts the applied load to the induced strains response of the tested specimens. At the peak load, the average axial compression strain monitored in the longitudinal bars was around 2800 $\mu\varepsilon$, which is about 14% of the ultimate tensile strain of the GFRP bars $\varepsilon_{frp,u}$, while the ultimate recorded compressive strength was 30% of $\varepsilon_{frp,u}$. These findings coincide with that mentioned by [3]. The average axial strains in the reinforcing bars were recorded and utilized to estimate the contributions of the

Table 3 Experimental test results

Column ID	P_{n1} (kN)	Δ_{n1} (mm)	$\varepsilon_{n1,conc.}$ (με)	$\varepsilon_{n1,bar}$ (με)	$P_{bar,1}$ (kN)	$\%bar_1$ (%)	$P_{n,2}$ (kN)	Δ_{n2} (mm)	$\varepsilon_{nf1,bar}$ (με)	Failure modes
HC-6G-80	2271	5.79	−2785	−2417	144	6.35	1490	9.21	−6795	1. Vertically microcracks started and propagated along the column height 2. Concrete cover spalling 3. Two GFRP bars rupture 4. Rupture initiation of one spiral
HC-8G-80	2381	6.63	−2865	−3553	283	11.88	1671	10.72	−3117	1. Vertically microcracks started and propagated along the column height 2. Concrete cover spalling 3. One GFRP bar rupture

(continued)

Table 3 (continued)

Column ID	P_{n1} (kN)	Δ_{n1} (mm)	$\varepsilon_{n1,conc.}$ (με)	$\varepsilon_{n1,bar}$ (με)	$P_{bar,1}$ (kN)	$\%bar_1$ (%)	$P_{n,2}$ (kN)	Δ_{n2} (mm)	$\varepsilon_{nf1,bar}$ (με)	Failure modes
HC-12G-80	2492	7.50	−3042	−2766	330	13.25	2154	12.60	−7195	1. Vertically microcracks started and propagated along the column height 2. Concrete cover spalling 3. Four GFRP bars rupture
HC-8G-W	2120	7.13	−2374	−2420	193	9.09	2043	7.35	−2299	1. Vertically microcracks started and propagated along the column height 2. Column bugling 3. Explosive manner collapse 4. Bars buckling have remarked
HC-P	2000	5.51	−2040	–	–	–	2000	5.51	–	1. Vertically microcracks started and propagated along the column height 2. Column bugling 3. Explosive manner collapse

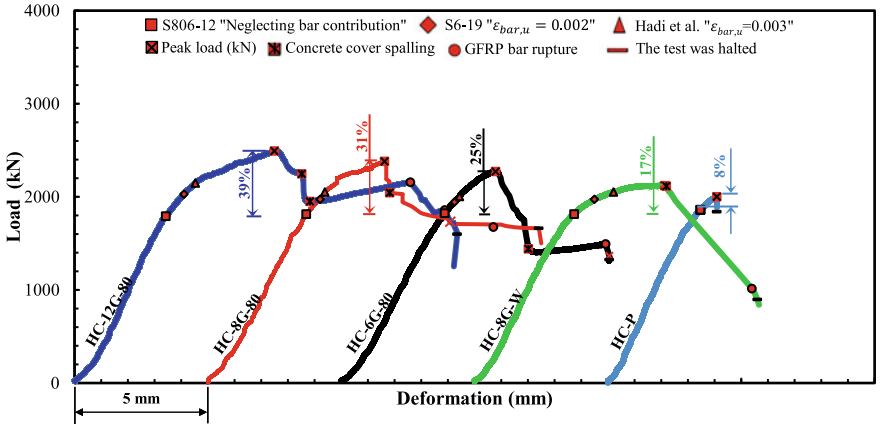

Fig. 3 Investigating the influence of the longitudinal reinforcement ratios on the load-axial deformation response ($\rho_l = 3.79\%, 2.53\%, 1.89, and\ nil$)

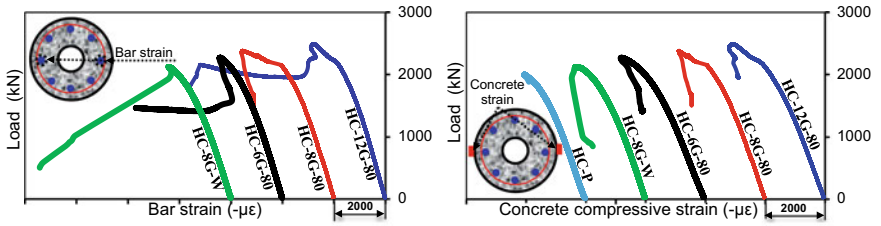

Fig. 4 GFRP-bars and concrete strains

compressive strength of the bars to the overall strength capacities, P_{bars}. P_{bars} was computed based on the measured strain at the peak load, ε_{bar}, the cross-sectional area of the bar, A_f, and the bar's modulus, E_f. The ratios $P_{bars}/P_{exp.}$ are reported in Table 3. The average contribution of the GFRP bars in compression was around 10% of the experimental peak load, contrary to the CAN/CSA S806-12, which neglecting the compressive strength of the GFRP bars. All measured concrete strains at the peak load were 3042, 2865, 2785, 2374, and 2040 με for the column specimens HC-12G-80, HC-8G-80, HC-6G-80, HC-8G-W, and HC-P, respectively, (on average 2620 με). The concrete strain readings were affected and became unreliable upon the cracks widened and propagated.

4 Experimental-to-Theoretical Ultimate Load Capacity

Table 4 presents a comparison between the peak loads obtained from the experimental testing and the ultimate load capacity estimated based on the CAN/CSA S806-12

Table 4 Experimental-to-theoretical ultimate load capacity evaluation

Column ID	Exp.	Theoretical							
		CAN/CSA S806-12 $disregard$		CAN/CSA S6-19 $\varepsilon_{GFRP} = 0.002$		Hadi et al. [11] $\varepsilon_{GFRP} = 0.003$		Tobbi et al. [16] and Afifi et al. [1, 2]	
	P_{exp} (kN)	$P_{Th.}$ (kN)	$P_{exp.}/P_{Th.}$	$P_{Th.}$ (kN)	$P_{exp.}/P_{Th.}$	$P_{Th.}$ (kN)	$P_{exp.}/P_{Th.}$	$P_{Th.}$ (kN)	$P_{exp.}/P_{Th.}$
HC-6G-80	2271	1824	1.25	1943	1.17	2003	1.13	2242	1.01
HC-8G-80	2381	1812	1.31	1971	1.21	2051	1.16	2369	1.01
HC-12G-80	2492	1789	1.39	2028	1.23	2147	1.16	2625	0.95
HC-8G-W	2120	1812	1.17	1971	1.08	2051	1.03	2369	1.12
HC-P	2000	1859	1.08	1859	1.08	1859	1.08	1859	1.08

and CAN/CSA S06-19, and proposed equations from past studies. These equations are shown as follow:

$$P_o = 0.85 f_c'\left(A_g - A_F\right) \text{ [7]} \tag{1}$$

$$P_o = 0.85 f_c'\left(A_g - A_F\right) + 0.002 E_f A_F \text{ (CAN/CSA S06 - 19)} \tag{2}$$

$$P_o = 0.85 f_c'\left(A_g - A_F\right) + 0.003 E_f A_F \text{ [11]} \tag{3}$$

$$P_o = 0.85 f_c'\left(A_g - A_F\right) + 0.35 f_{f,u} A_F \text{ [1, 2, 16]} \tag{4}$$

The experimental-to-theoretical ratios demonstrate that the ultimate capacity of hollow concrete columns reinforced with GFRP bars and spirals can be computed by considering the contribution of the longitudinal GFRP bars in compression. This study measured that the axial compressive strains in the longitudinal reinforcement which, on average, is equal to 0.0028. Hence, the equation reported by CAN/CSA S09-19 can reliably predict the axial-load capacity of hollow concrete columns reinforced with GFRP bars and spirals. These findings match with that reported by [17], since they assumed that the average axial strain of the GFRP bars at peak load is equal to 2000 με.

5 Conclusions

This study is part of a large experimental and analytical research project at the University of Sherbrooke investigating the behavior of GFRP-RC hollow columns concentrically and eccentrically loaded. The experimental program in this paper is designed to study the performance of five full-scale circular RC columns with hollow cross-sections and reinforced with different longitudinal reinforcement ratios. Based on the experimental investigations of this study, the following conclusions can be drawn:

1. All tested GFRP-RC hollow concrete columns revealed a compression-controlled failure in terms of gradual concrete cover spalling.
2. The difference in the peak load of hollow concrete columns reinforced with 12 GFRP bars (3.79%) increased from 5% at 8 GFRP bars (2.53%) to 10% at 6 GFRP bars (1.89%).
3. The GFRP longitudinal reinforcement significantly contributed to resisting the applied compression loads. The GFRP-RC hollow columns sustained an axial load exceeded the design load defined in CSA S806-12.
4. The average contribution of the GFRP bars in compression was around 10% of the experimental peak load, contrary to the CSA S806-12, which neglecting the compressive strength of the GFRP bars.

5. The ultimate strength of the GFRP-RC hollow columns can be reliably predicted by considering the contribution of the longitudinal reinforcement of 2000 με.

Acknowledgements This research was conducted with funding from the Tier-1 Canada Research Chair in Advanced Composite Materials for Civil Structures, the Natural Sciences and Engineering Research Council of Canada (NSERC), Mathematics of Information Technology and Complex Systems (MITACS), and the Fonds de recherche du Québec en nature et technologies (FRQ-NT). The authors thank the technical staff of the CFI structural laboratory in the Department of Civil Engineering at the University of Sherbrooke.

References

1. Afifi M, Mohamed HM, Benmokrane B (2013) Axial capacity of circular concrete columns reinforced with GFRP bars and spirals. J Compos Constr 18(1):04013017
2. Afifi M, Mohamed HM, Benmokrane B (2013) Strength and axial behavior of circular concrete columns reinforced with CFRP bars and spirals. J Compos Constr 18(2):04013035
3. AlAjarmeh OS, Manalo AC, Benmokrane B, Karunasena W, Mendis P (2019) Axial performance of hollow concrete columns reinforced with GFRP composite bars with different reinforcement ratios. Compos Struct 213:153–164
4. American Concrete Institute (ACI 318R-14) (2014) Building code requirements for structural concrete. ACI 318-14 and commentary, Farmington Hills, Michigan
5. American Concrete Institute (ACI 440.1R-15) (2015) Guide for the design and construction of structural concrete reinforced with FRP bars, Farmington Hills, MI, 44 p
6. ASTM (2012) Standard test method for compressive strength of cylindrical concrete specimens. ASTM C39/C39M-12, West Conshohocken, PA
7. Canadian Standards Association (CAN/CSA S806-12) (2012) Design and construction of building structures with fibre-reinforced polymers. Mississauga, Ontario, Canada, 206 p
8. Chaallal O, Benmokrane B (1993) Physical and mechanical performance of an innovative glass-fiber-reinforced plastic rod for concrete and grouted anchorages. Can J Civ Eng 20(2):254–268
9. De Luca A, Matta F, Nanni A (2010) Behavior of full-scale glass fiber-reinforced polymer reinforced concrete columns under axial load. ACI Struct J 107(5):589–596
10. Hadi MN, Hasan HA, Sheikh MN (2017) Experimental investigation of circular high strength concrete columns reinforced with glass fiber-reinforced polymer bars and helices under different loading conditions. J Compos Constr 21(4):04017005
11. Hadi MN, Karim H, Sheikh MN (2016) Experimental investigations on circular concrete columns reinforced with GFRP bars and helices under different loading conditions. J Compos Constr 20(4):1–12
12. Mohamed HM, Afifi M, Benmokrane B (2014) Performance evaluation of concrete columns reinforced longitudinally with FRP bars and confined with FRP hoops and spirals under axial load. J. Bridge Eng. 19(7):04014020
13. Liang X, Beck R, Sritharan S (2015) Understanding the confined concrete behavior on the response of hollow bridge columns. Department of Civil, Construction and Environmental Engineering. Iowa State University: California Department of Transportation
14. Maranan G, Manalo A, Benmokrane B, Karunasena W, Mendis P (2016) Behavior of concentrically loaded geopolymer-concrete circular columns reinforced longitudinally and transversely with GFRP bars. Eng Struct 117:422–436
15. Pantelides CP, Gibbons ME, Reaveley LD (2013) Axial load behavior of concrete columns confined with GFRP spirals. J Compos Constr 17(3):305–313
16. Tobbi H, Farghaly AS, Benmokrane B (2012) Concrete columns reinforced longitudinally and transversally with glass fiber-reinforced polymer bars. ACI Struct J 109(4):551–558
17. Tobbi H, Farghaly AS, Benmokrane B (2014) Behavior of concentrically loaded fiber-reinforced polymer reinforced concrete columns with varying reinforcement types and ratios. ACI Struct J 111:375

Lightweight Self-consolidating Concrete Bridge-Deck Slabs Reinforced with GFRP Bars Under Concentrated Loads

M. Aflakisamani, S. Mousa, H. M. Mohamed, E. A. Ahmed, and B. Benmokrane

1 Introduction

Lightweight aggregates are environmentally-friendly that can replace natural aggregates. Additionally, lightweight aggregates reduce the mass of construction which consequently led to reduce the cross-section and the amount of reinforcement used in concrete structures, and thus seismic resistance will be increased. The weight of bridge-deck slabs is considerably more than imposed traffic loads. In the case of using lightweight concrete (LWC) reinforced by FRP bars, the advantages are included the strength-to-weight ratio improvement and reduction in life cost of the structures. According to the investigations, ACI 318R-95 underestimated the flexural capacity of the LWC slabs [15]. Comparing the results of shear behavior of GFRP-reinforced lightweight one-way slabs with the shear strength predictions of the American Concrete Institute (ACI) 440.1R-06 recommendations (ACI 440.1R-06) showed that the use of ACI 440.1R-06 shear equations for lightweight concrete is less conservative than for normal-weight (NW) concrete [16, 17]. The experimental results from GFRP-reinforced lightweight panels showed that LW concrete panels

M. Aflakisamani (✉) · S. Mousa · H. M. Mohamed · E. A. Ahmed · B. Benmokrane
Department of Civil and Building Engineering, University of Sherbrooke, Sherbrooke, QC, Canada
e-mail: Mahdi.Aflaki.Samani@Usherbrooke.ca

S. Mousa
e-mail: Salaheldin.Mousa@Usherbrooke.ca

H. M. Mohamed
e-mail: Hamdy.Mohamed@Usherbrooke.ca

E. A. Ahmed
e-mail: Ehab.Ahmed@Usherbrooke.ca

B. Benmokrane
e-mail: Brahim.Benmokrane@Usherbrooke.ca

S. Walbridge et al. (eds.), *Proceedings of the Canadian Society of Civil Engineering Annual Conference 2021*, Lecture Notes in Civil Engineering 244,
https://doi.org/10.1007/978-981-19-0656-5_11

performed similar to NW concrete panels [17]. The shear predictions using Canadian [6] and Japanese recommendations [14] regarding shear strength of lightweight and normal weight concrete panels reinforced with Glass fiber-reinforced polymer (GFRP) bars are less conservative, hence a reduction factor is not required [14].

On the other hand, as the steel reinforcement easily corroded when exposed and routine maintenance should be conducted in reinforced concrete (RC) structures, FRP bars are increasingly used in construction industry instead of steel reinforcement. FRP bars have some significant specifications like high tensile strength, noncorrosive properties and lightweight. Due to their significant properties, they are an effective alternative for steel bars, particularly in marine structures, concrete bridge-deck slabs, and parking garages where they are exposing to chlorides and de-icing chemicals. As concrete bridge-deck slabs experience harsh environmental conditions, including routinely used de-icing salts, traffic loads, freeze-thaw cycles, and wet-dry cycles, they are more likely to deteriorated compare to any other bridge elements. FRP bars help reduce the cost of maintenance, repair, and rehabilitation because of their noncorrosive feature. According to the results of previous studies on the punching shear of FRP-reinforced concrete slabs, punching shear is the failure mode of FRP-RC slabs and the type of reinforcement (GFRP, carbon FRP (CFRP), or steel) had a negligible effect on the deflection behavior of reinforced concrete deck slabs [2, 11, 12]. Results from a recent research project conducted by [10] showed that conservative predictions are provided by ACI 440.1R [1] in terms of the punching-shear capacity of basalt FRP (BFRP)-RC deck slabs, however, CAN/CSA S806 [7] provided reasonable yet conservative predictions. FRP reinforcements can improve cracking performance and the induced strains of FRP-RC slabs by improving the bond between the concrete and reinforcing bars [10, 13].

There is no experimental data concerning the use of FRP bars as internal reinforcement for concrete bridge-deck slabs using as known by the authors. This is partially due to a lack of experimental data, which can describe the behavior of members reinforced with such materials. This experimental investigation has been carried out regarding the structural behavior of full-scale lightweight self-consolidated concrete (LWSCC) bridge-deck slabs internally reinforced with GFRP bars under concentrated loads simulating truck wheel loads.

2 Experimental Program

2.1 Material properties

2.1.1 Reinforcing Bars

In this study, helically wrapped GFRP bars (No. 5) were used. The GFRP bars are classified as Grade III according to CSA S807-19 [9]. While ribbed steel bars (15M)

Table 1 Mechanical properties of the reinforcing bars

Bars	Bar size	d_b (mm)	A_f (mm^2)	E_f (GPa)	f_{fu} (MPa)	ε_{fu} (%)	Surface configuration
GFRP	#5	15.9	199	64.1	1528	2.4	Helically Wrapped
Steel	M15	16	200	200	$fy = 460$	$\varepsilon_f = 0.23$	Ribbed

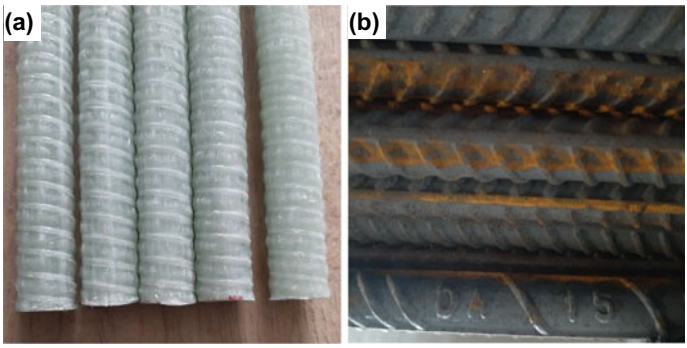

Fig. 1 Reinforcing bars used in this study: (a) Helically wrapped GFRP bars; (b) Steel bars

were used for the reference slab. Table 1 provides the properties of the reinforcing bars. Figure 1 shows the two reinforcing types used in this study.

2.1.2 Concrete

Lightweight self-consolidating concrete (LWSCC) was used in this investigation. LWSCC mixture is made with lightweight coarse and fine aggregates according to the specifications of [4] and natural normal weight sand. The maximum sizes of coarse and fine aggregates were 14 and 5 mm, respectively. Lightweight aggregates used in this study were expanded shale. The aggregates were pre-wetted separately before mixing with the rest of the materials to maintain a uniform water volume fraction of 0.33. The LWSCC were prepared using a ternary binder containing 70% general-use cement (GU), 25% fly ash (FA), and 5% silica fume (SF) complying with ASTM C150 [3]. A ready to use a polycarboxylate-based high-range water-reducing agent (HRWRA) with a solid content of 40% and a specific gravity of 1.09 density was used as a superplasticizer with air-entraining admixture. The specimens were cast on the same day. The curing process was initiated immediately after the casting by covering the concrete surface with polyethylene sheets. The slabs were unmolded after one day and the water-curing process was initiated for 7 days. The equilibrium density of the LWSCC was 1930 kg/m^3 and was measured according to ASTM C567 [5]. The concrete compressive strength of 46.1 MPa was based on the average value of tests performed on 12 concrete cylinders 100 $\times$ 200 mm on the day of testing.

Fig. 2 Overview of the assembled GFRP meshes and formworks prepared for casting

2.1.3 Test Specimens and Testing Procedure

The experimental program included testing of two full-scale concrete deck slabs measuring 3000 mm long × 2500 mm wide × 200 mm thick and span of 2000 mm (center to center), as shown in Fig. 2. The specimens were supported on two steel girders and were restrained at the edges in the longitudinal direction with 22 mm steel anchors. The concrete cover was equal to 30 and 25 mm at the top and bottom, respectively, as specified in Clause 16.4.5 of CAN/CSA S6 [8]. The slab thickness was selected to keep the supporting beams spacing to slab thickness ratio less than 18, as specified in Clause 8.18.3.1 of CAN/CSA S6 [8], and to represent the most used size of concrete bridge-deck slabs in Canada. The test setup and prepared specimen under the loading actuator are shown in Fig. 3. Each specimen consists of two meshes at top and bottom. The reinforcement details of the slabs were presented in Table 2. The specimens defined with G and S have GFRP and steel bars, respectively. The bar spacing in each direction for both meshes is 300 mm.

Each slab was loaded up to failure over a center-to-center span of 2000 mm under a monotonic single concentrated load. The load was applied to the slab center with a contact area of 600 × 250 mm, using a 70 mm thick steel plate to simulate the footprint of a sustained truck wheel load (87.5 kNCL-625 truck) as specified in CAN/CSA S6 [8]. An MTS actuator hydraulic jack with a capacity of 1000 kN and a ±250 mm stroke was used to apply the monotonic load up to failure at a displacement control rate of 0.3 mm/min. During the test, the slabs were observed until the first three cracks appeared in the transverse direction; the corresponding load was recorded. The LVDTs were installed at crack locations to record crack widths with the load increasing. The load was continuously increased until slab failure. The formation of the cracks on the sides and bottom surface of the deck slabs and corresponding loads were marked and recorded during the test.

Fig. 3 Test setup and the bridge-deck slab ready for testing

Table 2 Top and bottom reinforcement details for transverse and longitudinal direction

Slab ID	Reinforcement	ρ (%)	$\rho \times E$ (MPa)
G	16 mm @300 mm	0.37	237
S	15M @300 mm	0.37	733

3 Test Results and Discussion

The specimens were tested in terms of crack width, cracking pattern, deflection, cracking load, ultimate load, and failure mode. The results from experiments are presented in Table 3. The design service load (P_{serv}) and design factored load (P_{fact}) were calculated according to the CAN/CSA S6 [8]. The design service load of the deck slabs was taken as $1.4 \times 0.9 \times 87.5 = 110.25$ kN, where 87.5 is the maximum wheel load of the design truck (87.5 kN CL-625 truck), 1.4 is the impact coefficient, and 0.9 is the live-load combination factor. The design factored load was taken as $1.4 \times 1.7 \times 87.5 = 208.25$ kN, where 1.7 is the live-load combination factor.

Table 3 Test results of the punching shear capacities

Slab ID	f'_c (MPa)	P_{cr}	P_{max}	Deflection (mm)			Crack width (mm)		
				P_{serv}	P_{fact}	P_{max}	P_{serv}	P_{fact}	P_{max}
G	46.1	83.4	421.1	1.13	6.88	24.47	0.01	0.39	1.79
S		114.7	538.7	1.27	4.18	25.72	–	0.20	1.91

3.1 Cracking

A similar cracking pattern appeared after testing for both specimens, despite the different reinforcement type. Figure 4 shows the crack patterns on top and bottom surfaces of the specimens. On the bottom surface, the first cracks appeared in longitudinal direction under the loading area and then propagated in the radial direction away from the center to the edges and sides. Almost the same number of cracks appeared underneath of loading plate on the bottom surface for both slabs, which indicates that the performance of the slabs in case of crack appearance and propagation was similar, regardless of their reinforcement bar type. On the top surface, the same footprint appeared on both slabs.

The cracking loads were 108.1 and 114.7 kN for specimens G and S, respectively. The cracking loads were almost the same as the design service load (110.25 kN) as specified in the CAN/CSA S6 [8]. The cracking load recorded for specimen G is 94.2% that of specimen S, which indicates that the GFRP-reinforced slab behaved similarly to the steel-reinforced slab in terms of initial cracking.

The load-average crack width curves are presented in Fig. 5. The crack widths were measured with LVDTs and presented in Table 3. For slab G, the crack width recorded at service load was 0.01 mm which is less than the allowable limit defined by ACI 440.1R-15 and the CSA S6-19 of 0.5 mm for exterior exposure. However, for slab S, no crack appeared at the service load level (cracking load was higher

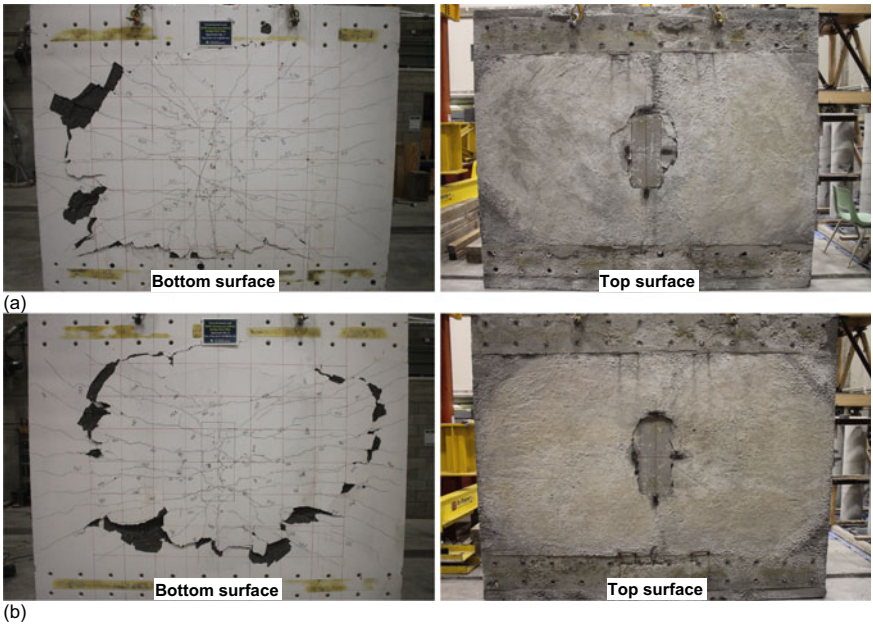

Fig. 4 Top and bottom surfaces of specimens after testing: (a) G; (b) S

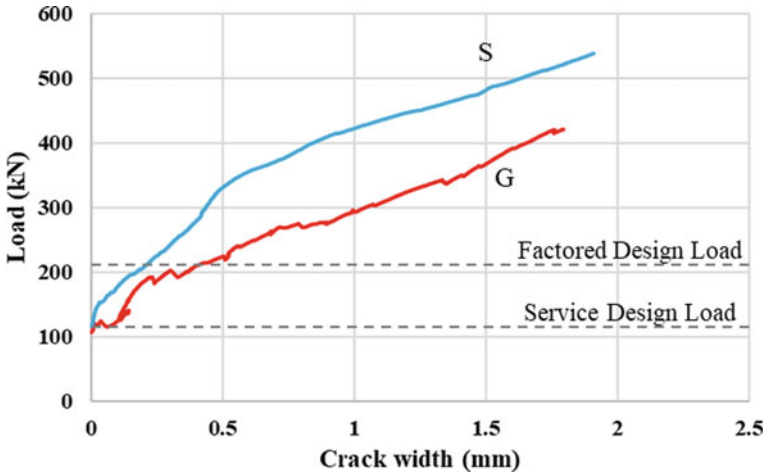

Fig. 5 The load-average crack width curves for bridge-deck slabs

than the service load). Approximately the same crack widths were recorded at the ultimate load. This confirms that the use of this type of GFRP reinforcing bars with a lower modulus of elasticity than steel bars has a minor effect on crack widths of the bridge-deck slabs. In general, cracking performance of the specimen reinforced with GFRP bars is approximately similar to that of steel-reinforced specimen.

3.2 Ultimate Capacity and Failure Mode

As it can be observed in Fig. 4, the same cracking pattern appeared on the surfaces of the slabs after testing. As no crushing was observed for the concrete and no bar was ruptured during the test, the punching-shear is considered as a failure mode of the slabs.

The ultimate punching-shear loads were recorded at the value of 421.1 and 538.7 kN for slab G and S, respectively. This indicates that the slab G could bear load up to 78% of the ultimate load recorded for slab S and it can be concluded that the higher axial-reinforcement stiffness can lead to the higher punching-shear capacity. Moreover, GFRP-reinforced slab showed 2.02 times the factored design load of 208.25 kN specified by the CSA S6-19. This value for the slab S was calculated 2.59. This is related to the fact that the specimens were designed according to the flexural failure, while the shear was the actual mode of failure.

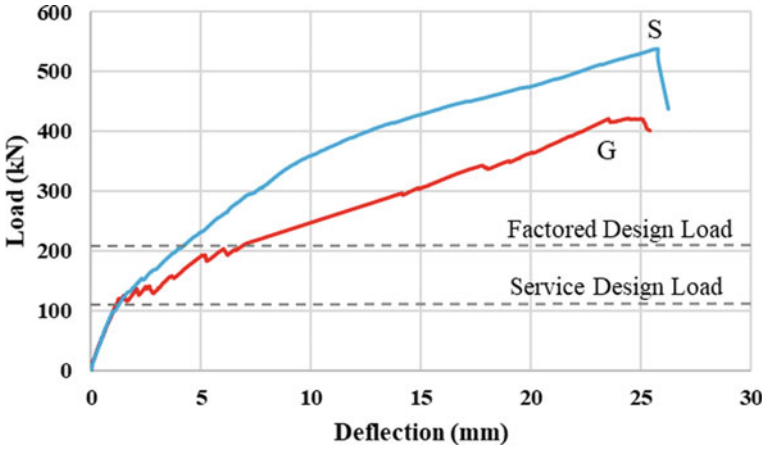

Fig. 6 Load-deflection curves of the bridge-deck slabs

3.3 Deflection Behavior

Figure 6 shows the load-deflection curves of the specimens. The maximum deflections at the ultimate load were 24.47 and 25.72 mm for slab G and S, respectively. The behavior of the slabs was similar up to failure and the bilinear load-deflection curves were drawn. Having more than three times of axial-reinforcement stiffness ($\rho \times E$) in slab S compared to the slab G had a significant impact on the maximum deflection at the same load level. The recorded deflections at service and ultimate load were approximately similar. This indicates that reinforcing bar type and modulus of elasticity have a major effect on the deflection behavior of the slabs.

4 Conclusions

Full-scale lightweight self-consolidating concrete bridge-deck slabs reinforced with steel and GFRP bars were tested under a single concentrated load simulating the footprint of a sustained truck wheel load (87.5-kN CL-625 truck) to investigate the structural behavior of load capacities. The results of this experimental study are as follows:

- A similar cracking pattern appeared on the bottom and top surfaces of the slabs after testing. Also, according to the readings from LVDTs, approximately similar maximum crack width was recorded at the ultimate load for the slabs. This confirms that GFRP-reinforced slab can show almost similar cracking behavior to the steel-reinforced slabs.
- The punching-shear mode of failure was evidenced for the slabs at the ultimate loads exceeded the factored designed loads specified by the CSA S6-19.

- The slab G bearded up to 78% of the ultimate load of slab S. This represents the acceptable behavior of the GFRP-reinforced slab by having a one-third the axial-reinforcement stiffness of slab S.
- At the same load level, slab G showed a higher maximum deflection and crack width. However, at the service designed load and ultimate load, approximately similar crack width and maximum deflection were recorded for the slab G and S. In general terms, this can prove that LWSCC GFRP-reinforced slabs showed acceptable structural behavior and can be used to reduced total construction mass and cross-sections of the elements.

Acknowledgements This research was conducted with funding from the Tier 1 Canada Research Chair in Advanced Composite Materials for Civil Structures, the Natural Sciences and Engineering Research Council of Canada (NSERC), the Fonds de la recherche du Québec en nature et technologies (FQR-NT), and the Canadian Foundation for Innovation (FCI), and for the technical help provided by the staff of the structural lab of the Department of Civil Engineering at the University of Sherbrooke. The authors would like to express their special thanks and gratitude to Northeast Solite Corporation for their generosity. Their donation of Solite® aggregate was instrumental to the success of the research project.

References

1. ACI Committee 440 (2006) Guide for the design and construction of structural concrete reinforced with FRP bars (ACI 440.1R-06). American Concrete Institute, Farmington Hills, MI, 44 pp.
2. Ahmad SH, Zia P, Yu T, Xie Y (1993) Punching shear tests of slabs reinforced with 3-D carbon fiber fabric. ACI Concr Int 16(6):36–41
3. ASTM C150/C150M-18 (2019) Specification for Portland cement. ASTM International, West Conshohocken, PA
4. ASTM C330/C330M-17a (2017) Standard specification for lightweight aggregates for structural concrete (Rapport technique). ASTM International, West Conshohocken, PA
5. ASTM C567/C567M (2014) Standard test method for determining density of structural lightweight concrete. ASTM International, West Conshohocken, PA
6. Canadian Standards Association (2002) Design and construction of building components with fiber reinforced polymers (CAN/CSA S806-02), Rexdale, Canada
7. Canadian Standards Association (2012) Design and construction of building components with fiber reinforced polymers (CAN/CSA S806-12), Rexdale, Canada
8. Canadian Standards Association (2019) Canadian highway bridge design code (CAN/CSA S6-19), Rexdale, ON, Canada
9. Canadian Standards Association (2019) Specification for fibre-reinforced polymers (CAN/CSA S807-19), Rexdale, ON, Canada
10. Elgabbas F (2016) Development and structural testing of new basalt fiber-reinforced-polymer (BFRP) bars in RC beams and bridge-deck slabs. Doctoral Dissertation, Université de Sherbrooke, Sherbrooke, Quebec, Canada
11. El-Gamal S, El-Salakawy E, Benmokrane B (2007) Influence of reinforcement on the behavior of concrete bridge deck slabs reinforced with FRP bars. ASCE J Compos Constr 11(5):449–458
12. El-Gamal S, El-Salakawy EF, Benmokrane B (2005) Behavior of concrete bridge deck slabs reinforced with FRP bars under concentrated loads. ACI Struct J 102(5):727–735

13. Hussein A, El-Salakawy E (2018) Punching shear behavior of glass fiber-reinforced polymer–reinforced concrete slab-column interior connections. ACI Struct J 115(4):1075–1088
14. Liu R, Pantelides CP (2013) Shear strength of GFRP reinforced precast lightweight concrete panels. Constr Build Mater 48:51–58
15. Osman M, Marzouk H, Helmy S (2000) Behavior of high-strength lightweight concrete slabs under punching loads. ACI Struct J 97(3):492–498
16. Pantelides CP, Besser BT, Liu R (2012) One-way shear behavior of lightweight concrete panels reinforced with GFRP bars. Compos Constr 16(1):2–9
17. Pantelides CP, Liu R, Reaveley LD (2012) Lightweight concrete precast bridge deck panels reinforced with glass fiber-reinforced polymer bars. ACI Struct J 109(6):879–888

Design Challenges of the Widening of an Existing Bridge with Post-tensioned Concrete Deck

A. Vosogh, A. Sadeghian, and M. Hassan

1 Introduction

As a part of the project of widening of a major highway, an existing bridge located in Edmonton, AB, had to be widened. The existing bridge in N-S direction carries three (3) 3.7 m wide lanes of traffic with a 2.5 m inside shoulder and 3.0 m outside shoulder (total 16.60 m clear width) in the south-bound direction and was built in 2005. The total width of the existing bridge including the barrier is 17.64 m. The bridge structures are in total 111.4 m long and have two spans, 49.0 m North span and 46.0 m South span, in addition to 2 approach spans of 8.2 m each. The bridge spans overpass perpendicular E-W roadways. The bridge superstructure is supported on center piers with fixed-bearing and expansion-bearings at the abutments. The longitudinal slope of the bridge deck is 0.514% from North to South. The bridge section has a 2% transversal slope from the crown.

The project scope of work includes the widening of the bridge by widening of its cross section to 24 m clear width between the barriers. A 7.4 m widening will be applied to the outside of the existing bridge. The widening will ultimately accommodate two extra 3.7 m lanes. The existing abutments, pier columns and foundations were not designed for future widening (Fig. 1).

1.1 Existing Super-structure

The existing superstructure consists of five precast pre-stressed and post-tensioned concrete NU girders with a reinforced concrete deck. The girders are continuous

A. Vosogh · A. Sadeghian · M. Hassan (✉)
Cima+ Inc., Montreal, Canada
e-mail: Munzer.Hassan@cima.ca

S. Walbridge et al. (eds.), *Proceedings of the Canadian Society of Civil Engineering Annual Conference 2021*, Lecture Notes in Civil Engineering 244,
https://doi.org/10.1007/978-981-19-0656-5_12

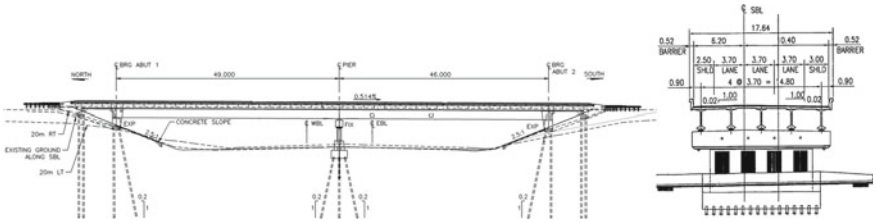

Fig. 1 Existing bridge Elevation (left) and section (right), (Alberta ministry of transportation)

over the center pier and are not integral with the pier. The girders support a 235 mm thick reinforced cast-in-place deck, with an 80 mm 2-course ACP wearing surface on 10 mm deck waterproofing.

The existing bridge girders are NU2000 × 175 girders spaced at 3.7 m. The deck cantilevers on each side of the bridge are 900 mm, and the barrier width is 520 mm. The width of the top and bottom flanges are 1,250 and 1,000 mm respectively and the thickness of the web is 175 mm. The intermediate diaphragms are steel X-bracings and are spaced at 9.8 m for the North span and 9.2 m for the South span. There is a 1,500 mm wide concrete diaphragm at the abutments to connect the girders. The concrete strength for these girders (28 days strength) is 70 MPa and pre-stressed strands in the bottom flange produced pre-stressing within the girders. Additionally, four 15.2 mm post-tensioning mono-strands in the top flange of each girder were added to achieve the desired deflections at transfer after pre-tensioning. The North (49 m) and South (46 m) girders were designed to have 96 and 91 mm camber at the time of erection. In addition to pre-stressing strands, there are three post-tensioning ducts in each girder, each duct contains post-tensioned low relaxation strands. The post-tensioning was carried out in two phases at the end of two separate construction stages of the cast-in-place slab. The girders were joined to each other at the splice joint located at 400 mm on the North side from the center pier axis. The superstructure is fixed to the sub-structure through bearings, transversely at the abutments and center pier, and is longitudinally fixed to the sub-structure only at the center pier.

2 Design Challenges

The first common solution for the widening of bridge decks is to use the same structural concept for the widening part of the deck i.e., use of pre-tension and post-tensioned NU 2000 girders. However, for the case of this bridge there have been several design challenges for widening the existing superstructure. Since the current 2% cross fall of the deck must be maintained in the widening portion of the deck, the available road clearance under the bridge spans will be reduced. The total thickness of the existing deck is 2.404 m that composes the height of the girder, haunch, slab, and ACP layers. Using the same NU 2000 girders and assuming that the new

exterior girder is located 7 m from the existing exterior girder, the road clearance would be reduced by 140 mm which falls under the minimum 5.6 m required road clearance by the authorities. It should be noted that the existing NU 2000 girders have been heavily prestressed by pre-tensioning strands and post-tensioning tendons to pass serviceability and ultimate limit states requirements. Also, considering actual camber variability, a thicker haunch is required for the new deck to ensure proper matching of existing and new deck's final grade. In addition, the existing bridge was designed for CS-750 truck loads. But according to the current design requirements the new deck must be designed for CL-800 loadings. Consequently, reducing the total thickness of prestressed concrete decks to overcome the clearance problem became a remarkable issue during the conceptual design phase.

On the other hand, the significant axial prestressing forces on the NU girders and the slab causes a major time dependent behaviour of both the widening deck and the existing deck. The existing structure was constructed in 2005 and based on the estimations by the formulations provided in CHBDC respectively more than 97% and 94% of girder and slab creep should be completed so far. But based on CHBDC recommendations only 89% and 49% of girder and slab shrinkage strains are expected to be completed at this point. Since a large portion of the of the creep and shrinkage deformation happen in the first couple of years after the concrete pour, a common method to reduce the effect of time-dependent deformation of new structures on the old deck is to delay the closure pour between the two superstructures. However, determining the minimum delay is a challenging subject for engineers. To determine the minimum delay, it is important to have an accurate estimation of the deformations due to creep and shrinkage over time. Comparison of creep and shrinkage completion by time suggested by AASHTO LRFD-2017 and CSA-S6-14 show a considerable difference between the two codes. The presented graph at Fig. 2 for the existing NU 2000 girders illustrates this difference. Evidently, the Canadian code predicts a much slower rate of completion, especially for shrinkage. CEB-FIP MODEL CODE 1990 was also consulted for comparison and its results were found similar to CSA-S6-14 results.

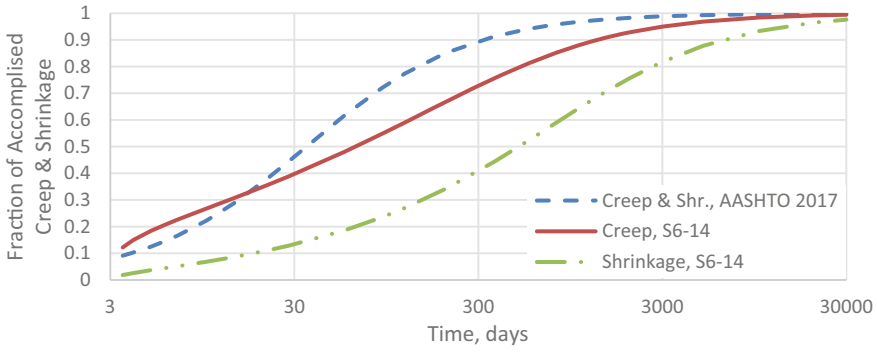

Fig. 2 Time development model of creep and shrinkage

From a mechanical perspective, the effects due to the differential deformations between the existing and new concrete decks are crucial. After merging the two decks, the existing deck will tend to decompress the new deck whereas the new deck tends to compress the existing deck. Also, continuous shortening in the new deck will impose transversal bending on the old deck and causes tension in far exterior existing girders and compression in near existing NU girders. Such actions are also dependent on the elastic modulus of the existing and new concrete deck. However, there are many uncertainties regarding the elastic modulus of concrete and accurate estimation of elastic modulus of the existing and new concrete is another challenging subject. As previously mentioned, in order to limit such restraint effects, the closure pour should be cast when the differential deformations are reduced to an acceptable limit. The acceptable time for merging two decks can be estimated from design code recommendations and should be verified based on field measurements during construction. For the case of the bridge under study, the preliminary calculations based on CSA-S6-14 provisions showed that the estimated time for the casting the closure pour should be around two years after the last stage of post-tensioning.

3 Proposed Solution

To avoid the challenges with the addition of a concrete deck, using steel composite beams for the new deck was proposed as a better option to limit total deck thickness, shorten the waiting time before casting the closure pour, eliminate the effects of time dependent deformations of concrete girders and to reduce the uncertainties pertinent to the actual camber of girders. Figure 3 illustrates the cross section of the proposed solution.

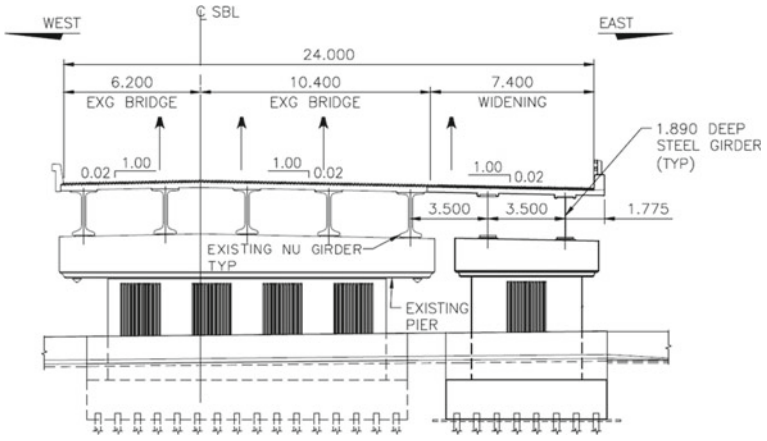

Fig. 3 Cross section of widened bridge

The connection of unsimilar deck systems introduces new challenges that need to be addressed appropriately. The major challenges are: i) Cracking of the slab of the composite steel girder deck around the pier due to negative bending moments; ii) Different stiffness of the steel girders and concrete NU girders; and iii) Difference in thermal coefficient of steel and concrete girders.

Due to negative bending moments caused by the superimposed dead loads (SDL) and live load, at service limit state, the slab of a common composite steel deck develops cracks. However, because of the post-tensioning, the existing deck slab experiences no cracking. This inconsistency in behaviour across the deck slab of the widened bridge is not favorable and will interrupt the load paths in the widened deck. An innovative solution was utilized to prevent cracking of new deck slab under permanent loads. According to this concept, the composite deck (steel girders and slab) was designed to be initially erected and poured at a higher elevation on temporary supports located at the pier (Fig. 4). Later when the poured concrete gains its characteristic strength, the deck will be lowered by removing the temporary supports and jacking down the deck to its final elevation. This approach will induce compression stresses in the new deck slab and will mimic the post-tensioning of the existing deck in the composite steel widening deck. This also results in more homogeneous stress distribution between the existing and new deck particularly around the centre pier. However, this approach also imposes permanent compression in new deck slab and introduces time dependent effects in the new deck that must be taken into consideration.

In order to have better live load distribution between the girders and predictable behaviour of the widened deck, it is necessary to adjust stiffness of composite steel girders with the existing prestressed deck. Therefore, the size of steel girder was determined to limit the variation of stiffness across the widened deck to less than 10%.

Thermal coefficients of concrete and steel are slightly different and the concrete slab along the deck closure must be capable of integrating different expansion/contraction between steel and concrete girders across the length of the bridge. In addition to different responses of concrete and steel girders to uniform raise or fall of ambient temperature, their responses to temperature gradient across the height of deck are also completely different.

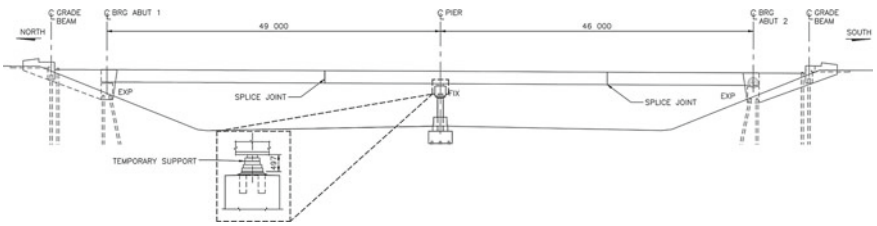

Fig. 4 Erection of superstructure on elevated temporary bearing

4 Deck Analysis

To investigate the effects of various loads imposed to the widened deck, a 3D finite elements model with staged construction was created in CSIBridge (Fig. 5).

To produce better estimates for the creep and shrinkage effects, the time dependent material properties for all concrete elements (concrete girders and deck slabs) were defined in the software based on CSA-S6-14/CEB-FIP Model Code 1990. In creating the analytical model, the following main steps were followed:

i) Modeling the old structure by considering the elapsed time; ii) Erection of new steel girders on the temporary bearing positioned 300 mm higher than permanent bearings, followed by pouring of new concrete slab; iii) 28 days waiting time to allow the young concrete to gain its 28 day strength; iv) Lowering the new deck to its permanent position and inserting the permanent bearings; v) 16 days waiting time to allow a fraction of creep to take place before connecting the old and new decks; vi) Demolishment of the existing barrier adjacent to the new deck and connection of the diaphragms between old and new girders. Pouring of the deck closure (start of the interaction between two decks); vii) Apply the loads of the new barrier and the wearing surface to the structure; viii) Run the analysis to calculate the induced actions due to the creep and shrinkage in the new deck slab up to the next 75 years.

Furthermore, the maximum and minimum temperature range and thermal gradient were calculated per CSA-S6 for both types of concrete girder and steel beam decks and were applied to the finite element model accordingly.

4.1 Slab Stresses

The short-term stresses due to lowering the new girders are shown in Fig. 6 with an average of −7.2 MPa (compressive) on the pier. Based on the formulations from CEB-FIB 1990 model code, 16 days after the deck lowering the slab, because of the

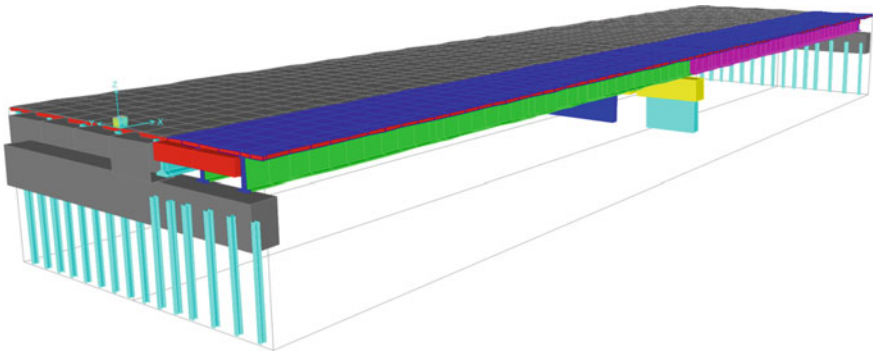

Fig. 5 An isometric view of the 3D analytical model

completion of a portion of creep and shrinkage strains, the stress will be decreased to −5.2 MPa (compressive) (Fig. 7).

The closure pour is a main element in the interaction of the old and new decks and was one of the major concerns during preliminary design. Figure 8 presents longitudinal stresses due to time dependent deformations during summer. Maximum tension in closure joint would be 1.6 MPa on the pier and maximum shear stress would happen adjacent to expansion joint with value of 0.8 MPa. These stresses are within acceptable range for concrete.

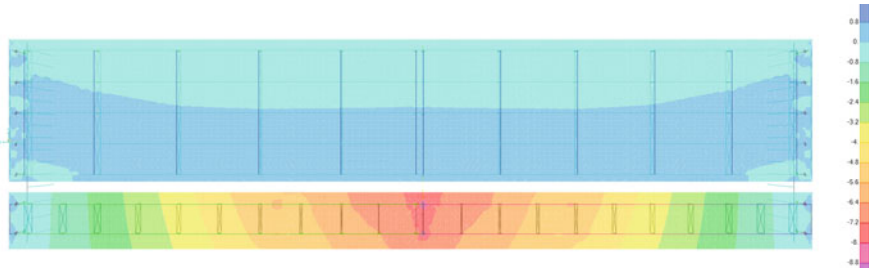

Fig. 6 Longitudinal stresses in new slab immediately after lowering

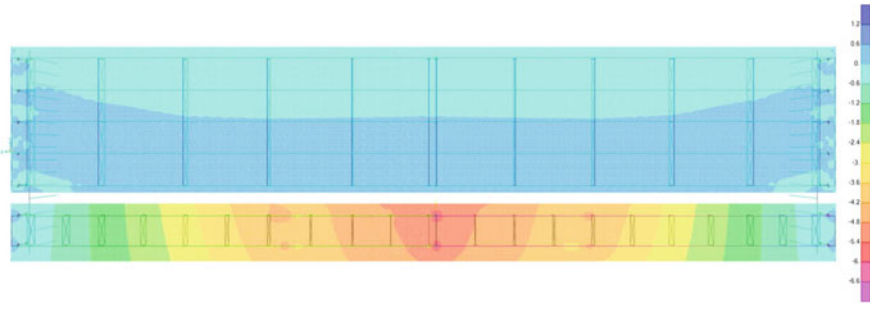

Fig. 7 Longitudinal stresses in new slab before casting of closure pour

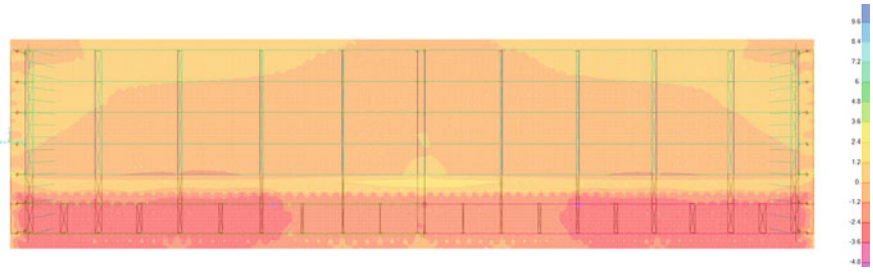

Fig. 8 Longitudinal stresses in slab due to Creep + Shrinkage + Temperature's rise in summer

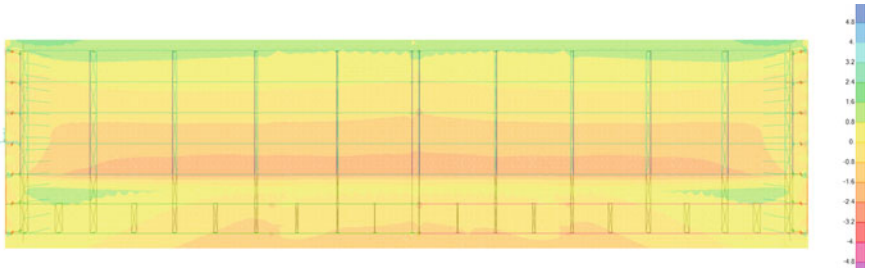

Fig. 9 Longitudinal stresses in slab due to Creep + Shrinkage + Temperature's fall in winter

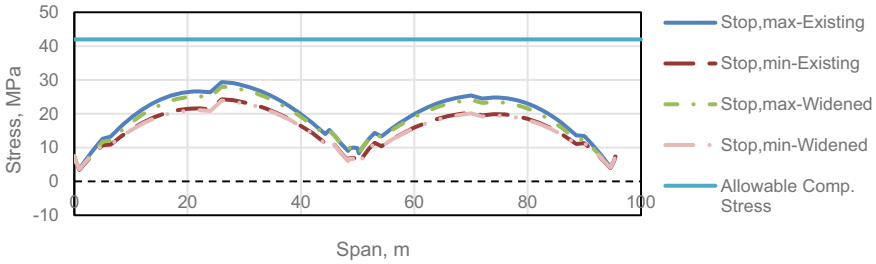

Fig. 10 Stresses in existing exterior girder-top extreme fiber

Figure 9 represents the final effect of shrinkage and creep that is combined with temperature stresses during the winter. Maximum stresses take place at the vicinity of expansion joints with magnitude of 1.3 and 1.6 MPa for longitudinal and shear forces respectively. Again, stresses are less than concrete strength.

4.2 Concrete Girder Stresses

The existing deck was analysed based on given information in as-constructed drawings and existing stresses were extracted to represent the current superstructure. Then, effects of extra loads on the widened deck including the creep and shrinkage of the composite steel portion of the widened deck and the thermal deformation were analysed and added to stresses of the existing concrete girder. Figure 10, 11, 12 and 13 present the status of stresses before and after widening. The jumps on the graphs represent the debonding of pre-tensioning strands and construction stages for slab pouring and stressing of post-tensioning tendons in the existing structure.

As it can be seen, the level of Serviceability Limit States stresses in the exterior NU girders are within allowable compression and tensile limits. The 3rd interior girder (nearest interior girder to new deck) has the most unfavourable stress state within the evaluation. Along a short length of this girder, the tensile stresses of the

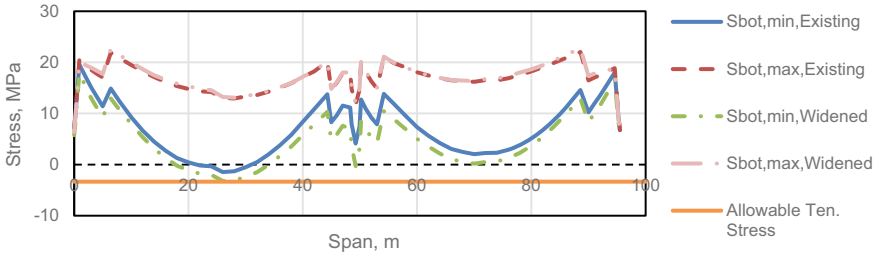

Fig. 11 Stresses in existing exterior girder-bottom extreme fiber

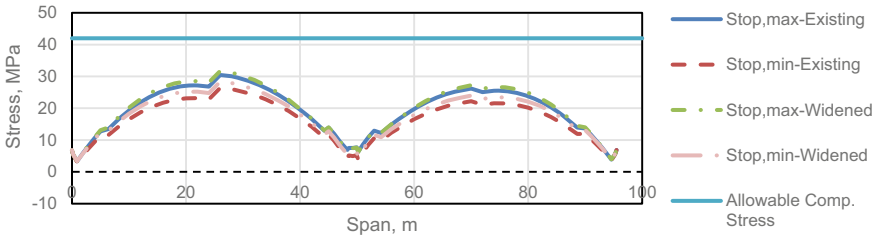

Fig. 12 Stresses in existing 3rd interior girder-top extreme fiber

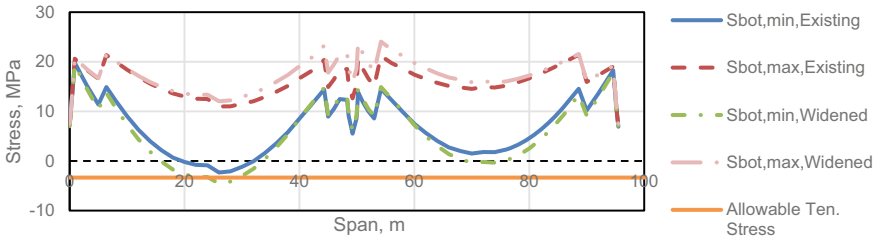

Fig. 13 Stresses in existing 3rd interior girder-bottom extreme fiber

bottom fiber drop beyond the cracking stress given by CSA-S6-14. Investigations show that this case happens when the CL-800 trucks move together during a hot summer day. After passage of the CL-800 trucks or colling down the girder the crack will be closed again. So, considering on the temporary nature of this load case and its low probability of occurrence, this exceptional case was accepted, since its effect on durability will be negligible.

5 Impact of Soil Settlement on the Existing and New Piles at the Abutments

The abutments of the existing bridges were structurally designed as semi-integral abutments including abutment seat, wing walls and roof slab. The abutment seats are supported by two rows of H310 × 110 steel driven piles, with each row consisting of eleven piles. The front row of abutment piles (towards the E-W roadway) consists of battered piles with 5V:1H inclination while the second row has all vertical piles.

Another challenging complication in this project was the impact of potential settlement, due to the addition of the new abutment backfill for the widening portion of the structure, on the existing and new driven steel piles at the abutments. The thickness of new embankment fills at the abutments reaches nearly 1.7 m in some areas. The settlement due to the weight of new embankment not only produces drag-down forces for both new and existing piles in direction parallel to the piles, but in case of the battered piles it also produces additional bending due to the settlement component in the direction perpendicular to the piles (Fig. 14).

The geotechnical investigations determined that around the new piles (widening area), the addition of backfill is expected to cause approximately 15 mm of vertical settlement at the surface. The settlement diminishes to zero at a depth of approximately 11 m below the ground surface. Additionally, around the existing piles, the surface settlement was determined to be approximately 7 mm, diminishing to zero at a depth of approximately 10 m below the ground surface.

To evaluate the induced loads along the piles, the soil settlement in the direction parallel to the pile axis was used in combination with the unit shaft and end-bearing resistances of the pile to estimate the axial drag loads. To evaluate the induced bending in the battered piles, the soil settlement in a direction perpendicular to the pile axis was used in combination with the soil spring forces provided to estimate the magnitude of soil loadings acting perpendicular to the pile axis.

The above-mentioned approach was utilised to implement finite element models in Advance Design America [6]. The model considered the section losses due to corrosion in the existing abutment piles (Fig. 15).

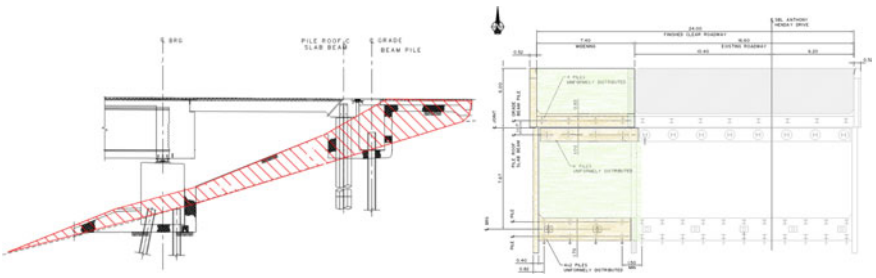

Fig. 14 Additional embankment required for abutment widening (left), plan of the widening abutment (right)

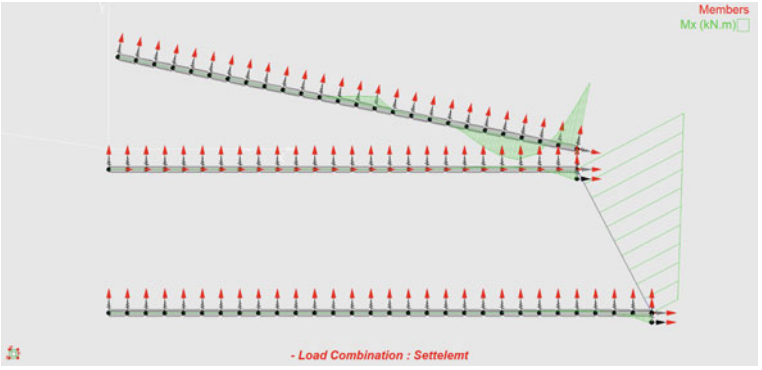

Fig. 15 Induced forces in the existing and new abutment and grade beam piles due to soil settlement caused by the addition of embankment

The results of the analysis show that the induced axial drag-down forces due to the soil settlements for the vertical piles would be 372 and 409 kN for the existing and new vertical piles respectively. The axial drag-down forces for the existing and new battered piles would be 365 and 401 kN respectively. The maximum additional induced bending moment due to the soil settlement in the existing and new piles would be up to 9.6 and 13.1 kNm respectively. The results of this study showed that the capacity of the existing and new piles to bear the induced forces due to the soil settlement in addition to the axial gravity loads from the structure was satisfactory.

6 Conclusion

Widening of post-tensioned concrete bridge decks has been a continuous challenge for bridge engineers. Widening using similar post-tensioned deck is specifically problematic since the time-dependent deformations in the new deck could increase the stress levels beyond the cracking threshold within the existing deck and common solutions may lead to significant construction delays.

This article introduces an innovative solution by using a steel composite deck that is initially erected at an elevated position and after sufficient hardening of the deck slab, is lowered to its final position. The analyses show that, as intended, the induced compressive stress within the new slab serve as prestressing forces and are expected to prevent cracking of this slab around the region with negative bending moments. The closure pour between the decks is intended to be cast 16 days following the lowering of the new deck to minimize the stresses caused by differential deformations between the existing and new decks. Such effects, and the increase of the design live load to CL-800 were investigated by developing a 3D finite element model. The study illustrates that along a short length of few girders the tensile stress can go slightly beyond the cracking stress allowed by code. Such a case occurs when CL-800 trucks

move together during a hot day of the summer. It was concluded that after the passage of the trucks the cracks will be closed again. When these two loads are not concurrent the tensile stress will not exceed the acceptable limits.

Additionally, the impacts of soil settlement due to new abutment embankment fills on the existing and new abutment piles were studied. As expected, the impact of the soil settlements on the battered piles was more significant than that of the vertical piles. However, the analysis showed that the additional efforts were not significant to cause damage within either the existing, or new, abutment piles.

Acknowledgements The authors would like to thank Alberta Ministry of Transportation for their assistance and authorising access to the materials used for writing this paper.

References

1. American Association of State Highway and Transportation Officials (2017) AASHTO LRFD bridge design specifications, customary U.S. units. American Association of State Highway and Transportation Officials, Washington
2. Alberta Ministry of Transportation (2018) NU girder design and detailing manual, vol 1. Version 1.0. Ministry of Transportation, Edmonton
3. Canadian Standards Association (2014) Canadian highway bridge design code (CAN/CSA Standard No. S6-14). Canadian Standards Association, Rexdale
4. Comite Euro-International Du Beton (1993) CEB-FIP MODEL CODE 1990. Default book series. Lausanne, Switzerland
5. Computers and Structures Inc. (2021) CSIBridge Ver. 21.2.0. Computers and Structures, Inc., Berkeley, California
6. Graitec Inc. (2019) Advance design America. Graitec Inc., Innovation SAS, BIÈVRES, France

Assessment of Fatigue Design Provisions for Bridge Elements with Very Short Influence Lines

A. Chehrazi, M. Y. X. Chien, and S. Walbridge

1 Introduction

Fatigue failure has always been a significant problem in bridge structures. Therefore, preventing this failure mode is a primary task for bridge designers. The typical design approach in bridge codes involves passing a truck model over the influence line of an element of interest and determining the stress range caused by the truck model. This stress range is then multiplied by a fatigue correction factor and compared with an allowable stress range, known as fatigue resistance. Inaccurate fatigue correction factors can significantly influence the reliability of this approach. The fatigue correction factor can be obtained/calibrated using a code truck model, a real traffic database, a bridge model, etc. Given the possibility of changes in the truck weight distribution of the real traffic, regular calibration of fatigue correction factors is essential.

Design codes typically specify two separate correction factors, one for finite and another for infinite life design. Several works have investigated finite life factors, also known as damage equivalence factors. [5] presented a simulation-based method to determine these factors for finite life design. [2] used this method to calibrate the finite life factors in North American bridge design codes for welded aluminum highway structures and evaluate the possible effects of overload trucks on these factors. [4, 7] discussed the influences of simultaneous truck crossings on the finite life factors, again for North American bridge design codes.

A. Chehrazi (✉) · M. Y. X. Chien · S. Walbridge
University of Waterloo, Waterloo, Canada
e-mail: achehraz@uwaterloo.ca

M. Y. X. Chien
e-mail: michelle.chien@uwaterloo.ca

S. Walbridge
e-mail: swalbrid@uwaterloo.ca

S. Walbridge et al. (eds.), *Proceedings of the Canadian Society of Civil Engineering Annual Conference 2021*, Lecture Notes in Civil Engineering 244,
https://doi.org/10.1007/978-981-19-0656-5_13

Despite these works on the finite life factors for details with varying influence line length, no study to date has studied these factors for components with a focus on very short influence lines (e.g., elements spanning transversally). With this in mind, the current paper first reviews the fatigue design criteria of the Canadian Highway Bridge Design Code, CSA-S6. It then presents the steps for determining the fatigue correction factors, and finally, evaluates these factors for elements with very short/short influence lines.

2 Background

2.1 Fatigue Design According to Canadian Bridge Design Code

According to [1], given normal traffic conditions, each structural detail must satisfy the following:

$$\lambda_1 \cdot f_{sr} < F_{sr} \tag{1}$$

where λ_1, the damage equivalence factor, is equal to 0.52 for all structural details except elements in bridge decks; f_{sr} is the nominal stress range at the structural component of interest due to the passage of the code truck, and F_{sr} is the fatigue resistance of the component and can be determined as follows:

$$F_{sr} = \left(\frac{\gamma}{N_c}\right)^{1/3} \tag{2}$$

$$\text{If } F_{sr} = \left(\frac{\gamma}{N_c}\right)^{1/3} < F_{srt} \text{ then } F_{sr} = \left(\frac{\gamma'}{N_c}\right)^{1/5} \geq \frac{F_{srt}}{2} \tag{3}$$

where γ and γ' are fatigue life constants, F_{srt} is the constant amplitude threshold stress range of the detail, and N_c is the estimated number of truck passages during the design life of the bridge and can be calculated as follows:

$$N_c = 365 \cdot y \cdot N_d \cdot ADTT_f \tag{4}$$

in which y is the design life (typically 75 years), N_d is the number of stress cycles for each passage of the code truck, and $ADTT_f$ is the single-lane average daily truck traffic.

2.2 Infinite Fatigue Life Correction Factor

Based on Eqs. 1–3, a component with "infinite" fatigue life must satisfy the following:

$$0.52 f_{sr} < \frac{F_{srt}}{2} \tag{5}$$

This equation can be rewritten as follows:

$$\lambda_2 \cdot f_{sr} < F_{srt} \tag{6}$$

Equation 6 is similar to Eq. 1. However, λ_2 is the infinite life correction factor and is equal to 1.04 (= 0.52·2) based on the current version of the CSA-S6 design code.

3 Methods

3.1 Damage Equivalence Factor, λ_1, Calculation Procedure

This paper employs the method described by [5] to determine damage equivalence factors for bridge structural elements. Based on this method, a damage equivalence factor can be determined using a real traffic database, a code truck model, and the influence line of a detail of interest. The calculation procedure is as follows:

1. The trucks in the real traffic database are passed over the influence line of the detail of interest.
2. The load effects are computed based on the axle loads of the trucks and the influence line of the detail, and the peak values of the load effects are recorded.
3. A rainflow cycle counting method (e.g., [3]) is used to generate a stress range histogram based on the peak values stored in Step 2. The histogram values are then divided by the total number of trucks in the real traffic database to generate a histogram with the average occurrence frequencies in each stress range bin.
4. The code truck model is passed over the influence line, and the stress range at the detail of interest due to single code truck passage is determined.
5. The stress range histogram in step 3 is scaled to the total expected number of passing trucks during the design life of the bridge, N_c.
6. The S-N curve for the detail category of interest is displaced vertically until the damage caused by the stress ranges in the histogram of Step 5, D_{real}, equals 1. Then, the parameter used to vertically displace the S-N curve is recorded, M_{real}:

$$Log_{10}(N) = Log_{10}(M) - m \cdot Log_{10}(\Delta S) \tag{7}$$

7. The S-N curve for the detail category of interest is displaced vertically until the damage caused by the code stress range, found in Step 4, in N_c cycles, D_{code}, equals 1. Then, M_{code} is recorded.
8. It can be shown that the damage equivalence factor can be determined as follows:

$$\lambda_1 = \left(\frac{M_{real}}{M_{code}}\right)^{\frac{1}{m}} \tag{8}$$

where m is the initial slope of the S-N curve.

3.2 Infinite Life Correction Factor, λ_2, Calculation Procedure

As shown in Eq. 6, for infinite life design, the code stress range is multiplied by the infinite life fatigue correction factor and then compared with a fatigue threshold. This factor accounts for the difference between the stress range caused by the code truck and the peak stress range in the real stress range histogram. A component under variable amplitude cyclic loading has an infinite life (for practical purposes) if only 0.01% of the cycles pass the constant amplitude threshold stress range according to various sources, e.g. [6]. This definition is mainly used for variable amplitude fatigue tests. However, generated histograms show that the average number of cycles per truck passage is usually more than one cycle, especially for elements with very short influence lines. Therefore, a per truck definition is used in the current study, and instead of a 1/10000 recurrence rate, a recurrence rate of 1/(10,000·average number of cycles per truck passage) is employed. An infinite life correction factor can be determined using a real stress range histogram and a code stress range, respectively based on Steps 3 and 4 of the method developed by [5]. Given the stress range with 1/(10,000·average number of cycles per truck passage) recurrence rate from the real stress range histogram, $\Delta S_{1/10000}$, and the code stress range, ΔS_{code}, the infinite life correction factor, λ_2, can be calculated as follows:

$$\lambda_2 = \frac{\Delta S_{1/10000}}{\Delta S_{code}} \tag{9}$$

Several methods can be used to determine $\Delta S_{1/10000}$ from the real traffic stress range histogram. In this paper, a normal distribution is fitted to the tail of the histogram. The following equation is used to fit the normal distribution to the stress range histogram of the real traffic:

$$\Delta f_p = m_{normal} \cdot \Phi^{-1}(p) + b_{normal} \tag{10}$$

where p is the percentile and Φ^{-1} is the inverse of the standard normal distribution. The top 10% range, i.e. the 90th to 99.9th percentiles, is used for tail fitting. Because of

the limited size of the real truck database, results in the top 0.1% range are inaccurate and therefore not used in the curve fitting process.

4 Simulation Parameters

Two real truck traffic databases from the Ontario Ministry of Transportation are used in this study. These databases include axle weights, and the spacing between the axles of each truck. The first database, obtained in 1995, includes 10,198 trucks and the second one, obtained in 2012, includes 45,192 trucks. The histograms of the gross vehicle weight, GVW, of these databases are shown in Fig. 1.

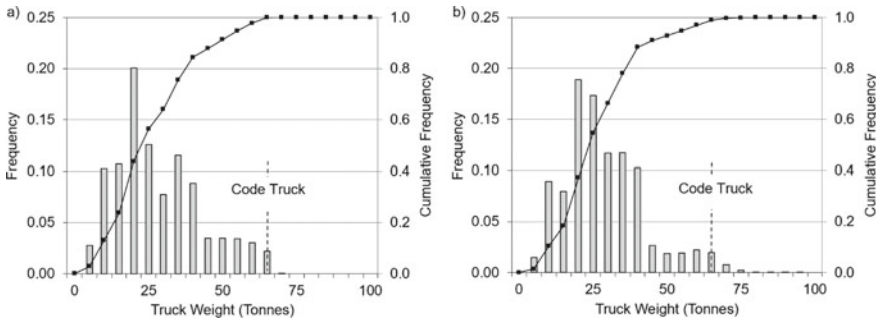

Fig. 1 GVW histograms for MTO 1995 **a** and MTO 2012 **b** databases

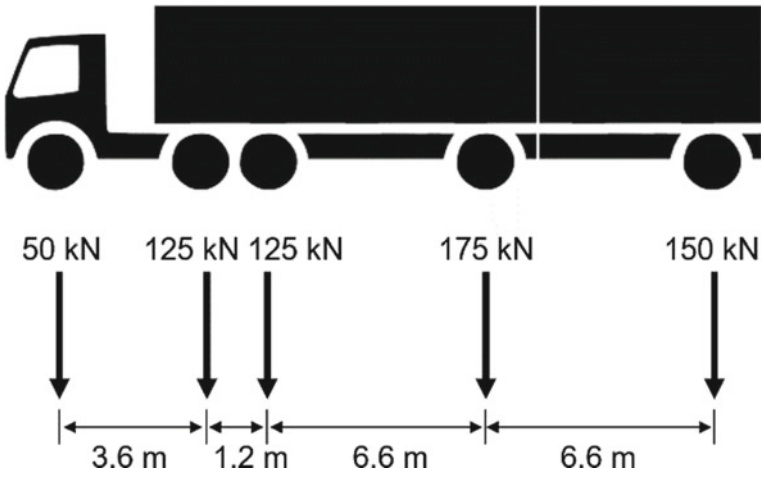

Fig. 2 CSA-S6 truck model

The design truck model from CSA-S6 is used in this work (see Fig. 2). This 5-Axle truck model has a GVW of 625 kN (62.5 tonnes). Based on the detail category, different dynamic load allowance, DLA, values are specified in CSA-S6. For example, this factor is 0.5 for deck joints, and 0.4 if only one axle of the design truck model is used. In this work, however, the DLA has no practical effect on the results because the same value is used for both real traffic and the design truck.

Four different highway classes, A, B, C, and D, with ADTTs of 50, 250, 1000, 4000 respectively, are evaluated in this work. Based on CSA-S6, an N_d value of 2 is employed for elements with influence lines shorter than 12 m, and an N_d value of 1 is used for elements with influence lines longer than 12 m. Three detail categories, A, C, and E, with different S-N curves are considered (see Fig. 3).

Two influence line types are employed to evaluate the possible effect of the shape of the influence line on the fatigue factors: ps-m, the positive bending moment at mid-span for a simply supported element, and ps-r, the support reaction of a simply supported element. To cover details with short influence lines, several influence line spans are considered, namely: 0.1, 0.2, 0.5, 1, 2, 3, 5, 10, and 20 m (Fig. 4).

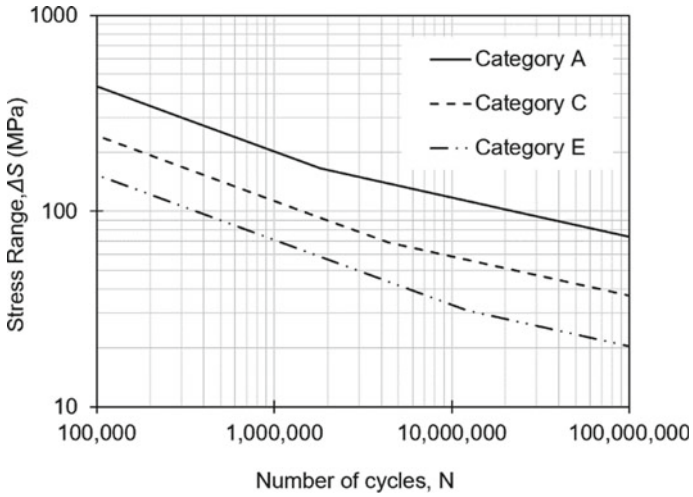

Fig. 3 S-N curve of evaluated detail categories from CSA-S6

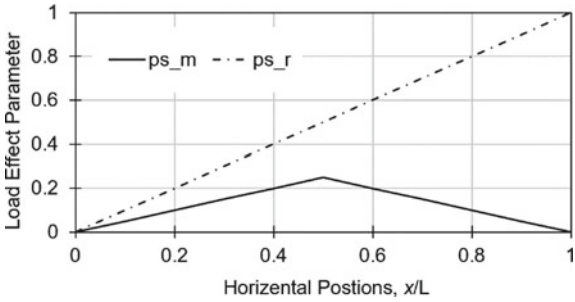

Fig. 4 Studied influence lines

5 Results and Discussion

5.1 Damage Equivalence Factor Results for Finite Life Design

Sample of damage equivalence factor results for the MTO 1995 and MTO 2012 databases are shown in Fig. 5. The results are the same for details with influence lines shorter than 1 m; because the spacing between the subsequent axles of the code truck is more than 1 m, and only a small percentage of the trucks in the real traffic databases have axle spacings shorter than 1 m. Therefore, the results based on influence lines with a length in this range are only a function of individual axles of the trucks, and the shape/length of the influence lines cannot affect the results. However, for elements with longer influence lines, the results are also a function of other parameters including the spacing between the axles of the trucks and the shape/length of the influence lines. As can be seen, for elements with longer influence lines, the correction factors generally increase with an increase in the length of the influence line. However, the combined effects of the several mentioned parameters cause slight fluctuations in the results.

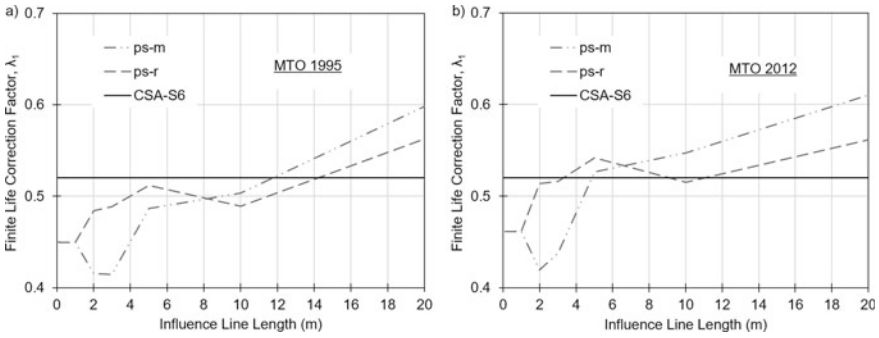

Fig. 5 Sample finite life factor results for a Category A detail with an ADTT of 4000, based on MTO 1995 database **a** and MTO 2012 database **b**

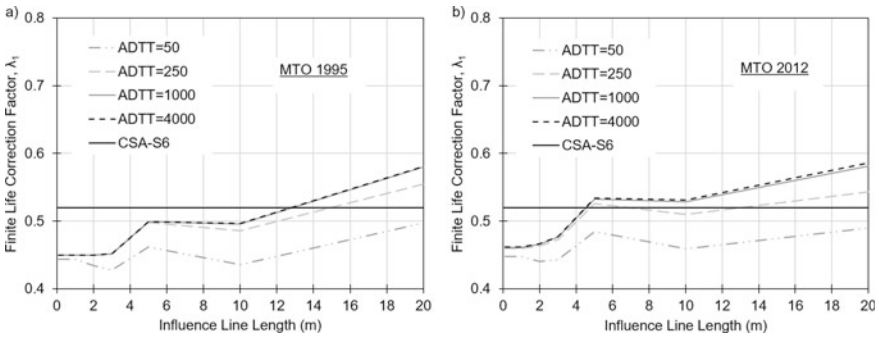

Fig. 6 The effect of ADTT on finite life factors for a Category A detail

Figure 6 shows the effect of ADTT on damage equivalence factors for a Category A detail. The factors in this figure are the average results for the two studied influence line shapes. As can be seen, the damage equivalence factors increase with an increase in ADTT. The results based on the MTO 2012 database are higher than the results based on the MTO 1995 database. This is because of the heavier trucks in MTO 2012 database, which can be seen in Fig. 1. The factors for details with influence lines shorter than 4 m are lower than the current code value (0.52) in all cases. However, factors for details with longer influence lines are higher than the code factor, especially when the MTO 2012 database is used.

In Fig. 7, the results for different detail categories with two commonly used ADTTs, 1000 and 4000, are compared. As can be seen, the results with an ADTT of 4000 trucks per day are very close to each other. However, slight differences can be seen in the results with an ADTT of 1000 trucks per day, especially for members with longer influence lines. The results for the different detail categories show that the code correction factor is conservative for elements with very short influence lines, where only the weights of single axles of the trucks are effective. However, for elements with longer influence lines, several factors affect the results, and the code factor may err on the unconservative side under certain conditions.

5.2 Infinite Life Results

The results for the infinite life fatigue correction factors are shown in Fig. 8. As can be seen, the fatigue correction factors are lower than the code value for very short influence lines ($L < 1$ m) for both the MTO 1995 and 2012 databases. In this range, only the individual axle loads of the trucks are playing a role. It can be seen that the code factor is unconservative for elements with longer influence lines; for these elements, the results are a function of the weight of the truck or the combined effects of more than one axle. Similar to the finite life damage equivalence factor, the infinite

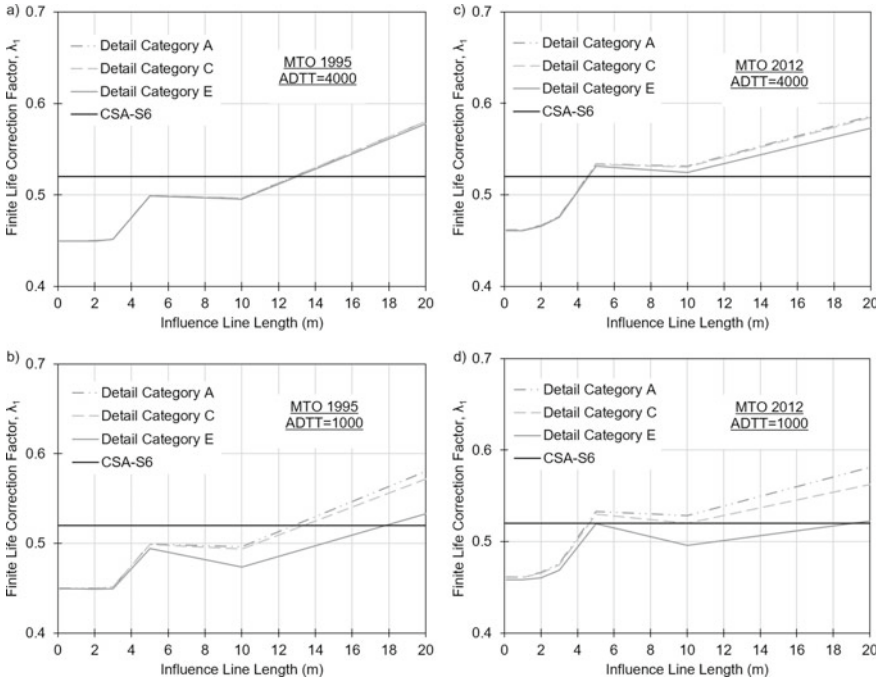

Fig. 7 The effect of detail category type on the finite life factors

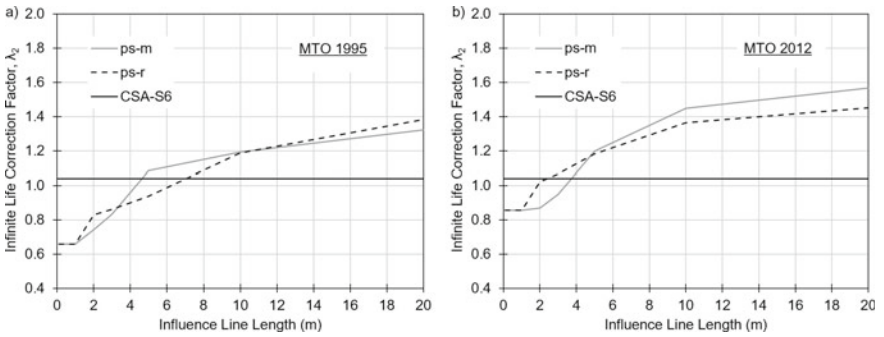

Fig. 8 Infinite life factors based on MTO 1995 **a** and MTO 2012 **b** databases

life factors are higher based on the MTO 2012 database, as it includes heavier trucks in comparison with the MTO 1995 database.

In Fig. 9, the histograms of the maximum axle weights of the trucks in the employed databases are shown. The weight of the heaviest axle of the code truck is 17.5 tonnes (175 kN). As can be seen, a very small percentage of the trucks in both databases has an axle heavier than 17.5 tonnes. However, the percentage of trucks that are heavier than the code truck is much higher. This is the main reason for the

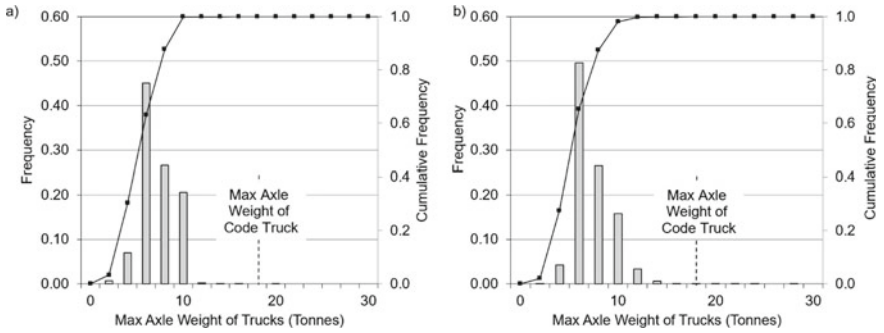

Fig. 9 Maximum axle weight histograms for trucks in MTO 1995 **a** and MTO 2012 **b** databases

higher fatigue correction factors for elements with longer influence lines; because the factors are a function of individual axle loads of the trucks for elements with very short influence lines, and a function of the combined effects of two or more axles of the trucks, or possibly even the gross vehicle weights of the trucks, rather than the individual axle loads, for elements with longer influence lines.

6 Conclusions

Based on the presented results in this paper, the following conclusions can be drawn:

- The fatigue factors in the Canadian bridge design code, CSA-S6, are conservative for elements with very short influence lines ($L < 1$ to 4 m) and it may therefore be reasonable to consider lower fatigue factors for the design and assessment of these elements.
- Fatigue factors increase with an increase in the length of the influence line of structural details. For very high traffic volumes and longer influence line spans, the calculated factors exceed the current code values of 0.52 (finite life) and 1.04 (infinite life). However, this may be due in part to the fact that only two influence line shapes were considered in the current study. (Note: other factors that may justify an increase in these factors for longer spans (e.g. the influence of simultaneous truck crossing events) are discussed elsewhere, and not considered in this paper.)
- The different findings in this paper for long and short spans can be explained by the fact that the available Ontario real truck databases appear to have a higher rate of occurrence of gross vehicle weights exceeding the weight of the code truck (62.5 tonnes) than individual axles exceeding the maximum axle weight of the code truck (17.5 tonnes).

Acknowledgements The idea for this paper of a focused calibration study on short spans came from discussions with G. Grondin at AECOM. M. Haalstra and A. Au at the Ministry of Transportation of Ontario (MTO) are thanked for their insights and providing access to the MTO 2012 survey data used in this study.

References

1. CSA (Canadian Standards Association) (2019) Canadian highway bridge design code. CAN/CSA-S6. CSA, Mississauga
2. Coughlin R, Walbridge S (2011) Fatigue correction factors for welded aluminum highway structures. Can J Civ Eng 38(10):1082–1091
3. Downing SD, Socie DF (1982) Simple rainflow counting algorithms. Int J Fatigue 4(1):31–40
4. Fischer V (2012) Effect of simultaneous vehicle crossings on the North American fatigue correction factors. Master's thesis report, École Polytechnique Fédérale de Lausanne, Lausanne, Switzerland
5. Hirt MA, Bez R, Nussbaumer A (2006) Traite de génie civil, vol. 10: construction métallique—notions fondamentales et méthodes de dimensionnement. Presses Polytechniques et Universitaires Romandes, Lausanne, Switzerland
6. Russo FM, Mertz DR, Frank KH, Wilson KE (2016) Design and evaluation of steel bridges for fatigue and fracture–reference manual. Report FHWA-NHI-16-016, Federal Highway Administration, Washington, DC
7. Walbridge S, Fischer V, Maddah N, Nussbaumer A (2013) Simultaneous vehicle crossing effects on fatigue damage equivalence factors for North American roadway bridges. J Bridg Eng 18(12):1309–1318

A Comparative Study: Seismic Deformability and Strength of Non-conforming Columns

F. Dameh and S. J. Pantazopoulou

1 Introduction

It has been observed in reconnaissance reports following previous strong ground motion events that many structural components constructed prior to the introduction of modern seismic design concepts (e.g. before the 1980's in the Western world) exhibit premature failures which prevent these components from developing their intended full deformation capacity and strength [15]. Structural deficiencies may be associated with substandard detailing and dimensioning that was mainly based on allowable stress design with no emphasis on the confining function of adequately anchored stirrups. Therefore, substandard R.C buildings may collapse due to localization of failure in few locations of the building prior to redistribution of stresses [2, 5, 9, 11]. Premature mechanisms leading to localized failures may include buckling of compression reinforcement, slip of longitudinal reinforcement due to the presence of poorly confined lap splices in the plastic hinge zone region-which was a common practice more than 40 years ago-, crushing of concrete in the member web, etc.). Those types of structural components which do not comply to modern seismic provisions are labeled henceforth nonconforming members [7].

Nonconforming members exist in a large number of concrete structures across Canada. They are a result of older methods of construction prior to the earthquake engineering community worldwide could reach a thorough understanding of the mechanics of seismic resistance of RC; such structures are deemed unsafe according to current building codes [14]. Therefore, there is a need for improved understanding of the critical mechanisms governing the deformation capacity and strength of RC structures, along with better calibration of the prevalent assessment model.

F. Dameh (✉) · S. J. Pantazopoulou
York University, Toronto, Canada
e-mail: Fardam96@yorku.ca

S. Walbridge et al. (eds.), *Proceedings of the Canadian Society of Civil Engineering Annual Conference 2021*, Lecture Notes in Civil Engineering 244,
https://doi.org/10.1007/978-981-19-0656-5_14

2 Analytical Models

Using an advanced finite element software (ATENA V.5 3D Engineering) a series of benchmark columns are modeled considering different effects of detailing representing nonconforming construction [4]. All columns are subjected to monotonic loading. Using ATENA Studio (ATENA Studio ×64V.5.6.1. 17,830) the resistance curves for the columns were calculated and the deformation and strength capacities were recorded to form a data base for a comparative study. Figure 1a presents the five different cases of column models considered, with differences in longitudinal reinforcement detailing: (1) The longitudinal reinforcement bars are fully anchored into the foundation with a 90° hook, (2) Bars are lap spliced over a lap length of $15D_{b,}$ (3) Bars extend into the foundation with an anchorage length of $15D_b$, (4) The column has a deep cross Secttion (700 mm depth), (5) A hinge is fabricated at the base of the column—where the longitudinal reinforcement crosses the center of the cross section and therefore produces a zero moment point. Each case of longitudinal detailing shown in Fig. 1a is modeled with different combinations of axial loading (10, 35, 50% of crushing), longitudinal reinforcement (shown in Fig. 1b) and stirrup spacing (100- and 200-mm stirrup spacing) with 8 mm stirrup diameter. The column identification code is as following: The first numeral following the letter C (for Column)-for example C35-corresponds to the normalized axial load ratio applied to the columns which in this case is 35% of the crushing load, followed by the section ID number (each section contains a different amount of longitudinal reinforcement, so as to control the hierarchy between flexural and shear demands as shown in Fig. 1b) whereas the last number digit in the numeral represents the stirrup spacing in cm along the length of the shear span of the column.

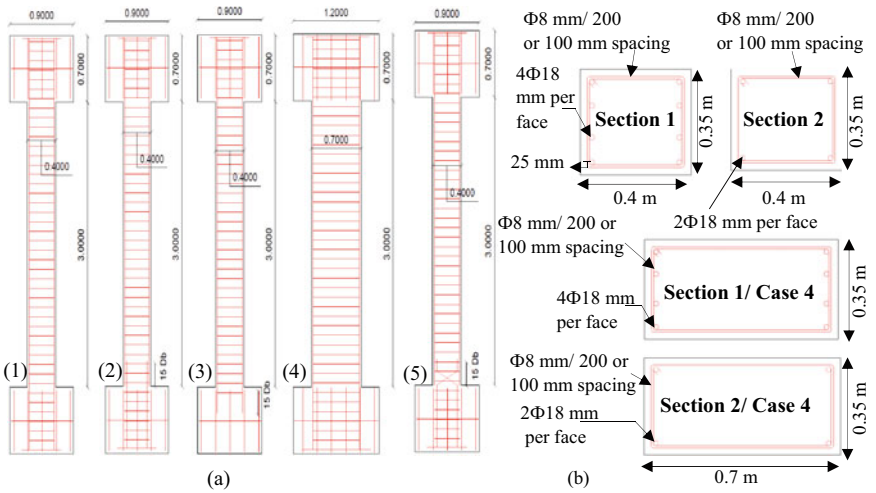

Fig. 1 **a** Column cases and detailing (all dimensions are in m). **b** Section geometry

The columns are modeled using 3D macro elements. The columns have a clear length of 3 m. The foundation is modeled as a block with dimensions (0.9 × 0.9 × 0.7) m. A symmetrical beam block is assumed at the top to enable application of lateral load. The dimensions of the foundation are increased for case 4 to (1.2 × 1.2 × 0.7) m.

2.1 Finite Element Model

The cases in Fig. 1a were modeled using a laterally swaying cantilever model with a shear span length equal to half of the column's deformable length (3/2 = 1.5 m). Moreover, due to symmetry half the cross section was modeled. The columns were discretized into 3D brick elements (8 nodded) with a brick size ranging between 0.025 m for the bottom portion of the column (0.5 m) and 0.05 m for the rest of the column. The reinforcement is modeled through 1D reinforcement truss elements. The columns were modeled with a stiff steel plate on the top and side of the column to eliminate localized failure when applying axial and lateral loads. The axial load was applied in the first analytical step followed by monotonic steps of 0.4 mm lateral displacement until columns would completely fail. The bottom surface nodes of the foundation are restrained from movement in x, y and z directions. The section's symmetrical plane was restrained from movement in the x-direction (the direction perpendicular to the symmetrical plane). Two monitor points were placed at the point of lateral displacement application. One for recording the reactions and one for displacements. The reported reactions represent the entire cross section. Therefore, the load-displacement (monotonic resistance envelopes) are obtained.

2.2 Material Models

2.2.1 Concrete and Reinforcement Stress-Strain Relationships

NonlinearCementitious2 User material was used to model concrete behaviour. This model uses a combination of plasticity and fracture relationships to simulate the full range of inelastic stress-strain behavior of concrete [3]. The cracked stiffness in this model was calculated using the help of the retention shear factor r_g as described in Eq. 1, whereas the strain value in tension or compression is calculated in this model as shown in Eq. 4 [3].

$$E_{ijij}^{'cr} = r_g . G/(1 - r_g) \tag{1}$$

$$G = r_g . G_{c,} \tag{2}$$

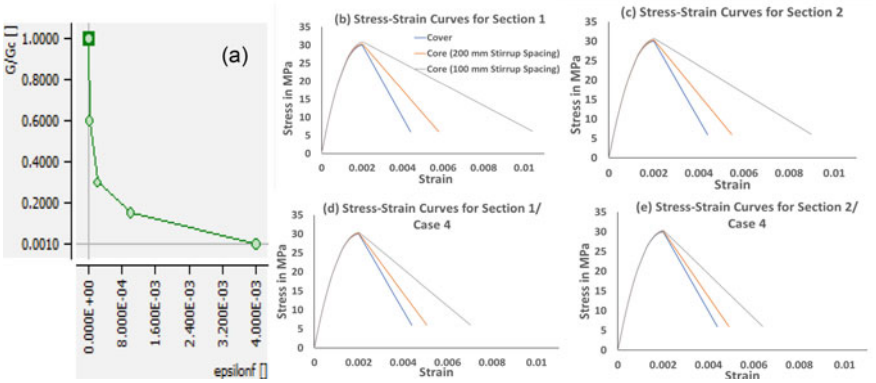

Fig. 2 Concrete stress strain curve for different sections and transverse stirrup spacing

$$G_c = E_c/2 \cdot (1 + \upsilon) \tag{3}$$

$$\text{If } \varepsilon_1^f < \varepsilon_{loc}^f, \quad \varepsilon = \varepsilon_1^f \quad \text{else} \quad \varepsilon = \varepsilon_{loc}^f + \left(\varepsilon_1^f - \varepsilon_{loc}^f\right)\frac{L_t}{L_{ch}^t} \tag{4}$$

In the above, $E_{ijij}^{'cr}$ is the cracked stifness, r_g is the minimum of the shear retention factor on cracks in both directions i and j, G is the elastic shear modulus, and the retention shear factor is defined in Fig. 2a. L_{ch}^c and L_{ch}^t in Eq. 4 represent a size for which the diagram in tension and compression is valid and decreases the dependency on the mesh [3]. For the column models 0.03 and 0.050 m are used for L_{ch}^c and L_{ch}^t respectively with trial and error so as to capture an appropriate response. L_t and L_c represent the crack band size and crush band size respectively. Parameter ε is the strain tensor at the finite element integration points. The localized softening strain in compression is defined as the strain corresponding to the maximum compressive strength after subtracting the linear portion of the stress strain curve [3]. The localized softening strain in tension is assumed 0 for plain concrete thus no hardening occurs after the first crack initiates [3]. Concrete compressive strength for the unconfined concrete used is $f_c = 30$ MPa, $E_c = 30{,}000$ MPa and $v = 0.2$. The stress strain curve of concrete was determined based on Hognestad's parabola [8] for the ascending branch. Kent and Park [10] softening branch model was used to model the concrete cover. Modified Park and Kent [16] was used to model the confined core. The stress strain relation for concrete is shown in Fig. 2 for all cases of longitudinal and transverse reinforcement ratios.The mechanical properties used for transverse and longitudinal reinforcement are listed in Table 1.

Table 1 Longitudinal and transverse reinforcement properties

	Longitudinal reinforcement: (ASTM A706 grade 60 ksi)	Transverse reinforcement: (ASTM A615 grade 40 ksi)
Yield strength	414 MPa	276 MPa
Ultimate strength	552 MPa	483 MPa
Strain rupture	120 mm/m	120 mm/m

2.2.2 Reinforcement Bond

The longitudinal reinforcement is connected to the concrete through interface springs endowed with a proper bond stress-strain relationship to allow the slip between the bar and concrete. In this manner pullout or splitting behavior of the longitudinal reinforcement can be considered. The bond stress-slip relationship was determined based on fib Model Code 2010 [13] assuming good bond conditions. Splitting failure is estimated to occur along the shear span of the column. For the case of 100 mm stirrup spacing the maximum bond strength was used as shown in Eq. 5. However, in the case of 200 mm stirrup spacing the unconfined maximum bond stress was used as shown in Eq. 6, as the effective confining pressure in this case is, $K_e < 0.3$. Equation 7, 8, 9 and 10 are used to calculate the milestone points of the bond-slip relationship. Bond strength T_{max} is calculated as $2.5\sqrt{f_c}$. The residual strength for the 100 mm stirrup spacing case is $0.4*T_{max}$. A value of 0 is assumed for the residual strength for lower confinement according to the code. The bond stress-slip relation used for the column models are shown in Fig. 3.

$$T^1_{u,split} = 8.(f_c/25)^{0.25} \tag{5}$$

$$T^2_{u,split} = 7.(f_c/25)^{0.25} \tag{6}$$

For slip calculations:

$$T_o = T_{max}.(s/s_1)^{0.4}, \text{ for } 0 <= s <= s_1 \tag{7}$$

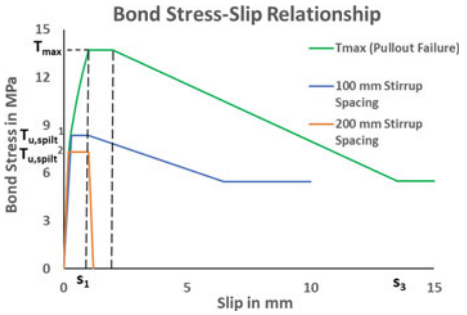

Fig. 3 Bond stress-slip relationship

$$T_o = T_{max}, \text{ for } s_1 <= s <= s_2 \tag{8}$$

$$T_o = T_{max}(T_{max} - T_f).(s - s_2)/(s_3 - s_2), \text{ for } s_2 <= s_3 \tag{9}$$

$$T_o = T_f, \text{ for } s_3 < s, \text{ where, } T_{max} = 2.5.fc^{0.5} \tag{10}$$

3 Results and Analysis

3.1 Deformation and Strength Capacities and Modes of Failure for Cantilever Models

Table 2 displays the deformation capacities and strengths for each case shown in Fig. 1a. The strength is plotted against the drift ratios (which is defined as the displacement divided by the length of the shear span (1.5 m)) as shown in Fig. 4. To make a fair comparison of the different resistance curves in order to reveal the influence of the parameters studied, the apparent loss of lateral load resistance owing to P-Δ effect was eliminated in the plots by adding the product of the axial load multiplied by the drift ratio at each point. Figure 5 depicts the failure of the columns under ultimate loading capacity.

4 ASCE/SEI 14/17 and Eurocode 8-Part III 2005 Deformation Capacity Correlation

The deformation capacities at different performance stages using the ASCE/SEI 14/17[1] and Eurocode 8 III 2005 were calculated. The performance levels are determined in the codes at Near Collapse (NC), Significant damage (SD) and damage limitation (DL) performance limit states in the Eurocode 8 [6] which corre spond to Collapse prevention (CP), Life safety (LS), Immediate Occupancy (IO) respectively in the ASCE/SEI 14/17. Figures 6a, b and c plots the 3 limit stages according with the ASCE/SEI 14/17 plotted against the model analytical data. Similarly, Fig. 6d, e and f illustrates the performance levels in the Eurocode 8 III [6] plotted against the model data.

Figure 5 depicts the mode failures of the columns. Where Fig. 5a is for set 1, b is for set 2, c is for set 4, and e is for set 5.

Table 2 Deformation and strength capacities for 5 different columns

Axial lo ad (%)	100 mm stirrup spacing						200 mm stirrup spacing					
	4Φ18 bars per face			2Φ18 bars p er face			4Φ18 bars per face			2Φ18 bars per face		
	Shear force (KN)	Δ_y *mm*	Δ_u *mm*	Shear force (KN)	Δ_y *mm*	Δ_u *mm*	Shear force (KN)	Δ_y *mm*	Δ_u *mm*	Shear force (KN)	Δ_y *mm*	Δ_u *mm*
Set 1 (full anchorage in foundation with 90° hook)												
10	153.12	9.8	43.6	107.01	7.8	55	153.5	9.4	37	106.54	7.4	38.7
35	242.96	11.2	42.3	194.47	8.8	33	237.5	10.4	23.6	192.14	8.5	21
50	261.17	10.6	31	212.65	8.2	25	246.49	8.8	19.4	205.6	7	17
Set 2 (lapped splice-270 mm lap length)												
10	146.63	12.2	26	104.64	10.2	36.2	143.64	11.2	17.2	103.01	9	26
35	224.60	11.5	38.8	181.81	8	34	211.13	9.1	22	173.31	6.8	20.2
50	233.82	9	31	192.81	7	25.5	223.46	7.8	15.8	185.83	6.5	15.2
Set 3 (short anchorage length)												
10	142.86	9	30.8	106.7	7.8	52.3	137.22	7.9	15	106	7.5	41
35	238.53	11	33.5	194.08	9	32	231.72	10	20.8	192.9	8.4	21.7
50	259.46	10.7	31	211.48	8.3	25.3	246.35	8.8	19.6	205.31	7.3	17.5
Set 4 (deep cross section)												
10	361.08	5.7	35	265.9	4	35.8	356.8	5.3	28.5	266.26	3.8	28.3

(continued)

Table 2 (continued)

Axial lo ad (%)	100 mm stirrup spacing						200 mm stirrup spacing					
	4Φ18 bars per face			2Φ18 bars p er face			4Φ18 bars per face			2Φ18 bars per face		
	Shear force (KN)	Δ_y *mm*	Δ_u *mm*	Shear force (KN)	Δ_y *mm*	Δ_u *mm*	Shear force (KN)	Δ_y *mm*	Δ_u *mm*	Shear force (KN)	Δ_y *mm*	Δ_u *mm*
35	638.14	6.3	23	549.71	5.5	20	625.37	5.9	17	544.51	5.1	15.1
50	704.5	6	15.5	608.94	5.2	14.2	673.8	5.5	11	588.46	4.8	11.2
Set 5 (hinge connection to the foundation base)												
10	82	8	53	70.71	6	44.8	77.75	6	41.6	68.35	4.8	47.5
35	161.36	5.5	39	153.34	5.5	30	159.39	5.4	21.5	152.04	5.2	19.8
50	190.51	6.2	28	179.48	6	20	185.99	5.8	14.8	175.99	5.8	13.4

Note The shear force is the maximum resistance attained by the column. Δ_y is the effective yield displacement found using ASCE/SEI 14/17 code standards. Δ_u is the displacement at 15% reduction in shear force on the post peak resistance curve

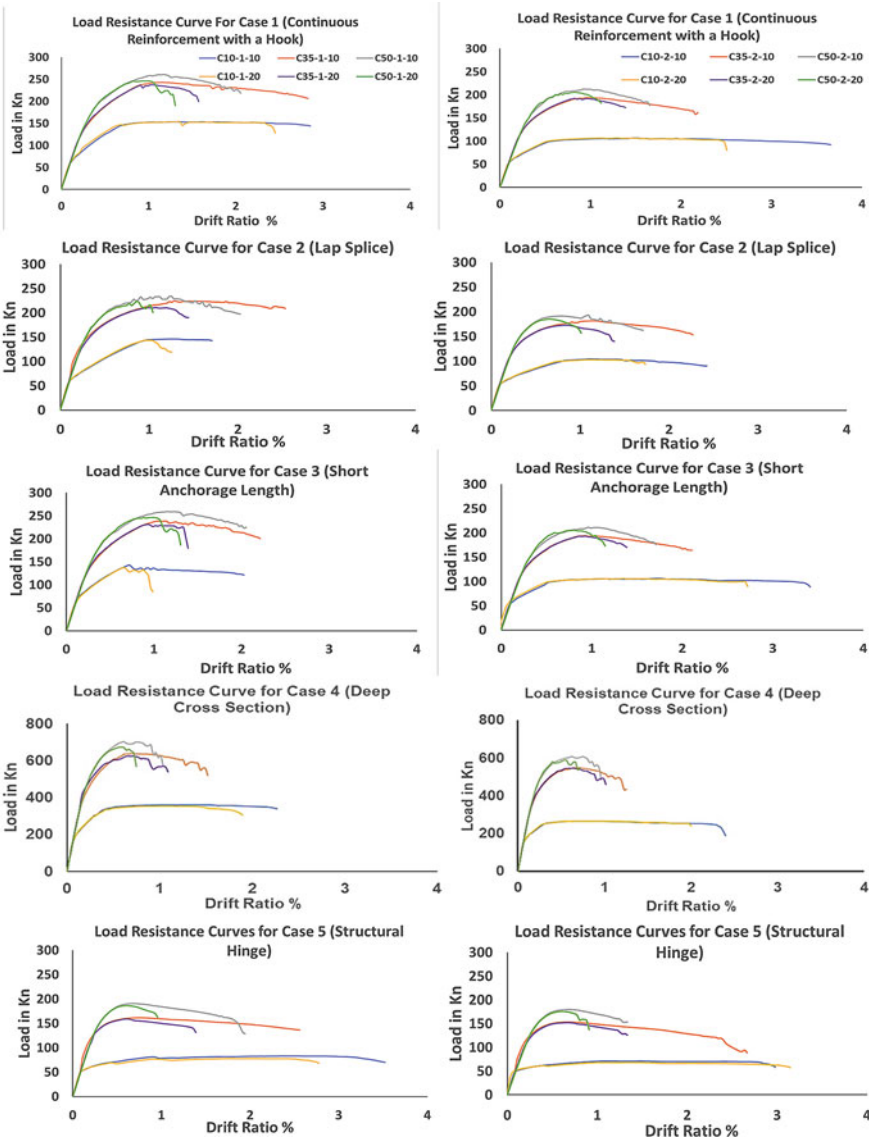

Fig. 4 Load-displacement for all cases of longitudinal reinforcement. Here, the drift ratio is defined as the displacement of the column divided by the column's shear span length

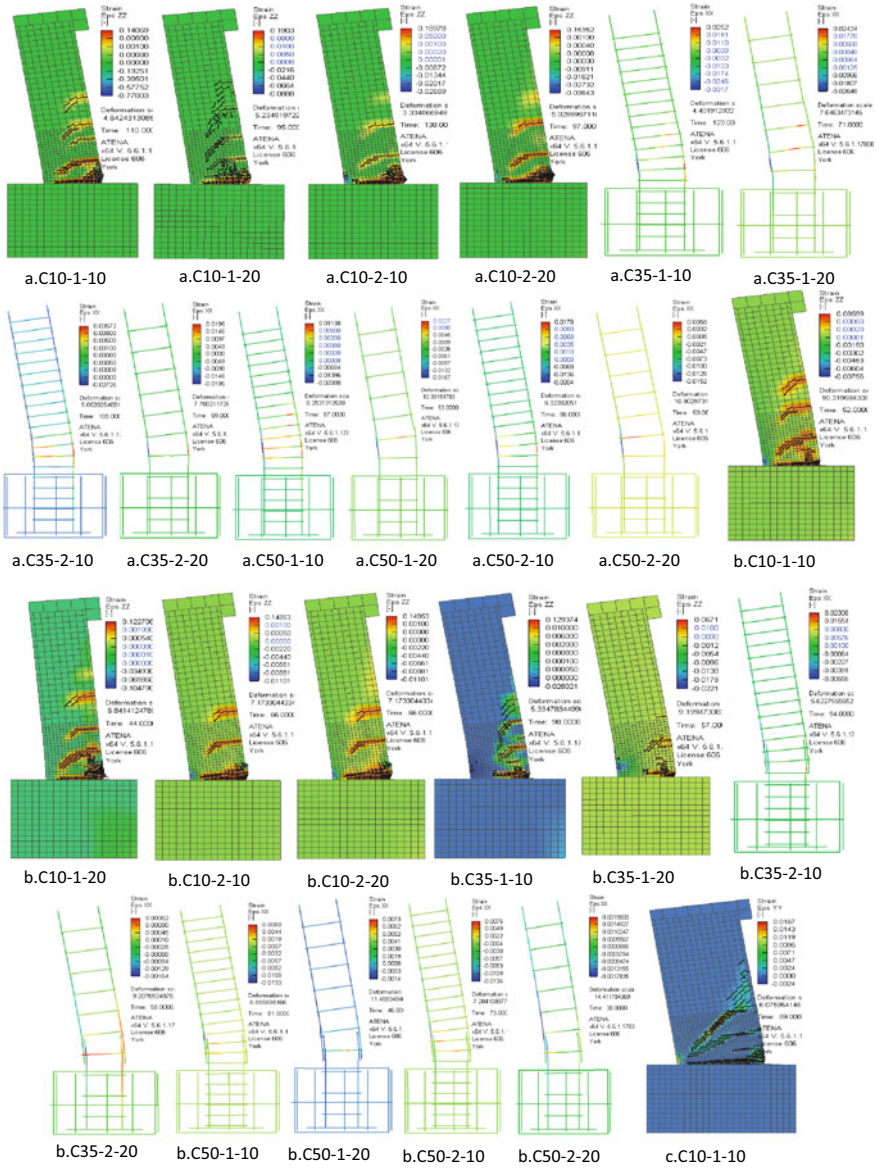

Fig. 5 Column failure modes at near collapse state. Strain XX are the longitudinal strains in reinforcement and strain ZZ are the strains in concrete

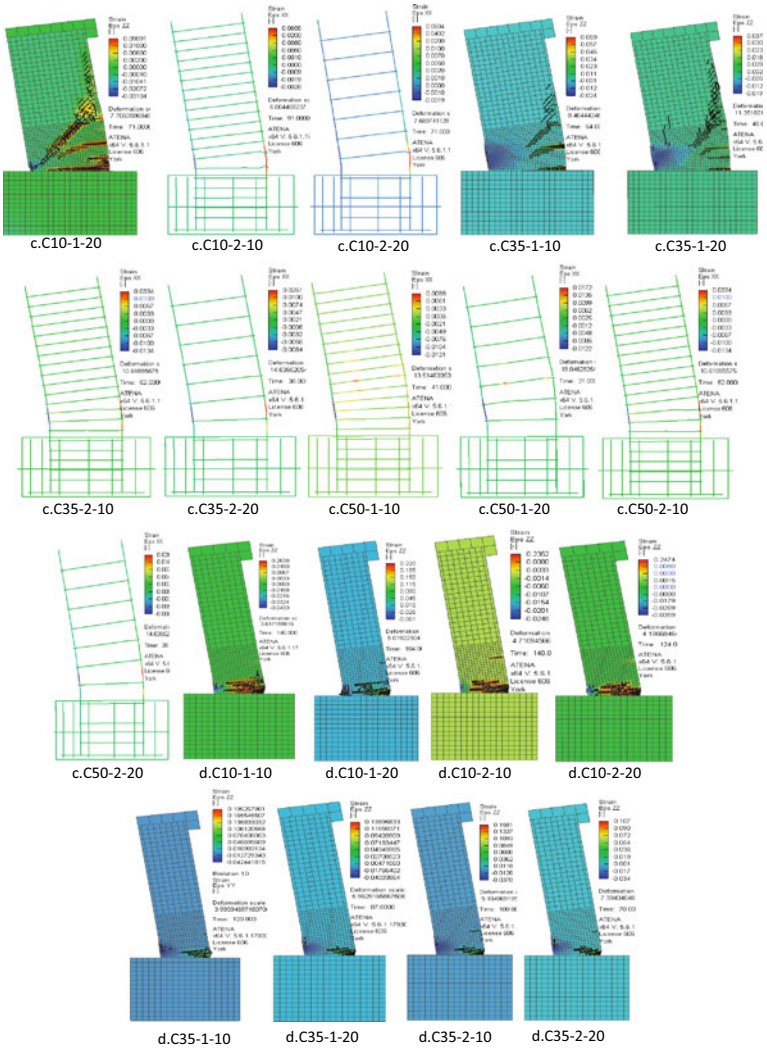

Fig. 5 (continued)

5 Discussion and Conclusions

This study investigated the deformation capacity and its correlation to the assessment codes at three performance levels (acceptance criteria). Columns with well confined stirrups provided larger deformation capacities. The column's shear strength started to vary at high axial loads, indicating stirrup yielding and shear failure. Moreover,

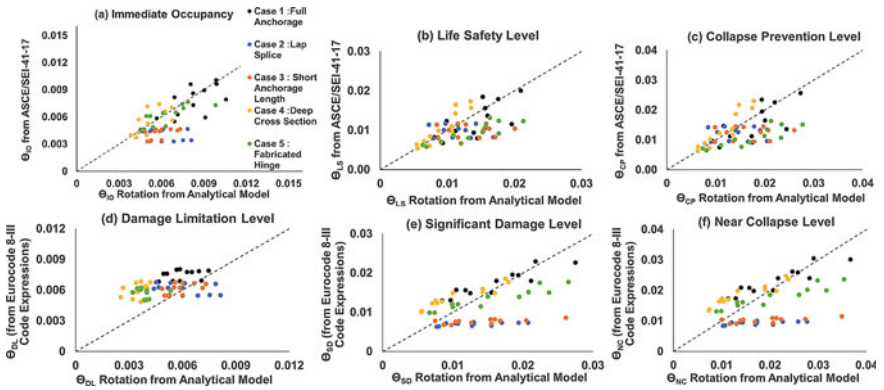

Fig. 6 Code estimated rotation capacities vs. values from F.E. Models **a–c** Limit states from ASCE/SEI 41-17; **d–f** Limit states from Eurocode 8-III

it wa s found that the effective yielding increased with the increase of the axial load. A decrease in the effective yielding at an axial load of 50% was found due to the occurrence of concrete crushing failure. The hinge fabrication at higher axial loads was excluded from this behaviour as reinforcement slips were present at lower axial loading. Moreover, column yielding was delayed at low axial loads in the case of lap spliced column. This is due to the delay in the longitudinal reinforcement yielding due to the increase of slip. It is also concluded that the column's deformation capacities decrease with an increase in the axial loads. Columns with low axial load failed due to splitting. The crushing of concrete is also present at 50% crushing load, limiting longitudinal bar yielding especially in the cases of low confinement. The effect of the longitudinal reinforcement detailing present in the lap splice and short anchored reinforcement was attenuated with the increase of the compressive loading. Thus, the reinforcement slip from the foundation was mitigated when lateral displacements were applied. At lower axial load stronger deterioration of ultimate deformation capacities occurred as these columns were dominated by the pullout slip of the reinforcement. It should also be noted that the pullout demand in these cases for columns lightly reinforced are less affected. This was observed due to the prevalence of flexural yielding. For deep cross sections, the larger internal lever arm also increased the shear demand. Shear failure could occur at lower shear strengths with lower deformation capacities.

The ASCE/SEI 41-17 procedures showed better correlation to the rotation at yielding when compared to deformation capacities from models as opposed to the Eurocode 8 III [6]. This is because shear force demands are considered in calculating the rotation capacities in the ASCE/SEI 41-17. For the second set (the lapped splice), the finite element models show a decrease in the yield rotation compared to columns in the first set (columns with continuous reinforcement). This increase is attributed to the increase of slip rotations along the reinforcement bar. However, this is not reflected in the assessment codes properly. The codes demand a decrease in the slip rotation in a lapped splice column at yielding compared

to columns with full anchorage. Generally, the assessment codes show a decrease in the life safety/significant damage state with the increase of the axial load for all column cases. However, from the finite element models it was found that this trend was not applicable to columns that fail ultimately due to reinforcement slips, which are columns in set 2 and 3 (lapped splice and short anchorage length) that have high reinforcement ratios. This is because the compression forces of the axial load mitigate the pullout forces when applying lateral load. In the case of 50% the ultimate rotations decrease, as the column were controlled by concrete crushing rather than pure slip. At Near Collapse or Collapse Limit state the scatter increased when the column was controlled by crushing of concrete according with the Eurocode at higher axial loads. However, according with the ASCE SEI 14/17, values successfully matched the calculated ones in computing the deformation capacities when concrete crushing failure controlled. The Eurocode 8 III [6] showed lesser correlation to the computational results for columns failing ultimately in buckling/shear.

References

1. ASCE-41-17 (2017) ASCE standard, ASCE/SEI, 41-17: seismic evaluation and retrofit of existing buildings. American Society of Civil Engineers, Reston
2. Augenti N, Parisi F (2010) Learning from construction failures due to the 2009 L'Aquila, Italy, earthquake. J Perform Construct Facil 24(6):55–536
3. Cervenka V, Jendele L, Cervenka J (2020) Theory. ATENA program documentation part 1. Cervenka Consulting, Prague
4. Chassioti SG, Syntzirma DV, Pantazopoulou SJ (2010) Codes of assessment of buildings: a comparative study. In: 9th US National and 10th Canadian conference on earthquake engineering 2010, including papers from the 4th international Tsunami symposium, vol 2, pp 1192–1201
5. Dogangun A (2004) Performance of reinforced concrete buildings. Eng Struct 26(6):841–856
6. EN 1998-3 (2005) Eurocode 8—design of structures for earthquake resistance—part 3: assessment and retrofitting of buildings. European Committee for Standardization (CEN), Brussels
7. FEMA 356 (2000) Pre-standard and commentary for the seismic rehabilitation of buildings
8. Hognestad E (1951) A study of combined bending and axial load in R.C. members. University of Illinois Engineering Experiment Station. Bulletin no. 399
9. Jeong SH, Elnashai AS (2004) Analytical and experimental seismic assessment of irregular RC buildings. In: 13th world conference on earthquake engineering, Vancouver, Canada
10. Kent DC, Park R (1971) Flexural members with confined concrete. J Struct Div ASCE 97(ST7):1969–1990
11. Lang AF, Marshall JD (2011) Devil in the details: success and failure of Haiti's non engineered structures. Earthq Spectra 27(S1):72–345
12. Lehman DE, Calderone AJ, Moehle JP (1998) Behavior and design of slender columns subjected to lateral loading. In: 6th US National conference on earthquake engineering, EERI, Seattle, Washington, 31 May–04 June 1998
13. Model Code 2010: final draft, fib—Bulletin 65, vol 1. www.fib-international.org.
14. National Research Council of Canada (1995) Guideline for seismic upgrading of building structures upgrading of building rehabilitation. Institute for Research and Construction NRC Publications Archive

15. Pantazopoulou SJ (2003) Strength and deformation capacity of non-seismically detailed components. Seismic assessment and retrofit of reinforced concrete buildings, fib Bulletin No. 24:91–150
16. Park R, Priestley MJN, Gill WD (1982) Ductility of square-confined concrete columns. J Struct Div 108:929–950

Fretting Fatigue Characterization of Bolted Steel Connections with Different Surface Treatments

Alireza Zangouie, Leon D. Wegner, and Jacob Muthu

1 Introduction

Slip-critical bolted steel connections are preferred over bearing-type connections when fatigue is a design consideration. However, they are prone to developing fretting damage caused by the inevitable micro slip between the contacting surfaces under repetitive loading conditions, which can lead to fretting fatigue failure [15]. Although significant progress has been made to improve the fretting fatigue performance of bolted connections, there is still a lack of understanding of the fatigue behaviour of slip-critical connections due to its intrinsic complexity.

Fretting is caused by a repetitive relative displacement between contacting surfaces in the presence of a force acting normal to the surface combined with an externally applied cyclic load acting parallel to the surface [5]. The small amount of relative displacement induces a frictional force along the contact interface. The combination of normal load, frictional force and cyclic axial load develops stress concentration sites resulting in the nucleation of surface micro cracks, which coalesce into a leading crack that will eventually result in failure [8]. In general, fretting fatigue failure occurs in two stages: crack initiation and crack propagation.

There are many factors that can affect the fretting fatigue behaviour of bolted steel connections, including bolt preload, surface finish, coefficient of friction, magnitude of relative displacement in the contact area, bolt arrangement, joint geometry, material properties, stress ratio and frequency of the applied cyclic loads [9]. A considerable amount of research has been carried out to provide a better understanding of the effects of these parameters on fretting fatigue, but among those requiring further investigation, the effect of surface finish is still not completely understood.

A. Zangouie (✉) · L. D. Wegner
University of Saskatchewan, Saskatoon, Canada
e-mail: alireza.zangouie@usask.ca

J. Muthu
University of Regina, Regina, Canada

S. Walbridge et al. (eds.), *Proceedings of the Canadian Society of Civil Engineering Annual Conference 2021*, Lecture Notes in Civil Engineering 244,
https://doi.org/10.1007/978-981-19-0656-5_15

There are various engineering techniques used to modify contact surface quality to enhance fretting fatigue strength, such as shot peening, laser peening, turning, grinding and coating [13]. Three different surface conditions are adopted for slip-critical connections in CAN/CSA-S16-14, including clean mill scale (Class A), blast-cleaned surface or blast-cleaned surface with class B coating (Class B) and hot-dip galvanized (Class C) [2]. Blast-cleaning (shot-blasting or sand-blasting) is a technical treatment that is used to remove scale and contamination from the surface by bombarding it with various media like metal shot or sand. Blast-cleaning can produce compressive residual stress on the surface of the material, which potentially reduces the risk of crack propagation [9]. This technique generates a localized plastic flow on contact surface leading to work hardening and surface roughening [16].

Although various research studies have been undertaken to investigate the effect of different surface treatments on the fretting fatigue life, a limited amount of research has been carried out on the fretting fatigue behaviour of blast-cleaned surfaces (Class B). Among the studies that address the topic, contradictory conclusions have been reported, as mentioned by [16]. For example, Naidu and Raman [9] reported that sand-blasting improved the fretting fatigue strength significantly, while Yue and Wahab [16] stated that increasing the surface roughness by sandblasting decreased the fretting fatigue life. On the other hand, Cullimore [3] and Frank and Yura [4] concluded that shot-blasting does not affect the fatigue strength noticeably. The present investigation was conducted to investigate experimentally the effect of different surface treatments identified in CAN/CSA-S16-14 [2] on the fretting fatigue behaviour of bolted connections in terms of severity of surface damage, crack initiation location, orientation of initiated crack, and total fatigue lifetime.

2 Experimental Details

2.1 Material and Specimen Geometry

A series of small-scale fatigue tests using double-lap joint bolted specimens was conducted. Double-lap joint (DLJ) specimens are preferred over single-lap joint specimens to avoid the undesirable bending effect caused by eccentric loading inherent in the single-lap joints. As shown schematically in Fig. 1, the test specimen consisted of three identical high strength steel plates made of CSA G40.21 300 W, and two single 3/4″ ASTM A325 bolts along with two suitable washers placed underneath the bolt head and the respective nut. The properties of the plate material are given in Table 1.

Before assembling the specimens, a two-step preparation process was performed which involved drilling bolt holes and applying the surface finish. Two standard 19.5 mm diameter bolt holes were drilled and reamed at the centre of the specimen with respect to its width, with an edge distance of 35 mm from the free edge of plate. A series of tests was performed using plates with a Class A surface finish, and

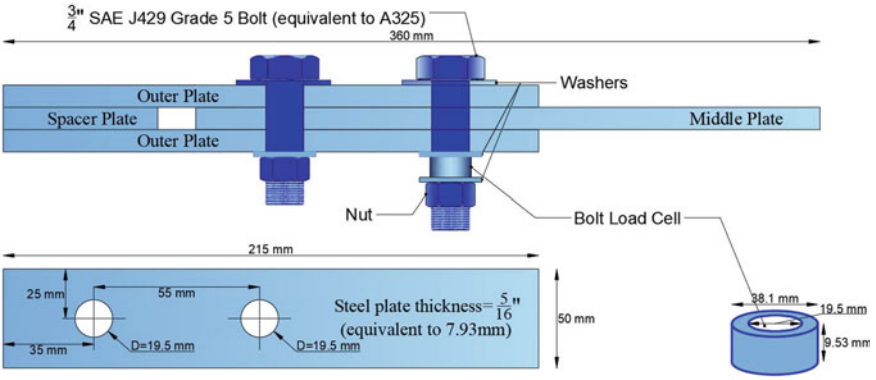

Fig. 1 Double lap joint bolted specimen used for fatigue tests

Table 1 Mechanical properties of CSA G40.21 300 W

Elastic modulus (GPa)	Yield strength (MPa)	Ultimate tensile strength (MPa)	Poisson's coefficient	Elongation (%)
219	393	483	0.29	28.5

another series using plates with a class B surface finish according to CAN/CSA-S16-14 [2]. The Class A surface was an unpainted clean scale finish that was achieved by polishing the drilled plate using fine sandpaper, and then wiping the plates with acetone to remove the oxide layer. The Class B surface finish was achieved by sand-blasting the cleaned surface. The bolts were tightened using a calibrated torque wrench to produce a pretension force of 145 kN in the bolt, as measured using a bolt load cell.

2.2 Testing Procedure

The bolted joint specimens were tested using an MTS servo-hydraulic testing machine with a capacity of 250 kN. The fatigue testing program is summarized in Table 2. The fatigue tests were performed with a stress ratio $R = -1$ at a testing frequency of 10 Hz using tension—compression cyclic loading (sine wave). Tests were conducted at three different axial load levels, and at least three replicate tests were performed for each condition.

Table 2 Experimental matrix of fretting fatigue tests

Label	Contact surface finish type	Fatigue load (kN)	Nominal stress amplitude (MPa)
F-A-145T-65	Class A	65	327
F-A-145T-80		80	403
F-A-145T-95		95	478
F-B-145T-65	Class B	65	327
F-B-145T-80		80	403
F-B-145T-95		95	478

3 Results and Discussion

3.1 Fretting Fatigue Life

Figure 2 shows the S-N curves obtained for specimens with the two surface treatments, as identified by plotting the mean values of fatigue life for each of the six conditions tested. Also shown is the standard curve for Detail Category B given in CSA S16-14 for reference. Of significance is the fact that the data from the fatigue tests lie above the standard S-N curve for bolted connections by a large margin, indicating that the design curve is very conservative for the particular cases investigated

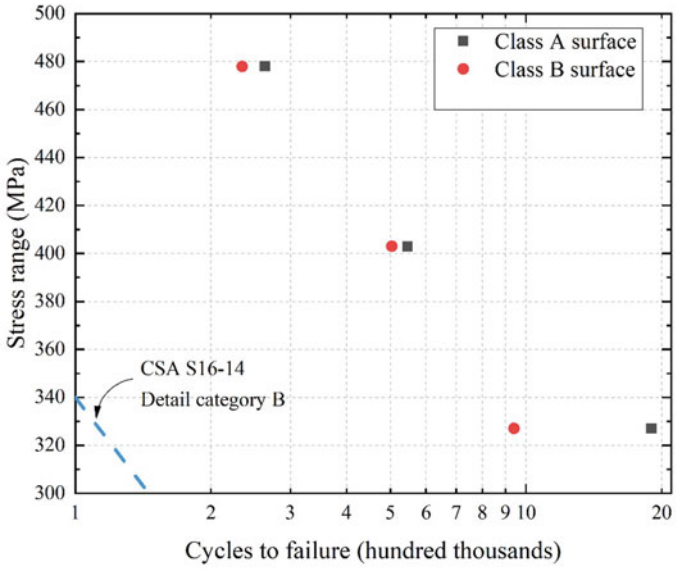

Fig. 2 Fretting fatigue stress range versus number of cycles to failure (S-N curves), with mean values for fatigue life plotted for the two surface finishes

here. From the experimental results, it can be concluded that using a Class A surface finish significantly improved the fretting fatigue life of the bolted joints compared to the Class B sand-blasted surface finish at the lowest stress amplitude. More specifically, sand-blasting significantly reduced the fretting fatigue life, by a factor of 50% at the lowest stress amplitude of 327 MPa, while there was a negligible reduction in the fretting fatigue life at the higher two stress ranges.

3.2 Surface Damage

All specimens were examined using microscope after failure to investigate the effect of axial stress range and surface type on the fretting fatigue behaviour of the bolted connections in terms of crack initiation site on the surface, crack initiation orientation and severity of wear. Fretting damage was visible in the contact area of all three plates of each specimen, but failure due to fretting fatigue occurred in the middle plate in all cases. On the side plates, fretting damage was more severe on the side closer to the bolt head, indicating that a higher stress concentration exists under the bolt head. Figure 3 confocal microscope images of the surfaces of the middle plate in the

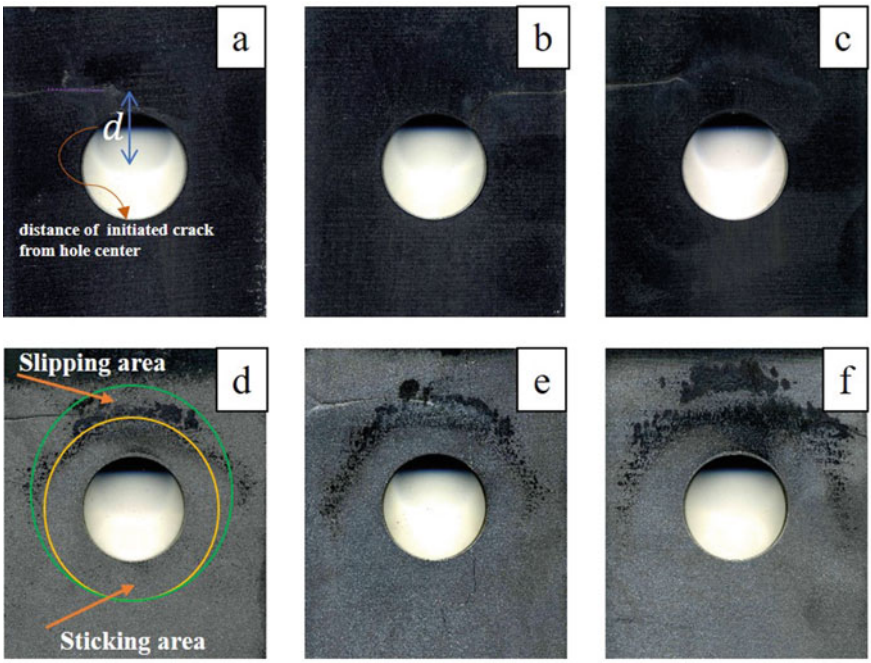

Fig. 3 Fretting damage on the surface of the middle plates for specimens **a** F-A-145T-65, **b** F-A-145T-80, **c** F-A-145T-95, **d** F-B-145T-65 **e** F-B-145T-80, and **f** F-B-145T-95

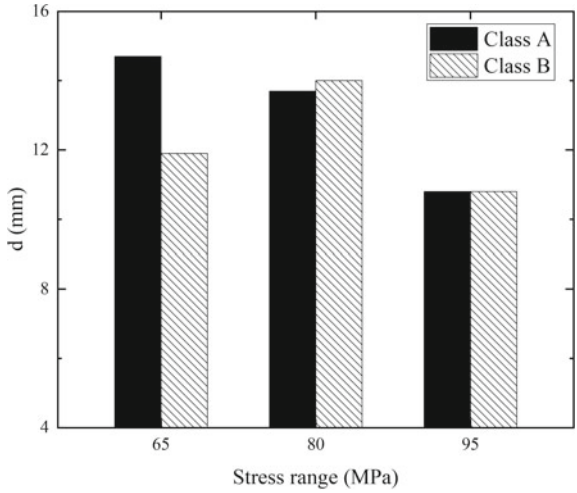

Fig. 4 Average radius of stick zone

vicinity of the bolt hole for representative samples for all six cases investigated. These images illustrate that the bolt hole is surrounded by two roughly semi-circular zones corresponding to the sticking and slipping regions. Crack initiation occurs some distance from the bolt hole along the boundary of the sticking and slipping zones (i.e., in the partial slip region) where the shear stress gradient is relatively high [1]. This location is identified as distance 'd', measured from the centre of the bolt hole, and is plotted in Fig. 4 for each case. This figure shows that, in general, the surface type did not change the average size of the sticking area significantly for specimens subjected to the same axial stress range. The only exception is the joints subjected to the lowest stress range, where using a sandblasted surface apparently decreased the size of stick area. This may be due to the higher coefficient of friction between faying surfaces that exists in the Class B surface compared to a Class A surface. All cracks were initiated in the partial slip zone along the boundary of the sticking and slipping areas, but crack initiation angle increased with increasing frictional force at the contact interface i.e. combination of normal and external load [7]. Moreover, the Class B surface type caused the cracks to initiate at an acute angle compared to Class A surface (Mode II). After crack initiation, the cracks propagated in a transverse direction, perpendicular to the direction of the cyclic loads under influence of tensile stress (Mode-I failure).

3.3 Fractographic Examination

All specimens were sectioned and the fracture surface was inspected by scanning electron microscope (SEM) to investigate the location of crack initiation, crack orientation through the thickness and crack growth rate. The fractographs for specimens

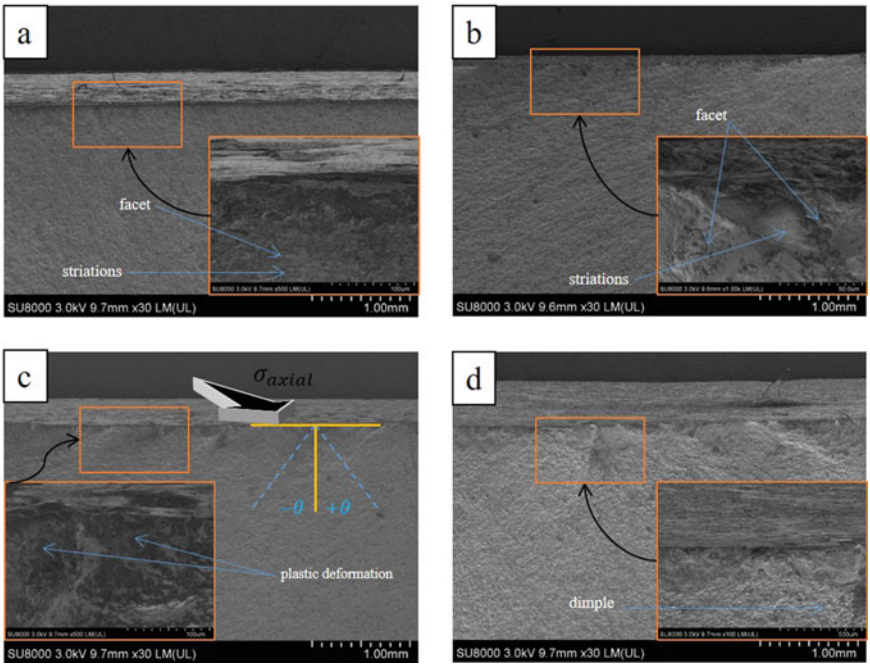

Fig. 5 SEM images of the fracture surfaces for specimens **a** F-A-145T-65, **b** F-B-145T-65, **c** F-A-145T-95, and **d** F-B-145T-95

subjected to the lowest and highest axial loads are presented in Fig. 5. It is evident that an increase of axial load and using a Class B surface type caused several cracks to be initiated; however only a few of them grew sufficiently large to cause failure. Cracks were initiated on the surface at angle of θ with respect to the surface under Mode II due to the presence of a frictional force. It was found that when the initiated cracks reached a critical length, they changed their orientation and propagated in a mixed mode, and then in Mode I under the influence of cyclic axial load (Fig. 5(c), (d)). It can be observed that primary cracks are orientated at $+59°$ and $-63°$ for specimens with a Class A surface subjected to lower and higher axial cyclic loads, respectively. On the other hand, the orientation of cracks in specimens with a Class B surface type were observed to vary from 25° to $+32°$. Moreover, the transition from Mode II to Mode I (the mixed mode transition) in the specimens under higher cyclic loads occurred at a shallower distance into the surface, which means that the effect of tensile stress on the crack propagation is more pronounced.

Faceted fracture with fine striations can be seen in Fig. 5(a), corresponding to the near-threshold or lower Paris law fracture mechanism [12]. As can be seen in Fig. 5(a) ratcheting of dislocations were formed along the persistent slip bands due to shear stress. The density of striations is lower in specimen F-B-145T-65 compared to F-A-145T-65, indicating that sand blasting has changed the mode of crack growth from the low Paris law regime to the higher fatigue growth regime. Furthermore,

the fine striations are less evident in the high amplitude of stress range due to the presence of plastic deformation around the crack tips, leading to accelerated crack growth rates (Fig. 5(c), (d)) [12].

3.4 Surface Roughness Measurements

The surface roughness of the contact surfaces of the middle plates along a line across the width of the specimen close to crack path was measured by means of a Mitutoyo SJ-201 roughness tester. Prior to the measurement, the fretted area was wiped by acetone to remove wear scars due to fretting wear. The average arithmetic mean deviation of the profile (Ra) for specimens subjected to the lowest and highest stress ranges before and after testing are shown in Fig. 6. Generally, the sandblasting process generated an initially rougher and more uniform surface as compared to the

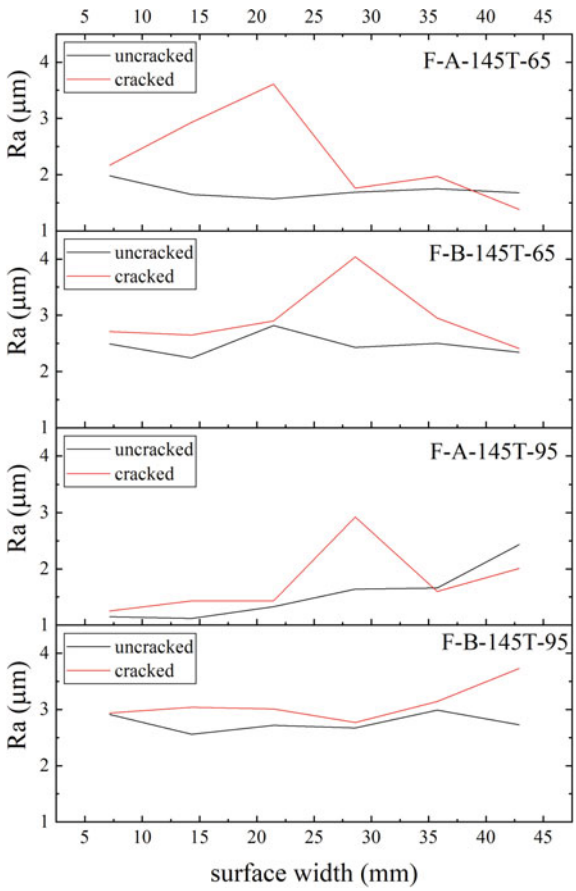

Fig. 6 Surface roughness profiles in the fretted areas

polished surfaces. It was found that the oxide film and any initial debris were worn down during the fatigue loading, and a new rougher surface formed in the slip region [11]. Figure 6 indicates that the increase of surface roughness due to fretting wear for specimens subjected to the lower stress range was larger than that of the specimens subjected to the higher stress range.

NIS-Elements Imaging software along with a Nikon optical microscope were employed to measure the intensity distribution of pixels over the surface. Intensity surface plot or pixel intensity is used to quantify the characteristic of damaged zones [10]. The intensity surface plot of specimens under low and high cyclic loads are presented in Fig. 7. According to the figure, the amplitude of cyclic loads does not noticeably affect the width and depth of fretting scars (indicative of the wear volume) in the specimens with the rougher contact surfaces (Class B sandblasted surfaces),

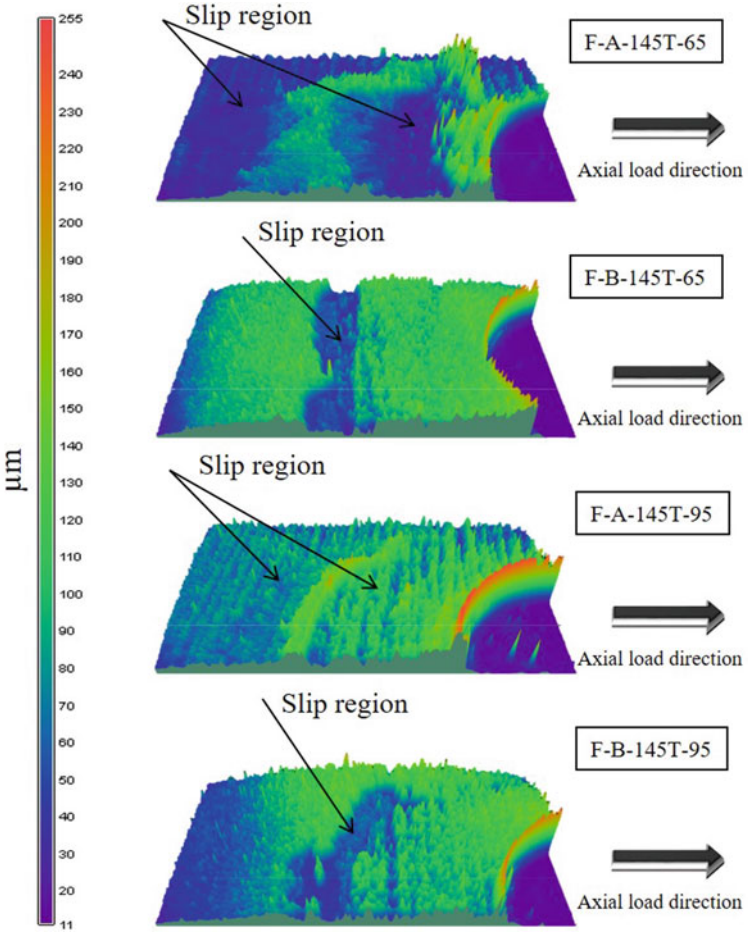

Fig. 7 Intensity of surface plot in the fretted areas

while the fretting scars of less rough surfaces (Class A polished surfaces) become wider and deeper by decreasing the axial stress range, which may be due to greater slippage in the contact area.

3.5 Discussion

Based upon the measurements and observations mentioned above, it can be concluded that the sandblasted specimens with a rougher surface developed a somewhat smaller slip area in the place of fretted scars and induced higher localized contact pressure in the partial slip area. Also, Fig. 7 indicates that the wear marks produced on the Class A surface were more uneven compared to the Class B surface, and as a result the contact pressure acting on fretting wear zone was decreased [14]. The normal contact pressure over the stick region is higher than in the slip zone, and this produces a high stress concentration at the boundary of the slip and stick areas. This stress concentration is higher in the sandblasted specimens than in specimens with a Class A surface. The higher stress concentration may contribute to the reduced the fretting fatigue life in Class B surface specimens at the lowest axial stress range. Sandblasting can produce a compressive residual stress in the surface layer, which is able to improve the fretting fatigue life, however, the experimental results show that the impact of the stress concentration is more dominant in this case.

It was also observed that the wear volume for the F-A-145T-65 specimens was the highest among all specimens tested. The increased wear results in the effective removal of existing flaws produced during the manufacturing process as well as the removal of wear particles, thereby increasing the fretting fatigue life in comparison to the sandblasted surface condition. On the other hand, the F-B-145T-95 specimens had the lowest wear volume, which resulted in trapping more of the wear particles in a smaller area and intensifying the stress concentration in the contact area, thereby leading to the lowest resistance to fretting fatigue.

Finally, Hisakado [6] observed that wear volume and shear strength are inversely proportional to the intensity of surface roughness. Since the sandblasted surface had a higher initial surface roughness than the Class A surface, a lower shear strength would be expected for the Class B surface, and this may also have contributed to the observed reduction in the fretting fatigue life of specimens with the sandblasted surface.

4 Conclusion

An experimental study was carried out to investigate the effect of two different surface types (clean scale—Class A; and sandblasted—Class B), as identified in CSA S16-14, on the fretting fatigue behaviour of double shear lap bolted joints subjected to three levels of fully reversed cyclic loads. Fretting damage was visible on the contact

surfaces of all plates in the double lap assemblies, but failure occurred due to fretting fatigue in the middle plates in all cases. Cracks initiated on the surface of the middle plates in the partial slip zone between sticking and slipping areas due to the presence of a steep shear stress gradient under Mode II loading, and then the cracks propagated in Mode I perpendicular to the applied cyclic axial loads until final rupture. Based on the experimental results, sandblasting the surface to produce a Class B surface finish decreased the fretting fatigue life of specimens subjected to the lowest cyclic loads, while it resulted in negligible decreases in fatigue life at higher cyclic loads. The reduction in fatigue life may be attributed to the higher frictional force that exists on the Class B surface in comparison to the Class A surface. Specimens with a Class A surface subjected to the lowest stress range developed higher wear volumes that effectively removed existing microcracks, thereby significantly increasing the fretting fatigue life. In addition, the smaller fretting area observed on the sandblasted Class B surfaces is indicative of higher localized contact pressure and greater stress concentration compared to the Class A surface, which reduced the number of cycles to crack initiation. These results suggest that a Class A surface is preferred for faying surfaces of bolted connections that are subjected to repetitive loading.

References

1. Benhaddou T, Stephan P, Daidie A, Chirol C, Tuery J-B (2012) Effect of axial preload on double-lap bolted joints: numerical study. In: ASME 2012 11th Biennial conference on engineering systems design and analysis. American Society of Mechanical Engineers Digital Collection, pp 769–776
2. CSA (2014) CSA-S16-14: design of steel structures. Canadian Standards Association, Toronto
3. Cullimore MSG (1982) Fatigue of HSFG bolted joints: effects of design parameters. International Association for Bridge and Structural Engineering, pp 715–723
4. Frank KH, Yura JA (1981) An experimental study of bolted shear connections. Technical, Austin, TX United States: Department of Civil, Architectural and Environmental Engineering, University of Texas Austin
5. Hills DA (1994) Mechanics of fretting fatigue. Wear 175(1–2):107–113
6. Hisakado T (1977) The influence of surface roughness on abrasive wear. Wear 41(1):179–190
7. Jacob MSD, Arora PR, Saleem M, Ahmed EM, Sapuan SM (2007) Fretting fatigue crack initiation: an experimental and theoretical study. Int J Fatigue 29(7):1328–1338
8. Liu D, Pons DJ (2018) Crack propagation mechanisms for creep fatigue: a consolidated explanation of fundamental behaviours from initiation to failure. Metals (Multi Digit Publishing Inst) 8(8):623
9. Naidu NKR, Raman SGS (2005) Effect of shot blasting on plain fatigue and fretting fatigue behaviour of Al-Mg-Si alloy AA6061. Int J Fatigue 27(3):323–331
10. O'Byrne M, Schoefs F, Ghosh B, Pakrashi V (2013) A comparison between pixel intensity and texture analysis based damage detection techniques. In: 7th international workshop NDT in progress, Dresden, Germany
11. Pereira K, Yue T, Wahab MA (2017) Multiscale analysis of the effect of roughness on fretting wear. Tribol Int 110:222–231
12. Shen W, Soboyejo WO, Soboyejo ABO (2004) An investigation on fatigue and dwell-fatigue crack growth in Ti-6Al-2Sn-4Zr-2Mo-0.1 Si. Mech Mater 36(1–2):117–140
13. Volchok A, Halperin G, Etsion I (2002) The effect of surface regular microtopography on fretting fatigue life. Wear 253(3–4):509–515

14. Wang J, Xu H, Su T, Zhang Y, Guo Z, Mao H, Zhang Y (2016) Fretting fatigue experiment and analysis of AlSi9Cu2Mg alloy. Mater (Multi Digit Publishing Inst) 9(12):984
15. Xu Y, Sun Z, Zhang Y (2016) Experimental and numerical investigations of fretting fatigue behavior for steel Q235 single-lap bolted joints. Adv Build Technol Constr Mater 2016:1–10
16. Yue T, Wahab MA (2017) Roughness effects on fretting fatigue. J Phys Conf Ser 843:012056

Time-Frequency Assisted Deep Learning for Crack Localization Using Acoustic Emission Data

Mohamed Barbosh, Kyle Dunphy, and Ayan Sadhu

1 Introduction

Large-scale infrastructures such as towers, bridges, roads, and dams are subjected to deterioration due to exposure to the surrounding environment and applied loads which significantly affects their overall life-span. The structural integrity of these infrastructures can be monitored and evaluated using sensor-based structural health monitoring (SHM) techniques. SHM is able to provide useful information about the existing condition of the structure that can prevent any abnormal behaviour and avoid catastrophic failure [1]. Acoustic emission (AE) is a nondestructive technique (NDT) that can monitor and detect minor cracks in civil structures [2]. AE phenomenon is defined as a transient elastic wave generated as an outcome of a material deformation due to damage initiation and damage propagation [3]. Essential and useful information of the health condition of structure can be extracted from AE parameters such as amplitude, counts, rise time, duration, signal strength, and energy. However, these traditional parameters can be sensitive to the surrounding environment, the level of damage and the presence of noise in the measured AE data. Therefore, this study aims to develop an AE sensing-based improved crack detection technique using a deep learning method augmented with time-frequency decomposition.

Researchers have paid great attention to AE technique as a damage detection tool due to its high sensitivity to minor damage. For example, AE technique was used to assess the microcracks in different structural elements such as fibre-reinforced concrete beams and multi-story buildings [4]. In [5], the authors proposed AE technique to detect the damage in a reinforced concrete slab subjected to dynamic load.

M. Barbosh (✉) · K. Dunphy · A. Sadhu
Department of Civil and Environmental Engineering, Western University, London, ON, Canada
e-mail: mbarbosh@uwo.ca

A. Sadhu
e-mail: asadhu@uwo.ca

S. Walbridge et al. (eds.), *Proceedings of the Canadian Society of Civil Engineering Annual Conference 2021*, Lecture Notes in Civil Engineering 244,
https://doi.org/10.1007/978-981-19-0656-5_16

On the other hand, AE technique was proposed to evaluate the existing health condition of the real-life bridge. AE sensors were placed at different locations of the bridge to collect AE signals under various loading conditions [6]. In another study, AE technique was utilized to detect the severity and location of damage in prefabricated and prestressed concrete elements. The performance of the proposed technique was verified using AE data collected from the reinforced-concrete beam specimens under different loading conditions [7]. AE analysis based on an advanced deep neural network approach was proposed to detect cracks in prestressed concrete specimens. The proposed technique was implemented to monitor two full-scale bridges under ambient conditions [8]. However, most of the above-mentioned studies are based on pattern recognition techniques that require a suitable selection of features to identify the severity and location of the damage [9].

Recently, Deep Learning (DL)-based artificial intelligence techniques have shown the increased prevalence in the field of SHM as they can extract features from 1 and 2D data without being pro-processed by the users [10]. As such, mechanical faults such as bearing deviations, stator and rotor friction, rotor breaks, and poor insulation can be extracted from 2D greyscale images using CNN as demonstrated by [11]. Though many studies have focused on using traditional greyscale or RGB images in DL-based damage detection methods, there are several studies which implement images based on time or frequency domain methods. [12] demonstrated that the CNN architecture, '*LeNet-5*' was able to efficiently and accurately diagnose faults of mechanical systems using CWT images. Similar conclusions were reached by [13], which demonstrated that '*LeNet-5*' was able to distinguish between various system health conditions from 2D spectrograms. However, 2D CNN based on time-frequency (TF) images have focused primarily on mechanical systems, and very few studies have contributed to the field of SHM. Therefore, this paper proposes a new method for the localization of damage in civil structures through the classification of CWT images extracted from the AE signals using CNNs.

2 Proposed TF-Based 2D CNN Method

2.1 Empirical Mode Decomposition (EMD)

EMD is a TF-based signal processing method that has been widely applied as a modal identification and damage detection tool for civil structures due to its high performance with nonlinear and non-stationary data [14]. EMD can decompose a multi-component signal into a set of oscillatory waveforms defined as intrinsic mode functions (IMFs) [15]. In order to consider the waveform as IMF, it should meet the following criteria [16]: (a) the difference between the number of extremums and the number of zero-crossings should be equal or differ at most by one in the entire data set, and (b) the mean value of the envelope defined by local maxima and minima is zero at any point. There are some steps that need to be followed to decompose any

signal, which is provided in [14]. Once the signal is decomposed, the input signal $x(t)$ can be written as:

$$x(t) = \sum_{i=1}^{m} IMF_i(t) + \varepsilon_m(t) \tag{1}$$

where $IMF_i(t)$ represents the IMF of the original signal and $\varepsilon_m(t)$ is the residual of $x(t)$. In this study, EMD is applied to eliminate the presence of noise in AE data and obtain the key AE components (IMFs) that belong to damage, which are used to generate the images using CWT.

2.2 Continuous Wavelet Transform (CWT)

WT is a TF method that can provide a TF representation of the signals in a multi-resolution framework. CWT is one of the powerful TF signal processing approaches that are used in different fields such as image compression, signal noise filtering, and pattern recognition [17]. The CWT of a signal $x(t)$ can be expressed as:

$$w_n^l(x) = \int_{-\infty}^{\infty} x(t)\psi^*(\frac{t-n}{l})dt \tag{2}$$

The inverse CWT (ICWT) can be determined by:

$$x(t) = \frac{1}{w_\beta} \iint_{-\infty}^{\infty} \frac{1}{|l|} w_n^l(z)\psi^*\left(\frac{t-n}{l}\right)dn\frac{dl}{l^2} \tag{3}$$

where w_β can be written as:

$$w_\beta = \int_{-\infty}^{\infty} \frac{|\psi(\omega)|^2}{|\omega|}d\omega < \infty \tag{4}$$

where l and n represent scale and translation of the mother wavelet, respectively. The basis function is called mother wavelet $\psi(t)$, where superscript (*) denotes its complex conjugate. With the appropriate choice of l and n, the CWT utilizes the shifted and scaled versions of ψ and subsequently performs its inner product with $x(t)$. In this paper, CWT is applied to generate spectrograms of key AE components (IMFs) that are used to feed the CNN model to detect and identify the approximate location of the damage.

2.3 Convolutional Neural Network (CNN)

CNNs are a subset of DL Algorithms which were inspired by the visual cortex of animals and the interconnectivity of neurons between the eye (input) and the brain (output) for decision-making processes based on visual data. These networks can consist of several blocks (neurons) which are used to extract the relevant information from the input data accurately. Features are autonomously extracted from input data (x) through convolutional layers, which implement dot product operations to extract weights (W) and bias (b) through a pre-defined kernel. The presence of specific features spatially within images is emphasized by activation functions such as rectified linear units or hyperbolic tangent units, which allows nonlinear relationships to be defined between the input and anticipated output of the data. Once feature extraction has been completed, the results of the convolutional layers are flattened using Fully Connected Layers. Finally, Softmax Layers are used to determine the probability of a particular classification occurring based on the output (Y) defined by:

$$Y = Wx + b \tag{5}$$

Following classification, the overall performance of the network can be evaluated using various indicators such as accuracy, precision, recall and F1 score based on comparing the predicted and true outputs of the inputted data.

2.4 Proposed Approach

Once AE data $y(t)$ is measured, EMD method is proposed to decompose the data and extract the key AE components (IMFs) of each AE sensor. Then, CWT is used to provide the TF representation of each IMF extracted from EMD, known as spectrograms. The resulting spectrogram of each IMF is used to feed into a 2D CNN model to identify the potential location of the damage. In this paper, a modified *VGG-16* developed by [18] is used to classify the spectrograms of the IMFs. The number of filters of each convolutional layer from the traditional VGG-16 network is reduced by a factor of 8 as the number of classifications and complexity of the features are dramatically reduced compared to the original capacity the network was designed for. Moreover, the length of intermediary fully connected layers is reduced from 4096 to 512, with the final fully connected layer having a length equivalent to the number of classes used in the study. The main steps of the proposed approach are illustrated in Fig. 1.

Fig. 1 The flowchart of the proposed approach

3 Numerical Illustration

3.1 Sine Example

In order to validate the performance of the proposed approach, a suite of sine signals containing four different frequencies (e.g., $f_1 = 1$ Hz, $f_2 = 3$ Hz, $f_3 = 5$ Hz, and $f_4 = 7$ Hz). However, a pure sine signal can generate only a single CWT image which is not enough to train the CNN model. To overcome this issue, an ensemble of sine signals with the same frequency is generated by adding noise to the original sine signal, as shown in Eq. (6):

$$X = \sin(2\pi f t) + a \tag{6}$$

Where f is the signal frequency, and α is the signal noise component that is a random and normal time-series sequence. Each signal is processed using CWT to create spectrograms, as shown in Fig. 2. 1000 images of each frequency class are extracted using the CWT method and then used to feed the CNN model. 70% of the images are used for training, 20% for validation, while the rest 10% are used for training. This resulted in 2800 images, 800 images and 400 images, respectively, that are used for training, validation and testing. The training is conducted over 30 epochs using a Stochastic Gradient Descent with Momentum (SGDM) solver with an initial learning rate of 0.0005, minibatch size of 128 and L2 regularization of 0.0005. Figure 3 shows the variation of the accuracy and loss throughout the training and validation process. The network is trained for 3 epochs resulting in 39 minibatch iterations. It can be observed that due to the high performance of the network, the accuracy reaches 100% relatively quickly while minimizing the loss function. The trained network is tested using 100 images of each frequency class. Therefore, The proposed CNN model can achieve 100% classification accuracy for all frequency classes.

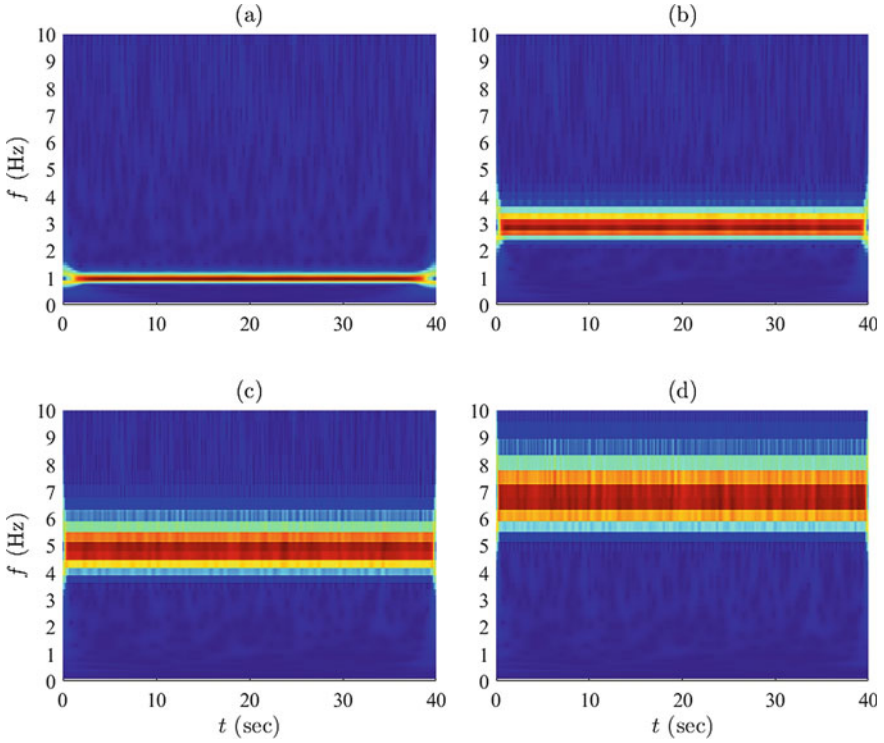

Fig. 2 Spectrograms of the sine signals with frequency **a** 1.0 Hz, **b** 3.0 Hz, **c** 5.0 **Hz** and **d** 7.0 Hz, respectively

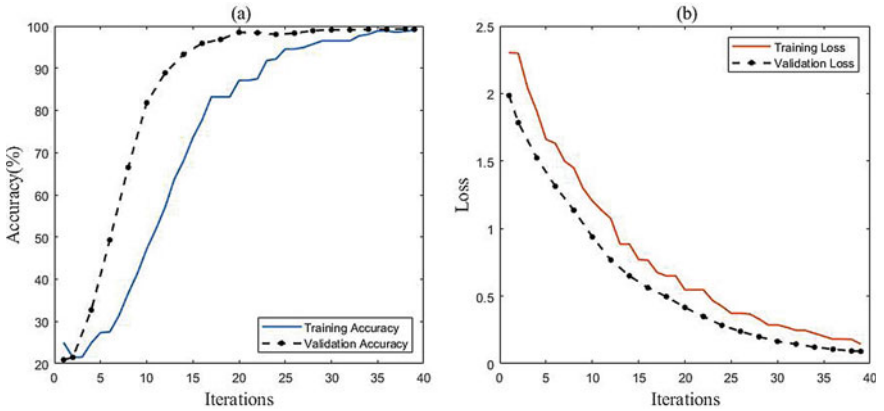

Fig. 3 Performance evaluation of the proposed CNN (modified VGG-16) network

4 Experimental Study

In order to validate the performance of the proposed method as a damage localization tool, an experimental test is conducted using an AE monitoring system on a wooden beam. In this study, a wooden beam was monitored using two AE sensors. These sensors have an operating range of frequencies between 20–450 kHz, which is suitable for the proposed application. A preamplifier is attached to the AE sensors to amplify AE signal. A decoupling box is connected with a preamplifier at one end, and the other end is connected with the data acquisition (DAQ) system. It is also attached with a direct current supply to power the AE sensor and collect the AE signal. A DAQ with four input measurement channels is attached to a computer. The sampling frequency of AE sensors is set to 20 kHz. Figure 4(a) presents the setup of the AE monitoring system. In order to evaluate the performance of the proposed method, AE

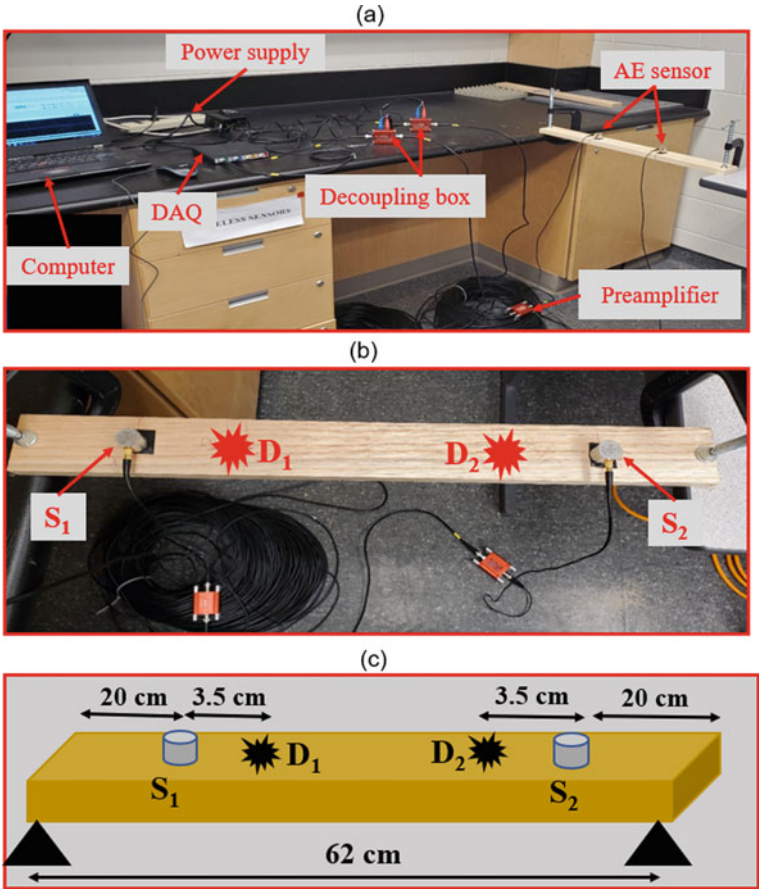

Fig. 4 **a** AE monitoring system and experimental setup **b** actual, and **c** the schematic

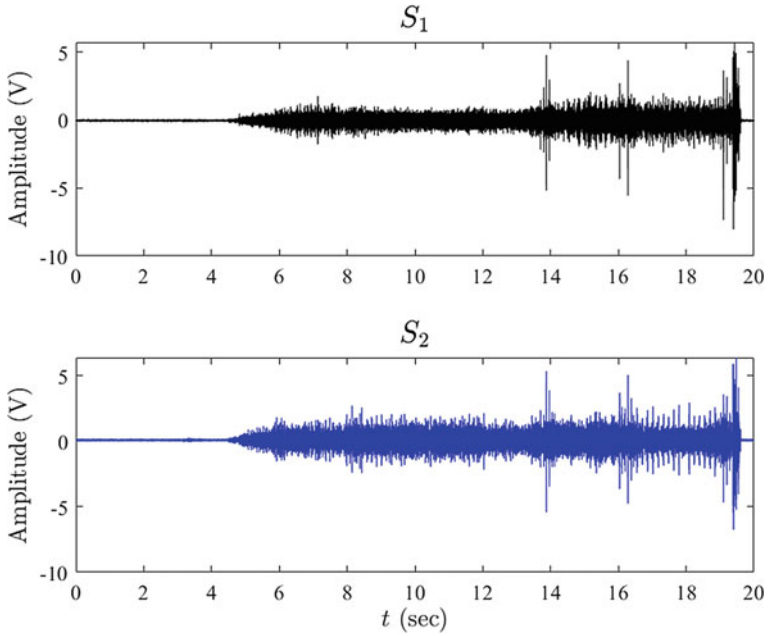

Fig. 5 Time-history of the measured AE data of damage at D_1

data collected from a wooden beam using two sensors (S_1 and S_2) is considered, as shown in Fig. 4(b). The dimensions of the beam are 62 cm in length, 6.5 cm width, and 2 cm thickness, respectively. Two damage locations were considered to check the capability of the proposed method for localizing the damage (e.g., location D_1: damage near S_1 and location D_2: damage near S_2) as shown in Fig. 4(b, c). A drilling machine was used to create the damage while the AE data was collected.

Figure 5 show the time-history of AE data collected from wooden beam using S_1 and S_2. The AE sensors produced big data due to the higher sampling frequencies. Therefore, the time-series of AE signal was divided into a finite number of windows (say, N). EMD method was applied to each segment separately, and a number of IMFs were extracted. Figure 6 represents the first IMF obtained from EMD and its Fourier spectra using AE data from (a, b) S_1 and (c, d) S_2. Then, the CWT method was used to generate the spectrogram of each IMF obtained from EMD. Figure 7 shows a typical coloured (original) spectrogram of IMFs using AE data collected from (a) S_1 and (b) S_2 for damage at D_1. This coloured spectrogram of IMFs obtained from CWT has a size of 936×1920, which were used as the training and testing data of the 2D CNN.

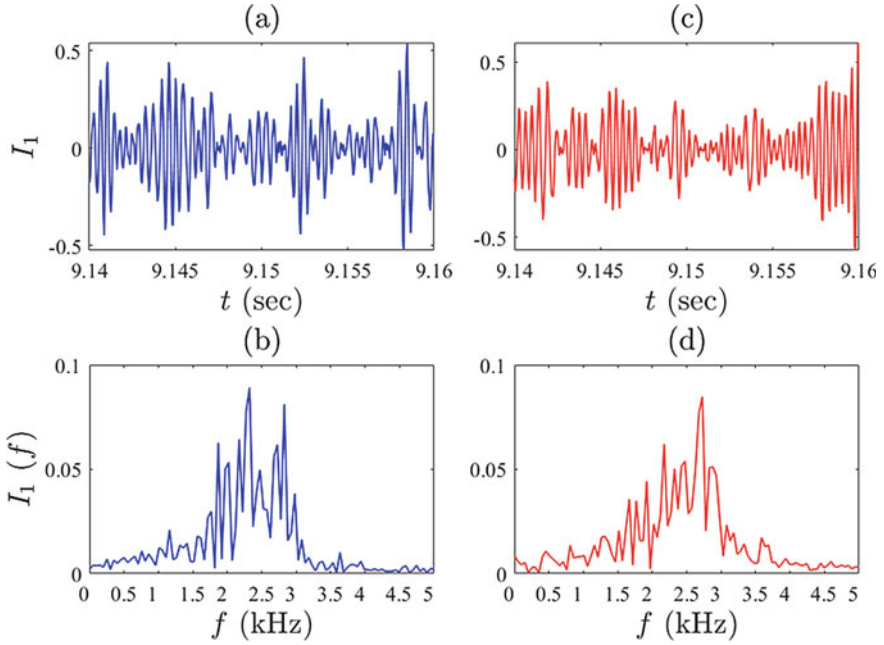

Fig. 6 IMF_1 and its Fourier spectra of AE data collected from (**a**, **b**) S_1 and (**c**, **d**) S_2 for damage at D_1

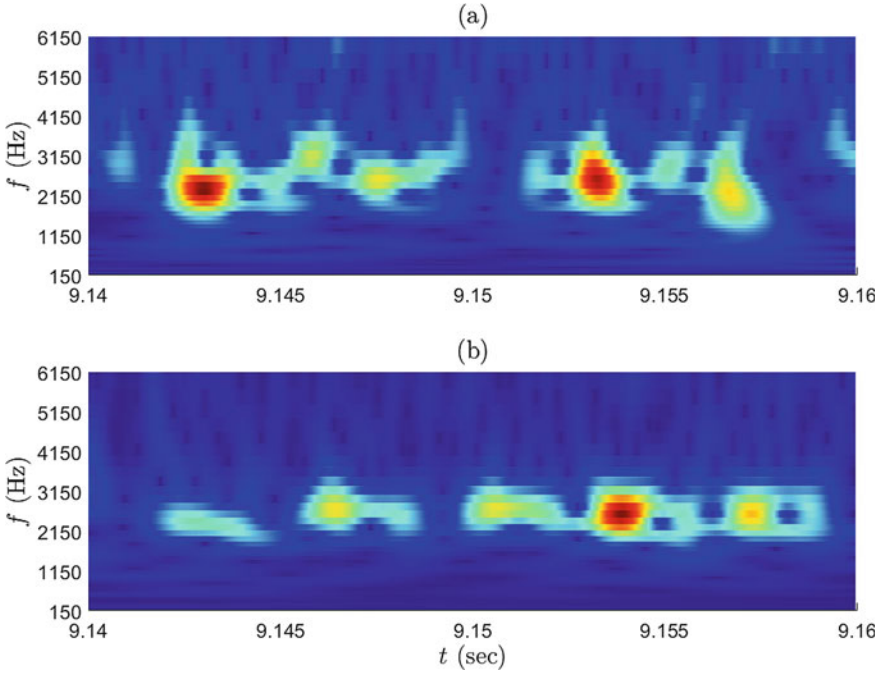

Fig. 7 Spectrograms of IMF using AE data from **a** S_1 and **b** S_2 for damage at D_1

In this study, 473 randomly selected images of each sensor class were used in the training process. An additional 135 images and 67 images of each sensor class were used in the validation and training process. Figure 8 shows the training process of the CNN model. The network was trained for 50 epochs using the same hyperparameters outlined in Sect. 3.1. Thus, a total of $135 \times 2 = 270$ images were used for validation while $67 \times 2 = 134$ images were used for testing. The confusion matrix, as shown in Fig. 9(a, b) displays the classification accuracy for the validation and testing datasets, respectively. The accuracy, recall, precision and F1 scores of the validation dataset and testing dataset are summarized in Table 1. The performance indicators calculated from the confusion matrices suggest an excellent damage identification using the proposed approach.

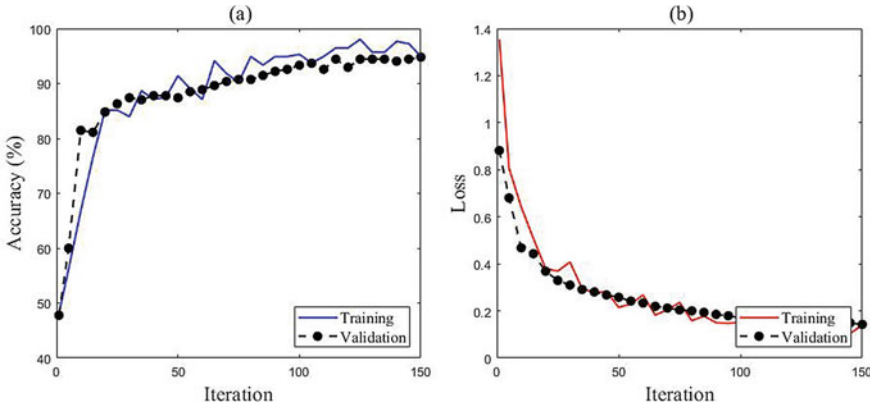

Fig. 8 Training and validation: **a** performance and **b** loss of the Modified VGG-16 using the CWT images

Fig. 9 Confusion matrices for **a** validation and **b** testing data of the wooden beam

Table 1. Performance indicators calculated from the classification of CWT images of close and far damage

Performance indicator	Validation dataset	Testing dataset
Accuracy (%)	93.7	93.2
Recall	0.93	0.93
Precision	0.95	0.94
F1 score	0.94	0.93

5 Conclusion

AE technique is considered as one of the powerful NDT techniques that is capable of detecting and localizing minor damage due to its sensitivity to damage initiation and propagation. For long-term AE monitoring of full-scale structure, AE sensors produce a huge amount of data due to the high sampling frequency. Dealing with such massive AE data using traditional feature extraction techniques can be time-consuming and computationally expensive. In this study, a 2D CNN model is proposed to automate the process of detecting and localizing the damage using massive AE data collected from structures. A set of numerical and experimental studies are conducted to validate the performance of the proposed approach as a damage detection tool using a limited number of AE sensors. The results show the high accuracy of the proposed approach to identify the approximate location of the damage in the structural element. The proposed approach can identify the approximate location of the damage with 93% accuracy, where it can be a suitable candidate for a damage detection tool.

Acknowledgements The first author would like to thank the University of Tripoli for funding this research through the Libyan Ministry of Education. The authors also thank Mitacs for providing financial support to the first author to conduct this research through the Mitacs Research Training award program. The authors also acknowledge the financial support provided by Western Research through the last author's NSERC WSS Accelerator Award.

References

1. Kralovec C, Schagerl M (2020) Review of structural health monitoring methods regarding a multi-sensor approach for damage assessment of metal and composite structures. Sensors 20(3):826
2. Saeedifar M, Zarouchas D (2020) Damage characterization of laminated composites using acoustic emission: a review. Comp Part B Eng 195:108039
3. Sarfarazi MP (1992) Acoustic emissions and damage constitutive characteristics of paper. Institute of paper science and technology, Project 3571
4. Carpinteri A, Lacidogna G, Niccolini G (2010) Damage analysis of reinforced concrete buildings by the acoustic emission technique. Struct Control Health Monit 18(6):660–673
5. Benavent-Climent A, Gallego A, Vico JM (2011) An acoustic emission energy index for damage evaluation of reinforced concrete slabs under seismic loads. Struct Health Monit Int J 11(1):69–81

6. Anay R, Cortez TM, Jáuregui DV, ElBatanouny MK, Ziehl P (2016) On-site acoustic-emission monitoring for assessment of a Prestressed concrete double-tee-Beam bridge without plans. J Perform Constr Facil 30(4):04015062
7. Worley R, Dewoolkar MM, Xia T, Farrell R, Orfeo D, Burns D, Huston DR (2019) Acoustic emission sensing for crack monitoring in prefabricated and Prestressed reinforced concrete bridge girders. J Bridg Eng 24(4):04019018
8. Ma G, Du Q (2020) Structural health evaluation of the prestressed concrete using advanced acoustic emission (AE) parameters. Constr Build Mater 250:118860
9. Barbosh M, Sadhu A, Sankar G (2021) Time–frequency decomposition-assisted improved localization of proximity of damage using acoustic sensors. Smart Mater Struc 30(2):025021
10. Sony S, Dunphy K, Sadhu A, Capretz M (2020) A systematic review of convolutional neural network-based structural condition assessment techniques. Eng Struc 226:111347
11. Hsueh Y-M, Ittangihal V, Wu W-B, Chang H-C, Kuo C-C (2019) Fault diagnosis system for induction motors by CNN using empirical wavelet transform. Symmetry 11(10):1212
12. Liu Q, Huang C (2019) A Fault diagnosis method based on transfer convolutional neural networks. IEEE Access 7:171423–171430
13. Zhang Y, Xing K, Bai R, Sun D, Meng Z (2020) An enhanced convolutional neural network for bearing fault diagnosis based on time–frequency image. Measurement 157:107667
14. Barbosh M, Singh P, Sadhu A (2020) Empirical mode decomposition and its variants: a review with applications in structural health monitoring. Smart Mater Struc 29(9):093001
15. Huang NE, Shen Z, Long SR, Wu MC, Shih HH, Zheng Q, Yen NC, Tung CC, Liu HH (1998) The empirical mode decomposition and the Hilbert spectrum for nonlinear and non-stationary time series analysis. Proc Royal Soc Math Phys Eng Sci 454(1971):903–995
16. Huang NE, Shen Z, Long SR, Wu MC, Shih HH, Zheng Q, Liu HH (2002) The empirical mode decomposition and Hilbert spectrum for nonlinear and non-stationary time series analysis. Proc Royal Soc A 454:903–995
17. Sadhu A, Sony S, Friesen P (2019) Evaluation of progressive damage in structures using tensor decomposition-based wavelet analysis. J Vib Control 25(19–20):2595–2610
18. Simonyan K, Zisserman A (2014) Very deep convolutional networks for large-scale image recognition. ICLR Conf 1409:1556

Laycock Park Pedestrian Bridge, Pushing the Limits of Timber Design

Hothifa Rojob, Peter Phillips, and Abul Rafiquzzaman

1 Background

Calgary is the most livable city in North America and the 5th in the world as per the global livability index by The Economist 2019 report [5]. The City maintains it's livability standards by upholding key environmental, social, and economic sustainable strategies. In 2004, City Council approved the Brundtland definition of sustainable development: "Sustainable development is a development that meets the needs of the present without compromising the ability of future generations to meet their own need" [6]. In the context of a pedestrian bridge, true sustainability is found in the efficient use of materials, improvement of the sociocultural environment, eco-friendly practices, and creation of a long-term positive effect for users and passers-by. This Laycock Park Pedestrian Bridge project was planned and executed taking into consideration The City's commitment to sustainability and in compliance with the City's 2020 Sustainability Direction 10-year plan, City's Triple Bottom Line policy framework, and the Calgary Transportation Plan.

Laycock Park is located on the Southwest corner of the intersection of 64th Avenue NE and Deerfoot Trail in Calgary, AB. The old bridge had reached the end of its useful life (Fig. 1) and was closed for pedestrian by The City due to concerns with scour holes opening up behind the abutment back-walls. Also, differential settlement of the piers and abutments had created dips in the existing bridge. There were also failures in some of the timber stringers supporting the deck. The closure of the bridge cut off community access across Nose Creek to the Park's parking lot, as well as to the regional pathway which traverses the park. The new bridge, designed by a local Calgary team, needed to promote active transportation, recreation, and to become a point of interest to the community. The new structure option was carefully designed to reflect its relationship to the natural environment surrounding the structure. As the

H. Rojob (✉) · P. Phillips · A. Rafiquzzaman
Parsons Inc., Calgary, Canada
e-mail: hothifa.rojob@parsons.com

S. Walbridge et al. (eds.), *Proceedings of the Canadian Society of Civil Engineering Annual Conference 2021*, Lecture Notes in Civil Engineering 244,
https://doi.org/10.1007/978-981-19-0656-5_17

Fig. 1 The old Laycock Park Pedestrian Bridge

existing Laycock Park site includes a former landfill, hazardous material management practices were designed as part of the project.

2 Wood—A Natural Sustainable Choice

The use of wood represents a particularly sustainable option for the project. Wood products have less embodied energy, are responsible for less air and water pollution, and have lower carbon footprints, than other construction materials such as steel and concrete [7]. The light carbon footprint of wood comes in two keyways—through carbon storage and through avoided greenhouse gas emissions.

For the 113 cubic meters of timber used in this bridge, the total estimated carbon benefit is about 138 metric tons, divided as 100 tons of carbon dioxide stored in the wood and 38 tons of carbon dioxide avoided greenhouse gas emissions, which would be the case if fossil fuel-intensive materials (i.e., steel and concrete) would have been used for the bridge's superstructure. U.S. and Canadian forests can grow the amount of wood used in the current project in 19 s [1].

The glulam timber girders are made of regionally sourced AYC, a species that is used where weather resiliency, durability, and workability are needed. The AYC is strongly aromatic and has a nearly yellow colour with fine texture and straight grains

[8]. It has superiority in weather resistance over other common wood species used in structural applications. Laminating stock was sourced through sustainable forest practices and fabricated by an FSC-certified company. Because AYC is not yet among the timber species recognized by certain Canadian structural design standards, we were required to provide our research on the species to the client before receiving their approval to use it for the glulam girders.

3 The Bridge Structural System

The bridge provides an aesthetically pleasing, elegant, robust, innovative, economical, durable, maintainable, and sustainable structure. The approximately 37-m-long bridge spans over Nose Creek and has 3-m approach slabs on each end, followed by 5% accessible at-grade ramps connecting into the adjacent Laycock Park, to the regional North-South pathway systems to the West, and to the Park's parking lot to the East. The bridge deck is 3 m wide, which is maintained through the approach slabs and ramps and widens to 3.5 m as it connects to the Eastern pathways. Among three different structural forms examined in the conceptual design phase, the chosen option was indeed most appropriate (Figs. 2, 3 and 4). Using a Multiple Account Evaluation, the use of exposed structural wood through-girders and GFRP-wrapped timber deck panels was found to be the most sustainable and constructible option within client schedule and budgetary limits. The use of a proprietary innovative GFRP-wrapped deck panel system was mandated by The City at the project Terms of Reference stage. The timber deck on floor beams and the through-girders on reinforced concrete abutments were supported by elastomeric bearings. The abutments were supported by cast-in-place concrete pile caissons into bedrock and were protected by riprap against waterway scour. Aesthetic 'natural stone finish' concrete formlined block retaining

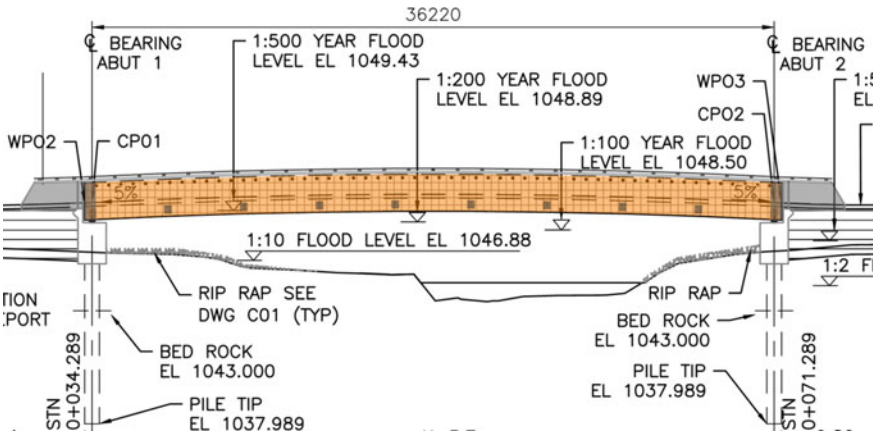

Fig. 2 The new bridge elevation

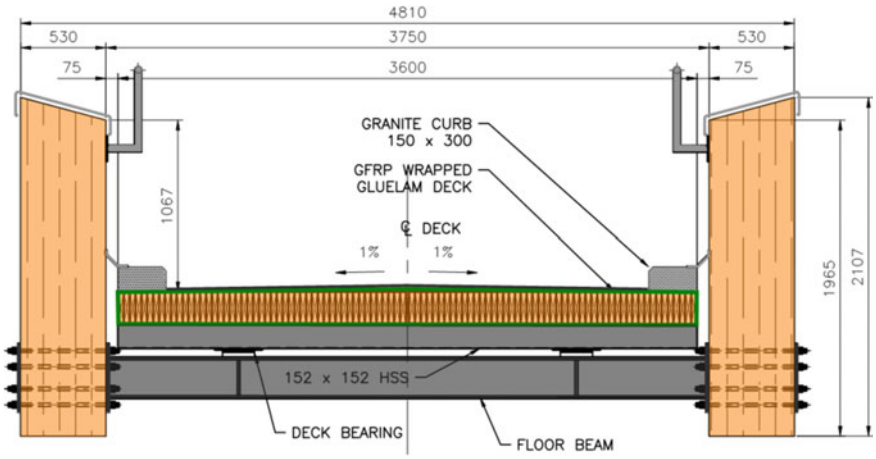

Fig. 3 The new bridge cross-section

Fig. 4 Completed Laycock Park Pedestrian Bridge, looking North

walls parallel to Nose Creek supported 'as-small-as-possible' earth berms on each side of the Creek which were required to raise the bridge's main-span above 1:100-year plus appropriate freeboard flood elevation. The bridge is designed for the 80 kN maintenance vehicle as per the Canadian Highway Bridge Design Code (CHBDC) [2] and 4 kPa of pedestrian loads (not simultaneous loading). The dynamic foot-fall analysis of the bridge was carried out to make sure that vibrations were within acceptable limits.

4 Design Innovations

4.1 Massive Glulam Girders

To improve the bridge's flood resiliency and reduce environmental impacts, instream construction works and lengthy regulatory permits (Alberta Environment and Parks, Water Act, and Department of Fisheries and Oceans, Authorization were minimized and avoided, respectively, i.e. clear spanning the Creek was imperative. However, the 37-m clear span pushed the design and fabrication limits of the glulam girders. The pieces had to be designed without moment splices, as moment splices are known in timber to be locations of uncertainty in design capacity vs. actual capacity. Each girder weighs about 20 metric tons and consists of a pair of 2,000 mm deep beams bolted side by side to constitute a full beam width of 530 mm (Figs. 5 and 6). Key to The City was the availability of multiple local fabricators that could fabricate that size was in order to get competitive bid prices. As it turns out, only three manufacturers in Canada can manufacture and ship that length in full pieces. Shipping and installation strategies were considered at the early stages of design for the girders, so the design team could be confident that their solution could actually be delivered and installed.

As mentioned previously, to improve the flood resiliency of this crossing, as compared to the original bridge that was removed at this site, the soffit of the new bridge needed to be raised up over current design flood elevations. However, maintaining the top of deck elevation as low as possible to tie-in with existing grades as quickly as possible with maximum 5% accessible slopes at each end of the new bridge

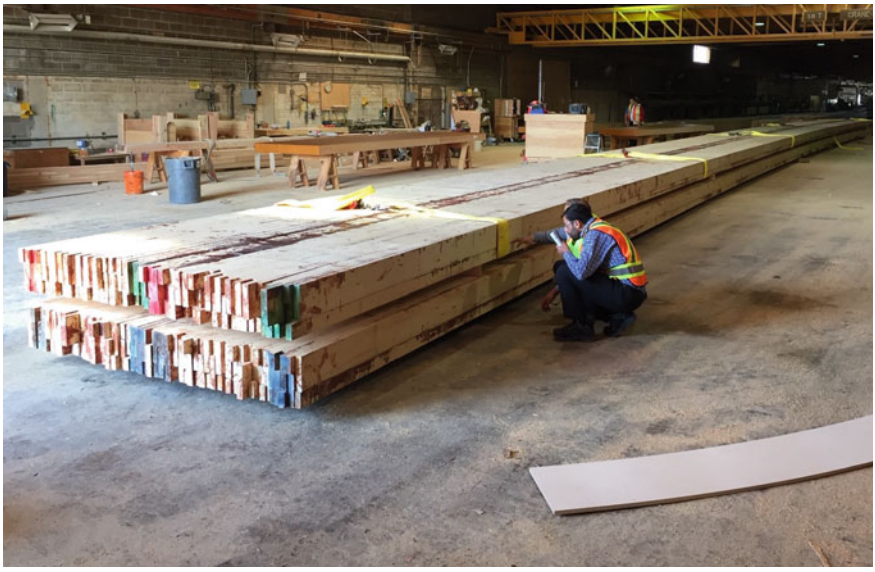

Fig. 5 Girders during fabrication

Fig. 6 Installation of glulam girders

was also important. Consequently, the girders are raised, and the deck is connected to the lower portion of the girders, which added an additional challenge in providing lateral stability to the top portions of the girders in compression. Girder sizes were carefully proportioned to prevent lateral buckling without the use of knee-bracings. The stability of the bridge was confirmed by numerical simulations. The tops of the girders were actually fabricated with slopes towards the inside (walkway) of the bridge to facilitate drainage and to discourage people from standing on their tops.

4.2 Dowel Connections

A unique design in the bridge engineering world for the steel floor beam-to-timber girder connections was implemented. The two pairs of beams (each pair forming one girder) were connected at the level of floor beams using twelve galvanized anchor rods running through pre-drilled holes and at their tops at regular intervals with threaded rods. The floor beams transfer loads from the deck to the lower portion of the timber girders (Fig. 7). To strengthen the girders at the connections, twelve 950 mm fully threaded, zinc-coated, and self-tapping screws were driven into the glulam girders from their bottoms to reinforce the connections and to provide additional capacity against the tensile forces perpendicular to the grain (Fig. 8). This technique engaged a larger volume of timber to resist the vertical loads. Section resistances were checked using a fracture mechanics-based model [3, 4]. The screws, with small heads countersunk 100 mm into the timber, provides additional protection against moisture infiltration and corrosion of the screws.

Fig. 7 Underside of bridge showing the connection between floor beams and glulam girders

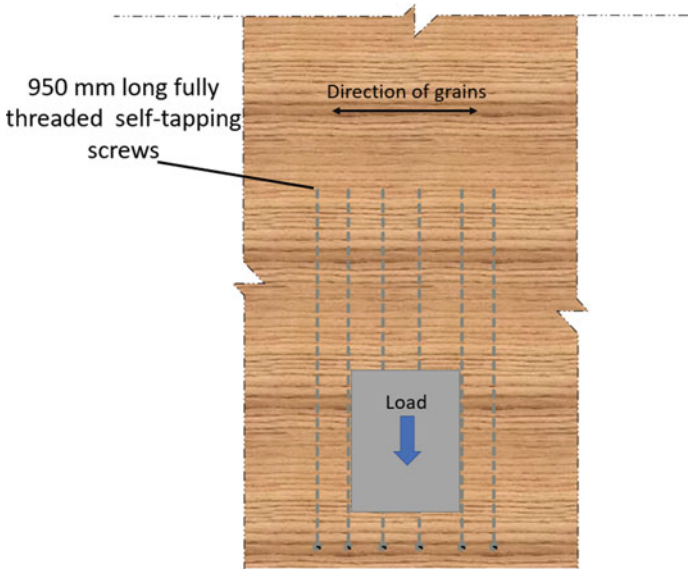

Fig. 8 Typical screw reinforcements for the floor beam connections

4.3 Moisture—Wood's Biggest Enemy

The key to a sustainable timber structure is careful planning and understanding of environmental loads that impact the structure. The bridge is designed to be inherently self-protecting by deflecting water away from the structural elements and by allowing the timber to breathe, i.e., allowing air circulation around the timber so it can dry quickly after being wet. Figure 9 highlights some details of our moisture management engineering. A stainless-steel cap protects the tops of glulam girders while maintaining gaps beneath for air circulation. Similarly, a stainless-steel flashing plate is provided to cover the gap between the glulam girders and the bridge deck and to direct dripping water away from the girders. In addition, for extra levels of precaution, various joints and interfaces between materials were caulked with silicone sealant to keep water out and the girders were oversized by 25 mm on each face to accommodate some future outer rot or damage. In order to facilitate drainage, the bridge deck has a built-in crowned of 1% cross slope in each direction (Fig. 3). Longitudinally, the bridge profile is made of a parabolic curve with 5% slopes at each end (Fig. 2). To summarize: water is directed towards the curbs, then to both ends

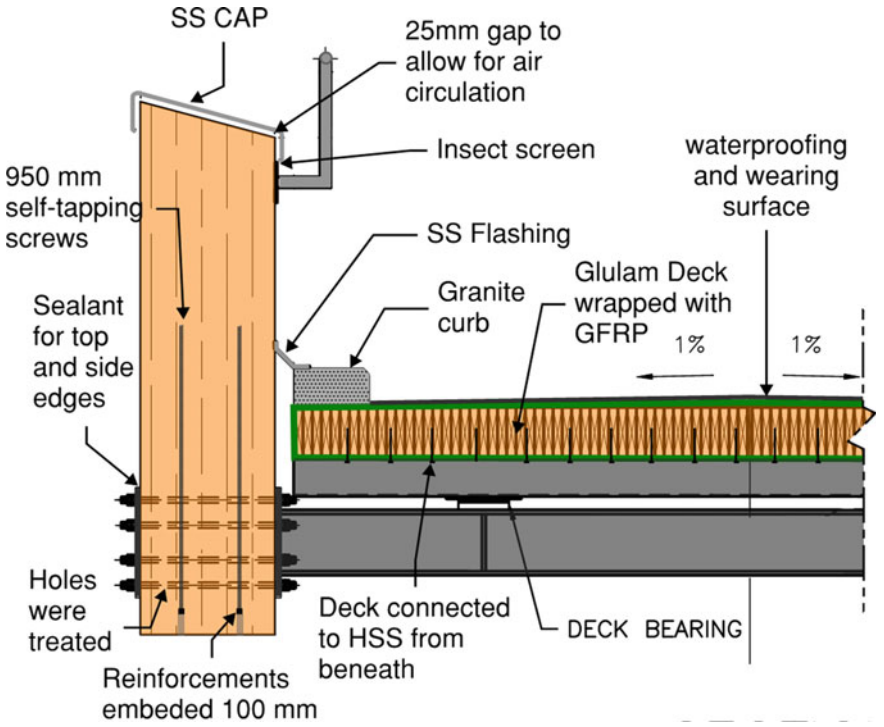

Fig. 9 Waterproofing methods employed

of the bridge into riprap drains. A water repellent, but breathable coating system is another defence against moisture.

4.4 Breathable Coating System

The CHBDC restricts the use of traditional wood treatment measures such as creosote for components in direct contact with pedestrians due to the toxicity of the chemicals involved in the treatment process but is relatively silent on acceptable alternatives. Therefore, as the glulam girders are exposed and within the reach of pedestrians, a safe, environmentally friendly, aesthetically appealing, and equally protective alternative solution needed to be researched. A breathable, three-layer proprietary coating system was ultimately chosen for its ability to repel moisture, protect from UV exposure, hinder the commencement of rotting and withstand weather fluctuations. The coating's pigment was carefully selected to reflect the natural colour and texture of the AYC while still protecting the timber against UV light.

4.5 GFRP-Wrapped Timber Deck Panels

A bridge deck is vulnerable to both abrasion and moisture; therefore, since the bridge deck was to be made out of timber, GFRP-wrapping of the deck timbers for both durability and strength with a post-applied wearing surface on the top of the panels was proposed (Fig. 10). As mentioned previously, The City mandated the use of a proprietary innovative GFRP-wrapped deck panel system at project Terms of Reference stage. The deck panels provide a service lifespan of more than 100 years. The timber core of the deck is made up of Black Spruce manufactured into glulam panels. The non-corrosive durable GFRP encasing protects the timber core against water ingress and UV light. The deck system is much lighter than other typical bridge deck systems made out of steel or concrete, and thus significantly reduces dead load requirements for the structure to accommodate. The panels were manufactured in three pieces and were just set end to end on-site. Providing additional waterproofing protection, a separate proprietary wearing course system was applied on-site on top of the deck panels and spanned the two panel-to-panel joints between the three deck panels.

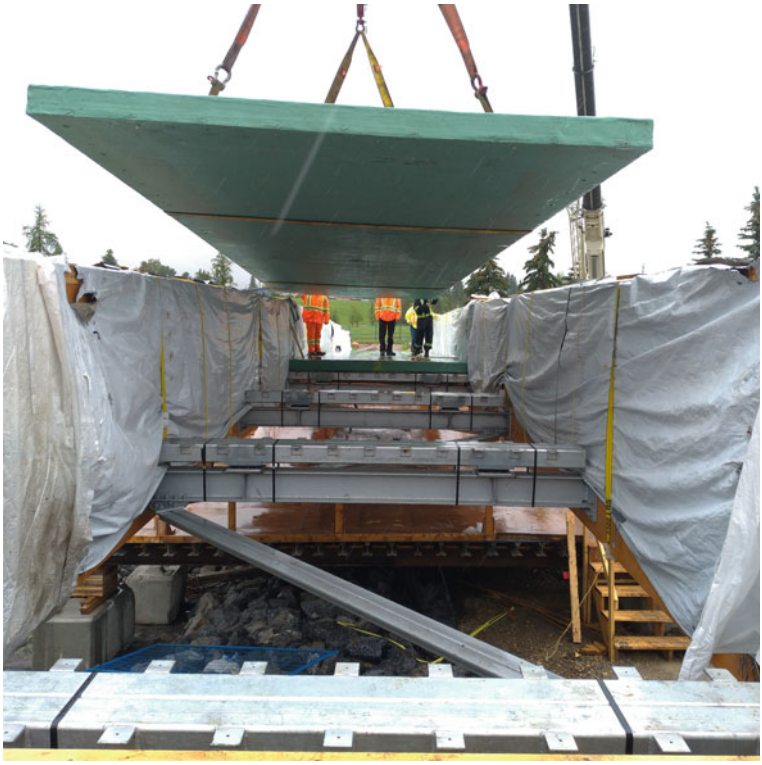

Fig. 10 Installation of GFRP-wrapped timber deck panels

5 Aesthetic Design Features

To match with the theme of other ongoing Park enhancements, redesign, and naturalization, which feature basalt stones for cladding and seating, matching coloured granite stones were used for the bridge's curbs (Fig. 11). The bridge also features stainless-steel caps and stainless-steel bike-rails (grabrails for accessibility are not required as all walkway slopes on the project are less than 5%).

Fig. 11 Bridge aesthetic features including granite curbs and stainless-steel caps and bikerail

6 Conclusions

The new Laycock Park Pedestrian Bridge promotes sustainability by using renewable materials. This aligns with The City's vision for sustainable development and coincides with the public interest in protecting the environment and fighting climate change. For sustainable timber bridges, attention should be given to moisture and water-shedding details, the selection of a proper pedestrian-friendly coating system, and the use of proper wood species. It is also important to make sure that timber is harvested and fabricated in accordance with applicable sustainability standards—which can be imposed by requesting FSC certifications for the timber and from the fabricators.

Acknowledgements The Authors would like to acknowledge The City for encouraging the design team to explore sustainable and renewable materials, the Contractor, Volker Stevin, for their efforts to make the construction of the bridge a success despite the novel materials and details, the bridge Architect, FAAS Architecture, for their assistance in complementing/incorporating the bridge into The City's naturalized vision for the Park, the glulam girders' Fabricator, Western Archrib, the Geotechnical Engineer, Thurber Engineering, the coating Supplier, SANSIN Corporation, Wildlife Specialists, Omnia Ecological Services, Aquatic Environmental Specialist, Grassroots Environmental Services, the GFRP-Wrapped Timber Deck System Developer and Fabricator, Guardian Bridge Rapid Construction, including their Engineer, Blackwell Engineering, the miscellaneous steel Fabricator, Sundance Portable Welding Ltd, the Piling Sub-contractor, Red Deer Piling Inc.

and Ki International Ltd, the wearing surface installation Sub-contractor, Place-Crete Systems L.P., the bearing and expansion Joints Fabricator, LCL-Bridge Products Technology Inc., the Erection Engineer, LEX3 Engineering, and the Redi Rock retaining walls Designer, E2K Engineering.

References

1. Canadian Wood Council (2021) Carbon Calculator. https://cwc.ca/design-tools/carbon-calculator/. Accessed Feb 2021
2. CSA (2014) CSA S6-14, Canadian Highway Bridge Design Code, CSA Group, Mississauga, Ontario, Canada
3. Dietsch P (2016) Reinforcement of timber structures – a new section for Eurocode 5. In: World conference on timber engineering (WCTE 2016), Vienna, Austria
4. Jensen J, Girhammar U, Quenneville P, Kallsner B (2012) Reinforcement of timber structures – a new section for Eurocode 5. In: World conference on timber engineering (WCTE 2012), Auckland, North Island
5. The Economist, Intelligence Unit (2019) The Global Liveability Index 2019. https://www.eiu.com/public/topical_report.aspx?campaignid=liveability2019. Accessed Feb 2021
6. The City of Calgary, The office of sustainability (2020) The City of Calgary's 10-year Plan towards sustainability. https://www.calgary.ca/pda/pd/office-of-sustainability/office-of-sustainability.html. Accessed Feb 2021
7. Oliver C, Nassar N, Lippke, McCarter J (2014) Carbon, fossil fuel, and biodiversity mitigation with wood and forests. J Sustain Forestry **33**(3):248–275
8. Wood Database (2021) Alaskan Yellow Cedar. https://www.wood-database.com/alaskan-yellow-cedar/. Accessed Feb 2021

The Role of Cementitious Liners on the Structural Preservation of Overburdened Buried Concrete Pipes

R. J. Jackson, I. D. Moore, and A. S. Genikomsou

1 Introduction

Reinforced and unreinforced concrete storm and sanitary sewers rely on gravity flow so are often installed at deep burials exceeding five-metre covers [8]. Concrete pipes are designed to resist earth and surface loads such that unreinforced structures do not crack, and reinforced concrete structures have limited crack widths. Cracking also leaves pipe walls susceptible to stormwater infiltration and consequently corrosive and abrasive damage [5]. Corrosive and abrasive damage may create even more cracks in the walls, reducing the load-resisting capacity of the pipe. After enough deterioration-cracking cycles, the damaged pipe will lose capacity such that it can no longer carry the required earth and surface loads, leading to collapse.

In Canada, reinforced concrete pipes are manufactured in accordance with the ASTM C76-11 standard. ASTM C76-11 categorizes the buried reinforced concrete pipes into five classes where each class has three separate wall types. Lower classes, such as Class 1 and 2, correspond to pipes having smaller load-resisting capacities whereas higher classes are selected for burial conditions with harsher loading. Within each class, Wall Types A through C denote increasing wall thicknesses and resistance elements. An image annotated to depict the nomenclature commonly used to denote the four key locations around the pipe circumference is provided in Fig. 1.

Rigid pipes are conventionally selected from the C76-11 standard using either the Direct or Indirect Design Methods [1]. It is widely recognized that in rigid buried

R. J. Jackson (✉) · I. D. Moore · A. S. Genikomsou
Queen's University, Kingston, Canada
e-mail: 15rjlj@queensu.ca

I. D. Moore
e-mail: Ian.moore@queensu.ca

A. S. Genikomsou
e-mail: ag176@queensu.ca

S. Walbridge et al. (eds.), *Proceedings of the Canadian Society of Civil Engineering Annual Conference 2021*, Lecture Notes in Civil Engineering 244,
https://doi.org/10.1007/978-981-19-0656-5_18

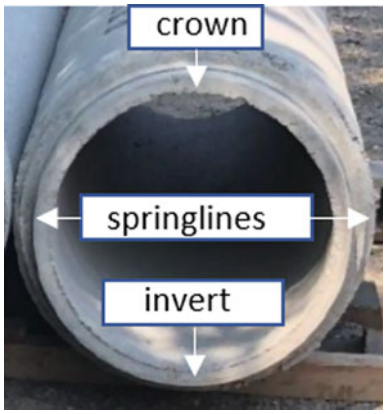

Fig. 1 Diagram of relevant locations around a pipe's circumference

pipes, bending moment should be regarded as the critical design mechanism [12]. Therefore, rigid pipes are designed to limit moment-induced cracking, specifically at the pipe crown or invert where bending moments are most severe. The Indirect Method for reinforced concrete pipes is based around computing the required D-Load to induce a 0.3 mm crack. These computations consider live loading, earth loading, and the required pipe diameter. The moments associated with earth and live loading can be calculated using bedding factors, empirical quantities that account for the reductions in moment resulting from soil support, with various burial conditions defined by AASHTO quoted in the ACPA design manual [3]. Pipes are then selected based on the required D-Load (the capacity of the pipe to resist vertical force applied across the vertical diameter, assessed using strength tests which feature two or three-point loading applied until it fractures) to prevent unsafe levels of cracking after burial. An alternative is to use the Direct Design Method, where bending moment is calculated explicitly with a finite element analysis. AASHTO employs the Heger earth pressure distributions for use in that structural analysis [10].

Many Canadian sewers are approaching the ends of their service lives and have reached unsafe levels of deterioration or loading, or the joints are leaking, and permitting the ingress of groundwater. Rather than replacing these pipes, which is a costly process with excavations that impede traffic and lead to other indirect costs, many Canadian municipalities opt to rehabilitate buried pipes with trenchless solutions. Different trenchless methods for pipe rehabilitation exist, where each method is suitable for different types of pipes and burial conditions. Cementitious liners are centrifugally cast with a spinning head that travels along the interior of the pipe or sprayed by hand. Once the liner is applied over the pipe interior it is left to cure until tensile strength is adequate. All stormwater flow is rerouted prior to liner application to ensure the cementitious admixture sets properly. In scenarios where pipe degradation has led to critical decreases in load-resisting capacity, the strength contribution of the liner can be essential to ensuring continued structural integrity. Additionally, some intact pipes may be subjected to additional surface loads after installation. In

those instances, the application of the liner may be required to increase the cracking capacity of a pipe such that it can meet load demands and prevent deterioration.

While cementitious liners have been studied for rehabilitation of corrugated steel (flexible) pipes (e.g. Moore and Becerril García [14], little guidance exists regarding the selection of cementitious liner thickness to restore the hydraulic or structural integrity of rigid (vitrified clay or concrete) pipes. The objective of the current research is to develop a procedure for selecting liner thicknesses based on numerical modelling and applications of soil-pipe interaction theory. While future instalments from this research project will encompass lining methods for a range of pipe deterioration states, this report addresses the potential need to line intact pipes to prevent leakage or strengthen them to withstand additional earth loads after installation.

2 Loading and Expected Bending Moment

Moore [15] adapted the Indirect Design Method for buried pipes to estimate the bending moments that develop in a buried rigid pipe repaired with a sprayed liner, responding to a combination of earth loads and vehicle loads. Live load bedding factor of 1.1 and earth load bedding factor of 1.7 from [1] were used to relate the moment in a buried pipe to the D-load condition. Bending moments were then reduced to account for the soil-pipe interaction, using a moment arching factor (reductions because their work focussed on sprayed liners within buried flexible pipes).

Royer and Allouche [17] considered three different bending moment values in their study of reinforced concrete pipes with sprayed liners, none of which involve explicit consideration of the soil-pipe interaction. The first value arose from consideration of a ring subjected to uniform external pressure (a loading condition that produces negligible bending moments, and so could not be expected to provide design that prevents cracking due to moments in a buried pipe). The second is based on an equation from Watkins (1999) for the moment at the centre of a 90-degree arch with pinned supports having radius r, and subjected to uniform vertical pressure P, producing peak moment of $0.0062\,\mathrm{Pr}^2$. This moment value is approximately one percent of the peak moment for a ring subjected to that same vertical pressure loading, if the resulting vertical force was applied at the crown ($\frac{2\mathrm{Pr}^2}{\pi} = 0.63\,\mathrm{Pr}^2$ for this D-load condition, so implicitly implies that the repaired pipe has a bedding factor of $0.63/0.0062 > 100$). The third moment value was also based on an expression from Watkins [18], where the pipe has invert moment of $0.05872\,\mathrm{Pr}^2$ (so implicit bedding factor of $0.63/0.0625 > 10$). All moment values considered by Royer and Allouche [16] appear much lower than values that could be expected to develop in a buried rigid pipe.

In the current study, stress resultants (moments and thrusts) that develop in buried rigid structures will be estimated using the Hoeg solution [11]. Hoeg's soil-pipe interaction theory defines pipe behaviour in terms of its response to the uniform and

non-uniform components of earth pressures. The uniform component of earth pressure produces wall-thrusts and the non-uniform component results in circumferential bending moments. The accuracy of the Hoeg solution is limited by the assumptions of linear elastic soil and either a no-slip (i.e. bonded) or perfectly smooth response assumed to apply around the soil-pipe interface.

The Hoeg solution uses dimensionless stiffness ratios, C and F, which relate soil stiffness to pipe stiffness. In rigid sewers the pipe stiffness is large relative to soil stiffness so C and F can be assumed to approach zero. On this basis Moore [13] suggests a simplified version of the Hoeg solution in Eq. 1,

$$M_{applied,crown} = \frac{\sigma_v r^2 (1 - K)(1 - \nu)}{3 - 4\nu} \tag{1}$$

where $M_{applied,crown}$, σ_v, r, K, and ν denote the crown bending moment, vertical (overburden) stress, external pipe radius, coefficient of lateral earth pressure and Poisson's ratio of the soil respectively [13]. This equation will subsequently be referred to in this paper as 'rigid pipe theory'.

Vehicle loading can be defined in accordance with AASHTO [1]. The design manual states that at soil covers less than 0.6 m, wheel loads shall be distributed directly to the top slabs of culverts. At burials deeper than 0.6 m a live-load distribution factor (LLDF) is introduced which increases the length over which vertical load is applied in each horizontal direction by 1.15 times the depth of the fill. The LLDF applies until the area sustaining vertical loads reaches a maximum value when the soil cover reaches 2.4 m. At covers deeper than 2.4 m, surface loads are assumed to have negligible effects. Given reinforced concrete sewers are typically buried at covers greater than five metres, the effects of live loading will be ignored.

A liner is typically applied to pipes after burial, meaning the concrete pipe actively resists earth loads prior to the liner installation. However, the current study will estimate the required liner thickness to restore structural capacity to rigid pipes by assuming the liner is applied before the concrete pipe is subjected to earth loads. This assumption may result in conservative estimates of the tensile stresses seen in the liner, as liners applied after pipe burial would attract proportionally less load relative to the fully loaded concrete pipe.

3 Resistance Models

The design models developed by Moore [15] were for sprayed liners within flexible (corrugated steel) pipes, where circumferential bending moment at the crown is limited to prevent the liner from cracking under the tensile stress induced at its extreme fibre, with both composite and non-composite calculation options provided. They compared their design calculations with measurements of cracking loads observed in the two buried pipe tests reported by Moore and Becerril García [14] for spray-lined corrugated steel pipes tested under surface loads and showed that the

calculations based on composite response were the most successful. That work could provide a useful starting point for the current study, provided the strength assessment was modified to consider liners sprayed within reinforced concrete rather than corrugated steel pipe.

Royer and Allouche [16] considered the use of two different kinds of resistance models. The first assumes that the pipe is allowed to crack, but with maximum crack widths limited to either 0.01 or 0.0625 inches. Analysis was undertaken assuming that the neutral axis of the lined pipe is at the interface between the concrete and the liner. The second resistance model they considered involved application of a strength equation developed by Bazant and Cao [4] for unreinforced concrete pipe. Those researchers related the nominal stress in the unreinforced concrete at failure to the tensile strength of the concrete as well as a 'characteristic dimension' for the structure, and a series of empirical parameters obtained by Bazant and Cao [4] using best fits to their strength data for unreinforced concrete pipes. Bazant and Cao [4] however, reported that the performance of their empirical strength correlations was poor. Neither the crack width nor the empirical strength model appears suitable for the current study, since unreinforced material like the sprayed liner should be designed to prevent cracking (rather than to achieve a non-zero crack width), and it would require many sprayed concrete pipe tests to generate data sufficient for the empirical correlation.

There is a clear need for a design method for liner thickness selection that is based on realistic levels of bending moment, and which addresses the composite behaviour of a sprayed concrete pipe. In the current study, the resistance of the pipe will be evaluated on the basis that the bending moment at the crown shall not exceed the cracking moment of the pipe wall. This assumption helps ensure that the repaired pipe will not leak through joints or undergo crack-deterioration cycles over its service life. Buckling is not considered to be a critical design mechanism as the deteriorated pipe will support most of the compressive thrust, leaving the liner responding primarily in bending. The liner thickness is selected to prevent two potential strength limit states at the crown and invert:

a. cracking at the innermost fibre of the liner (the inner surface of the rehabilitated sewer).
b. cracking at the innermost fibre of the concrete pipe wall (where it contacts the liner, since a strain concentration would then develop that cracks the liner where it spans across the crack in the concrete).

It is not necessary to make any 'a priori' assumption regarding the location of neutral axis. Instead, its location can be computed geometrically using force equilibrium. Once the location of the neutral axis is obtained, stress-strain distributions can be computed under the assumption of linear strain distribution through the liner-concrete composite (based on perfect bond at the interface between the liner and the concrete). Liner thicknesses are then selected by setting the applied moment based on the Hoeg solution equal to the allowable moment (when tensile stress in the liner or concrete pipe reaches the tensile strength limit i.e., rupture stress, or tensile strain reaches the tensile strain limit). Closed-form solutions were created to investigate

the peak tensile liner stresses that develop from perfect bond and complete debond between the liner and the host pipe. The solutions show that tensile stresses are higher in the bonded case, indicating that the assumption of perfect bond is conservative for the purposes of this study. Further investigation on the implications of partial debonding between the liner and the host pipe will be included in future research studies.

This study will illustrate this resistance assessment by investigating the effects of repairing concrete pipes with two alternative materials: the cementitious liner examined by Moore and Becerril García [14] which had a tensile stress limit of 11.3 MPa [16], and then a cement mortar having a tensile stress limit of 7 MPa [6]. Applying a safety factor of 2 to the tensile strength of each material, tensile stress limits of 5.65 and 3.5 MPa will be used for the liner and mortar respectively. For the case where the concrete pipe cracks before the inside surface of the liner (case b. above). Equation 2, is used to estimate the allowable tensile stress limit of the concrete in the pipe as 2.05 MPa for Class III and Class IV pipes, and 2.51 MPa for Class V. The coefficient of 0.65 in this equation represents the resistance factor specified for concrete [7].

$$\mathrm{fr} = 0.65 \times 0.6\lambda\sqrt{\mathrm{f'c}} \tag{2}$$

4 Numerical Modelling

A series of finite element analyses (FEA) were conducted using the ABAQUS/CAE software [2] to evaluate the results of the design approach. In the FEA, two-dimensional solid, plane-strain elements were used to model the soil, the concrete, and the liner. The liner thicknesses computed in the design model were used to create replicas of the soil-pipe-liner system in the FEA. The numerical analyses were used to obtain the values of the maximum tensile stress in the liner. An example mesh for a Class IV-Wall B pipe at a five-metre burial depth is shown in Fig. 2. Distance to the

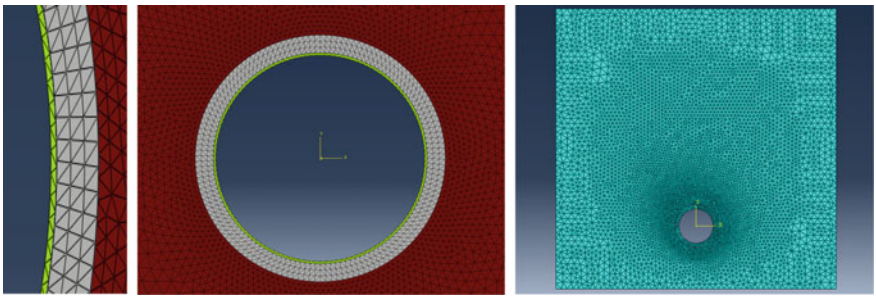

Fig. 2 Image of a meshed soil-pipe model created in ABAQUS/CAE

side boundaries of the mesh from the springlines of the pipe was set to 4.25 m, and a 1.75-m soil foundation was created between the invert and the bottom boundary. Lateral soil distances between springlines and boundaries were selected on the basis that rigid pipes attract more load than just the weight of the soil prism directly above the pipe. Rather, rigid pipes are stiff relative to the soil beside it, forcing the sewer to resist the weight of a larger volume of soil that extends outwards towards the side boundaries. This concept is known as negative arching.

The soil, concrete and the liner were modelled as homogenous, deformable elements with elastic material responses. Elastic response until shear failure, and thereafter elastic-plastic behaviour was defined for soil but not the pipe, since the pipe was loaded up to a maximum of half the fracture (cracking) stress given safety factors of 2 are applied in the design model. Mohr-Coulomb plasticity behaviour was defined for the soil elements to capture the effects of plastic strain resulting from the shear stresses which develop at the shoulders and haunches. Reinforcing steel was not included in this analysis, since steel was assumed to have a negligible impact on the moment for this uncracked pipe (the steel has modest effect on the intact section's flexural rigidity). The interface between concrete and liner was modelled with a tie connection to simulate perfect bond. This idealization may not always be realized in practice as the success of the bond is a function of the liner installation process, and it may be investigated further in a subsequent study. The soil-pipe interface was also modelled with a tie connection which matches the no-slip condition assumed in the design model. The no-slip condition is a reasonable assumption given the high coefficient of friction expected between the soil and concrete.

Material properties used in the FEA models are reported in Table 1. Material strengths for concrete were taken from C76-11. There are several techniques to numerically model horizontal soil stress behaviour over increasing soil depths. The analysis of a block of soil under self-weight was undertaken with full restraint against lateral deformation along each of the vertical side boundaries. To ensure the lateral earth pressures that then developed were in accordance with the assumed value of coefficient of lateral earth pressure, $K = 0.335$, used in the design model, Poisson's ratio, ν, was set to $K/(1 + K) = 0.25$. When the soil deforms under its self-weight, the lateral earth pressure coefficient of 0.335 will then result based on the well-known relationship for one-dimensional elastic deformation shown in Eq. 3.

Table 1 Material values used for the FEA and the design model

Material	Young's modulus (MPa)	Density (kg/m^3)	Poisson's ratio, ν	Friction angle (degrees)	Dilation angle (degrees)	Cohesion stress (kPa)	K
Concrete	23,632	2400	0.2	–	–	–	–
Liner	25,900	2400	0.2	–	–	–	–
Soil	40	1834	0.25	45	23	3	0.335
Concrete (Class V)	28,943	2400	0.2	–	–	–	–

$$K = \nu/(1 - \nu) \tag{3}$$

All model components were meshed with six-node modified quadratic plane strain triangles. Nodes close to the pipe were seeded at three-centimetre spacings around the pipe circumference. The displacement of the left and right boundaries of the soil system were restricted in the x-direction (where the x and y-directions denote the horizontal and vertical directions in the model respectively). The displacement at the bottom edge is fixed in both the x and y-directions. Self-weight due to gravity was applied over the entire model.

5 Results

A MATLAB script of the design model was created to relate the cracking moment to the applied moment due to earth loads for a rigid pipe (Eq. 1). Using the geometric and material parameters for different pipe classes and wall types outlined in C76-11, the script iterates through increasing liner thicknesses until the allowable moment meets the demands of the earth load. The required liner thicknesses for a Class III-Wall A, Class IV-Wall B and Class V-Wall C buried at 4, 5, and 7-m covers respectively were obtained from the design model and are presented in Table 2 below. Burial depths were selected on the basis that earth loading would surpass the allowable moment capacity of the host-pipe and that the required liner thickness was small enough that the hydraulic area remains unobstructed. For all three burials, cracking occurs when the pipe interior reaches its tensile rupture stress and not when the liner ruptures (as the stresses in the concrete pipes have all reached their respective tensile limits). This is a result of using a liner with a high tensile stress limit in comparison to the concrete pipe. The results shown in Table 2 will be compared to reference numerical models in subsequent sections of this paper.

A plot illustrating the changing cracking capacity of the pipe with increasing liner thickness for the Class IV-Wall B pipe buried at a five-metre cover is presented in Fig. 3. The applied moment remains constant as the simplified Hoeg solution is independent of changing pipe properties apart from the external pipe radius which remains constant. The pipe's cracking moment capacity increases steadily with increasing

Table 2 Required cementitious liner thicknesses for three different burial conditions

Pipe	Burial depth (m)	Computed liner thickness (mm)	Max stress in concrete pipe (MPa)	Max stress in the liner (MPa)
Class III, Wall A	4	22.81	2.05	3.58
Class IV, Wall B	5	21.94	2.05	3.60
Class V, Wall C	7	25.36	2.51	3.19

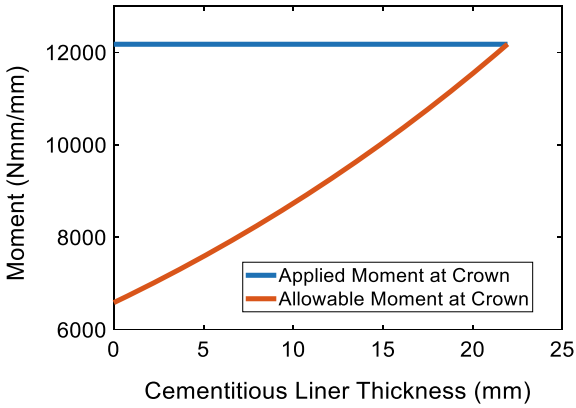

Fig. 3 Plot of increasing allowable moment with additional cementitious liner thickness, for the Class IV pipe specified in Table 2

liner thickness as the addition of the liner shifts the neutral axis of the section downwards through the concrete. A liner thickness of 21.9 mm was required to set the estimate of the cracking moment equal to the estimate of the applied moment, at the point of intersection of the two lines.

Numerical models were then used to evaluate the results of the soil-pipe interaction solution used in the design model. Using the required liner thickness for the Class IV-Wall B pipe, a 2-D model was created. An in-plane stress-contour of this model can be seen in Fig. 4. The red contours denote regions of tensile stress and compressive zones are shown in blue. The FEA captures the formation of peak tensile zones at the interior of the crown as assumed in the design model. Tensile zones also appear at the exterior of the springlines but were smaller in magnitude. A mesh refinement analysis was completed where element sizes were decreased by 50%. The mesh refinement resulted in a 0.4% difference in the maximum stresses observed in the model. A plot of the stress distribution around the top half of the liner's interior circumference is presented in Figs. 4 and 5. The negative values at the edges of the plot correspond with 4.07 MPa compressive stress maxima at the springline interiors.

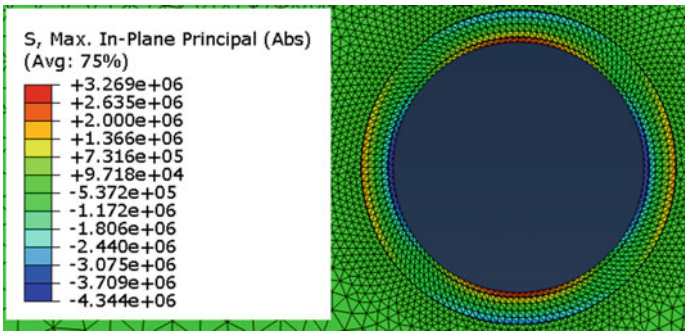

Fig. 4 Stress contours around a Class-IV, Wall B pipe at a 5-m burial depth

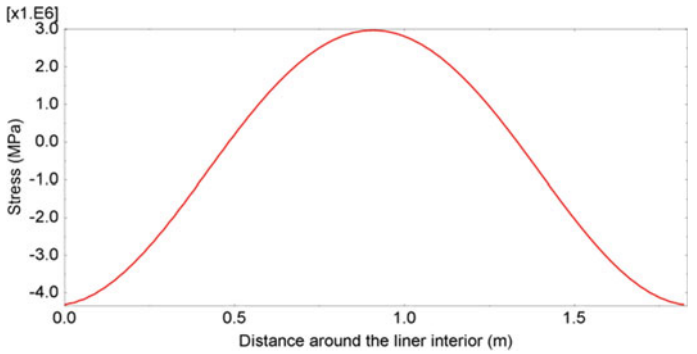

Fig. 5 Stress plot around the internal liner circumference for the top half of the Class-IV, Wall B pipe

The liner stress approaches zero at the shoulders of the pipe which is characteristic of the typical hourglass stress distribution around buried pipes. The tensile stress in the liner reaches a maximum value of 2.98 MPa at the crown interior.

The strain distribution through the pipe-wall at the crown is shown in Fig. 4. The dashed blue line represents the strain distribution calculated with the design model based on the Hoeg solution assuming composite behaviour between the liner and the concrete pipe. The solid red line represents the somewhat curved strain distribution obtained from the FEA, with a maximum difference of 0.000025 strain observed between the two lines. This finite element calculation supports the simplifying assumption of linear strain distribution used in the design model. The point of zero-strain, or the neutral axis, can be seen at approximately 70 mm from the top of the section. Figure 6 also shows that for a liner with a tensile stress limit of 11.3 MPa (5.65 MPa after dividing by a safety factor equal to 2), the required liner thickness to

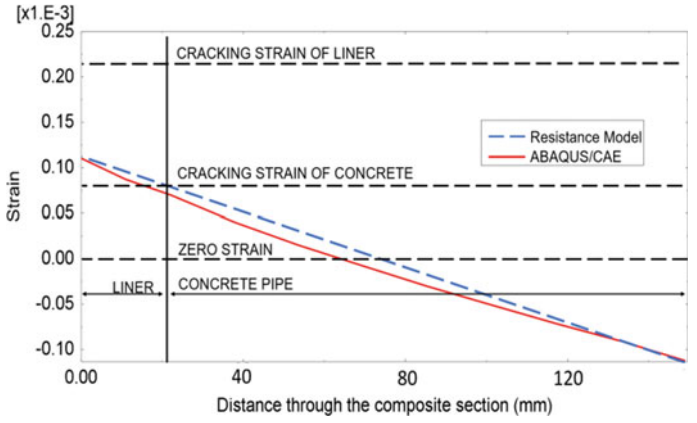

Fig. 6 Plot showing the strain distribution through the composite section measured from the inner surface of the cementitious liner

prevent cracking is governed by the tensile strain limit of the concrete pipe rather than the tensile strain limit of the liner. This is shown by the intersection of the design model and the line denoting the cracking strain of concrete. The tensile limit of concrete governs the required liner thickness to prevent cracking because the tensile strain limit of the liner greatly exceeds the tensile strain limit of the concrete. Thus, for a linear strain distribution, the concrete will reach its rupture capacity before the liner cracks.

This solution also reveals that the a priori assumption made by Royer and Allouche [16] regarding the position of the neutral axis (at the interface between the concrete pipe and the liner) is not accurate for this design example. In future installments of this research, the resistance and numerical models will be extended to address cases where the host pipe is cracked.

For intact reinforced concrete pipes repaired with materials having lower tensile strain limits than the liner considered previously, such as cement mortars, the selection of liner thickness may be governed by the tensile strain limit of the mortar liner rather than the tensile stress limit of the concrete pipe. The strain distribution of the Class IV-Wall B pipe repaired with mortar is shown in Fig. 7. The intersection of the design model and the dashed line corresponding to the mortar liner's tensile cracking strain shows that this failure is governed by the tensile strain limit of the mortar liner.

Finally, the three pipes repaired with cementitious liner analyzed with the Hoeg solution as presented earlier in Table 2 were compared to finite element analyses. The results of those comparisons are shown in Table 3 below. As explained earlier, critical concrete rupture stresses of 2.05, 2.05 and 2.51 MPa were used for the Class III, Class IV, and Class V pipes respectively, and so all values of maximum tensile stress used in the design model were either 2.05 or 2.51 MPa. As shown in the table, all the finite element calculations produced values of liner and concrete tensile stress

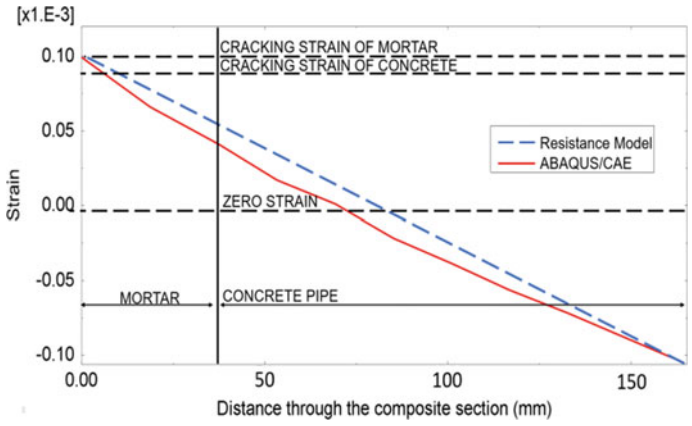

Fig. 7 Strain distribution through the composite section measured from the inner surface of the mortar

Table 3 Maximum tensile stress comparisons between the design model and ABAQUS/CAE simulations for three different pipes

Pipe	Burial depth (m)	Computed liner thickness (mm)	Max stress in the concrete pipe, design model (MPa)	Max stress in concrete pipe, ABAQUS/CAE (MPa)	Max stress in the liner, design model (MPa)	Max stress in the liner, ABAQUS/CAE (MPa)
Class III, Wall A	4	22.81	2.05	1.54	3.58	2.91
Class IV, Wall B	5	21.94	2.05	1.72	3.60	2.98
Class V, Wall C	7	25.36	2.51	2.42	3.19	3.11

that fell below their respective rupture values, indicating that the simplified Hoeg theory gives a reasonable, conservative approximation to the FEA.

In the design calculations, all pipes were assumed to be perfectly rigid meaning they were infinitely stiff compared to the surrounding soil (where Hoeg factors C and F are approximated as zero, [13]). This simplification results in an upper limit for negative arching where the pipe's tendency to attract soil load reaches a maximum. This additional attraction of soil load results in increased bending moments and tensile liner stresses at the crown in the design model. In the finite element calculations, the pipe stiffness and soil stiffness were explicitly defined, producing arching corresponding to the actual pipe and soil stiffnesses, resulting in moments that fall below the rigid pipe (upper bound) limit. The simplification of perfect rigidity used in the design model based on rigid pipe theory (Eq. 1) is consistently conservative compared to moments from FEA, with that conservatism dropping from 32 to 1% as the pipe being relined goes from Class III to Class V (since moment approaches the rigid pipe limit for the Class V pipe).

6 Conclusions

A design solution for estimating the required liner thickness to prevent cracking in intact pipes strengthened using liners to resist increased surface loads has been developed, using the 'buried rigid pipe' limit to the Hoeg solution. Two criteria were considered—the first involving cracking of the liner before the concrete pipe, and the second involving cracking of the concrete pipe before the liner. Preventing cracks within the host pipe ensures that the liner is not subjected to large stress concentrations that would inevitably cause the liner to crack.

Example calculations were presented for a Class IV pipe repaired using a sprayed cementitious liner available in the market, and a mortar. For the sprayed liner, cracking is expected to develop in the concrete pipe before the liner, whereas the mortar lining

that was examined would be expected to crack before the concrete. Finite element calculations were used to evaluate the results of the design model for both liner choices. In each case, the numerical analysis provided strain distributions that were somewhat curved but having a maximum strain difference relative to the design model of 0.000025. For both cases, it appears that the linear strain approximation used in the design model represents a safe and effective simplification. Further calculations were presented for the sprayed liner applied within Class III, Class IV, and Class V pipes, based on the design model and finite element analysis. Maximum tensile stresses calculated using the design model were always higher than those from the finite element analysis, with differences decreasing from 35 to 1% for the Class III to Class V pipes, because the buried rigid pipe approximation provides conservative estimates of bending moment. Future work includes extending the design model to address different pipe deterioration states and undertaking experimental evaluations.

References

1. AASHTO (2020) AASHTO LRFD bridge design specifications. By American Association of State Highway and Transportation AASHTO. AASHTO
2. ABAQUS CAE (2019) ABAQUS documentation. Dassault Systems
3. ASTM (2011) C76-11. Standard Spec. for Reinforced Concrete Culvert, Storm Drain, and Sewer Pipe
4. Bazant Z, Cao Z (1989) Size effect in brittle failue of unreinforced pipes. ACI J
5. Cai X, Ge Z, Tang S, Chen X (2016) Abrasion erosion characteristics of concrete made with moderate heat Portland cement, fly ash and silica fume using sandblasting test. In: Construction and building materials, Wuhan, China, vol 127, pp 804–814
6. Chen X, Wu S, Zhou J (2013) Influence of porosity on compressive and tensile strength of cement mortar. Construc Build Mater 40:869–874
7. CSA (2016) Design of concrete structures. Cement Association of Canada
8. Doherty I (2020) Interview regarding current cementitious liner practices for deteriorated reinforced concrete pipes
9. Elshimi TM, Moore ID (2013) Modeling the effects of backfilling and soil compaction beside shallow buried pipes. J Pipeline Syst Eng Pract 4:04013004
10. Heger FJ (1980) Design method for reinforced concrete pipe and box sections. Transportation Research Board
11. Hoeg K (1968) Stresses against underground structural cylinders. Soil Mechanics and Foundations Engineering, ASCE
12. Marston A, Anderson AO (1913) The theory of loads on pipes in ditches and tests on cement and clay drain, tile and sewer pipe. Engineering Experimental Station
13. Moore ID (2001) Buried pipes and culverts. In: Geotechnical and Geoenvironmental Engineering Handbook, pp 541–567
14. Moore ID, Becerril García D (2015) Ultimate strength testing of two deteriorated metal culverts rehabilitated with spray-on cementitious liners. Transp Res Rec (2522): 139–147
15. Moore ID (2019) Design of sprayed cementitious liners within corrugated steel pipes. American Society of Civil Engineers
16. Paragon Systems (2012). Laboratory report on concrete/polymer sample. Paragon Systems
17. Royer JR, Allouche E (2016) Laboratory testing and analysis of geopolymer pipe-lining tech. for rehab. of sewer & stormwater conduits. NASTT's 2016 No-Dig Show. Dallas, Texas
18. Watkins RK (1999) Structural Mechanics of Buried Pipes. Boca Raton

FE Analysis to Simulate Pressure Pipe Liners Spanning Across Perforations

R. Qiu, I. D. Moore, and N. A. Hoult

1 Introduction

Leakage from damaged pressurized water mains leads to the loss of potable water into the surrounding soil [9], and has been a major problem for developed countries since the late twentieth century. Traditional excavation and replacement methods generally involve high direct and indirect costs and cause long disruptions to residents in the service area [11]. In the past two to three decades, a new technology called cured-in-place-pipe (CIPP) was developed and introduced into the water main rehabilitation industry [4]. CIPP is a type of technology where specific type of polymer liner is introduced into damaged host pipe via resin and fixing cracks and potentially enhance overall structure integrity. A simple image showing a standard CIPP configuration can be found in Fig. 1. It can reduce costs associated with traditional replacement methods and largely mitigate the aforementioned disruption. Despite more than twenty years of use, CIPP is still a relatively new technology and limited research has been undertaken investigating the interaction between the host pipes and liners [3]. Finite element analysis (FEA), when used in conjunction with robust experimental data sets, offers the possibility to investigate these complex interactions. Previous research has demonstrated that FEA can be used to gain an understanding of the interaction between perforated pipes and polyester-polyurethane composite rehabilitation liners under pressurized loading conditions [6–8]. The development of distributed fibre optic sensors (DFOS) has since made the measurement of the

R. Qiu (✉) · I. D. Moore · N. A. Hoult
Department of Civil Engineering, Queen's University, Kingston, ON, Canada
e-mail: ranlin.qiu@queensu.ca

I. D. Moore
e-mail: ian.moore@queensu.ca

N. A. Hoult
e-mail: neil.hoult@queensu.ca

S. Walbridge et al. (eds.), *Proceedings of the Canadian Society of Civil Engineering Annual Conference 2021*, Lecture Notes in Civil Engineering 244,
https://doi.org/10.1007/978-981-19-0656-5_19

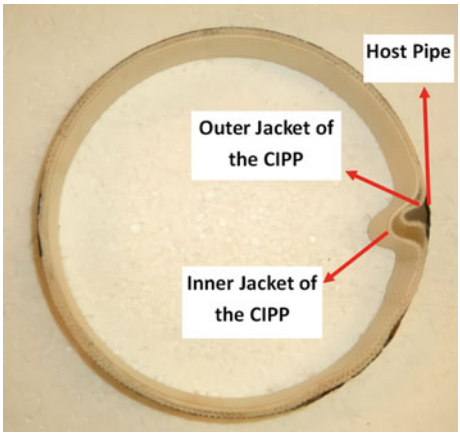

Fig. 1 A typical CIPP configuration [5]

complex strain distribution within the liner possible [3, 5]. The robust data sets provided from these experiments enable the evaluation of computer analyses, which can then be used to conduct parametric studies into the behaviour of these pipe-liner systems that would be unrealistic from both a time and cost point of view if they had to be undertaken using physical experiments.

This study aims to evaluate the use of FEA to calculate the strains that develop in a liner under internal pressure, so that the model can then be used to conduct parametric studies in subsequent investigations. This paper presents preliminary comparisons between the FEA results and previously published experimental data [5], to assess the performance of the analysis.

2 Methods and Procedures

2.1 Introduction

To achieve the objective, as noted previously this study will be using the results from an experimental program as a baseline for comparison. A laboratory test was conducted on a pressurized liner spanning across a perforation with a diameter of 25 mm in a steel pipe [5]. A set of finite element models were then developed, considering an optimum balance between processing run time and accuracy. This section describes the methods used in the analysis, while the optimization process will be reported elsewhere, and the final version of the FE model will be used in subsequent studies to conduct parametric analyses.

2.2 Creating a Set of Simplified Models

The test setup of [5] involved a perforation cut through the wall of a plain steel pipe. The damaged pipe was then repaired using a commercial grade liner called Sanexen Aquapipe. The ends of the repaired pipe were sealed and restrained at both ends as seen in Fig. 2, and a 700 kPa internal pressure was applied by adding pressurized water into the system.

The dimensions used in the experimental campaign and the finite element model can be found in Table 1 [5].

The FEA was performed using ABAQUS [2] (ABAQUS will hereafter be referred to as the FE software package). The FE software package has two built-in model types: standard and explicit mode. Standard mode is used to analyse static systems where the overall system will not exert significant shape changes such as yielding or cracking [2]. On the other hand, explicit mode is able to solve more complex problems such as dynamic systems and to model cracking behaviour [2]. The explicit mode

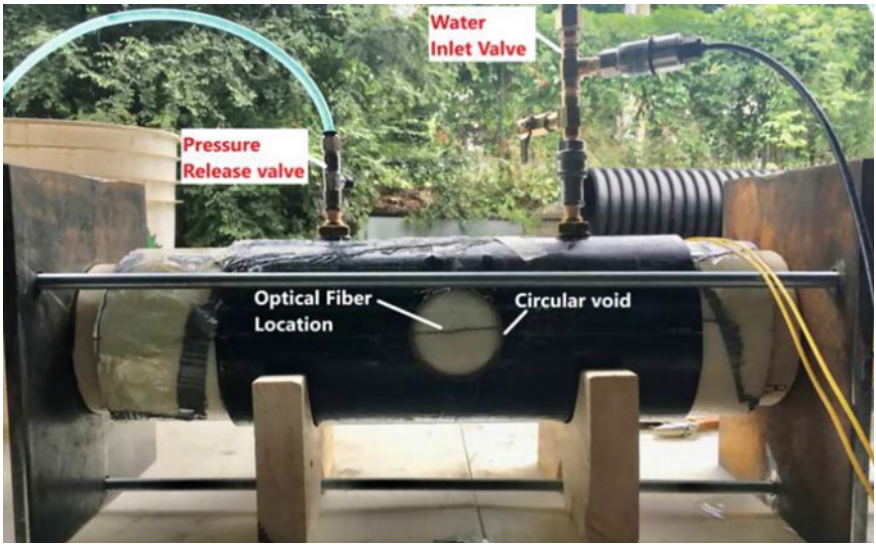

Fig. 2 The test setup [5]

Table 1 Physical dimensions of each component

Component	Dimensions (mm)
Steel Pipe (NOVA TUBE ASTM A53 steel pipes)	154 inner diameter, 300 length 7.1 wall thickness, 25 diameter perforation
Liner	155 outer diameter, 4.7 wall thickness

requires more input parameters to run and usually takes more computational power to solve.

The maximum internal pressure applied to the system for the experiment was 700 kPa [5]. This applied internal pressure is not high enough to rupture the liner or the pipe. Based on these considerations, the standard mode was used for this analysis.

Three models were constructed in this study, the first two models were designed to be used as a proof of concept. The first model will use the same dimensions as the experimental set up and the other one will reduce the length of the pipe and liner by half while keeping the perforation size unchanged. In order to speed up the process of concept validation, these two models were simulated using simplified material properties. These two models were constructed to shed light on model choices such as element selection, physical dimension of the model, and increment size. In the end, the final model, which uses the optimum parameter choices from the two previous models, was used for the final simulation with a set of more detailed liner material properties.

2.3 FE Model Set up

The following section describes the modelling choices that were made in an attempt to balance computational efficiency and the accuracy of the numerical results.

2.3.1 Material Models

The FE model for this study consists of two individual components: the outer steel pipe and the inner polymer liner. After the shapes of these components are constructed, the next step is to define material properties for both components. The liner properties were obtained from coupon tests and the steel pipe was manufactured according to the ASTM standard [1], and the material properties for both materials reported by [5] are reproduced in Table 2. Standard linear elastic (isotropic) material properties can be selected from the FE software package employing only two parameters: Young's modulus and Poisson's ratio. For materials with different linear

Table 2 Linear-elastic material properties [5, 7]

Material	Young's Moduli (MPa)	Poisson's Ratios	Shear Moduli (MPa)
Polymer Liner (Simplified)	2165	0.31	N/A
Polymer Liner (Engineering Constant)	E1 = 2000 E2 = 2857 E3 = 2158	V13 = 0.44 V23 = 0.31 V12 = 0.31	G12 = 1079 G13 = 1079 G23 = 1428
ASTM Pipe Steel	200,000	0.305	N/A

elastic behaviour based on testing orientation (hoop, axial and radial direction based on one fixed coordinate system), a better way to define this type of material is to use the 'engineering constants' material model [2]. This function requires modulus of elasticity, Poisson's Ratio and shear moduli in all three directions (hoop, axial and radial) directions [2]. More detailed material properties should result in better accuracy in terms of the simulation result and it was decided to use this approach for the final simulation with the updated model. Some of the parameters for the engineering constants model, such as the Young's modulus in the axial and hoop directions and all the Poisson's ratios, were collected using material testing [5]. The rest were based on previous research [6, 7]. Since the internal pressure loading was 700 kPa, and this does not exceed the linear range of both materials, the use of linear material behaviour in the analysis was deemed appropriate. All of these properties can be found in Table 2.

2.3.2 Interface Elements and Applied Load

The only interface interaction modeled in the analyses occurs between the outer surface of the liner and the inner surface of the steel pipe. The interaction between these two materials was defined using the friction angle function in the FE software package with an assumed friction angle of 30° (based on previous studies: [6–8]). The utilization of an approximate isotropic Coulomb friction model in the FE software package will have an uncertain impact on the final simulation result [6, 7], and the impact of this simplification may be a future research topic. Load applied in the analysis was in the form of a uniform internal pressure normal to the internal surface of the liner that was increased up to the maximum value of 700 kPa to simulate water pressure within the lined pipe.

2.3.3 Mesh

Meshing of the component is one of the most crucial steps in the modeling process, as it influences the quality of the simulation result. Tetrahedral elements are widely used in FE analysis of contact mechanics due to their high compatibility with automatic meshing. The linear tetrahedral element has the advantages of ease of implementation via auto meshing, while saving computation power since each element only contains four nodes [10]. The quadratic tetrahedral element provides the same ease of use in terms of auto-meshing while generating better simulation accuracy but with the trade-off of longer computational run time. In this study, both linear tetrahedral (denoted as C3D4) and quadratic tetrahedral elements (denoted as C3D10) were used and compared. The assembled model with C3D10 mesh can be found in Fig. 3.

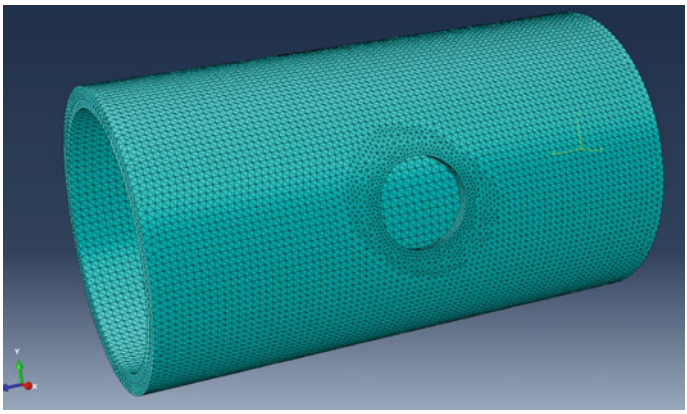

Fig. 3 A meshed assembly of the FE model

2.3.4 Boundary Conditions

As seen in Fig. 1, both ends of the pipe were fixed during testing [5]. Thus, in the FE model both ends of the steel pipe were fixed against displacement and rotation in all three directions, see Fig. 4. Similar to the data collected from the tests, the 300 mm overall length is more than enough to mitigate the influence of boundary conditions at the ends of the specimen on the region of interest (the liner area under and near the perforation) [5]. Additionally, the impact of reducing overall pipe length on simulation accuracy was also investigated.

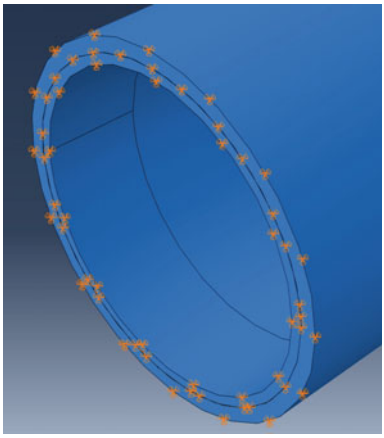

Fig. 4 Boundary conditions on one end of the model

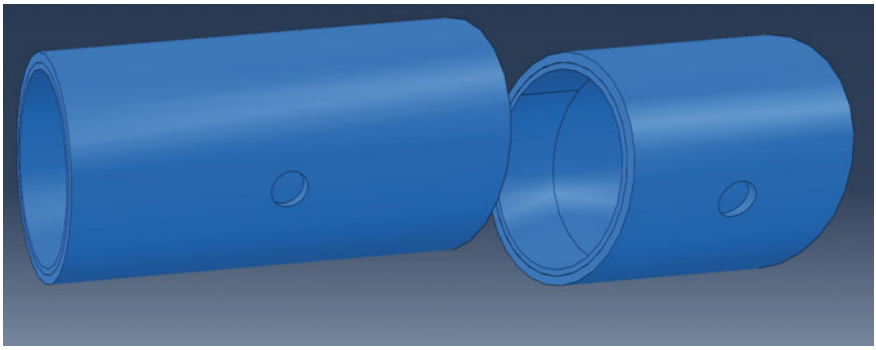

Fig. 5 Full length model (left) and Shorter length model (Right)

2.3.5 Solving the System

Two FE models, one matching the full length of the experiment and one that was half that length (see Fig. 5), were run. Both models were run with both types of element (C3D4 and C3D10).

The final step of running the FE analysis involves defining load steps and desired outputs. Since the analysis includes modeling of a frictional interface between the liner and the steel pipe, loading representing the internal water pressure must be applied in a series of steps up to the maximum applied pressures. The impact of increment size on simulation runtime and accuracy of results was examined by solving the same model twice, once with 20 and then again with 100 increments.

2.4 Evaluation of Finite Element Modeling Choices

Three aspects of the FEA design were investigated via the two aforementioned models: element choice between C3D10 and C3D4, model length: half or full length, and use of 20 or 100 load increments in the analysis. The subsequent section presents comparisons to the test measurements. To check the effect of the half-length analysis on the simulation accuracy, the half-length model and the full-length alternative were assigned C3D10 elements and solved using 100 increments. The peak (largest compressive) axial strain values are calculated to occur on the inner surface of the liner at the midpoint where it passes across the perforation, and this largest compressive strain is presented in Table 3.

To test the difference between calculations using the C3D10 and C3D4 elements, the full length model was assigned each type of element and solved using 100 increments. As Table 4 indicates, the C3D4 element generated a very different peak compressive strain compared to the simulation based on the C3D10 element. It will

Table 3 Peak compressive liner strain calculated at the mid-point of the perforation; results from analyses using both full length and half length FE simulations

	Full length	Half length
Strain	−0.00108	−0.00113

Table 4 Peak compressive liner strain calculated at the mid-point of the perforation; full length model assessed using both C3D4 and C3D10 elements

	C3D10	C3D4
Strain	−0.00108	−0.000384

be shown in the next section that the peak strain measurement is much closer to the C3D10 result, so no further analysis is undertaken using the C3D4 option.

Solving the model with 100 increments naturally results in an increased analysis time compared to a solution with 20 increments. In order to seek alternatives that can reduce the analysis time for the final simulation, the full length model with C3D10 elements was solved using both 20 and 100 increments. After comparing the results from both simulations (see Table 5), the use of 20 increments is found to have little impact on the calculations, and is used in all subsequent analyses.

Based on all the evaluations conducted above, the model parameters used in the comparisons presented in the next section were chosen: the full length model, using 'engineering constant' orthotropic elastic material properties for the liner, C3D10 elements, and solved using 20 increments. Additionally, to increase the accuracy of the final simulation result while keeping the overall computation run time within a reasonable range, the mesh for the liner was further refined as presented in Fig. 6. At the middle of the liner, where the liner deformed the most due to the perforation and the largest-magnitude compressive strains are calculated, the mesh was refined to further increase the simulation accuracy. For the sections at both ends, the mesh was made coarser to reduce computation run time.

Table 5 Peak compressive liner strain calculated at the mid-point of the perforation; full length model assessed using both 20 and 100 increments

	100 Increments	20 Increments
Strain	−0.00108	−0.00108

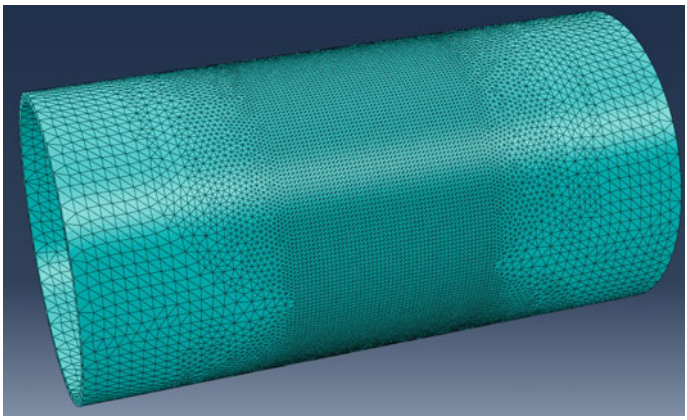

Fig. 6 Assigned mesh for the final model simulation

3 Comparison Between FE Model and Experimental Results

After the FE model was solved, the deformed liner shape could be plotted using the FE software package post processor as shown in Fig. 7. The deformed shape shows general correlation with the visual observation result from the testing (i.e. that the liner deformed outwards at the perforation). To further verify the accuracy, a data comparison between simulation-generated data and the laboratory measurements from the distributed fibre optic sensors was prepared.

The testing involved strain measurements using fiber optic sensing technology, with a fibre glued to the inner surface of the liner and running parallel to the pipe

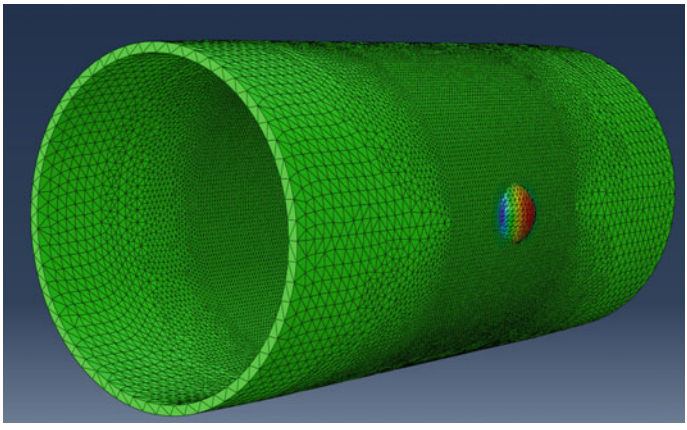

Fig. 7 Liner deformations calculated using the FE software package

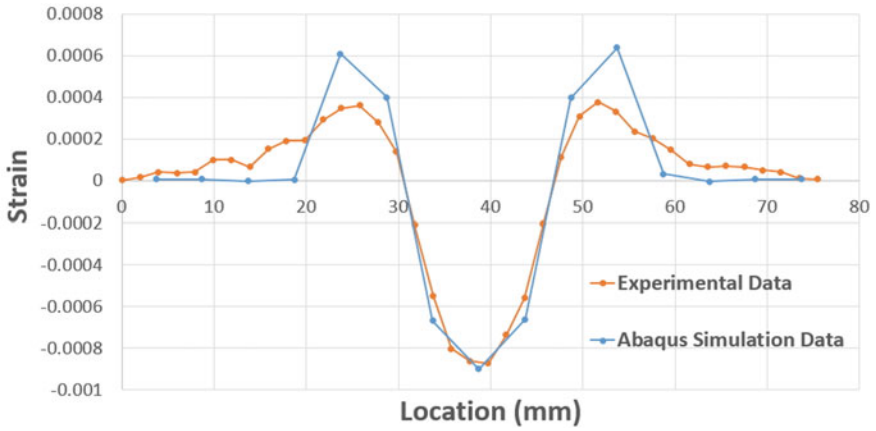

Fig. 8 Axial strain comparison between FE results and the measurements of [5], distribution of strain along on the inner surface of the liner parallel to the pipe axis

axis [5]. That fibre passed directly under the perforation. Figure 8 shows the distribution of axial strains along the inner surface of the liner, with axial location of the measurement shown along the x axis of the figure and the strain measurement on the vertical axis. The centre of the perforation is located at an x position of approximately 38 mm.

Based on the results seen in Fig. 7 and Table 6, which presents the peak strain from the experiment and the final model, it is concluded that the analysis provides a reasonable approximation to the test measurements, where the peak compressive strain calculated is within 3% of the peak measured value. The analysis reflects the general trend in terms of strain distribution along the liner where it spans across the perforation, though with higher positive peak strain in the liner adjacent to the perforation, and more rapid attenuation of those strains to zero with increasing distance from the perforation. These details will be investigated using further analysis to evaluate parameters like liner-steel pipe interface roughness (a lower friction angle between the liner and the steel host pipe than the value used in the analysis might have led to the slower attenuation observed in the experiment).

Table 6 Peak compressive strain and from the final model and the test of [5]

	Final model	Experiment
Strain	−0.000900	−0.000873

4 Conclusions

This study presented modeling choices used in the analysis of an experiment conducted on a polymer liner spanning across a circular perforation in a steel test pipe. Three different modeling choices were investigated–the length of the pipe and liner system that was modeled, the element type used in the analysis, and the number of load steps employed. Analysis was then undertaken using a more detailed mesh, and a comparison presented between the axial strains measured along the inside of the liner during the experiment, and the finite element calculations. This revealed that the analysis was reproducing the correct pattern of axial strains, with the peak (most compressive) strain under the centre of the perforation estimated within 3% of the measurement. Greater differences were, however, observed at and beyond the perimeter of the perforation, possibly due to the choice of friction angle modeled between the liner and the steel pipe. The use of a friction angle of 30° produced an overestimate of the maximum strain at the perimeter of the perforation while underestimating the attenuation length beyond the perforation.

Acknowledgements This research was funded by the Natural Sciences and Engineering Research Council (NSERC) of Canada through a Strategic Research Grand to the second and third authors. Thanks also to Dr. Titilope-Oluwa Adebola for providing her research results used to design the model and for the test comparisons.

References

1. ASTM (2020) Specification for pipe, steel, black and hot-dipped, zinc-coated, welded and seamless. ASTM International. https://doi.org/10.1520/A0053_A0053M-20
2. ABAQUS/CAE User's Manual (v6.6). n.d. https://classes.engineering.wustl.edu/2009/spring/mase5513/abaqus/docs/v6.6/books/usi/default.htm?startat=pt03ch14s03s02.html. Accessed 16 Feb 2021
3. Adebola T (2019) Service performance of a cured in place polymer pipe liner for deteriorated cast iron pressure pipes. Doctoral Thesis, Department of Civil Engineering, Queen's University at Kingston, Canada
4. Adebola T, Hoult NA, Moore IDM (2020) Distributed strain sensing to study a composite liner for cast iron water pipe rehabilitation. J Test Eval 48(6):4283–4303. https://doi.org/10.1520/JTE20170497
5. Adebola T, Moore ID, Hoult NA (2021) Use of optical fibers to investigate strength limit states for pressure pipe liners spanning across circular perforations. J Pipeline Syst Eng Pract 12(2):04021006. https://doi.org/10.1061/(ASCE)PS.1949-1204.0000523
6. Brown MJP, Moore ID, Fam A (2014) Performance of a cured-in-place pressure pipe liner passing through a pipe section without structural integrity. Tunn Undergr Space Technol 42:87–95. https://doi.org/10.1016/j.tust.2014.01.005
7. Brown MJP, Moore ID, Fam A (2014) Design recommendations for performance limits for cured in place liner in cast iron water pipe. No Dig Show, NASTT, Orlando, MM: T3-03
8. Brown MJP, Moore ID, Fam A (2020) Analysis of a cured-in-place pressure pipe liner spanning circular voids. Tunn Undergr Space Technol 101:103424. https://doi.org/10.1016/j.tust.2020.103424

9. Folkman S (2018) Water main break rates in the USA and Canada: a comprehensive study, vol 49
10. Four-Node Tetrahedral Element (C3D4 and F3D4). http://web.mit.edu/calculix_v2.7/CalculiX/ccx_2.7/doc/ccx/node32.html. Accessed 10 Feb 2021
11. Tetreault J, Moore ID, Hoult NA, Dicksen T, Maher MLJ (2018) Development of a sustainability evaluation system for culvert replacement and rehabilitation projects. J Pipeline Syst Eng Pract 9(2):04018004. https://doi.org/10.1061/(ASCE)PS.1949-1204.0000315

Practical Considerations for Implementing SHM Systems in Highway Bridges

E. MacLeod, B. Wyman, J. Matthews, and K. Arjomandi

1 Introduction

As infrastructure ages, conditions and natural hazards such as corrosion, fatigue, scour and earthquakes can deteriorate its performance [2]. According to the Canadian Society of Civil Engineers' "Canadian Infrastructure Report Card," currently in Canada $13 billion worth of bridge infrastructure needs rehabilitation or replacement, a number which is anticipated to keep increasing in the future. It is therefore important to develop efficient condition-based monitoring strategies such as the structural health monitoring (SHM) approaches, which can continuously monitor structures during their lifespan. The main objective of SHM techniques is to enable more effective performance and safety assessments. Structural Health Monitoring systems (SHM) are comparable to regular checkups performed by physicians and are essential when dealing with critical structures used by the public [3].

Oversize and overweight vehicles have become a common concern worldwide as the demand to structural capacity ratio is continuously increasing due to changes in traffic and aging of bridge structures. Overweight trucks can cause serious damage to bridges and accelerate the degradation, causing fatigue problems and shortening service life. The province of New Brunswick, located in Atlantic Canada, is home to 770,000 residents and more than 3000 bridges. The large number of bridges per capita combined with a high ratio of heavy commercial vehicle traffic and a small number of commercial vehicle enforcement officers, makes overweight loading a significant concern for the New Brunswick Department of Transportation and Infrastructure (NBDTI). There is a growing desire for the development of real-time

E. MacLeod (✉) · B. Wyman · K. Arjomandi
University of New Brunswick, Fredericton, Canada
e-mail: ethan.macleod@unb.ca

J. Matthews
New Brunswick Department of Transportation Infrastructure, Fredericton, Canada

S. Walbridge et al. (eds.), *Proceedings of the Canadian Society of Civil Engineering Annual Conference 2021*, Lecture Notes in Civil Engineering 244,
https://doi.org/10.1007/978-981-19-0656-5_20

remote monitoring programs to monitor the frequency of over weight loading events and the effect they have on the bridge structures.

Most health monitoring efforts are isolated applications of single SHM techniques. Therefore, a research project was proposed to NBDTI that aims to develop an integrated framework using data from various SHM methods, visual inspections, and previously collected data by NBDTI. This framework will incorporate multiple established techniques into a single low-cost continuous monitoring system capable of assessing the bridge structural safety in real time. The system will also be deployed as a Bridge Weigh in Motion (BWIM) system that can measure the axle weight and spacing of trucks crossing the bridge at the highway speed [5]. The system includes state of the art instruments and equipment and comprises of, strain gauges, accelerometers, thermocouples, a camera, a programable data acquisition system, and network communication hardware. This research and development project addresses several key areas with significant importance to NBDTI and UNB. These areas include:

1. The development of a convenient and practical method for measurement of structural safety of major bridges in real time;
2. The development of a cost-effective weigh-in-motion solution for temporary and permanent measurement of traffic characteristics;
3. Development of a real time, modular, and scalable bridge monitoring system that can be deployed on a network of bridges which supports the bridge designers and bridge management strategies.

This paper aims to highlight some of the practical considerations to implementing a SHM system for NBDTI at the Westfield Route 7 overpass (asset W475) in Westfield New Brunswick. The paper will cover the selection and preliminary analysis of the structure, sensor selection and placement, data acquisition system selection, system installation and some lessons learned.

2 Case Study Bridge Selection

The structure chosen for instrumentation is the Westfield Route 7 overpass (asset W475). The bridge is a 58 m three span bridge built in 1986 consisting of six continuous prestressed concrete girders shown in Fig. 1. When selecting a structure to instrument, it is essential to consider the applicability to the project goals, suitability for analytical purposes, and feasibility of instrumentation. Considering the project goals, W475 was found to be a suitable candidate for achieving all three. As the bridge is on a major traffic corridor the bridge safety is of a high priority, therefore it is suitable for the development of a practical real-time SHM system. Route 7 is a heavy trucking route with mostly through traffic, making it a good test structure for estimating the traffic characteristics of commercial vehicles passing between the cities of Saint John and Fredericton. W475 is a very common overpass design in New Brunswick and as one of the project goals is to develop a scalable system,

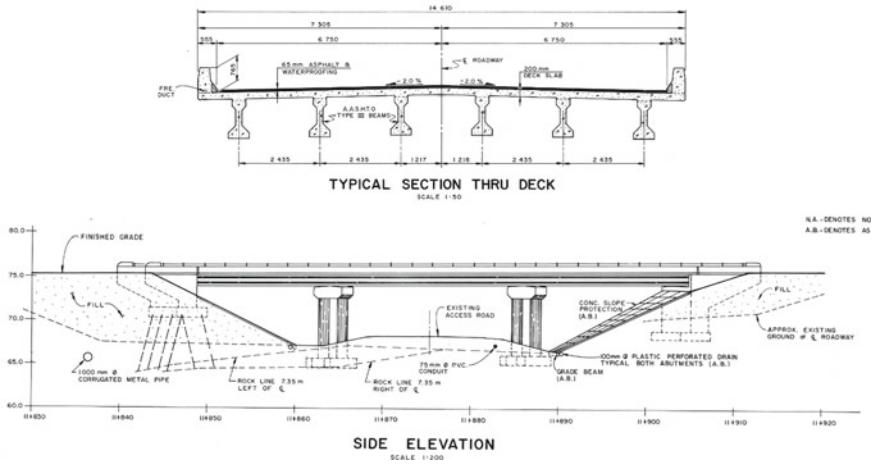

Fig. 1 W475 elevation and typical deck cross section

it is beneficial that the developed techniques could be readily applied to numerous structures in the network.

The second major consideration for selection is the suitability of the structure for the desired analysis. In order increase the likelihood of completing successful modal identification from vibration monitoring, it is necessary that the structure has suitable dynamic characteristics. In the case of W475, the structure does not posses any significant nonlinearities, is relatively flexible due to its length, and also has simple symmetric geometry. When performing BWIM it is desirable for the vehicles to be traveling at a constant velocity across the bridge structure. The ramps for the Westfield overpass are located a considerable distance before and after the bridge, seen in Fig. 2, allowing enough of an approach for traffic to reach a constant velocity while crossing the bridge. The bridge also has one lane in each travel direction. This eliminates the occurrence of side by side vehicles traveling in the same direction which can greatly increase the complexity of analysis. The structure has some undesirable characteristics for BWIM as well. For example, multiple spans can allow multiple vehicles to be present on the bridge simultaneously adding complexity to the analysis. As there will always be compromise when selecting a structure for instrumentation it was the authors' opinion that the benefits of selecting this bridge outweighed the potential challenges.

The final consideration, which can often be the limiting factor, is the feasibility of instrumentation. There were a number of factors that contributed to selecting W475 as a feasible bridge to instrument. As it was not built over a waterway, it was possible to install all instrumentation from below the structure using a lift. This ensured no disruption to the highway traffic on the bridge and only moderate disruption to the traffic below. It is necessary to consider if all areas of the bridge are accessible with the equipment available. In the case of the Westfield overpass, the available boom lift was not able to reach the approach spans from the road, therefore the drainage

Fig. 2 Satellite image of Westfield Route 7 overpass (asset W475) showing orientation and ramps

ditches were used to access the underside of the approach spans as seen in Fig. 3a. At the north approach span, the ground was too soft for the lift. Therefore, as shown in Fig. 3b a temporary earth ramp was constructed to allow access. Access to electrical can also be a limiting factor when designing a SHM system and often the only option is to use batteries or solar. Due to the high power demands and reliability requirements of our real-time system, these power alternatives were not on a viable option. A tie-in to existing wires which was already present at W475 from previous maintenance the expansion joints was required. As the SHM system must be able to communicate results to NBDTI in real-time over a wireless internet connection it was necessary to determine that there was adequate cellular coverage at the site.

Fig. 3 **a** boom lift utilized for project. **b** temporary earth ramp

3 Preliminary Analysis of the Structure

A preliminary analysis of the structure was performed in order to determine the necessary number, type, and location of sensors. In BWIM systems, axle detection techniques are used to estimate vehicle velocity, axle spacing, and axle position in the lane. This information can be incorporated into weight estimation techniques [7]. Free-of-axle detector (FAD) algorithms have been developed where sensors, typically strain gauges, are placed underneath the bridge and the vehicle properties can be extracted from the localized structural response [6]. Typically, two FAD sensors are allocated to each lane where one of the sensors should be mounted at around 20–40% of the span and the other at around 60–80% of the span [4]. To determine the ideal orientation of the FAD sensors, an influence surface analysis was conducted in CSiBridge using a finite-element model of the W475 bridge shown in Fig. 4. The deck elements were modelled using four-node quadrilateral shell elements with the maximum submesh size set to 100 mm which is less than the expected contact length of a tire. This is small enough to capture a realistic influence surface for the localized stress response expected by FAD sensors. A comparison between longitudinal and transverse measurement directions was performed. The result of the influence surface analysis is presented in Fig. 5. Longitudinal sensor placement resulted in a much smaller influence area width compared to transverse sensor placement, although their peak prominences are similar. The influence area width in both cases is bound between the two nearest girders making them insensitive to vehicles travelling in the other lane. However, influence in the transverse direction is more prominent as the vehicle deviates from the expected wheel path. These results align with the results of the experimental tests conducted by Brown [1]. The authors decided to use transversely oriented strain gauges placed on the underside of the deck in the approach span at 33% of the span length. This orientation will increase the width of the wheel path to get more reliable results when the vehicle deviates from the middle of the lane. The approach span was selected to minimize the dynamic

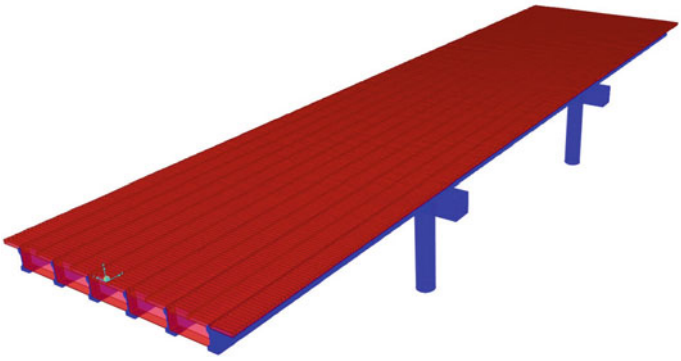

Fig. 4 W475 finite-element model in CSiBridge

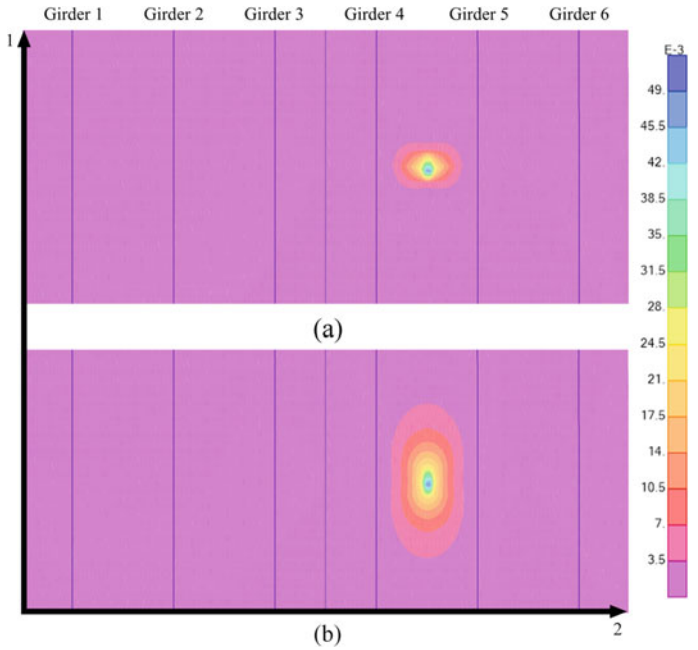

Fig. 5 Influence surface for the bottom stress (in MPa) of a shell element representing the deck soffit longitudinally located at 33% of span 1 and transversely located in the expected wheel path: **a** S11, the longitudinal stress; **b** S22, the transverse stress

effects of the bridge. Strain gauges are installed at midspan which is the location of maximum bending strain to measure bending and the vehicle response. To avoid damaging the prestressing in the bottom flange, the gauges are placed in the web above the chamfer of the bottom flange avoiding stress concentrations. The sensor layout is shown in Fig. 6.

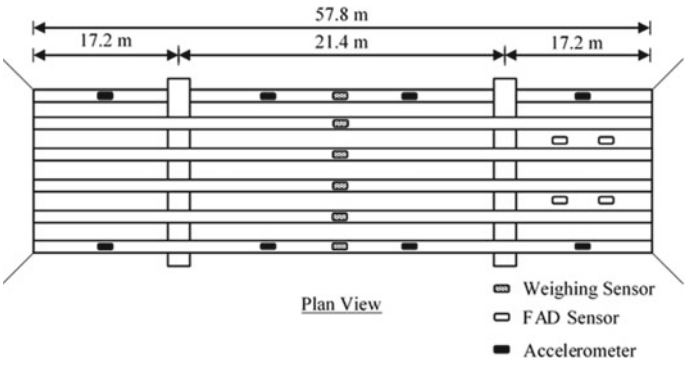

Fig. 6 Sensor placement showing weighing and axle detection sensors as well as accelerometers

Table 1 Sensor types and model as well as the key specification for considered for selection

Sensor type	Model	Specifications
Strain Gauge	BDI ST 350	• Rugged construction and weather proof • Strain Range of ±4000 με is more than adequate to capture expected strain of 30 με • Temperature Rating: −50 to +80 °C adequate for expected environment
Accelerometer	PCB Uniaxial Low Frequency Industrial ICP	• Sensitivity (±5%) of 500 mV/g will provide good resolution for modal analysis • Freq 0.2–6000 Hz encompasses estimated first 6 natural frequencies • Hermetic sealing for weatherproofing • Operating Temperature Range −54 to 121 °C adequate for expected environment
Camera	Basler acA1440-73gc with EO C Series 35 mm Lens	• 73 frames per second adequate for capturing moving traffic • 1.6 MP resolution enables identification of vehicles • LabView compatible for ease of programming
Thermocouple	NI T-Type	• Field cuttable for ease of installation • Operating Temperature Range −200 to 260 °C encompasses expected temperatures on site

A simplified 3D beam model representative of the bridge structure was constructed in SAP2000 to determine the location and number of accelerometers necessary to capture the dominant mode shapes when performing Operational Modal Analysis (OMA). After performing a modal analysis of the model, the number of inflection points was identified for each calculated mode shape. It was then possible to determine the required number of sensors to fully capture each mode shape, as one sensor is required per inflection point. Based on these results it was decided to use eight accelerometers to capture the first six mode shapes. Higher mode shapes can often be difficult to excite and contribute less to the overall structural response. It was decided that capturing higher modes did not justify the added cost of more sensors and channels. Accelerometers are installed along the underside of the exterior beams in both the main and approach spans seen in Fig. 6 to fully capture the first 6 mode shapes.

Fig. 7 **a** BDI ST 350 strain gauge, **b** PCB Uniaxial Low Frequency Industrial ICP, **c** Basler acA1440-73gc camera, **d** NI T-Type thermocouple

4 Sensor Selection

Once the number of sensors and location has been established it is necessary to determine the specific sensors (makes and models) based on the required capabilities and operating conditions. The sensors selected for this project and the main specifications considered in their selection are summarized below in Table 1 and shown in Fig. 7.

5 Data Acquisition System Selection

The data acquisition system (DAQ) consists of two main components: 1) a National Instruments CompactRIO (Real-time Industrial Controller), cRIO-9047 with a 1.60 GHz Quad-Core CPU, 4 GB RAM and 8 card slots; 2) a Dell OptiPlex 7070 with Intel® Core™ i5-9500 T (2.2 GHz) processor, 8 GB RAM and a 256 GB SSD. The cRIO-9047 is a rugged modular data acquisition system that runs a Linux Real-Time OS which results in reliable long-term performance and determinism. The hardware enables the use of National Instruments LabVIEW programing language which has many useful built-in functions for data acquisition applications. Though the cRIO-9047 can run headlessly once programmed the Dell OptiPlex was added to the system to increase its capabilities and ease of access. Having a Windows PC on site allows remote network access to monitor performance and deploy and debug

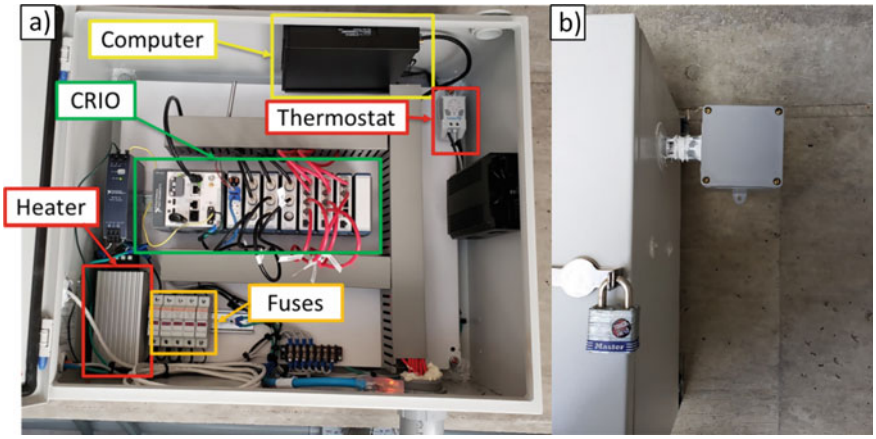

Fig. 8 **a** DAQ enclosure and contents. **b** external cellular antennae enclosure

new code modules. The PC has the ability to communicate data to a database on a UNB server and also has greater internal expandable storage for data locally. Finally, the PC enables some of the computationally expensive and non-time critical tasks to be unloaded from the cRIO to ensure the real-time system stays deterministic.

Once the acquisition system is selected a suitable enclosure must be sized and designed to meet the needs of the system. If the enclosure is openly accessible to the public, it should be locked and secured to avoid theft or vandalism and preferably placed out of direct line of sight from traffic or pedestrians. The enclosure selected for Westfield shown in Fig. 8a is a durable locking enameled steel enclosure. It is anchored to the abutment between the girders and is therefore not easily visible from the roadway. The enclosure is a weatherproof construction to withstand the elements and has a vent and drain to reduce internal moisture and condensation. It is also important to consider the operating temperatures of the electronic hardware in the acquisition system. The cRIO-9047 is rated for a temperature range of −40 to 70 °C which is adequate for our application. However, the Dell OptiPlex is only rated for 0 to 70 °C. Therefore, a heater was added to the system to ensure the interior of the enclosure remains at 15 °C for optimal performance. The addition of fuses can also be beneficial to isolate sensitive equipment from surges or shorts. Fuses were included in the enclosure design to isolate each component from both the external power source and internal power supplies. It is essential to guarantee a sufficient cellular signal if a cellular modem will be used. Due to the construction of the box no signal was available from the interior and an external antennae enclosure was added as shown in Fig. 8b. Finally, to improve ease of access and ensure proper connection, it is suggested the electrical wiring be neat and consistently coloured and cable trays used to keep data cables organized and orderly.

6 Programming and Data Management

Data processing and acquisition is performed using LabVIEW, the native programing language for National Instruments. This enables seamless integration with the cRIO system and has many useful toolboxes and functionalities. The system programming is still currently under development and a basic system is currently running at the site while a more comprehensive version is developed by researchers at UNB. The current program is a real-time system where the acquisition is performed on the cRIO and then transferred over the network to the host PC to be saved to disk. This system is not deterministic and contains no comprehensive error handling or performance monitoring, however, it is suitable to record continuous raw data. The comprehensive version in development will build on the current system and improve performance and reliability. This will be achieved by separating deterministic and non-deterministic tasks on the cRIO, ensuring that no data is lost or dropped. Data will both be saved on a USB flash-drive at the real-time target for ease of access and on a solid state disk on the host computer for backup and processing. Advanced specific and central error handling will be employed to minimize downtime and the addition of error logging will aid in future debugging and diagnostics. A system watchdog and a monitoring process will be utilized to ensure the program is running smoothly and alert researchers if any problems are discovered. Finally, event triggering will be added to capture events of interest which will be transferred to a UNB server via a database connectivity module.

7 System Installation

Many SHM systems in the literature are designed for short to medium term duration and therefore do not need to be installed with durable or protected hardware. This project is to be permanent and in place for multiple years, therefore a lot of attention was spent developing a system that would be secure and durable. Often, in short term applications, bare cables can be taped or strapped to the structure being monitored. Instead, to improve weatherproofing, the entire system at Westfield is enclosed in rigid and flexible PVC schedule 40 conduit seen in Fig. 9a. Junction boxes are used at the conduct intersections and sensor locations, shown in Fig. 9b, for ease of installation and maintenance. The rigid conduit and junction boxes were installed first to ensure proper fit and avoid damaging the sensors and cables. The conduit was installed in the web just above the chamfer to provide a flat surface for clamping. Anchors and brackets were used that did not fully penetrate the concrete cover and risk damaging the steel reinforcement. A string was installed in the conduit to allow the cabled to be pulled through as the sensors were installed afterwards. This was done beginning furthest from the DAQ and working back towards it. To facilitate the cable pulling, a low conduit utilization was used and the cables were bundled together and pulled as one unit to reduce friction and winding.

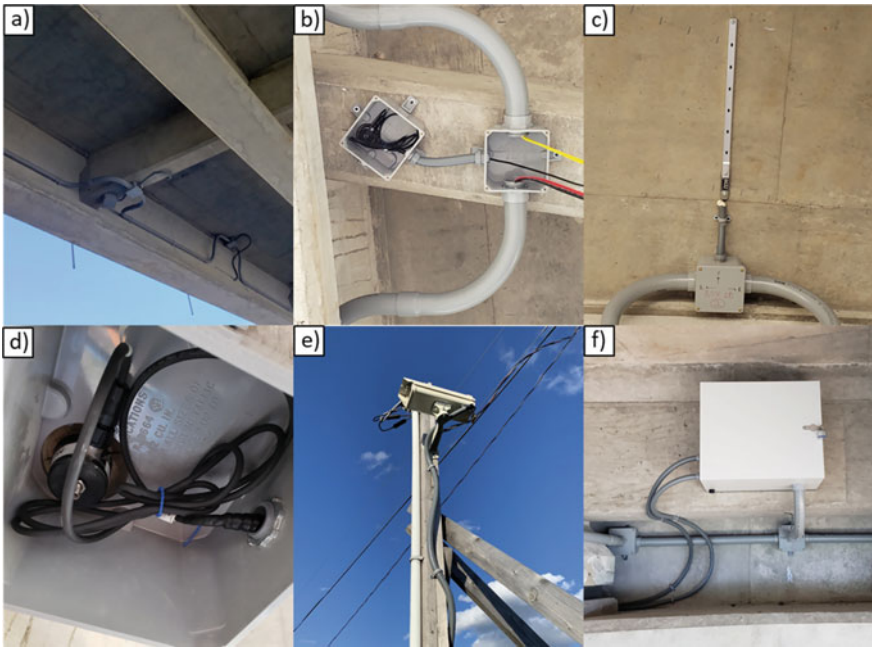

Fig. 9 **a** rigid and flexible PVC schedule 40 conduit, **b** custom drilled junction boxes **c** strain gauge with 24 inch expander bar **d** accelerometer mounting **e** camera and power pole **f** DAQ enclosure

When mounting the sensors considerations had to be given to durability, the ease of installation from the lift, if special tools or hardware were required, how the mounting method would affect the quality of the signal, and finally, if the mounting method could inflict damage to the concrete structure. The strain gauges were mounted with 24 inch expander bars, shown in Fig. 9c, to ensure average strain in the concrete (and not aggregate strain) was being measured. The gauges were mounted with 0.25 inch diameter anchor studs that were drilled 1.125 inches into the concrete to stay in the concrete cover. All of the studs and hardware are stainless steel to avoid corrosion. The accelerometers were mounted to the bridge with a custom threaded stainless steel rod secured into a seismic drop-in anchor seen in Fig. 10d. The anchor was selected for its shallow embedment depth which is less than the thickness of cover and its performance in cracked concrete. The custom fabricated rod, shown in Fig. 10, was necessary to interface between the 3/8″-16 thread of the anchor and the internal 1/4″-28 thread of the accelerometer. The middle portion of the shaft was unthreaded to ensure that the accelerometer was "free floating" and clamped to the bridge with the top nut, rather than threaded to the rod itself. This is to eliminate the natural frequency of the rod from the measured spectrum. A spherical washer assembly was used between the sensor and concrete to account for any out of plumbness of the hole and ensure an even contact interface. Again, all hardware is stainless steel to reduce corrosion. The camera was mounted to the existing power poke in a weatherproof

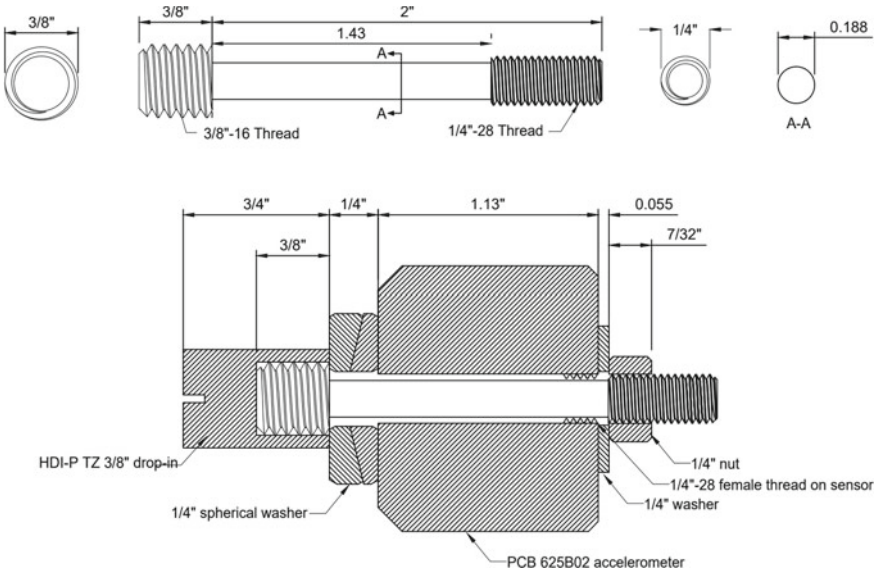

Fig. 10 Custom threaded 3/8″-16 to 1/4″-28 stainless steel rod

enclosure as seen in Fig. 9e, with the cables run in a flexible conduit buried in the embank. Finally, the DAQ enclosure is mounted on the abutment on two sections of square channeling with the power and camera cables entering from the side and the data cables entering from the bottom as shown in Fig. 10f.

8 Lessons Learned

The authors would like to conclude this paper with some lessons learned throughout the process of installing a hybrid SHM system in Westfield NB. One aspect that proved more difficult than expected was pulling the cables through the conduit. The long runs and sharp 90° bends can add significant friction to the point it was no longer possible to make any progress. Lubricating the cables with a cable lubricant solved this problem and enabled the installation to be completed without damaging the cables. When designing the system the skew of the bridge was ignored, however, this created challenges as the system was designed to meet at right angles along the diaphragm and had to be adapted on site. It is therefore essential to carefully consider all bridge geometries as well as sketch the planned system, to scale, to ensure proper fit. In a large project good organization is key to ensure hardware is installed correctly and delays are limited. For this project each intersection and junction followed a coding system and the components for that junction were labeled accordingly. This increased efficiency and facilitated confirming the correct hardware was selected. Hardware and conduit was first dry-fit on the ground to expedite the installation to.

This ensured that all hardware necessary was present and that everything fit properly before beginning to install the components in the lift as it was easier to modify components on the ground than in the lift. Finally, expect delays and stay flexible as problems and delays will most certainly arise and need to be overcome. In this regard it helps to have some extra time worked into you're schedule to ensure the project can still be completed on deadline.

Acknowledgements The authors would like to thank the Natural Sciences and Engineering Research Council of Canada (NSERC) and the New Brunswick Department of Transportation and Infrastructure (NBDTI) for supporting this research.

References

1. Brown AJ (2011) BRIDGE weigh-in-motion deployment opportunities in Alabama
2. Ettouney MM, Alampalli S (2011) Infrastructure health in civil engineering, vol II, p 696
3. Frangopol DM, Strauss A, Kim S (2008) Bridge reliability assessment based on monitoring. J Bridg Eng 13(3):258–270
4. Kalin J, Žnidarič A, Lavrič I (2006) Practical implementation of nothing-on-the-road bridge weigh-in-motion system. In: Proceedings 9th intenational symposium on heavy vehicle weights and dimensions, vol 207, pp 3–10
5. Richardson J, Jones S, Brown A, O'Brien E, Hajializadeh D (2014) On the use of bridge weigh-in-motion for overweight truck enforcement. Int J Heavy Veh Syst 21(2):83
6. WAVE (2001) Weighing-in-Motion of Axles and Vehicles for Europe (WAVE): Report of Work Package 1.2. Work. Laboratoire Central des Ponts et Chaussées, Paris
7. Yu Y, Cai CS, Deng L (2016) State-of-the-art review on bridge weigh-in-motion technology. Adv Struct Eng 19(9):1514–1530. https://doi.org/10.1177/1369433216655922

Fatigue Assessment of Shear Studs for Steel-Concrete Composite Bridges Using the Hot-Spot Stress Approach

S. Arbuckle and S. Walbridge

1 Introduction

The use of nominal stress (NS) methods for the fatigue evaluation of shear studs in steel-concrete composite bridges is the norm within research and in practice. Additionally, the current design provisions are not based on full-beam tests, rather, they are based on a conservative 'push-out' direct shear test, and the test results are lacking in the high-cycle fatigue life domain for which most bridges are designed. Another direct shear testing method was recently developed, called the 'push-plate' method, which can enable efficient testing in the high-cycle domain and thus offer a formal basis for establishing an endurance limit. However, this method is highly-conservative in contrast to a full composite beam test. In order to relate results from these different test types to each other and to expected behaviour in the field, local stress approaches can be used to capture the effects of various factors attributed to the boundary conditions. This paper presents a hot-spot stress (HSS) analysis of 18 push-plate fatigue tests in the intermediate-life domain and presents a parametric study performed using the developed FE model.

2 Background

Hot-spot stress (HSS), also called 'structural stress', considers the effect of local stress concentrations due to geometrical variations at the crack initiation site of a structural detail. The membrane and bending stresses are considered in the HSS calculation, but the non-linear stress peak, shown in Fig. 1, is neglected [10]. The

S. Arbuckle (✉) · S. Walbridge
University of Waterloo, Waterloo, ON, Canada
e-mail: sdarbuckle@uwaterloo.ca

S. Walbridge et al. (eds.), *Proceedings of the Canadian Society of Civil Engineering Annual Conference 2021*, Lecture Notes in Civil Engineering 244,
https://doi.org/10.1007/978-981-19-0656-5_21

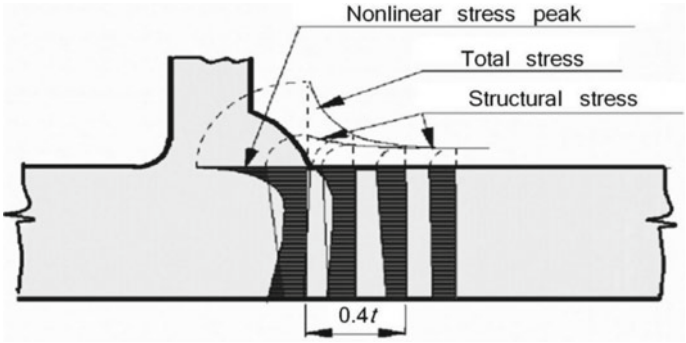

Fig. 1 Stress distribution across the plate thickness for a fillet-welded attachment undergoing transverse loading [8]

effect of the notch is considered in the experimentally determined S-N (stress-life) curves, and this enables a simplified stress analysis, which allows for the consideration of complex geometries and/or boundary conditions when paired with finite element (FE) models.

The International Institute of Welding (IIW) provides recommendations for estimating the HSS based on linear or quadratic extrapolation methods, for either fine or coarse FE model meshes [7]. Equation 1 and Eq. 2 are used in conjunction with a fine mesh model to determine Type A (membrane plus bending stress present) and Type B HSS (membrane stress only), respectively:

$$\sigma_{HS,\,A} = 2.52\sigma_{0.4t} - 2.24\sigma_{0.9t} + 0.72\sigma_{1.4t} \tag{1}$$

$$\sigma_{HS,\,B} = 3\sigma_{4mm} - 3\sigma_{8mm} + \sigma_{12mm} \tag{2}$$

where, $\sigma_{HS,\,A}$ is the Type A HSS, and $\sigma_{0.4t}$, $\sigma_{0.9t}$, and $\sigma_{1.4t}$ are the stresses along the surface of the plate/stud located a distance of 0.4, 0.9, and 1.4 times the plate/stud thickness/diameter away from the weld toe, respectively; $\sigma_{HS,\,B}$ is the Type B HSS, and σ_{4mm}, σ_{8mm}, and σ_{12mm} are the stresses along the surface of the plate located at a distance of 4, 8, and 12 mm away from the weld toe, respectively. These extrapolation methods, along with the possible failure locations on a shear stud, are shown in Fig. 2, where the toe/shank, "T/S" and the toe/plate, "T/P" failure modes are identified.

In practice, the fatigue life of shear studs is evaluated using the nominal stress (NS) approach. The provisions of the Canadian Highway Bridge Design Code (CHBDC) were formed based on push-out tests performed by [13], and later refined based on the regression analysis of a large push-out test database by [14]. In 2010, shear studs were defined as Category D, following the log-log curve shown in Eq. 3; however, in 2019, a new category, 'Category S', was created to address the overly conservative Cat. D endurance limit [5, 6]. In general:

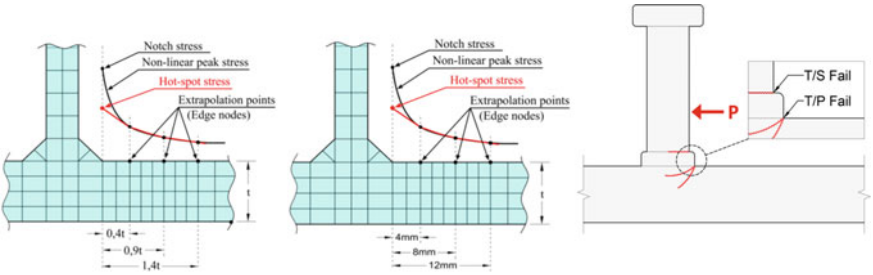

Fig. 2 Quadratic extrapolation of Type A (left) and Type B (centre) HSS used for the T/P failure mode [3], T/S and T/P failure modes illustrated on a shear stud (right)

$$S = \left(\frac{\gamma}{N}\right)^{1/m} \tag{3}$$

where, S and N are the nominal stress range (MPa) and fatigue life (no. of cycles), respectively, and γ and m are equal to $721 \cdot (10^9)$ and 3, respectively, above the constant amplitude fatigue limit (CAFL) for Cat. D and S details. Below the CAFL of 48 MPa for Category D and 70 MPa CAFL for Category S, the slope, m, changes to $m' = 5$, and γ becomes $\gamma' = 1.66 \cdot (10^{15})$ and $3.43 \cdot (10^{15})$, respectively. The curves bottom out at a variable amplitude fatigue limit (VAFL), which is somewhat arbitrarily declared to be half of the CAFL (i.e., 24 MPa and 35 MPa for Cat. D and Cat. S, respectively). Figure 3 shows the CHBDC design curve alongside the semi-log AASHTO curve, as well as the log-log curve from Eurocode 4, which has a slope of 8 and no fatigue limit [2, 4, 5]. Also, a cloud of push-out test results from the literature, with information about failure type disseminated by [11], and initial stud failures from full-beam tests done by [12] are plotted. It is evident here that

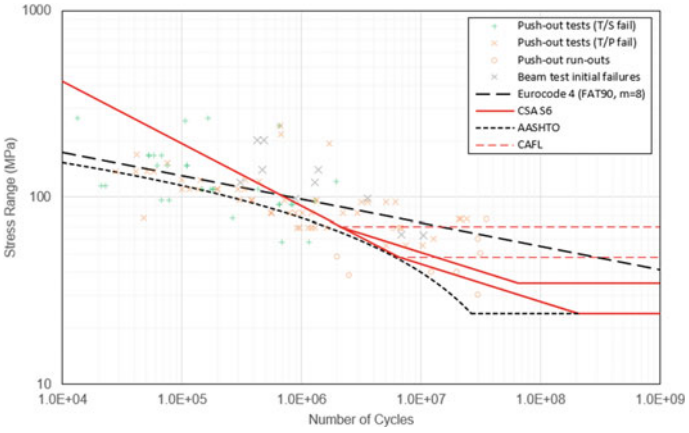

Fig. 3 S-N curve comparison for various design codes

the T/S failures into the stud shank are generally only associated with higher stress levels and lower fatigue lives.

The first and only known application of the HSS method with shear studs was reported in a study by [9]. The familiar push-out test apparatus, as seen in the seminal work done by [13] and several other experimental studies, was analysed using FE models to determine the Type A HSS for failure at the weld-plate interface (T/P failure). The researchers found that the standard S-N curve obtained via HSS was consistent with design curves recommended by the IIW. The significance of HSS being a valid fatigue evaluation approach is that it can be used to account for factors that are otherwise ignored by the NS approach (e.g., varying stud pitch, stud eccentricity, concrete creep, material plasticity, etc.). It can also consider other critical factors that are of interest in the current study,namely, plate thickness, as well as the point-of-application of an equivalent point load (lever arm), which is a function of the stud height.

3 Description of Push-Plate Test and FE Model

The push-plate test configuration, shown in Fig. 4, consists of a headed stud (22 or 25 mm diameter) welded to a mild steel (300 W) plate, a second plate with an overhang extending into the test frame grips, and a third plate functioning as a spacer. Another plate with a two-way radius machined to match the stud geometry is placed in the opposing end of the test frame and then moved to contact the stud shank. A 100-kN capacity frame with constant-amplitude loading applied at 10 to 15 Hz was utilized.

Two model variants were developed using the finite element (FE) analysis software ABAQUS (Fig. 5). The contact interaction between the load-plate and stud was included in the initial model; however, this was replaced with a load applied directly

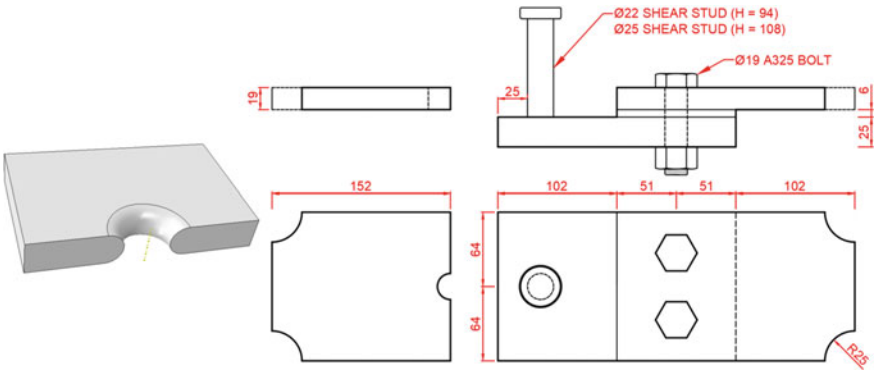

Fig. 4 Stud contact plate geometry (left) and push-plate specimen configuration (right) (units in mm)

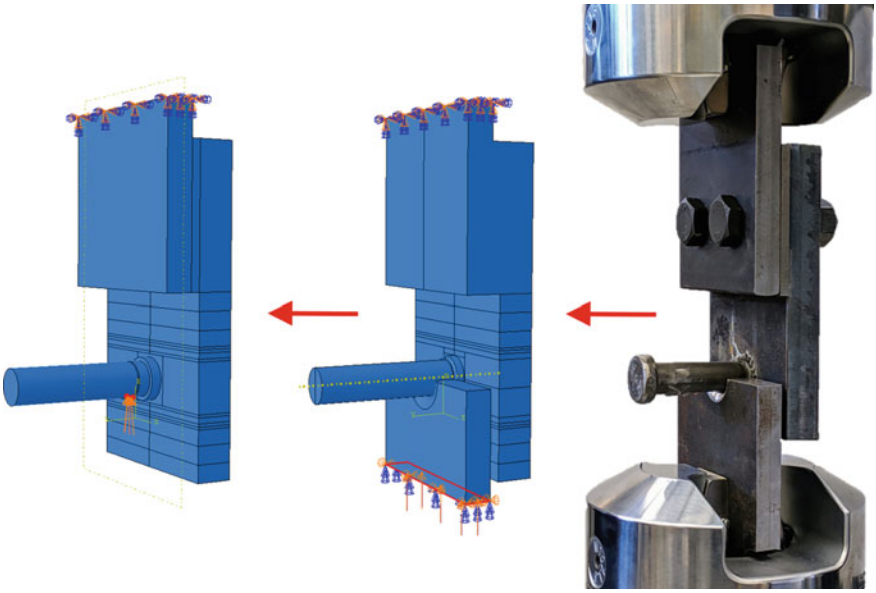

Fig. 5 Progression from the test set-up (right), to the initial (centre) and final (left) FE models

to the stud shank to reduce computational effort. The base plate was partitioned to obtain the stress at the locations required to estimate the HSS. The weld geometry was modelled without a radius. The width and height of the weld profile used was 2.5 and 6.5 mm, respectively, for the 22 stud, and 2.9 and 7.4 mm, respectively, for the 25 mm stud.

A Young's modulus of 200 GPa and Poisson's ratio of 0.3 was used to model the stud and steel plates in a 3D elastic analysis. The meshes for the two FE models are shown in Fig. 6. Both models used an element size of 2 mm, but the model with the contact plate required a finer mesh around the point of contact. The first

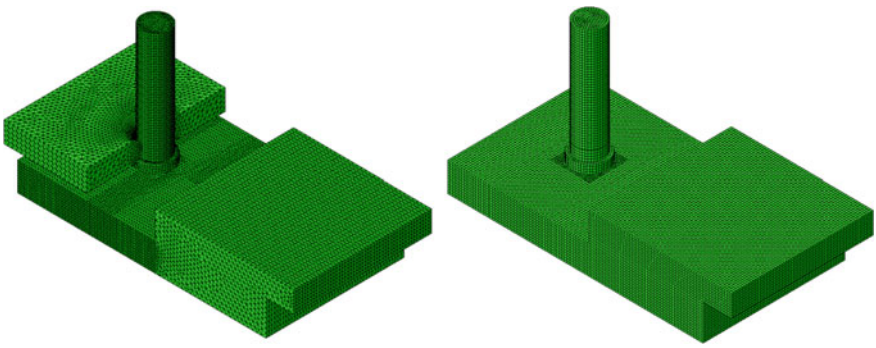

Fig. 6 Mesh of the initial (left) and final (right) FE model

model utilized 10-node quadratic tetrahedron elements, whereas the second model utilized 8-node linear brick elements with reduced integration and hourglass control throughout, and 6-node triangular prism elements within the region around the base of the stud.

4 Results

4.1 Experimental Test Results

The fatigue test results are shown in Fig. 7 for the ten 25-mm diameter studs and eight 22-mm diameter studs welded to 25-mm-thick base plates. NS results are plotted for the tests, along with HSS at the T/P and T/S locations, which where computed using the results obtained from the FE model and the Type B quadratic extrapolation method, shown previously in Eq. 2. It should be noted that even though the structural stress for this geometry included bending and membrane components at both crack locations, the compactness of the specimen geometry makes the application of Eq. 1 (Type A HSS) problematic.

The observed failure type is also indicated in Fig. 7, and T/S failures (cracking through the shank) appeared for high stress, low-cycle tests, and not frequently, which is consistent with the push-out test failures reported in the literature. Also, curves with a slope, m, of 5, following the Eurocode "FAT" fatigue design curve convention (i.e., FAT stress level corresponding to $2 \cdot (10^6)$ cycles), are plotted for the HSS for each type and stud size [4]. For example, the FAT67 curve (m = 5) passes through the point at $2 \cdot (10^6)$ cycles and a stress range of 67 MPa. FAT157 and FAT162 curves are shown for the Type B HSS at point T/S for the 22 and 25 mm studs, respectively.

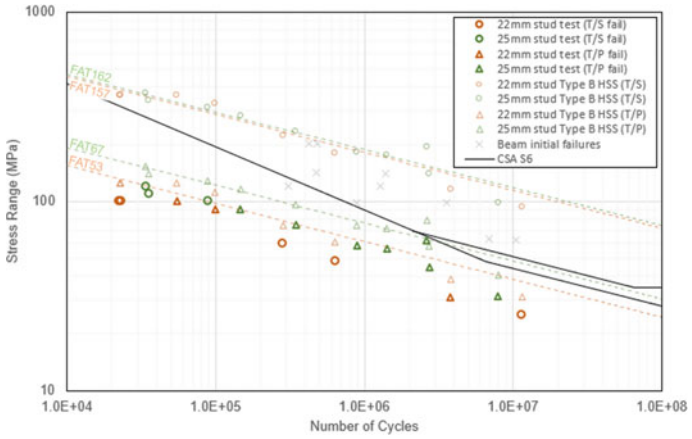

Fig. 7 Stress-life fatigue test results with corresponding Type B HSS obtained from FE model

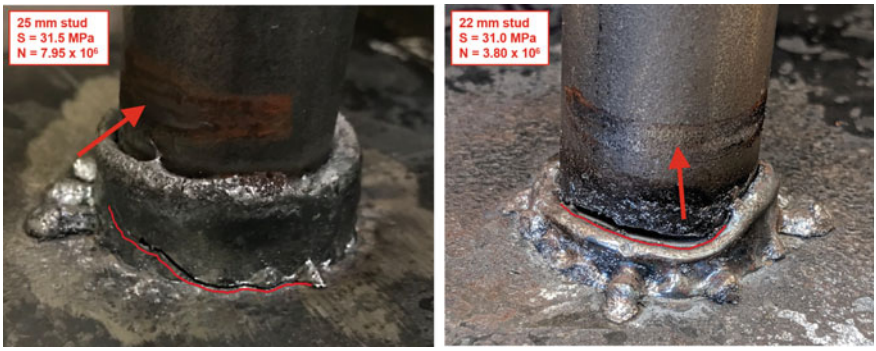

Fig. 8 Observed T/P (left) and T/S (right) fatigue failures, with direction of load indicated

Similarly, the FAT curves shown point T/P are for Type B HSS and are FAT53 and FAT162 for the 22 mm and 25 mm studs, respectively.

The push-plate test method is shown to be conservative (i.e. it yields lower NS results) compared to CSA S6 curve (which corresponds to mean push-out results) and compared to the beam tests done by [12]. It is suspected that the lack of confinement provided by concrete, and the resulting boundary conditions (e.g., local compressive stresses, friction), contribute to this conservatism. Also, it is evident that the higher HSS at the point T/S determined using the FEA with a geometrical-defect-free model does not capture the true fatigue behaviour of the studs. Failure at the point T/P is more prevalent, likely due to the defect-prone weld/plate interface and the prevalence of imperfect welds that do not form a uniform weld profile around the circumference of the stud shank. This phenomenon also be a function of the plate thickness and load lever arm used, which will be investigated in the parametric study.

Examples of both failure types are shown in Fig. 8, which also illustrates the potential for variation in weld geometry and quality, which are critical factors for fatigue life.

4.2 Parametric Study

The parametric study investigated the influence of stud size, base plate boundary conditions, and base plate thickness on HSS at the T/P and T/S points, looking at different stud sizes, as the distance from the stud base to the point-of-application of the load, or lever arm, d, was varied. This is meant to simulate an equivalent point load acting on a stud embedded in concrete due to the shear stress distribution along the stud height. A load corresponding to a nominal shear stress of 60 MPa was used throughout. Figure 9 shows the Type A and Type B HSS at the point T/S for the two stud sizes (22 and 25 mm).

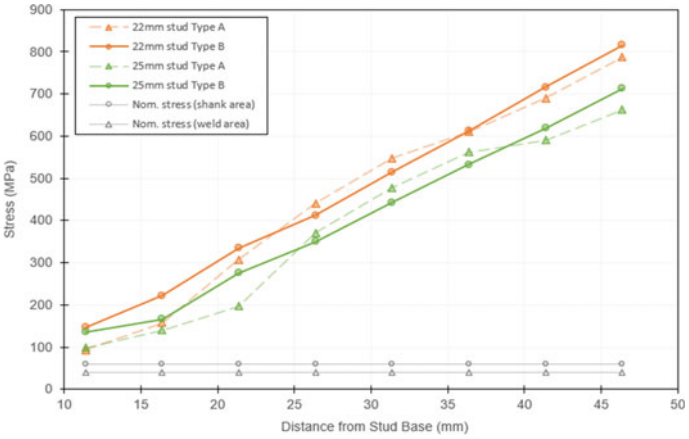

Fig. 9 Lever arm length vs. HSS at T/S for different stud diameters

The results indicate that the smaller stud experiences a greater HSS at the T/S point, and this effect increases as the lever arm increases. The curves deviate from a straight line because of the local stresses near the point-of-application of the load, this is overly apparent for Type A HSS due to the location of the stress extrapolation points along the stud shank. This study shows that the HSS at the point T/S can be estimated as Type B. Next, the boundary conditions were varied for the 22-mm stud specimen to investigate the effect on HSS at the point T/P. The end of the base plate remained unchanged (free) in one case, and in the other case, movement of the end of the base plate was restricted as if the underside was welded to the web of a beam (i.e., no displacement normal to the axis of the base plate is permitted). Also, the comparable unconstrained 25 mm stud model is plotted. The results are shown in Fig. 10.

Finally, the effect of the base plate thickness on the HSS at T/P is investigated. The results for the 22 mm stud and various base plate thicknesses at 5-mm increments down from the 25.4-mm thick base plate used in the experimental testing are presented in Fig. 11. A graphical representation of the Type A and Type B HSS at T/P for each plate thickness and a constant lever arm of 16 mm is shown in Fig. 12.

This study helps explain the relatively low HSS at the T/P location computed for the experimental specimen, which had a base plate thickness of 25.4 mm. When using the HSS approach for shear studs, it is apparent that the base plate (flange) thickness is an important parameter to consider when evaluating test results. The S-N curve reported by [9] was based on the Type A HSS at the T/P location for a push-out specimen with a flange thickness of 11 mm. They determined an average hot-spot fatigue strength of FAT187 and a FAT107 standard fatigue design curve, which is much greater than what was found in the current study for the push-plate test (c.f. a range of FAT16 to FAT67). The results reported by [9]—with a nominal stress of 60 MPa corresponding to a Type A HSS of 172 MPa—are in line with the results of the current parametric study, specifically, looking at the Type A HSS at T/P for the

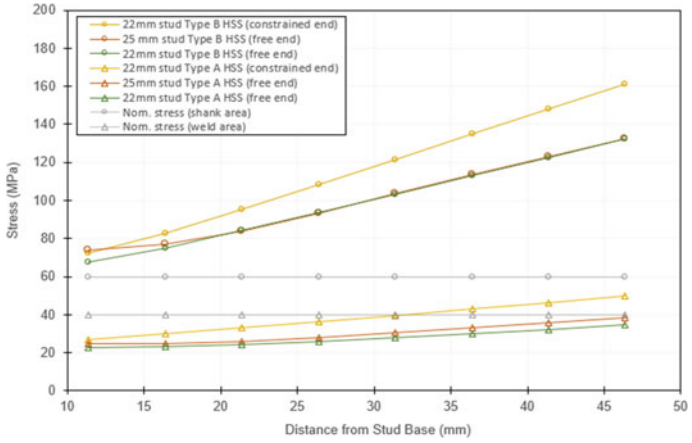

Fig. 10 Lever arm length vs. HSS at T/P for different base plate boundary conditions and stud diameters

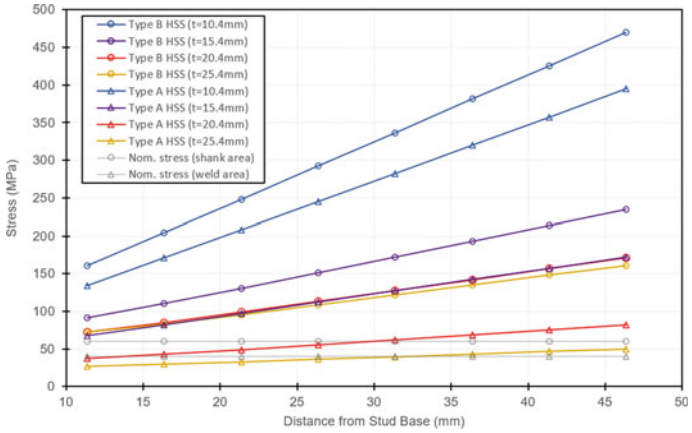

Fig. 11 Lever arm length vs. HSS at T/P for different base plate thicknesses

FE model with a comparable plate thickness (10.4 mm). Thus, it can be concluded that a modification to the test results may be necessary to draw comparisons between analyses involving HSS with different plate thicknesses, as well as other specimen geometrical features such as stud height and specimen configuration (i.e., push-plate, push-out, or full beam test). Also, failure at the T/S location should be investigated in conjunction with this. Overall, T/S failure is more desirable in practice since it is contained to the individual stud and is does not have as much potential to be detrimental on a global scale. This failure has a greater likelihood of occurring in the case of a smaller stud diameter, thicker base plate, and longer lever arm.

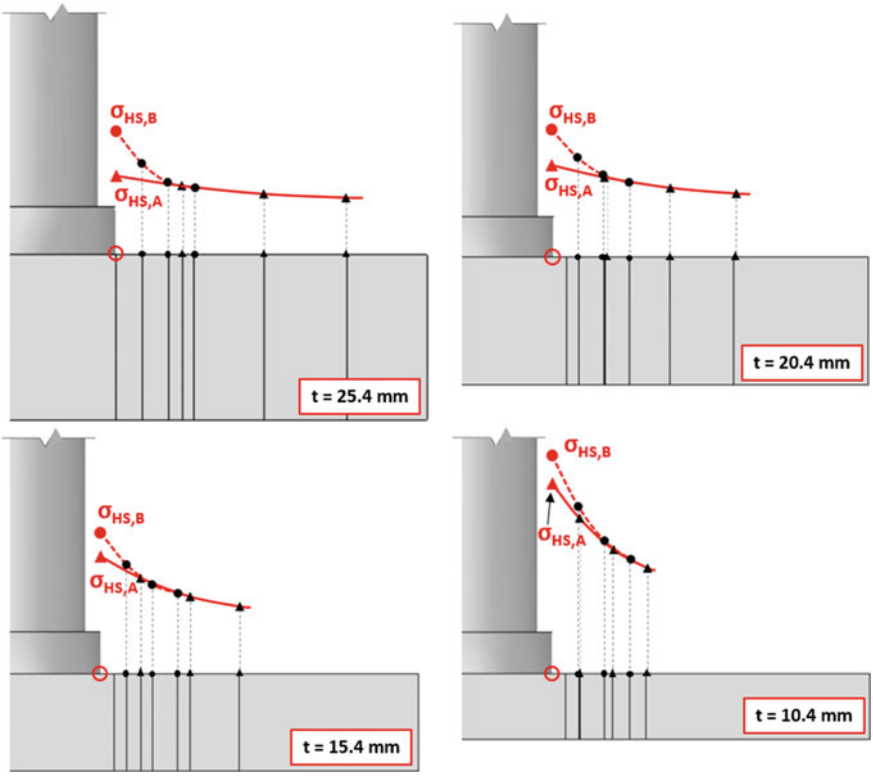

Fig. 12 Type A and Type B HSS at T/P plotted for various base plate thicknesses (lever arm = 16 mm)

5 Conclusions and Recommendations

Based on the results presented in this paper, the following conclusions are made:

- Despite its conservatism, the simple push-plate testing apparatus proved to be effective in producing repeatable fatigue tests with S-N results that follow a trend, and the fatigue failures and their corresponding failure type were similar that of push-out tests in the literature. Future fatigue testing should be completed in the high-cycle domain to establish an endurance limit.
- It was observed that the drawn-arc stud welding process produces welds that can range significantly in both their quality (e.g., consistency around the circumference of the stud) and profile geometry and can therefore influence the predictability of the crack initiation site location (T/P or T/S failure) and the overall fatigue life. Future work should consider the notch effect for various weld geometries using the effective notch stress (ENS) method so the failure mode can be more accurately predicted.

- The final simplified FE model used was able to produce results in a reasonable runtime and allowed for a time-effective parameter study; however, further work should be done to study the effect of the element size, and experimental tests measuring strain at various point along the base plate and stud shank should be done to validate the model.
- The hot-spot stress of studs at the point T/P was influenced by the location of the applied load (lever arm), the base plate boundary conditions, and the thickness of the base plate (flange). Future FE modelling should be done for push-out tests to compare the results of the push-plate tests with the S-N curves in design codes, as well as for full composite beams to align the push-plate and push-out test results to reality and improve fatigue design practices.
- Design practice should consider the two failure modes (T/S and T/P), e.g. separate S-N curves for each, as the governing mode can be influenced by the aforementioned parameters, particularly stud diameter.

Acknowledgements The authors would like to thank the Ontario Ministry of Transportation (MTO) and Canadian Institute of Steel Construction (CISC) for their financial support. Additionally, the University of Waterloo Structures Lab technicians, Peter Volcic and Richard Morrison, are thanked for their assistance with laboratory testing.

References

1. ABAQUS (2017) Version 2018, Dassault Systèmes, USA
2. AASHTO (American Association of State Highway Transportation Officials) (2014) AASHTO LRFD Bridge Design Specifications. Washington, DC, USA
3. Al-Emrani M, Aygül M (2014) Fatigue design of steel and composite bridges. Report 2014:10, Göteborg, Sweden
4. CEN (European Committee for Standardization) (2005) Eurocode 4, ENV 1994: Design of composite steel and concrete structures. Brussels, Belgium, EU
5. CSA (Canadian Standards Association) (2019) CAN/CSA-S6-19, Canadian Highway Bridge Design Code. Mississauga, Ontario, Canada
6. CSA (Canadian Standards Association) (2010) S6.1S1-10 Commentary on CAN/CSA-S6-06. Mississauga, Ontario, Canada
7. Hobbacher A (2016) Recommendation for fatigue design of welded joints and components. The International Institute of Welding (IIW). Wilhelmshaven, Germany, EU
8. Lee JM et al (2010) Comparison of hot spot stress evaluation methods for welded structures. Int J Naval Archit Ocean Eng 2:200–210
9. Liu R, Hao Z, Zhiqiang F, Haohui X, Yuqing L (2020) Fatigue evaluation on headed stud connectors with toe-plate failure mode using hot spot stress approach. Eng Failure Anal 117. Article 104972
10. Niemi BE, Marquis G (2002) Introduction to the structural stress approach to fatigue analysis of plate structures (pp. 73–90).
11. Ovuoba B (2017) On the fatigue of headed shear studs in steel-concrete composite bridge girders. Unpublished Doctor of Philosophy in Engineering. University of Arkansas, Fayetteville, Arkansas, USA

12. Sjaarda M (2018) The fatigue behaviour of welded and bolted shear connectors in composite highway bridges. Unpublished Doctor of Philosophy in Civil Engineering. University of Waterloo, Waterloo, Ontario, Canada
13. Slutter RG, Fisher JW (1966) Fatigue strength of shear connectors. No. 316.2. Lehigh University Institute of Research. Bethlehem, Pennsylvania, USA
14. Zhang Q (2007) Fatigue resistance of shear stud connectors. Unpublished Master of Engineering in Structural Engineering. University of Alberta, Calgary, Alberta, Canada

A Computational Analysis for an Adaptive Tensegrity-Based Four-Module Roof Structure

S. Paul and A. C. Sychterz

1 Introduction

In addition to the building industry's contribution of 29% of total waste in the United States [11], current over-conservative design practices are a burden on natural resources. The viable solution for future infrastructure, such as adaptive and tensegrity structures, will optimize material usage with sustainable control systems. Adaptive structures can undergo shape-change [14] to meet design requirement in response to external loads [26]. These structures can be active, deployable, controllable, and include sensory as well as machine learning systems [27], which are properties that are easily studied using tensegrity structures. Tensegrity structures are closely coupled, pin-jointed structures composed of a set of bars in compression, surrounded by a network of cables in tension and are held stable in a state of self-stress [4, 20].

Active vibration control has been used to tackle heavy dynamic loading such as earthquake and wind loads [23]. This concept has been studied for tall buildings suing tendons as active control [1], the bracing systems [15] to control the response for vibrational forces [3]. Active control is used in cable stayed bridges to control the displacements [19] and [28]. Cable tendons are also used in adaptive prestressing and control algorithms were developed for load induced optimized prestressing [21]. Tensegrity structures are costlier than passive structures [22]. However, this extra cost can manage to reduce the effect on environment and integrating the concept of adaptivity can further lower the cost by helping to reduce effective load on the structure.

Tensegrity structures feature unique visualization qualities and topological characteristics. It has been studied on space structures that through active control, tensegrity

S. Paul (✉) · A. C. Sychterz
Department of Civil and Environmental Engineering, University of Illinois at Urbana-Champaign, Urbana, IL, USA
e-mail: sagnikp2@illinois.edu

S. Walbridge et al. (eds.), *Proceedings of the Canadian Society of Civil Engineering Annual Conference 2021*, Lecture Notes in Civil Engineering 244,
https://doi.org/10.1007/978-981-19-0656-5_22

structures have the potential to widen the scope of research in the areas of lightweight, reusable and innovative structural systems [5, 10]. One of the important characteristics of tensegrity structures is that it is deployable. Deployable structures can be defined as structures which changes shape, to change size [14]. The mechanism of a deployable hollow-rope tensegrity footbridge structure is studied and implemented through the actuation of its cables [16–18]. Deployable tensegrity structures have also been studied for masts [7]. Apart from these, tensegrity structures have wide scope of applications in civil and architectural systems like towers, large domes, roofs and tent structures [7].

Only two proposed tensegrity roof structures are "tensegrity roof structures for atrium roofs" in Reuters headquarters in London, which was never built, while the other one is the new La Plata Stadium (Argentina) based on a concept by architect Roberto Ferriera [9]. In terms of computational research, half-cuboctahedron tensegrity grid is studied for roof structures which was found to be more suitable for large span structures [24]. An older study proposed dismountable tensegrity grid as an alternative to roof structure. Advantages to these structures include ease of production, construction, and disassembly [13]. Variable geometry truss (VGT) and origami concepts have been used to study foldable roof structures [12] and [8]. In 2011, a novel mechanism called scissor-hinge was proposed for convertible roof [2, 6]. Although there are some ideas presented separately in the areas of tensegrity structure and adaptive roofs, there is hardly any literature in conjunction with the two ideas. Tensegrity structures are deployable and adaptive roofs are something of great interest in recent times, an adaptive tensegrity roof structure is something apt for exploration.

In this paper, a four-module tensegrity roof structure is proposed which is inspired from the hollow tensegrity footbridge structure proposed by Motro [17]. The four-module roof structure is formed by using the upper part of the footbridge structure. A computational analysis of this four-module tensegrity roof structure is performed using dynamic relaxation (DR) method. Combinations of actuated struts are studied to change the overall shape of the roof structure. This is one of the ways a roof can adapt itself to counteract the different loads it can experience through its lifetime due to various hazards. A comparison is made between the set struts actuated in terms of the observed change of shape to the total length of actuation of the struts.

2 Methodology

2.1 Description of the Proposed Roof Structure

A four-module tensegrity roof structure inspired from the hollow tensegrity footbridge structure proposed by Motro is proposed (Fig. 1). It consists of a combination of cables and bars (struts). The Young's modulus and cross-sectional area considered for the cables and bars are 240 kN/cm^2 and 0.018 cm^2, and 340 kN/cm^2 and 0.64

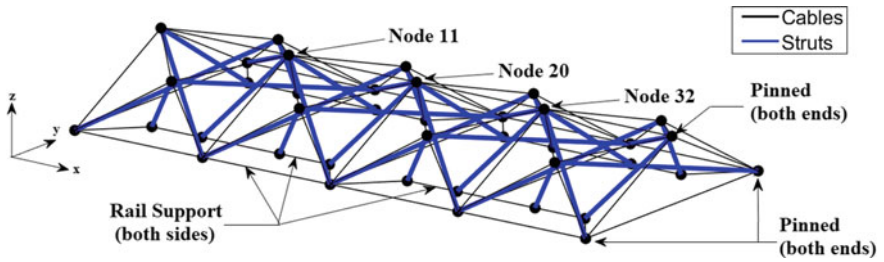

Fig. 1 3D view of the proposed tensegrity roof structure

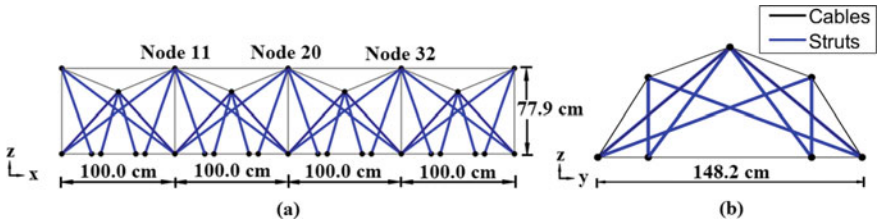

Fig. 2 2D view of the structure along **a** x-z plane **b** y-z plane

cm^2 respectively for the computational analysis. All the nodes lying on the x-y plane are considered to be laid on rails along the x-axis, that is, these nodes are only free to move in the x-direction. All the end nodes are pinned, that is, it cannot move in any direction. The rest of the nodes are free to move along all directions.

The two-dimensional view of the tensegrity roof structure along the x-z plane and y-z plane is depicted in Fig. 2 along with the dimensions. The length of each module is 100 cm. The structure is 400 cm in length, 77.9 cm in height and 148.2 cm in width. Three top nodes at the intersection of two adjacent modules are marked as Node 11, 20 and 32.

2.2 Adaptation by Dynamic Relaxation

Dynamic relaxation (DR) method has been applied successfully for the shape control of tensegrity structures [25]. DR method is used as the tool for computational analysis of the roof structure undergoing change of shape. The change of shape is studied under 5 different cases and another special case by changing the actuating struts. A detailed description of the struts actuated in each case is presented in Table 1.

Through various simulation trials, it was determined that actuation of struts was the key to the aspired change of shape of the struts. Actuation of some cables forced the tensegrity roof structure to lose its structural integrity, while some others proved ineffective by moving the nodes in the opposite direction. Actuation of cables also

Table 1 Description of the various cases studied

Case	Actuating struts
A	All struts connecting to Node 20
B	All struts connecting to Node 11 and 32
C	All struts connecting to Node 11, 32 and 20
D	Only shorter struts connecting to Node 11, 32 and 20
E	Only longer struts connecting to Node 11, 32 and 20
Special case	Same as Case D but shorter nodes connected to Node 20 are actuated at a higher rate

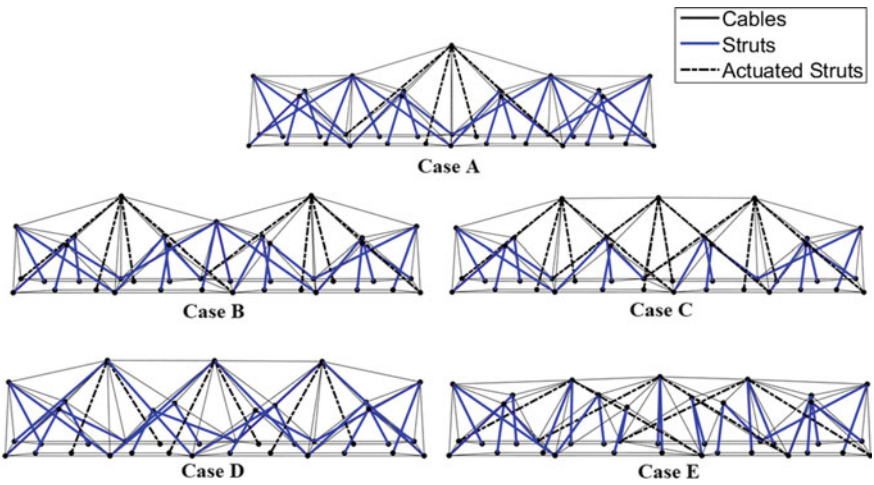

Fig. 3 Adapted shapes of the roof structure after undergoing complete actuation studied under different cases

proved to be ineffective when actuated along with struts. Hence, actuation of struts was found out to be the best way to attain the pre-cambering of the roof structure.

Combination of actuating struts are chosen such that the adapted form of the structure helps in counteracting gravitational loads. Each of the actuating struts in each case is made to undergo a total length increment of 20 cm. The final shapes of the roof structure obtained in each case is depicted in Fig. 3. Gravitational loads will be better counteracted if an upward curved shape is formed by the roof structure, similar to pre-stressing in concrete. One of the ways to achieve that is to vertically rise the position of the Nodes 11, 20 and 32 along z-axis.

Raising the positions on Nodes 11, 20 and 32 are crucial in achieving the aspired adapted shape of the structure. This process of pre-cambering will not only help the structure to counter gravitational loads but also help in drainage system of rainwater by forming a slope in a particular direction. Hence, the primary objective of the adaptation of this tensegrity-based roof structure lies in the change of position of the

Nodes 11, 20 and 32 in z-axis. The different cases studied, as described in Table 1, will be investigated to choose the best set of actuated struts that makes the most efficient use of energy to achieve the required goal. Two methods, effective position change and effective length change method are proposed next in order to make an assessment and compare the most effective choice of actuating struts.

Effective Position Change

The change in position with respect to z-axis for the Nodes 11, 20 and 32 are defined as $(\Delta z)_{N11}$, $(\Delta z)_{N20}$ and $(\Delta z)_{N32}$ respectively. The total length actuated can be defined as the sum of the change of length of the actuating struts in each case. For example, in case A, 4 struts are actuated by a length of 20 cm each, hence the total length actuated is $\Sigma L_a = 4 \times 20\,\text{cm} = 80\,\text{cm}$. The effective position change is defined as:

$$(\Delta z)_{eff} = \frac{sum\ of\ change\ of\ position\ in\ z\ axis\ for\ Nodes\ 11,\ 20\ and\ 32}{total\ length\ actuated}$$

$$\rightarrow (\Delta z)_{eff} = \frac{(\Delta z)_{N11} + (\Delta z)_{N20} + (\Delta z)_{N32}}{\Sigma L_a}$$

Hence, for case A, Nodes 11, 20 and 32 moves along z-axis by a distance of 0.42 cm. 25.92 cm and 0.42 cm respectively. So, the effective position change can be computed as follows:

$$(\Delta z)_{eff} = \frac{(\Delta z)_{N11} + (\Delta z)_{N20} + (\Delta z)_{N32}}{\Sigma L_a} = \frac{0.46\,\text{cm} + 24.79\,\text{cm} + 0.46\,\text{cm}}{80.00\,\text{cm}} = 0.32$$

A summary of observed change of position along the z-axis for the Nodes 11, 20 and 32, and the effective change of position for each case studied is shown in Table 2.

The effective position change ($(\Delta z)_{eff}$) is a measure of the obtained change of position along z-axis of the concerned nodes that helps in adapting the shape of the structure per unit length actuated. Hence, the more change in position attained per unit length of actuation, the more effective is the use of energy towards the aimed

Table 2 Observations of change of position along z-axis and effective position change for each case

Case	A	B	C	D	E
No. of struts actuated	4	8	12	6	6
ΣL_a (cm)	80.00	160.00	240.00	120.00	120.00
$(\Delta z)_{N11}$ (cm)	0.46	27.74	27.84	16.06	2.79
$(\Delta z)_{N20}$ (cm)	24.79	4.48	28.62	13.40	6.06
$(\Delta z)_{N32}$ (cm)	0.46	27.74	27.84	16.06	2.79
$(\Delta z)_{eff}$	0.32	0.38	0.35	0.38	0.10

adapted structure. Thus, a higher value of $(\Delta z)_{eff}$ should be preferred while choosing the combination of actuating struts.

From Table 2, it is observed that in case A, Node 20 gets vertically displaced by a much larger distance compared to its adjacent nodes Node 11 and 32. Case B presents a shape where the opposite happens. Node 11 and 32 gets vertically displaced by a much larger distance compared to the middle Node 20. This adapts to a shape of bi-modal roof where the set of two modules on either side creates a curved form. However, the trough in the middle is not helpful to counteract gravity loads nor the drainage of water. Case C is a combination of the previous two cases A and B where it is observed that all the three nodes get almost equally vertically displaced. In all the above three cases, the $(\Delta z)_{eff}$ values are very similar to each other. Two different variations of case C are shown through cases D and E. Only the two shorter of the four struts joining at Nodes 11, 20 and 32 are actuated in case D, while only the longer struts are actuated in case E. The adapted shape in case D is similar to that of case C, however the change of position of each of the three nodes is about 10 cm less than that of case C. The better part here is that the $(\Delta z)_{eff}$ value is 8% greater than case C and the $(\Delta L)_{eff}$ value is even lower than case A. Case E, contrary to case D shows the worst adaptive behaviour of all cases studied. This happens because two of the actuated nodes are connected to pinned nodes at the which prevents the movement of the elements after a certain stage, saturating the change of position. This behaviour is reflected through the $(\Delta z)_{eff}$ value of 0.10 (about $1/4^{th}$ to that of case D). Although Case C achieves the highest amount of vertically displacement, Case D shows a more efficient use of energy obtaining the shape. A little lack in the amount vertically displacement is compensated by the energy efficiency, and hence should be considered as the best choice of all the five cases.

Effective Length Change

The second method that can be used to measure the efficiency of the adaptation process is the effective length change method. While the struts are theoretically actuated to undergo an increase of 20 cm in length, the actual increment in length is not exactly 20 cm due to restraints caused by boundary conditions. For example, in case A, 4 struts are actuated by 20 cm each, however the actual length of actuation are 19.30 cm, 19.97 cm, 19.30 cm and 19.97 cm. So, the term effective length change is defined as:

$$(\Delta L)_{eff} = \frac{total\ length\ actuated\ -\ sum\ of\ actual\ length\ actuated}{total\ length\ actuated} \times 100\%$$

$$\rightarrow (\Delta L)_{eff} = \frac{\Sigma L_a - \Sigma L_{act}}{\Sigma L_a} \times 100\%$$

Hence, for case A,

$$(\Delta L)_{eff} = \frac{\Sigma L_a - \Sigma L_{act}}{\Sigma L_a} \times 100\% = \frac{(4 \times 20\,\text{cm}) - (19.54\,\text{cm} + 19.90\,\text{cm} + 19.54\,\text{cm} + 19.90\,\text{cm})}{4 \times 20\,\text{cm}} \times 100\%$$

Table 3 Summary of (ΣL_a), sum of actual length actuated (ΣL_{act}) and effective length change ($(\Delta L)_{eff}$) for each case studied

Case	A	B	C	D	E
No. of struts actuated	4	8	12	6	6
ΣL_a (cm)	80.00	160.00	240.00	120.00	120.00
ΣL_{act} (cm)	78.89	156.74	235.38	118.6	110.50
$(\Delta L)_{eff}$ (%)	1.39	2.04	1.93	1.17	7.92

$$\rightarrow (\Delta L)_{eff} = \frac{(4 \times 20\,\text{cm}) - (19.54\,\text{cm} + 19.90\,\text{cm} + 19.54\,\text{cm} + 19.90\,\text{cm})}{4 \times 20\,\text{cm}} \times 100\%$$

$$\rightarrow (\Delta L)_{eff} = \frac{80\,\text{cm} - 78.89\,\text{cm}}{80\,\text{cm}} \times 100\% = 1.39\%$$

Similar calculations are performed for the other four cases. A summary of total length of actuation (ΣL_a), sum of actual length actuated (ΣL_{act}) and effective length change ($(\Delta L)_{eff}$) for each case studied is shown in Table 3.

The effective length change ($(\Delta L)_{eff}$) is a measure of the difference between the actual change of length desired to the change of length achieved to the actuated length. Hence, it is an estimate of the energy wasted in the process. Thus, a lower value of ($(\Delta L)_{eff}$) should be preferred.

In terms of $(\Delta L)_{eff}$ values, from Table 3, case A shows a slightly lower value than the Cases B and C. Out of cases A, B and C, case C serves the purpose the most in terms of change of position. Case D exhibits the lowest value of $(\Delta L)_{eff}$, while Case E shows a $(\Delta L)_{eff}$ value of 7.92% (about 6 times to that of case D). Once again, by this method, Case E shows a very poor performance compared to the best adaptation behaviour exhibited by case D. This method draws the same conclusions as before by the method of effective position change.

From the above discussion, it is quite evident that case D is the better choice of all the cases. Although the change of position achieved is slightly lesser, it is the most effective in terms of effective position change $(\Delta z)_{eff}$ as well as effective length change $(\Delta L)_{eff}$ values, which implies better use of energy. However, the adapted shape obtained is not exactly a curve. The middle two modules of the adapted roof structure seem almost flat. The process of pre-cambering is not very effective by this method of actuation. To mitigate this issue, a concept of differential actuation is implemented.

2.3 Differential Actuation

In the previous section, it is concluded that case D is the most appropriate choice for adaptation of this roof structure. However, the adapted shape is not exactly a curve and the pre-cambering is not the most effective. Hence, a concept of differential

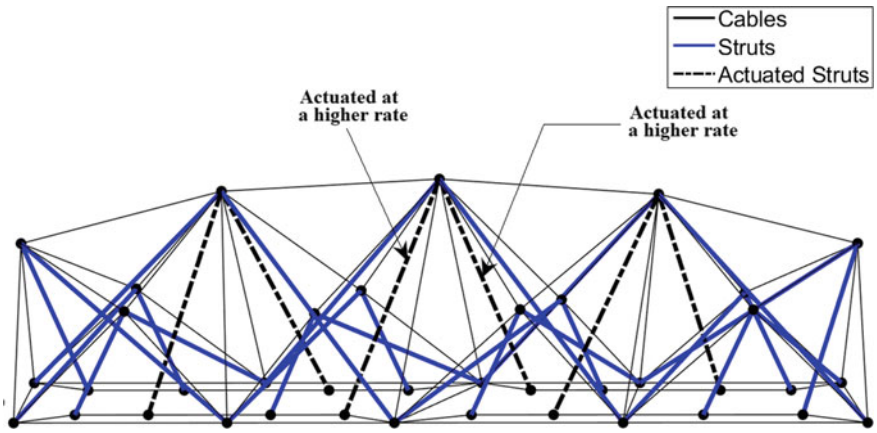

Fig. 4 Adapted shape of the roof structure after undergoing differential actuation

Table 4 Summary of outputs for differential actuation

No. of struts actuated	ΣL_a (cm)	$(\Delta z)_{N11}$ (cm)	$(\Delta z)_{N20}$ (cm)	$(\Delta z)_{N32}$ (cm)	$(\Delta z)_{eff}$	ΣL_{act} (cm)	$(\Delta L)_{eff}$
6	140.00	17.33	21.88	17.33	0.39		1.16%

actuation is implemented here. The actuating struts are kept same as that of case D. Only the actuated struts joined to Node 20 are actuated at a rate 50% higher than that of the other four actuated Hence, the total intended change of length is 30 cm for the actuated struts connected to Node 20, while it is 20 cm for the actuated struts connected to Nodes 11 and 32. The adapted shape of the roof structure undergoing differential actuation is shown in Fig. 4.

From Fig. 4, it is observed that the concept of differential rate of actuation produces a much better adapted curved shape of the roof tensegrity structure. The change of positions of the Nodes 11, 20 and 32, the effective position change value, the effective length change value and other associated details are summarized in Table 4. Since two of the total six actuating struts are actuated at a rate of 50% higher, the total actuated length is calculated as $\Sigma L_a = 4 \times 20\,\text{cm} + 1.5 \times 2 \times 20\,\text{cm} = 140\,\text{cm}$.

From Table 4, it is observed that the values of the effective position change $(\Delta z)_{eff}$ and effective length change $(\Delta L)_{eff}$ remain same as that of Case D. However, in this special case, the visual appeal of the adapted shape of the structure and pre-cambering is more effective geometrically. The process also ensures efficient use of energy. Thus, it can be concluded that differential rate actuation of struts proves to be successful in obtaining a more desired adapted shape of the roof structure.

3 Discussion

Two parametric methods, the effective position change $(\Delta z)_{eff}$ and effective length change $(\Delta L)_{eff}$, are introduced as a measure to choose the best set of actuating struts. Both the methods calculate a value that represents the efficiency energy utilization in actuation of struts. A high value of $(\Delta z)_{eff}$ is preferred and a low value of $(\Delta L)_{eff}$ is preferred to ensure the most effective process of shape adaptation.

Based on the results of case E, it is advisable to actuate struts where both end nodes are free to move and adapt. If the actuating members are unable to undergo a complete change of length through actuation due to boundary conditions, it will lead to the formation of unwanted stresses in the elements and inefficient use of energy. This will make the member prone to buckling and hence the stability of the structure.

Comparing the performances of Case C and Case D, often it is more effective to achieve less absolute change of position of nodes and compensate it with the effective change of position in order to attain an overall improved adapted shape of the structure.

4 Conclusion

Dynamic relaxation (DR) method confirms as a successful and robust tool to computationally study the adaptive shape control of tensegrity roof structures. Actuating struts instead of cables enables the proposed tensegrity roof structure to obtain the maximum change of position of the desired nodes. However, a concept of differential rate of actuation of different struts is introduced which enables the structure to adapt its shape into a proper curve ensuring better pre-cambering, which will help in counteracting gravitational loads and drainage systems.

The study presents a computational analysis of an adaptive tensegrity roof structure through the actuation of struts. This opens an opportunity to study on the topic on actuation of compression members practically, which is relatively tougher than actuating tension members.

References

1. Abdel-Rohman M, Leipholz HH (1983) Active control of tall buildings. J Struct Eng 109(3):628–645. https://doi.org/10.1061/(asce)0733-9445(1983)109:3(628)
2. Akgün Y, Gantes CJ, Sobek W, Korkmaz K, Kalochairetis K (2011) A Novel adaptive spatial scissor-hinge structural mechanism for convertible roofs. Eng Struct 33(4):1365–1376. https://doi.org/10.1016/j.engstruct.2011.01.014
3. Bani-Hani K, Ghaboussi J (1998) Nonlinear structural control using neural networks. J Eng Mech 124(3):319–327. https://doi.org/10.1061/(asce)0733-9399(1998)124:3(319)

4. Calladine CR (1978) Buckminster fuller's 'tensegrity' structures and Clerk Maxwell's rules for the construction of stiff frames. Int J Solids Struct 14(2):161–172. https://doi.org/10.1016/0020-7683(78)90052-5
5. Fest E, Shea K, Domer B, Smith IFC (2003) Adjustable tensegrity structures. J Struct Eng 129(4):515–526. https://doi.org/10.1061/(asce)0733-9445(2003)129:4(515)
6. Gantes CJ (2001) Deployable structures: analysis and design. WIT Press, Southampton
7. Gilewski W, Kłosowska J, Obara P (2015) Applications of tensegrity structures in civil engineering. Procedia Eng (TFoCE) 111:242–248. https://doi.org/10.1016/j.proeng.2015.07.084
8. Del Grosso AE, Basso P (2010) Adaptive building skin structures. Smart Mater Struct 19(12):124011. https://doi.org/10.1088/0964-1726/19/12/124011
9. Jáuregui, VG (2020) Tensegrity structures and their application to architecture
10. Kawaguchi K, Hangai Y, Pellegrino S, Furuya H (1996) Shape and stress control analysis of prestressed Truss structures. J Reinf Plast Compos. https://doi.org/10.1177/073168449601501204
11. Kofoworola OF, Gheewala SH (2009) Estimation of construction waste generation and management in Thailand. Waste Manage 29(2):731–738. https://doi.org/10.1016/j.wasman.2008.07.004
12. Kurita K, Inoue F, Furuya N, Shiokawa T, Natori M (2001) Development of adaptive roof structure by variable geometry Truss. In: Proceedings of 18th international symposium on automation and robotics in construction
13. Panigrahi R, Gupta A, Bhalla S (2009) Dismountable steel tensegrity grids as alternate roof structures. Steel Compos. Struct. 9(3):239–253. https://doi.org/10.12989/scs.2009.9.3.239.
14. Pellegrino S (2002). Deployable structures. https://doi.org/10.1007/978-3-7091-2584-7
15. Reinhorn AM, Soong TT, Lin, RC Riley MA, Wang YP (1992) Active bracing system: a full scale implementation of active control. National Center for Earthquake Engineering Research
16. Rhode-Barbarigos L, Veuve N, Ali NBH, Motro R, Smith IFC (2012) Mechanism-based approach for the deployment of a tensegrity-ring module. J Struct Eng 138(4):539–548.https://doi.org/10.1061/(asce)st.1943-541x.0000491
17. Rhode-Barbarigos L, Veuve N, Ali NBH, Motro R, Smith IFC (2011) Deployment of a pentagonal 'Hollow-Rope' tensegrity module tensegrity-ring module topology. In: IABSE-IASS symposium 2011: taller, longer, lighter, London (UK), pp 1–8, 20–23 September 2011
18. Rhode-Barbarigos L, Veuve N, Ali NBH, Motro R, Smith IFC (2013) A transformable tensegrity-footbridge system. In: Conference transformables, pp 1–6, September 2013
19. Rodellar J, Mañosa V, Monroy C (2002) An active tendon control scheme for cable-stayed bridges with model uncertainties and seismic excitation. J Struct Control 9(1):75–94. https://doi.org/10.1002/stc.4
20. Schenk M, Guest SD, Herder JL (2007) Zero stiffness tensegrity structures. Int J Solids Struct 44(20):6569–6583. https://doi.org/10.1016/j.ijsolstr.2007.02.041
21. Schnellenbach-Held M, Steiner D (2014) Self-tuning closed-loop fuzzy logic control algorithm for adaptive prestressed structures. Struct Eng Int J Int Assoc Bridge Struct Eng (IABSE) 24(2):163–172. https://doi.org/10.2749/101686614X13830790993528
22. Senatore G, Duffour P, Winslow P (2018) Exploring the application domain of adaptive structures. Eng Struct 167:608–628. https://doi.org/10.1016/j.engstruct.2018.03.057
23. Soong T (1988) Active structural control in civil engineering. Eng Struct 10(4):74–84. https://doi.org/10.1016/0141-0296(88)90033-8
24. Sulaiman S, Parthasarathi N, Geetha B, Satyanarayanan KS (2016) The performance of half-cuboctahedron grid tensegrity systems in roof structures. Indian J Sci Technol 9(32). https://doi.org/10.17485/ijst/2016/v9i32/98636
25. Veuve N, Sychterz AC, Smith IFC (2017) Adaptive control of a deployable tensegrity structure. Eng Struct 152:14–23. https://doi.org/10.1016/j.engstruct.2017.08.062
26. Wada B (1989) Adaptive structures. Struct Struct Dyn Mater Conf 42(12):72. https://doi.org/10.2514/6.1989-1160

27. Wada BK, Fanson JL, Crawley EF (1990) Adaptive structures. J Intell Mater Syst Struct 1:157–174
28. Xu B, Wu ZS, Yokoyama K (2003) Neural networks for decentralized control of cable-stayed bridge. J Bridg Eng 8(4):229–236. https://doi.org/10.1061/(asce)1084-0702(2003)8:4(229)

Applications of Artificial Intelligence Techniques for Optimization of Structural Steel Connections

E. Duong, A. Darras, R. G. Driver, M. Essa, and A. Imanpour

1 Introduction

Applications of artificial intelligence (AI) techniques within the steel construction industry offer the potential for optimization of connections in ways not possible without utilizing advanced computational resources. In Canada, steel connections in building projects are typically designed with the aid of connection design software, spreadsheets, and design tables, while complex connections may involve numerical behavioural simulations using commercial finite element analysis software. Designing what may be thousands of connections in a typical project can be an extremely time-consuming process, especially when aspects of the design change throughout the lifecycle of the project. Unfortunately, changes are common and unavoidable in the construction industry and have left connection designers redoing or recalculating a large number of their designs, leading to a loss of efficiency and productivity [9]. Development of design tools that utilize AI-driven techniques can provide instant feedback to designers on how certain changes affect cost, constructability, and sustainability, while allowing for the efficient design of connections and better integration of the workflow across different disciplines [7].

This study investigates the practicality of an optimization tool that utilizes evolutionary algorithms (EA) to optimize shear connections such as shear tabs, welded–bolted double- and single-angle connections, and all-bolted double- and single-angle connections, shown in Fig. 1. To illustrate the main principles, a shear end-plate connection is explored using the demand-to-capacity ratio as the optimization criterion. The various aspects that contribute to the development of the optimization

E. Duong (✉) · A. Darras · R. G. Driver · M. Essa · A. Imanpour
The Steel Centre, Edmonton, Canada
e-mail: eduong1@ualberta.ca

University of Alberta, Edmonton, Canada

S. Walbridge et al. (eds.), *Proceedings of the Canadian Society of Civil Engineering Annual Conference 2021*, Lecture Notes in Civil Engineering 244,
https://doi.org/10.1007/978-981-19-0656-5_23

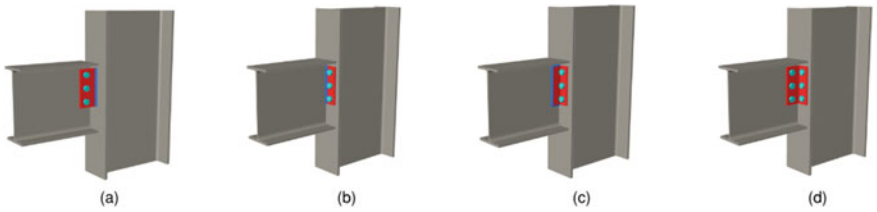

Fig. 1 Simple shear connections: **a** Shear tab, **b** Shear end plate, **c** Welded–bolted angle connection, **d** Bolted angle connection

design tool, as well as the limitations of this tool, are explored in the following sections.

2 Methodology

2.1 Virtual Connection Test Matrix

The shear connections evaluated in this study were chosen based on an industry survey conducted by the Steel Centre at the University of Alberta [12]. The survey was sent to local steel fabricators in Edmonton, Canada, where connection designers ranked common steel shear connections on a scale of one to five, with one corresponding to "rarely used" and five corresponding to "heavily used". The results of the survey were averaged, and the top six connections were incorporated into the optimization design tool. In addition to six different connection types, the design tool consists of a beam-to-girder connection, beam-to-column-flange connection, as well as a beam-to-column-web connection, all shown in Fig. 2. Within the tool, the user can opt to use codified limit states design provisions or component-based finite element modelling (CBFEM) to determine the capacity of the connection. The design of a shear end plate in a beam-to-column-web connection through the proposed optimization tool

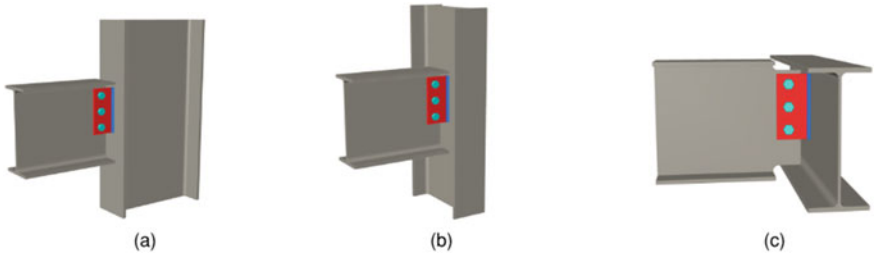

Fig. 2 Selected connection configurations: **a** Beam-to-column-flange connection, **b** Beam-to-column-web connection, **c** Beam-to-girder connection

Table 1 Modelling parameters for shear connections

Connection type	Parameters
Shear end plate	Plate thickness, number of bolt rows, fillet weld size
Shear tab	Plate thickness, gauge distance, number of bolt rows, number of bolt columns, fillet weld size
Welded–bolted double angle	Angle designation, number of bolt rows, fillet weld diameter
Welded–bolted single angle	Angle designation, number of bolt rows
Bolted double angle	
Bolted single angle	

is illustrated in this paper. The results are then compared to end plate connection design example in the Handbook of Steel Construction [3].

2.2 Proposed Connection Optimization Tool

In order to perform generative design, a parametric model is developed through Grasshopper, a visual scripting plugin for Rhino3D [13] used for parametric design, where Rhino3D is a 3D computer graphics and computer-aided design application software. Parametric modelling is the creation of a digital model based on a series of pre-programmed rules. That is, instead of the model or elements being manually manipulated, they are generated automatically by internal logic arguments. Typically, parametric rules create relationships among different elements of the design. For example, a rule might be created to ensure that the pitch between rows of bolts remain a specified distance; if the number of bolt rows changes, the distance between adjacent bolt rows remains the same.

The user interface of the proposed optimization tool allows the designer to choose the connection type, beam and column size, steel grade, bolt diameter, number of copes, and bolt pitch. For each connection type, the parametric attributes outlined in Table 1 are then used to control the design for the respective connection. Aspects of the connections, such as edge distance, bolt spacing, bolt hole diameter, plate thickness, weld size, etc., are constrained through limitations prescribed by the Canadian steel design standard CSA S16 [4].

2.3 Evolutionary Algorithms (NSGA-II)

EA are optimization algorithms that search for optimal solutions by mimicking the biological mechanisms of mutation, recombination, and natural selection [2]. In the presence of multiple objectives in a problem, which is often the case in connection design, a set of optimal solutions arises as opposed to one optimal solution. Because of this, applications of EA in structural engineering are often referred to as generative

design, which is the act of generating thousands of design iterations with the intent of having an engineer choose one solution from a set of optimal solutions.

Over the last decade, numerous EA have been developed as technology rapidly advances and the field of AI becomes more prominent. For this study, a sorting-based multi-objective EA called nondominated sorting genetic algorithm II (NSGA-II) is used [5].

NSGA-II solves multi-objective optimization problems (MOPs) through Pareto dominance and a sorting procedure known as non-dominated sorting. A solution is considered to dominate another solution if all its fitness values, determined from the user-defined objective criteria, are lower than or equal to another solution's fitness values. For the proposed optimization tool, the fitness values are based on the demand-to-capacity ratios determined through the two analysis methods. An example of non-dominated sorting for a double objective problem is illustrated in Fig. 3. During non-dominated sorting, solutions are compared against each other and are assigned ranks based on dominance. Lower ranks refer to better fitness values and are associated with solutions that have higher dominance. In MOPs, a solution is said to be a Pareto optimal solution if it is not dominated by any other solution of the MOP. There exists more than one Pareto optimal solution for an MOP due to the conflicting nature of objectives. The projection of Pareto optimal solution set in objective space is called the Pareto front. At each generation of NSGA-II, non-dominated sorting is first employed to select solutions with lower ranks from the parent and offspring population, and crowding distance is used as the secondary metric to distinguish solutions in the same rank by favouring solutions with a large crowding distance [16].

Within the optimization tool, NSGA-II is utilized through Wallacei [11], an evolutionary engine that allows users to run evolutionary simulations in Grasshopper. Wallacei employs a simple user interface, as shown in Fig. 4, to run the NSGA-II based on user-defined objective criteria and parameters. The engine can then be used to analyze the results and export phenotypes.

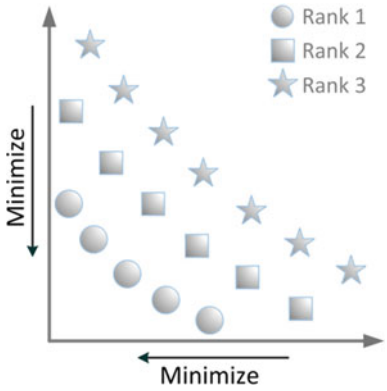

Fig. 3 Illustration of non-dominated sorting with the population divided into three ranks [16]

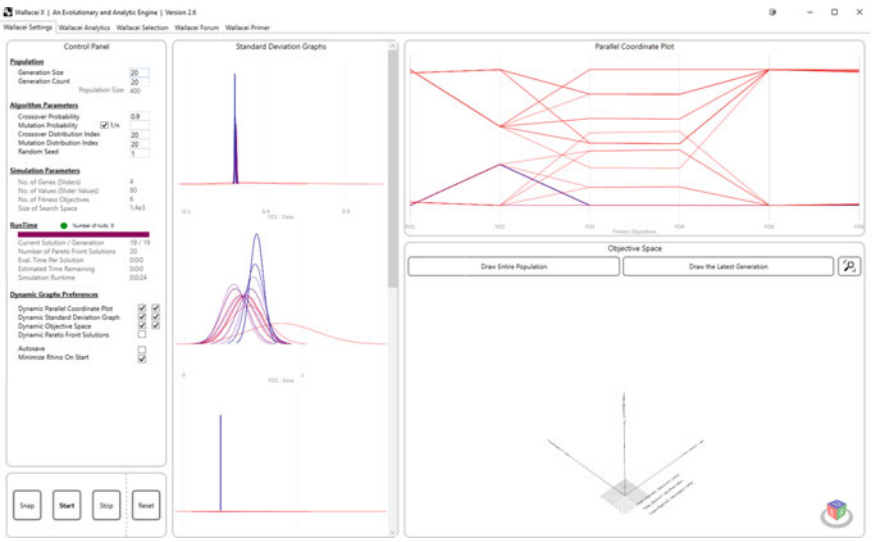

Fig. 4 Wallacei evolutionary engine user interface

To use the evolutionary solver, the user must define a set of genes (parameters) and fitness objectives (optimization criteria). The fitness objectives are represented by values that the user aims to minimize. If the user wishes to maximize a fitness objective, the value must be inversed. For instance, if the user wishes to minimize the fitness objective x, the value should be represented as x. However, if the user wishes to maximize the fitness objective y, the value should be represented as 1/y. The accuracy and duration of the optimization process is determined by the generation size and count specified. Generation size refers to the number of offspring produced for every generation, while generation count refers to the number of generations produced overall. For example, if the user specifies a generation size of 20 and a generation count of 30, the total population produced will be 600. For every generation, the EA evaluates the populace against the defined fitness objectives. Offspring with parameters that favour the defined fitness objectives are crossbred together, while the others are discarded. This process is repeated for the specified generation count with the intent of producing a set of optimal solutions from which the user chooses the most appropriate solutions. Figure 5 showcases the individuals generated for a single generation during the optimization process of a shear end plate connection.

2.4 Standards-Based Solution (Limit States Design)

The optimization tool is split into two design methodologies: a standards-based solution using limit states design and a solution determined through CBFEM. The standards-based solution is derived from the provisions of CSA S16-19. Limit states

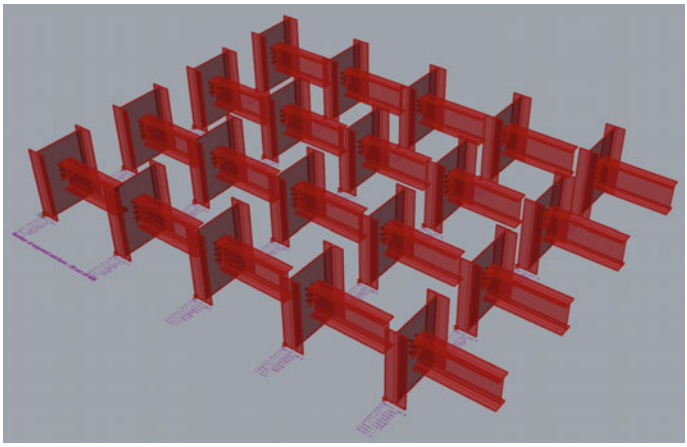

Fig. 5 Solutions generated using the optimization tool for a shear end plate connection through Wallacei

that are not covered in CSA S16-19 are supplemented by equations defined in AISC 360-16 [1].

Due to the simplistic nature of common shear connections, limit states design is relatively straight forward, requiring few computational resources for the evolutionary solver to generate a solution. This drastically decreases the overall optimization duration in comparison to the finite element (FE) based solution. However, the standards-based solution is limited to simple steel connections, as standards provisions may not be adequate for complex connections requiring design software.

The optimization criteria presented for the standards-based solution aims to maximize the demand-to-capacity ratio, while maintaining a ratio equal to or less than 1.0 to satisfy strength requirements.

2.5 Finite Element-Based Solution

The FE-based solution of the optimization tool uses IDEA StatiCa [10], a connection design software that utilizes CBFEM. CBFEM is a combination of the component method and the finite element method. The component method is a technique whereby components are individually modelled as complex springs that reflect the strength, stiffness, and deformation capacity of the component, and the behaviour of a joint can then be determined by assembling the individual components with help of mechanical models [15]. CBFEM removes the restrictions and most simplifications used in the component method. In CBFEM, plates are modelled by shell elements, while the components, e.g., bolts or welds, are modelled by nonlinear springs with their properties based on design codes and research. CBFEM provides code checks

of failure modes that may not be captured by finite element analysis alone, such as weld fracture [14].

Although finite element analysis is a powerful analysis method for simple steel shear connections, the time required for the evolutionary solver to generate a single solution can become significantly greater in comparison to the standards-based solution. Similar to the standards-based solution, the optimization criteria presented for the FE-based solution aims to maximize the utilization ratio of the bolts and welds, and the plastic strain of the plate while remaining below a certain threshold to satisfy strength requirements.

3 Shear End Plate Connection Case Study

The optimization tool is used to design a shear end plate connection. The results are then be compared against the design from the Handbook of Steel Construction. The end plate connection consists of a W410 × 60 beam framing into the web of a W760 × 134 girder, both of ASTM A992 steel, with a factored reaction of 325 kN. The connection material consists of a G40.21 Grade 300 W steel plate, ¾ in. (19.1 mm) diameter ASTM A325 bolts, and E49XX electrodes. Both the FE- and standards-based solutions are evaluated.

The end plate is assumed to have sheared edges with an edge distance rounded up to 35 mm. An 80 mm bolt pitch is used. Input parameters for the optimization tool are shown in Fig. 6(a). The generation size and count are both set to 20. The plate thickness parameter ranges from 6 to 10 mm, as suggested by the Handbook of Steel Construction, to obtain adequate flexibility. Furthermore, the number of bolt rows range from 2 to 4, which is compatible with the bolt pitch and depth of the

Fig. 6 **a** Parameters inputted in the user interface for the optimization process **b** Wallacei interface using the standards-based solution, **c** Wallacei interface using the FE-based solution

beam. Finally, the fillet weld size ranges from 3 to 10 mm. Although the minimum and maximum fillet weld sizes are constrained by parameters such as the end plate thickness and girder-web thickness, these constraints were ignored for this study to expand the search space of the EA.

3.1 Standards-Based Solution Results

In the standards-based solution, the factored reaction is divided by each limit state capacity to obtain the demand-to-capacity ratio. The results are then inversed and any values below 1.0 are filtered out as null solutions, which are ignored by the EA. Thus, any connection design that the user exports from the optimization results will be one that satisfies strength requirements. It should be noted that implementing null solutions into the design problem should be avoided unless the user understands its origins. Optimization parameters used in the evolutionary solver are shown in Fig. 6(b).

After the optimization is complete, the user can export any solution to display the resulting fitness values and parameters, as shown in Fig. 7, wherein the three data inputs refer to the plate thickness (mm), number of bolt rows, and fillet weld size (mm), respectively. Every solution can be plotted onto a parallel coordinate plot, as shown in Fig. 8. The solution highlighted in black in the figure represents the solution with the lowest average inversed demand-to-capacity ratio of all the limit

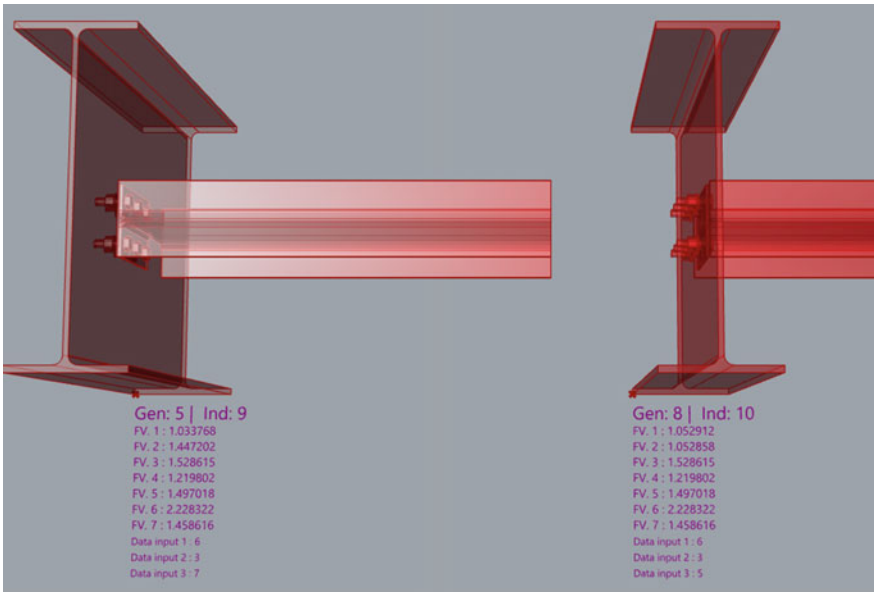

Fig. 7 Fitness values and parameters of individuals generated through the standards-based solution

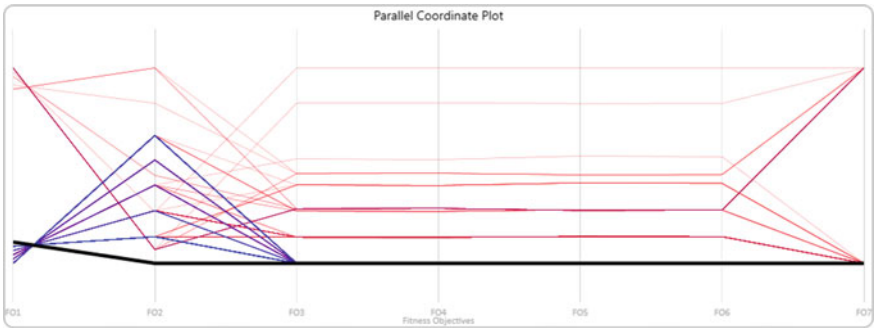

Fig. 8 Parallel coordinate plot of the solutions generated through the standards-based solution

states considered. This represents the solution with the highest demand-to-capacity ratio not exceeding 1.0. For this study, this solution is considered to be the optimal solution. The optimal design determined from the standards-based solution is an end plate connection with plate size PL170 × 6 × 230 mm, 3 rows of bolts with a gauge distance of 100 mm.

3.2 Finite Element-Based Solution Results

The FE-based solution uses results from the connection design software to determine the fitness values. Three fitness objectives are defined for the FE-based solution including maximizing the plastic strain of the plate while remaining below 5%, maximizing the utilization of the bolts while remaining below 100%, and maximizing the utilization of the weld while remaining below 100%. The limiting value of 5% for the plastic strain is suggested in the Eurocode [8]. To quantify the fitness objective for the plate strain, the results are divided into 5, while any results below 1.0 are discarded. Similarly, to quantify the fitness objective for the bolt and weld utilization, the results are divided into 100, while any results below 1.0 are discarded. Optimization parameters for the FE-based solution are identical to those for the standards-based ones shown in Fig. 6(c).

The parallel coordinate plot of the optimization process is shown in Fig. 9. Similar to the standards-based solution, the optimal solution using the FE-based method is an end plate connection with plate size PL170 × 6 × 230 mm, 3 rows of bolts with a gauge distance of 100 mm, as shown in Fig. 10.

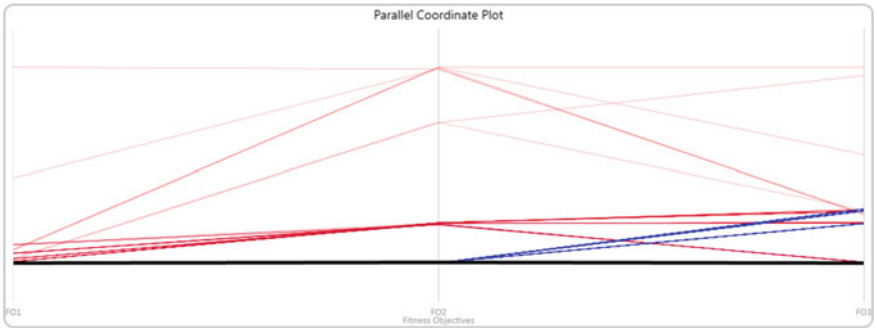

Fig. 9 Parallel coordinate plot of every solution generated through the FE-based solution

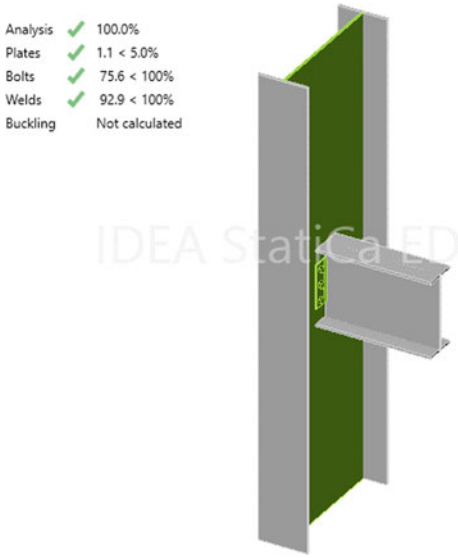

Fig. 10 Verification of the optimal design of an end plate connection using IDEA StatiCa

3.3 Evaluation of Two Solution Approaches

It can be shown that even through a parametric study, the FE- and standards-based solution both result in the same answer given the same parameters and objective criteria. The solution in the example given in the Handbook of Steel Construction specifies a PL160 $\times$ 6 $\times$ 230 mm end plate connection. The difference between the solution obtained through the optimization tool and what is specified in the Handbook is the plate size. In the optimization tool, the plate is assumed to have sheared edges which requires a slightly larger edge distance, resulting in a larger plate width. Although the design given in the Handbook is not necessarily an optimized solution, it is encouraging that the results for both solutions match.

Even though the FE- and standards-based solutions gave an identical connection design, the optimization runtime for the standards-based solution was 22 s, while the runtime for the FE-based solution was more than 85 min, as shown in Figs. 6(b) and (c). This indicates that the standards-based solution may be more favorable for such simple shear connections.

Ideally, MOPs should have thousands of generations and generation sizes to ensure that the optimization process converges to an optimal set of solutions. However, due to simplistic nature of the problem in this study, only a small number of individuals were generated: 400. It should be noted that the search space for this study includes only 120 possible solutions. This means that there are individuals produced with identical genes. However, this does not indicate that every possible solution was searched during the optimization process. As the EA searches for an optimal set of solution, Pareto optimal solutions can be the same if the gene pool is relatively small.

4 Potential and Drawbacks

Although the shear end plate connection explored in this paper utilizes few parameters and a simple objective criterion, the proposed tool has the capability to parametrize additional connection details such as bolt pitch, edge distance, and add additional bolt columns. The objective criteria can also be expanded to reduce net fabrication and erection costs by considering material, labour, fabrication and erection constraints, machinery availability, and available inventory based on the steel fabricator's preferences. All these additions can provide instant feedback to designers on how certain changes affect cost and constructability, while allowing for the automated design of connections.

By combining the optimization capabilities of EA with CBFEM, this tool can be extended to encompass more complex connections. Leveraging connection design software through this tool streamlines the design process as users only need to check the output of the connection design software. One drawback to using CBFEM for analysis is the long optimization time which would be increased for complex connections. This process, however, can be exported to external servers to be run on cloud computers, greatly reducing the optimization runtime, or the number of objective functions can be refined to achieve a more efficient design process. Increasing the efficiency of the software itself can also reduce the optimization runtime. For example, the software could be programmed to not fully analyze a solution if the early analysis results are not within a certain threshold.

Solving MOPs are not limited to NSGA-II; there are countless multi-objective EA and other algorithms that can be used to optimize structural steel connections. For example, the particle swarm optimization, an algorithm that mimics the unpredictable nature of a bird flock to determine an optimal solution [6], can also be used.

Additional add-ons such as integration of structural models to allow users to import member sizes and pass-through forces directly into the optimization tool can provide another level of automation to a typical connection design workflow. Connection

designers could import, design, optimize, and export multiple optimal solutions that suit their preferences in a matter of minutes through an entirely automated process. This would aid in addressing the issue of constantly adjusting designs due to changes that arise throughout the life cycle of a project.

5 Conclusions and Future Work

Automated optimization of structural steel connections can be achieved through evolutionary algorithms and parametric modelling. This paper focuses on the optimization of a shear end plate connection design through an optimization tool proposed here, which takes advantage of both limit states design and finite element modelling approaches. The results of the optimization of the shear end plate connection are nearly identical with the example end plate connection given in the Handbook of Steel Construction. Although only the demand-to-capacity ratio of the connection was optimized in this study, it showcases the application of generative design and EA within the steel construction industry. The advantages of using these optimization processes include reducing the number of re-designs during the lifecycle of a project, minimizing connection costs, reducing repetitive tasks in connection design, and providing designers with feedback on how certain changes affect other parameters within a steel connection.

Additional parameters should be added in future to better represent the realistic design process of a connection designer. With the help of Canadian steel fabricators and connection designers, additional objective criteria such as reducing material, crane operation, welding, labor, and energy costs can all be implemented into the tool. A case study can be performed in partnership with Canadian steel fabricators to verify optimization results and determine the applications of this optimization tool in industry practice. Implementation of the ability to export joints from structural models can also further automate connection design, drastically improving the typical workflow. This tool can finally be extended to encompass utilizing other AI techniques and compare the optimization speed between different algorithms.

References

1. American Institute of Steel Construction (AISC) (2016) Specification for structural steel buildings (ANSI/AISC 360-16). IL, USA
2. Bagavathi C, Saraniya O (2019) Deep learning and parallel computing environment for bioengineering systems. Elsevier Academic Press, New York
3. Canadian Institute of Steel Construction (CISC) (2017) Handbook of steel construction, 11th edn, Ontario, Canada
4. Canadian Standards Association (CSA) (2019) Design of steel structures (CAN/CSA Standard No. S16-19), Ontario, Canada
5. Deb K, Pratap A, Agarwal S, Meyarivan T (2002) A fast and elitist multi-objective genetic algorithm: NSGA-II. IEEE Trans Evol Comput 6(2):182–197

6. Eberhart R, Shi Y (2001) Particle swarm optimization: developments, applications and resources. In: Proceedings of the 2001 congress on evolutionary computation, Seoul, South Korea, pp 81–86
7. Ebrahim K, Sadegh A, Atefeh M (2020) Applying artificial intelligence within the AEC industry: collecting and interpreting data. In: Proceedings of the 2020 construction research congress (CRC). ASCE, Reston, VA
8. European Committee for Standardization (CEN) (2005) Eurocode 3: design of steel structures – Part 1-1: general rules and rules for buildings (EN1993-1-5), Belgium, Brussels
9. Greco L (2018) Machine learning and optimization techniques for steel connections. In: Proceedings of IASS annual symposia, IASS 2018 Boston symposium: metal gridshell structures, connections and stability. International Associated for Shell and Spatial Structures (IASS), Madrid, Spain
10. IDEA StatiCa (2021) IDEA StatiCa connection. V. 20.1.5115,1 IDEA StatiCa. Windows
11. Makki M, Showkatbakhsh M, Song Y (2019). Wallacei primer 2.0. [Online] https://www.wallacei.com/
12. Oosterhof S, Driver R (2014) Behaviour of steel shear connections for assessing structural vulnerability to disproportionate collapse. Steel Centre engineering Report no 003. Steel Centre, Edmonton, Alberta
13. Robert McNeel & Associates (2021) Rhinoceros3D. V. 7.3. Robert McNeel & Associates. Windows
14. Sabatka L, Wald F, Kabeláč J, Gödrich L, Navrátil J (2014) Component based finite element. Model of structural connections. In: 12th international conference on steel, space and composite structures. CL-Premier Pte Ltd, Praque
15. Steenhuis M, Jaspart JP, Gomes F, Leino F (1998) Application of the component method to steel joints. In: Proceedings of the COST C1 international conference, publications office of the European communities, Liege, Belgium, vol 18854, pp 125–143
16. Tian Y, Wang H, Zhang X et al (2017) Effectiveness and efficiency of non-dominated sorting for evolutionary multi- and many-objective optimization. Complex Intell Syst 3:247–263

Considering Non-stationary Loading Due to Climate Change in the Reliability Analysis of Structures

Mohammad Barkhori and Scott Walbridge

1 Introduction

Different climate systems regulate the natural environment of our planet. Any disturbance to the harmony of these systems, natural or man-made, is a threat not only to natural ecosystems but also socio-economic ecosystems through complex cascading effects. In recent years, changes in the average temperature compared to historical data have provided pronounced evidence of climate change, which is attributed to the increase of GHG emissions. According to the Intergovernmental Panel on Climate Change (IPCC), by the end of the twenty-first century, the mean global temperature might rise from 1.5 to 4 °C above the 1850–1900 average depending on different considered emission scenarios [8]. Such a change may impact precipitation and snowfall patterns, and the occurrence of high winds and other extreme weather loading events. These changes can affect the performance of infrastructure in different ways: (1) higher intensity and frequencies of extreme events such as flooding and wind can reduce the reliability of infrastructure systems; (2) it can result in faster deterioration rates and, as a result, reductions in the service life of infrastructure; and (3) it can necessitate changes in the allowable capacities of infrastructure systems (e.g. bridge scour can cause a reduction of the capacity of foundations piles, which might require closure to traffic). As a result, the effect of climate change on different infrastructure systems has attracted the attention of many researchers in recent years in a variety of disciplines. In this regard, several research studies indicate that even small changes in the global climate might have great impacts on long-term structural reliability. Despite this growing body of knowledge, studies on prioritizing adaptation measures are lacking. It is noteworthy that there is always a limit to the expendable resources for adaptation. Therefore, identifying infrastructure systems with higher failure consequences and sensitivity to climate change can help authorities with decision making and planning. In an effort to contribute to broader initiatives aimed at

M. Barkhori (✉) · S. Walbridge
Department of Civil and Environmental Engineering, University of Waterloo, Waterloo, Canada
e-mail: mbarkhor@uwaterloo.ca

S. Walbridge et al. (eds.), *Proceedings of the Canadian Society of Civil Engineering Annual Conference 2021*, Lecture Notes in Civil Engineering 244,
https://doi.org/10.1007/978-981-19-0656-5_24

achieving this goal, the current paper describes and demonstrates several possible approaches for considering non-stationary load effects in the reliability analysis of structures.

2 Reliability Analysis

2.1 Failure Probability and Design Load Factors

In order to design engineered components and systems (including structures) properly, it is essential to consider the uncertainties involved in the demands on these components or systems and their capability in responding to these demands. Reliability methods can be employed to address this need. In this context, defining the limit state function as the demand, S, minus the capacity, R, (i.e., $G = R - S$), failure occurs when $G \leq 0$ [7]. Several reliability methods, including: Monte Carlo Simulation (MCS) and first and second-order reliability methods are available for analyzing probability of failure. However, due to the complexity of applying such methods in general engineering practice, other methods such as Limit States Design (LSD) are implemented in design codes to ensure safety.

2.2 Load Factors and Reliability Index

This section demonstrates the mathematical relation of load factor and reliability index (β), which is related to the probability of failure through the following equation:

$$p_f = \Phi(-\beta) \tag{1}$$

In general design problems, the demand on the engineered component or system usually involves a combination of different loads, each of which is given its load factor in modern design codes. The simultaneous presence of dead and wind load effects on a structure is a simple example of such a condition. In this regard, the limit state function can be redefined as $G = R - (D + W)$ where D and W are random variables representing dead and wind load effects. Accordingly, given the nominal design values, the reliability index can be mathematically computed through the following equation:

$$\beta = \mathrm{LN}\left(\Omega\sqrt{\frac{1+\varsigma_{z_W}^2}{1+\varsigma_{z_U}^2}}\right)/\sqrt{\mathrm{LN}\left[\left(1+\varsigma_{z_W}^2\right)\left(1+\varsigma_{z_U}^2\right)\right]} \tag{2}$$

Here, $U = R - D$, and Ω is given in Eq. (3), in which $\alpha_{w,}$ α_D, and ϕ_R denote wind load factor, dead load factor and resistance factor, respectively:

$$\Omega = \frac{\overline{z}_R}{\overline{z}_W \phi_R}\left[\alpha_W - \frac{D_n}{w_n}\left(\frac{\phi_R \overline{z}_D}{\overline{z}_R} - \alpha_D\right)\right] \tag{3}$$

where the mean value of each variable is denoted by a bar (e.g. $\overline{z}_D$) while their COV is denoted with a ς, and their standard deviation is shown by σ. In this paper, the lognormally distributed random variables for load and resistance are replaced by normalized variables for simplification purposes:

$$z_R = \frac{R}{R_n}, z_W = \frac{W}{W_n}, z_D = \frac{D}{D_n}, z_U = \frac{U}{U_n} \tag{4}$$

where the 'n' subscript denotes "nominal value".

2.3 Time-Dependent Reliability Analysis Considering Climate Change Effects

The current design of engineered components and systems is generally based on an assumption of stationarity of loads and resistance over their lifetime. However, the projected changing weather stressors over the lifespan of infrastructure systems demands a method capable of capturing the relevant non-stationary essence of loading in calculating future reliability and service life. In this regard, Eq. (5) provides the time-dependent reliability (i.e. the probability of survival) of ageing structures in the presence of non-stationary loads and degradation during a time interval of (0, t) [5]:

$$L(t) = \mathrm{EXP}\left\{-\int_0^t \lambda(\zeta)[1 - F_s(R(\zeta))]\mathrm{d}\zeta\right\} \tag{5}$$

where $F_S()$ represents the cumulative distribution function (CDF) of demand. While $\lambda(\zeta)$ and $R(\zeta)$ respectively denote the time-varying occurrence rate of the loading and resistance functions. It is worthwhile to note that $[1 - F_S\,(R(\zeta))]$ is the instantaneous failure probability at time ζ. Depending on the considered hazard type, parameters of $F_S()$ can be redefined so the occurrence of loading forms a Homogenous Poisson Process with the time-independent occurrence rate, λ. In such a case, by discretizing time to years, Eq. (5) can be simplified as follows:

$$L(t) = \mathrm{EXP}\left(-\sum\nolimits_{i=1}^{N} \lambda P_i\right) \tag{6}$$

In which P_i denotes probability failure during the i^{th} year, and N is the number of years in time interval (0, t).

3 Illustrative Example

In this section, the effects of nonstationary wind loading, as one of the climatic stressors on the performance of a structural element located in London, Ontario, Canada is investigated. It is assumed that the element is a flexural member on a bridge, and fails when the flexural moment in it surpasses its capacity. Nevertheless, the employed method is general and applicable to other structural elements and load types. In this example, wind pressure and dead load effects are the only stressors, and strength deterioration is negligible during the service life. The element is designed based on an LSD approach and fails when the stochastic values of wind and dead load surpass the randomly distributed resistance.

3.1 Limit State Function and Design Load Combination

According to the Canadian Highway Bridge Design Code [3] a bridge component with nominal flexural resistance R_n can be designed according to the following condition:

$$\phi R_n > \alpha_W W_n + \alpha_D D_n \tag{7}$$

where, W_n and D_n are nominal values for the wind and dead load flexural effects on the component, and α_W, α_D, and ϕ represent the wind load, dead load, and resistance factor, respectively. Considering the load effect and factor values in Table 1, a component with the nominal resistance of $R_n = 505$ kN·m is satisfactory according to Eq. (7).

The component fails when the stochastic values of wind and dead load surpass the randomly distributed component resistance. The limit state function can be defined as:

$$G = z_R R_n - (z_w W_n + z_D D_n) \tag{8}$$

In the next section, the procedure for calculating the mean and standard deviation of these parameters is presented.

Table 1 Loads and load factors

α_W	α_D	ϕ	W_n	D_n
1.4	1.1	0.95	200 kN·m	200 kN·m

3.2 Load and Resistance Models

3.2.1 Resistance Model

The flexural resistance of the component is assumed to be a linear function of $F_y \cdot S$, where F_y and S are the yielding strength of the material and section modulus with related bias coefficients of z_{Fy} and $z_{S,}$ respectively. The component resistance model exhibits error in the prediction of the exact value of resistance, which can be represented with random variable z_{Mod}. Therefore, the combined bias coefficient for resistance can be calculated as follows:

$$z_R = z_{Mod} z_{Fy} z_S \tag{9}$$

Assuming independence of the variables in Eq. (9), the mean and variance of z_R can be computed, according to the following equations:

$$\overline{z}_R = \overline{z}_{Mod}\overline{z}_{Fy}\overline{z}_S,\ var_R = \prod_{i=1}^{3}(var_{zi} + \overline{z}_l^2) - \prod_{i=1}^{3}\overline{z}_l^2 \tag{10}$$

Table 2 presents the values of mean and COV of the variables used to define the resistance model [2].

3.2.2 Dead Load Model

The bias factor of the dead load is assumed to have a mean of 1.03 and COV of 0.08, based on [2, 6].

3.2.3 Wind Load Model

According to [2], the design horizontal wind load pressure can be calculated as:

$$p = C_e C_g C_h q \tag{11}$$

where C_e, C_g, and C_h are exposure, gust effect, and horizontal effect coefficients and q is the air pressure, which is related to the wind velocity (V) through the following equation:

$$q = \frac{1}{2}\rho V^2 = CV^2 \tag{12}$$

where ρ is the density of air. If V is in km/h, the constant $C = 0.05$ can be used to compute q in Pa. Defining a_C as the analysis coefficient for the conversion of the

Table 2 Resistance model parameters

Variable	Mean	COV
z_{Fy}	1.06	0.051
z_S	0.99	0.021
z_{Mod}	1.09	0.045
z_R	1.14	0.071

wind load into a load effect and A as the exposure area, the general equation for the wind load effect is:

$$W = a_C C_e C_g C_h C V^2 A \tag{13}$$

According to [2], the mean and COV of the wind bias coefficient can be computed using the following equations:

$$\overline{z}_W = \overline{z}_{a_C} \overline{z}_{C_e} \overline{z}_{C_g} \overline{z}_{C_h} \overline{z}_C \overline{z}_{V^2} \overline{z}_A \tag{14}$$

$$\varsigma_{z_W} = \sqrt{\varsigma^2_{z_{a_C}} + \varsigma^2_{z_{C_e}} + \varsigma^2_{z_{C_g}} + \varsigma^2_{z_{C_h}} + \varsigma^2_{z_C} + \varsigma^2_{z_{V^2}} + \varsigma^2_{z_A}} \tag{15}$$

The statistical values of the parameters used in this study to define wind loading are adopted from [2] and presented in Table 3. It is noteworthy that the values for z_{V^2} in this table represent climate conditions in the Year 2000.

The values defining the distribution of wind velocity during extreme events mostly rely on statistical analyses of historical weather data. However, new studies predict the deviation of these values from historical data in future decades. The following section discusses the procedure used for the computation of the parameters of the wind velocity distribution.

3.2.3.1 Wind Velocity

According to [4] the probability distribution of maximum hourly wind speeds can be modelled with an Extreme Value Type I (or Gumbel) distribution, as follows:

$$F_V(v) = P(V \leq v) = \text{EXP}\{-\text{EXP}[-a(v - \mu)]\} \tag{16}$$

where a and μ are the scatter and central tendency of the distribution. The mean $\overline{V}$ and standard deviation σ_V of the distribution can be computed using Eqs. (17) and (18).

$$\sigma_V = 1.282/a \tag{17}$$

Table 3 Statistical parameters used in defining wind load

Variable	Mean	COV
z_C	1.00	0.025
z_{C_e}	1.00	0.080
z_{a_C}	1.00	0.050
z_A	1.00	0.000
z_{V^2}	0.332	0.587
z_{C_h}	0.71	0.140
z_{C_g}	1.02	0.075
z_W	0.24	0.616

$$\overline{V} = \mu + 0.577/a \tag{18}$$

Indicating the return period of the extreme wind event in the subscript (e.g., a_1, μ_{100}), the statistical parameters of the annual maximum hourly wind speed (i.e., a_1, μ_1) can be calculated through [2]:

$$a_1 = [\mathrm{LN}\left(\frac{100}{10}\right)]/[\overline{V}_{100} - \overline{V}_{10}],\ \mu_1 = \overline{V}_{10} - [\mathrm{LN}(10) + 0.577]/a_1 \tag{19}$$

where the values of $\overline{V}_{10}$ and $\overline{V}_{100}$ are available in [3].

3.2.3.2 Square of Wind Velocity

The distribution for the 75-year wind velocity is derived in the previous section. However, according to Eq. (12), the reference wind pressure depends on the square of the wind velocity, which requires the transformation of the distribution of wind velocity to the distribution of the square of wind velocity. As load and resistance usually follow lognormal distributions, fitting a lognormal distribution to the square of the velocity is reasonable. This process begins with finding the parameters of maximum hourly wind speed, a and μ, and generating data for the wind speed and then its square based on the CDF of maximum hourly wind speed given in Eq. (16). Then, a lognormal distribution can be fitted to the upper tail (right-hand side) of the generated data through the probability paper plotting method.

3.3 Climate Change Projections

This section discusses future weather projections considered in this study. Several global climate models (GCMs) and regional climate models (RCMs) are available to make projections of future climate. The uncertainties involved in these projections arise from different factors. To capture the uncertainty of future climate change trends due to human behaviour, [9] suggests considering four different Representative Concentration Pathways (RCPs) covering a range of low (RCP 2.6) to high (RCP 8.5) for future emissions. A separate study by Environment and Climate Change Canada (ECCC) provides the predicted changes in climatic variables for different locations and RCP scenarios to facilitate the development of climate-resilient codes and standards for Canada's Buildings and Core Public Infrastructure (B&CPI) [1]. Using the projections of ECCC, the changes in the 10-year and 100-year wind pressures for London, Ontario are evaluated for various RCP levels during the twenty-first century and presented Fig. 1. Additionally, using this figure and Eqs. (14) and (15), the mean and COV of the annual wind load bias on the considered member are determined and depicted in Fig. 2.

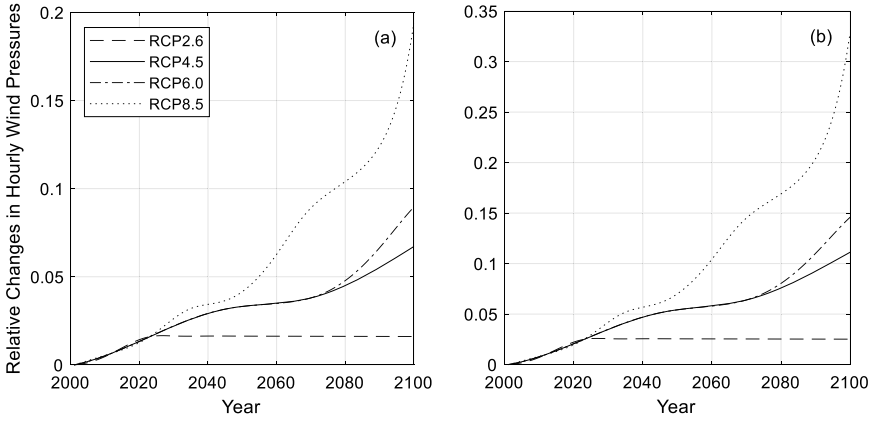

Fig. 1 Changes in wind pressures for London, Ontario in the 21st century. **a**, 10-year wind pressures, and **b**, 100-year wind pressures

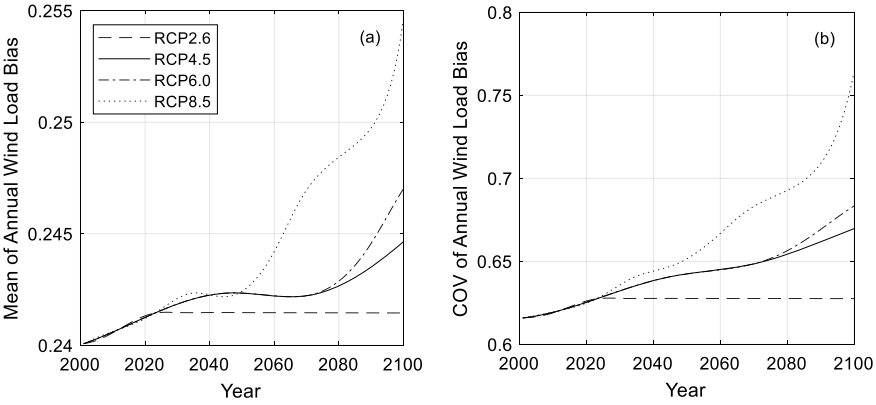

Fig. 2 Changing properties of wind load on the bridge member. **a**, mean of annual wind load bias, $\overline{Z}_W$, and **b**, COV of the annual wind load bias, ς_{zW}

3.4 Probability of Failure

In this section, probabilities of failure of the case study structure are calculated with various climate change scenarios considered. Given the changes in wind pressures, the inverse of Eq. (12) is used to translate 10-year and 100-year level wind pressures to wind velocities (i.e. $\overline{V}_{10}$ and $\overline{V}_{100}$). These values are then substituted in Eq. (2) to determine distributions of the annual maximum wind speeds. To compute wind load effect distribution parameters, the procedure explained in Sect. 3.2.3 is applied. Equations (2) and (1) are then used to calculate time-varying annual reliability indices

and probabilities of failure, according to the changes in the annual wind load statistical parameters for each scenario.

3.4.1 Annual Probability of Failure

Figure 3 presents the annual probability of failure of the structure under the nonstationary increasing wind loads associated with different RCP scenarios for the service life of a structure constructed in the Year 2000. It is worth noting that the curve for RCP4.5 is neglected as it is so close to the RCP6.0 curve. As expected, RCP2.6 and RCP8.5 respectively result in the lowest and highest changes in the reliability. Under all scenarios, the probability of failure begins with $4.6{\cdot}10^{-5}$ in the first year of service in the Year 2000, and constantly increases through 2023 to $5.6{\cdot}10^{-5}$. Then while the RCP2.6 curve remains constant until the end of this century, the RCP6.0 and RCP8.5 curves continue growing to $1.6{\cdot}10^{-4}$ and $4.7{\cdot}10^{-4}$, which is equivalent to 248 and 921% growth compared to the beginning year of service.

3.4.2 Cumulative Probability of Failure

The lifetime reliability of the structure, $L(T)$, is calculated using Eq. (6) in which P_i is the annual probability of failure of the i^{th} year under maximum annual wind loading ($\lambda = 1$). As reliability can be thought of as a measure of the probability of survival, the cumulative probability of failure through the j^{th} year of service (P_{T_j}) can be easily computed using the following equation:

$$P_{T_j} = 1 - L(T) = 1 - \text{EXP}\left(-\sum_{i=1}^{j} \lambda P_i\right) \tag{20}$$

Figure 4 shows the cumulative probability of failure versus time. In these figures, the solid green line is drawn as a reference and is related to a scenario in which the wind loading is stationary and without change for 100 years. The other lines are related to different RCP scenarios. As shown, the cumulative probability of failure of the structure under all the global warming scenarios is larger than the one assuming stationarity of the wind loading over the analysis period. For instance, for a structure established in the Year 2000, with a design service life of 75 years, the total probability of failure over the duration of the servce life for RCP8.5 is $6.48{\cdot}10^{-3}$, which is 1.89 times that of the stationary scenario ($3.43{\cdot}10^{-3}$).

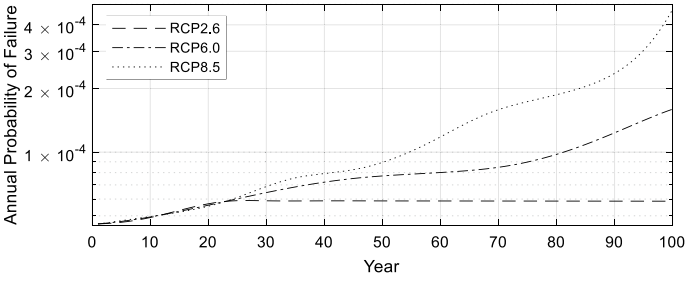

Fig. 3 Annual probability of failure for the case study flexural member in London, Ontario

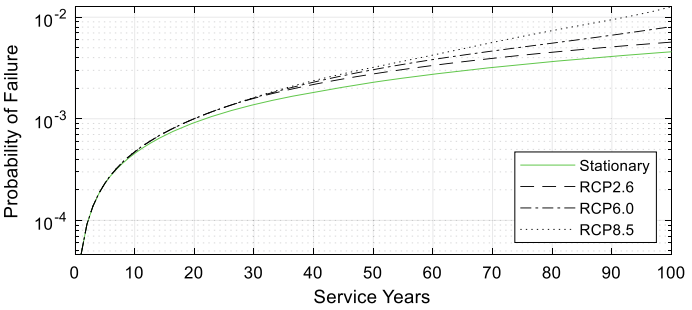

Fig. 4 Cumulative probability of failure for different RCPs

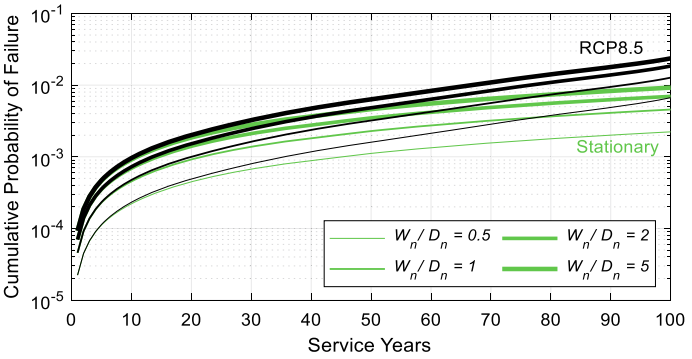

Fig. 5 Comparison of cumulative probability of failure of various structures with different wind/dead load ratio under stationary load condition and RCP8.5 scenario

To evaluate the effects of the ratio of the nonstationary (wind) to stationary (dead) load ratio on the probability of failure, a sensitivity study was performed, the result of which is depicted in Fig. 5. In this figure, two groups of green and black curves respectively represent the cumulative probability of failure of the structure under the stationary and RCP8.5 scenarios. In each group, there are four curves for different values of wind-to-dead load ratios (WDR), covering a range of 0.5–5 where the upper limit is realistic for aluminum structures designed with light weight in mind. As shown, the curves for structures with larger WDRs (the thicker curves) are higher for both groups, meaning that these structures are relatively more prone to failure even though the design basis is the same under all WDRs. However, the probability of failure of the structures with lower WDRs is slightly more sensitive to future climate changes. For instance, at the 75th year of service, the probability of failure of a structure with WDR = 5 grows by 80% ($6.93{\cdot}10^{-3}$ to $1.25{\cdot}10^{-2}$) under the RCP8.5 compares to the stationary condition, while for a structure with WDR = 0.5 under the same conditions otherwise, the change is 98% ($1.67{\cdot}10^{-3}$ to $3.30{\cdot}10^{-3}$).

Figure 6 shows the probability of failure sensitivity to changes in the mean and standard deviation of the annual maximum wind speed. In this analysis, a 1:1 wind-to-dead load ratio is assumed. The solid green line represents the probability of failure under stationary conditions. The other lines consider a linear annual increase to reach a change in the parameter of interest in Year 100 (i.e., a 10 or 20% increase). As can be seen in this figure, the curve for a 10% increase in the standard deviation is above the curve for a 10% change increase in the mean. The same is true for the 20% increase curves. This suggests probability of failure is more sensitive to changes in the standard deviation in the wind speed than its mean.

All the previous analyses were performed using the mathematical approach (i.e., closed form expressions) described in this paper. This approach ignores the correlation of load and resistance from one year to the next. To evaluate the effect of correlation of the load and resistance parameters in successive years of service, a Monte Carlo simulation (MCS)-based approach was employed, the result of which is depicted in Fig. 7 for the RCP8.5 climate change scenario. The applied MCS involves many trials, each of which assesses the limit state function, for every single

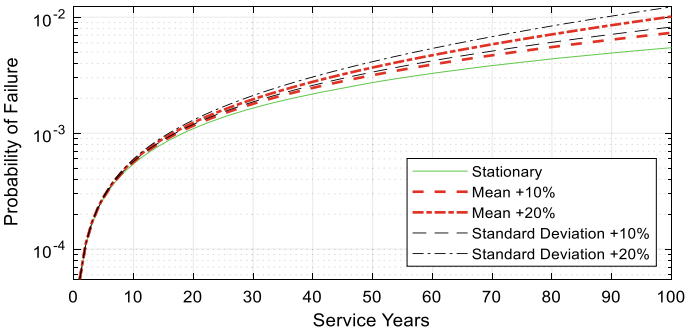

Fig. 6 Sensitivity to the increase in annual maximum wind speed parameters

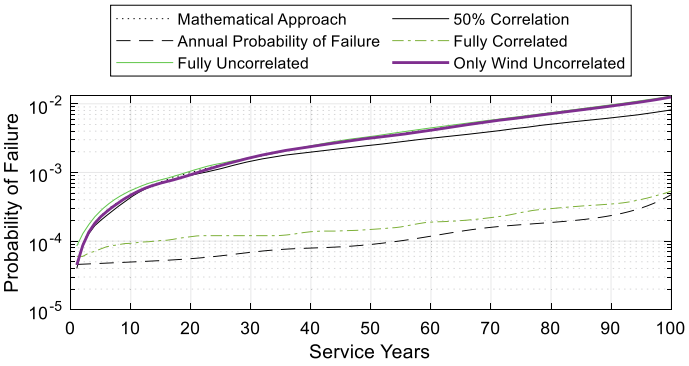

Fig. 7 Effect of correlation of random variables between adjacent years (RCP8.5)

year of service. The correlation of variables in different years is modelled by a correlation matrix, R(X), in which $X = [x_1, x_2, \ldots, x_n]$ is the vector of random variables in different years (e.g., wind load effect in successive years of service) and the element r_{xixj} defines the correlation between variables in i^{th} and j^{th} year. Considering the structure as a non-repairable system, the first service year where the loads exceed the resistance is recorded as the failure year in that trial. Then the generated data for the failure year is used to capture the cumulative distribution function of failure time. The black dot and black dash lines in Fig. 7 respectively show the cumulative and annual probabilities of failure predicted by the so-called "mathematical approach". The other four curves depict the cumulative probabilities of failure generated by MSC with various assumptions about the correlation of random variables (i.e., resistance, wind load effect, and dead load effect) in successive years of service.

Generated under the assumption the loads and resistance in different years are completely independent, the "Fully Uncorrelated" curve perfectly matches the result of the "mathematical approach". The "Only Wind Uncorrelated" curve is close to the mathematically generated curve assuming no correlation as well. This curve assumes the dead load and resistances of different years of service are fully correlated, while the maximum annual wind loads are independent. This is a logical assumption in many cases where the values for resistance and dead loads remain constant throughout the service life of the structure. The "Fully Correlated" and "50% Correlated for all of the Variables" curves respectively assume a correlation of 100 and 50% between random variables in successive years of service (i.e., the non-diagonal elements of correlation matrix respectively are 1 and 0.5 for 100 and 50% correlation). As shown, with the increase in correlation, the cumulative probability of failure decreases and eventually converges on the annual probability of failure curve obtained using the mathematical approach.

4 Conclusions

This paper demonstrates several methods for assessing the impact of climate change on the reliability of civil engineering structures during their service life. Particularly, in a case study, the nonstationary effects of wind load on the reliability of a simple structural element located in London, Ontario were evaluated. For a 100-year analysis period, the results show that the lifetime probability of failure can be as much as 1.9 times greater than the baseline (stationary) analysis if climate change effects are considered, while the annual probability of failure in the final year of service is almost four times of what it would have been in the beginning year in 2000. The effect of the nominal wind-to-dead load ratio was evaluated. For the considered example, it was illustrated that with an increase of this ratio the structure becomes more prone to failure even though the design basis remains unchanged. However, the probability of failure of the structure with a lower wind-to-dead load ratio is more sensitive to future climate changes. A sensitivity analysis indicated the total probability of failure is more sensitive to the COV of annual maximum wind speed

than its mean. This finding indicates the importance of inclusion of variability of projected changes of climatic design values into future research. Lastly, the effects of the correlation of random variables in different years of service were investigated through Monte Carlo simulation. It is shown that with an increase in correlation, the probability of failure curve shifts downwards (i.e., to a lower probability of failure for a given year).

References

1. Cannon A, Jeong D I, Zhang X, Zwiers FW (2020) Climate-resilient buildings and core public infrastructure: an assessment of the impact of climate change on climatic design data in Canada
2. CSA (2007) Calibration Report For CAN/CSA-S6-06 Canadian Highway Bridge Design Code
3. CSA Group (2019) CSA S6:19, Canadian Highway Bridge Design Code. Canadian Standards Association (CSA), Mississauga
4. Kupper LL (1971) Probability, statistics, and decision for civil engineers. Technometrics 13(1):211–211. https://doi.org/10.1080/00401706.1971.10488770
5. Li Q, Wang C, Ellingwood BR (2015) Time-dependent reliability of aging structures in the presence of non-stationary loads and degradation. Struct Saf 52(PA):132–41. https://doi.org/10.1016/j.strusafe.2014.10.003
6. Nowak AS, Grouni HN (1994) Calibration of the Ontario highway bridge design code 1991 edition. Can J Civ Eng 21(1):25–35. https://doi.org/10.1139/l94-003
7. Shayanfar MA, Barkhordari MA, Barkhori M, Barkhori M (2018) An adaptive directional importance sampling method for structural reliability analysis. Struct Saf 70:14–20. https://doi.org/10.1016/j.strusafe.2017.07.006
8. Stocker TF, Qin D, Plattner G-KK, Tignor MMBB, Allen SK, Boschung J, Nauels A, Xia Y, Bex V, Midgley PM (2014) Climate change 2013: the physical science basis working group I contribution to the fifth assessment report of the intergovernmental panel on climate change. intergovernmental panel on climate change, vol 9781107057. Cambridge University Press. https://doi.org/10.1017/CBO9781107415324
9. van Vuuren DP, Edmonds J, Kainuma M, Riahi K, Thomson A, Hibbard K, Hurtt GC et al. (2011) The representative concentration pathways: an overview. Climatic Change 109(1):5–31. https://doi.org/10.1007/s10584-011-0148-z

Achieving an Optimized Solution for Structural Design of Single-Storey Steel Buildings Using Generative Design Methodology

A. Torres, B. Mahmoudi, A. J. Darras, A. Imanpour, and R. G. Driver

1 Introduction

Single-storey buildings constructed using structural steel are commonly used in Canada for shopping centres, recreation facilities, and industrial buildings. During the design development phase of a project, engineers evaluate multiple design parameters to achieve the owner's objectives within a limited time before the detailed design begins. The current single-storey design workflow in design offices is mostly manual and tedious. Moreover, miscommunication and human error may occur during design due to overlapping tasks. Regardless of these disadvantages, the design process has the capability not only to become automated, but also to seek innovative new solutions [1, 21]. GD is a specific application of artificial intelligence (AI) that can quickly generate thousands of high-performing design scenarios [16]. It has been applied to architectural designs in Canada [18], but has not yet been realized in structural design. One important factor that structural engineers prioritize during the design stage in order to achieve an optimum design is the total weight of the structure. While optimizing the weight cannot be said to not produce the lowest cost or optimal structure, it is used in this case study as a proxy for labour cost, material cost, and environmental effects, etc., caused by the manufacturing and fabrication processes.

In this paper, an automation design tool is developed using Rhino3D [22], a 3D modeling software, and Grasshopper [23], an algorithmic modelling plugin for Rhino3D. The design tool takes the user inputs and feeds it to a metaheuristic single-objective optimization algorithm. The application and performance of various algorithms used in Grasshopper are studied and considered for future implementation. In this case study, the algorithm's sole objective is to reduce the structures steel tonnage. However, other essential objectives and constraints in the design of steel structures are studied and considered. For the structural analysis portion of this design tool,

A. Torres (✉) · B. Mahmoudi · A. J. Darras · A. Imanpour · R. G. Driver
University of Alberta, Edmonton, Canada
e-mail: atorres@ualberta.ca

S. Walbridge et al. (eds.), *Proceedings of the Canadian Society of Civil Engineering Annual Conference 2021*, Lecture Notes in Civil Engineering 244,
https://doi.org/10.1007/978-981-19-0656-5_25

a link between Grasshopper and S-Frame [5] is being developed to incorporate an FEA solver into the tool. Enhancements to the geometry of the single-storey structure generated in Rhino3D are proposed. After discussing the preliminary results of this research, future steps to enhance the automation tool is outlined.

The main objective of this research is to gain a deep understanding of GD's possibilities towards structural optimization, which will lead to an automation tool that can design safer and lighter single-storey structures in Canada. The method has the potential to reduce material usage, minimize construction waste, and improve productivity in the Canadian construction industry. Furthermore, this research has strong potential to provide Canadian practitioners in the steel construction industry with an automated process to design single-storey buildings.

2 Optimization in Structural Design

2.1 Optimization Algorithms

An evolutionary solver used in this project's optimization tool is responsible for finding the optimal solution for the design problem by implementing a metaheuristic single-objective algorithm. Various evolutionary solvers are discussed in the literature. Most of these algorithms share the same concepts, as they are developed based on the group behaviour of different creatures in nature and how they evolve. The main advantage of these algorithms is that they are derivative-free. Whereas other mathematical approaches require a well-defined and differentiable objective function and attempt to find the optimal solution by computing the derivative of the objective function, metaheuristic algorithms search the domain just by assessing the objective function's value. Since optimization of engineering systems requires evaluating sophisticated objective functions that are not usually differentiable, metaheuristic algorithms have gained popularity among researchers. The key stages of the optimization process are illustrated in Fig. 1 and summarized below. In this figure, N is the number of solutions considered for the first generation, and m is the total number of generations considered for limiting the loop of updating the generations. It is worth noting that the design variable considered here is only the spacing between the columns, and the objective function is the total weight of the structure. The penalty function increases the total weight of structure when the results obtained from structural analysis software do not pass the design codes' requirements.

1) Stage 1: the algorithm creates a set of random solutions by varying design variables associated with the problem. This set is also referred to as the first generation. Each solution returns a specific value for the objective function defined for the optimization problem and by inspecting these values, different solutions can be ranked against each other.
2) Stage 2: in every optimization problem, solutions are subject to different constraints with a feasible space defined. The algorithm applies these constraints

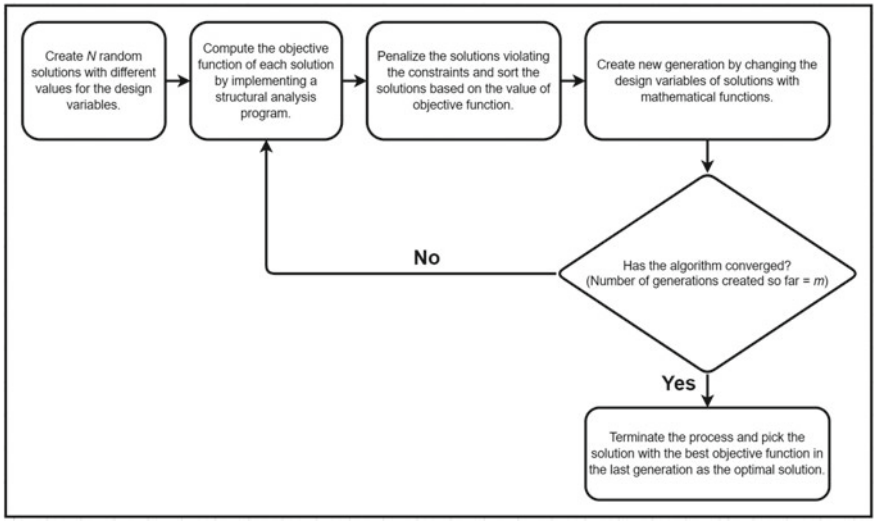

Fig. 1 Optimization process stages

to the solutions by a penalty function. If a solution meets all constraints, the value of its objective function remains the same. However, if the solution's design variables violate these constraints, it would get penalized by a multiplier in its objective function so that it would not be able to compete with feasible solutions of the generation when it comes to rank them based on their objective function.

3) Stage 3: once the set is sorted based on the objective function of the solutions, the algorithm applies certain mathematical functions to the generation and adjusts their design variables, leading to a new set of solutions (i.e., the next generation). The mathematical functions vary for different algorithms. For instance, particle swarm optimization (PSO) algorithm updates the solutions with the velocity function [14] and genetic algorithm generates new solutions with mutation and crossover functions [11]. The algorithm's main goal is to modify the solutions by generating and guiding the solutions toward the global optimum of the problem. While these functions focus on obtaining the best solutions of each generation and improving them in subsequent generations, randomness is also formulated within them, which helps the algorithm search the entire feasible domain of the problem and prevent getting trapped in zones where local optima are located.
4) Stage 4: it has been proven mathematically that the functions responsible for generating new solutions help the optimization algorithm converge at the end if it undergoes a sufficient number of iterations. There are two ways to specify when an algorithm should terminate the loop of creating new generations and bypass performing the second and third stages. The preferred approach is to consider a total number of generations for the algorithm before it has stared generating solutions. The second approach involves checking the convergence

at each iteration by comparing the best solutions of the last two generations with each other. If the difference between the value of the objective function of these two solutions is less than the specified tolerance, it is assumed that the algorithm is no longer capable of finding a better solution, so it is allowed to stop generating new ones. The latter approach might not be appropriate because sometimes the algorithm might get stuck around a local optimum. Terminating the loop does not let the randomness considered in mathematical functions help the algorithm discover new regions in the domain that may contain more optimal solutions.

2.2 Grasshopper Algorithms

The efficiency of optimization algorithms strongly depends on the number of variables, constraints, and objective functions. Past studies showed that Optimus, a tool based on the jEDE algorithm, outperforms several other single-objective optimization tools of Grasshopper in the optimization of a frame structure [9]. The following is a list of the tools that Optimus was compared against, and the algorithms that they use: Galapagos [24], based on the genetic algorithm, SilverEye [6, 7], using the PSO algorithm, and Opossum [26], using an RBFOpt algorithm [8]. In this study, the performance of Wallacei [15], a tool based on the NSGA-II algorithm, which is primarily developed for solving multi-objective optimization problems, with the four Grasshopper optimization tools introduced above to determine which tool yields the best result for optimizing single-storey buildings. By introducing the new nondominated sorting concept, the nondominated sorting genetic algorithm II (NSGA-II) allows us to solve optimization problems with more than one objective function with the help of fundamental components of the genetic algorithm, which can only be used for solving single-objective problems [10].

2.3 Wallacei

Wallacei is an evolutionary multi-objective optimization and analytic engine. This evolutionary solver can consider several objective functions simultaneously to determine the optimum solution. In this case study, there is only one objective function, reducing steel tonnage. However, the ability to run several objective functions is a highly valuable property considering the automation tool requires more objectives, as mentioned in Sect. 3.1. In addition, the solver allows the user to store and save arbitrary data for each iteration of the design. Compared to other Grasshopper components such as Galapagos, Wallacei has specific features that give the user better control over the optimization, graphs, and plots to follow the optimization [12]. The basic interface for the Wallacei component in Grasshopper is shown in Fig. 2.

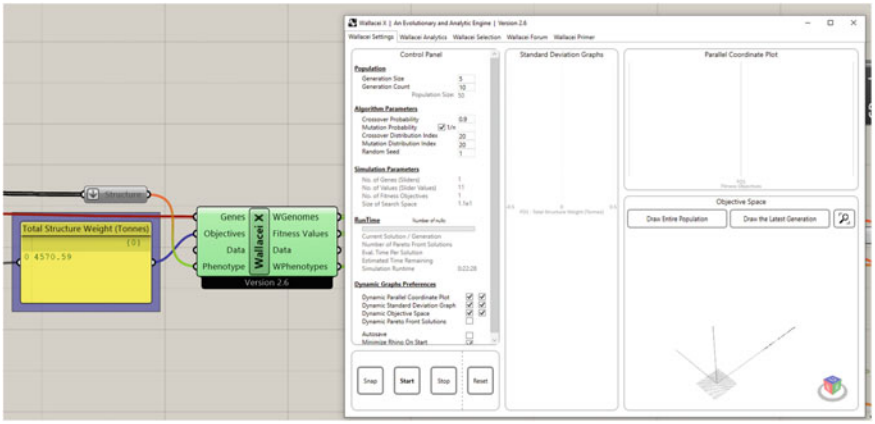

Fig. 2 Wallacei interface in Grasshopper

3 Proposed Automation Tool for Structural Design

3.1 Description of Automation Tool

GD methodology developed for the purpose of single-storey building design can generate a large number of layout options according to the designer's specific requirements. The project's GD workflow has three main components: generate, evaluate, and evolve (shown in Fig. 3). The designer can specify the length, width, and height of the building inside the Grasshopper script, shown in Fig. 4a. This generates the first design option in real-time within Rhino 3D, as shown in Fig. 4b. The evolutionary solver Wallacei is then used to produce a large number of options by varying the equal column spacing used in each direction to obtain the most cost-effective option, taking into account the weight of structural steel only, a standard method

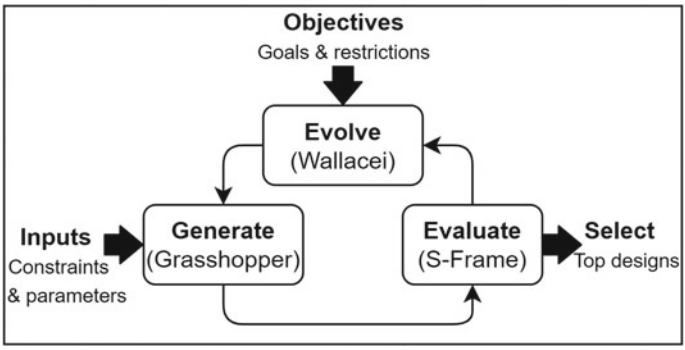

Fig. 3 Project's GD workflow

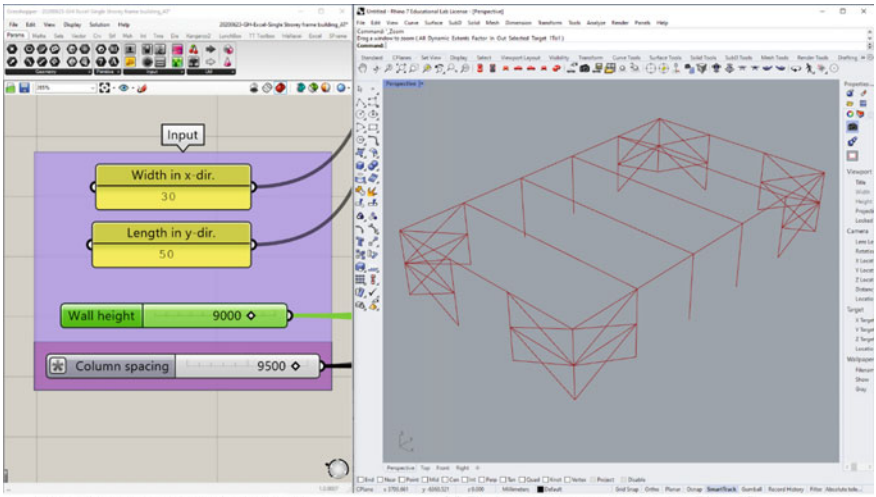

(a) User inputs in Grasshopper script (b) Design option generated inside Rhino3D

Fig. 4 Single-storey structure automation tool

implemented by fabricators in approximating the cost. This process leads to various plausible design options with respective design data, aiding the designer to make a judgment call on which options to proceed with.

3.2 Structural Analysis Component

The current analysis method in the automation tool mentioned in Sect. 3.1 uses Excel. After Excel performs a simplified calculation to select the structure's members, a summary of the structure's weight is created. From this summary, the weight of the beams, struts, and bracing is totalled and represents the total weight of steel for the structure. This total steel weight is the driving factor for comparing various layouts that the script produces. However, using Excel is a very simplified method of structural analysis and needs to be replaced with a more advanced means of analysis.

3.3 Implementation of Finite Element Method for Structural Analysis

To analyze the structure using the structural analysis program S-Frame, a link between the scripts in Grasshopper and S-Frame is needed to transfer the model's data from Rhino3D to S-Frame. Since there is no current API that exists to connect Grasshopper and S-Frame, a middleware text file is required to create this link between software.

This text file will export the necessary information from Grasshopper and import it into S-Frame to create the structure model. To create such a text file, a template text file is made that holds all the semi-constant information that can later be filled out with the remaining data to match the desired model. Filling out the remaining data can be performed with a C# script that grabs all the needed geometry data from Grasshopper and inserts it into the text file. Once this is done, the text file can be opened with S-Frame, creating the S-Frame model and allowing the FEA solver to analyze the structure. This creation of this link is almost complete, as the only data left to transfer is the bracing geometry. The transfer of the model's data between software is shown in Fig. 5.

To create the C# script that fills out the needed text file, a custom Grasshopper component was created and shown in Fig. 6. This custom component takes the user inputs such as the number of bays in each direction, the wall height, and bay spacing, which are used to generate all the remaining data required for the text file. This data consists of design codes, geometry, loads, section and material properties, etc. This is intended to create a fully-parametric tool that can update the text file for S-Frame as soon as one of the model's parameters changes inside Grasshopper.

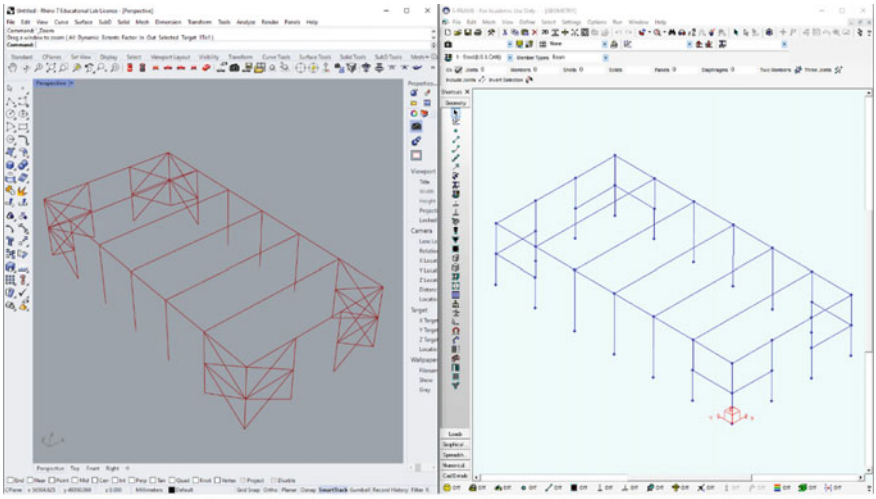

Fig. 5 Transfer of model's data between Rhino3D and S-Frame

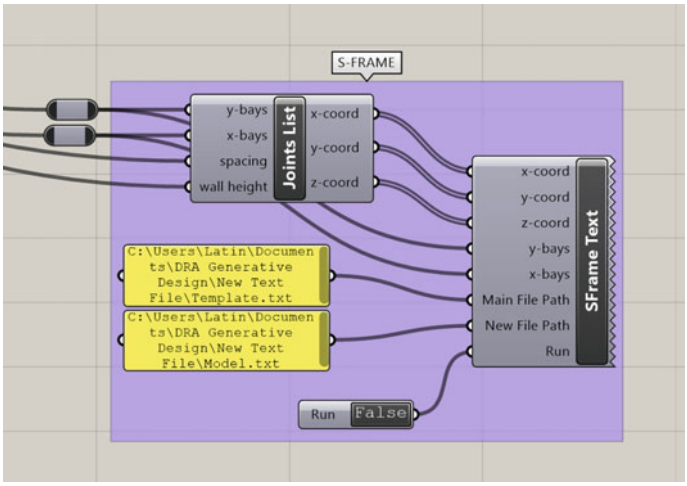

Fig. 6 Custom Grasshopper component created from C# script

4 Preliminary Results and Future Research

4.1 Cost Estimate

In practice, designers estimate the steel structure cost in the design development stage based on steel tonnage. The steel tonnage can be considered a key metric to evaluate and compare design options. However, the total weight of steel can only provide an approximate estimate of the project's total cost. Other important variables are also required to improve the estimate's accuracy, since the total construction cost of structural steel framing is not necessarily a function of its weight [2]. The three primary components of the total cost are a function of the material, fabrication, and erection costs, as shown in Fig. 7 [3]. The material category is defined as structural shapes, plates, steel joists, steel deck, bolting products, welding products, painting

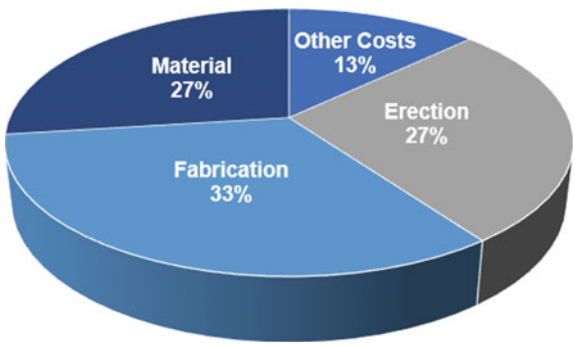

Fig. 7 Distribution of the total cost of structural steel framing [4]

products, and any other products purchased and incorporated into the project. The fabrication category includes the detailing and fabrication labour required to prepare and assemble the shop assemblies of structural shapes, plates, bolts, welds, and other materials. The erection category includes the erection labour needed to unload, lift, place, and connect the structural steel frame components. Lastly, other costs are defined as all cost items not specifically included in the three previous categories [4]. As shown in Fig. 7, the material costs only constitute one-quarter of the total cost, and the majority of costs are associated with the fabrication and erection of structural steel framing. From the results shown in the mentioned studies, it is evident that the proposed automation tool needs to incorporate other cost estimating factors to provide a more realistic estimate of the project's total cost.

4.2 Building Geometry

The current lateral load resisting system of the single-storey building consists of cross-bracing placed at the corners. However, other bracing configurations such as chevron bracing, V-bracing or single diagonal bracing can also be used in such low-rise buildings. The possibility of different bracing configurations (Fig. 8), number

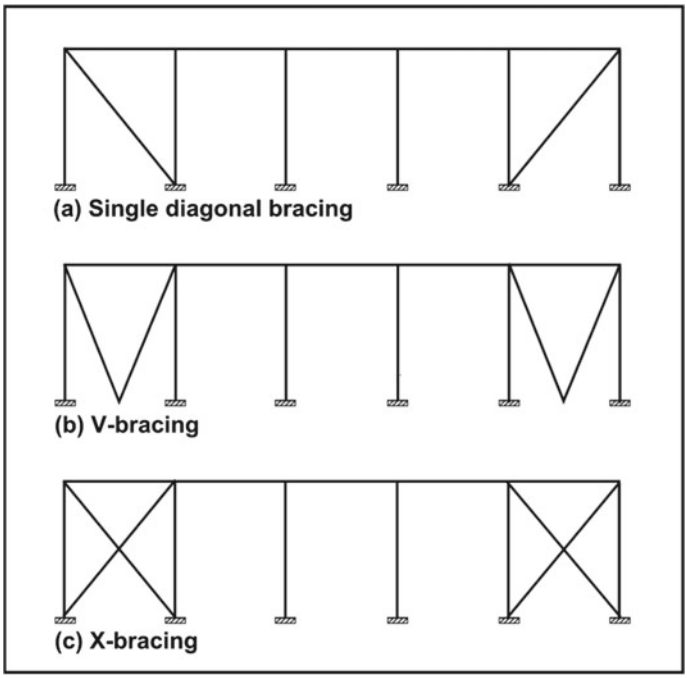

Fig. 8 Typical bracing configurations for portal frames [19]

of braced frames and bracing locations will be studied in the future. Note that the application of X-bracing, inverted V-bracing, and diagonal bracing options for a simple portal frame structure were evaluated in the past using a python script built in Grasshopper [25]. Furthermore, other steel frame geometric parameters such as height to eaves, the pitch of frame, and haunch length are so far missing in the design. Other research has included such parameters in optimizing steel frame buildings [13, 20]. Adding different bracing configurations and other frame geometric parameters will widen the design space's scope and create a more realistic structure.

4.3 Future Direction

While the current study shows promising results obtained using the proposed automation tool, it is still rudimentary and requires further refinement and development before it could be implemented in practice. Further improvements to the proposed automation tool are as follows:

- Incorporate finite element analysis into the project's workflow by completing the link between Grasshopper and S-Frame.
- Incorporate additional factors in the overall cost estimation process to obtain an accurate value.
- Consult with fabricators and erectors to better understand their preferences in the construction of single-storey steel buildings and implement this industry knowledge into the optimization process.
- Expand the scope of the generated frame geometry to produce a more realistic structure and improve optimization.
- Implement multi-objective optimization algorithms by adding more design variables and objectives.
- Explore and compare different optimization algorithms used in structural applications and determine if better results can be obtained.
- Combine a connection design optimization tool with the current automation tool.

5 Conclusions

An automated optimization tool is proposed here for the structural design of single-storey steel structures by reducing steel tonnage in the design stage. The preliminary results show the evolutionary algorithm adopted can result in optimized design options in the design development stage to help the designer select an efficient, better design option. Future studies will incorporate other key design objectives including member availability, connection type, and different frame geometries into the proposed automated design tool to achieve a more accurate estimate of construction costs.

References

1. Almusharaf A, Elnimeiri M (2010) A performance-based design approach for early tall building form development. In: 5th international conference proceedings of the Arab society for computer aided architectural design, Illinois Institute of Technology, Chicago, IL, USA, vol 1, pp 39–50
2. Ashworth A, Skitmore M (1983) The effectiveness of estimating in the construction industry, Master's Degree, The Charted Institute of Building, Englemere, Berkshire, England
3. Barg S, Flager F, Fischer M (2018) An analytical method to estimate the total installed cost of structural steel building frames during early design. J Build Eng 15:41–50
4. Carter C, Schlafly T (2008) "$ave More Money". Modern Steel Construction, American Institute of Steel Construction
5. Casoli G (1998) S-Frame. V. Enterprise. S-Frame Software Inc. Windows
6. Cichocka JM, Migalska A, Browne WN, Rodriguez E (2017) SILVEREYE—the implementation of particle swarm optimization algorithm in a design optimization tool. In: Proceedings of the international conference on computer-aided architectural design futures, Istanbul, Turkey, 10–14 July 2017, pp 151–169
7. Cichocka JM, Migalska A, Browne WN, Rodriguez E (2017) SILVEREYE – the implementation of particle swarm optimization algorithm in a design optimization tool. In: Çağdaş G, Özkar M, Gül L, Gürer E (eds) Computer-aided architectural design. Future trajectories. CAADFutures 2017. Communications in Computer and Information Science, vol 724. Springer, Singapore
8. Costa A, Nannicini G (2018) RBFOpt: an open-source library for black-box optimization with costly function evaluations. Math Program Comput 10(4):597–629
9. Cubukcuoglu C, Ekici B, Tasgetiren MF, Sariyildiz S (2019) OPTIMUS: self-adaptive differential evolution with ensemble of mutation strategies for grasshopper algorithmic modeling. Algorithms 12(7):141
10. Deb K, Pratap A, Agarwal S, Meyarivan T (2002) A fast and elitist multi-objective genetic algorithm: NSGA-II. IEEE Trans Evol Comput 6(2):182–197
11. Goldberg DE (1989) Genetic algorithms in search, optimization and machine learning, 1st edn. Addison-Wesley Longman Publishing Co., Boston
12. Granberg A, Wahlstein J (2020) Parametric design and optimization of pipe bridges, Master's Degree, KTH Royal Institute of Technology
13. Hernández S, Brebbia CA, De Wilde WP (2012) Computer aided optimum design in engineering XII. WIT Press, Southampton
14. Kennedy J, Eberhart R (1995) Particle swarm optimization. In: Proceedings of ICNN'95 - international conference on neural networks, vol. 4. IEEE, Perth, pp 1942–1948
15. Makki M, Showkatbakhsh M (2018) Wallacei. Wallacei
16. McKnight M (2017) Generative design: what it is? How is it being used? Why it's a game changer. In: The international conference on design and technology, KnE Engineering, Geelong, Australia, vol. 2, pp 176–181
17. Microsoft (2000) C#. V. 7.3. Microsoft. Windows
18. Nagy D, Villaggi V, Benjamin D (2018) Generative urban design: integrating financial and energy goals for automated neighborhood layout. In: SpringSim: spring simulation multiconference, vol 25. Society of Computer Simulation International, San Diego, pp 1–8
19. Portal Frames (2021). www.steelconstruction.Info. https://www.steelconstruction.info/Portal_frames
20. Phan DT, Lim JBP, Sha W, Siew CYM, Tanyimboh TT, Issa HK, Mohammad FA (2013) Design optimization of cold-formed steel portal frames taking into account the effect of building topology. Eng Optim 45(4):415–433
21. Rempling R, Mathern A, Ramos D, Fernández S (2019) Automatic structural design by a set-based parametric design method. Autom Constr 108:102936
22. Robert McNeel & Associates (1998) Rhinoceros 3D. V. 7.0. Robert McNeel & Associates

23. Rutten DG (2007) V.1.0. Robert McNeel & Associates. Windows
24. Rutten D (2013) Galapagos: on the logic and limitations of generic solvers. Archit Design 83:132–135
25. Vasilev L (2020) parametric modeling in structural design, Double Bachelor's Degree, LAB University of Applied Sciences
26. Wortmann TO (2017) Introducing and evaluating a model-based optimization tool for grasshopper. In: Proceedings of the CAADRIA 2017, Hong Kong, China, 5–8 July 2017

Calculation of Longitudinal Strain Parameter Used in CSA A23.3:19 Torsion Provisions for Reinforced Concrete Members

A. Kuan, E. C. Bentz, and M. P. Collins

1 Introduction

The two key parameters used in the CSA A23.3:19 [6] shear and torsion provisions for reinforced concrete are β and θ. β, a factor which accounts for the shear resistance of cracked concrete, is used to calculate the shear capacity attributed to the concrete, V_c, while θ, the angle of inclination of diagonal compressive stresses which result from shear and torsion, is used to calculate the shear capacity attributed to the reinforcement, V_s, as well as the torsional resistance of the member, T_r. Although these parameters are affected by many factors, the CSA A23.3 provisions, beginning with the 2004 code [2], harmonized their calculation by relating them a single quantity, the longitudinal strain in the member at the mid-depth, ε_x. For members which contain at least minimum amounts of transverse reinforcement, the resulting equations for β and θ are:

$$\beta = \frac{0.40}{(1 + 1500\varepsilon_x)} \tag{1}$$

$$\theta = 29^\circ + 7000\varepsilon_x \tag{2}$$

In lieu of a more detailed analysis, CSA A23.3:19 suggests using the following equation, which is based on the applied loading and the characteristics of the longitudinal reinforcement, to calculate ε_x. The derivation of Eq. 3 assumes that if the flexural compression zone is uncracked, the longitudinal strain at the mid-depth of the member can be conservatively estimated as half of the strain in the flexural tension reinforcement, as shown in Fig. 1.

A. Kuan (✉) · E. C. Bentz · M. P. Collins
University of Toronto, Toronto, Canada
e-mail: allan.kuan@mail.utoronto.ca

S. Walbridge et al. (eds.), *Proceedings of the Canadian Society of Civil Engineering Annual Conference 2021*, Lecture Notes in Civil Engineering 244,
https://doi.org/10.1007/978-981-19-0656-5_26

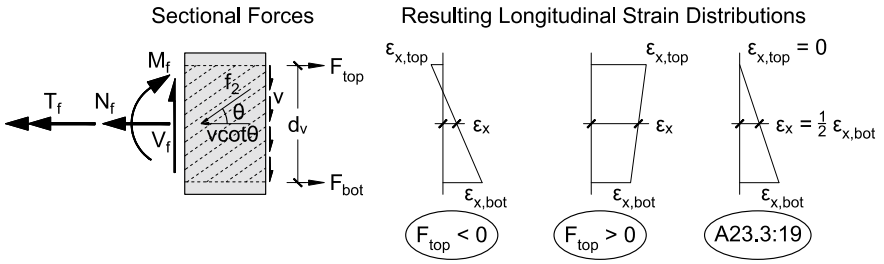

Fig. 1 Section of a reinforced concrete member subjected to sectional actions (left) and resulting longitudinal strain distributions (right)

$$\varepsilon_x = \frac{\frac{M_f}{d_v} + \sqrt{\left(V_f - V_p\right)^2 + \left(\frac{0.9 p_h T_f}{2A_o}\right)^2} + 0.5N_f - A_p f_{po}}{2\left(E_s A_s + E_p A_p\right)} \leq 0.003 \qquad (3)$$

When using the CSA A23.3:19 General Method, Eqs. 1–3 must be used together to determine the shear and torsion resistance of the member. If a more direct alternative is desired, the Simplified Method, which uses $\beta = 0.18$ and $\theta = 35°$, can be used instead. These values of β and θ are obtained if ε_x is chosen to be 0.85×10^{-3} which, assuming 400 MPa steel and using Eq. 3, corresponds to a stress of $\phi_s f_{yl} = 0.85 \times 400 = 340$ MPa in the flexural reinforcement. Because it is derived based on a conservative value of ε_x, the Simplified Method typically gives lower estimates of capacity than the General Method.

Although it is reasonable to assume that the flexural compression zone remains uncracked when designing members for shear, this is not always the case for situations involving torsion. Experimental evidence has shown that torsion, either alone or in combination with other actions, can cause cracking around the full perimeter of the cross section. When this occurs, Eq. 3 will underestimate ε_x, potentially leading to unconservative values of β and θ. To remedy this issue, CSA A23.3:19 includes an accompanying clause which suggests that if axial tension causes the compression zone to crack, the value obtained from Eq. 3 should be doubled. However, this clause does not consider the possibility of full-depth cracking caused by torsion and does not provide a rational basis for calculating the resulting increase in ε_x if it occurs.

This paper will present a simple mechanics-based approach, previously mentioned in another paper [16] but explained in more detail here, to account for the effect of torsion on ε_x. The proposed method addresses the shortcomings of CSA A23.3:19 by providing engineers a means to (1) determine when cracking of the flexural compression zone occurs and (2) calculate its effect on β and θ. Validation of the method against 291 torsion experiments found in the literature shows that this method improves the accuracy and safety of the General Method in CSA A23.3:19.

2 Derivation of Proposed ε_x Equation for Torsion

The proposed method for calculating ε_x is obtained by following the derivation of Eq. 3 but relaxing the requirement that the flexural compression zone remains uncracked. Consider the section of a reinforced concrete member shown in Fig. 1 with a flexural lever arm d_v which resists an axial load N_f, a bending moment M_f, a shear force V_f, and a torsion T_f. If the shear force is carried in the concrete by a field of diagonal compressive stresses only and the torsion is temporarily neglected, the force in the flexural compression region is equal to:

$$F_{top} = -\frac{M_f}{d_v} + 0.5V_f \cot\theta + 0.5N_f \tag{4}$$

The presence of torsion, T_f, causes an additional longitudinal tension which must be carried by longitudinal reinforcement distributed around the perimeter of the member. If it is assumed that θ is constant on each face of the cross section, this tension, $N_{Torsion}$, can be calculated using the following equation:

$$N_{Torsion} = \frac{T_f p_o}{2A_o} \cot\theta \tag{5}$$

In Eq. 5, A_o is the area enclosed by the shear flow path and p_o is the perimeter of the shear flow path. These terms can be approximated as $A_o = 0.85A_{oh}$ and $p_o = 0.9p_h$, where A_{oh} and p_h are the area enclosed and perimeter defined by the centreline of the stirrups, the same way that they are defined in CSA A23.3:19.

The resulting longitudinal tension caused by the combined effects of shear and torsion can calculated by taking the square root sum of squares of the individual terms. This is done instead of simply adding the terms together because under combined loading, θ is generally not constant around the cross section and the assumed values of A_o and p_o are affected by the presence of shear. Performing this operation and including the terms associated with prestressed reinforcement results in the following equation for F_{top}:

$$F_{top} = -\frac{M_f}{d_v} + 0.5\cot\theta\sqrt{\left(V_f - V_p\right)^2 + \left(\frac{0.9T_f p_h}{2A_o}\right)^2} + 0.5N_f - A_p' f_{po}' \tag{6}$$

In Eq. 6, V_p is the vertical component of prestress acting in the direction of the applied shear, A_p' is the area of prestressing reinforcement on the flexural compression side and f_{po}' is the stress in the prestressed reinforcement on the flexural compression side when the surrounding concrete strain is equal to zero. The force on the flexural tension side, F_{bot}, can be calculated in a similar manner by simply changing the sign on the M_f term and using the analogous definitions for A_p and f_{po}:

$$F_{bot} = \frac{M_f}{d_v} + 0.5\cot\theta\sqrt{\left(V_f - V_p\right)^2 + \left(\frac{0.9T_f p_h}{2A_o}\right)^2} + 0.5N_f - A_p f_{po} \quad (7)$$

With the longitudinal forces known, the corresponding longitudinal strains in the reinforcement on the flexural compression and tension sides, $\varepsilon_{x,top}$ and $\varepsilon_{x,bot}$ respectively, can now be determined. If $\cot\theta$ is conservatively approximated as 2.0 and only positive strains are considered, applying Hooke's law to Eqs. 6 and 7 yields the following equations for $\varepsilon_{x,top}$ and $\varepsilon_{x,bot}$:

$$\varepsilon_{x,top} = \frac{-\frac{M_f}{d_v} + \sqrt{\left(V_f - V_p\right)^2 + \left(\frac{0.9T_f p_h}{2A_o}\right)^2} + 0.5N_f - A_p' f_{po}'}{E_s A_s' + E_p A_p'} \geq 0 \quad (8)$$

$$\varepsilon_{x,bot} = \frac{\frac{M_f}{d_v} + \sqrt{\left(V_f - V_p\right)^2 + \left(\frac{0.9T_f p_h}{2A_o}\right)^2} + 0.5N_f - A_p f_{po}}{E_s A_s + E_p A_p} \geq 0 \quad (9)$$

Finally, the longitudinal strain at the mid-depth is found by taking the average of the top and bottom longitudinal strains. It is suggested that the upper limit of 0.003 on ε_x, which applies to Eq. 3 to avoid relying on excessive amounts of redistribution within the member, be maintained [2].

$$\varepsilon_x = \frac{\varepsilon_{x,top} + \varepsilon_{x,bot}}{2} \leq 0.003 \quad (10)$$

The proposed method, which is a simple reworking of Eq. 3, provides a check for when cracking of the flexural compression zone takes place and considers the influence of the flexural compression reinforcement on ε_x when it occurs. In situations where the tension caused by the torsion exceeds the compression from the moment, $\varepsilon_{x,top}$ will be positive, leading to larger values of ε_x and θ than those obtained using the General Method. Conversely, if the compression from the moment dominates the tension caused by the torsion, then the numerator of Eq. 8 will be negative, leading to $\varepsilon_{x,top} = 0$. When this happens, Eq. 10 converges to Eq. 3 and the proposed method will give the same results as the General Method.

3 Validation of Proposed Method Against Experiments in the Literature

The proposed method for calculating ε_x was validated against a large database of experiments from the literature. Of the 291 tests considered, 154 were beams tested in pure torsion and 137 were beams tested under combined bending and torsion. The size of each member's cross section, which were all rectangular in shape, varied from

102 mm x 203 mm to 500 mm x 725 mm, and 46 were hollow. The concrete strengths varied from 14.3 MPa to 105.7 MPa, and the yield strength of the reinforcing bars used varied from 248 MPa to 690 MPa. The quantity of longitudinal reinforcement, expressed as the volumetric ratio of longitudinal steel $\rho_l = A_l/A_c$, varied from 0.16% to 3.88%, and the quantity of transverse reinforcement, expressed as the volumetric ratio of transverse steel $\rho_t = A_t p_h/A_c s$, varied from 0.15% to 2.49%. Beams which failed by crushing of the concrete before yielding of either direction of steel were not considered in the study because the CSA A23.3:19 equation used to predict crushing is not a function of ε_x.

To obtain the failure load of each specimen using the proposed method, ε_x was first calculated using Eqs. 8–10, and then Eq. 2 was used to calculate θ. The CSA A23.3:19 equations for torsional strength, shown below, were then used to determine both the failure load and predicted mode of failure.

$$\sqrt{\left(\frac{V_f - V_p}{b_w d_v}\right)^2 + \left(\frac{T_f p_h}{1.7 A_{oh}^2}\right)^2} \leq 0.25 \phi_c f_c' \tag{11}$$

$$T_r = 2A_o \frac{\phi_s A_t f_{yt}}{s} \cot\theta \tag{12}$$

$$F_{lt} = \frac{M_f}{d_v} + 0.5N_f + \cot\theta \sqrt{\left(V_f - 0.5V_s - V_p\right)^2 + \left(\frac{0.45 p_h T_f}{2A_o}\right)^2} \leq \phi_s A_s f_{yl} + \phi_p A_p f_{yp} \tag{13}$$

$$F_{lc} = -\frac{M_f}{d_v} + 0.5N_f + \cot\theta \sqrt{\left(V_f - 0.5V_s - V_p\right)^2 + \left(\frac{0.45 p_h T_f}{2A_o}\right)^2} \leq \phi_s A_s' f_{yl} + \phi_p A_p' f_{yp} \tag{14}$$

Equations 11–14 correspond to failure modes associated with crushing of the concrete before yielding of any reinforcement (11), yielding of the transverse reinforcement (12), and yielding of the longitudinal reinforcement on the flexural tension (13) and flexural compression (14) sides of the member. f_{yt}, f_{yl} and f_{yp} are the yield strengths of the transverse, longitudinal, and prestressing steel respectively, and f_c' is the compressive strength of the concrete. When performing the validation study, the value of each resistance factor (ϕ_c, ϕ_s and ϕ_p) was taken as 1.0 in order to evaluate the true predictive capabilities of the method.

Table 1 contains a summary of the analysis results obtained using the proposed method. The quality of each strength prediction was evaluated by calculating the ratio of the experimentally observed failure torque and the predicted failure torque, Test/Pred. The process was repeated using the CSA A23.3:19 General Method, which calculates ε_x using Eq. 3, and the CSA A23.3:19 Simplified Method, which uses $\theta = 35°$. Examining the statistics based on the full dataset, the proposed method has the most accurate Test/Pred of the three methods on average, as well as the smallest

Table 1 Summary of analysis results

Type	Investigators	Test/Pred statistics	Proposed method	CSA A23.3:19 general method	CSA A23.3:19 simplified method
Pure torsion	[1] [3] [7] [9] [10] [11] [12] [13] [14] [15] [17] [20] [21] [22] [23] [25] [26]	Count	154	154	154
		Mean	1.33	1.27	1.37
		COV	15.8%	17.9%	21.1%
		1st percentile	0.840	0.740	0.696
Combined torsion and bending	[5] [8] [11] [18] [20] [21] [24] [25]	Count	137	137	137
		Mean	1.22	1.30	1.31
		COV	16.0%	21.3%	19.9%
		1st percentile	0.765	0.655	0.703
Total		Count	291	291	291
		Mean	1.27	1.28	1.34
		COV	15.9%	19.4%	20.5%
		Max	2.20	3.46	2.79
		Min	0.71	0.69	0.73
		1st percentile	0.800	0.701	0.700

coefficient of variation (COV). Furthermore, the first percentile Test/Pred value of the proposed method, based on a normal distribution fitted to the lower half of the data, was 0.800, which is higher than the corresponding values for the other two methods. If the reliability heuristic suggested by MacGregor [19] is used to interpret these values, the resistance factor required to offset the 1% probability of failure for the proposed method would be 0.800, which is less severe than the 0.701 needed for the General Method and 0.700 needed for the Simplified Method. Overall, all of these metrics suggest that the proposed method makes safer and more accurate predictions of torsional capacity than both of the methods currently used in CSA A23.3:19.

The following sections discuss the application of the proposed method for pure torsion and combined torsion and bending in more detail.

3.1 Members Subjected to Pure Torsion

Pure torsion tests are the simplest and most common form of torsion experiment, even though pure torsion does not occur in practical situations. In the absence of other actions, using Eqs. 8–10 to calculate ε_x becomes straightforward. If the longitudinal reinforcement is equally distributed on the top and bottom of the member, then $A_s = A_s' = A_l/2$. This results in the following equation for ε_x for non-prestressed members:

$$\varepsilon_x = \frac{0.9T_f p_h}{A_o A_l E_s} \tag{15}$$

Figure 2 shows the Test/Pred values for each of the 154 beams tested in pure torsion when analyzed using the proposed, CSA A23.3:19 General, and CSA A23.3:19 Simplified methods. The horizontal axis, $\rho_l f_{yl}/\rho_t f_{yt}$ is a measure of the relative tensile strength of the longitudinal reinforcement compared to the transverse reinforcement. A large value of $\rho_l f_{yl}/\rho_t f_{yt}$ indicates that the member is more likely to fail due to yielding of the stirrups and a small value of $\rho_l f_{yl}/\rho_t f_{yt}$ indicates that yielding of the longitudinal reinforcement is more likely to govern the ultimate load.

The CSA A23.3:19 General and Simplified methods tend to be very conservative for members which fail due to yielding of the longitudinal reinforcement. This is because the CSA methods, which calculate ε_x assuming that half of the member is uncracked, tend to use values of θ which are shallower than those observed experimentally. Lower values of θ increases the demand on the longitudinal reinforcement, which results in more conservative estimates of strength. The opposite occurs for members with a larger $\rho_l f_{yl}/\rho_t f_{yt,}$ where the CSA A23.3:19 methods tend to give

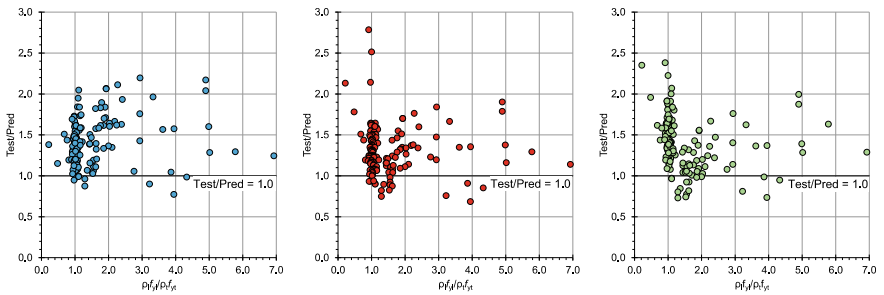

Fig. 2 Experimental validation, pure torsion. Proposed method (left), CSA A23.3:19 general method (centre), CSA A23.3:19 simplified method (right)

less conservative predictions of strength. In these cases, the shallower θ overestimates the torsional strength provided by the transverse reinforcement, resulting in many Test/Pred values below 1.0 the General Method is used. Because the Simplified Method uses the same assumption as the General Method to calculate its value of $\theta = 35°$, it too has several Test/Pred values under 1.0. However, it is usually more conservative than the General Method because its assumed value of θ is usually larger than the θ obtained using the General Method. The proposed method, which always uses larger values of ε_x and θ than both of the CSA methods in situations of pure torsion, gives more consistent and accurate predictions across the full spectrum of reinforcement arrangements.

3.2 Members Subjected to Combined Torsion and Bending

The response of reinforced concrete members subjected to torsion in combination with bending is strongly influenced by the behaviour of the longitudinal reinforcement. If the ratio of the applied bending moment to the torsion is defined as $\omega = M_f/T_f$, then Eqs. 13 and 14 can be rearranged to express the torsional resistances offered by the flexural compression and flexural tension steel respectively:

$$T_r = 2A_o \frac{\phi_s A_s f_{yl} d_v \tan\theta}{0.9 p_h d_v + 2A_o \omega \tan\theta} \tag{16}$$

$$T_r = 2A_o \frac{\phi_s A_s' f_{yl} d_v \tan\theta}{0.9 p_h d_v - 2A_o \omega \tan\theta}, \text{ only positive values of } T_r \text{ should be considered.} \tag{17}$$

When using Eq. 17, negative values of T_r will be obtained if the longitudinal steel on the flexural compression side of the member remains in compression under the effects of T_f and M_f. When this happens, the flexural compression reinforcement cannot fail by yielding in tension and hence these values should be discarded.

Figure 3 shows the Test/Pred values obtained using the three methods for each of the 137 beams considered in this study. Many of these tests contained more longitudinal reinforcement on the flexural tension side than on the flexural compression side, meaning that failure could be governed by yielding of the longitudinal steel on only one side of the beam. Members tested under a high ratio of M/T tended to fail by yielding of the flexural tension reinforcement, while members tested under a low ratio of M/T tended to fail by either yielding of the stirrups or of the flexural compression steel.

As with the case with pure torsion, the proposed method tends to give more uniformly accurate and safe predictions over a wide range of ω. For flexure-dominated tests with a large M/T ratio, the General Method and the proposed method give the same results. This is because the high bending moments cause the flexural compression zone to stay uncracked, resulting in the proposed method converging

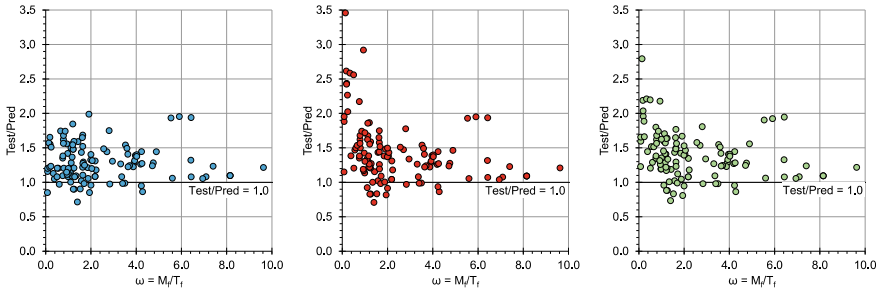

Fig. 3 Experimental validation, combined torsion and bending. Proposed method (left), CSA A23.3:19 general method (centre), CSA A23.3:19 simplified method (right)

to the General Method. For lower values of ω, which correspond to situations where the flexural compression zone can crack from the torsion, the predictions obtained using the General and Simplified methods are much worse than those made using the proposed method. In situations where yielding of the longitudinal reinforcement governs the failure, the smaller values of θ overestimates the demand on the flexural compression reinforcement, producing several predictions which are conservative by more than a factor of 2.5. For members which instead fail by yielding of the stirrups, the shallower choice of θ used by the CSA methods results in some unconservative predictions for the same reasons mentioned for the pure torsion tests.

A study of the TBU ("Torsion Bending Under-reinforced") series of beams tested by Onsongo [24] was performed to evaluate the methods in situations of combined torsion and bending in more detail. Details of the specimens and experimental failure loads can be found on the torsion-bending interaction plot shown in Fig. 4. Also plotted on Fig. 4 are the predicted interaction curves obtained using the proposed, CSA A23.3:19 General and CSA A23.3:19 Simplified methods. The theoretical response of these non-symmetrically reinforced beams has been previously discussed by Collins and Lampert [4]: for low M/T ratios, failure is governed by yielding of the reinforcement on the flexural compression side. Increasing the M/T ratio increases the load which the member can resist until an optimal point is reached, after which the failure load reduces as yielding of the flexural tension steel begins to govern the failure.

The interaction curves predicted by the CSA General and Simplified methods shown in Fig. 4 exhibit three distinct regimes. The methods correctly predict that yielding of the top longitudinal reinforcement governs failure for low M/T ratios, although the shallow values of θ used by the methods overestimate the tensile demand in the steel, resulting in very conservative predictions for TBU5. The flat region is where Eq. 11 predicts a crushing failure of the beams, which gives accurate predictions for TBU3 and TBU4. For large values of M/T, yielding of the flexural tension steel governs the calculated capacity, with the General Method predicting a steeper reduction in strength than the Simplified method because it uses a smaller value of θ. When performing the calculations using the CSA methods, the torsional resistance attributed to yielding of the transverse reinforcement never governs.

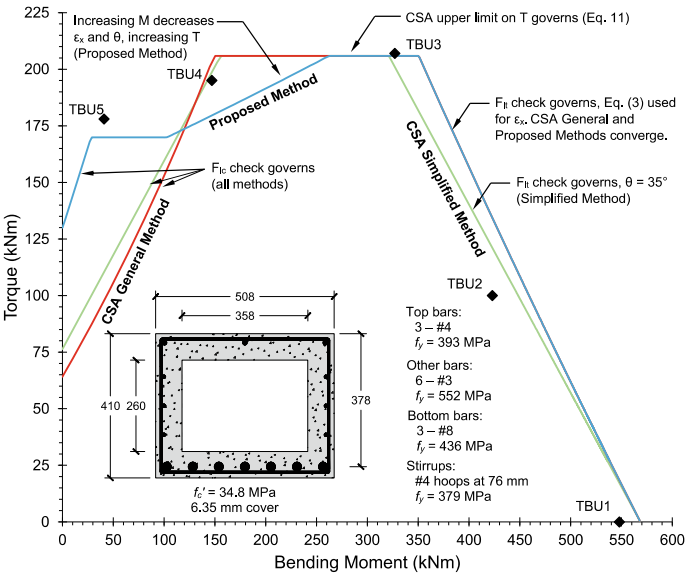

Fig. 4 Torsion-bending interaction, TBU series. Proposed method (blue), CSA A23.3:19 general method (red), CSA A23.3:19 simplified method (green)

The additional considerations used to calculate ε_x with the proposed method results in a more complex torsion-bending interaction curve. Like the General and Simplified methods, for low values of M/T, failure is governed by yielding of the top longitudinal steel. However, because the method predicts that the compression zone cracks, larger values of ε_x and θ are used which result in more accurate predictions. The constant region on the interaction diagram where T = 170 kN corresponds to failure being governed by yielding of the transverse steel, which caps ε_x and θ at 0.003 and 50° respectively. The subsequent ascending region corresponds to when yielding of the stirrups governs the strength of the member, but the presence of moment causes the torsional strength to increase. Because the member has less longitudinal reinforcement on the top than on the bottom, the decrease in $\varepsilon_{x,top}$ from the flexural compression is greater than the increase in $\varepsilon_{x,bot}$ from the flexural tension. Increasing the moment therefore causes a net decrease in ε_x and θ, which in turn increases the efficiency of the stirrups and increases T_r. For larger values of M/T, the proposed method predicts the same behaviour as the General Method (crushing according to Eq. 11 followed by yielding of the flexural tension steel).

The interaction curve obtained using the proposed method matches the experimental failure loads and observed behaviour more closely than those obtained using the General and Simplified methods. In particular, the predictions made for low M/T ratios using the methods in CSA A23.3:19 are very conservative and do not adequately capture the effect of the flexural compression reinforcement on the specimens' capacity.

4 Concluding Remarks

Although designing reinforced concrete members to resist torsion shares many similarities with designing for shear, some assumptions used in shear design are no longer valid when torsion is present. In this paper, the assumption that the flexural compression region stays uncracked when calculating ε_x is examined. Although appropriate for shear design, the presence of torsion causes the CSA A23.3:19 General and Simplified methods to make relatively poor strength predictions of 291 beam tests found in the literature (average test-to-predicted torsional strengths of 1.28 and 1.34 with COV of 19.4 and 20.5% respectively). The strength of members which fail by yielding of their transverse reinforcement tends to be overestimated, while the strength of those governed by yielding of the longitudinal reinforcement tends to be underestimated.

This paper presents an alternative method of finding ε_x which instead calculates it as the average of the longitudinal strains on the top and bottom of the member. Using this procedure instead of the default ε_x equation in CSA A23.3:19 results in a similar average test-to-predicted value of torsional strength, 1.27, but improves the COV to 15.9%. It is suggested that future editions of CSA A23.3 include this method to both improve the accuracy of the design provisions and also draw attention to this unique aspect of torsion design.

Acknowledgements The financial support provided by the Natural Science and Engineering Research Council of Canada (NSERC) is gratefully acknowledged.

References

1. Bernardo LFA, Lopes SMR (2009) Torsion in high-strength concrete hollow beams: strength and ductility analysis. ACI Struct J 106(1):39–48
2. Bentz EC, Collins MP (2006) Development of the 2004 Canadian Standards Association (CSA) A23.3 shear provisions for reinforced concrete. Can J Civ Eng 33:521–534
3. Chiu HJ, Fang IK, Young WT, Shiau JK (2007) Behavior of reinforced concrete beams with minimum torsional reinforcement. Eng Struct 29:2193–2205
4. Collins MP, Lampert P (1972) Torsion, bending and confusion - an attempt to establish the facts. J Am Concr Inst 69(8):500–504
5. Collins MP, Walsh PF, Archer FE, Hall AS (1968) The ultimate strength of reinforced concrete beams subjected to combined torsion and flexure. Am Concr Inst Spec Publ SP-18:379–402
6. CSA (2019) Design of concrete structures. Standard CAN/CSA A23.3:19, Canadian Standards Association, Mississauga, ON, Canada
7. Fang IK, Shiau JK (2004) Torsional behaviour of normal- and high-strength concrete beams. ACI Struct J 101(3):304–313
8. Goode CD, Helmy MA (1968) Ultimate strength of reinforced concrete beams in combined bending and torsion. Am Concr Inst Spec Publ SP-18:357–378
9. Hsu TTC (1968) Torsion of structural concrete - behavior of reinforced concrete rectangular members. Am Concr Inst Spec Publ SP-18:261–306
10. Ibrahim MS, Gebreyouhannes E, Muhdin A, Gebre A (2020) Effect of concrete cover on the pure torsional behavior of reinforced concrete beams. Eng Struct 216:110790

11. Iyengar KTSR, Rangan BV (1968) Strength and stiffness of reinforced concrete beams under combined bending and torsion. Am Concr Inst Spec Publ SP-18:403–440
12. Jeng CH, Peng SF, Chiu HJ, Hsiao CK (2014) New torsion experiment on large-sized hollow reinforced concrete beams. ACI Struct J 111(6):1469–1480
13. Joh C, Kwakh I, Lee J, Yang IH, Kim BS (2019) Torsional behavior of high-strength concrete beams with minimum reinforcement ratio. Adv Civil Eng 2019:1432697
14. Kemp EL (1968) Behavior of concrete members subject to torsion and to combined torsion, bending, and shear. Am Concr Inst Spec Publ SP-18:179–202
15. Koutchoukali NE, Belarbi A (2001) Torsion of high-strength reinforced concrete beams and minimum reinforcement requirement. ACI Struct J 98(4):462–469
16. Kuan A, Bruun EPG, Bentz EC, Collins MP (2020) Alternative design procedures for torsion in ACI 318-19: a comparative study. Am Concr Inst Spec Publ SP-344:64–91
17. Lampert P, Thurlimann B (1968) Torsionsversuche an Stahlbetonbalken, Bericht Nr. 6506-2. Institut fur Baustatik, ETH Zurich, Switzerland
18. Lampert P, Thurlimann B (1969) Torsions-Biege-Versuche an Stahlbetonbalken, Bericht Nr. 6506-3. Institut fur Baustatik, ETH Zurich, Switzerland
19. Macgregor JG (1976) Safety and limit states design for reinforced concrete. Can J Civ Eng 3(4):484–513
20. Mardukhi J (1974) The behaviour of uniformly prestressed concrete box beams in combined torsion and bending, M.A.Sc thesis, Department of Civil Engineering, University of Toronto, Toronto, ON, Canada
21. McMullen AE, Warwaruk J (1967) The torsional strength of rectangular reinforced beams subjected to combined loading, Report no. 2, Civil Engineering Department, University of Alberta, AB, Canada
22. McMullen AE, Rangan BV (1978) Pure torsion in rectangular sections – a re-examination. ACI J 75(10):511–519
23. Mitchell D, Collins MP (1978) Influence of prestressing on torsional response of concrete beams. J Prestressed Concr Inst 23(3):54–73
24. Onsongo WM (1978) The diagonal compression field theory for reinforced concrete beams subjected to combined torsion, flexure, and axial load, PhD thesis, Department of Civil Engineering, University of Toronto, Toronto, ON, Canada
25. Pandit GS, Warwaruk J (1968) Reinforced concrete beams in combined bending and torsion. Am Concr Inst Spec Publ SP-18:133–164
26. Peng XN, Wong YL (2011) Behaviour of reinforced concrete walls subjected to monotonic pure torsion – an experimental study. Eng Struct 33(9):2495–2508

Use of Structural Health Monitoring Data in Reliability-Based Analysis of Existing RC Corbel Considering Teflon Degredation

Connor Petrie, Fadi Oudah, and Glen Norlander

1 Introduction

Structural Health Monitoring (SHM) allows owners to measure their structures in response to changing loads over time, to assess for the effects of deterioration, and to improve risk-based decisions around maintenance. With a growing number of SHM programs being implemented in North America, there is a need for research investigating the incorporation of SHM data into assessing the safety of structural components. Depending on the locations and type of measurements taken as part of the ongoing SHM program, reliability-based techniques can be employed to estimate the changing safety of the structure over time. Location of the measurements will depend on the structure and the nature of loading. Large multi-story buildings, like the one examined in this study, are typically monitored at the expansion joints, through measurement of the movement of these joints over time.

The present case-study examines a multi-story institutional building located in Alberta. At the expansion joints, south side floor girders are continuous with the column, north side floor girders sit on corbels with sliding Teflon bearing pads. The expected relative movement at the expansion joints has several reasons including shrinkage and creep of concrete members, elastic deformation under load, and temperature cycles. These movements should have been considered in the original design. However, the building has experienced additional unexpected movement, with the cause attributed to excessive differential settlement and soil rebound. The owner has developed a SHM program, monitoring at the expansion joints where excessive movements are occurring, and as a result has monitored movement since 1996. The continuation of increasing relative movement of building sections at expansion joints is thought to be a primary limitation to the expected life of the structure.

C. Petrie · F. Oudah (✉) · G. Norlander
Norlander Oudah Engineering Ltd. (NOEL), Calgary, Canada
e-mail: Fadi.Oudah@Norlander-Oudah.com

S. Walbridge et al. (eds.), *Proceedings of the Canadian Society of Civil Engineering Annual Conference 2021*, Lecture Notes in Civil Engineering 244,
https://doi.org/10.1007/978-981-19-0656-5_27

In addition, the Teflon bearing pads used at expansion joints will degrade with time, further increasing the lateral force on the corbel by increasing the coefficient of friction of the sliding surface. The increasing force adversely affects corbel reliability (i.e., reduce the safety over time). The proposed reliability framework incorporates SHM data, in the form of measurements of horizontal movements at the expansion joints, taken over 30 years, as a random variable (RV) in the reliability analysis.

An upper floor along an expansion joint with the largest recorded movements was selected for analysis. The horizontal movement data was extrapolated and used for statistically-based structural assessments, known as structural reliability. Regression was used to fit and project curves of the anticipated movement until the end of the assumed service life (75 years). Descriptive statistics (bias, coefficient of variation (COV), and distribution type) were determined for eccentricity model error. Statistics for loads and material strength were taken from the values used to calibrate the Canada National Building Code [5]. Monte Carlo Simulation (MCS) was employed to calculate the reliability index of the corbel for the assumed remaining service life. To investigate the effect of Teflon degradation, a parametric study was also conducted by bounding the coefficient of friction of the Teflon and taking a range of deterministic values.

The following sections describe in more detail the methodology and input used to conduct the reliability analysis. Section 2 describes the used SHM data and the techniques used to calculate the descriptive statistics of the RVs. Section 3 deals with the load and resistance models used. Sections 4 and 5 describe the reliability analysis and study on the effects of Teflon degradations.

2 Structural Health Monitoring Data

A SHM program has been in place to monitor the building's unexpected soil related movements. Measurements are taken bi-annually during the winter and summer seasons. The program measures horizontal movements of the expansion joints at each floor by measuring the relative movement to a fixed point. This data can be incorporated into reliability analysis to calculate the change in reliability of the corbel over time by introducing a new RV of eccentricity model error. This new variable is based on the mean bias and standard deviation of the measurements through regression analysis to fit predictive curves to the data, while the distribution type of the model error was found using MATLAB's built-in distribution fitting tool.

2.1 Data Selection

Review of recorded horizontal movements, from 1996 to 2019 was conducted and horizontal movement data of the expansion joint with the largest movement was

extracted, at each corbel location. The data was sorted into two databases, Database A and Database B, representing winter and summer movement, respectively. The goal of the separate databases is to eliminate the year-to-year movement from typical seasonal temperature differences and examine the extreme movement trends year-to-year, so that the changing reliability over time of the corbel can be established. Regression analysis and distribution fitting allow for the descriptive statistics of the new RV of eccentricity model error to be found.

2.2 Regression Analysis

Regression analysis was performed with the software MATLAB on each set of horizontal movements in the two databases. Best fit curves predict the yearly movements of each corbel. Each curve derived was used to project predicted relative movement at each corbel until 2036 (the assumed remaining service life of the building). Bias values were obtained (bias is defined as the actual value divided by the predicted value) for every year with recorded movement. Statistical parameters (bias, COV & distribution type) for eccentricity were obtained. The mean bias and COV obtained were used as inputs for reliability analysis and were found to be 1.00 and 0.172, respectively.

2.3 Distribution Fitting

To obtain the distribution of the eccentricity bias, fitting of typical distributions (normal, lognormal, Weibull, extreme) was performed using MATLAB for each corbel location along the expansion joint. It was found that a lognormal distribution best fit the eccentricity bias data at this location.

3 Load and Resistance Models

A predictive model in SAP2000 was constructed to model the geometry and loads of the building. Static non-linear gravity load analysis was conducted to obtain the loads imposed on the corbels. Flexural resistance models to describe the capacity of the corbel, based on its internal reinforcement were used to make the limit state. The following subsections describe each model in detail.

3.1 SAP2000 Predictive Model

A Predictive SAP2000 model, consisting of the building's main structural components, was used to yield the gravity loads imposed on the corbels. A static non-linear analysis of dead and live loads was completed to obtain unfactored axial and normal forces at the corbels.

3.2 Resistance Model

Resistance models were formulated based on reinforcement type to find the capacity of the reinforced concrete corbels. A classical bending resistance model based on CSA A23.3-14 [3] was developed to compute the capacity of embedded built-up structural steel plates, used as primary resisting members, in the corbels. The primary resisting plates are embedded in the column, at the corbel location, and extend into the corbel to provide flexural capacity. Moment resistance of the corbels is calculated given the random inputs from MCS.

4 Reliability Analysis

MCS was selected to perform the reliability analysis for its robustness in handling several different distribution types of random variables that make up the limit state, coupled with its relative simplicity to set up. An excel sheet was programed to preform 100,000 runs of the given flexural limit state, for each corbel and season. Reliability index values were calculated at 5-year intervals from 2010 until 2035, showing the trends in the changing safety of the corbel.

Descriptive statistics and distribution type for eccentricity found in this study are given in Sects. 2.2 and 2.3, respectively. Descriptive statistics for the other statistical parameters for load and material strength are based on studies conducted by [1, 2, 4, 6]. The bias and COV were 1.12 and 0.10, respectively, for steel yield strength; 1.18 and 0.16, respectively, for concrete strength; 1.05 and 0.10, respectively, for dead load; 0.90 and 0.17, respectively, for live load; and 1.00 and 0.206, respectively, for transformation to load effect. These statistical parameters are used with the load and resistance models to carry out MCS.

5 Parametric Study: Teflon Degredation

The effects of degradation of the Teflon sliding surface were considered by adjusting the coefficient of friction, μ, of the Teflon-steel sliding surface. Three deterministic

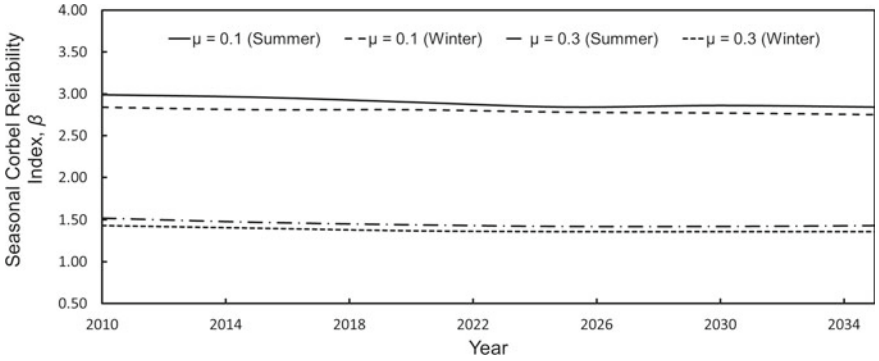

Fig. 1 Corbel seasonal reliability index, β, over remaining service life

values, $\mu = 0.04, 0.1, 0.3$ are used. These coefficients represent optimum as manufactured, design value, and steel on steel (fully degraded) sliding conditions. MCS was conducted as described in Sect. 4 for each value of μ, for the remaining service life of the structure in 5-year intervals from 2010 to 2035. Figure 1 shows the changing reliability index, β, over the remaining service life for a critical corbel. Reliability index values are shown for both seasons, and, for μ values of 0.1 (design) and 0.3 (steel on steel):

The figure shows that based on the variation in material strength and loads, combined with the projected eccentricity, the safety of the corbel does not degrade uniformly with time or between each season. Furthermore, bearing pads on buildings are typically inaccessible for assessment. As the Teflon degrades toward steel on steel ($\mu = 0.3$), the reliability drops significantly as compared to the design condition ($\mu = 0.1$). The decrease in reliability from the Teflon degradation is much more significant than that resulting from an increase in eccentricity and could be the limiting factor when estimating the remaining service life.

6 Conclusion

The present work examines the application of a simple reliability framework to assess the changing safety of RC corbels, part of a buildings expansion joint system. It shows how practicing engineers can incorporate structural health monitoring (SHM) data into reliability analysis to quantify the changing safety of a corbel, while also considering Teflon degradation. The proposed methodology will have significance to practicing engineers and provide a rational basis for assessing the useful remaining life of a corbel as part of the structure, based on data from a SHM program.

The proposed framework can aid to address the probabilistic side of risk assessment, allowing for improved planning of milestones for major repair or decommissioning. Furthermore, considering Teflon degradation of the bearing pad within the

corbel assembly is needed, as this may the limiting factor to the remaining service life of the structure as shown in this case study. Further studies to investigate how the condition of Teflon components within a corbel expansion joint system affects the reliability are recommended.

References

1. Bartlett M, Hong HP, Zhou W (2003a) Load factor calibration for the proposed 2005 edition of the National Building Code of Canada: statistics of loads and load effects. Canad J Civil Eng **30**(2):429–439
2. Bartlett M, Hong HP, Zhou W (2003b) Load factor calibration for the proposed 2005 edition of the National building code of Canada: companion-action load combinations, Canad J Civil Eng **30**(2):440–448
3. CSA A23.1-14/A23.2-14, Concrete materials and methods of concrete construction/Test methods and standard practices for concrete, Canadian Standards Association, Mississauga (Ontario)
4. Galambos TV, Ravindra MK (1976) The basis for load and resistance factor design criteria of steel building structures. Can J Civ Eng 4(1):178–189
5. NBCC (2015) National building code of Canada, National Research Council, Ottawa (Ontario)
6. Wang N, Ellingwood BR (2015) Limit state design criteria for FRP strengthening of RC bridge components. Struct Saf 56(1):1–8

The Behaviour of Reinforced Concrete Under Impact Loading: Review

M. George, M. Abdallah, and H. Hajiloo

1 Introduction

Columns are a key aspect of public infrastructure such as bridges and buildings as they provide the primary structural support to ensure the structures remain standing. Columns utilized in these structures can vary in material type (concrete, steel, hybrid, timber, etc.), size, orientation, and cross-sectional geometry (rectangular, spherical, square, etc.).

Lateral impact loads can most commonly occur due to vehicle collisions with the structural columns. These collisions can be accidental such as a car losing control or a distracted driver [9], but they can also be intentional such as an act of terrorism [2] or suicide [10]. The consequences of such an impact can cause the failure of the column and the structure which can have fatal results. The I-40 bridge in Webbers Falls, Oklahoma was a concrete bridge for vehicle travel over the Arkansas River which collapsed in 2002. The failure was caused by a barge collision with the supporting columns which resulted in a partial collapse of the bridge and killed 14 people [3].

The consequences of failure occurring can be catastrophic with large loss of life, especially if this failure were to occur in a high-rise residential or commercial structure. To prevent this loss of life it is important to develop ways to mitigate the possibility of collapse. Some strategies for mitigating failure due to lateral impact loads include material supports such as steel tubes or fibre reinforced polymers (FRP), and design solutions such as developing improved lateral impact resistance designs for columns. This literature review will explore some research done into material mitigation factors for resisting lateral impact loads such as concrete-filled FRP tubes,

M. George (✉) · M. Abdallah · H. Hajiloo
Department of Civil and Environmental Engineering, Carleton University, 1125 Colonel By Drive, Ottawa K1S 5B6, Canada
e-mail: MickeyGeorge@cmail.carleton.ca

S. Walbridge et al. (eds.), *Proceedings of the Canadian Society of Civil Engineering Annual Conference 2021*, Lecture Notes in Civil Engineering 244,
https://doi.org/10.1007/978-981-19-0656-5_28

concrete-filled FRP-steel double-skin tubes, spiral reinforcement (SR), and ultra-high-performance fibre-reinforced concrete (UHPFRC). This research will be used to explore the impact resistance of concrete-filled glass FRP (GFRP) tube columns and evaluate how the GFRP tube improved the impact resistance of reinforced concrete (RC) columns.

The effects of dynamic loads are difficult to accurately calculate and are often estimated with a numerical equation that uses several assumptions. These methods for estimating the equivalent static loads often have a large margin for error. Subsequently, it is harder to effectively reinforce the columns to resist dynamic loadings without accurate knowledge of how these materials improve the performance of the column. The effects of lateral impact loads on columns are being studied to provide a better understanding of how impact loads can compromise the structural integrity of columns and the structures as a whole. This improved understanding will aid the development of more accurate lateral strength capacity estimates for columns, and material or design solutions to improve the performance of columns subjected to impact loads.

2 Background

2.1 Testing Methods

The impact testing method used by researchers ideally should simulate the conditions that occur in an impact loading scenario and replicate the failure modes and responses likely to occur in this event. In the reviewed studies, there were three primary testing methods used to evaluate the impact resistance of the specimens. These methods were (1) drop weight apparatus, (2) horizontal impact apparatus with a truck or trolley, and a (3) finite element (FE) model simulating a truck impacting the column. A monotonic test was also implemented by Qasrawi et al. [14] to evaluate the static load enhancements provided by FRP jackets. These tests were performed using a variety of impact weights, drop heights, and impact velocities. There are advantages and drawbacks associated to each of the testing methods utilized to test impact resistance.

Drop weight apparatuses are the most common method for impact testing as they can more closely resemble impact damage in field conditions while also having a built-in fail-safe mechanism that can stop the motion of the weight. However, if the weight does not immediately separate from the specimen after impacting the specimen then the weight will move with the specimen and the additional weight needs to be account for in the determination of the impact response [6]. Additionally, if there needs to be an increase in the impact energy/velocity, this can require increasing the height of the drop weight apparatus or strengthening the guide columns of the weight to support a heavier mass.

Aghdamy et al. [1] developed a horizontal impact testing system (HITS) which used a pneumatic instrumented striker to deliver the impact load. The drawbacks for both of the HITS and drop weight systems are that they have difficulty accurately simulating the effects of a vehicle collision due to their limited applied impact energy capacity. The horizontal impact apparatus using a trolley system was used by Chen et al. [6] as this system can reproduce full-scale crash tests. Similar systems were also used for various researchers to study the effects of collisions with columns.

An FE model was also used to study the effects of a full-scale crash at velocities typically experienced around bridge columns. This system for testing the impact resistance can be effective but only if the model is properly validated, which can be an exhaustive process that requires experimental results to compare the model. Due to this, the FE model is only as reliable as the data used to validate the results and can be time intensive if the experimental data is going to be collected through the study. These methods were used to study the impact resistance enhancement provided by various materials typically used to strengthen structural members.

2.2 Effects of Strengthening Materials on Lateral Impact Resistance

2.2.1 Effects of Spiral Reinforcement on Lateral Impact Resistance

A numerical study on the dynamic response of reinforced concrete columns by Cai et al. [5] determined that the impact force-time histories can be divided into three stages: the oscillation stage, stabilization stage, and attenuation stage. The oscillation stage is caused by the initial impact lifting the impact force to its peak, which is increased with a higher impact weight and velocity. There is then a fast decay before the curve begins to increase steadily in the stabilization stage. As the impact energy dissipates, the impact force reduces to zero in the attenuation stage which concludes the impact process. Similar to the force-time history, the deflection-time history consists of the ascent stage, descent stage, and the damped vibration stage. The numerical analysis conducted by Demartino et al. [7] yielded similar force-time histories as those found by Cai et al. [5] There were some discrepancies between the two force-time histories primarily that the Demartino et al. [7] histories did not display the stabilization stage found by Cai et al. [5]. This discrepancy can likely be attributed to the Cai et al. [5] impact location being at the top of the columns, and the columns having a square cross-section whereas the Demartino et al. [7] columns were circular with the impact location near the base of the column.

The experimental study conducted by Demartino et al. [7] showed that the formation of damage occurs faster in higher velocity impacts and that the severity of the damage also increases as impact velocity increase. The study by Cai et al. [5] also concluded that the increase in impact velocity leads to a linear increase in maximum displacement. However, the severity of the damage is improved by reducing the

distance between stirrups in the columns which increases the shear resistance and could provide sufficient resistance after concrete cracking. The addition of spiral reinforcement was suggested by Chen et al. [6] to improve the ductile behaviour of columns subjected to impact loading.

2.2.2 Effects of FRP on Lateral Impact Resistance

The force-time histories provided in the study conducted by Chen et al. [6] showed that the addition of GFRP tubes improved the shear and global impact behaviours of the columns. The importance of the GFRP was also shown to be more significant with an increase in impact energy. The specimens with thicker GFRP tubes exhibited higher local stiffness and damping, which lead to an increase in the duration of the impact. The force-time histories of the concrete-filled FRP tube (CFFT) columns were similar to those for reinforced concrete, with an initial and steep rise in impact force, followed by a sharp decline and stabilization before a steady decay to zero. The specimen with a thicker GFRP tube exhibited a sharper decline than the specimens with a thinner GFRP tube. The shallower decline exhibited by the specimens with a thinner tube remained relatively constant with an increase in impact velocity. This suggests that increasing the thickness of the GFRP tube will increase the rate of decay of the impact force while increasing the overall duration by improving the damping of the column.

Pham and Hao [13] reviewed of the impact resistance provided by FRP and concluded that FRP materials were an efficient way to improve the impact resistance of concrete structures. The addition of FRP was shown to increase the load-carrying capacities of columns, while also increasing the ductility and energy absorption. This is supported by the findings of Chen et al. [6] which concluded that increasing the thickness of GFRP tubes leads to an increase of energy absorption and a decrease in the maximum displacement of CFFT columns. They also showed that the tensile strength of the FRP increases as the strain rate increases and that an increase in compressive strength can be attributed to the addition of FRP tubes. The experimental results from Qasrawi et al. [14] showed that the addition of an FRP jacket increased the energy required to cause the failure of a reinforced concrete column by a significant amount. The FRP jacket also reduced permanent displacements and the occurrence of concrete crushing or spalling in the columns. The ductility of the columns was shown to increase with the addition of an FRP jacket. For columns with a 1.2 and 2.4% reinforcement ratio the energy required to cause failure increased by 1223 and 467% respectively, indicating that there is a greater benefit to columns with lower reinforcement ratios. Wang et al. [16] showed that increasing the thickness of the FRP tube leads to a decrease in impact load and residual lateral deformation. It was also stated that the FRP fibres were oriented in the hoop direction and that further research should be conducted into the effect that the orientation of the fibres has on the impact resistance of the member.

2.2.3 Effects of FRP and Spiral Reinforcement on Lateral Impact Resistance

The lateral impact resistance of concrete columns is improved through the addition of FRP tubes or spiral reinforcement. Qasrawi et al. [14] showed that the addition of FRP tubes to a column with spiral reinforcement drastically improved the impact energy capacity of the column. Chen et al. [6] showed that concrete columns reinforced with only FRP tubes reduced the maximum displacement and increase the energy absorption of the column, but that it exhibited a brittle failure mechanism. The study concluded that the brittleness of the FRP tubular columns could be improved with the addition of spiral reinforcement. Thus, the configuration of FRP tubes and spiral reinforcement not only increases the impact resistance of the column, but also improves the ductility of the element. It was also concluded that for columns carrying heavier axial loads the configuration of FRP tubes and spiral reinforcement is optimal for resisting lateral impact loads. A study of axial impact resistance conducted by Huang et al. [11] concluded that the configuration of FRP tubes and spiral reinforcement provided better impact resistance than either of the materials separately.

2.2.4 Effects of Other Strengthening Materials on Lateral Impact Loads

Steel tubes are a viable strengthening material to improve the lateral impact resistance of concrete columns. In a study conducted by Chen et al. [6], it was found that the residual lateral deformations of a column with a hollow steel tube interior (DSTC) were roughly 40% lower than the concrete columns reinforced with just an FRP tube (CFFT). This indicated that the members with steel tubes had lower local stiffness and higher global stiffness. The DSTC members are also able to absorb more energy than the CFFT members under the same impact velocity.

Ultra-high-performance fibre-reinforced concrete (UHPFRC) is considered to be a promising material to improve the resistance of impact loading. Fan et al. [8] conducted a study to evaluate the impact resistance provided by UHPFRC using a numerical analysis. Compared to conventional RC columns, the UHPFRC jacket reduced displacement by at least 50% and exhibited less severe damage under similar impact velocities. The thickness of the UHPFRC jacket significantly affected the impact resistance of the column under low-velocity impacts, but when the impact velocity was high increasing the jacket thickness had minimal effect on the residual capacity after impact.

2.2.5 Summary of the Column Damage

The various support materials used to reinforce the columns impact the amount of damage sustained by the column. Generally, it can be seen that the addition of any

material typically reduces the amount of damage and increase the impact energy capacity. However, the FRP-steel double skin tubular columns were able to sustain the most amount of impact energy and exhibited lower damage when compared to the conventional reinforced concrete columns and the columns reinforced with other materials. A summary of the damage sustained by various columns reinforced with material supports, the loading conditions, and section properties can be seen in Table 1.

2.3 Effects of Strengthening Materials on Axial Impact Loads

2.3.1 Effects of Steel Tubes on Axial Impact Loads

Steel tubes have been shown to have a positive effect on the lateral impact resistance of concrete columns, but a study by Zhu et al. [17] investigated the potential benefits of concrete-filled steel tube (CFST) columns on axial impact resistance. The study showed that the circular columns were able to sustain significantly higher impact forces and exhibited lower maximum displacements and a shorter impact duration. It was concluded that circular columns were optimal for resisting axial impact loads as a result of the shape characteristics allowing more impact force to be distributed to the concrete core. Increasing the steel strength was able to increase the axial impact resistance of the CFST columns, but the impact of this was more visible in non-circular columns due to their increased sensitivity to local buckling.

2.3.2 Effects of FRP and Spiral Reinforcement on Axial Impact Loads

Columns reinforced with FRP and spiral reinforcement were shown to be an effective configuration for lateral impact resistance. A study by Huang et al. [11] looked into the axial impact resistance of circular columns with GFRP and SR. The impact damage resistance of the columns was shown to be improved by the configuration of GFRP and SR than either of the two reinforcement materials separately. The configuration was shown to increase the impact stress duration and that a higher stress level was reached after the peak, indicating that the confinement improves the energy dissipation capacity of the column. Increasing the number of GFRP layers and SR volumetric ratio was able to increase the convergence of dynamic peak stress towards the static peak stress. These findings were consistent with those found by Huang et al. [12] which showed that columns with CFRP and SR demonstrated higher impact load resistance compared to columns with either of these materials separately. The ductility of the column was also improved by the addition of CFRP and SR, with the failure mode being less brittle. Similar to Huang et al. [11], the addition of CFRP and SR increased the maximum impact load, larger energy dissipation capacity, and more durability at high levels of stress. These two studies concluded that increasing

Table 1 Summary of experimental studies on the effects of impact loads on columns types

Reference	Specimens	Dimension (mm)	Mass of impactor (kg)	Impact energy (kJ)	Damage that occurred
[7]	Reinforced Concrete	d = 330 s = 330	1582	7.21	1 diagonal crack. Some capacity reserved
		d = 330 s = 100		6.98	1 diagonal crack. Some capacity reserved
		d = 330 s = 330		15.66	1 diagonal crack. Some flexural cracking along rear followed by failure
		d = 330 s = 100		15.45	1 diagonal crack. Some flexural cracking along rear followed by failure. Damage reduced when stirrup distance reduced
[14]	GFRP and SR	d = 200, ρ(%) = 1.2	561	8.7	Sustained 1 impact; GFRP failed
		d = 200, ρ(%) = 2.4			Sustained 5 impact; GFRP failed
[6]	DSTC	$d_{con} = 300$, $d_{st} = 140$, $t_{FRP} = 7$	1580	61.9	Minimal damage; concrete spalling of abutment at fixed end
		$d_{con} = 300$, $d_{steel} = 140$, $t_{FRP} = 7$		85.2	Noticeable damage at point of impact. Failure resulting from fibre rupture of the GFRP in hoop direction at fixed regions
		$d_{con} = 300$, $d_{steel} = 140$, $t_{FRP} = 7$		108	Noticeable damage at point of impact. Failure resulting from fibre rupture of the GFRP in hoop direction at fixed regions
		$d_{con} = 300$, $d_{steel} = 140$, $t_{FRP} = 10$		108	Noticeable damage at point of impact. Failure resulting from fibre rupture of the GFRP in hoop direction at fixed regions

(continued)

Table 1 (continued)

Reference	Specimens	Dimension (mm)	Mass of impactor (kg)	Impact energy (kJ)	Damage that occurred
[16]	Reinforced concrete with Interior steel tube	d = 114, t_{steel} = 2.1, 6 bars with d = 6, d_{ties} = 4 at s = 50	230	0.56	Slight damage in impact region. 17.8 mm of residual deformation
		d = 114, t_{steel} = 2.1, 6 bars with d = 6, d_{ties} = 4 at s = 50	230	1.13	Significant cracks observed at the bottom of the column and concrete crushed at the concrete base. 29.5 mm of residual deformation
		d = 114, t_{steel} = 2.1, 6 bars with d = 6, d_{ties} = 4 at s = 50	230	2.25	Major cracks observed in specimen. 53.9 mm of residual deformation

the thickness of the FRP and SR ratio greatly improves the impact resistance of the columns.

2.4 Future Considerations

There remains a gap in knowledge indicated in these studies that are to be accounted for in future research. Wang et al. [16] stated that the effect of the orientation of the FRP fibres on lateral impact resistance was unclear, and for that study, the fibres were oriented in the hoop direction of the member. Due to this uncertainty, the orientation of the fibres in the FRP should remain constant for all members tested to ensure homogeneity amongst the test specimens. Pham and Hao [13] reviewed numerous studies into the impact resistance provided to concrete structures by FRP reinforcement. It was stated that the debonding mechanism, stress-strain relationship, and the rupture strain of the FRP subjected to impact loading were unclear through the review. Future research is needed to determine the effect that impact loading has on these subjects.

3 Research Methodology

This review is the first step towards developing a systematic research plan on the impact resistance of conventional reinforced concrete columns and CFFT columns confined with GFRP tubes. It was revealed that there is considerable research performed on the impact resistance of concrete columns reinforced with different materials. However, there exists minimal research conducted that directly compares the improvement provided by CFFT columns to conventional reinforced concrete

columns with respect to lateral impact resistance. Research into the impact resistance of CFFT columns must be furthered to enhance the knowledge on the integrity and reliability of infrastructures against impact loads.

Currently, an experimental work is conducted at Carleton Univesity to investigate the impact resistance of CFFT columns and conventional reinforced concrete columns. The objective of this study is to understand the performance of columns with the CFFT material configuration compared to reinforced concrete columns subjected to loads simulating the effects of vehicle collisions with bridge piers.

Although the drop mass test apparatus was the most adopted to understand the impact behavior of structural members, it is difficult to simulate the vehicle collision due to their limited applied impact energy capacity. The pendulum impact was designed to induce impact loading on concrete members in several studies [4, 15] and [18] and proved to be an efficient way to simulate vehicular impact characteristics. Thus, in this study, a pendulum machine of 221 kg is used to apply impact loading on the specimens. Test setup is shown in Fig. 1. The pendulum was lifted with designated angles using a pulley system connected to a winch and then released to generate the impact loading on the top of the columns. The impact angle was achieved by pulling the pendulum weight backwards to a distance corresponding to

Fig. 1 Test set-up of lateral impact test using pendulum machine

the impact angle by cranking the winch. The winch was mounted on a steel reaction frame. The pulley system was connected by passing a high tensile strength rope from the winch to a fabricated rolling rod at a height above the winch, and then to a hook on the pendulum weight system. A release mechanism was achieved using a fabricated rod with a rope attached to it. The rod was connected to its hook such that it unlocked from the hook once the attached rope was pulled.

All specimens have a height of 1800 mm with two different internal diameters of 152 and 210 mm. All columns are reinforced with 6–10 M longitudinal reinforcement. Circular ties of 10 M and with 100 mm pitch, are added along the height of the columns to increase their structural performance. A steel base with a hollow steel section of 152 diameter and 450 mm height was fabricated to provide a fixed boundary condition to the bottom of the columns. The steel base is attached to the ground of the strong floor lab using four high-strength anchor bolts. A normal strength concrete was used to cast the column specimens. The maximum aggregate size was 20 mm. The average compressive strength of the concrete was around 35 MPa. The yield strength of the longitudinal bars and ties was 447 MPa and the elastic modulus was 200 GPa. To investigate the effects of different FRP tube parameters, two types of glass FRP tubes with a different wall thickness of 2.9 mm and 6.4 mm are used. The tube wall consisted of continuous glass fibers wound in an epoxy resin matrix. Dimensions and mechanical properties of the used GFRP tubes are shown in Table 2. The equipment used in the experimental program included Celesco string potentiometers (SP1-25), 50-kip compression load cell, and Yokogawa DL750P Data Acquisition system as the oscilloscope. The load cell and string potentiometers were calibrated at the laboratory to determine their capacities, mode of operation and to give accurate results for the tests. In addition, A series of strain gauges are mounted to the column to record the strain of the steel bars and GFRP tubes during impact.

Table 2 Dimensions and mechanical properties of fiber-reinforced polymer tubes

Tube type	Internal diameter (mm)	Thickness (mm)	Number of layers	Stacking sequence	E_1 (MPa)	E_2 (MPa)
I	152	2.9	8	$[\pm 60]_4$	20,860	8785
II	152	6.4	16	$[\pm 61_2, \pm 43_2, \pm 61_4]$	23,630	9270
II	210	6.4	26	$[\pm 74, \pm 60_4, \pm 74, \pm 60_4, \pm 74_4]$	24,720	10,250

4 Conclusion

There were several reinforcing materials that showed promise to improve the impact resistance of concrete columns. These materials included spiral reinforcement, FRP, FRP-SR configurations, steel tubes, and UHPFRC jackets.

1. Spiral reinforcement alone was shown to improve the severity of the damage that occurred due to impact loading by improving the shear resistance of the column. It was also shown that the addition of spiral reinforcement improved the ductility of the beams and results in less brittle failure modes. An analysis of the force-time histories of columns with spiral reinforcement showed that circular reinforced concrete columns exhibited a rapid decay of the impact force after the initial peak.
2. FRP confinement is an efficient means to improve the impact resistance of the concrete column by increasing the load-carrying capacity, energy absorption, and ductility of the member. It was determined that increasing the thickness of the FRP tube also enhanced the benefits provided to the column.
3. The combination of both FRP and spiral reinforcement was determined to provide more improvement to the impact resistance than either of the two materials separately. This configuration was also determined to be optimal for resisting impact loads if the column is required to carry sufficiently heavy axial loads.
4. The steel tubes were shown to be a viable material for improving the impact resistance of concrete columns, with the addition of a hollow interior steel tube reducing residual lateral deformation by 40%.
5. The UHPFRC jackets improve the impact resistance of columns, with significant improvement over reinforced concrete columns at high-velocity impact loads.
6. Regarding the axial impact resistance of concrete columns, Steel tube confinement was shown to significantly improve the axial impact resistance of the columns which reduced maximum displacements and impact duration while increasing the impact force capacity. The strength of the steel tube increased the axial impact resistance but did not have as much of an effect on circular columns due to the shape characteristics. The FRP-SR configuration was shown to be effective in improving the axial impact resistance of the column. The FRP confinement was indicated to improve the energy dissipation capacity of the column, and that increasing the FRP thickness or SR volumetric ratio further improves the resistance of the member.
7. it has been shown that the FRP-SR configuration for reinforcing circular concrete columns is effective in improving the lateral impact resistance. This configuration with GFRP will be compared to reinforced concrete columns in future research to study the behaviour of these columns under dynamic impact loading.

References

1. Aghdamy S, Thambiratnam DP, Dhanasekar M (2016) Experimental investigation on lateral impact response of concrete-filled double skin tube columns using horizontal-impact-testing system. Exp Mech 56:1133–1153
2. Anderson C (2018) Uzbek Asylum Seeker Gets Life in Prison for Deadly Truck Attack in Sweden. New York Times. https://www.nytimes.com/2018/06/07/world/europe/sweden-truck-attack-rakhmat-akilov.html.
3. Burton W (2017) Ceremony set to honor I-40 bridge collapse victims. *Muskogee Phoenix*. https://www.muskogeephoenix.com/news/ceremony-set-to-honor-i-40-bridge-collapse
4. Buth CE, Brackin MS, Williams WF, Fry GT (2011) Collision loads on bridge piers: phase 2. Report of guidelines for designing bridge piers and abutments for vehicle collisions. Rep FHWA/TX-11/9-4973-2, Texas Transportation Inst., College Station, TX; 2011.victims/article_374575c6-27e0-582c-b632-a3fab0b6b319.html
5. Cai J, Ye J, Wang Y, Chen Q (2017) Numerical study on dynamic response of reinforced concrete columns under low-speed horizontal impact loading. Proc Eng 210:334–340
6. Chen Z, Wang J, Chen J, GangaRao H, Liang R, Liu W (2020) Responses of concrete-filled FRP tubular and concrete-filled FRP-steel double skin tubular columns under horizontal impact. Thin-Walled Struct **155**
7. Demartino C, Wu J, Xiao Y (2017) Experimental and numerical study on the behavior of circular RC columns under impact loading. Proc Eng 199:2457–2462
8. Fan W, Xu X, Zhang Z, Shao X (2018) Performance and sensitivity analysis of UHPFRC-strengthened bridge columns subjected to vehicle collisions. Eng Struct 173:251–268
9. Gutschke L (2020) Rule woman dies after vehicle strikes bridge column near I-20 in north Abilene. Abilene Reporter News. https://www.reporternews.com/story/news/2020/06/26/rule-woman-traci-lynn-farwell-dies-after-vehicle-crash-north-abilene-near-i-20-interestate-20/3262790001/
10. Hogan J (2020) Woman Crashes vehicle into bridge at M-24/I-69 in suicide attempt. The County Press. https://thecountypress.mihomepaper.com/articles/woman-crashes-vehicle-into-bridge-at-m-24-i-69-in-suicide-attempt/
11. Huang L, Kasal B, Yan L, Sun X (2017) Impact behavior of concrete columns confined by both GFRP tube and steel spiral reinforcement. Constr Build Mater 131:438–448
12. Huang L, Kasal B, Yu T, Yan L, Gao C (2018) Experimental and numerical studies of CFRP tube and steel spiral dual-confined concrete composite columns under axial impact loading. Comp Part B 152:193–208
13. Pham TM, Hao H (2016) Review of concrete structures strengthened with FRP against impact loading. Structures 7:59–70
14. Qasrawi Y, Heffernan PJ, Fam A (2015) Dynamic behaviour of concrete filled FRP tubes subjected to impact loading. Eng Struct 100:212–225
15. Silva PF, Mesia WD, Marzougui D, Badie SS (2009) Performance evaluation of flexure impact resistance capacity of reinforced concrete members. ACI Struct J 106(5):726
16. Wang R, Han LH, Zhong T (2015) Behavior of FRP-concrete-steel double skin tubular members under lateral impact: experimental study. Thin-Walled Struct 95:363–373
17. Zhu Y, Yang H, Yang X, Sun F (2020) Behavior of concrete-filled steel tubes subjected to axial impact loading. J Construct Steel Res 173
18. Zhang X, Hao H, Li C (2016) Experimental investigation of the response of precast segmental columns subjected to impact loading. Int J Impact Eng 95:105–124

Concentric and Eccentric Material Characterization of Polyurethane Disc Bridge Bearings

Nicholas Thibodeau, Alan Lloyd, and Hassan Fatemi

1 Introduction

Bridge bearings are used to accommodate a superstructure's translational and rotational displacements independently from the substructure while appropriately transferring loads. A common type of bearing, high load multirotational bridge bearings (HLMR), have been widely utilized in larger structures given their ability to resist high loads and permit rotations about any horizontal axis. Included in which are pot, disc and curved sliding bearings, with notable research on their behaviour and mechanics coming from NCHRP Report 432 [8]. Disc bearings, in particular, utilize an unconfined polyether-urethane disc (polyurethane disc) sandwiched between steel plates with a high strength shear pin in the center to resist horizontal loads. The hard elastomeric polyurethane can resist high compressive demands without excessive vertical deflections, while accommodating the superstructure's rotations. Although disc bridge bearings are not a modern invention, their origin of being a proprietary technology has limited their utilization and public knowledge on the behaviour of the bearing and the material within. To facilitate widespread use of disc bearings in Canada, material characterization on the polyurethane's response under compressive and rotational loads is required to properly design, model, and understand the bearings limitations.

Being an elastomeric material, the polyurethane seen in disc bridge bearings is visco-hyperelastic and experiences a non-linear elastic response under high compressive demands that is dependent not only on its inherent material properties, such as hardness, but also its shape, temperature, loading boundary conditions, and rate

N. Thibodeau (✉) · A. Lloyd
Department of Civil Engineering, University of New Brunswick, Fredericton, Canada
e-mail: nthibod4@unb.ca

H. Fatemi
Goodco Z-Tech a Product of CANAM Bridges, Laval, Canada

S. Walbridge et al. (eds.), *Proceedings of the Canadian Society of Civil Engineering Annual Conference 2021*, Lecture Notes in Civil Engineering 244,
https://doi.org/10.1007/978-981-19-0656-5_29

of loading [7]. Since elastomers are considered to be an incompressible material, meaning uniaxial compressive deflection is accommodated not by volume change but by displacement of the material via bulging, the shape of the material influences its compressive resistance. This effect is generally characterized using shape factor or the area under compression over the area free to bulge. The influence shape factor has on the compressive stiffness is directly dependent on the loading boundary condition, or with respect to disc bearings, the friction between the polyurethane and its bearing plates. Previous work on the relationship between polyurethane-plate friction and its stiffness concluded the influence shape factor has on the polyurethane's compressive stiffness increases alongside the increase in friction between the plates and polyurethane since it resists lateral sliding of the disc [2]. Additional information on the characteristics of elastomeric material that may be relevant for bridge bearing applications can be seen in Chapter 33 – Mechanical Properties of Rubber in Harris' Shock and Vibration Handbook, or the NCHRP Report 248 [6, 7].

This paper describes an experimental research program, completed at the University of New Brunswick, designed to characterize the response of polyurethane seen in disc bearings under a bridge's compressive and rotational demands for various shape factors. Concentric and eccentric tests completed on small-scale polyurethane specimens of shape factors varying from 1.5 to 4 with boundary conditions and properties seen in disc bearings are summarized. The resulting characterization will give bridge designers the means to appropriately predict the polyurethane's behaviour at various loading stages, such as during the initial placement of the superstructure, subsequent variations of compressive load, and rotations experienced during the life of the structure.

This work is part of a more extensive study between the University of New Brunswick and Goodco Z-Tech that aims to better understand the behaviour of disc bridge bearings and polyurethane under conditions seen in Canadian bridges.

2 Experimental Program

In this study, small-scale polyurethane disc samples containing properties and boundary condition interactions similar to what would be seen in a disc bridge bearing were manufactured and tested under cyclic concentric and eccentric compression. These testing programs were developed to characterize the compressive and rotational behaviour under parameters seen within a Canadian bridge.

2.1 Specimen Details

Six groups of polyurethane disc specimens of uniform thickness were manufactured with varying diameters to achieve shape factors of 1.5, 2.0, 2.5, 3.0, 3.5 and 4.0, respectively, using the equation for shape factor of a solid disc in terms of thickness

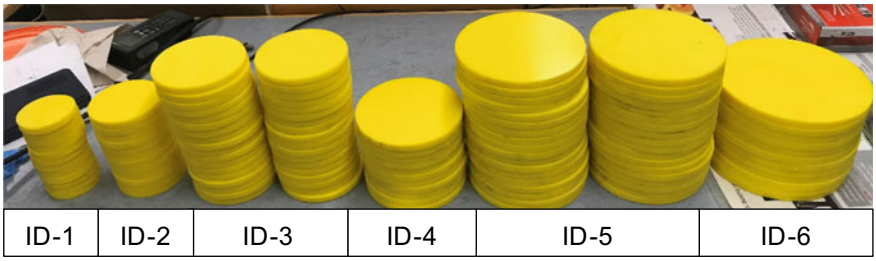

Fig. 1 Polyurethane specimens used for concentric, eccentric, and future testing

Table 1 Dimensions of polyurethane specimen sample size groups

Sample ID	Shape factor (SF)	Diameter (mm)	Thickness (mm)
1	1.5	75	12.5
2	2.0	100	12.5
3	2.5	125	12.5
4	3.0	150	12.5
5	3.5	175	12.5
6	4.0	200	12.5

(t) and diameter (D) shown in Eq. 1. Specimens can be seen in Fig. 1 with their dimensions outlined in Table 1.

$$\text{Shape Factor (SF)} = \frac{\text{Area Under Loading}}{\text{Area Free to Bulge}} = \frac{\frac{\pi D^2}{4}}{\pi Dt} = \frac{D}{4t} \tag{1}$$

These sizes were chosen so that the range of typical polyurethane shape factors used in a disc bridge bearing are captured and that enough sizes are tested to validate the material characterization results. The specimens were manufactured with uniform manufacturer specified hardness of Shore 90A and an average measured hardness of 36D.

Since it was unknown what temperatures the specimens experienced during shipment, they were conditioned at room temperature in the laboratory for a week prior to testing to ensure any low-temperature effects on the polyurethane's properties are avoided.

Additionally, 19.05 mm thick steel bearing plates finished in the same manner as a disc bridge bearing were used to properly simulate the contact interaction between the polyurethane and steel plates in an actual bearing. One set of plates were used for each set of sample sizes, with each plate having a diameter 25.4 mm larger than its respective polyurethane specimen.

2.2 Cyclic Concentric Compression Test Setup

Thirty specimens, five of each sample size, were tested under cyclic uniaxial compression by the self-reacting compression machine shown in Fig. 2. The specimens were centred to the cross-head motion of the machine then cycled five or ten times at a continuous deformation rate of ±1.3 mm/min, reaching a maximum stress of 55 MPa and minimum load of 1335 N (0.04 to 0.3 MPa depending on specimen size). Five cycles were performed on four out of the five specimens within a sample size, with the fifth specimen being tested under ten cycles. The five-cycle amount was chosen to ensure the cyclic behaviour approaches a harmonic state, with the ten-cycle test being used to validate its harmonic state. The loading rate of ±1.3 mm/min was chosen to follow that of ASTM D695, in-lieu of faster rates found in standards related to compressive tests on rubbers/elastomers, in order to be conservative in keeping the dynamic viscoelastic properties of the rigid polyurethane to a minimum [1]. The maximum stress of 55 MPa was chosen as it represents around 150% of the CSA S6-19 specified allowable service load compressive pressure on the polyurethane element in a disc bridge bearing of 35 MPa [3]. Using 150% of this condition is an approximate representation of the ultimate stress experienced by the polyurethane within a bearing. The minimum load was used to ensure all components remained in contact throughout testing.

Stress-strain relationships were obtained for each tested specimen. The average vertical strain was monitored by using two 25 mm linear variable differential transformers (LVDTs) at either end of the specimen, 180° from each other. Data acquisition software was used to simultaneously monitor the LVDTs displacement and load output from the compression machine at a rate of 10 Hz. Figure 3 depicts a typical cyclic compression concentric test setup.

Additionally, the diameter of two specimens from each sample size was measured incrementally for over one week following their initial test to evaluate the recovery of the material's bulging from compressive deformation. These specimens were then re-tested under the same cyclic concentric compression procedure to investigate the response of a specimen that has had time to recover from high stresses.

Fig. 2 Compression machine

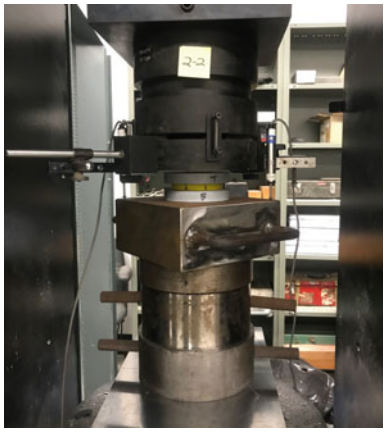

Fig. 3 Cyclic compression test setup

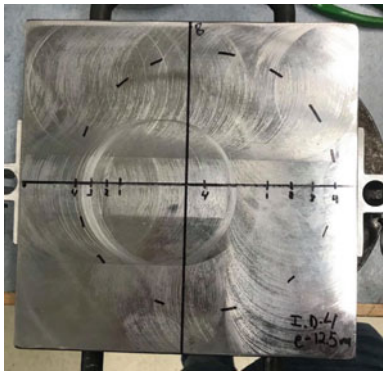

Fig. 4 Eccentric test template for sample ID-4

2.3 Cyclic Eccentric Compression Test Setup

To explore the rotational stiffness of the polyurethane disc samples, cyclic uniaxial compression tests with an eccentric load was performed on the specimens of varying shape factors. The largest sample, ID-6 having a shape factor of 4.0, was omitted from these tests due to capacity constraints of the compression machine. The eccentricity values were selected to be 5.5 mm for ID-1 specimens, 8.5 mm for ID-2 specimens, 10 mm for ID-3 specimens, 12.5 mm for ID-4 specimens and 14 mm for ID-5 specimens. These values were selected as they represent an eccentricity of around 7–8.5% of the specimen's diameter, below the 10% limit set out by CSA S6-19 for mitigating uplift of the polyurethane disc within a disc bridge bearing [3].

The specimens were positioned with these eccentricities by marking a template on the bottom plate holding the specimen and its respective bearing plates, as seen in Fig. 4, so when the bottom plate is centred with the cross-head motion of the compression machine, the specimen is appropriately offset. A custom load head was

also built for the compression machine, seen in Fig. 5, consisting of a 50 mm thick steel plate pinned to a high strength steel rod.

The 50 mm steel plate was loosely pinned to the steel rod that was fixed to the upper portion of the compression machine so that the plate could rotate freely as the specimen rotates, while remaining centred in-between tests. Two LVDTs measuring displacement throughout the test were located on either side of the specimen, perpendicular to the axis of rotation, and evenly spaced from the center of the cross-head motion. The resulting displacement values were used alongside the distance between the LVDTs to determine rotations of the sample following the test. Data acquisition software was used to simultaneously monitor the LVDTs and load output from the compression machine at a rate of 10 Hz.

The test procedure consisted of installing the samples at the appropriate eccentricity and applying five compression cycles at a continuous rate of ± 1.3 mm/min to a peak rotation of 0.02–0.022 rad and a minimum load of 2225 N. The peak rotations were chosen as it represents the approximate ultimate rotation of the polyurethane element in a disc bridge bearing. Since the compression machine could not be programmed based on the rotation of the specimen, displacement control of the compression machine's cross-head motion was used instead. However, since the point of the eccentric test was to determine the rotational stiffness of the polyurethane, the needed specimen deflection to induce the peak rotation at the location of the cross-head was unknown. To overcome this, the needed peak displacement was initially estimated for each sample size using the 50–55 MPa secant modulus from the cyclic concentric tests, then tested on a previously used specimen from the cyclic concentric tests. The values were then adjusted to obtain a target peak rotation of 0.02 rads before using an eccentric specimen. Peak rotations were calculated following each eccentric test and cross-head displacement adjusted, if needed, to remain in the 0.02–0.022 rad range of rotation. The displacement rate was chosen for the same reasoning as the cyclic concentric tests, and the minimum load was used to ensure all components remained in contact throughout testing.

Fig. 5 Eccentric sample test setup

3 Experimental Results

The experimental results of the polyurethane specimen tests focus on the stress-strain relationship for concentric tests, and the moment-rotation relationship along with the deflection of the two extreme ends of rotation throughout testing for eccentric tests. The primary objective is to characterize the compressive and rotational behaviour of the polyurethane for various shape factors.

3.1 Concentric Test Results

Typical stress-strain relationships obtained from the five cycle concentric compression tests are shown in Fig. 6 for a specimen with a shape factor (SF) of 2.0, and Fig. 7 for a specimen with a shape factor of 3.5. The specimens' diameter and thickness were measured at four distinct locations prior to testing and averaged in determining the engineering stress-strain values. Displacement of the specimens was calculated using the average of the two LVDTs to account for possible minute rotations of the

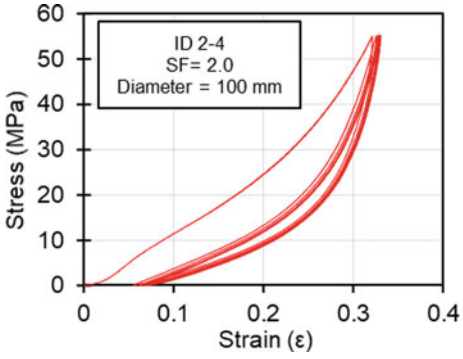

Fig. 6 Five cycle concentric compressive stress-strain results for specimen ID 2–4

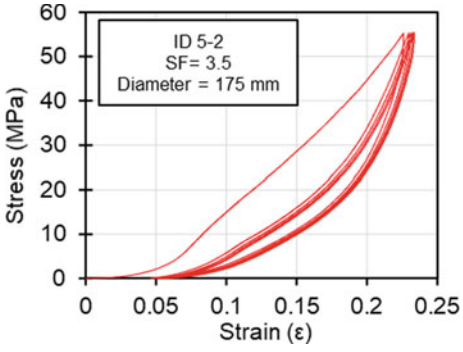

Fig. 7 Five cycle concentric compressive stress-strain results for specimen ID 5–2

specimen during testing. The data acquisition system captured the load values in unison with the displacement readings.

Mullins effect is observed following the initial loading cycle (virgin curve), as the reloading response follows closely to that of the initial cycles unloading curve [5]. After unloading of the first cycle, the specimens exhibited unrecovered strain, or residual strain, causing the second loading cycle to start from the residual strain location. Additional residual strain was seen in the following cycles, with its magnitude reducing after each cycle. This trend was apparent in all tested specimens, with the ten cycle tests confirming a continuous reduction in residual strain following each cycle, an example of which is shown in Fig. 8.

The data collected for the five specimens tested in each sample size under cyclic concentric compression were averaged and corrected so that loading starts at zero strain and zero stress. The results may be used in comparing responses between polyurethane shape factors. Figure 9 shows the average virgin curve in addition to the average fifth loading curve for each sample size.

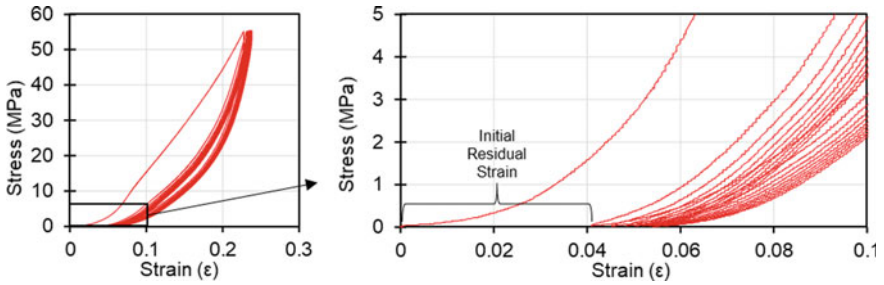

Fig. 8 Ten cycle concentric compressive stress-strain results for specimen ID 3–5 (Shape factor = 2.5 & Diameter = 125 mm)

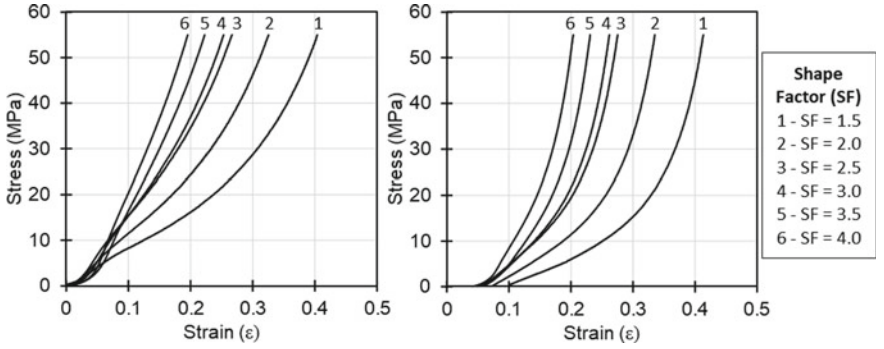

Fig. 9 Averaged virgin loading curve (Left) and average fifth loading curve (Right) per sample size

3.1.1 Recovered Samples Re-test Results

A number of specimens from each sample size were re-tested under the same conditions a minimum of one week following the initial cyclic concentric compression test. An example of re-tested stress-strain results in comparison to its original test can be seen in Fig. 10, corrected so that loading of both tests starts at zero stress and zero strain. To investigate recovery of the specimen's shape, the average diameter was measured incrementally between the initial test and re-test. It was observed that the specimens did not fully recover and exhibited permanent bulging, Fig. 11. The majority of recovery occurred 6 h following the initial test with an average of 35% of the bulging recovered between all re-tested specimens, and an additional average of 16% after approximately seven days.

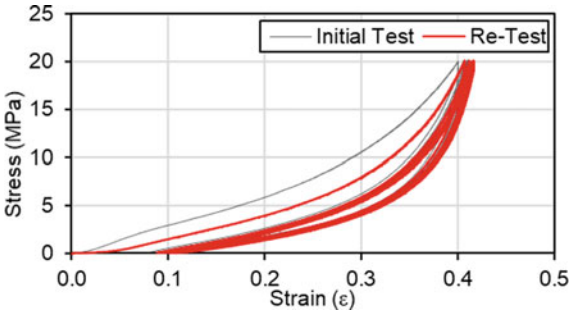

Fig. 10 Specimen ID 1–2 cyclic concentric compressive initial vs recovered re-test results (Shape factor = 1.5 & Diameter = 75 mm)

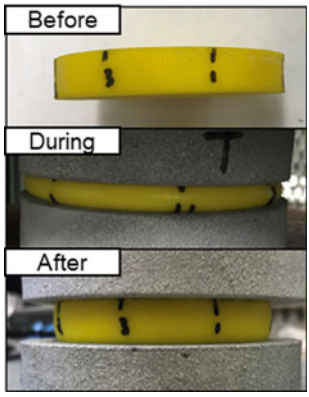

Fig. 11 Pictures of specimen ID 1–2 from the initial test

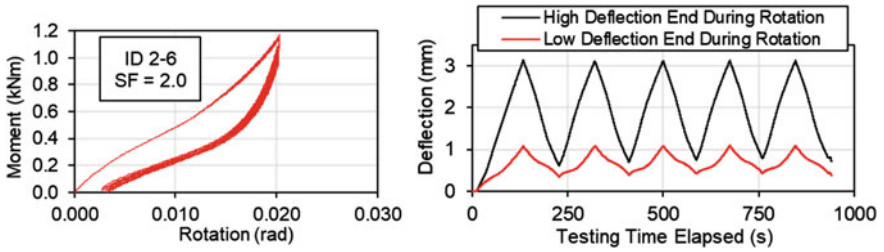

Fig. 12 Specimen ID 2–6 cyclic eccentric compressive results of moment-rotation (left) and deflection of the extreme ends during rotation over testing time (right), Diameter = 100 mm, Thickness = 12.5 mm

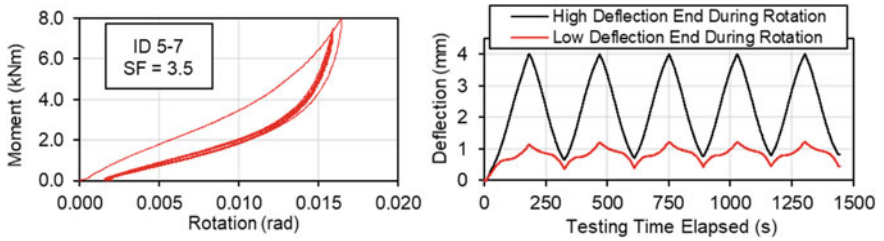

Fig. 13 Specimen ID 5–7 cyclic eccentric compressive results of moment-rotation (Left) and deflection of the extreme ends during rotation over testing time (Right), Diameter = 175 mm, Thickness = 12.5 mm

3.2 Eccentric Test Results

Typical results for the five-cycle eccentric compressive test can be seen in Fig. 12 for a shape factor of 2.0 and Fig. 13 for a shape factor of 3.5. Included is the moment-rotation relationship and displacement of the two extreme ends of the specimen during rotation. Moment-rotation was derived from the force and LVDT displacement readings along with the given eccentricity and distance between LVDTs, with the displacement for the two extreme ends during rotation determined using the LVDT readings and the distance to its respective specimen end.

4 Analysis and Discussion

4.1 Tangent Modulus

For all shape factors tested, the concentric compressive experimental results depicted non-linear behaviour for stresses up to and exceeding the 35 MPa service load compressive stress limit specified by CSA S6-19 for both the virgin loading curve and

following cycles [3]. It is essential to examine this trend considering the polyurethane element inside a disc bearing may be designed assuming linear elastic behaviour [4]. Linear approximation of the polyurethane's compressive behaviour is completed by simplifying the compressive stress-strain relationship into an effective modulus, such as the secant modulus outlined in ASTM D695 [1]. However, according to the experimental data, this may lead to an unrealistic estimation at the stress magnitude of interest given the non-linearity. A more valid method to explore the stiffness relationship of the polyurethane may be to plot the variation of tangent modulus over the applied stress. This is completed for each specimen by taking the tangent of the average five data point sets before and after the stress level of interest and plotting it against set stress for each loading cycle. The resulting variation of tangent modulus over applied stress for all specimen's virgin and consecutive loading curves, respectively, are shown in Fig. 14.

It is observed from the tangent moduli of the virgin curves that a softening occurs at relatively low strains for the initial loading of a new specimen followed by an increase in stiffness as the loading continues. During the consecutive loading cycles, a similar softening at lower strains to that of the virgin curve is seen as the shape factor of the sample increases. For all shape factors, rapid stiffening of the specimens at higher compressive strains is observed. The same process of taking the tangent

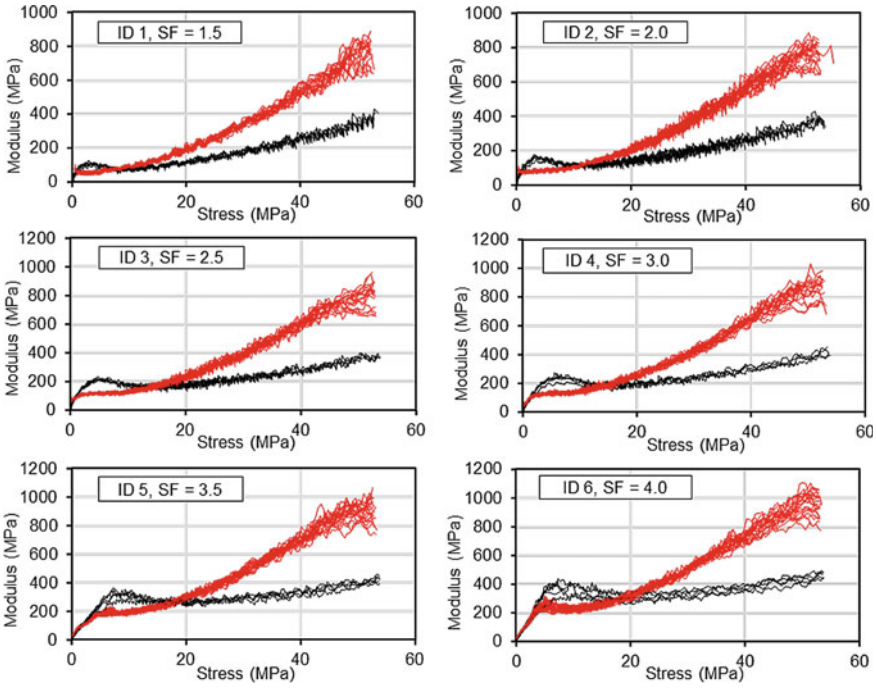

Fig. 14 Tangent modulus of the virgin loading curve (black) and subsequent loading curves (red) against stress for all the cyclic concentric specimens

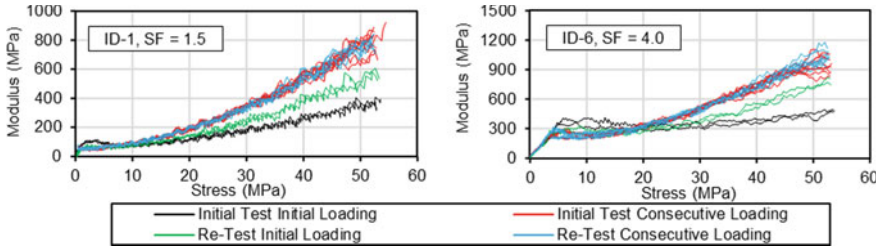

Fig. 15 Examples of the tangent modulus of the virgin loading curve and consecutive loading cycles for both the initial test and re-test on the recovered sample

modulus may be completed for the recovered samples, examples of which can be seen in Fig. 15 for shape factors of 1.5 and 4.0.

4.2 Discussion on Concentric Results and Implications for Disc Bearing Design

It is seen in Fig. 9 that the compressive stress-strain response of polyurethane, with properties and boundary conditions as what would be used in the design of disc bearings, is highly dependent on its shape factor. As the shape factor increases, the overall compressive stiffness increases as well. For comparison purposes, the range of cyclic loading tangent moduli at the CSA S6-19 service stress of 35 MPa varies between 400 to 500 MPa for specimens with a shape factor of 2.0, and 550 MPa to 650 MPa for specimens with a shape factor of 3.5. This suggests that the shape factor is of high importance when evaluating the response of the polyurethane element in designing a disc bridge bearing.

As previously mentioned, non-linearity of the compressive stress-strain response that will vary between the initial loading and subsequent variations of loads is seen, which may bring forth concerns when designing the polyurethane element in a disc bearing. In lieu of a linear assumption for the entire stress-strain relationship, it may be beneficial for designers of disc bearings to use the tangent modulus of the polyurethane in a range of stresses that the disc bearing will experience. The varying stress-strain response between initial and subsequent loadings must also be considered in designing bearings for the initial placement of the bridge on the bearing and subsequent variations of gravity loads, respectively. The main reasoning for the variation of stiffness after the virgin curve is currently unknown; however, it is speculated that it may be caused by the new polyurethane specimens, that have never been stressed, experiencing permanent damage or the material being "broken in". This could also explain the reasoning for consecutive loading cycles showing characteristics similar to that of the initial loading cycle as the shape factor increases, such as the softening at lower strains, considering total volume of material increases in higher shape factors resulting in less material being damaged or broken in.

Furthermore, the initial loading of a polyurethane specimen that has had time to recover after experiencing high stresses will respond differently compared to a new specimen. The response falls in between that of the subsequent loading cycles and initial loading of a new polyurethane specimen, while both sets of cyclic loading follow the same response, as seen in Fig. 15. It may be beneficial to investigate the initial loading of a recovered specimen with varying historic peak stresses, for example, one that has experienced a peak stress of the CSA recommended service load value of 35 MPa in place of the 55 MPa used. This could also enlighten the cause of variations between the stiffness responses of the initial and subsequent loading cycles and whether the speculated breaking in or damage of the material has any validation.

4.3 Discussion on Eccentric Result

It is evident in the cyclic eccentric compressive tests that the polyurethane's rotational stiffness depends on its shape factor as the moment to rotation relationship dramatically rises in correlation to the increase of shape factor. Furthermore, the trend of higher stiffness resulting from increased stress or strain seen in the concentric compressive results can be used to justify rotational behaviour.

As the specimen is loaded eccentrically and rotations are induced, the polyurethanes cross-section experiences non-linear stiffness as the highly stressed end during rotation becomes stiffer in relation to the end with the lowest stress. This increases the internal resisting moment as the eccentric load is applied, which in conjunction with the lowest stressed end being able to deform more readily than the highest, results in higher moments needed to induce further rotation. This relation is evident when examining the deflection time history of Figs. 12 and 13 as the deflection rate on the low stressed end of rotation increases compared to that of the high stressed end. This is more prominent as the specimen's shape factor increases since a larger diameter causes higher strains when trying to induce the target rotation. For the largest sample in the rotation tests, ID-5 having a shape factor of 3.5 and diameter of 175 mm, the rate of deflection on the end experiencing the lowest stresses approaches that of the opposite end, limiting its ability to rotate any further, which explains why the peak rotation was approximately 0.016 rads instead of the desired 0.02–0.022 rads. An additional test was completed in an attempt to increase the total rotation of the 175 mm specimens by increasing the compressive machine's cross-head motion; however, as it approached 0.016 rads, the results became asymptotic in nature, with the applied moment rapidly increasing with minimal change in rotation.

5 Conclusion

Based on preliminary cyclic concentric and eccentric compressive test results, the following conclusions may be drawn on the compressive and rotational behaviour of polyurethane under conditions seen in disc bridge bearings:

- Shape factor of the polyurethane highly influences its compressive stiffness. Higher shape factors resulted in higher compressive stiffness.
- The polyurethane exhibits residual strain after its initial loading cycle, with the subsequent cycles exhibiting near-harmonic behaviour with minimal additional residual strain following each cycle.
- The stiffness response of the initial loading and following loadings cycles on new polyurethane varies. It is recommended that different values be used to design the initial loading of the bearing and subsequent variations in gravity loads.
- After being stressed to high levels (55 MPa in these tests), polyurethane exhibits unrecoverable bulging, with the response of the initial loading on a previously stressed sample varying for polyurethane that has never previously been stressed.
- During rotation, the non-linearity of the polyurethane's compressive stress-strain response causes non-linear stiffness among the polyurethane's cross-section that may impede its ability to rotate under eccentric loads low enough to mitigate uplift.

For further validation and expansion upon the results, it is recommended to complete similar tests on larger scale samples with dimensions similar to that of the polyurethane element in a disc bearing. In addition, since CSA S6-19 specifies a range of applicable polyurethane hardness', it is recommended to complete the test on samples of varying Shore D hardness.

Acknowledgements The authors would like to thank Goodco Z Tech a product of Canam Bridges for supplying materials and technical expertise as the project continues. They would also like to acknowledge the MITACS Accelerate Program and Goodco Z Tech for their financial support. Lastly, special thanks to the University of New Brunswick, specifically lab technicians Andrew Sutherland, Chris Forbes and Gregory Greer, for providing expertise essential in completing the research.

References

1. ASTM (2015) ASTM D695-15–Standard test method for compressive properties of rigid plastics. ASTM. International, West Conshohocken, PA
2. Choi E, Lee JS, Jeon H, Park T, Kim H (2010) Static and dynamic behavior of disk bearings for OSPG railway bridges under railway vehicle loading. Nonlinear Dyn 62:73–93
3. CSA Group (2019a) CSA S6:19 – Canadian highway bridge design code. Canadian Standards Association, Mississauga, Ontario, Canada
4. CSA Group (2019b) Commentary on CSA S6:19 – Canadian highway bridge design code. Canadian Standards Association, Mississauga, Ontario, Canada

5. Mullins L (1969) Softening of rubber by deformation. Rubber Chem Technol 42(1):339–362
6. Schaefer RJ (2009) Chapter 33 - Mechanical properties of rubber, shock and vibration handbook, 6th edn. McGraw-Hill Companies Inc., New York, NY, USA
7. Stanton JF, Roeder CW (1982) Elastomeric bearings design, construction, and materials. NCHRP Report **248**. Transportation Research Board National Research Council, Washington, DC, USA
8. Stanton JF, Roeder CW, Campbell IT (1999) High-load multi-rotational bridge bearings. NCHRP Report **432**. Transportation Research Board National Research Council, Washington, DC, USA

Effect of Core Fill Timing on Shear Capacity in Hollow-Core Slabs

Taylor Quinlan, Alan Lloyd, and Sajjadul Haque

1 Introduction

Prestressed hollow-core concrete slabs (PHCS) are commonly used in flooring systems. They are designed to minimize weight and maximize the span. This is done by removing material from the center of the member and using prestress forces to pre-camber the span. The lack of material in the cores can create shear issues at the member end where there are high shear demands. In high shear scenarios, it is common practice to fill some or all of the cores with concrete. This selective core filling keeps the weight low in the center of the member, while maintaining shear capacity in the high shear regions at the end of the span.

Most PHCS are cast on a bed using an extruder, which prevents the use of shear steel reinforcement. The PHCS are constructed by first prestressing the steel strands, and then an extruder compacts zero slump concrete which forms the PHCS over the length of the bed. This allows for multiple members of different lengths to be cast, with individual members cut from the whole. A typical casting bed used in this procedure is shown in Fig. 1.

When void filling is required the flange above the core to be filled is removed, and a plug is installed at the desired location beyond which no core filling is required. Self-consolidating concrete is then placed in the void. This is typically done before the prestress loads are transferred into the member by cutting the prestress strands near the jacking point. After loads are transferred the members are cut to length and placed into storage. In some cases, the void fill is placed in the member after the prestress has been transferred and the specimen is fully cured. This is generally done on the construction site using grout. Depending on when the fill is placed, the member could be fully or partially cured, and prestress loads could be present

T. Quinlan (✉) · A. Lloyd
University of New Brunswick, Fredericton, Canada
e-mail: t.quinlan@unb.ca

S. Haque
Strescon Limited, Saint John, Canada

S. Walbridge et al. (eds.), *Proceedings of the Canadian Society of Civil Engineering Annual Conference 2021*, Lecture Notes in Civil Engineering 244,
https://doi.org/10.1007/978-981-19-0656-5_30

Fig. 1 Extrusion casting bed for hollow core members

or not. These two constraints can affect the capacity of the member. This research focuses on determining how the shear capacity might change based on the timing of fill placement.

2 Background

2.1 Transfer Length

The prestress forces in the member decrease near the end due to the transfer length of the strands, resulting in a lower shear capacity at that location. Transfer length is specified as fifty bar diameters in the Canadian CSA Standard A23.3 Design of Concrete Structures [3]. This has been shown to be a simplification of the actual mechanism by many authors. Floyd compiled an extensive review of past researchers' equations for transfer length [4]. ACI 318-14 recognized the effect of the initial wire stress in the bonding length, using the non-empirical equation given in equation one.

$$L_t = \frac{f_{se} d_b}{20.7} \quad or \quad L_t = \frac{f_{se} d_b}{13.8} \tag{1}$$

where: f_{se} is the strand stress, d_b is the bar diameter, and the equation is chosen based on which length creates a more critical effect (ACI 318 2014). Long transfer lengths will reduce the benefit that prestressing delivers to shear capacity, thus increasing member cost, and shorter transfer lengths can increase the risk of failure in the end

regions [6]. Aside from concrete strength and prestress level, the effect of several other variables on the transfer length has also been studied. These include W/C ratio [5], cut procedure [8], and shape of voids [9].

2.2 Components Contributing to Shear Capacity

Shear capacity is impacted by the decrease in prestress level at the member end. This can be clearly demonstrated using the modified compression field theory (MCFT). CSA A23.3 standards specify shear using the Simplified modified compression field theory [2], to compute the contributions of shear steel, concrete aggregate interlock, and harped prestressing steel [3]. One of the primary benefits of the MCFT is the ability to estimate shear behavior of members without stirrups [2]. Prestress loads in this theory apply internal compression to the member which keeps cracks small and thus increases aggregate interlock.

The issue of PHCS shear in the transfer region is also affected by the possibility of web-shear failure. Most members fail in flexure-shear, where the cracks first form vertically due to flexure. These cracks then propagate at an angle as the shear forces widen the cracks. Alternately, web-shear failure begins in the smaller webs of the member due to concrete tension stresses. Research has shown that the transfer length was an important variable in web-shear capacity [11]. Palmer and Shultz completed a thorough study on the web-shear phenomenon, and how it was likely the cause of underestimations in design codes for shear in multi-webbed members [9].

2.3 Effect of Core Filling

The complexity of the end region makes study of the effect of core fill on shear capacity vital to safe and efficient design. The loading will transfer to the core fill via interfacial shear, and timing of core-fill will affect prestress level within the fill concrete. The bond between the two surfaces is generally described with three components; shear friction, cohesion, and dowel action [10]. The existing concrete strength does not exhibit a significant effect on the transfer strength with low levels of roughness [1]. Since this study used shear reinforcement and shear keys, it is possible the base block strength could make a difference without reinforcement. Hollow-core slabs do not have shear reinforcement unless it is included when the cores are filled. Another parameter that could affect the interfacial shear transfer is the presence of the bond along multiple surfaces, instead of one side of the member. The sawtooth model described by Bass and Carrasquillo demonstrates how lateral movement of a concrete-concrete surface will also result in vertical movement [1]. If the sawtooth model is accurate, a bond on both sides of the member could dramatically increase the friction. Most interfacial shear testing is along one surface, as explored by Bass

and Carrasquillo [1]. However, horizontal and vertical casting positions do not show significant differences in capacities if the concrete was well consolidated [1].

Very little has been done to describe the effect of plain core fill timing. McDermott performed a study on the effectiveness of core filling, including cold-joint, reinforced, and plain concrete. Their research did not consider the timing of prestress transfer, or at what point in the casting procedure the fill concrete was placed. The prestressed behavior of the core fill decreased over time due to concrete shrinkage decreasing the concrete-concrete bond [7].

3 Purpose of Research

This research attempts to determine how the timing of fill placement will affect the specimen shear capacity. This will be done by casting specimens with plastic bond breaks applied between the PHCS concrete and the core-fill, approximating the effect of waiting until concrete is cured before placement. Since the amount of material and the surface roughness is the same the only component of the bond that is affected is the chemical bonding. Several specimens will also be filled after the prestress load is transferred into the concrete, to demonstrate the capacity of specimens filled onsite after more curing has taken place.

4 Experimental Program

4.1 Loading Scenario

Specimens were cast at Strescon Limited's precast facility in Saint John, New Brunswick in a single extrusion and cut to 3.05-m (10′) lengths. Specimens that required void fill were filled over a length of 305 mm (12″) at the member end, in all cores according to standard practice. Compressive strength tests using standard cylinder samples were conducted on the fully cured concrete, which showed the hollow-core concrete had an average strength of 86 MPa, and the void fill had an average strength of 58 MPa. The specimens were tested at UNB using a 500 kN servo-electric controlled hydraulic actuator set to load at 2 mm/min until first cracking; coinciding with failure in prestressed members under shear. The loading rate was increased to 4 mm/min due to the gradual failure of this loading type once the concrete section was clearly damaged. The members were loaded with a 76 mm (3″) wide steel load tree to create an approximate line load over the width of the member at 305 mm from the member end. While the length of void fill and location of the loading are the same, this was coincidental. The load was placed at this location to ensure failure occurred within the transfer length. Since the concrete surface is rough, wooden shims were placed under the load point to ensure a uniform distribution of

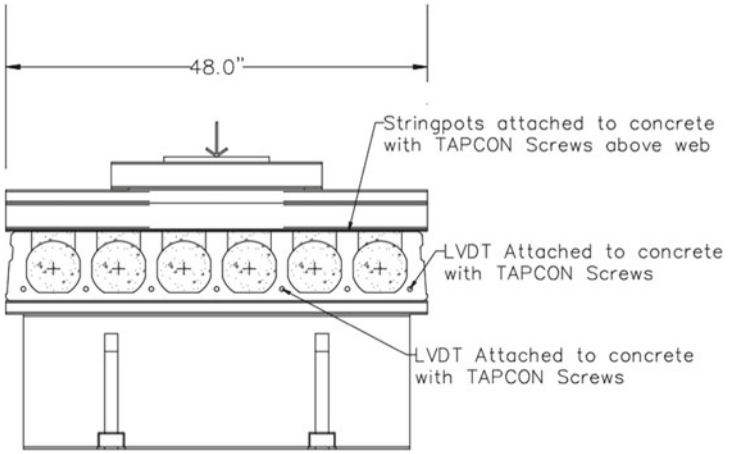

Fig. 2 Longitudinal view of testing setup

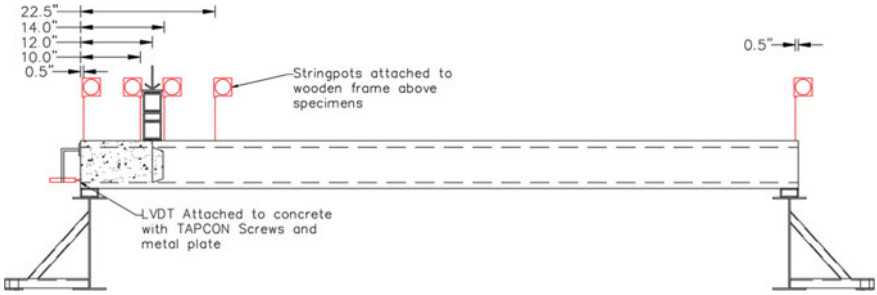

Fig. 3 Transverse view of testing setup

load over the width of the specimen. The testing diagram is shown in Figs. 2 and 3. The load point was directly above the end of the filled cores. The members were supported by a 76 mm wide rectangular HSS support. This was selected to represent the typical bearing width for PSHC used in internal design documents.

4.2 Data Collection

Data was collected to measure the specimen's deflection and strand slippage. Two Linear variable displacement transducers (LVDT) were placed on the strands. They were magnetically attached to a metal plate that was screwed onto the member, shown in Fig. 4a. This allowed the measurement to be relative to the concrete itself. These gave another indication that failure had occurred. Spring loaded wire potentiometers (string pots) were placed above both the supports, either side of the load point, and

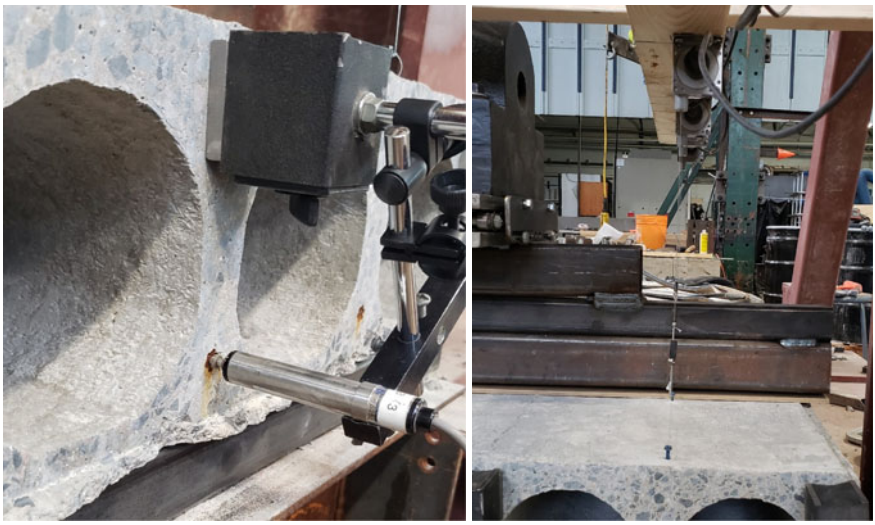

a) Placement of LVDT b) Attachment of stringpots

Fig. 4 Location of data collection devices

nine inches from the loading point and used to measure specimen displacement. They were attached to the member using TAPCON screws above the interior web, shown in Fig. 4 (b). The data was collected from the same locations on all members. Figures 2 and 3 show the locations where data was collected along the member.

4.3 Naming Convention

Five specimen types were tested to determine the effect of interfacial shear on HC shear strength. Each member had all cores filled up to one foot from the member end except for the plain hollow core. Two specimens were filled with void fill before prestress load was transferred into the member, and two were created after the specimen was released from the casting bed. A plastic bag was used as a bond break on one specimen type before and one specimen type after release. To distinguish different specimens and their potential loading effects, a naming convention was created. The first letter describes if the voids were filled with concrete (F) or were plain HC (P). The second letter describes the time of prestress transfer, with before transfer (B), after transfer (A), or Not Applicable (N). The third letter describes the presence of a plastic bond break (B), or no bond break (N). So the specimen type FBB would be a bond broken slab filled with void fill before prestress transfer. During casting the FAN/FAB specimens were first cut as 6.1 m (20′), which were then cut into two 3.05-m sections after the void fill was placed. This is shown in Table 1.

Table 1 Naming convention

	No bond break applied	Bond break applied
Not filled	PNN	N/A
Void filled before transfer	FBN	FBB
Void filled after transfer	FAN	FAB

5 Preliminary Results

Due to the loading scenario, most members showed vertical cracking at the load point. The exception was the plain hollow core, which had developed diagonal shear cracking. This also explains the lower capacity of the FBB members. Since a plain hollow core fails in flexure shear, the filled core with no bond gives a lower capacity. A comparison of the ultimate capacity of each specimen is shown in Fig. 5, with the cracking capacity shown in Fig. 6.

The cracking strength of both the FBN and FAN members was not significantly different, however the FAN members showed a higher average ultimate capacity. This is worth nothing due to the different levels of prestressing within the cores. The casting method would place a larger prestress load on the FBN cores, but that did not appear to create an increase in cracking load. Despite the larger prestress load, FBN members did not have as large an ultimate capacity. The larger capacity in FAN members could be due to the increased time for the hollow-core concrete to cure, or the lack of prestress loads. However, the additional work and time required to create the FAN specimen's is not practical and would only be beneficial if cracking were acceptable in the member. After fracturing the FAB specimens, it became clear that the core fill concrete did not completely fill the void. This resulted in a capacity lower than the PNN members, and they could not be accurately compared to the FBB specimens which were filled before transfer.

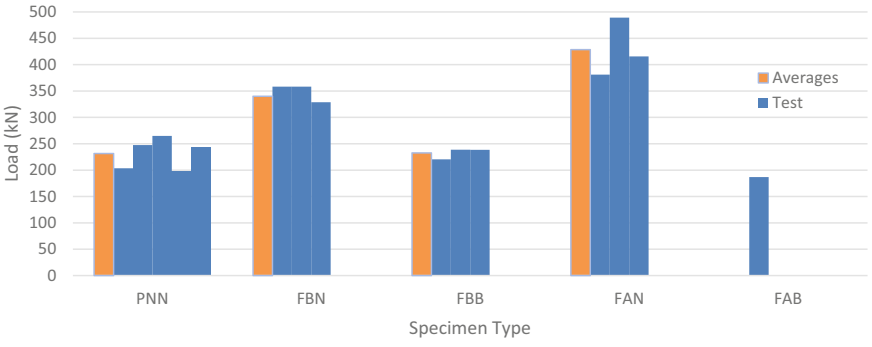

Fig. 5 Member ultimate capacity

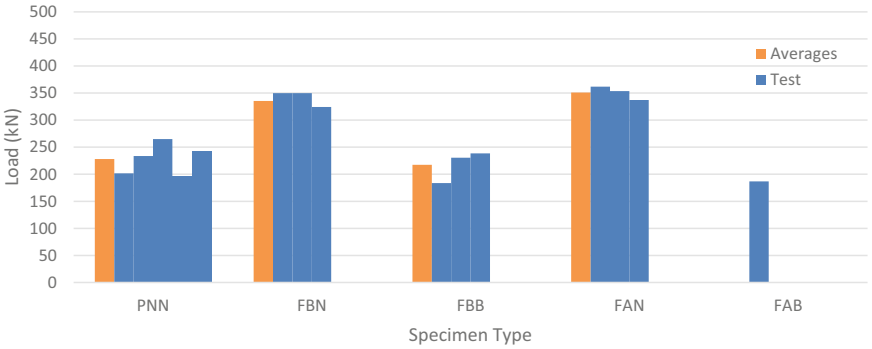

Fig. 6 Member initial cracking load

Design models will be created for each member type and the results will be compared against the experimental results to draw conclusions about what mechanism is driving the difference between members. It appears that the presence of void fill in this loading scenario is aiding the prestress wire bond strength. After initial cracking, and wire slippage, the ultimate capacity increases. This would suggest that the bond on the wires increases due to the presence of prestressing materials. This is clearly shown in Fig. 7, where loading increases after slippage occurs in both the FBN and FAN samples. Figure 8 shows the PNN member increasing in capacity for a smaller amount of slippage.

Strand slippage occurred at the moment of first cracking in all members. Failure occurred in each member at the point of loading, except for the plain members (PNN). Some of the PNN members failed vertically, but the majority failed with a diagonal crack formation common in flexure shear. Figure 9 shows a typical example of the crack pattern in each member type. The cracks are very similar in all the filled members, where vertical cracking occurs at the end of the core filling. There are also diagonal cracks that formed along the outside of the core fill in the web. While the

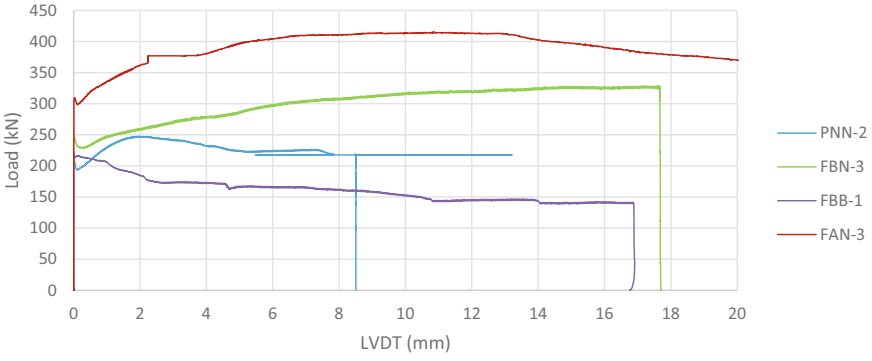

Fig. 7 Loading vs strand slippage

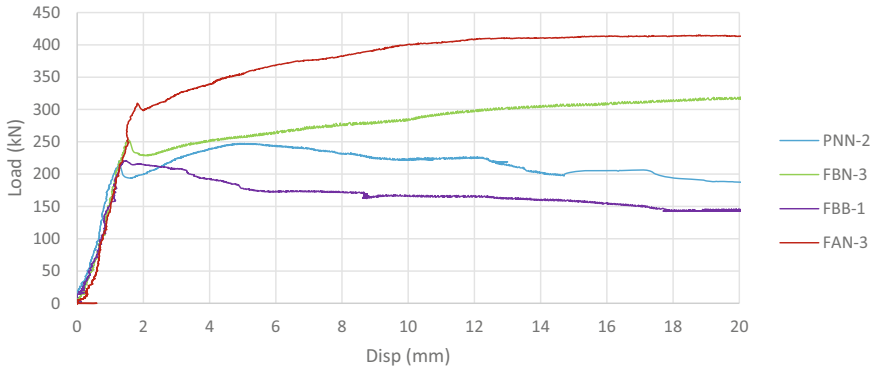

Fig. 8 Loading vs member displacement

Fig. 9 Typical failure of each member type

vertical cracking shown in Fig. 9d appears to be flexure cracking, it is more likely to be shear failure pushed through the high stress point at the end of the core fill.

Most members had several smaller cracks around the failure area, but the PNN member was the only one that had cracks extending to the front of the member. Some FBB members also had similar cracks, since the PHCS concrete did not bond to the void fill concrete. The void fill concrete was not normally fractured after these tests, only happening once in all ten filled tests. If the void fill were extended beyond the load point it is possible that the core filling would fracture as well. The location of the load point on a high stress point on the member was a factor in the failure mode of all member types except PNN.

6 Conclusions

Four different configurations of void filled PHCS were tested under shear. This was done to determine if the casting methods could be optimized to maximize shear capacity in the member end. Several members were also cast with a bond break installed, to simulate a cold joint before transferring the prestress load into the specimen. Based on the work to date, the following conclusions can be drawn:

1. Most specimens failed in a vertical cracking pattern at the back of the void fill. The only specimens that did not fail in this way were the PNN and FBB members. Some FBB members had cracking along the outside web.
2. Some specimens exhibited a higher ultimate capacity after the strands had slipped. This seems to be due to the concrete-steel bond increasing in capacity as slippage occurred. The helical orientation of the strands could be a cause of this.
3. Members that had partial prestress transfer into the void fill (FAN) showed a higher overall capacity than other members. However, it did not have a significantly higher cracking load, and so is not practical in almost all applications.
4. The placement of the load point and the stress concentration at the core fill end created a consistent failure at the high stress location behind the void fill. This generally did not allow the concrete in the cores to crack.

Acknowledgements The authors would like to thank Strescon Limited for supplying materials and technical expertise to the research program. They would also like to thank the MITACS Accelerate program and Strescon Limited for their financial support. Also special thanks to UNB, specifically the lab technicians Andrew Sutherland, Chris Forbes, and Gregory Greer. Without their expertise the research would not have been possible.

References

1. Bass RA, Carrasquillo RL, Jirsa JO (1989) Shear transfer across new and existing concrete interfaces. ACI Struct J 86:383–393
2. Bentz EC, Collins MP (2006) Development of the 2004 Canadian Standards Association (CSA) A23.3 shear provisions for reinforced concrete. Can J Civ Eng 33:521–534
3. CSA (2019) CSA Standard A23.3 - Design of Concrete Structures. Canadians Standards Association
4. Floyd RW, Howland MB, Hale MW (2011) Evaluation of strand bond equations for prestressed members cast with self-consolidating concrete. Eng Struct 33:2879–2887
5. Marti-Vargas JR, Serna P, Navarro-gregori J, Bonet JL (2012) Effects of concrete composition on transmission lengh of prestressing strands. Constr Build Mater 27:350–356
6. Marti-Vargas JR, Micah Hale W (2013) Predicting strand transfer length in pretensioned concrete: Eurocode versus North American practice. J Bridge Eng 18(12):1270–1280
7. McDermott MR, Dymond BZ (2020) Shear capacity of hollow-core slabs with concrete-filled cores. PCI J 65:59–74
8. Moon DY, Zi G, Kim J-H, Lee S-J, Kim G (2010) On strain change of prestressing strand during detensioning procedures. Eng Struct 32:2570–2578
9. Palmer KD, Schultz AE (2010) Factors affecting web-shear capacity of deep hollow-core units. PCI J 55:123–146
10. Soltani M, Ross BE, Khademi A (2018) A statistical approach to refine design codes for interface shear transfer in reinforced concrete members. ACI Struct. J. 115:1341–1352. https://doi.org/10.14359/51702239
11. Yang L (1994) Design of Prestressed hollow core slabs with reference to shear failure. J Struct Eng 120(9):2675–2696

Explainable Machine Learning for Seismic Vulnerability Assessment of Low-Rise Reinforced Concrete Buildings

M. Midwinter, C. M. Yeum, and E. Kim

1 Introduction

Earthquake vulnerability assessment methods for buildings are key to planners and policymakers for managing seismic risk. Given structural failures are the largest source of losses in earthquake events, proactive assessment of their potential risk allows decision-makers to best allocate time and resources to mitigate the effect of earthquakes through pre-emptive rehabilitations, insurance, or reinsurance [1]. Knowledge of the building stock and which buildings are most vulnerable can also help prioritize rescue efforts and actions against possible aftershocks.

Rapid structural performance screening methods rely on easily collected data, simple calculations, and workable accuracy to predict the seismic vulnerability of buildings. One of the simplest and most popular methods is the Hassan-Sozen Priority Index (PI) [4], which has been used by researchers around the world to prioritize a large inventory of low-rise monolithic reinforced concrete buildings. The PI is computed using easily measured geometric dimensions of a building and is inversely related to the structure's vulnerability in an earthquake. The PI is defined as the sum of the wall index (WI) and column index (CI) which are ratios of the effective wall and column areas to the total building floor area above the base (A_{ft}) calculated as follows:

$$PI = WI + CI \tag{1}$$

$$WI = (A_{cw} + A_{mw}/10)/A_{ft} \tag{2}$$

M. Midwinter (✉) · C. M. Yeum · E. Kim
University of Waterloo, Waterloo, Canada
e-mail: mxxmidwi@uwaterloo.ca

S. Walbridge et al. (eds.), *Proceedings of the Canadian Society of Civil Engineering Annual Conference 2021*, Lecture Notes in Civil Engineering 244,
https://doi.org/10.1007/978-981-19-0656-5_31

Table 1 Datasets used in this study

Earthquake	Magnitude (M_w)	Sample size	Reference
Duzce, Turkey (1999)	7.2	55	[11]
Bingol, Turkey (2003)	6.4	116	[11]
Nepal 2015	7.8	135	[9]
Ecuador 2016	7.8	344	[12]
Taiwan 2016	6.4	106	[8]
Pohang, S. Korea (2017)	5.4	74	[13]

$$CI = (A_{col}/2)/A_{ft} \tag{3}$$

where A_{cw} and A_{mw} are the total cross-sectional areas of reinforced concrete (cw) and unreinforced masonry filler walls (mw) at the base, and A_{col} is the total column area above the base. Masonry wall areas are divided by to indicate that masonry walls contribute to the lateral resistance of the structure but an order of magnitude less than concrete walls. The column areas are divided by 2 since columns act in long and short directions of a typical structure. PI can be calculated for both long and short directions, but the minimum is chosen as the overall PI.

Since its original application to the Erzincan earthquake of 1992, the PI has been used in numerous earthquake reconnaissance missions around the world and a large volume of post-earthquake structural performance data were published through Datacenterhub, a popular research data sharing platform maintained by Purdue University. The datasets are well structured and documented for scientific study and future reuse. This study uses data collected from the six earthquakes listed in Table 1.

This large dataset of structural features collected for the PI presents an opportunity for the application of machine learning (ML) methods. It is possible that each structural measurement, considered for the PI encodes additional information that is lost when calculating PI due to quantization and it is theorized that ML algorithms could identify a more accurate damage rating estimation model by learning more complex relationships than is used to define the PI.

Moreover, while ML methods have been successfully applied in civil engineering, including earthquake vulnerability assessment and structural performance screening [15, 16], machine learning's Achilles heel is a lack of intuitive explanations. Without model explanations, it is difficult to judge a model's quality and suitability using accuracy metrics alone. In this paper, the goal is to create the best earthquake vulnerability classifier possible using PI data, however, it is not possible to judge what is a 'good' and 'intuitive' prediction accuracy due to the limited scope of the dataset (i.e., using only PI features). To address this and supplement the regular accuracy metric, SHapley Additive exPlanations (SHAP) [5] is used to evaluate the quality of the model.

2 Overview of the Approach

The underlying idea is to use machine learning approaches to identify a relationship between the geometric information of buildings and the level of damage expected in an earthquake. The PI is oversimplified in terms of the contribution of the input parameters, and does not provide specific thresholds or rules for relating the index itself to damage ratings. In this study, using post-earthquake reconnaissance data from the earthquakes identified in Table 1, a random forest (RF) algorithm is used to develop a robust and accurate damage rating model and SHAP is used to test the model transparency.

The data used in this study are publicly available on DataceterHub. The available data includes general information (e.g., date of collection, GPS coordinates, images), building geometry measurements, and damage ratings. The damage level for each building in the dataset is classified as no damage, light damage, moderate damage, and severe damage. Descriptions of each damage level are provided in Table 2.

It should be noted that among the data available, only seven parameters are necessary for computing the PI: 1) column area, 2) the number of floors, 3) floor area, and 4) concrete wall area in the two horizontal directions (east-west and north-south), and 5) masonry wall area in the two horizontal directions.

For the six earthquakes identified in Table 1, data for a total of 830 low-rise reinforced concrete buildings are available. A popular ensemble learning method, RFclassifier, was used to train a model with the building parameters as the input features and the damage rating as the output target. The best model was identified using hyperparameter tuning and the accuracy of the model was evaluated using cross-validation. Whereas in the PI, the contribution of each input parameter to the index is clearly identified, it is difficult to quantify how much each input parameter contributes to the output (damage rating). SHAP was applied to the trained model to address this issue and investigate how individual input parameters are correlated with the output. This makes it possible to understand and validate the input measurements to determine the output damage rating. This workflow consisting of training, tuning, and explaining, was repeated until a high-fidelity machine learning model was obtained.

Table 2 Damage descriptions used in the dataset

Material	Damage level	Description
Reinforced concrete	Light	Hairline cracks (<0.25 mm) and/or flexural cracks
	Moderate	Inclined cracks, spalling or loss of cover
	Severe	Loss of concrete core, reinforcement buckling or fracture, shear failure, or visually apparent permanent drift in structure
Masonry	Light	Hairline cracks (<0.25 mm) or flaking of plaster
	Moderate	Inclined cracking or flaking of large pieces of plaster
	Severe	See-through wall cracks

In this study, we made some important assumptions to develop the model using the real-world earthquake reconnaissance data:

- All measurements of building geometry and damage rating assessments are reasonably accurate and consistent.
- Initial construction quality, differences in seismic design standards, and the effect of aging, all of which could affect the damage rating, are neglected.
- Site effects and other factors that affect earthquake forces in a building are neglected. This means two buildings with similar geometric properties are assumed to experience the same earthquake forces.

Note that it is important to note that the data used in this study was collected by many different engineers over the last 20 years. As such, it is not possible to check the data collection quality and no other information is available (e.g., year of built, structural drawings). Thus, there might have outliers in the dataset for whichsome of these assumptions are invalid. However, the overall validity of the assumptions is verified through the model accuracy as well as model interpretation using SHAP.

3 Model Development and Explainability

3.1 Machine Learning

The RF model is an ensemble learning method that was developed upon on the concept classification and regression tree (CART) models. The CART model, from the root node, attempts to create internal nodes and leaf nodes that will separate the data into mutually exclusive subspaces. The CART model accomplishes this by applying a greedy algorithm to the impurity score, which defines a node's ability to separate the dataset. Finally, a CART model is pruned where some leaf nodes are removed, and the internal node is made into a leaf. The motivation of pruning a CART model is to prevent overfitting and increase robustness. However, CART models still suffer from overfitting and high variance, which are both addressed by RF models through bagging, which consists of two steps: bootstrapping and aggregating. Essentially, the RF model creates numerous models on random subsets (booststrapping) of the whole dataset and at each internal node, a random subset of features is considered to determine the best split. Generating a prediction from the RF model involves running the features through every tree, created with each bootstrapped dataset, and aggregating the resulting prediction. In other words, the RF model creates a large number of random tree models through bagging, and the prediction is determined by the majority vote. Like CART, RF models are quick training and easy to implement. Unlike CART, however, the RF can achieve higher accuracy and robustness to overfitting due to the randomness introduced by bagging and selection of features to split. Lastly, RF models are robust to hyperparameter changes (i.e. number of trees, minimum sample split etc.), unlike multi-layered perceptron (MLP) where the

choice of optimizer and learning-rate can drastically affect learning outcomes. Many RF model hyperparameters deal with controlling the size of the learned trees such as the number of estimators, maximum features for the split, minimum samples for the split, minimum impurity decrease, and minimum samples in leaf nodes. Due to the relatively limited number of samples in the dataset used in this study, controlling the growth of these decision trees was not necessary.

3.2 Model Explainability Using SHAP

In this work, the SHAP library, especially TreeSHAP, based on the theory of Shapley values, was used to explain the trained RF model. With its roots in game theory, the Shapley value tries to determine how best to distribute a payout among players in a collaborative game where the players are features and the payout is the prediction [10]. Shapley values have found wide application in economics but the most intuitive way to understand it may be in the context of a group project. The underlying idea of the Shapley value is that while each group member can attempt the group project on their own, they could achieve a higher grade if they all work together. Assume a function, υ, calculates the final grade of the group based on the contributions of group members. N is the set of all group members, S is an arbitrary subset of group members and i is a person in the group. Then the Shapley value ϕ_i for group member i

$$\phi_i(N, \upsilon) = \frac{1}{N!} \sum\nolimits_{S \subseteq N\{i\}} |S|!(|N| - |S| - 1)![\upsilon(S \cup \{i\}) - \upsilon(S)] \tag{4}$$

ϕ_i is the weighted average marginal contribution of group member i, calculated for every possible subset of members.

The Shapley value is attractive for explaining complex models due to its efficiency and conformity to the axioms of efficiency, symmetry, dummy player, and additivity [10]. Continuing with the group project analogy, it is noted that Shapley is mathematically fair. Group members who do the same work receive the same grade, a group member who does nothing receives a zero, and the contribution of each member is additive to the whole. Despite these desired properties, the calculation of the Shapley values requires the calculation through every combination of subset S in N features which is extremely computationally expensive. Therefore, to use Shapley values, it is necessary to estimate them using approximation methods to reduce computation time [14]. TreeSHAP is a specially developed algorithm to estimate Shapley values for tree-based ensemble models (Lundberg et al., 2018). The combination of Monte Carlo sampling feature combinations, efficient estimation of marginal contributions, and a novel recursive algorithm in TreeSHAP reduces the computation cost of Shapley values from exponential to polynomial time (Lundberg et al., 2018). A limitation of TreeSHAP is that the dummy axiom may not be fulfilled if the feature is correlated with another feature that does have an effect on the prediction (Lundberg

et al., 2018). To address this, a bivariate analysis was conducted to best understand the SHAP results.

4 Results

The dataset was split into training and validation sets, an RF model (M1) was naively fit and tested. Accuracies in this paper are the calculated F1 measure, which is a function of precision and recall, which are commonly used to describe a model's output compared the ground-truth label. The model M1 achieved an average accuracy of 73.5%, with class accuracies of 67, 63, and 83% for the light, moderate and severe damage classes respectively. This appeared to be a very good result but the SHAP analysis returned an interesting observation which is graphically presented in Fig. 1. For actual usage, engineers simply measure seven parameters from each building, which are used for training the model. Then, the model provides its potential damage rating.

Figure 1 shows the average impact (SHAP value) of each feature on the model prediction where each colour band corresponds to the predicted damage class ("L" = Light Damage, "M" = Moderate Damage, "S" = Severe Damage). This SHAP analysis tells us how input parameters are contributing to the model's estimate of potential damage to buildings. The results indicate that reinforced concrete walls are a less impactful feature than unreinforced masonry filler walls when intuition would indicate the opposite. We found that the reason this phenomenon occurs is due to the imbalanced distribution of structures with and without concrete walls. If we only validate the model performance using classification accuracy through typical metrics (e.g., precision and recall, confusion matrix), such an important model relationship cannot be found. This is a well-known challenge of explainability in ML models. Based on this observation, we decided that two separate models were created: M2 for structures with concrete walls, and M3 for structures without concrete walls.

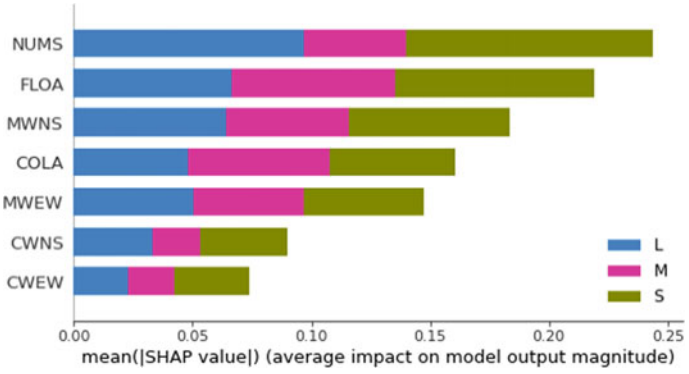

Fig. 1 SHAP summary plot for model M1

In Fig. 2 (a), it can be seen that for buildings with concrete walls, the most important features are the cross-sectional area of the concrete walls while Fig. 2 (b) shows that the most important feature in buildings without concrete walls is the number of stories. Interestingly, M2 has an accuracy of 58%, class accuracies 65, 35 and 64% for light, moderate and severe damage; while M3 has an accuracy of 83%, class accuracies 87, 67 and 87% for light, moderate and severe damage (Table 3).

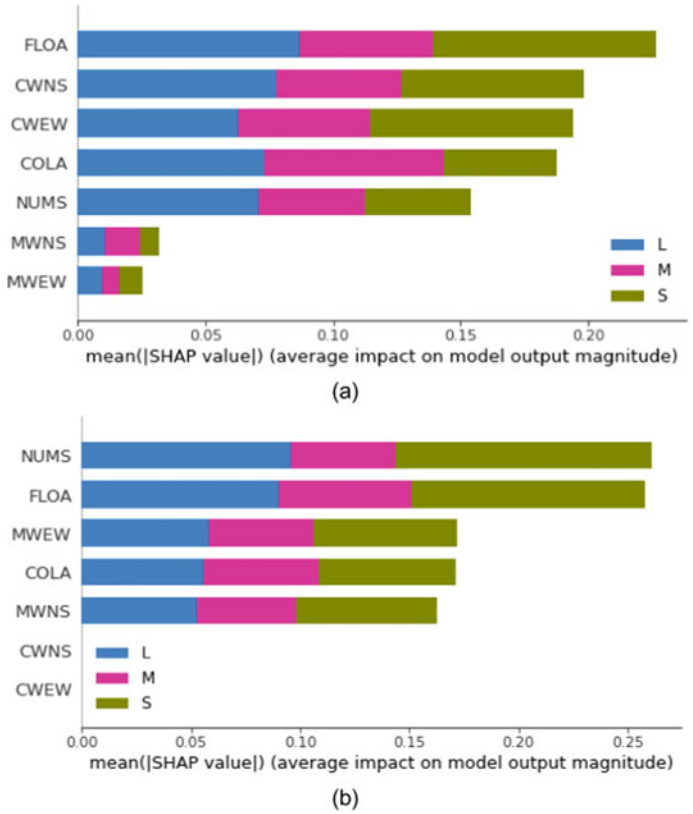

Fig. 2 SHAP summary plot for models **a** M2 **b** M3

Table 3 Model accuracies

Name	Description	Class accuracies (L, M, S)	Weighted model accuracy
M1	Full dataset	(67%, 63%, 83%)	73.5%
M2	Only structures with concrete walls	(65%, 35%, 64%)	58%
M3	Only structures without concrete walls	(87%, 67%, 87%)	83%

This result implies that structures with concrete walls behave in a different and potentially more complex manner than those without concrete walls. Further investigation and more samples are needed to more conclusively determine whether a reliable structural vulnerability classifier can be created for structures with concrete walls will require more data. Additionally, it can be seen that the accuracy of the moderate class is significantly lower than light and severe; this is partly due to a lack of moderate damage records. The authors also conducted a bivariate SHAP analysis, this plotted the SHAP value of two features in cartesian plot, while a third variable could be used to colourized the bivariate plot. The authors confirmed their results by plotting the training data, however it makes more sense to plot the testing data, which is too sparse to interpret. These bivariate SHAP plots will be published in a follow-up paper, where more data will be used for analysis.

5 Conclusion

Motivated by the simplicity of the Hassan-Sozen PI, this study used post-earthquake structural performance data for 830 low-rise reinforced concrete buildings from six different earthquakes to train a RF classifier to predict structural vulnerability using only easily attainable geometric parameters. The data was used to create a classifier (M1), which achieved a cross-validated accuracy of 73.5%. Then using a simple SHAP analysis showed discrepancies, which was addressed by developing structural vulnerability classifiers for buildings with reinforced concrete walls (M2), and those without (M3). M2 and M3 achieved accuracies of 58 and 83% respectively. Using the SHAP method, we can gain valuable insights about the performance of the model. Further analysis of the SHAP values should be able to reveal other hidden learned trends about what trends the model has learned. The authors hope to follow up this work with an in-depth comparison between Hassan-Sozen PI and our RF classifier.

References

1. Calvi GM et al (2006) Development of seismic vulnerability assessment methodologies over the past 30 years. ISET J Earthq Technol 43(3):75–104
2. Dönmez C, Pujol S (2005) Spatial distribution of damage caused by the 1999 earthquakes in Turkey. Earthq Spectra 21(1):53–69. https://doi.org/10.1193/1.1850527
3. Pyper Griffiths JH, Irfanoglu A, Pujol S (2007) Istanbul at the threshold: an evaluation of the seismic risk in Istanbul. Earthq Spectra 23(1):63–75. https://doi.org/10.1193/1.2424988
4. Hassan AF, Sozen MA (1997) Seismic vulnerability assessment of low-rise buildings in regions with infrequent earthquakes. Am Concrete Inst Struct J 94(1):31–39
5. Lundberg SM, Lee SI (2017) A unified approach to interpreting model predictions. In: Conference on Neural Information Processing Systems, Long Beach, California, USA
6. Lundberg SM, Erion GG, Lee SI (2019) Consistent individualized feature attribution for tree ensembles. https://arxiv.org/pdf/1802.03888.pdf

7. Ozcebe G, et al. 1 May 2003 Bingol Earthquake. Engineering Report (Tubitak, NSF, October 30, 2003). https://datacenterhub.org/dv_dibbs/file/1012:dibbs/?f=/1012/data/files/experiments/reports/3136/Bingol%20Report.pdf
8. Purdue University. "Performance of Reinforced Concrete Buildings in the 2016 Taiwan (Meinong) Earthquake" (NCREE, 2016). https://datacenterhub.org/resources/14098
9. Shah P, et al. (2015) "Database on Performance of Low-Rise Reinforced Concrete Buildings in the 2015 Nepal Earthquake" https://datacenterhub.org/resources/238
10. Shapley, LS Stochastic Games. In: Proceedings of the National Academy of Sciences of the United States of America, Mathematics, vol 39 pp 1095–1100 June 17, 1953. https://doi.org/10.1073/pnas.39.10.1095.
11. Sim C, et al. "Database of Low-Rise Reinforced Concrete Buildings with Earthquake Damage (Duzce, Bingol)" March 22, 2015. https://datacenterhub.org/resources/123
12. Sim C, et al. "Performance of Low-Rise Reinforced Concrete Buildings in the 2016 Ecuador Earthquake" August 24, 2016. https://datacenterhub.org/resources/14160
13. Sim C, et al. "2017 Pohang Earthquake - Reinforced Concrete Building Damage Survey" April 7, 2018. https://datacenterhub.org/resources/14728
14. Strumbelj E, Kononenko I (2014) Explaining prediction models and individual predictions with feature contributions. Knowl Inf Syst 41:647–665. https://doi.org/10.1007/s10115-013-0679-x
15. Xie Y et al (2020) The promise of implementing machine learning in earthquake engineering: a state-of-the-art review. EERI Earthq Spectra 1:1–33. https://doi.org/10.1177/8755293020919419
16. Zhang Y et al (2018) A machine learning framework for assessing post-earthquake structural safety. Struct Saf 72:1–16. https://doi.org/10.1016/j.strusafe.2017.12.001

Form-Finding of a Negative-Gaussian Curvature Cable Dome Using a Genetic Algorithm

Elshaimaa Ahmed, Ashraf El Damatty, and Ashraf Nassef

1 Introduction

Cable structures have been widely used for covering large areas such as arenas and stadiums because of their lightweight, adaptable forms and for their architectural impact. They can be classified into three categories; pure tension, tensegrity (cable-struts structures), and hybrid tensile structures [1]. As one of the most widely used applications of hybrid tensile structures, cable domes were initially proposed by Geiger and employed in roofing the Olympic Gymnastics Hall and the Fencing Hall for the Korean Olympics in Seoul [3]. The largest existing example of cable domes is Georgia Dome which was designed for the Atlanta Olympics Games in 1996 by Levy [8]. Since the self-stressed equilibrium between cables and struts should eventually achieve the rigidity of a cable dome, a specific shape wouldn't be maintained unless an appropriate initial prestress is assigned first. Accordingly, determining the initial prestress is an important step when designing cable domes. For many researches, the approach of form-finding, characterized by integrating the shape with the self-stress state, is considered when discovering a new geometry [15]. The aim of form-finding process is to obtain, at least, one state of self-stress without external forces by considering nodal coordinates, for example, as the main variables while searching for special configurations. However, the prestress distribution of the new shape that satisfies the equilibrium equations is not unique and can be chosen by designers according to the mechanical properties of the structure, which is called force-finding or prestress optimization.

E. Ahmed (✉) · A. El Damatty
Western University, London, ON, Canada
e-mail: eahmed23@uwo.ca

A. El Damatty
e-mail: damatty@uwo.ca

A. Nassef
The American University in Cairo, New Cairo City, Egypt

S. Walbridge et al. (eds.), *Proceedings of the Canadian Society of Civil Engineering Annual Conference 2021*, Lecture Notes in Civil Engineering 244,
https://doi.org/10.1007/978-981-19-0656-5_32

In the past decades, many studies focused on the form-finding of pin-jointed structures. Hanaor [6] proposed the flexibility method for designing the prestress of prestressable structures. Pellegrino [12] was the first who applied the Singular Value Decomposition technique (SVD) on the equilibrium matrix of the structure and reached the independent self-stress modes and the inextensible displacement modes. In [20], the authors developed the force density method, that originally proposed by Linkwitz and Schek [9] for cable nets, and extended its application to cable domes. Zhang et al. [21] applied the dynamic relaxation method with kinetic damping on the form-finding of new tensegrity configurations. For cable domes with multiple self-stress modes, such as Kiewitt dome, Xingfei Yuan et al. [19] modified the method of SVD and proposed the Double Singular Value Decomposition technique (DSVD) that can search for the optimal geometric configuration and the prestress distribution. In [16], the authors proposed another double-SVD technique that performs the singular value decomposition method on the equilibrium and force densities matrices in an iterative algorithm to reach the feasible prestress of a unique configuration of the structure by specifying an independent set of nodal coordinates. In [4], the authors proposed an iterative method based on Newton-Raphson technique (NR) taking into account the external loads to reach the feasible prestress distribution of cable domes. They applied this technique on typical cable domes of Geiger and Keiwitt type. They also extended the method to update the geometry of a new form of Geiger cable dome with negative-Gaussian curvature, where the initial proposed geometry has no self-stress state, and to achieve a final feasible geometry.

Despite all the above methods of form-finding, there is no method that is able to directly control the configuration of the unfeasible geometry of tensegrity structures such as the negative-Gaussian curvature cable domes. In addition to their aesthetic view and stable structural behavior, the feasible geometry of this saddle-shape dome should achieve a predefined configuration for some designing purposes. In other words, the rise and sag of the positive and negative curves of the saddle surface respectively, and the smoothness of the saddle-shape should be maintained at the end of the form-finding process to satisfy the required design. Therefore, this paper proposes a two-stage form-finding technique based on the SVD method, using a genetic algorithm followed by a multidimensional constrained optimization to obtain a feasible geometry of a cable dome with a predefined configuration. The configuration of the dome is controlled using a NURBS surface to maintain a smooth layout of the struts' elevation under given rise and sag. The proposed method is applied on a saddle-shape cable dome of Geiger type. However, it is applicable to other types of cable domes such as Levy and Keiwitt. Also, it can be used to control the configuration of the typical positive curvature cable domes when optimizing the structure under frequency and stability constraints. This paper is organized as follows. Section 2 demonstrates the basic principles of the proposed form finding method. Section 3 proposes a two-stage optimization algorithm to solve the problem of form-finding. Section 4 illustrates an example to verify the proposed method. Section 5 concludes the results.

2 Principles of the Form-Finding Procedure

2.1 The Feasible Prestress Basis Mode

The fundamental contributions of matrix analysis of pin-jointed tensegrities using the SVD method are due to the work done by Pellegrino [12] and Tibert and Pellegrino [15]. According to this method, for a d-dimensional (d = 2 or 3) cable dome with b members and n_s nodes (divideded into n free nodes and n_f fixed nodes), its topology can be expressed by the connectivity matrix $C_s\left(\in \mathbb{R}^{b\times n_s}\right)$ as illustrated in [17] and using their notations. If member k connects node i and j, the i^{th} and j^{th} elements of the k^{th} row of C_s are set to 1 and −1, respectively.

$$C_{s(k,p)}\begin{cases} 1 & \text{for } p = \min(i, j) \\ -1 & \text{for } p = \max(i, j) \\ 0 & \text{otherwise} \end{cases} \tag{1}$$

By numbering the free joints first, then the fixed joints, C_s can be divided into two parts as follows:

$$C_s = [C \;\; C_f] \tag{2}$$

Where $C\left(\in \mathbb{R}^{b\times n}\right)$ and $C_f\left(\in \mathbb{R}^{b\times n_f}\right)$ describe the connectivity of the members to the free and fixed nodes, respectively. The projected length of all members l_x ($\in \mathbb{R}^b$), l_y ($\in \mathbb{R}^b$), and l_z ($\in \mathbb{R}^b$) can be calculated using the following equations:

$$l_x = Cx + C_f x_f \tag{3}$$

$$l_y = Cy + C_f y_f \tag{4}$$

$$l_z = Cz + C_f z_f \tag{5}$$

Where x, y, z ($\in \mathbb{R}^n$) and x_f, y_f, z_f ($\in \mathbb{R}^{n_f}$) are the nodal coordinated for the free and fixed nodes in x, y, z directions, respectively. The vector of length of all members l ($\in \mathbb{R}^b$) can be calculated using:

By applying the equilibrium equations of the free nodes in each direction as in [17] and [14], neglecting external loads at each node and self-weight, the equilibrium matrix A ($\in \mathbb{R}^{dn\times b}$) of the structure without considering the fixed nodes can be calculated as follows:

$$A = \begin{pmatrix} C^T \mathrm{diag}(l_x) \\ C^T \mathrm{diag}(l_y) \\ C^T \mathrm{diag}(l_z) \end{pmatrix} L^{-1} \tag{7}$$

Where L ($\in \mathbb{R}^{b\times b}$) = diag(l). The equilibrium equation of the structure in the compact form is (Af = 0), where f ($\in \mathbb{R}^{b}$) is the vector of prestress in all members. To solve the equilibrium equation and obtain the prestress of all members in the structures, Pellegrino [12] applied the SVD on the equilibrium matrix:

$$A = UVW^{T} \tag{8}$$

Where U ($\in \mathbb{R}^{dn_s\times dn_s}$) and W ($\in \mathbb{R}^{b\times b}$) are the orthognal matrices and V ($\in \mathbb{R}^{dn_s\times b}$) is a diagonal matrix of non-negative singular values of A in descending order. The columns of matrix W can be expressed as:

$$W = [W_1 W_2 \ldots\ldots W_r | f_1 \ldots.. f_s] \tag{9}$$

Where fj ($\in \mathbb{R}^{b}$, j = 1,2, …, s) are the s independent states of self-stress of the dome which can be expressed as (s = b – r), where r is the rank of the equilibrium matrix A.

The feasible geometry and, in turn, the feasible prestress of cable domes can't be achieved unless these conditions are satisfied a) symmetry condition of the prestress distribution, b) unilateral condition of all elements, i.e., cables under tension and struts under compression, c) equilibrium condition at each node, i.e., minimizing the unbalanced prestress forces at all free nodes, and d) stability condition, i.e., positive definite tangent stiffness matrix [17].

2.2 Equilibrium Requirement

In order to ensure that the feasible prestress of the dome satisfies the equilibrium requirement, the euclidean norm of the unbalanced forces at all free joints, referred to as the design error ε, should be less than a very small value according to the desired level of accuracy. Tran et al. [17] recomends design error to be as small as 10^{-8}, while Pellegrino [12] recommends a value of 10^{-3}. After several try and errors and comparing the results with similar structures, it's worth noting that this number highly affects the max displacement resulting from the nonlinear analysis under the design level of presress. To maintain the max displacement of order 10^{-5} m when applying a max prestress of order 10^{7} N, the design error should be kept below 10^{-7}. Then, the objective function of the form-finding algorithm is to minimze ε which is the euclidean norm of the unbalanced force vector [Af] as follows:

$$\varepsilon = \|Af\|_2 = \sqrt{(Af)^{T}(Af)} \leq 10^{-7} \tag{10}$$

2.3 Stability Requirement

After obtaining the feasible geometry of the dome, the stiffness matrix should be checked for stability. This can be done in two cases: 1) If the force density matrix D is positive semi-definite regrdless of the properties of sections nor the level of prestress, 2) If not, the eigenvalues of the tangent stiffness matrix K_T should be positive and in a descending order. A detailed description of this requirement is shown in [11]. The force density matrix D ($\in \mathbb{R}^{n\times n}$) and the tangent stiffness matrix K_T ($\in \mathbb{R}^{dn\times dn}$) can be calculated using the following equations [20]:

$$D = C^T Q C \tag{11}$$

$$K_T = K_E + K_G \tag{12}$$

$$K_E = (A)\mathrm{diag}\left(\frac{E_k A_k}{l_k}\right)(A)^T \tag{13}$$

$$K_G = I_d \otimes D \tag{14}$$

Where $Q = \mathrm{diag}(f)\, L^{-1}$, K_E and K_G are the linear and geometric stiffness matrix respectively, I_d ($\in \mathbb{R}^{d\times d}$) and $\otimes$ are the unit matrix and tensor product, respectively, and E_k, A_k, l_k are the young modulus, cross sectional area and length of all b members in the dome.

3 Numerical Form Finding Algorithm

The aim of the numerical algorithm is to find a feasible geometry with a predefined configuration of a saddle cable dome. The predefined configuration involves the arrangement of cables and struts, the rise and sag values of the positive and negative curves, repectively, comprising the outer surface and their span lengths, and the lenght of all struts. The numerical algorithm is supposed to find the appropriate elevation of all struts that leads to a feasible geometry with at least one self-stress state. However, employing the elevation of struts directly as the variables of the optimization algorithm may lead the algorithm to fall in a local minimum and lose control over the curvature of the developed surface. Therefore, this study proposes a two-stage algorithm; the first stage is a global optimization technique (a Real-coded Genetic algoritm, RCGA) that searches the landscape of the objective function and deliver the optimum solution to the second stage. The second stage, in turn, is a local optimization technique (a multidimensional constrained optimization using Sequential Quadratic Programming, SQP) aims at enhancing the accuracy of the optimum solution. The proposed algorithm takes the advantage of the randomicity,

rapidity and wholeness of the genetic algorithm and the high accuracy of the SQP algorithm. Moreover, this method employs the control points of a NURBS surface, which passes through the higher points of struts, as the variables of the first stage. This surface provides adequate control on the shape of the saddle dome and ensures that RCGA will not fall in a local minimum. The proposed numerical model invovles interaction between a NURBS surface, a Genetic algorithm, and SQP algorithm. This section provides a brief description of each tool, the interaction between the various components, and the sequence of solution.

3.1 NURBS Surface

The saddle surface (negative-Gaussian curvature) can be mathematically represented by sweeping two curves on each other as shown in Fig. 1(b). One of the two curves has a negative curvature ($K_1 = -$ve), while the other has a positive curvature ($K_2 = {}_+$ve). The curvature of the developed surface at any point ($K = K_1\ K_2$) should be negative. The two curves can be easily represented by two parabolas resulting in a hyperbolic paraboloid surface. However, the feasibility of the developed surface cannot be achieved in saddle cable domes. Also, representing the two curves with a p^{th} polynomial has many limitations and disadvantages. If such polynomial is used, the independent variables employed in the optimization algorithm would be the polynomial coefficients, which have no physical meaning. In this study, two NURBS curves are used to represent the surface. NURBS are the abbreviations of a Non-Uniform Rational Basis Spline. NURBS curves are piecewise polynomials that can describe complex polynomials with lower-degree polynomials (Basis functions). Also, the great advantage of handling such polynomials with some local control properties makes NURBS curves adequate for most of shape optimization problems [13]. The applications of the NURBS curves can also be extended to the structural optimization problems as in [7] or topology optimization as in [2]. A NURBS curve

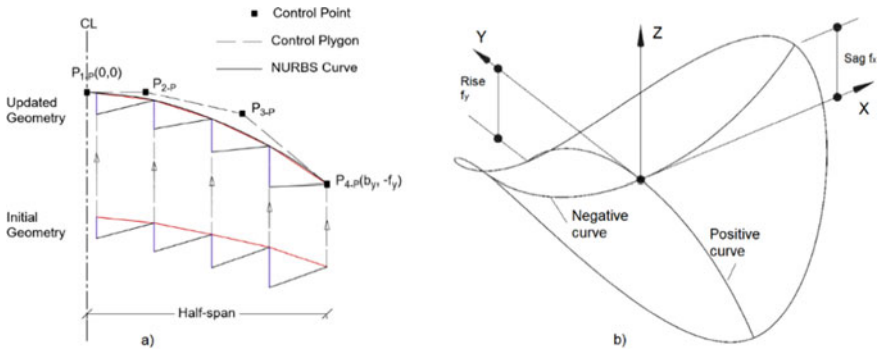

Fig. 1 **a** Updating geometry using NURBS curve **b** Developed surface

is the rational form of a B-spline curve and can be expressed as follows:

$$C(t) = \frac{\sum_{i=0}^{n} N_{i,p}(t) w_i P_i}{\sum_{i=0}^{n} N_{i,p}(t) w_i} = \sum_{i=0}^{n} R_{i,p}(t) P_i \tag{15}$$

where

$$R_{i,p}(t) = \frac{N_{i,p}(t) w_i}{\sum_{j=0}^{n} N_{j,p}(t) w_j} \tag{16}$$

$R_{i,p}(t)$ are the piecewise rational basis functions of the NURBS curve, w_i is the weight of the control point P_i and must be a non-negative real number. The weights give the NURBS curve more freedom to generate a large variety of shapes. $N_{i,p}(t)$ are the same basis functions of the non-rational B-spline curve given by:

$$N_{i,1}(t) = \begin{cases} 1 \text{ if } t_i \leq t \leq t_{i+1} \\ 0 \text{ otherwise} \end{cases} \tag{17}$$

$$N_{i,p}(t) = \frac{t - t_i}{t_{i+p+1} - t_i} N_{i,p-1}(t) + \frac{t_{i+p} - t}{t_{i+p} - t_{i+1}} N_{i+1,p-1}(t) \tag{18}$$

Where p (degree+1) is the order of B-spline curve, and $[t_0, t_1, \ldots, t_{n+p}]$ is the knot vector that represents the distribution of the parameter t along the curve. The relation between the order of the curve p, the number of control points $n + 1$, and the number of knots $m + 1$ is given by $(m = n + p)$.

After several try and errors, the NURBS curves used in this study are of order 3 and each of them has 4 control points as shown in Fig. 1(a). The knot vector that represents the t parameter is [0, 0, 0, 0. 5, 1, 1, 1] as discussed in details in [18]. It is worth noting that increasing the number of control points than 4 points causes the optimization algorithm to diverge. Moreover, choosing a NURBS curve of order 4 restricts the freedom of the curve and causes the optimization algorithm to hardly capture the optimum solution. The lower/upper bound of weights w_i and coordinates (x_i, y_i) of the control points of the NURBS curves are shown in Table 1 where a_x and b_y are half-spans of the negative and positive curves, respectively, while f_x and f_y are their corresponding sag and rise values.

3.2 *Real-Coded Genetic Algorithm*

Using the direct search method with different starting points can easily prove that the objective function, i.e., the design error, has many local minima. Therefore, a global optimization algorithm is needed to ensure that the algorithm will not be trapped in a local minimum. Based on the above, real-coded Genetic algorithm is selected in the current study to minimize the design error.

Table 1 The lower/upper bound of weights and coordinates of the control points of the NURBS curves

Control point P_i (x_i, y_i, w_i)		Fixed values	Variables	
			Lower bound	Upper bound
Positive curve	$P_{1\text{-}P}$	(0, 0, 1)		
	$P_{2\text{-}P}$		(0, 0, 0)	(b_y, 0, 2)
	$P_{3\text{-}P}$		(x_i ($P_{2\text{-}P}$), $-f_y * x_i(P_{3\text{-}P})/b_y$, 0)	(b_y, 0, 2)
	$P_{4\text{-}P}$	(b_y, $-f_y$, 1)		
Negative curve	$P_{1\text{-}N}$	(0, 0, 1)		
	$P_{2\text{-}N}$		(0, 0, 0)	(a_x, 0, 2)
	$P_{3\text{-}N}$		(x_i ($P_{2\text{-}N}$), 0, 0)	(a_x, $f_x * x_i(P_{3\text{-}N})/a_x$, 2)
	$P_{4\text{-}N}$	(a_x, $+f_x$, 1)		

The real-coded Genetic algorithm is a variant of the traditional Genetic algorithm in which the design variables are employed directly instead of encoding them into a binary string. The algorithm uses some mutation and crossover operators to handle the variables. The mutation operators allow searching in remote areas of the objective function landscape. In this study, the mutation operators used are boundary mutation, non-uniform mutation, and uniform mutation. The crossover operators produce new populations from the parent population having good objective function values. This study uses arithmetic, uniform, and heuristic crossovers. A detailed description of each operator can be found in [10]. The total number of instances (population size) used in this algorithm is 100; 4 instances are applied for each of the boundary, uniform and non-uniform mutation operators, and 2 instances are applied for each of the arithmetic, uniform and heuristic crossover operators.

3.3 Form-Finding Algorithm

As stated above, the form-finding algorithm is composed of two stages. The first stage P1 is a real-coded GA, in which the variables are the location of the control points of the two curves and their corresponding weights. The lower and upper bounds of each variable along with the known parameters of the two curves are shown in Table 1.

$$P_1 = \begin{cases} \text{minimize } F(x) = \varepsilon \\ \text{s.t.} \begin{cases} f_j > 0 \ (f_j \in \Omega_c) \\ f_k > 0 \ (f_k \in \Omega_s) \end{cases} \end{cases} \tag{19}$$

In which Ω denotes the total set of the initial self-stress forces, Ω_c is the set of the initial self-stress forces for cable members, and Ω_s is the set of the initial self-stress forces for strut members. f_j and f_k in Eq. (19) are the initial self-stress forces. The constraints are implemented using a penalized objective function, in which a penalty function is applied to the infeasible solutions that violate the constraints. The penalized objective function with n constraints is given by:

$$F_p(X) = F(X) + \sum_{i=1}^{n} \alpha_i \delta_i \tag{20}$$

where $\begin{cases} \delta_i = 1 \text{ if constraint i is violated} \\ \delta_i = 0 \text{ if constraint i is satisfied} \end{cases}$

$F_p(X)$ is the penalized objective function, whereas the F(X) is the unpenalized function, X is the design variables, α_i is a certain suitable constant imposed for violation of constraint i. This constant can be static or dynamic and can be estimated by performing a Monte Carlo simulation prior to the optimization step. In this study, the value of the constant α_i is assumed to be 10^6 for the two constraints (i.e., the number of cables and struts not satisfying the unilateral conditions).

The second stage P2 starts with the results of the first stage and can be called the (enhancement stage). This stage aims at further minimization of the design error by changing the elevation of each group of struts by a value Z_i ($Zi \in [-0.1, 0.1]$m, $i = 1, 2, \ldots, N_G$ where N_G is the number of groups of struts) away from the optimum NURBS surface. The multidimensional constrained optimization (SQP) implemented in MATLAB can efficiently obtain the optimum solution by specifying the starting point properly (i.e., the solution of the first stage). P1 and P2 have the same objective function and the same constraints, but the variables are different. Both optimization algorithms are implemented in MATLAB. A detailed flow chart of the two stages is shown in Fig. 2.

The feasible geometry obtained at the end of the form-finding process must be checked for stability as described above. The level of prestress, i.e., the magnification factor of the basis of prestress f_j ($\in \mathbb{R}^b$, $j = 1, 2, \ldots, s$), and the cross sectional properties should be assigned properly to check the tangent stiffness matrix of the feasible geometry. The eigenvalues λ_i ($i = 1, 2, \ldots, dn$) of the tangent stiffness matrix should be positive and in a descending order.

4 Numerical Example

To verify the effeciency of the proposed method, a saddle Geiger dome in [5], shown in Fig. 3(a), was selected for the form-finding problem. This study sets target sag and rise values of 8.7 and 11.3 m, respectively, to match with the results of the selected dome. The dome is circular with diameter of 100 m. The difference between the highest and lowest point of the outer beam is 20 m. Ridge cables are arranged every

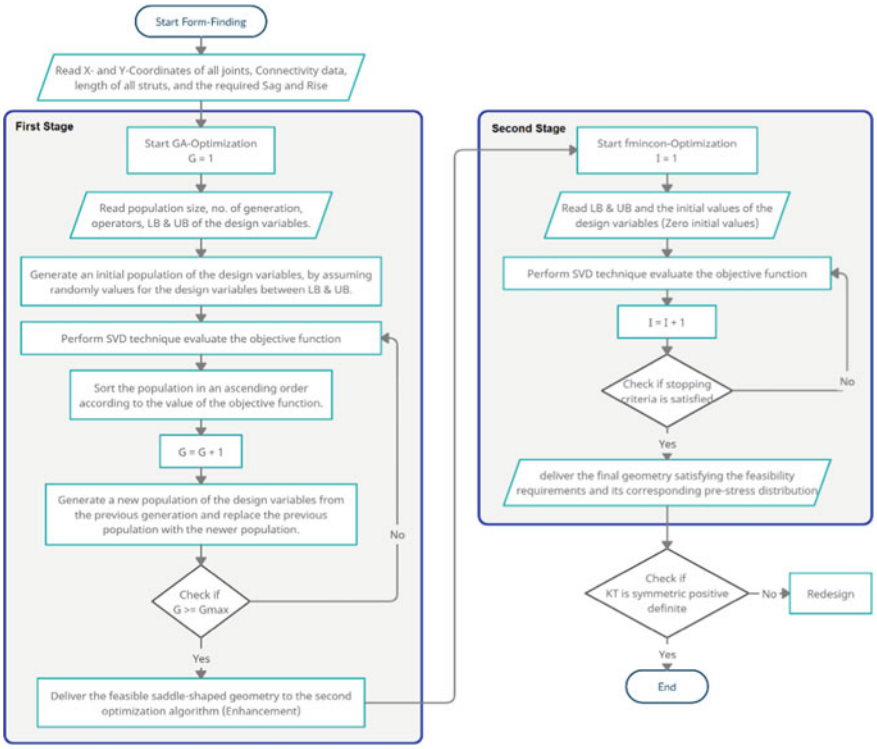

Fig. 2 Flow chart for the two stages form-finding algorithm of a saddle dome

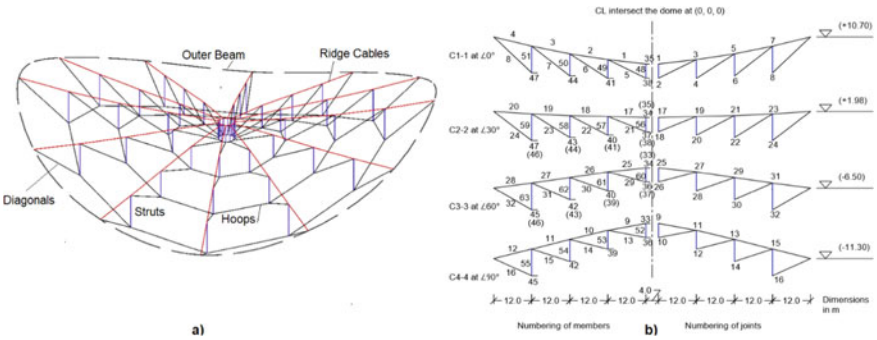

Fig. 3 **a** 3-D view of the saddle dome example **b** Numbering of joints and members

30°. Struts' lengths are 4.5, 6, 7, and 8.5 m arranged from the inner hoop to the outer hoop. The control points and their corresponding weights of the optimum NURBS curves obtained from the first stage are shown in Table 2. The fitness values of the objective function of the first stage, shown in Fig. 4(a), indicate the convergence of

Table 2 Location (x_i and y_i in m) and weights w_i of control points of the optimum solution of GA

		x_i	y_i	w_i			x_i	y_i	w_i
Negative curve	$P_{1\text{-}N}$	0.00	0.00	1.00	Positive curve	$P_{1\text{-}P}$	0.00	0.00	1.00
	$P_{2\text{-}N}$	4.24	0.00	1.46		$P_{2\text{-}P}$	4.94	0.00	0.84
	$P_{3\text{-}N}$	32.65	4.06	1.19		$P_{3\text{-}P}$	32.20	−6.78	0.68
	$P_{4\text{-}N}$	50.00	8.70	1.00		$P_{4\text{-}P}$	50.00	−11.30	1.00

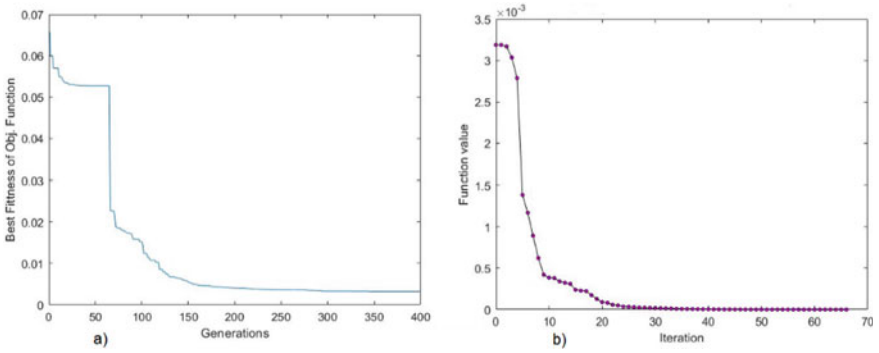

Fig. 4 Fitness values of **a** P_1 (GA) **b** P_2 (SQP)

GA after 300 generations, while in Fig. 4(b), the convergence of the second stage was achieved after 30 iterations. The design error achieved at the end of form-finding was about (2.5903×10^{-7}) which proves the efficiency of the algorithm. Meanwhile, the design error resulting from the first stage only was about (3.2×10^{-3}) which indicates that the second stage was able to enhance the accuracy of the feasible prestress obtained from this algorithm. The obtained feasible geometry is shown in Fig. 3(b) and z-coordinates of the higher joints of the struts at the end of form-finding are tabulated in Table 3. It is worth noting that the predefined rise and sag values are maintained during the form-finding process which is considered as a remarkable advantage of the proposed method compared to other methods in the literature.

The base prestress f_m obtained is shown in Table 4, where m is the total number of groups of cables and struts (47 group of cables + 16 groups of struts). The base prestress is scaled to the prestress of member 35 and magnified by 1×10^7 N to

Table 3 z-coordinates of the higher joints of struts in the final feasible geometry.

Joint	z (m)	Joint	z (m)	Joint	z (m)	Joint	z (m)
1	0.0560	9	−0.1034	17	0.0139	25	−0.0644
3	1.4952	11	−2.2954	19	0.3833	27	−1.3863
5	3.2879	13	−5.2158	21	0.6478	29	−3.1815
7	5.7500	15	−8.2964	23	1.1798	31	−4.9337

Table 4 Base prestress (f_m) of cables and struts ($\times 10^7$ N)

m	f_m	m	f_m	m	f_m	m	f_m	m	f_m	m	f_m	m	f_m
1	0.521	11	0.670	21	0.061	31	0.056	41	0.148	51	−0.001	61	−0.044
2	0.580	12	0.722	22	0.085	32	0.026	42	0.100	52	−0.019	62	−0.035
3	0.663	13	0.058	23	0.060	33	1.000	43	0.102	53	−0.056	63	−0.019
4	0.721	14	0.078	24	0.029	34	1.002	44	0.100	54	−0.046		
5	0.063	15	0.054	25	0.520	**35**	**1.000**	45	0.044	55	−0.025		
6	0.090	16	0.025	26	0.580	36	0.109	46	0.046	56	−0.019		
7	0.065	17	0.517	27	0.656	37	0.109	47	0.045	57	−0.026		
8	0.031	18	0.574	28	0.706	38	0.109	48	−0.019	58	−0.023		
9	0.526	19	0.650	29	0.058	39	0.147	49	−0.004	59	−0.014		
10	0.590	20	0.702	30	0.080	40	0.150	50	−0.002	60	−0.019		

Table 5 The lowest 10 eigenvalues of K_T in ascending order ($\times 10^4$)

0.54	1.72	2.37	3.74	3.82	3.95	5.25	6.85	7.34	8.21

satisfy the load carrying capacity of the dome. The tangent stiffness matrix K_T, formed using the magnified prestress and the same cross sections of the reference dome, is symmetric positive definite and its lowest 10 eigenvalues in ascending order are shown in Table 5. A nonlinear analysis using SAP2000 is performed by applying the scaled prestress only on cables and struts resulting in a max displacement of 2.2944×10^{-6} m, while in the reference example the max displacement was 4×10^{-5} m. All requirements of feasibility stated above are achieved for the geometry and obtained from the proposed form-finding method. This proves the efficiency and robustness of this algorithm in controlling the form-finding of saddle cable domes to a predefined sag and rise values. On the other side, the max displacement of the feasible geometry under self-weight is 0.1489 m which can be minimized by a structural optimization for the cross-sectional properties of all elements subject to strength and stability requirements.

5 Conclusion

This paper proposes a form-finding algorithm for cable domes with negative-Gaussian curvature with predefined sag and rise values. The algorithm consists of two stages based on a GA optimization as a first stage and a constrained local optimisation as a second stage. The objective function of the two sages is the design error of the base prestress obtained using SVD technique. A numerical example of a saddle cable dome of Geiger type is employed. The convergence of the proposed algorithm and the feasibility of the obtained geometry are checked and discussed in

details, proving the efficiency and robustness of the proposed method. The proposed algorithm can be applied on other forms of cable domes. However, a structural optimization might be needed for optimizing the distribution of the cross sections in order to minimize the displacement under the design and service loads.

Acknowledgements The authors would like to thank the Egyptian Ministry of Higher Education and Scientific Research for funding this research.

References

1. Albertin A, Malerba PG, Pollini N, Quagliaroli M (2012) Prestress optimization of hybrid tensile structures. In: Bridge maintenance, safety, management, resilience and sustainability: proceedings of the sixth international IABMAS conference
2. Costa G, Montemurro M, Pailhès J (2019) NURBS hyper-surfaces for 3D topology optimization problems. Mech Adv Mater Struct 28(7):665–684
3. Geiger DH, Stefaniuk A, Chen D (1986) The design and construction of two cable domes for the Korean Olympics. In: Proceedings of the IASS symposium on shells, membranes and space frames
4. Guo J, Jiang J (2016) An algorithm for calculating the feasible pre-stress of cable-struts structure. Eng Struct 118:228–239
5. Guo J, Zhu M (2016) Negative Gaussian curvature cable dome and its feasible prestress design. J Aerosp Eng 29(3):04015077
6. Hanaor A (1988) Prestressed pin-jointed structures—flexibility analysis and prestress design. Comput Struct 28(6):757–769
7. Hassan MM, Nassef AO, El Damatty AA (2012) Determination of optimum post-tensioning cable forces of cable-stayed bridges. Eng Struct 44:248–259
8. Levy MP (1994) The Georgia Dome and beyond: achieving lightweight-longspan structures. In: Spatial, lattice and tension structures
9. Linkwitz K, Schek H-J (1971) Einige bemerkungen zur berechnung von vorgespannten seilnetzkonstruktionen. Ingenieur-Archiv 40(3):145–158
10. Michalewicz Z, Fogel DB (2013) How to solve it: modern heuristics. Springer, Heidelberg
11. Ohsaki M, Zhang J (2006) Stability conditions of prestressed pin-jointed structures. Int J Non-Linear Mech 41(10):1109–1117
12. Pellegrino S (1993) Structural computations with the singular value decomposition of the equilibrium matrix. Int J Solids Struct 30(21):3025–3035
13. Pourazady M, Xu X (2000) Direct manipulations of B-spline and NURBS curves. Adv Eng Softw 31(2):107–118
14. Quagliaroli M, Malerba PG, Albertin A, Pollini N (2015) The role of prestress and its optimization in cable domes design. Comput Struct 161:17–30
15. Tibert AG, Pellegrino S (2003) Review of form-finding methods for tensegrity structures. Int J Space Struct 18(4):209–223
16. Tran HC, Lee J (2013) Form-finding of tensegrity structures using double singular value decomposition. Eng Comput 29(1):71–86
17. Tran HC, Park HS, Lee J (2012) A unique feasible mode of prestress design for cable domes. Finite Elem Anal Des 59:44–54
18. Yanase K (2017) A gentle introduction to isogeometric analysis: part 2 NURBS curve and surface. Fukuoka Univ Rev Technol Sci 99:1–8
19. Yuan X, Chen L, Dong S (2007) Prestress design of cable domes with new forms. Int J Solids Struct 44(9):2773–2782

20. Zhang JY, Ohsaki M (2006) Adaptive force density method for form-finding problem of tensegrity structures. Int J Solids Struct 43(18–19):5658–5673
21. Zhang L, Maurin B, Motro R (2006) Form-finding of nonregular tensegrity systems. J Struct Eng 132(9):1435–1440

Experimental Testing of the Shear Strength of CLT-Concrete Composite Sections Utilizing Screws as Shear Connectors

Osama Sam Salem and Vikram Virdi

1 Introduction

Cross-laminated timber (CLT) is a proprietary mass timber product that is prefabricated using wood laminations arranged in alternating perpendicular layers (commonly ranging from 3 to 9) with the outer layers oriented in the direction of the major strength axis. CLT is advantageous to manufacture as the finished product has more desirable mechanical properties than those of the individual lamination. The latest National Building Code of Canada [3] is now allowing wood as the primary material in the construction of up to twelve-storey buildings, which will result in an enduring increase in the application of mass timber sections. Evidently, it can be demonstrated that with the technical information and documentations that recently have been developed, new timber buildings such as those made of glued-laminated timber (glulam) framing systems that are supporting CLT floor panels can be designed to successfully achieve the limit state design requirements for both strength and serviceability. Accordingly, several tall buildings made primarily of timber are increasingly being constructed worldwide. Floor systems in such buildings can even be made stronger and span longer distances to allow designers greater versatility in terms of floor plan and to promote open concept design in modern buildings by adding a top layer made of concrete. Addition of a concrete layer can allow the formation of Timber-Concrete Composite (TCC) floor system if adequate shear connections can be developed. In such floor composite systems, the advantageous mechanical properties of both materials (timber and concrete) are efficiently utilized and thus, several advantages can be achieved for a more robust floor system. Among the several advantages of utilizing TCC floor systems are greater strength, durability, and better acoustics and vibration performance characteristics [12].

O. S. Salem (✉) · V. Virdi
Department of Civil Engineering, Lakehead University, Thunder Bay, ON, Canada
e-mail: sam.salem@lakeheadu.ca

S. Walbridge et al. (eds.), *Proceedings of the Canadian Society of Civil Engineering Annual Conference 2021*, Lecture Notes in Civil Engineering 244,
https://doi.org/10.1007/978-981-19-0656-5_33

TCC floor systems are developed by creating adequate shear connections between the timber section carrying the tensile forces and the concrete layer carrying the compressive forces. The composite action and behaviour of such system is defined mainly by the rigidity of the shear connections between the two materials. The primary technique for shear connections in TCC systems is a wide variety of metal connectors [8], grooved connections [9], or adhesive connections [10]. Strength and stiffness of TCC sections can be determined using the Mechanically Jointed Beams Theory (gamma-method) from Annex B of Eurocode 5 [6], especially when considering conventional floor systems where the span is at least 25 time the depth of the section [2]. While the design of TCC sections with the use of various mechanical shear connectors is well addressed in different design codes in the EU, there are no provisions in the current Canadian standard for Engineering design in wood [4] for their design. The only design guide that recently became available for engineers in Canada is the *Design Guide for Timber-Concrete Composite Floors in Canada*, which provides guidance for the design of TCC systems in ambient and fire conditions [5].

The study presented in this paper aimed to experimentally investigate the shear characteristics of medium-size CLT-Concrete composite sections that utilize metal screws as shear connectors. Two study parameters were considered, the screw spacing (150 and 200 mm) and the number of screw rows within the width of the composite section (two and three rows).

2 Experimental Program

The shear characteristics of CLT-Concrete composite sections that utilized metal screws as shear connectors have been investigated throughout the experimental program of the study presented in this paper. Two study parameters were considered, the screw spacing (150 and 200 mm) and the number of screw rows within the width of the composite section (two and three rows). A total of eight composite sections, each with 600 × 1000 mm shear interface between the CLT panel and the concrete layer, were experimentally examined under direct shear forces until failure. Four composite sections were tested at concrete age of 14 days, while the other four duplicated sections were tested at 28-day concrete age.

2.1 Materials

2.1.1 CLT Panels

The 3-ply CLT panels utilized in the composite sections were cut to 600 mm wide × 1200 mm long with the external laminations oriented in the longitudinal direction of the test specimen. The CLT panels were all made of spruce-pin-fir (S-P-F) planks.

Table 1 Mechanical properties of CLT panels (adopted from Nordic Structures [11])

Property	Allowable strength (MPa)
Comp. parallel to grain	19.3
Comp. perp. to grain	5.3
Tension parallel to grain	15.4
Modulus of elasticity	11,700
Shear modulus	731.25

Table 2 Mechanical properties of self-tapping screws (adopted from ICC-ES Evaluation report [7])

Property	Allowable strength (MPa)
Bending strength	1175.0
Tensile strength	1298.0
Shear strength	881.0

The principle mechanical design properties of the CLT panels in the longitudinal direction as provided by the supplier [11] are listed in Table 1.

2.1.2 Self-Tapping Screws

The self-tapping screws (STS) utilized in the sections were made of 8-mm diameter rugged structural steel screws with 100 mm length. The screws were made of specially hardened steel to provide greater torque, tensile, and shear strengths. In comparison to regular screws or nails, the employed STS were designed with special thread that helped in enlarging the screw hole to allow easy penetration in wood without the need of pre-drilled holes, which also increases the withdrawal resistance of the screws. The mechanical properties of the utilized screws as per the ICC-ES Evaluation report [7] are provided in Table 2.

2.1.3 Concrete

The targeted compressive strength of the concrete required for the 50-mm thick concrete layer of the composite sections was 30 MPa. Accordingly, a concrete mix that is composed of 300 kg (40%) fine aggregate; 300 kg (40%) coarse aggregate; 90 kg (12%) cement; and 60 kg (8%) water was prepared to cover the amount of concrete required for the eight test specimens (total concrete volume of 0.288 m^3). Total of six cylinders were prepared from the concrete mix to determine the actual compressive strength of concrete after 14 days (3 cylinders) and 28 days (3 cylinders) from the concrete casting time.

2.2 Fabrication Process and Tests Assemblies Details

After cutting down the CLT panels needed for the composite sections to their final dimensions (600 mm wide × 1200 mm long) the STS were installed in four different patterns based on the number of rows (two or three rows along the width of the section) and the spacing between screws along each row (150 and 200 mm). Each different test specimen was duplicated to allow testing one specimen at 14-day and the other at 28-day concrete age. Table 3 shows the test matrix of the study presented in this paper.

In sections A and B that utilized two rows of screws, a 100 mm edge distance was left on both sides of the 600 mm width of the CLT panel, which allowed a 400 mm middle spacing between the two rows of screws. Whereas in sections C and D that utilized three rows of screws, each of the side rows had only 50 mm edge distance and 250 mm intermediate spacing with the middle row. The STS were driven into the CLT panels at 45° angle of inclination with the panel top surface. Most of the screw length (100 mm) was driven into the CLT panel keeping the screw head at 25 mm distance perpendicular to the panel top surface (50% of the concrete layer thickness). At each screw junction, there were two screws driven into the CLT and inclined in two opposite directions along the longitudinal direction of the panel, as shown in Fig. 1.

After installing the required number of STS in each CLT panel, cut-off strips of plywood were attached to the CLT panel to build a formwork that was used to allow casting the 50-mm thick concrete layer of the composite section. The formwork was designed to allow a CLT-Concrete interface area of 600 mm wide × 1000 mm long with a 200-mm overhang in each of the concrete layer and the CLT panel with respect to each other at the two opposite ends in the longitudinal direction of the composite section, as shown in Fig. 1. The development of the said overhangs was mainly to allow the load application solely on the top end of the CLT panel while the entire composite section is supported solely on the bottom end of the concrete layer (see Sect. 2.3 for test setup details).

Before pouring the concrete, the prepared CLT panels were laid down and leveled on the floor. Concrete was evenly spread over the CLT panel, around the screw junctions, along the edges and in the formwork corners. After the poured concrete reached slightly higher level than the top edges of the formwork, it was made sure that the concrete surface was levelled and flushed with the top edges of the formwork

Table 3 Test matrix including all eight CLT-Concrete composite sections

Composite section ID	Number of screw rows	Spacing between screws (mm)	Number of replicates	Number of screw junctions
A	2	200	2	10
B	2	150	2	14
C	3	200	2	15
D	3	150	2	21

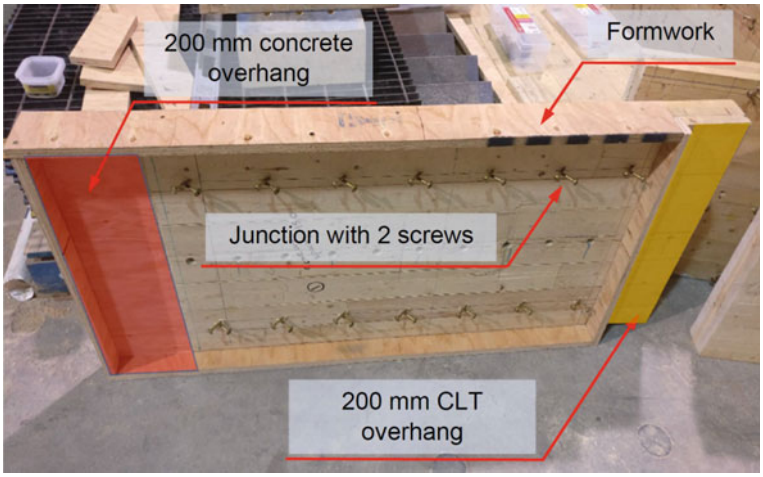

Fig. 1 CLT panel with STS and concrete formwork installed

using a magnesium float to ensure the 50 mm thickness required for the concrete layer.

To maintain the temperature and dampness for proper curing, the poured concrete layers were watered and covered with polyethylene sheeting for the first seven days of the concrete age. However, the formworks were removed after only two days of pouring the concrete, as shown in Fig. 2.

Fig. 2 CLT-Concrete composite sections after removing formworks

2.3 Test Setup and Procedure

To allow the load application solely on the top end of the CLT panel while the entire composite section is supported solely on the bottom end of the concrete layer as well as to restrain the test specimen against any lateral or transversal displacement, a strong steel supporting rig was designed and fabricated. The supporting rig was then placed on top of a strong, long bottom steel girder within the Universal Testing Machine (UTM) accommodated in the Civil Engineering's Structures Laboratory at Lakehead University. Before sliding the supporting rig to be positioned between the upper and lower crossheads of the UTM, the heavy CLT-Concrete composite test specimen was aligned in a vertical orientation into the supporting rig using an overhead crane. After the top end of the CLT panel of the test specimen was centered under the upper crosshead of the UTM in both lateral and transversal directions, displacement transducers were installed on the specimen. Two linear variable differential transformers (LVDTs) were attached to the left- and right-side edges of the CLT panel (namely LVDT-1 and LVDT-2) with their rods were bearing against little steel brackets that were glued to the left- and right-side edges of the concrete layer, respectively. The two LVDTs were utilized to continuously measure the relative slips between the CLT and concrete layer near the left- and right-side edges of the test specimen during loading. Figure 3 illustrate the test setup for a general test specimen placed within the UTM with both LVDTs installed. After the initial readings of the installed LVDTs were checked, the load was applied gradually at a rate of 8.0 kN per minute. The relatively slow rate of loading was deliberately chosen to avoid unnecessary premature cracks in the concrete that would have developed due to faster application of the load. Also, force-controlled loading (kN/min) instead of displacement-controlled loading (mm/min) was deliberately selected due to the same preventative measure of not loading the test specimens too quickly.

3 Results and Discussion

3.1 Concrete Cylinder Tests

To verify the targeted compressive strength for the concrete mix, which is 30 MPa, cylinders with 14-day and 28-day concrete age were tested for their actual compressive strength using the same UTM. The compressive strength tests were performed according to ASTM C39/C39M-20 standard for concrete cylinder tests [1]. The average compressive strength attained by the three cylinders with the 14-day concrete age was 23.1 MPa, while the average strength attained by the other three cylinders with the 28-day concrete age was 29.98 MPa. All concrete cylinders exhibited cone failure.

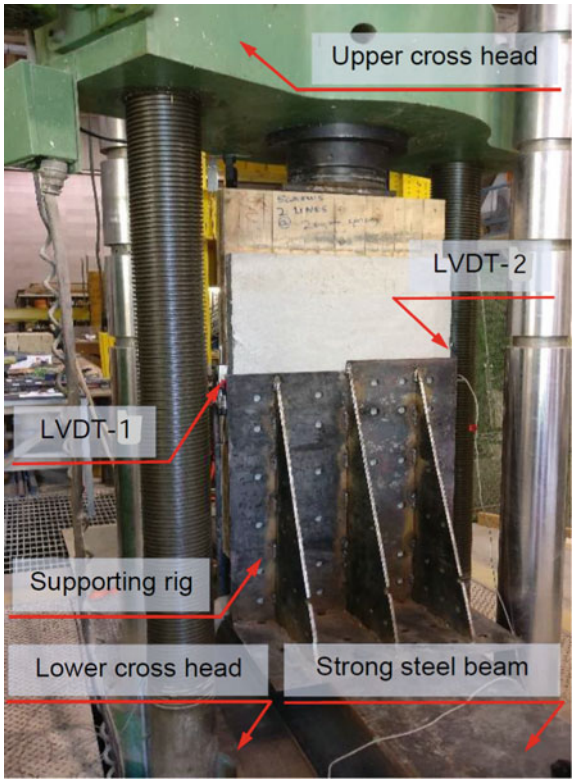

Fig. 3 Test setup for a general test specimen with instrumentation installed

3.2 CLT-Concrete Composite Section Tests

Figure 4 shows the load–displacement relationships developed using the measurements of the installed LVDTs against the loads applied by the UTM for the four CLT-Concrete composite sections that employed two rows of screws with 200 and 150 mm screw spacings. The ultimate load attained by the sections with 200 mm screw spacings and concrete of 14- and 28-day age is 131 and 180 kN, as shown in Fig. 4(a) and (b), respectively. While for the sections with the smaller screw spacings (150 mm), the ultimate load was increased to 225 and 234 kN for the sections with concrete of 14- and 28-day age, respectively, Fig. 4(c) and (d).

Figure 5 shows the load–displacement relationships for the four CLT-Concrete composite sections that employed three rows of screws with 200 and 150 mm screw spacings. The ultimate load attained by the sections with 200 mm screw spacings and concrete of 14- and 28-day age is 225 and 239 kN, as shown in Fig. 5(a) and (b), respectively. While for the sections with the smaller screw spacings (150 mm), the ultimate load was increased to 258 and 287 kN for the sections of concrete of 14- and 28-day age, respectively, Fig. 5(c) and (d).

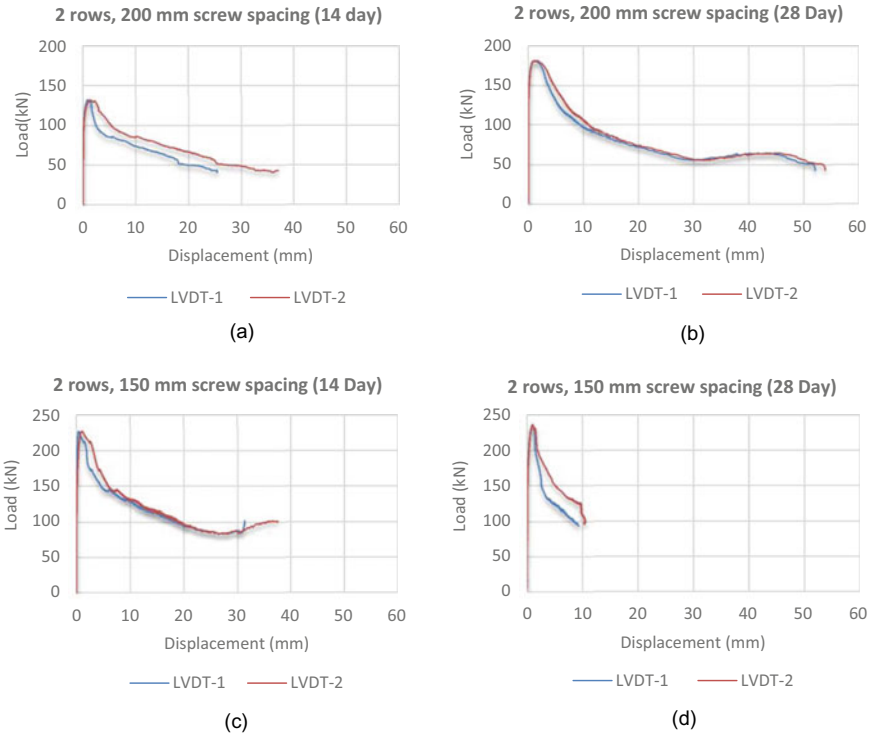

Fig. 4 Load–displacement relationships for composite sections that utilized two rows of screws with 200 and 150 mm screw spacings at 14- and 28-day concrete age

Table 4 summaries the test results of all eight CLT-Concrete composite sections experimentally examined in the study presented in this paper.

3.3 Effect of Concrete Age on the Ultimate Load of the Composite Sections

Comparing Fig. 4(a) and (b), the ultimate load of the sections that utilized two rows of screws with the larger screw spacings (200 mm) increased by approximately 37% because of the increase in the compressive strength of concrete due to longer curing time (28 days vs 14 days). Whereas this increase in the ultimate load was negligible for similar sections that utilized two rows of screws but with the smaller screw spacings (150 mm), as it was determined at approximately 4% only, Fig. 4(c) and (d).

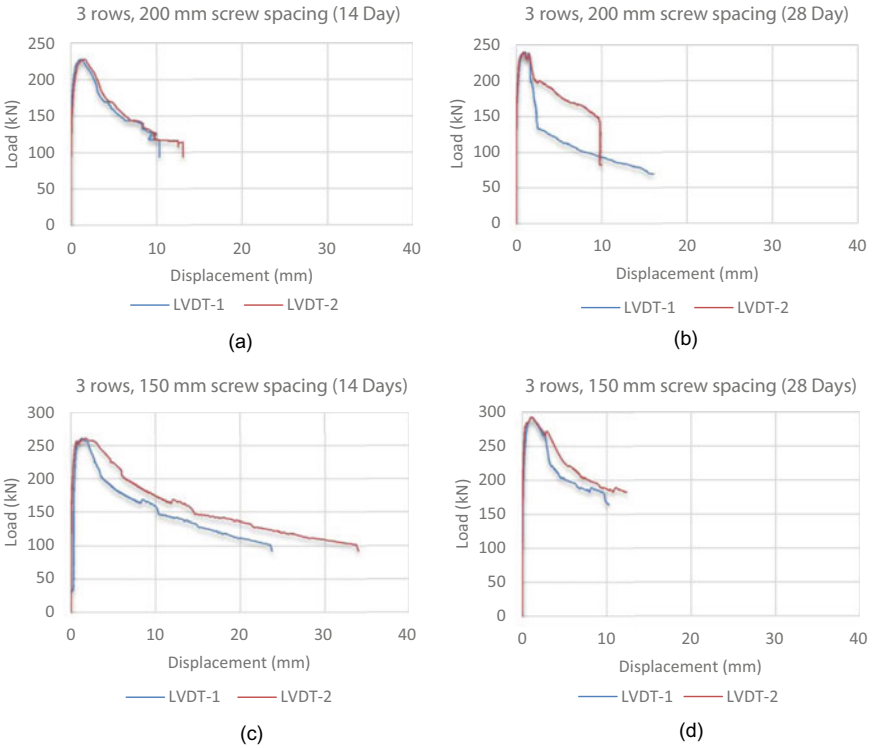

Fig. 5 Load-displacement relationships for composite sections that utilized three rows of screws with 200 and 150 mm screw spacings at 14- and 28-day concrete age

Table 4 Tests results for all eight CLT-Concrete composite sections

Composite section ID	Number of screw rows	Spacing between screws (mm)	Concrete age (days)	Maximum load (kN)
A	2	200	14	131
A	2	200	28	180
B	2	150	14	225
B	2	150	28	234
C	3	200	14	225
C	3	200	28	239
D	3	150	14	258
D	3	150	28	287

Comparing Fig. 5(a) and (b), the ultimate load of the sections that utilized three rows of screws with the larger screw spacings (200 mm) increased marginally by approximately 6% after 14 days additional of concrete curing time (28 days vs 14 days). Whereas this increase in the ultimate load was slightly more noticeable for similar sections that utilized three rows of screws but with the smaller screw spacings (150 mm), as it was determined at approximately 11%, Fig. 5(c) and (d).

3.4 Effect of Number of Screw Rows on the Ultimate Load of the Composite Sections

From Fig. 5(a) and (b), the ultimate load attained by the sections that utilized three rows of screws with the larger screw spacings (200 mm) increased by approximately 72% and 32% compared to similar sections with the same larger screw spacings but utilized only two rows of screws with 14- and 28-day concrete age, respectively, as shown in Fig. 4(a) and (b). Whereas this increase in the ultimate load was less for similar sections that utilized three rows of screws but with the smaller screw spacings (150 mm), as it was determined at approximately 15% and 22% compared to similar sections with the same smaller screw spacings but utilized only two rows of screws with 14- and 28-day concrete age, respectively, as shown in Fig. 4(c) and (d) in comparison to Fig. 5(c) and (d).

3.5 Effect of Screw Spacings on the Ultimate Load of the Composite Sections

Comparing Fig. 4(c) and (d) with Fig. 4(a) and (b), the ultimate load attained by the sections that utilized two rows of screws with the smaller screw spacings (150 mm) increased by approximately 72% and 30% compared to similar sections that utilized two rows of screws but with the larger screw spacings (200 mm) and 14- and 28-day concrete age, respectively. Whereas this increase in the ultimate load was less for similar sections with the smaller screw spacings (150 mm) but utilized three rows of screws, as it was determined at approximately 15% and 20% compared to similar sections that utilized three rows of screws but with the larger screw spacings (200 mm) and 14- and 28-day concrete age, respectively, as shown in Fig. 5(c) and (d) in comparison to Fig. 5(a) and (b).

(a) **(b)**

Fig. 6 Failure modes of the composite sections that utilized two rows of screws, **a** with the larger screw spacings (200 mm); **b** with the smaller screw spacings (150 mm)

3.6 Failure Modes

In the CLT-Concrete composite sections that utilized two rows of screws, the failure started with the development of a longitudinal crack in the concrete layer along one of the two rows of screws, as shown in Fig. 6(a). This crack propagated further and separated one edge of the concrete layer in the composite sections with the smaller screw spacings (150 mm), as shown in Fig. 6(b).

While in the composite sections that utilized three rows of screws, the failure started with a longitudinal crack that was developed at both sides of the concrete layer. The side crack was aligned longitudinally with the locations of the screw heads impeded at the middle of the thickness of the concrete layer, as shown in Fig. 7(a). Afterwards, those side cracks propagated laterally towards the sides and caused the concrete layer to separate from the CLT section after the concrete surrounding the screw junctions along the side rows of screws was damaged, as shown in Fig. 7(b). This failure can be attributed to the small edge distance between the side row of screws and the respective side of the concrete layer.

(a) (b)

Fig. 7 Failure modes of the composite sections that utilized three rows of screws with the smaller screw spacings (150 mm), **a** shortly before failure; **b** at failure

4 Conclusions and Recommendations

Based on the results obtained from this experimental study on the shear strength of CLT-Concrete composite sections, the following conclusions can be drawn.

- The shear strength of the composite sections of 28-day concrete age increased by a minimum of 4% and 6% compared to that of the respective sections of 14-day concrete age that utilized two and three rows of screws, respectively.
- The shear strength increased by slightly less increments when the screw spacings reduced from 200 to 150 mm compared to those increments attained due to increasing the number of screw rows from two to three along the composite section width.
- Composite sections that utilized three rows of screws exhibited more cracks in both longitudinal and lateral directions compared to those that utilized two rows of screws which exhibited only longitudinal cracks along one of the screw rows. This is mainly attributed to the less number of screw junctions in the sections with two rows of screws.
- CLT-Concrete composite sections exhibited considerable shear strength with a maximum failure load of 287 kN attained by the specimen that utilized three rows of screws with the smaller screw spacings (total of 21 screw junctions), while the specimen that utilized two rows of screws with the larger screw spacings (total of 10 screw junctions) failed at only 180 kN.

– Either reducing the screw spacings from 200 to 150 mm or increasing the number of screw rows from two to three rows increases the shear strength of the CLT-Concrete composite sections almost equally. However, increasing the number of screw rows is recommended since it is not only increasing the shear strength of the composite sections with slightly greater increments but also allow more uniform distribution of the shear stresses along the width of the composite section.

Acknowledgements This research project was funded partially using the NSERC-Discovery Grant and the Mass Timber Institute Research Grant awarded to the first author. The authors would like to thank lab technologists C. Hubbard and R. Timoon for their assistance in the Civil Engineering's Structures Laboratory at Lakehead University.

References

1. ASTM (2020) ASTM C39/C39M-20, Standard test method for compressive strength of cylindrical concrete specimens. ASTM International, West Conshohocken
2. Bajzecerová V (2017) Bending stiffness of CLT-concrete composite members - comparison of simplified calculation methods. Proc Eng 19:15–20
3. Canadian Commission on Building and Fire Codes (2020) National Building Code of Canada, National Research Council of Canada, Ottawa
4. Canadian Standards Association (2019) CSA O86-19, Engineering design in wood, Mississauga
5. Cuerrier-Auclair S (2020) Design guide for timber-concrete composite floors in Canada. FPInnovations, Montréal
6. European Committee for Standardization (2004) Eurocode 5: Design of timber structures. Part 1-1: General–common rules and rules for buildings. EN 1995-1-1. CEN, Brussels
7. GRK Fasteners, A Division of Illinois Tool Works Inc. (2017) Rugged Structural Screws. ICC-ES Evaluation Report. ESR-2442. Bartlett. Illinois. http://itwcpc.ca/wp-content/uploads/2019/07/ICC-ESR-2442-GRK-RSS.pdf.
8. Kanócz J, Bajzecerová V, Šteller Š (2013) Timber-concrete composite elements with various composite connections, Part 1: Screwed connection. Wood Res 58(4):555–570
9. Kanócz J, Bajzecerová V, Šteller Š (2014) Timber-concrete composite elements with various composite connections, Part 2: Grooved connection. Wood Res 59(3):627–638
10. Kanócz J, Bajzecerová V, Šteller Š (2015) Timber-concrete composite elements with various composite connections, Part 3: Adhesive connection. Wood Res 60(6):939–952
11. Nordic Structures (2019) Design properties of Nordic Lam. In: Technical Note S01. Nordic Structures, Canada
12. Tannert T, Gerber A, Vallee T (2019) Hybrid adhesively bonded timber-concrete-composite floors. Int. J. Adhes. Adhesiv. 97:102490

Bridgebase: A Knowledge Graph Framework for Monitoring and Analysis of Bridges

Kunal Tiwary, Sanjaya Kumar Patro, and Bibhudatta Sahoo

1 Introduction

Computing devices are commonly used for analyzing and processing large-scale knowledge. Knowledge Graph structures are needed to infer useful models and provide a query framework (which could even support a question–answer based system) over the models [11]. Knowledge graphs have proven its ability to represent a huge data set in a more readable form than tabular representation or structured data [10]. In this work, we exploit the features of the knowledge graph to essentially monitor and do real-time analysis of bridges.

New bridges are constructed frequently whose maintenance is very essential and its cost grows simultaneously. Some bridges are completely replaced or rehabilitated due to monetary constraints which might be deficient in terms of budget, although the condition of bridges is identified [9]. These situations lead to the initiatives of the programs which can help us monitor and repair rather than rehabilitate. To perform a deep study about the parameters related to performance degradation procedure related to various structures, a sample distribution may be needed [9]. If similar groups are identified correctly, the repair work of all such extensions can be performed at a time optimally. Certain bridge structures need to be monitored based on a more cost-effective approach. The information related to bridges (more than 6,00,000) in the United States is stored in the National Bridge Inventory (NBI) [6, 11]. The ASCE report card issued every four years (issued last in 2017), has reported America's infrastructure as D+ , whose evaluation is based upon 16 different categories with each category to be equally weighted. The grades have degraded from C+ (2013)

K. Tiwary (✉) · S. K. Patro
VSS University of Technology, Burla, India

S. K. Patro
e-mail: skpatro_ce@vssut.ac.in

B. Sahoo
National Institute of Technology, Rourkela, India
e-mail: bdsahu@nitrkl.ac.in

S. Walbridge et al. (eds.), *Proceedings of the Canadian Society of Civil Engineering Annual Conference 2021*, Lecture Notes in Civil Engineering 244,
https://doi.org/10.1007/978-981-19-0656-5_34

to D+ (2017). A deficient competitive infrastructure can lead to an investment that is equivalent to the GDP of Germany. Improving grades is directly related to better investments at every level [2 GPA: D+). Clustering is a method to bring alike objects together [8]. According to the strategies for the answer to this problem provided by the ASCE report card, cluster analysis is adopted in this work. The problem arises when there is a lack of labeled data (like which bridges are similar) or the data is sparse.

Deepwalk is used to learn the latent representations of vertices in a network by using a collection of random walks even in lesser labeled data [18]. Deepwalk learns latent features of the nodes by searching similarities of the graph structure. Further, the learned latent vectors could go through any clustering technique to figure out similar vectors in n-dimension space. Deepwalk, could essentially convert a knowledge graph node to a latent n-dimensional vector using the node connectivity semantics (example—a common property node between two bridge nodes). The node to vector latent conversion uses a set of random walks and then captures the sequences of random walks to build an essential vocabulary. Deepwalk uses the built vocabulary and *skip-gram* to build latent vectors. The major contributions of the work done in this paper can be summarized as follows:

- Modeling of the NBI bridge data set to knowledge-graph, which structurally captures the similar properties of bridges in terms of common knowledge graph nodes.
- Using deepwalks to create bridge nodes latent vectors and then using the latent vectors to figure out similar bridges using density-based clustering.
- Evaluating deepwalks efficiency in terms of captured features while building latent vectors in the presence of partial knowledge graphs using F1 scores.

The paper presents a knowledge graph approach to model the NBI data set of bridges, which makes it efficient to create clusters of similar bridges by using embeddings from deepwalk.

1.1 Literature Review

Bridges are highly sensitive with a lot of varying loads (dead load, live load, wind load, etc.). The frequency of capturing these parameters makes it difficult to handle the huge volume of data and take the decision in real-time. Wired and wireless sensors are deployed in many long-span bridges that give more measurements for a high volume of parameters every second [21]. Such huge data needs to be handled, and monitoring of all such bridges with similar attributes needs attention. Typically this involves building complex Machine Learning pipelines (which captures features from the dataset and then learns a model from extracted features) to get useful information in real-time [7, 18].

As presented in [9], a class of bridges is identified using a group of attributes found in the national bridge inventory. Error in measurements and missing of labeled data

is a very common phenomenon in real-time data or even in visual inspections. In such a case where variance in data occurs, latent class clustering techniques prove to be sensitive [15]. The formation of latent-vectors seems an already known mechanism, which auto-captures the essential features which could be then consumed by a Machine Learning pipeline to give useful information in real-time. In literature, unsupervised clustering was done to identify similar bridges and also the variety of work by fuzzy c-mean clustering algorithms [20]. In [1], future bridge networks were predicted for the planning of rehabilitation work by use of tensor factorization. Similar algorithms from data mining have shown a wide range of applications in civil infrastructural systems for prediction of the condition rating classes in the National Bridge Inventory (NBI) dataset [3]. The main problem that restricts these methods is that these methods need to consider the entire dataset to make the pipeline work (hence making them challenging for streaming applications). Also while considering the entire dataset when the volume of data gets exponentially high, it again creates challenges in processing the high volume i.e.—efficient memory management, complex feature engineering, etc. In this work, we try to create a system that brings similar kinds of bridges together even with real-time data collection in a more readable form. The work done in this paper models the NBI dataset into a knowledge graph and then converts the bridge nodes into latent vectors even with the partial knowledge graph (or a subset of knowledge graph). This makes the latent-vector conversion more compute efficient for even processing streaming data.

2 Illustration of the NBI Data

The data which is utilized to build the knowledge graph is directly taken from the Federal Highway Administration (FHWA) at the end of 2019 [6]. At first, this informational collection contained a total of 617,085 bridges. Also, the data can be directly taken and utilized from [1] but in this work, we preferred data from the inventory. There are two kinds of datasets available, elemental data and the whole data. The performance, structural, and functional behavior is described by different variables and is stored in the whole data of National Bridge Inventory. It includes variables like the age of the structure, average daily traffic (ADT), condition ratings of deck, substructure, and superstructure. These variables are recorded and stored in the inventory under the specifications provided by FHWA [5]. The data available in the inventory can be clearly understood by reading the coding guide. After analyzing the whole data, a rejection process is opted which helps to find the exact attributes needed to monitor. The attributes chosen have a direct connection with the structural identity and its performance.

2.1 Description of the Variables

Variables are used to define either the structural performance of the bridge or for its identification purposes. For brief information, the code can be directly referred to.

- **Structure Number—**It is a unique number designated to the structure and is used for the identification of the structure in the graph.
- **Year Built and Year Reconstructed—**It represents the age of the structure with respect to the current year.
- **ADT and ADTT—**ADT depicts the particular average daily volume of traffic and ADTT represents the average daily volume of truck traffic.
- **Design Load—**It is the live load for which the structure has been designed.
- **Structure Type—**The first digit of which suggests the material type and the second constitute the type of design. For example, the concrete slab is represented by 11.
- **Condition Ratings—**It represents the condition of the structure and is rated accordingly. It includes the ratings of the Deck, superstructure, substructure, channel, culverts. If the rating is given "N", it concludes that the particular rating is not applicable for that structure.
- **Structural Evaluation—**It depicts the overall evaluation of the structure.
- **Critical Feature Inspection—**It denotes critical features, needed for special inspection during monitoring. It includes underwater details, fracture-critical inspection, and other inspections. The code "Y" suggests special attention, while "N" denotes vice versa.
- **Protective System—**It broadly contains information on three categories, surface type, membrane type, and deck protection.

3 Knowledge Graph

The knowledge graph comprises nodes (vertices) and relationships (edges) which helps in linking objects to other objects of the same properties. In this work, we use a graph database *Neo4j* for modeling of our data [17]. The prime work of *Neo4j* is to create a knowledge graph and store it. The whole data was converted from a CSV format to a knowledge graph format. Every individual bridge is a node in the graph and it is connected to other nodes (attributes) by the characterized relationship. A sub-plot of the original graph is presented in Fig. 1. There are three distinct bridges (nodes) that are linked to their attributes likewise, they share some common highlights which can be seen in the diagram. The plot contains 26 nodes in the graph among which there are three bridge nodes and all are associated with distinct relationships. These three bridges have the same culvert condition and consequently, the node is common for all. Additional information about any node can be obtained by tapping on it or by utilizing read clauses.

In Fig. 1, the bridge nodes are represented by their structure number respectively. The relationship between nodes are taken directly from the inventory and abbreviations are used (its details can be found in Table 1). For example, Bridge 1 which contains a structure number as 00000000000S702, Inventory and its details can be obtained from the coding guide.

3.1 Query System (for a Question Answer System)

Knowledge graph stored in *Neo4j* uses various clauses like, *OPTIONAL MATCH* which is used to get all nodes likewise as per their labels or as per their relationships. It returns null as a result of the missing parts of the pattern. For instance, the bridges having a channel condition of 6 can be obtained as the first and third bridge according to the NBI data. Similarly, a specific property can be searched and the respective nodes are described or, counting of the number of rows, and also counting the group of relationship types can be accomplished by *WHERE* and *COUNT* clause respectively. This also shows the capability of the knowledge graph to fill in as a question–answer framework.

Likewise, the nodes obtained by use of *OPTIONAL MATCH* or *WHERE* or *COUNT* based upon certain properties or labels can be then used to find clusters of other bridges which are similar in features/properties. For example, if *B24, B56, B44, B100 have* a common property which needs attention. But this way of figuring out bridge clusters is quite complicated and needs high human interference or attention (as it needs to figure out commonalities between bridges manually).

4 Node Embedding Using Deepwalk

Once the data is modeled as a graph, Deepwalk does a set of random walks starting from different bridge nodes to capture the relationship that each bridge node has with its adjoining nodes. Each walk returns a sequence of a specific length. The length of the random walk decides the number of times the process is repeated. Then a network (as per *skip-gram* algorithm [18]) is trained to learn the relationships each node has with its adjoining node. It's one form of self-supervised learning wherein modeling of a bridge node as a vector representation in terms of the relationships it has with adjoining nodes is done. The whole graph is converted into a corpus with every self-explanatory random walk sequence and the context defines it nearby. For example, bridge *B10* is facing a critical deck condition, and Bridge *B23* also faces the same, Deepwalk will transform node *B10* and node *B23* to close or near-by vector space. Similarly, if node *B210* and node *B4* also have similar issues then the closeness of node *B210* and node *B4* increases in vector space. Word2vec (which uses the skip-gram approach) works on neural networks and converts word embeddings

Table 1. Abbreviation

Symbol	Definitions
AGE	Year Built
CC	Channel Condition
ADT	ADT
CLC	Culvert Condition
SBC	Substructure Condition
DC	Deck Condition
STRK	Structure Kind
SPC	Superstructure Condition
STRE	Structural Evaluation
DL	Design Load

(random walk sequences in our case) to vectors. These vectors are represented in a n-dimensional space and are not spread aimlessly. Each vector is positioned according to some properties.

The word2vec understands the meaning of the whole system by replacing random words in a context and thus learning to create a difference between real phrase and corrupted phrase likewise, adjusting its weights. The vector space is created by a set of random walks and learning the context by understanding the meaning of the words used to create relationships. For example, Bridge *B1* and *B6* have the same substructure and superstructure ratings but little different deck ratings, those bridges are close to each other in terms of condition ratings.

To classify the most preferable node to be the neighbor for the current node, Word2vec takes the whole problem as a classification problem. It feeds the input sequence in a single layer neural network and the output contains a greater context word (softmax). The entire method is called *skip-gram* [18]. It maximizes the probability of the occurrence of the neighboring vector, thus creating a map for the whole context.

4.1 Streaming Advantages with Deepwalk

When the complete graph is absent or the knowledge is deficient, the model is updated by walks of smaller lengths being passed to the learning code skip-gram. The learning rate needs to be initialized to a lesser constant value because the original learning rate is impossible when data is sparse. By doing this, the system takes more time to understand but gives results which are important for analysis.

The general question being answered in the literature with such complex data analysis algorithms is regarding similar bridges. The algorithms presented in [7] provide results but need to be trained every time the new data comes in. A large number of queries (What, if) can be fired in the proposed system which can be answered in a fraction of second with a knowledge graph approach.

The flowchart representing the whole methodology of the proposed work is shown in Fig. 2. Every time the user doesn't need to execute commands in *Neo4j* to transform

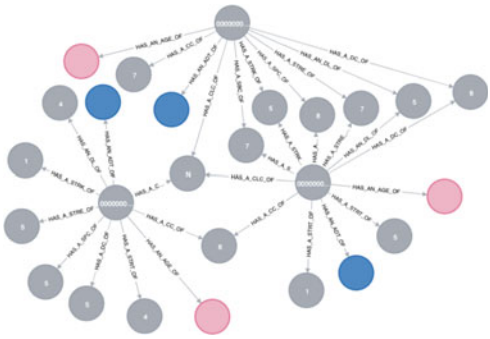

Fig. 1 Knowledge with 3 bridges

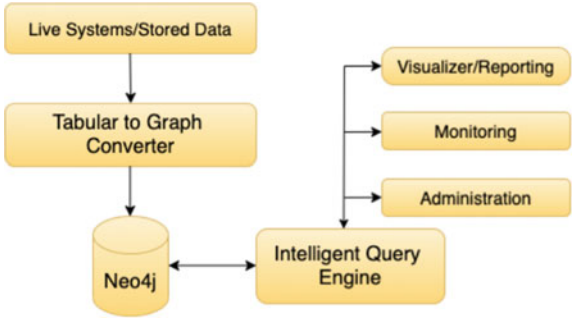

Fig. 2 Procedure of proposed system

the bridge data or data in tabular form to a knowledge graph. It can be done when the data is passed on to a python script—Tabular to Graph Converter (this script also exposes a set of REST endpoints to be consumed by IoT devices or sensor gateways) where certain libraries are referred, to convert new data from tabular form to graph network. Neo4j then stores the data in a knowledge graph format which is used by machine learning algorithms for clustering. The knowledge graph is then passed to the Query engine (which is again a python script) where a set of random walks is performed to learn vector representations and find the similarity between nodes by using deepwalk. The query engine can also fire queries into *Neo4j* through which read clauses can be passed. The Visualizer/Reporting engine makes API calls to Intelligent Query Engine (IQE) which can return the desired results. The Visualizer can ask for similar bridges around a property, similar properties or even multiple bridge clusters around multiple properties. The IQE always pulls only the required amount of data for processing and not all. This makes it highly scalable. In a nutshell the Visualizer/Reporting tool provides the users an user interface using which the users can execute queries and the IQE in the backend performs all the processing. The last step of the whole monitoring process is not a continuous monitoring plan rather an on demand task. Example of one such exposed API from Visualizer is *get_common_bridges* which takes an array of properties like Channel Condition and outputs common bridges by running Deepwalk. So initially the IQE figures out all the

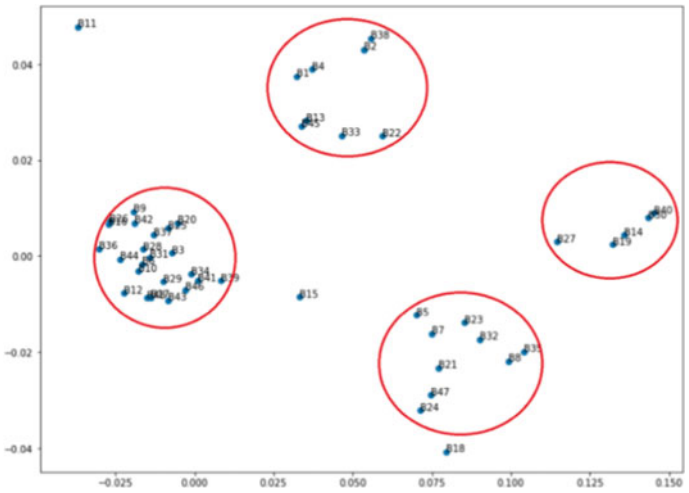

Fig. 3 Cluster formed taking 50 bridges

property nodes and then performs the Deepwalk from any of the bridges connected from the same property node can be obtained.

5 Result Analysis

This section shows the performance of Deepwalk when compared to other clustering algorithms considering the same dataset. A sample of 50 bridges was considered and clusters were formed as shown in Fig. 3. A total of 617,085 can be considered for clustering, but we only consider *50*, making it more readable for the readers. Four clusters of bridges are formed based on the node vectors formed from the computed knowledge graph (NBI Data). *B1* stands for the first bridge, *B2* for the second and so on. It is evident that *B11*, *B15*, and *B18* do not lie in any cluster. When the complete dataset is taken for analysis, there are a small number of bridges that are left out which may be monitored differently. These are also considered noisy inputs.

We use the DBScan Clustering method to get the clusters of similar bridges based on the node vectors. The hyper-parameters of DBscan are taken as, Eps (radius of circle of cluster) to be 0.175 and MinPts (Minimum points in a cluster) to be 15. Unlike k-means, DBScan does not presume any initial number of clusters in the beginning. For training purposes, it does not need labeled data of bridge classes and hence is an unsupervised system. As observed in Fig. 3, the difference between clustering performed by DBScan and clustering by human intervention is almost 0%. We verified the results of DBScan i.e. number of clusters, noisy points, and deviations in clusters from HDBScan also, which showed the same results as DBScan (Concepts: Relational to Graph—Developer Guides). The results obtained as clusters were of

high dimensionality which was converted to two-dimensional space by principal component analysis and is shown in Fig. 3.

Before evaluating Deepwalk, we evaluate DBscan to check the efficiency of the labelled data that we infer to evaluate Deepwalk. We use Density based clustering evaluation (DBCV) which calculates the density inside the clusters and between the clusters. A high value of density inside clusters and low density between clusters indicate good results [16]. The DBCV for 50 bridge data set was found to be 0.97 which indicates excellent clusters and thus the labels are used to evaluate the embeddings of Deepwalk.

The proposed work has been evaluated in terms of efficiency and accuracy. The metrics used are, Micro-F1 and Macro-F1 scores. We extensively use less labeled data to evaluate Deepwalk even when the data is sparse. We have created two groups for training and testing purposes [13]. The average of the total number of observations is taken and used as Macro F1 and Micro F1 scores. The experimental setup for testing of deepwalk using F1 scores includes clustered data (or the labeled data) obtained from DBscan. The complete evaluation becomes a multi-label classification problem by transforming the labels obtained into one vs rest which was carried out in LibLinear [19]. We compare deepwalk with a number of other node embedding algorithms like.

- **Spectral clustering:** It uses graph networks to form embeddings of less dimensions by the use of smallest eigenvectors of the graph Laplacian. It assumes no shapes of clusters and is an iterative process to find local minima. Please refer to [13] for better clarity on its working.
- **Modularity** [12]: This method also forms a representation of the graph network by using values (top) from the modularity matrix or simply from the eigenvectors, which contains features extracted from the graph. It is a comparative system which compares the nodes in a particular cluster with an assumed cluster created in an assumed graph with the same number of nodes. The clusters are thus adjusted and made more precise.
- **Edge cluster** [12]: It is almost similar to Modularity in terms of performance but uses k-means for clustering the adjacency matrix. It also has advantages like scaling data which are difficult for spectral decomposition.

The results are presented in Table 2. We vary our labeled nodes from 10 to 90% and calculate both macro-F1 and micro-F1. The result shows how Deepwalk performs better than Spectral Clustering, Modularity, and Edge cluster in sparse data. It outruns Edge Cluster proving it to be better in terms of scalability. Deepwalk wins in scalability mainly as it runs random walks of shorter lengths from any one of the bridge nodes and does not need the entire graph rather just a very small subset of the original graph where the size of the data to be processed depends on just the length of random walks. We observe that the accuracy is sensitive to the random walk length (as shown in Fig. 4). If the length is very short, the accuracy is low, as it seems like node embeddings are not able to capture sufficient features. Whereas, a high random walk length seems some fair with accuracy but needs more graph nodes (or data) for node embeddings. In Table 2, the evaluation was done with random walk length set to 6. The deepwalk algorithm is an efficient approach as with optimal values of

Table 2 Evaluation scores (micro and macro-F1 scores)

% Label nodes	Deepwalk micro macro	Spectral clustering micro macro	Edge cluster micro macro	Modularity micro macro
10%	38.0 21.0	33.1 23.2	30.0 18.1	29.4 19.3
20%	40.1 25.7	36.9 25.4	32.8 21.1	32.8 22.0
30%	41.2 27.8	39.2 27.2	33.9 22.4	33.9 22.8
40%	42.8 29.3	40.9 28.1	35.0 24.1	35.1 23.8
50%	43.2 30.2	41.8 29.1	36.2 25.1	36.2 24.6
60%	43.7 31.3	42.9 30.4	37.1 25.7	38.2 25.4
70%	43.9 32.0	43.5 30.7	37.1 26.0	38.1 25.8
80%	44.0 33.2	44.2 31.0	37.9 26.8	39.3 26.2
90%	44.0 33.6	44.3 31.4	38.2 27.1	40.2 26.9

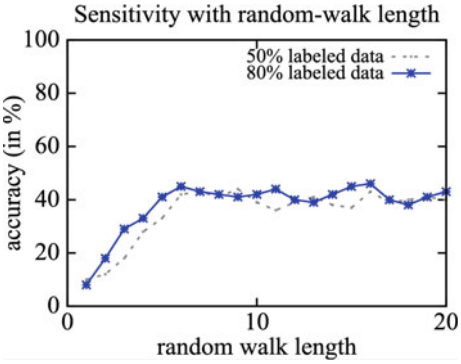

Fig. 4 Accuracy vs random-walk length

random walks it obtains higher accuracy even with very sparse data processing. The graphs presented in Fig. 5, presents throughput of deepwalk clustering and PSO + K-Means methods as presented in [7]. Here the PSO + K-Means method was just given input of 800 bridges (as with complete data the response time was nearly very low). We implement both the approaches on IQE (by exposing consumable APIs) and measure the response time for an hour.

In a nutshell as the tabular bridge data is already modeled as a knowledge graph, Deepwalk takes the advantage of community membership of bridge properties to perform node embedding with sparse data and hence, making it consumable for streaming applications.

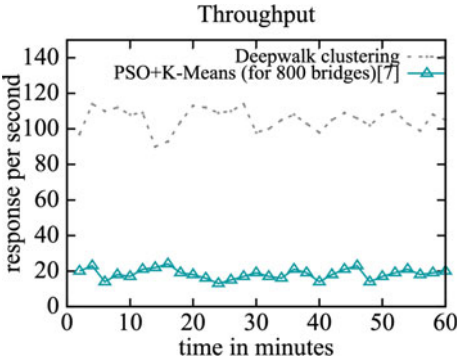

Fig. 5 Throughput comparison graph

6 Conclusion

The work presents a knowledge graph framework for monitoring of bridges, which embeds the graph nodes to latent-vector using Deepwalk. Knowledge graph proves to be more readable than other forms to store data in the inventory. It also marks how Deepwalk is a powerful tool which can be used to form embeddings and then clustering knowledge is easier. The clusters thus formed can be useful for managing similar bridges. The pipeline presented in the work also helps to easily extract node embeddings for bridges even without the need of an entire knowledge graph (hence making it better for streaming applications). It also forms a query system where a large number of queries can be fired and answered with time efficiency. We used DBscan clustering which forms classes based upon node vectors. The results obtained from DBscan are used to create labels or find out similar bridges. The accuracy of the proposed pipeline is measured in terms of Micro-F1 and Macro-F1 scores and compared to existing work in terms of response per second. The respective F1 scores of SpectralClustering, Modularity and EdgeCluster were calculated for comparison purposes and it is observed that Deepwalk outruns all in sparse data.

References

1. Adarkwa O (2015) Tensor factorization in civil infrastructure systems. J Infrastruc Syst 23(3): 04016044-1. American Society of Civil Engineers (ASCE)
2. ASCE (2017) 2017 report card for America's infrastructure, ASCE, Reston. http://www.infrastructurereportcard.org/. Accessed 9 July 2015
3. Bektas BA, Carriquiry A, Smadi O (2013) Using classification trees for predicting national bridge inventory data. J Infrastruc Syst 19(4):425–433. American Society of Civil Engineers (ASCE)
4. Chase S, Small E, Nutakor C (2000) An in-depth analysis of the national bridge inventory database utilizing data mining, In: GIS and advanced statistical methods, 3 March 2015
5. Federal Highway Administration (FHWA) (1995) Recording and coding guide for the structural inventory and appraisal of the nation's bridges. FHWA-PD-96-001. https://www.fhwa.dot.gov/bridge/bripub.cfm

6. FHWA (2019). National Bridge Inventory (NBI). U.S. Dept. of Transportation, FHWA, Washington, DC, https://www.fhwa.dot.gov/bridge/nbi.cfm.
7. Galván-Núñez S, Attoh-Okine N (2016) Hybrid particle swarm optimization and K-means analysis for bridge clustering based on national bridge inventory data. J. Risk Uncertain. Eng. Syst. Part A Civil Eng 3(2):F40160011. ASCE-ASME
8. Jain AK (2010) Data clustering: 50 years beyond k-means. Pattern Recogn Lett **31**(8), 651–666
9. Knight M, Cooil B (2005) Infrastructure investigation using latent class cluster analysis. In: International Conference on Computing in Civil Engineering, vol. 1, pp.1–10. ASCE, Cancun, Mexico
10. Knowledge Graph vs RDBMS. https://neo4j.com/developer/graph-db-vs-rdbms/. [accessed 22–10–2020]
11. Liang Y, Xu F, Zhang S-H, Lai Y-K, Mu T (2018) Knowledge graph construction with structure and parameter learning for indoor scene design. Comput Visual Media 4:123–137
12. Tang L, Liu H (2011) Leveraging social media networks for classification. Data Min Knowl Disc 23(3):447–478
13. Tang L, Liu, H (2009) Relational learning via latent social dimensions. In: Proceedings of the 15th ACM SIGKDD international conference on knowledge discovery and data mining, pp 817–826. KDD, ACM, New York, USA
14. Tang L, Liu H (2009) Scalable learning of collective behavior based on sparse social dimensions. In: Proceedings of the 18th ACM conference on Information and knowledge management, pp 1107–1116. ACM
15. Green MJ (2014) Latent class analysis was accurate but sensitive in data simulations. J Clin Epidemiol 67(10):1157–1162
16. Moulavi DA, Jaskowiak P, Campello R, Zimek A, Joerg S (2014). Density-based clustering validation. In: SIAM International Conference on Data Mining (SDM), Philadelphia, PA
17. Neo4j Server version: 4.1.1 [Computer software]. https://neo4j.com/
18. Perozzi B, Al-Rfou R, Skiena S (2014) DeepWalk: online learning of social representations. In: Proceedings of the ACM SIGKDD international conference on knowledge discovery and data mining, pp 701–710
19. Fan R-E, Chang K-W, Hsieh C-J, Wang X-R, Lin C-J (2008) LIBLINEAR: a library for large linear classification. J Mach Learn Res 9:1871–1874
20. Tsai Y, Yang C (2004) Constrained fuzzy c-mean clustering algorithm for determining bridge let projects. J Comput Civil Eng 18(3):215–225. American Society of Civil Engineers (ASCE)
21. Webb G, Vardanega P, Middleton C (2015) Categories of SHM deployments: technologies and capabilities. J Bridge Eng 20(11):04014118-1. American Society of Civil Engineers (ASCE)

Performance of Safety Netting Under Low Velocity Impact Loading

A. Lloyd and P. Barry

1 Introduction

Safety netting may be employed as a temporary or permanent method of preventing debris from impacting people or other sensitive items in dangerous environments. From a civil engineering perspective, these nets may be used in active construction zones in populated areas [4], mining applications, or as part of protective barriers between roadways and populated areas, among other applications. Debris retention netting is commonly used to restrain falling rock [5, 8], in sporting stadiums [1], and in unique applications like car racing windows [6]. In this paper, nets are tested under impact that may be more easily characterized by falling construction debris, but the safe design principals are constant for all applications: protect life safety by eliminating impacts or reducing impact energy.

The risk to human life safety from impact is complicated by variables including projectile size, hardness, velocity, and where it strikes on the body. However, generally agreed upon critical energy levels are present for low velocity (subsonic) strikes of rigid projectiles. [7] summarized the 80 J rule as simply the kinetic energy threshold where impacts present a high risk of death. More nuanced approaches, such as the Lewis formula, which is also summarized by Valsamos, incorporate more information but lead to similar conclusions. Figure 1 shows the velocity and mass combinations that would result in high probability of human death from both the Lewis formula and the 80 J rule. Overlayed on that figure is the mass and range of velocity used in this study. As can be seen, there are several combinations of mass and velocity

A. Lloyd (✉)
Department of Civil Engineering and Ballistics and Mechanical Test Lab, University of New Brunswick, Fredericton, Canada
e-mail: alan.lloyd@unb.ca

P. Barry
Barry Cordage Ltd., Montreal, Canada

S. Walbridge et al. (eds.), *Proceedings of the Canadian Society of Civil Engineering Annual Conference 2021*, Lecture Notes in Civil Engineering 244,
https://doi.org/10.1007/978-981-19-0656-5_35

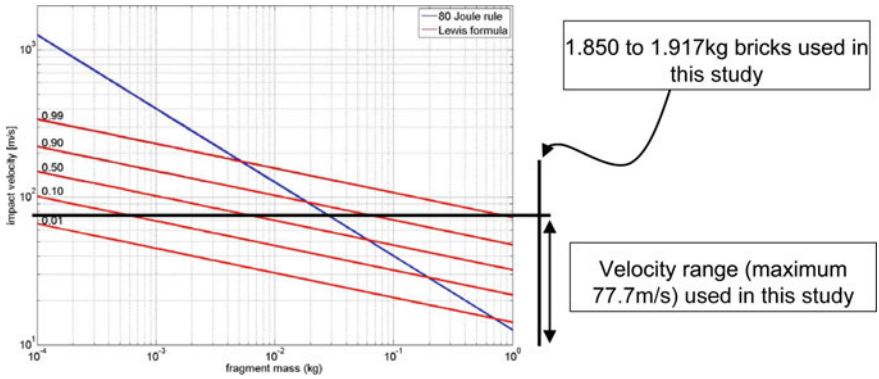

Fig. 1 Human death risk thresholds to impact (adapted from [7])

employed in this study that would be above the 80 J iso-damage line (and those of some of the Lewis curves as well).

This program explores the capacity of different configurations of safety nets under low velocity impacts. The impactor in this study is a common clay brick, often used in residential and commercial construction for facades, infill walls, and load bearing walls. The nets are commercially available heavy duty and light duty safety nets made from nylon and PVC coated polyester fibre.

2 Testing Program

2.1 Ballistics Test Lab

Testing for this project was conducted at the University of New Brunswick's Ballistics and Mechanical (BAM) Test Lab in Fredericton, New Brunswick. This lab is equipped with an array of ballistic launchers including multiple configurations of light gas guns capable of firing projectiles at hyper-velocities up to approximately 8000 m/s and multiple configurations of subsonic, air-driven launchers. This project employed a large bore foreign object debris (FOD) gun shown in Fig. 2 is capable of launching projectiles up to 250 mm in cross-section dimension at velocities up to approximately 300 m/s depending on mass.

This gun operates by charging a pressure reservoir with desired driver pressure using a computer-controlled interface. Once the desired pressure is achieved, an electronic trigger is switched, causing a fast opening butterfly valve to open and release the pressure in the reservoir. This pressure then acts upon the sabot housing the projectile in the breach of the barrel causing it to accelerate down the length of the barrel. Once the sabot reaches the end of the barrel, a stripper mechanism removes

Fig. 2 Large bore FOD gun at UNB BAM Lab

a) Empty sabot

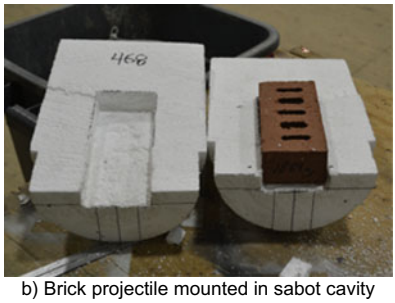

b) Brick projectile mounted in sabot cavity

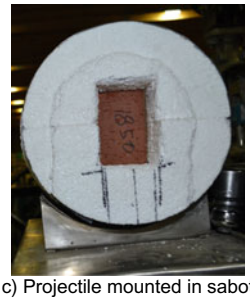

c) Projectile mounted in sabot

d) Loaded sabot mounted in breach

e) Stripped sabot retained in barrel after shot

Fig. 3 Sabot used in FOD gun

the sabot from the projectile allowing the projectile to continue towards the target and retaining the sabot in the barrel of the gun.

For the testing in this project, the sabot was formed by machining a 350 mm long cylinder of expanded polystyrene to the barrel diameter (250 mm). Once the cylinder was made, it was sawed in two equal pieces along the length and a cavity for the projectile was carved out of the foam on each side of the cut. Once the projectile was tightly fit in the cavity (Fig. 3b), the two sides of the sabot were taped together (Fig. 3a) such that the projectile was inset by 50 mm from the end of the sabot foam (Fig. 3c). The sabot used in this project is shown mounted in the breach in Fig. 3d and the stripped sabot after a shot in Fig. 3e. Sabots were consumable and needed to be replaced after each shot.

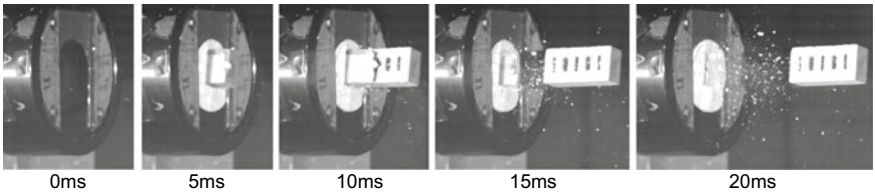

Fig. 4 Brick projectile exiting FOD barrel during test

Fig. 5 High speed camera array

A view of the projectile exiting the barrel is shown in Fig. 4 over a 20 ms period. In this figure, it is evident that the projectile housed by the sabot reaches the end of the barrel where the sabot is stopped by the stripper plate and the projectile slips from the sabot and continues towards the target. Variations in friction and the precision of the sabot cavity to house the brick had slight implications on variability of velocity during testing. All reported velocities in this paper were those recorded during the test.

An array of high-speed cameras were used to monitor these tests as shown in Fig. 5. The cameras included two Photron SA-X cameras that recorded the overall performance of the net from different angles and also were used for motion tracking of the projectile to record impact velocity and impact angle along with exit velocity or rebound velocity if applicable. The SA-X cameras recorded at 3000 frames per second at 1024 by 1024 pixel resolution. An additional high speed (AOS S Motion in Fig. 5) camera recording at 1000 frames per second was used to monitor the projectile exit from the barrel to ensure proper firing of the gun was achieved. All cameras were set to record data on a continuous loop, saving data to an internal camera buffer. Once the gun was triggered, an electrical impulse was sent to the cameras and the data was saved for a period of approximately 7 s. That full video record was reduced to

approximately 1 to 2 s of images that contained the impact and full response of the specimens in post processing.

2.2 Test Specimens

For this program, a total of 12 tests were performed on a total of 8 different netting specimens. Some specimens were tested multiple times if no damage was detected on the first test. Of the 8 different specimens, there were at total of 4 different net materials. Some tests were conducted on single-layered materials, and some were conducted on combinations of materials layered together.

All nets were supplied by Barry Cordage Ltd. of Montreal, Canada. The nets were comprised of either knotless (raschel) nylon or PVC coated polyester netting with different cord diameters, mesh opening sizes and break-strengths. Netting types used in this project are classified as light or heavy duty, or as debris mesh and each serve different industrial applications. The properties of each type of net are provided in Table 1.

Each of the nets used in this project are shown at approximate scale in Fig. 6. The two smaller types of nets used in this project, the nylon FN100-0.5 and PVC-coated polyester fibre BTMLC1, are shown in combination with one of the higher capacity nets (FN700-1.5 or FN700-2.5) as they were tested in a multi-layer configuration.

The nets were connected to a structural steel frame which was then bolted to the laboratory floor. The structural steel frame, shown in Fig. 7, was made from HSS102 $\times$ 102 $\times$ 4.8 steel sections welded together. The frame was built to accommodate the 3.048 m square nets. Gusset plates were added in the corners to accommodate steel shackles used to connect the net to the frame. Additional interior supports at 1/3 span points around the perimeter were included using eyebolts and either cable ties or rigid steel links to connect to the perimeter cable of the net.

The interior connections for all but one of the nets were comprised of doubled up cable ties with specified break strength of 445 N each or an assumed 890 N in pairs. These ties were used to remove the slack in the net while allowing for a progressive

Table 1 Safety net properties [2]

Designation	Material	Cord diameter	Mesh size (mm)	Mesh strength	Type
FN700-2.5	Knotless Nylon	6.35 mm	63.5 $\times$ 63.5	3114 N	Heavy Duty
FN700-1.5	Knotless Nylon	6.35 mm	38.1 $\times$ 38.1	3114 N	Heavy Duty
FN100-0.5	Knotless Nylon	1.59 mm	12.7 $\times$ 12.7	445 N	Light Duty
BTMLC1	PVC-coated polyester fibre	1000 denier	6.35 $\times$ 6.35	32.9 N/mm (warp) 20.0 N/mm (fill)	Debris Mesh

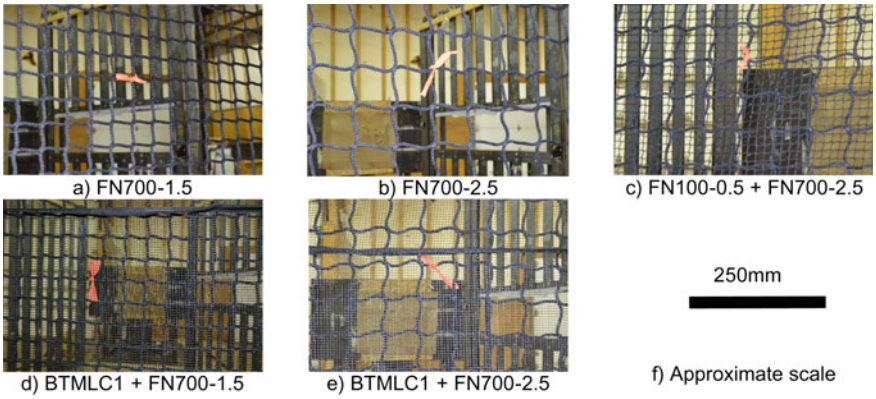

Fig. 6 Different safety nets tested in project

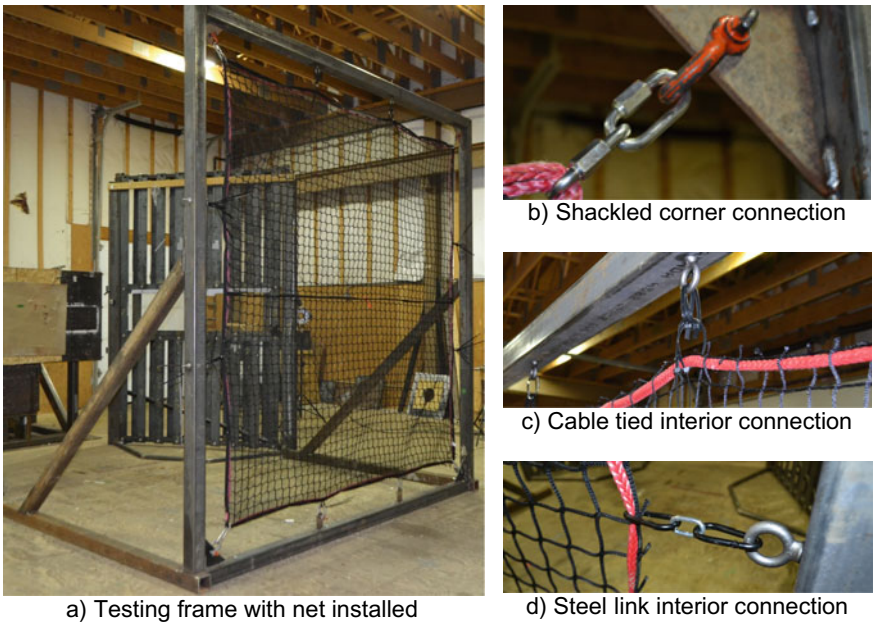

Fig. 7 Steel reaction frame and net-to-frame connections

failure mode with the idea that the ties would break under large impact forces prior to the net allowing the projectile to pass through. The large deformation in those extreme events was determined to be acceptable over failure to prevent pass through of the projectile. One net was connected at interior points with a rigid steel link system and tested to allow for direct comparison of behaviour with the cable tied nets. Figure 7 shows the interior and corner connections used in this test program.

Table 2 Net configurations and impact performance

Test	Configuration	Impact mass (g)	Velocity (m/s)			Energy (J)		
			Impact	Exit	Rebound	Impact	Exit	Rebound
1	FN700-1.5	1853	15.7	-	Low	228	-	-
2	FN700-1.5	1869	14.1	-	Low	186	-	-
3	FN700-1.5	1870	41.7	-	11.5	1626	-	124
4	FN700-2.5	1917	28.2	-	7.3	762	-	51
5	FN700-2.5	1866	25.5	-	Low	607	-	-
6	FN700-2.5	1867	40.1	-	12.5	1501	-	146
7	FN700-1.5	1873	36.6	-	12.7	1254	-	151
8	FN100-0.5 + FN700-2.5	1850	27.4	-	Low	694	-	-
9	FN100-0.5 + FN700-2.5	1875	77.7	72.4	-	5660	4914	-
10	BTMLC1 + FN700-1.5	1870	37.1	-	-	1287	-	-
11	BTMLC1 + FN700-1.5	1867	40.7	-	-	1546	-	-
12	FN700-2.5	1872	39.5	19.1	-	1460	341	-

Table 2 provides information on the nets tested in this project including the test number, the configuration of nets, the impact mass of the brick projectile and the impact velocity. The impact energy is also computed as the kinetic energy of the brick at the time of impact. Additional information on rebound and exit velocity and energy of the projectile is provided in Table 2, these are discussed later in this paper.

Table 2 shows that 4 of the 12 specimens tested had double net configurations (tests 8, 9, 10, and 11). In each of these tests, the lighter net (FN100-0.5 or BTMCL1) was placed on the impact side of the configuration such that the projectile impacted the smaller net first then the higher capacity backing net (FN700-1.5 or FN700-2.5). These nets were installed without any gap between the pairs.

3 Experimental Results

3.1 Single Layer Net Tests

This testing was conducted to try to determine the approximate capacities of the nets for the given brick impactor. Tests 1 to 7 explored the performance of the high capacity nets (FN700-1.5 and FN700-2.5) under various impact conditions. In general, these nets saw no failure up to 41.7 m/s impact velocity and a corresponding impact energy of 1626 J. For the low velocity tests (such as Test 1 and Test 2) typically none or

Fig. 8 Performance differences based on interior support conditions

very few of the interior cable tie supports for the nets failed whereas for the high velocity tests (Tests 3 and 6) all of the interior cable ties failed. Views of these nets at maximum displacement condition are shown in Fig. 8a and b where it is evident that all of the ties did break allowing for more deformation in the net along with the energy absorption and reduction in stiffness that allowed the nets to restrain the projectile completely. Figure 9a and b show the response of the high velocity tests on the FN700-1.5 (Test 3) and FN700-2.5 (Test 6) nets that were supported using cable ties over time.

Test 12 tested the same type of net as Test 6, FN700-2.5, under a similar velocity. However, Test 12 employed rigid steel links supporting the interior of the net rather than the cable ties. This net failed early on in response, approximately 33 ms after the first impact, as the projectile broke the cords in the net and passed through with a significant exit velocity. In this case, the exit velocity was 19.1 m/s with a corresponding 341 J of kinetic energy, well above the critical injury threshold of 80 J. The side view of Test 12 is shown at various times in comparison with other similar nets in Fig. 9c and the net condition at the time of failure is shown in Fig. 8c.

3.2 Rebound Hazard and Multi-layer Configurations

Even if the net does restrain the projectile, one potential hazard is the projectile rebounding backwards at a high enough velocity to become dangerous. Depending on the end use case of safety netting, this may not be a significant design consideration, but if people or items of concern are present on the impacted side of the net, rebound may become a concern. In this testing program, several of the nets had significantly high rebound velocities such that the rebound energy was above the potential critical injury threshold of 80 J. Figure 10 shows the rebound of the projectile from Test 3. In this test, the rebound energy was 124 J, enough to be considered critical if impacting humans, with the velocity of 11.5 m/s. In Fig. 10d the projectile can be

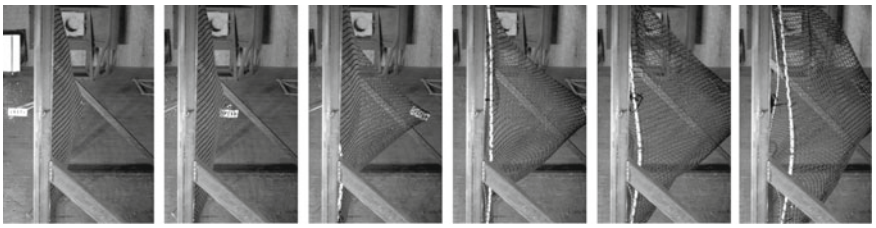

a) Test 3 FN700-1.5 at 41.7m/s (cable tie interior supports)

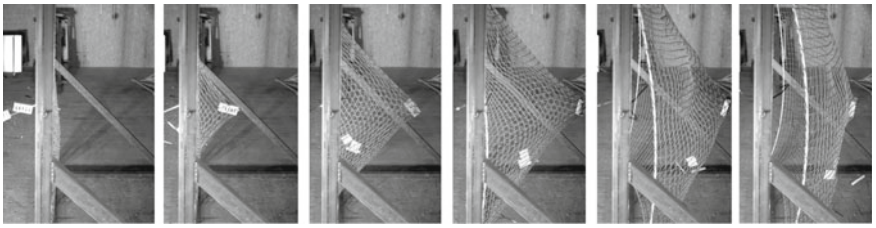

b) Test 6 FN700-2.5 at 40.1m/s (cable tie interior supports)

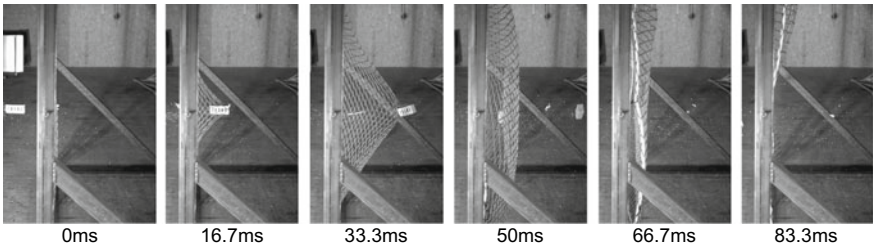

c) Test 12 FN700-2.5 at 39.5m/s (rigid steel link interior supports)

Fig. 9 Response of select nets under high energy impact over time

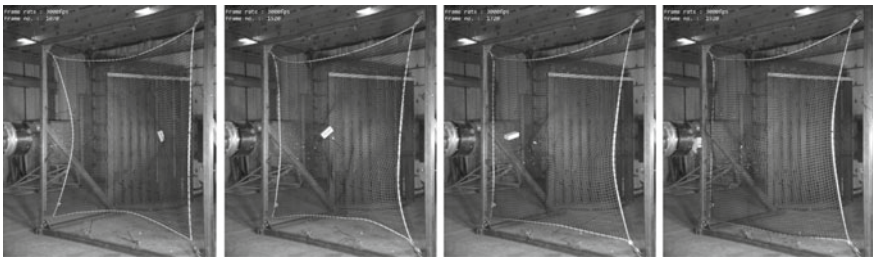

a) Maximum deformation b) 150ms after maximum c) 217ms after maximum d) 283ms after maximum

Fig. 10 Test 3 FN700-1.5 with an impact velocity of 41.7 m/s and a rebound velocity of 11.5 m/s

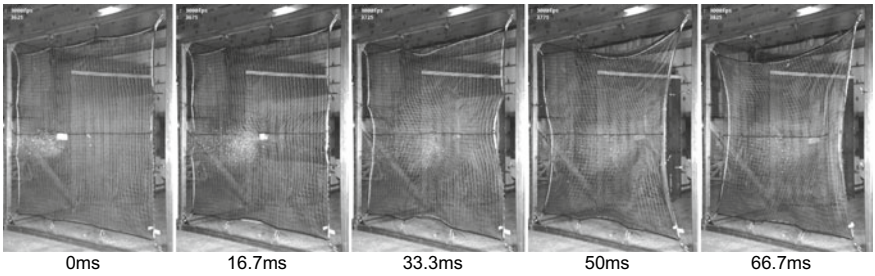

Fig. 11 Brick being retained by combination BTMLC1 and FN700-1.5 net in Test 11 at 40.7 m/s

seen shattering on the barrel of the launcher located approximately 2 m away from the net.

Test on the double layer nets show that prevention of rebound may be achieved by employing the incremental failure of the net pairs such that the projectile may become trapped between layers of the net. Careful design could result in systems that are elastic up to the point where rebound energy becomes critical. At that point, the failure of the first net could be used to entangle the projectile and prevent rebound completely. This was observed in Tests 8, 10, and 11 of this program, with Fig. 11 showing the retention of the projectile in Test 11. Test 9, however, shows that double layer configurations do have limitations as the projectile impact velocity and energy were high enough to break through both layers of the net with an exit velocity of 72.4 m/s, only a slight reduction from the 77.7 m/s impact velocity, and an exit energy well above critical levels at 4914 J.

4 Conclusions

Several different types of safety netting were tested under low velocity impacts representative of falling debris or industrial accidents. Different velocities, boundary conditions, and layup configurations of nets were used in this testing.

The following conclusions may be drawn from the observations made during this experimental program:

- Correctly designed nets may be effective in restraining projectiles.
- The nets tested in this study that were restrained with sacrificial cable ties were able to restrain the brick projectiles up to a velocity of 41.7 m/s without projectile pass through.
- Rebound of projectiles may be of significant energy to present a hazard. This rebound hazard was observed to be present in moderate velocity tests that did not cause significant damage to the nets.
- High enough impact energy and velocity will cause rapid failure of the nets and result in pass through of the projectile with little reduction in velocity and energy.

This was observed in conditions of high impact velocity (Test 9 at 77.7 m/s) and moderate impact velocity with rigid interior supports (Test 12 at 39.5 m/s)

- Light duty netting may be employed effectively in concert with heavy duty net to restrain projectiles from both passing through the net and from rebounding from the net.
- The use of sacrificial interior connections, cable ties in this case, allowed the nets to be securely installed for service conditions and to absorb impact energy during impact events. These sacrificial elements clearly demonstrated their contribution to enhanced impact performance over rigid connections by direct comparison of performance between Test 6 and Test 12.

Further validation of safety nets under different impact conditions including impact velocity, impactor configuration, impact angle, and overall net geometry and materials should be done to fully generalize these conclusions.

Acknowledgements The authors would like to acknowledge Barry Cordage Ltd. for financially supporting this project.

References

1. Bohm H, Schwiewagner C, Senner V (2007) Simulation of puck flight to determine spectator safety for various ice hockey board heights. Sports Eng 10:75–86
2. Collections (2021) Barry Cordage Ltd. https://www.barry.ca/collections/. Accessed 4 Mar 2021
3. Debek C, Wasileqicz A, Czyz T (2017) Investigation and FEM analysis of mineshaft rope safety platforms in underground mining. J South Afr Inst Min Metall 117:373–380
4. Krishnamurthy N (2013) Safety during steel erection. In: The Pacific Structural Steel Conference PSSC, Singapore
5. Nicot F, Cambou B, Mazzoleni G (2001) Design of rockfall restraining nets from a discrete element modelling. Rock Mech Rock Eng 34(2):99–118
6. Patalak J, Gideon T, Krueger D (2014) Design development and testing of an improved stock car driver's window net mounting system. SAE Int J Transp Saf 2(1):165–181
7. Valsamos G, Casadei F, Larcher M, Solomos G (2015) Implementation of flying debris fatal risk calculation in EUROPLEXUS. Institute for the Protection and Security of the Citizen. Joint Research Centre of the European Commission, Luxembourg
8. Yang J, Chen Y, Xhang Z, Luo R (2018) Falling weight impact test of a new-type flexible rock-shed. Eng Rev 38(20):242–252

Experimental Testing of the Shear Strength of CLT-Concrete Composite Sections Utilizing Adhesive for Shear Connections

Osama Sam Salem, Xi Chen, and Sherine Ali

1 Introduction

Cross-laminated timber (CLT) is a mass timber product that is manufactured using wood laminations arranged in alternating perpendicular layers with the top and bottom layers oriented in the direction of the major strength axis. CLT panels can be prefabricated to lengths that can reach approximately 20 m and width of approximately 3 m. The recent changes in the National Building Code of Canada (NBCC 2020) along with the recent amendments in several provincial building codes have resulted in a persistent surge in the application of mass timber structural elements, such as glued-laminated timber (glulam), cross-laminated timber (CLT) and nailed-laminated timber (NLT) panels, and others.

Floor systems in such buildings can even be made stronger and span longer distances by adding a top layer of concrete, which can allow the development of Timber-Concrete Composite (TCC) floor systems. In such floor composite systems, the advantageous mechanical properties of both materials (timber and concrete) are efficiently utilized and thus, several advantages can be achieved for a more robust floor system, if compared to timber floors such as those made solely of cross-laminated timber (CLT) panels. Among the several advantages of utilizing TCC floor systems are greater strength, durability, and better acoustics and vibration performance characteristics [13]. However, to exploit TCC floor systems, the connection between the two materials shall be rigid enough to ensure an effective composite action. Nevertheless, in many applications it is difficult to achieve such composite action as it can be impaired by the deformability of the shear connectors utilized in

O. S. Salem (✉) · X. Chen
Department of Civil Engineering, Lakehead University, Thunder Bay, ON, Canada
e-mail: sam.salem@lakeheadu.ca

S. Ali
Hatch Ltd., Mississauga, ON, Canada

S. Walbridge et al. (eds.), *Proceedings of the Canadian Society of Civil Engineering Annual Conference 2021*, Lecture Notes in Civil Engineering 244,
https://doi.org/10.1007/978-981-19-0656-5_36

the TCC system. In such systems, the two components (timber section and concrete layer) are working integrally with the use of various shear connections which can be achieved using either discrete or continuous shear connectors that are located where the maximum shear forces are expected.

The composite action and behaviour of such TCC systems is defined mainly by the rigidity of the shear connections between the two materials. The primary technique for shear connections in TCC systems is a wide variety of metal connectors [6], grooved connections [7], or adhesive connections [8]. Both short- and long-term tests have shown that adhesive shear connections can achieve greater flexure strength and stiffness than those obtained in shear connections that mainly rely on mechanical fasteners or in grooved connections [13]. Usually, TCC floor systems with adhesive connections can be produced in two ways: cured concrete slabs can be glued to mass timber panels and then shipped to construction sites, or more advantageously a wet-on-wet process can be followed. In this wet-on-wet process, it is required that the adhesive agent to be applied on top of the timber section and then fresh concrete to be poured on top of it before the adhesive has set [12]. A great advantage of this process is that it can offer a practical and efficient solution to retrofitting older buildings with deteriorated timber floor systems to increase the overall performance of the structure. In addition, the wet-on-wet method has other advantages such as the removal of steel reinforcement and concrete formworks required in traditional construction practice, as well as the enhanced flexure strength with the activation of the composite action of TCC system in a more efficient approach.

In a study conducted by [3], the use of wet-on-wet method to develop TCC sections was introduced. Fresh concrete was poured onto epoxy-based adhesive while the adhesive was still unhardened. In a study by [10] experimental tests on 6-m long TCC beam-type floor systems that utilized eight different shear connector types were performed. A numerical study of a single connector to verify the impact of the shear connection on the mechanical properties and behaviour of the TCC section was also conducted as part of the later study. In the said study, 2-mm thick steel sheets epoxy-glued to timber beams were utilized to develop the shear connections required for the composite section. The employed steel sheets allowed linear response throughout the test, nearly up to failure. Test results show that the flexure strength of that TCC beam-type floor system has approximately 2.5 folds the flexure strength of similar floor system but without the composite action between the concrete slab and timber beam, which was provided due to the use of the epoxy-glued steel sheets (approximately 90% of full composite action). Bathon and Graf [2] introduced a TCC system in which a steel mesh inserted and glued into a longitudinal slot made on the top side of a timber beam. A concrete slab was then cast on top of the beam with the extended portion of the steel mesh embedded in the concrete. Test results show that the shear connections developed in the described composite system was rigid enough to achieve the required flexure strength yet offered reasonable degree of ductility compared to TCC sections that employed other types of shear connections.

In the study presented in this paper, the shear characteristics of CLT-Concrete composite sections that utilized adhesive for shear connections have been experimentally investigated. The wet-on-wet method using an industrial adhesive was applied

Table 1 Mechanical properties of CLT panels (adopted from Nordic Structures 2019)

Property	Allowable strength (MPa)
Comp. parallel to grain	19.3
Comp. perp. to grain	5.3
Tension parallel to grain	15.4
Modulus of elasticity	11,700
Shear Modulus	731.25

to fabricate four identical TCC sections, each with 600 × 1000 mm shear interface between the CLT panel and concrete layer. Test specimens were experimentally examined under direct shear forces until failure.

2 Experimental Program

The shear characteristics of CLT-Concrete composite sections that utilized a commercially available industrial adhesive for shear connections have been investigated throughout the experimental study presented in this paper. A total of four identical composite sections, each with 600 × 1000 mm shear interface between the CLT panel and the concrete layer, were experimentally examined under direct shear forces until failure. Two composite sections were tested at concrete age of 14 days, while the other two duplicated sections were tested at 28-day concrete age.

2.1 Materials

2.1.1 CLT Panels

The 3-ply CLT panels utilized in the composite sections tested in this study were 600 mm wide × 1200 mm long. The external laminations were oriented in the longitudinal direction of the test specimen and the applied load. The CLT panels were all made of spruce-pin-fir (S-P-F) planks. The principle mechanical design properties of the CLT panels in the longitudinal direction as provided by the supplier [9] are listed in Table 1 below.

2.1.2 Concrete

The targeted compressive strength of the concrete required for the 50-mm thick concrete layer of the composite sections was 30 MPa. Accordingly, a concrete mix that is composed of 150 kg (40%) fine aggregate; 150 kg (40%) coarse aggregate; 45 kg (12%) cement; and 30 kg (8%) water was prepared to cover the amount of

concrete required for the four test specimens (total concrete volume of 0.144 m^3). Total of six cylinders were prepared from the concrete mix to determine the actual compressive strength of concrete after 14 days (3 cylinders) and 28 days (3 cylinders) from the concrete casting time.

2.1.3 Adhesive

The commercially available adhesive Sikadur-35 Hi-Mod LV was used to develop the shear connections in the four CLT-Concrete composite sections experimentally tested in this study. The said adhesive is a two-component, 100% solid, moisture-tolerant, low-viscosity, high-strength, multipurpose, epoxy resin adhesive. Herein, this type of adhesive can be used for "can't dry" surfaces. From Sika official product data sheet [11], at temperature of 23 °C and after 28 days curing time, the compressive strength of this adhesive can reach 13,000 psi (89.7 MPa).

2.2 Fabrication Process and Test Assemblies Details

After cutting each CLT panel to its final dimensions (600 × 1200 mm), cut-off strips of plywood were attached to the CLT panel to build a formwork that was used to allow casting the 50-mm thick concrete layer of the composite section. The formwork was designed to allow a CLT-Concrete interface area of 600 mm wide × 1000 mm long with a 200-mm overhang in each of the concrete layer and the CLT panel with respect to each other at the two opposite ends in the longitudinal direction of the composite section, as shown in Fig. 1. The development of the said overhangs was mainly to allow the load application solely on the top end of the CLT panel while the entire composite section is supported solely on the bottom end of the concrete layer (see Sect. 2.3 for test setup details).

Before pouring the concrete, the prepared CLT panels were laid down and leveled on the floor. Following the adhesive application instructions provided in [11], the two components of the adhesive were mixed in the ratio of 1-part component 'B' to 2 parts component 'A' by volume in a clean pail. The two components were mixed thoroughly for at least 3 min with a paddle attached to an electrical drill on a speed of (400–600 rpm) until uniformly blended. The prepared adhesive was then poured on the CLT panel top surface and smeared evenly, as shown in Fig. 2. This step was carried out simultaneously with mixing the concrete in order for the adhesive not to set hard before pouring the concrete on top of it.

Concrete was then evenly spread over the CLT panel, along the edges and in the formwork corners. After the poured concrete reached slightly higher level than the top edges of the formwork, the concrete surface was levelled and flushed with the top edges of the formwork using a float to ensure the 50 mm thickness required for the concrete layer. To maintain the temperature and dampness for proper curing, the

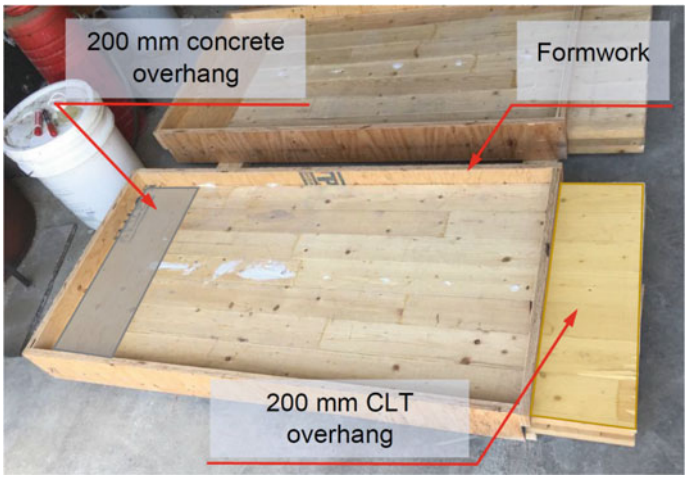

Fig. 1 A CLT panel with concrete formwork installed to allow concrete casting

Fig. 2 The mixed adhesive being smeared evenly on top of the prepared CLT panel

poured concrete layers were watered and covered with polyethylene sheeting for the first seven days of the concrete age.

2.3 Test Setup and Procedure

To allow the load application solely on the top end of the CLT panel while the entire composite section is supported solely on the bottom end of the concrete layer, as well as to restrain the test specimen against any lateral or transversal displacement, a strong steel supporting rig was designed and fabricated. The supporting rig was then placed within the Universal Testing Machine (UTM) accommodated in the Civil Engineering's Structures Laboratory at Lakehead University. After the top end of the CLT panel of the test specimen was centered under the upper crosshead of the UTM in both the lateral and transversal directions, displacement transducers were installed on the specimen. Two linear variable differential transformers (LVDTs) were attached to the left- and right-side edges of the CLT panel (namely LVDT-1 and LVDT-2) with their rods were bearing against little steel brackets that were glued to the left- and right-side edges of the concrete layer, respectively. The two LVDTs were utilized to continuously measure the relative slips between the CLT and concrete layer near the left- and right-side edges of the test specimen during loading. Figure 3 illustrates the test setup for a general test specimen placed within the UTM with both LVDTs installed. After the initial readings of the installed LVDTS were checked, the load was applied gradually at a rate of 8.0 kN per minute. The relatively slow rate of loading was deliberately chosen to avoid unnecessary premature cracks in the concrete that would have developed due to faster application of the load. Also, force-controlled loading (kN/min) instead of displacement-controlled loading (mm/min) was deliberately selected due to the same preventative measure for not loading the test specimens too quickly.

3 Results and Discussion

3.1 Concrete Cylinder Tests

To verify the targeted compressive strength for the concrete mix, which is 30 MPa, cylinders with 14- and 28-day concrete age were tested for their actual compressive strength using the same UTM. The compressive strength tests were performed according to ASTM C39/C39M-20 standard [1] for concrete cylinder tests. The average compressive strength attained by the three cylinders with the 14-day concrete age was 23.6 MPa, while the average strength attained by the other three cylinders with the 28-day concrete age was 30.2 MPa. All concrete cylinders exhibited cone failure.

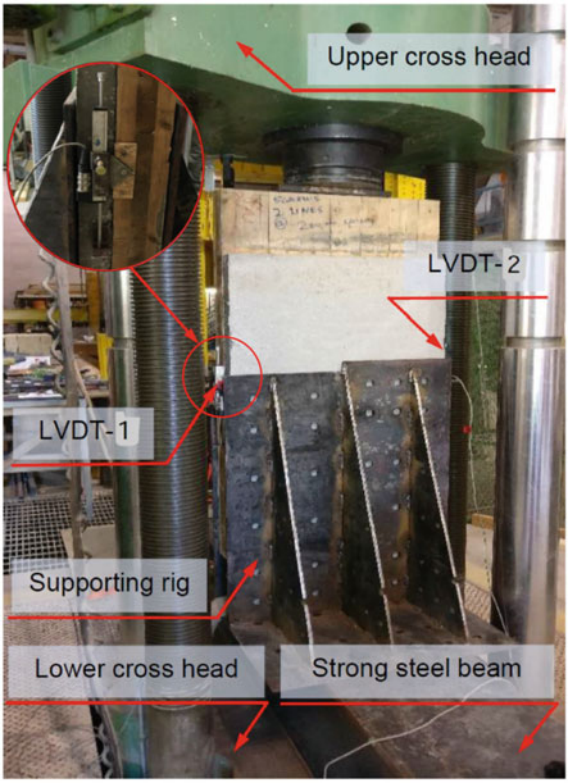

Fig. 3 Test setup for a general test specimen with instrumentation installed

3.2 CLT-Concrete Composite Section Shear Tests

Figure 4 shows the load-slip relationships developed using the measurements of the installed LVDTs against the loads applied by the UTM for one of the CLT-Concrete composite sections of 28-day concrete age, since all four specimens performed in very similar trend under the applied loads. As shown in Fig. 4, the maximum slip occurred at the interface between the CLT panel and concrete layer was recorded at only 0.04 mm, which is utterly negligible. Regardless of the different concrete age (two sections of 14-day and two sections of 28-day concrete age), there was no difference observed in terms of the load-slip behaviour between the four CLT-Concrete composite sections tested in this study.

The maximum load attained by the four composite sections exceeded 530 kN when the tests had to be terminated after the CLT panel started to crush under the heavy load applied. Figure 5 shows the relationship between the penetration values of the loading steel plate into the top edge of the CLT panel and the applied load for one of the CLT-Concrete composite sections of 28-day concrete age. The values of the penetration into the CLT panel increased in a relatively linear trend with the increase of the applied load, as shown in Fig. 5. The maximum penetration value was

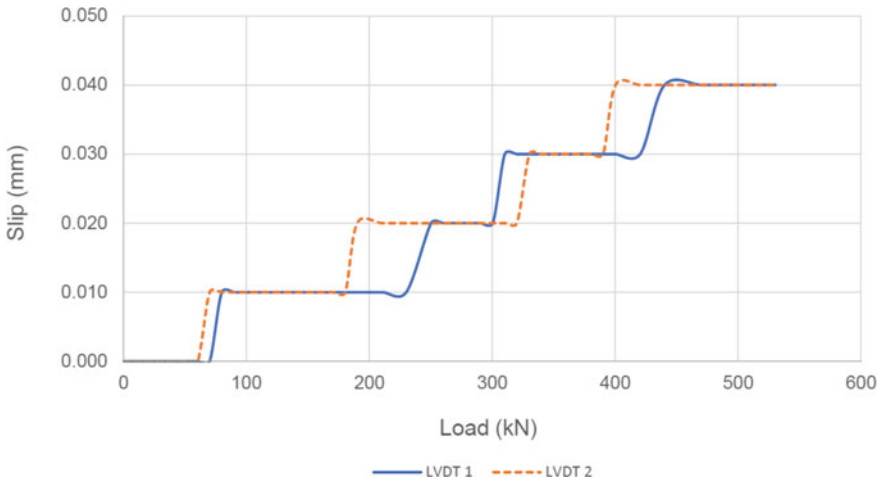

Fig. 4 Load-slip relationships for a CLT-concrete composite section of 28-day concrete age

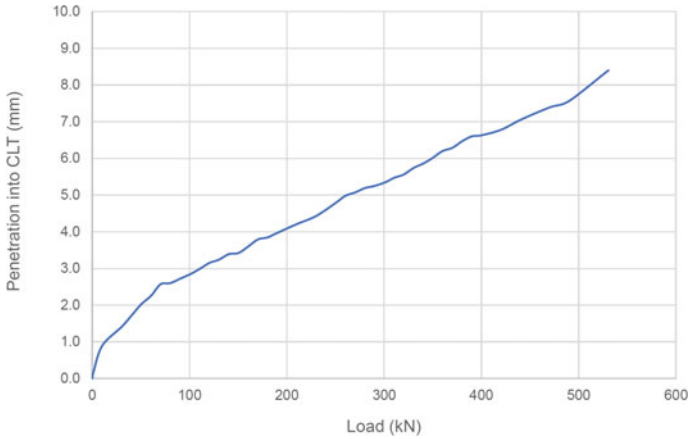

Fig. 5 Load-penetration relationship for a CLT-concrete composite section of 28-day concrete age

recorded at slightly more than 8 mm when a maximum load of 530 kN was attained by the composite section.

3.3 Failure Modes

Essentially, all four CLT-Concrete composite sections did not fail with the reach of a maximum load of 530 kN; however, the shear tests had to be terminated after the top edge of the CLT panel started to crush under the heavy load applied, Fig. 6(a).

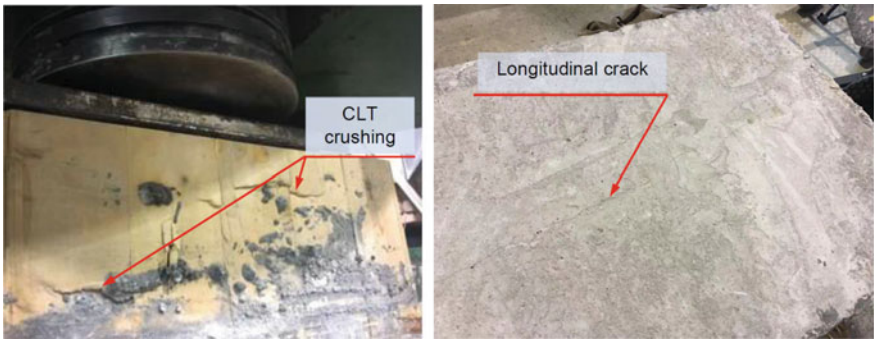

Fig. 6 Failures observed in the CLT-concrete composite sections, **a** CLT top edge crushing; **b** longitudinal crack observed in the concrete layer

Only the composite sections of 14-day concrete age exhibited the development of longitudinal crack in the concrete layer late in the tests at very high loads, Fig. 6(b).

4 Conclusions and Recommendations

Based on the results obtained from this experimental study on the shear strength of CLT-Concrete composite sections that utilized adhesive for shear connections, the following conclusions can be drawn.

- All four specimens performed in very similar manner under the applied loads since the maximum slip occurred at the interface between the CLT panel and concrete layer was recorded at only 0.04 mm, which is utterly negligible.
- Regardless of the different concrete age (two sections of 14-day and two sections of 28-day concrete age), there was no difference observed in terms of the load-slip behaviour between the four CLT-Concrete composite sections tested in this study.
- The maximum load attained by the four composite sections exceeded 530 kN when the tests had to be terminated after the CLT panel started to crush under the heavy load applied.
- The maximum value of penetration into the CLT panel was recorded at slightly more than 8 mm when a maximum load of 530 kN was attained by the composite sections.
- It is recommended to use adhesive to develop completely rigid shear connections since the outcomes of this study confirmed the assumption of the rigid connection between the CLT panel and concrete layer in such TCC glued sections, as all four specimens were able to attain more than 530 kN load without any shear interface failure observed.

Acknowledgements This research project was funded in part using the NSERC-Discovery Grant and the Mass Timber Institute Research Grant awarded to the first author. The authors would like to thank lab technologists C. Hubbard and R. Timoon, and graduate student V. Virdi for their assistance in the Civil Engineering's Structures Laboratory at Lakehead University.

References

1. ASTM (2020) ASTM C39/C39M-20, Standard test method for compressive strength of cylindrical concrete specimens, ASTM International, West Conshohocken, PA
2. Bathon L, Graf M (2000) A continuous wood-concrete-composite system. In: Proceedings of the 6th world conference on timber engineering, July 31–Aug 3. British Columbia, Canada
3. Brunner M, Romer M, Schnüriger M (2007) Timber-concrete-composite with an adhesive connector (wet on wet process). Mater Struct 40(1):119–126
4. Canadian Commission on Building and Fire Codes (2020) National building code of Canada, National Research Council of Canada, Ottawa
5. Canadian Standards Association (2014) CSA O86-14, Engineering design in wood, Mississauga
6. Kanócz J, Bajzecerová V, Šteller Š (2013) Timber-concrete composite elements with various composite connections, Part 1: screwed connection. Wood Res 58(4):555–570
7. Kanócz J, Bajzecerová V, Šteller Š (2014) Timber-concrete composite elements with various composite connections, Part 2: grooved connection. Wood Res 59(3):627–638
8. Kanócz J, Bajzecerová V, Šteller Š (2015) Timber-concrete composite elements with various composite connections, Part 3: adhesive connection. Wood Res 60(6):939–952
9. Nordic Structures. Design properties of Nordic lam. In Technical Note S01. Nordic Structures, Canada, 2019.
10. Piazza M, Ballerini M (2000) Experimental and numerical results on timber-concrete composite floors with different connection systems. In: Proceedings of the 6th World Conference on Timber Engineering, July 31–August 3, British Columbia, Canada
11. Sika Canada Inc. (2017) Product data sheet: Sikadur-35 Hi-Mod LV. Point-Claire, QC, Canada
12. Tannert T, Endacott B, Brunner M, Vallée T (2017) Long-term performance of adhesively bonded timber-concrete composites. Int J Adhes Adhes 72:51–61
13. Tannert T, Gerber A, Vallee T (2019). Hybrid adhesively bonded timber-concrete-composite floors. Int J Adhes Adhes 97:102490.

Vibration Testing of Truss Members Consisting of Multiple Eyebars for Estimating Axial Load Distribution

M-A. Chainey and M. Chaaraoui

1 Introduction

Tension members with multiple eyebars (members) are generally designed to share the applied load uniformly between individual eyebars (elements). However, deterioration due to multiple factors such as wear and tear, damage, corrosion and geometric variation due to construction tolerances can lead to uneven load sharing of tensile forces among elements of a member. Considering eyebar elements of equal cross section, length, and restraint conditions, eyebar elements with lower tensile forces include a lower natural vibrating frequency compared to eyebar elements with higher tensile forces.

Load sharing behaviour of multiple eyebar members is of interest in the evaluation of truss bridges for multiple reasons including:

- Accurate determination of stress levels in the individual eyebars for refined analysis including fatigue stress cycles;
- Assessment of the bending or shear stresses in the pin of the affected truss node due to the load sharing behaviour of eye bar members;
- Designation of eye bars as being subject to sudden loss of capacity with little or no warning by the Canadian Highway Bridge Design Code (CHBDC) (CL 14.12.3.(a) - CAN/CSA S6-19) [4].

A novel eyebar vibration testing method using a smart phone and a 3D printed case was developed to evaluate axial load distribution between separate eyebars of a member. Seventeen (17) eyebar members of a large true-pin cantilevered steel

M.-A. Chainey (✉) · M. Chaaraoui
Dillon Consulting Limited., Ottawa, Canada
e-mail: mchainey@dillon.ca

M. Chaaraoui
e-mail: mchaaraoui@dillon.ca

S. Walbridge et al. (eds.), *Proceedings of the Canadian Society of Civil Engineering Annual Conference 2021*, Lecture Notes in Civil Engineering 244,
https://doi.org/10.1007/978-981-19-0656-5_37

truss bridge were selected for testing to provide a representative sample of eyebar element behaviour, and to assess instances of suspected non-uniform loading between elements.

1.1 Background

The CHBDC Code and Commentary do not provide specific guidance with respect to load distribution assumptions for eyebar members. Previous studies on the topic have suggested that only one eyebar element be utilized in calculating the capacity of members consisting of only two elements [2]. This approach may be appropriate for structures with significant non-uniform element loading, but may be overly conservative for structures with only modest non-uniformity in eyebar element load distribution.

Following a first principles approach derived by Timoshenko et al. [1], the Manual for Railway Engineering (MRE) [5] provides a procedure to estimate the dead load stress in each element of an eye bar member by correlating force to the natural vibrating frequency. The MRE approach determines of the natural vibrating frequency by visually observing a number of cycles within a time period following a forced excitation of the element. An additional study by Mazurek included eyebar vibration testing in the lab and field utilizing accelerometers and data loggers rather than the visual observation method proposed in the MRE. Mazurek found that estimation of dead load stress in an eyebar is dependent on its end fixity, and that the estimated stresses utilizing the MRE procedure is only accurate if an equivalent fixed length is considered. While the magnitude of the estimated stresses were highly dependent on fixity, Mazurek determined that the load sharing variation between members can be calculated accurately based on the variation in frequencies between bars and suggested that vibration testing is a suitable technique for estimating load sharing effects [3].

2 Methods

The methodology for determining the load sharing distribution between eyebars is based on first principles and is directly correlated with the natural frequency of an eyebar in tension. The methods and techniques utilized in this study were based on an established procedure as described in MRE and as studied by Mazurek.

2.1 Structure and Member Selection

Eyebar vibration testing was conducted on a large true-pin steel truss bridge containing eyebar tension members in Ontario in the Fall of 2020. The eyebar vibration testing was selected to facilitate a more accurate structural evaluation of eyebar members accounting for the effects of load sharing between eyebars. The vibration testing and analysis was performed on a total of 17 members selected for vibration testing to cover a wide array of configurations and behaviours. In addition to representative and random selections, members suspected to demonstrate a higher load sharing variation based on field observations were also selected.

2.2 Materials and Methods

Rather than using visual observation to count the oscillations of an eyebar member as described in AREMA or using specialized accelerometer instrumentation, a simplified and easily repeatable procedure for field application was developed without specialized equipment or data loggers. The materials utilized consisted of a smartphone device (Samsung Galaxy s10) with a built in accelerometer (LSM6DSO), a custom plastic 3D-printed phone mounting case, standard C-clamps, and a free data logging phone app (Physics Toolbox). The vibration testing apparatus setup (Fig. 1) had an effective sampling rate of approximately 400 Hz.

The methodology used for conducting vibration testing was as follows:

- The smartphone device was mounted to the first eyebar element of the selected member, and phone application was set to record accelerometer data..

Fig. 1 Vibration testing set-up used for eyebar vibration testing. Smart phone display shows the g-force meter under nominal conditions (no forced excitation)

- The eyebar was manually excited by hand to achieve a sufficient vibration amplitude, and then the subsequent damped free vibration was recorded for a minimum of 25 cycles..
- The process was repeated on all remaining eyebar elements in the member..
- Selected eyebars of the same member were re-tested to ensure the results were consistent and repeatable.
- Acceleration data was exported to a.csv file by the app for data post-processing.

Vibration testing was performed with limited to no live load to assess the dead load distribution between the eyebar elements. Repeat testing of some members was performed on a separate date and the results were found to be congruent.

2.3 Analysis

The measured acceleration data was processed to calculate the natural frequencies of individual eyebars using a peak-picking algorithm to determine the oscillation period (Fig. 2). The processed data was then analysed to determine the variation in load sharing of eyebar elements.

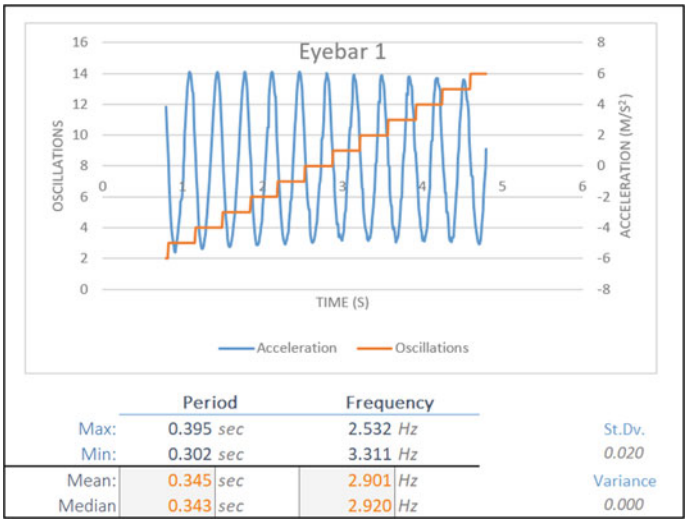

Fig. 2 Example of the processed acceleration data for a single eyebar

3 Results

For the current case study, the results of the analysis confirmed non-uniform load distribution for elements of a member, and the extent of non-uniformity varies from member to member. Compared to the nominal (average) force of an eyebar element in a member, the maximum force of an individual eyebar element was measured to be 0.3 to 37.4% above the nominal element force with a calculated average of 7.8% above the nominal element force. The distribution of results is shown below in Fig. 3.

The eyebar vibration testing methodology provided a rational approach for estimating axial loads in eyebar elements. A normal distribution was used to summarize the test results of the 17 members tested. The normal distribution statistical parameters are provided in Table 1. Based on a review of the data, a reasonable load multiplier was determined for the evaluation of eyebar members on the structure.

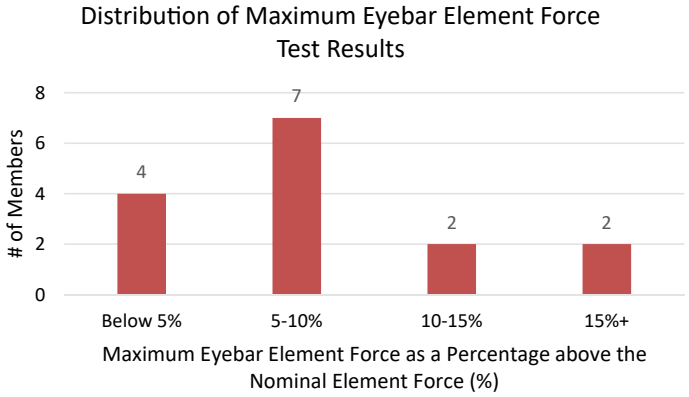

Fig. 3 Summary of test results showing the distribution of calculated maximum eyebar force relative to the nominal eyebar force for a member

Table 1 Eyebar vibration testing distribution results

Parameter	Max / Nominal Force for an individual Eyebar Element
Mean	7.8%
Standard Deviation	5.2%
75th percentile	9.8%
90th percentile	15.5%

4 Discussion

This case study confirmed that the dead load distribution in eyebar elements of tension members on the evaluated bridge are non-uniform. Considering the potential brittle failure mode of eyebars as indicated by the CHBDC, for this case study a 15% increase in eyebar element load above the nominal value was proposed for the evaluation of eyebar members (approximately aligned with the 90th percentile of the measured data sample). A *Load Multiplier* of 1.15 was applied to the nominal force of an individual eyebar to address potential non-uniform load distribution.

In addition to the load sharing behaviour, the eyebar vibration results were used for comparison as follows:

- The expected dead load forces in the eyebar members were determined by a finite element model.
- The relationship between tensile stress and the natural frequency provided in the MRE was utilized to calculate the estimated tensile stress of individual eyebar elements.
- The sum of the estimated forces in the eyebar elements was compared against the expected dead load forces.

The estimated forces in the eyebars did not correlate well with the expected forces produced by the finite element model. Several factors may affect this lack of correlation including assumptions in assumptions in in the modelled behaviour, determining the effective length of the eyebars, deteriorated state (i.e. section loss) of the eyebar elements, thermal stress in the members and nominal transient loading (live and wind) at the time of the vibration monitoring. However, this analysis remains adequate for determining the relative load sharing between eyebar elements as shown by Mazurek.

4.1 Limitations

The findings presented in this case study are based on a small sample size specific to the structure being evaluated. Only 17 data points (members) were available while a minimum of 30 data points is typically recommended for normality. The selection process was naturally skewed towards examples believed to include higher variations based on the observed condition. A larger, more representative sample size may show that a load multiplier of 1.15 corresponds to a higher percentile in the data than presented in this case study for the structure being evaluated.

References

1. Timoshenko SP, Weaver W, Young, D.H (1974) Vibration problems in engineering, 4th edn. Wiley, New York
2. Bakht B, Jaeger LG (1990) Bridge testing—a surprise every time. J Struct Eng 116(5):1370–1383 (1990). https://doi.org/10.1061/(asce)0733-9445(1990)116:5(1370)
3. Mazurek DF (2016) Vibration-based estimation of tension stress in steel eyebars. J Struct Eng 142(12). https://doi.org/10.1061/(asce)st.1943-541x.0001613
4. Canadian Highway Bridge Design Code (2019). CSA Group, Toronto
5. Manual for Railway Engineering (2011) AREMA, Landover

A New Panelized Roof Design Approach for Offsite Fabrication of Light-Frame Wood Residential Construction Projects

Md Saiful Islam, Ying Hei Chui, Mohammed Al-Hussein, and Mohammed Sadiq Altaf

1 Introduction

Off-site construction is a manufacturing process where building components, elements, or modules are pre-assembled in a controlled plant environment and subsequently transported to the construction site for installation [7]. This process reduces project duration, reworks, safety risks, life cycle costs, and adverse environmental effects. At the same time, it improves predictability, productivity, life-cycle performance, sustainability, and profitability [7, 14]. By relocating approximately 80% of the building construction activity from the original location, significant site disruption and vehicular traffic are reduced, which increases overall safety and security from the owner's perspective [12]. Among the several off-site construction approaches, the panelized construction process is popular because of its design flexibility and associated on-site assembly cost-savings. Panelized construction subdivides a building model into subassemblies such as wall panels, floor panels, and volumetric roof elements, that are manufactured in an off-site facility and then shipped to the site for installation

Typically, a light-frame panelized-building production facility encompasses several workstations such as wall framing location, sheathing assembly section, floor production line, and roof assembly section (Fig. 1). The corresponding panel types are fabricated as these workstations/sections capitalizing on building information modelling (BIM) and CNC machines, making the process highly efficient, with minimal waste of material and high productivity. As a result, the panelized construction method is faster and more competent compared to the traditional stick-built

M. S. Islam (✉) · Y. H. Chui · M. Al-Hussein
University of Alberta, Edmonton, Canada
e-mail: mdsaiful@ualberta.ca

M. S. Altaf
ACQBUILT Inc., Edmonton, Canada

S. Walbridge et al. (eds.), *Proceedings of the Canadian Society of Civil Engineering Annual Conference 2021*, Lecture Notes in Civil Engineering 244,
https://doi.org/10.1007/978-981-19-0656-5_38

Fig. 1 Typical factory-based home construction facility: **a** Wall framing station, **b** Floor station, **c** Wall sheathing station, and **d** Roof production station [3]

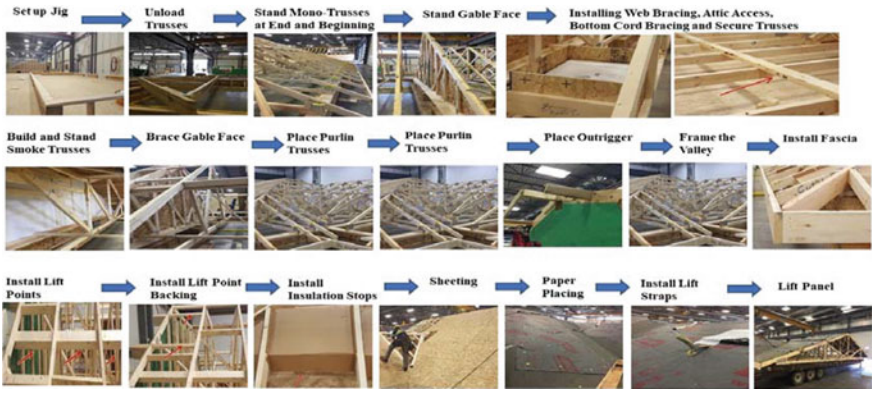

Fig. 2 Work breakdown of current roof module production process [3]

process. However, presently, this light frame offsite home construction method is best described as partially panelized since the roofs can only be prefabricated as a single volumetric module (Fig. 1d) or constructed on-site. In summary, current roof production in panelized construction method has the following 5 key steps and involves 19 manual tasks as illustrated in Fig. 2:

1. The roof trusses are designed and fabricated by a truss fabricator.
2. The roof trusses are shipped to the penalized production facility.
3. Trusses are unloaded and transferred to the designated roof production workspace where they are laid out according to the plan.
4. Wood-based sheathing panels and blocking are attached to the trusses using fasteners to form a roof module.
5. Roof finishing is added to the completed module

Producing roof structures in this manner entails the following deficiencies that can be addressed through innovation:

a) There are some non-value-added activities such as loading and unloading of trusses which lead to a relatively long setup time for the production line assembly

b) The manual (stick-built) approach employed for roof fabrication in current practice results in an imbalance of overall production (i.e., taking into account the effect on production flow at other workstations).
c) Transporting the roof requires a relatively large number of trailers (to be specific four trailers for a 1600 sq ft single-family home), and on-site loading and unloading increases the overall work duration, leading to high transportation cost [3].
d) The site installation process is complex due to the size of the roof modules. In the case of very congested construction sites, it becomes impossible to transport large roof modules; as a consequence the roof must be built entirely at the site (similar to the traditional stick-built process), increasing project cost and duration. Thus, the offsite construction goal is not achieved.
e) Considerable space is occupied in the factory while producing the roof module, again making it difficult to balance wall and floor panel production with roof fabrication for a given number of homes.
f) The additional cost of sub-contracting the roof trusses to the truss manufacturer raises the price of a home package.

A novel type of system that addresses these deficiencies could improve the efficiency of roof manufacturing. This paper discusses a novel approach to the roof design that allows home manufacturers to produce the roof component in-house using their existing production facility and thereby overcome the above-mentioned challenges.

2 Holistic Approach to Roof Prefabrication

In the conventional approach to the construction of residential low-rise buildings in Canada, the roof is built using closely spaced wood trusses that support sheathing and roofing materials (on the upper-chord) and ceiling materials (on the lower-chord). These trusses are arranged at a spacing of 610 mm or less. Lateral bracing of such a wood roof truss system is provided by wood-based sheathing panels, thereby achieving an extremely efficient structural system. However, as mentioned above, this truss-based structural design fails to accommodate the panelized construction constraints that exist in the production lines of panelized-home manufacturers.

A novel structural design is thus proposed that satisfies industry requirements while using existing panelized production lines to produce roof panels that can be assembled on-site with minimal effort. This approach will allow prefabricated home builder to move from partial towards full panelized manufacturing. To increase the productivity of the roof production process, panel dimensions and other roof components must accommodate the following limitations of the framing stations [3]:

a) The maximum allowable height of a framing module is 3,200 mm (10 ft) if it is produced at a wall framing station and 12,200 mm (40 ft) for the floor production line

b) The minimum permissible height of a framing module is 1,600 mm (5 ft) if it is built at the wall framing station
c) The maximum length allowed for a framing module is 12,200 mm (40 ft) in the wall production line whereas for the floor production line it is 3,200 mm
d) The Stud direction for the panel should be parallel to the short direction of the component if it is fabricated at the wall framing station
e) The roof design should minimize the crane lifting sequence on-site

In devising this holistic approach, we first analyze a case architectural 3D model and then subdivide the entire roof into several rectangular subsections. The dimensions of these subsections must comply with the production line constraints, transportation trailer capacity, crane lifting limitations, and on-site installation considerations. The resulting system for a typical two-storey building with a gable roof comprises the following components (Fig. 4):

a) Roof panels
b) Support wall panels
c) Celling frames
d) Beams spanning between two support walls
e) Inter-component connections, including the inclined roof panel and support wall, ceiling frame and shear wall, and the support wall and ceiling frame.

The dimensions of the roof panel, ceiling frame, and support wall are selected in such a manner that they accommodate the constraints of the production line and transportation limitations (Table 1). The roof panels and support wall are produced in the wall production line using laminated strand lumber (LSL) and oriented strand board (OSB). Details of the panel design are discussed in a later section. Ideally, the production process of the roof panels is the same as the wall production; for example, framing operation is performed in the framing station (Fig. 1a) and attaching the OSB on the finished frame is completed in the multifunction bridge (Fig. 1c) of the wall line. Whereas the ceiling frame can be produced in the wall line framing station or floor line depending (Fig. 1a and 1b) on the cost and efficiency of production. Other components such as roof panel to support wall connection requires manual operations. Details of the ceiling frame analysis can be found in Islam et al. [9]. Cost analysis for a gable roof with an 11 × 6.1 m building footprint shows that production cost is \$66.70/m^2 following the existing fabrication process, whereas manufacturing

Table 1 Constraints for roof panel and ceiling frame size

Component dimension	Production constraints	Transportation constraints
Maximum height (mm)	3,200	3,050
Maximum length (mm)	12,200	12,192
Minimum height (mm)	1,600	n/a
Minimum length (mm)	1,200	n/a

using the proposed system will cost $69.4/m^2. Therefore, the proposed system is a cost-competitive production process with the conventional system. As a matter of fact, this holistic approach is more efficient and economical since it will reduce the hauling number in transporting the roof and deliver higher utilization of automated and semi-automated production lines.

3 Panel Design

As mentioned in the previous section, the roof panel is produced in the wall line following the same procedure as the wall panel production process. As such, a gable roof with an 8/12 slope and 6,096 mm span requires a total of four panels. The corresponding width for the Panel-A type (Fig. 4) is 1,938 mm, whereas type Panel-B has a width of 1,838 mm. The material selection for this panel, it should be noted, is critically important as regards strength, stiffness, and production efficiency. In this regard, off-site home manufacturers typically prefer engineered wood products over traditional lumber because of their dimensional stability, high strength, and high stiffness. For example, if traditional lumber is used, then the top-plates and studs will need to be manually adjusted, often with considerable force applied, in order to fit the workbench at the framing station. Even operations such as cutting birdsmouth notches may not be consistent if traditional lumber is used. Given these issues with traditional lumber, for the panelized roof design, LSL and OSB are the preferred material. The gravity load path of this panelized roof is shown in Fig. 4. It can be noted from Fig. 4 that Panel-B has supports at both ends and if we assume simply support condition then half of the gravity load is transferred to the load-bearing wall at the eave line and half of the load is transferred to the support wall. For Panel-A, full gravity load is transferred to the support wall.

The panel design starts with the selection of OSB sheathing thickness. Following the design Table 2.1.2A and 2.1.2B in CWC [4], for the maximum spacing of the rafters 600 mm minimum 9.5 mm thick OSB can be used for specified roof Snow loads less than 2.0 kPa and 11 mm for specified roof Snow loads greater than 2.0 kPa. The studs of the panel can be designed similar to the traditional rafter analysis considering simply supported conditions for a span of the panel width. Since both Panel A and B are subjected to both out-of-plane loading and in-plane loading, the stud design would require checking for bending and compression (CSA 086 19 [5] clauses 6.5.4.1 and 6.5.6.2.3) member since the panel is subjected to both out-of-plane loading and in-plane loading. This simplified process gives an estimate as an individual member of the panel however the panel is a system itself with Top plate (76 mm 140 mm), Studs (38 mm 140 mm) spaced at 600 mm and OSB sheathing (9.5 to 11 mm thick). As such, it behaves as a plate rather than as a rafter system. Also, the edge of the top plate requires an additional OSB sheathing opposite side of the main sheathing (Fig. 5a) to make it more rigid and facilitate connections at the apex and support wall.

As can be observed in Fig. 5b, the proposed apex connection is a triangle hinge connection with a self-locking mechanism that requires studs on both sides of the triangle to connect both panels at the ridge of the roof. However, the spacing of this connection may require omitting some studs of the panel and thus the rigidity of the top plate-to-studs connection must be sufficient so that load can be transferred to the nearest apex connection zone. By nailing secondary OSB sheathings (Fig. 5a) at the edge of the top plate it is possible to facilitate an economical apex connection. The nail connection of the secondary OSB, it should be noted, is subjected to both lateral and axial load because of the slope orientation of the roof panel. Although CSA 086 19 [5] provides a design guideline for laterally loaded nail joints that is easy to implement for OSB sheathing in typical shear walls, the design in which the OSB sheathing-to-stud nail connections are subject to both withdrawal and lateral force is a special case. To obtain a detailed characterization of the behaviour of this panel, as well as to determine optimum nail spacing for the secondary OSB sheathing (300 mm wide), finite element (FE) modelling is required. The FE modelling, in turn, requires several types of nail connection tests, which are discussed in the next section.

3.1 Nail Connection Tests on Manufactured Panel

Experimental tests were carried out to assess the strength and stiffness of OSB-to-LSL stud and LSL top plate-to-LSL stud nail connection. The test method described in Sect. 13 of ASTM D1761-12 [1] covers the determination of the resistance to lateral movement offered by a single screw in wood members. Following the same loading protocol and measurement process, a modified test setup was designed for this study to obtain the load–displacement of the connections. The nail joint test program involved four types of connection (Fig. 6), in total, 24 nail joint specimens were fabricated at an offsite construction facility. Since the specimens were built in the same offsite environment of the home fabrication process, the nail connection samples represent a reasonable portion of actual production that accounts for the construction defects and variability. The test setup used for testing nail joints was similar to the one previously used by Plesnik et al. [15] and Spasojevic [18]. The setup had two parts: a) the test section at the top, and b) a dummy section at the bottom. The dummy section was overdesigned to make it very rigid so that it can maintain the geometry of the specimen. It was fabricated using ten 12-gauge screws that provided the dummy section with high stiffness and resisted any movement of that end. The test section of sample type-a was constructed with four nails and consisted of 38 $\times$ 140 mm LSL stud, and the 9.5 mm thick OSB on both sides (Fig. 6a). Whereas the test section of the type-b samples was fabricated using one 38 mm 140 mm LSL piece in horizontal plank orientation and two 38 $\times$ 140 mm LSL parts in stud orientation. Four nails were used to connect the LSL parts which represents the nail connection with a top plate to studs and test results of this sample represent the displacement of joints in x-direction as shown in the coordinate system in Fig. 6b.

Table 2 Summary of nail connection test samples

Joint type	Load	Head-side	Point-side	Peak load (kN)		Initial stiffness (N/mm)
				Mean	S.D	
Framing stud-to-top plate X-axis	Lateral	LSL	LSL	1.403	0.020	712.34
OSB sheathing-to-LSL framing	Lateral	OSB	LSL	1.035	0.188	2,622.93
Framing stud-to-top plate Y-axis	Lateral	LSL	LSL	1.199	0.138	758.51
Framing stud-to-top plate Z-axis	Axial	LSL	LSL	0.862	0.186	3,608.57

The test sample of type-c was constructed using three 38 × 140 mm LSL and two 9.5 mm OSB sheathing. The sheathing provided a surface that connected the dummy section and test section (Fig. 6c). To achieve high rigidity, twenty 12-gauge screws were used on both sides of the dummy and test section. Total four nails were used to connect the LSL sections which represents the nail connection of top plate-to-stud and test results of this sample represent the displacement of joints in the y-direction. Two Linear Variable Differential Transformers (LVDTs) were attached to both sides OSB of the specimen to record the relative displacement of the LSL sections. Finally, the test section of the type-d sample was fabricated using one 38 × 140 mm LSL in horizontal plank orientation and two 38 × 140 mm LSL in stud orientation (Fig. 6d). Four nails were used to connect the LSL sections that represent the connection of the top plate to the stud and test results of this sample represent the displacement of joints in the z-direction. It is worthy to note that this is ultimately the nail withdrawal test. Figure 7 illustrates the load–displacement plot of the tested sample and Table 2 summarizes all the test results. The characteristics of the individual sheathing-to-framing, LSL top plate-to-studs joints in roof panel are crucial in defining the strength and the stiffness of the panel. The results of this nail connections test were used to develop a finite element model of the panel which is described in the next section.

3.2 Finite Element Analysis of Manufactured Panel

Finite-element modelling can be applied to cost-effectively evaluate the structural response of a range of light-framed buildings [17]. Many researchers had used this tool to understand the structural response of light-frame timber construction. For this study, we used general-purpose finite element software Abaqus to develop a FEM of roof panel that can be used to build a gable roof with a slope of 8/12. The proposed 3D FE model used connector elements to model the load–displacement properties of the sheathing-to-LSL framing joint and LSL top plate-to-LSL stud joint. By defining

Table 3 Mechanical properties for OSB and LSL

	OSB	LSL
E_1	7,425	8,965
E_2	2,520	1,350
G_{12}	15,74	490
G_{13}	1,194	195
υ_{12}	0.183	0.298
υ_{13}	0.364	0.500
Bending 0^o	18.9	21.65
Bending 90^o	6.00	8.86
Shear strength 0^o	3.80	5.39
Shear strength 90^o	2.40	2.47

their properties nonlinear and introducing (nonlinear) single spring elements or spring pair elements, the proper connection behaviour can be captured in the model [16, 17, 19]. The load slip curves of the tested connections mentioned in the previous section were used to define the parameters for the nonlinear springs that characterize the OSB-to-Studs and Top plate-to-stud connection. An S4 shell element is used to represent sheathing panels and LSL studs. However, the top plate LSL was modelled using an 8-node linear brick element. S4R is a 4-node doubly curved general-purpose shell element with finite membrane strains permitted, and each node has 6 degrees of freedom. The properties of OSB and LSL material were defined based on values reported in the literature. OSB sheathing properties were adopted from [8, 10, 20]. LSL wood properties were defined on the basis of the test results of Moses and Prion [11], CCMC [6] and Niederwestberg et al. [13] (Table 3). The Tasi-Hill criterion was used to define the failure of OSB and LSL materials in bending. Since the gable roof is symmetric only half of the roof panel was modelled with a representative longitudinal length of 2,400 mm. The FEM was modelled using 9.5 mm secondary OSB sheathing at the edge of the top plate and connector elements with their local coordinate system were defined in that zone for top plate-to-OSB and stud-to-OSB connections (Fig. 8a). As shown in Fig. 9a symmetry boundary conditions at the ridge were defined for the studs 1,200 mm apart to represent the apex connection and the stud in between was connected to the top plate and secondary OSB by nails only. Thus, the model redistributes the load to adjacent supported studs and by analyzing the connector force output the optimum number of nails for the secondary OSB can be obtained. It should be noted that the nail withdrawal test results had a maximum mean load capacity of 862 N and according to CSA 086 19 for nail withdrawal case ϕ factor is 0.6, so for design maximum connector withdrawal threshold was set to 517 N. Results from the FEM shows that for a gravity load 4.0 kPa with 9.5 mm thick secondary OSB two rows of four nails are sufficient to comply the design requirement and the withdrawal forces in the fastener close to the unsupported studs remain below the design threshold.

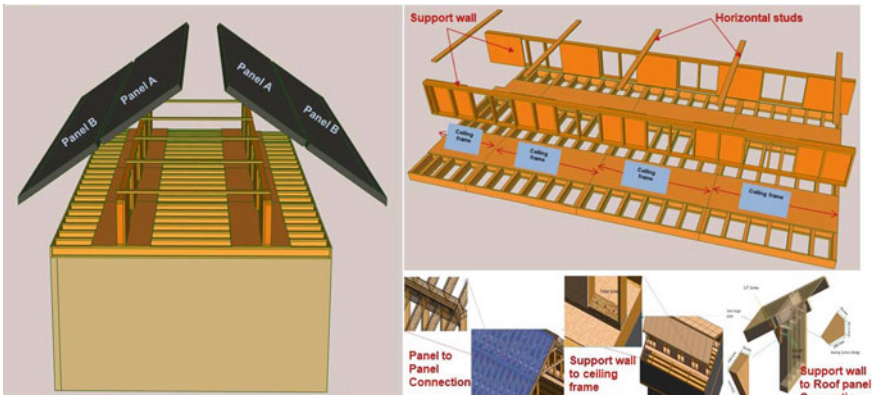

Fig. 3 Panelized roof concept

Figure 9b shows the load-displacement output from the model that confirms the fastener force is well below the threshold level. The same FEM model was used to simulate the three-point bending test of the panel and obtained the load-displacement response (Fig. 9a) until failure of the system. The predicted peak load was 33.75 kN and following the procedure described in ASTM D1037 [2] the bending stiffness of the panel was obtained to be 339×10^6 N-mm^2/mm. To develop FEM for the complete panelized roof which includes support wall, ceiling frame and all inter-component connections an equivalent super element fictitious plate can use with the equivalent bending stiffness of the actual panel. However, to model the FEM of the complete assembly of a panelized roof system load response of all the connections shown in Fig. 3 is essential. So, an experimental campaign was carried out at the laboratory of the Department of Civil and Environmental Engineering of the University of Alberta for the above-mentioned connections type. Details of the connection test and ceiling frame analysis can be found in Islam et al. [9]. Results from ceiling frame analysis show that the ceiling frames can be produced either at the wall line using LSL material or in-floor production line using wood I-Joist. Choice of the ceiling frame production depends on the production efficiency of the manufacturer's facility. The panelized roof design in this study is independent of the ceiling frame production method since the developed connection system can be applied to any type of ceiling frame. The experimental results of support wall-to-roof panel and panel-to-panel connection show that available analytical models for screws can be used to obtain good estimates of design values for all the connections of the panelized roof.

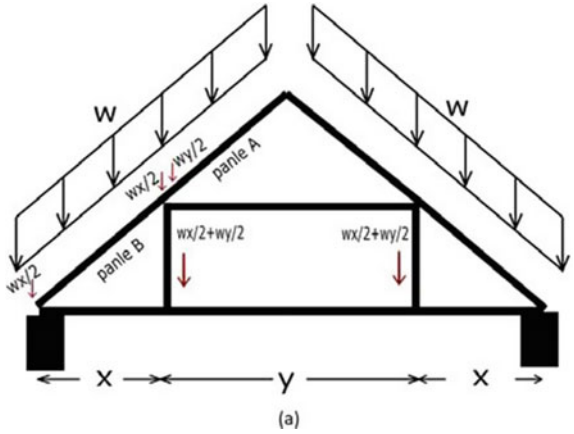

Fig. 4 Gravity load distribution in a cross-section of the panelized roof

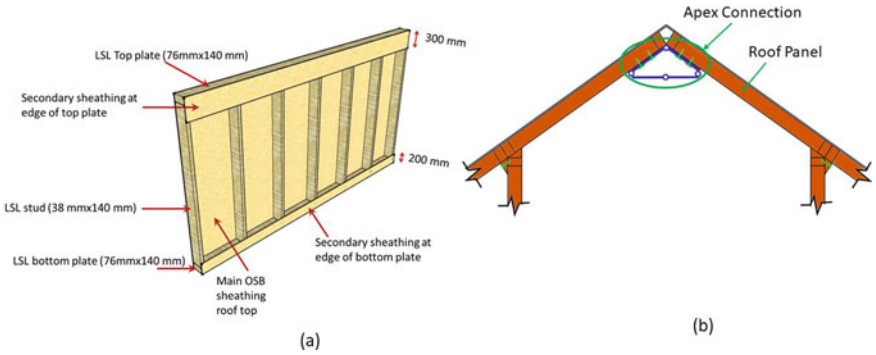

Fig. 5 **a** Typical panel for the panelized roof system, **b** Roof panel placed with apex connection

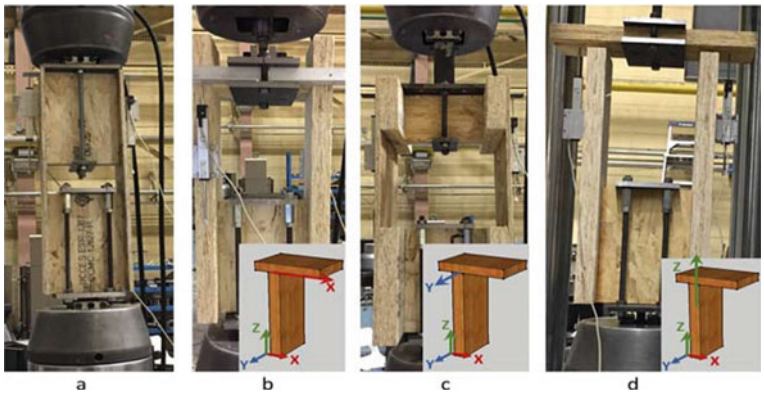

Fig. 6 Nail connection testing **a** nail connection OSB-to-LSL stud (type-a), **b** LSL to plate-to-LSL stud along the x-direction (type-b), **c** LSL to plate-to-LSL stud along the y-direction (type-c), and **d** Nail withdrawal (type-d)

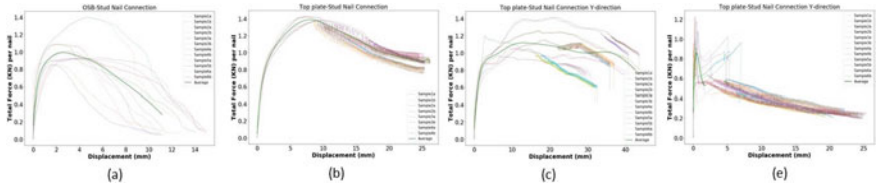

Fig. 7 Load displacement curves for **a** nail connection OSB-to-LSL stud, **b** LSL to plate-to-LSL stud along the x-direction, **c** LSL to plate-to-LSL stud along the y-direction, and **d** Nail withdrawal

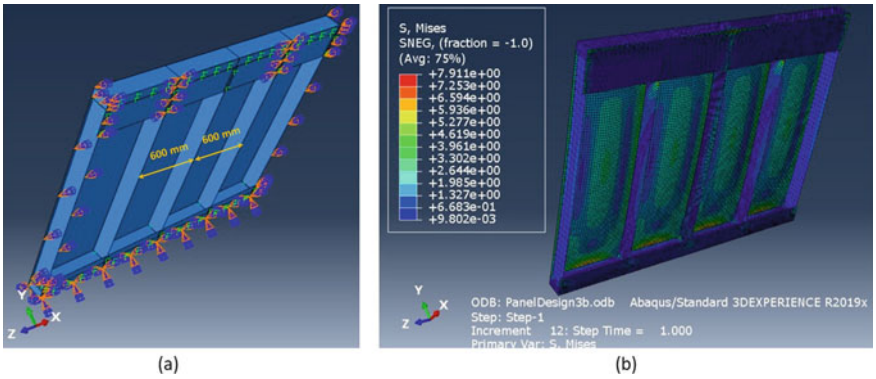

Fig. 8 **a** Assembly view of the FEM **b** results of the FEM

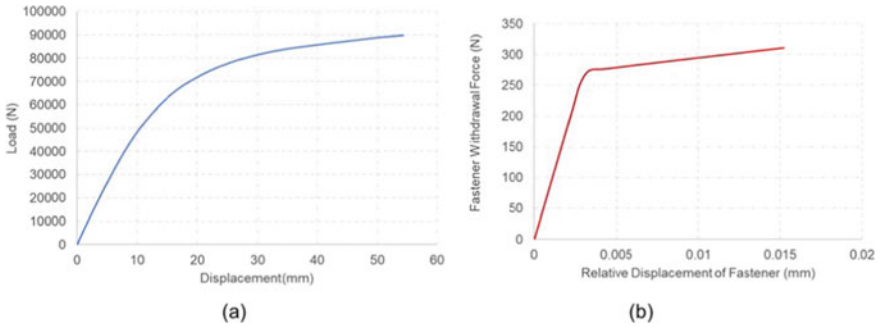

Fig. 9 **a** Load response of three-point bending test of panel **b** Fastener withdrawal force

4 Conclusion

The roof panel analysis and connection test results described above provide the basis for the FE model of the entire roof assembly (which is essential for understanding the load response behaviour of the overall system itself). In this regard, the FE modelling to be carried out in future work will reveal the expected load response behaviour of

the proposed novel roof system and will extend the approach to several other types of roofs in the North American construction market, such as hip, dormer, and gable with valley. The main limitation of this system is that it cannot be used in the case of a commercial facility with a large roof span.

Acknowledgements We thank ACQBUILT Inc., Rothoblaas and Simpson Strong-Tie Inc. for material supplies and technical support. This work was supported by a grant from the Natural Sciences and Engineering Research Council of Canada through the Engage Grant and Industrial Research Chair programs.

References

1. ASTM (2012) Standard test methods for mechanical fasteners in wood. Designation: D 1761–12
2. ASTM (2020) Evaluating properties of wood-base fiber and particle panel materials. Designation: D1037−12
3. ACQBUILT (2019) ACQBUILT Inc. company database and personal visits for images. http://www.acqbuilt.com/
4. Canadian Wood Council (CWC) (2014) Engineering guide for wood frame construction. 2014 edn, CWC, Ottowa, Canada
5. CSA (2019) CSA O86-19. Engineering design in wood. CSA Group, Mississauga
6. Canadian Construction Materials Centre (CCMC) (2019) Evaluation report CCMC 12627-R TimberStrand LSL. https://www.weyerhaeuser.com/application/files/8715/6115/1801/12627-R.pdf. Accessed 2 Jan 2020
7. Goodier C, Gibb A (2007) Future opportunities for offsite in the UK. Constr Manag Econ 25(6):585–595
8. Islam MS, Islam MN, Alam M (2017) Properties of oriented strand board (OSB), and timber to evaluate the stiffness of timber I-Joist. In: CSCE conference May 31–June 3 2017,Vancuver, Canada
9. Islam MS, Chui YH, Altaf SM (2021) A holistic design approach for innovative panelized light-wood frame roof construction. In: World conference on timber engineering (WCTE) 2021, 9–12 August, Santiago, Chile
10. Karacabeyli E, Lau P, Henderson CR, Meakes FV, Deacon W (1996) Design rated oriented strandboard in CSA standards. Can J Civ Eng 23(2):431–443
11. Moses DM, Prion HGL (2002) Anisotropic plasticity and the notched wood shear block. For Prod J 52(6):43–54
12. MBI (2015) First, let's describe what modular construction is. http://www.modular.org/htmlPage.aspx?name=why_modular. Accessed 9 Apr 2019
13. Niederwestberg J, Zhou J, Chui YH, Gong M (2018) Shear properties of innovative multi-layer composite laminated panels. In: Proceeding of World Conference on Timber Engineering, Korea National Institute of Forest Science, Seoul
14. Pan W, Goodier C (2012) House-building business models and off-site construction take-up. J Archit Eng 18(2):84–93
15. Plesnik T, Erochko J, Doudak G (2016) Nailed connection behaviour in light-frame wood shear walls with an intermediate layer of insulation. ASCE J. Struct. Eng. **142**(7):04 016045
16. Shivarudrappa R, Bryant GN (2013) Sensitivity of load distribution in light-framed wood roof systems due to typical modeling parameters. J Perform Constr Facil 27(3):222–234
17. Satheeskumar Henderson NDJ, Ginger JD, Wang CH (2017) Three-dimensional finite-element modeling and validation of a timber-framed house to wind loading. J. Struct. Eng.143(9):4017112

18. Spasojevic M (2019) Structural and Hygrothermal Performance of Light Wood-Frame Walls with Insulated Sheathing. Thesis University of Alberta, MSc
19. Vessby J, Erik S, Olsson A (2010) Coupled and uncoupled nonlinear elastic finite element models for monotonically loaded sheathing-to-framing joints in timber-based shear walls. Eng Struct 32(11):3433–3442
20. Zhu EC, Guan ZW, Rodd PD, Pope DJ (2005) A constitutive model for OSB and its application in finite element analysis. Holz Roh- Werkst 63(2):87–93

Application of the Building Code to Existing Buildings: Background, Objectives, and Interesting Tricks

Thomas Morrison

1 Introduction

The engineering community needs to improve its treatment of existing buildings. This has become increasingly important as a societal and as a climate control issue. A recent study [14] showed that the construction and operation of buildings account for approximately 32% of global carbon emissions, with construction accounting for an estimated 12% of total emissions. It has also been estimated that the construction industry contributes 45% by volume of waste to landfills. The industry has a responsibility to address these climate issues and improve the sustainability of the built environment. This is consistent with an engineer's responsibilities to ensure protection of the environment, the public, and the workplace [1].

Studies and organizational standards have identified that the renovation and repurposing of existing buildings is an effective solution in addressing the carbon emission and landfill issues. The importance of finding better ways to use existing buildings has been highlighted by such diverse groups as the International Panel on Climate Change and the U.S. Department of Defence. A U.S. Department of Defence report [9] concluded that the continued use of existing buildings should always be the default approach when seeking building space. The study also showed that successful projects require professionals with specialised knowledge. There is evidence of a trend to more construction activity with existing buildings. The American Institute of Architecture found that 44% of current design activity is dedicated to existing buildings [2]. A literature review could not confirm whether this is true in Canada but, it is probable that this is also representative of Canadian building activity. Where existing buildings are being repurposed, or renovated, there will be the need for structural analysis and design. However, the National Building Code of Canada [NBCC],

T. Morrison (✉)
Heritage Standing Inc., Fredericton, Canada
e-mail: tmorrison@heritagestanding.ca

S. Walbridge et al. (eds.), *Proceedings of the Canadian Society of Civil Engineering Annual Conference 2021*, Lecture Notes in Civil Engineering 244,
https://doi.org/10.1007/978-981-19-0656-5_39

and referenced design standards, contain limited content dedicated to existing buildings. The NBCC and the National Research Council Canada [NRCC] provide some guidance, but not to the extent provided for new buildings.

It is the objective of this article to outline the current guidance in the NBCC for existing buildings, summarize current NBCC initiatives to address existing buildings, identify other technical resources on this subject and finally present a process for structural engineers to use for existing building projects.

2 National Building Code – Division A

Prior to the first edition of the NBCC (published in 1941) there were a patchwork of regional and municipal codes. It was the responsibility of the structural designer to understand the technical background necessary to assign loads and develop a safe design. Most structural information pertained to loads, with live loads such as 100 pounds per square foot (4.8 kPa) being referenced since the mid 1800's. From the time of the first 1941 edition of the NBCC, to the fourteenth edition in 2015, many changes have occurred in the code. Code references in this paper refer to the 2015 NBCC.

The 2015 NBCC, Division A, includes Compliance, Objectives and Functional Statements which form the basis of the code intent. Division A Part 1: Compliance outlines where the Code applies and how it applies. The NBCC is an objective based code [5], and these are provided under Division A Part 2 Objectives. Division A Part 3: Functional Statements, provides additional guidance in understanding the objectives. The first question for a designer is - does the code apply to existing buildings?

The answer is that the code does apply under specific circumstances. Division A Clause 1.1.1.1.(1). states "This Code applies to the design, construction and occupancy of all new buildings, and the alteration, reconstruction, demolition, removal, relocation and occupancy of all existing building. (See Note A-1.1.1.1.(1))". This clause indicates that if a construction project relates to an existing building then the code applies [7]. However, the indicated "Note" must be considered for context.

The Division A Note (NBCC A-1.1.1.1.(1)) evolved from a January 1984 article by the National Research Council of Canada [10]. This article provides one of first technical discussions exploring code application to existing buildings. The article focuses on fire and life safety requirements. Structural considerations introduced at this time acknowledged the idea that compromise may be needed, and that existing performance should be considered in evaluation. The article states that "to successfully apply building codes to existing construction, two qualities are necessary: a knowledge of the subject and a constructive attitude". The current NBCC appendix note adopts this philosophy with changes having been made as the code evolved. Table 1 provides quotes from this appendix note that are relevant to structural requirements. The second column of the table provides the author's interpretation/experience related to the application of the requirements.

Table 1 Division a note 1–1.1.1.1.(1) discussion

NBCC division A: A 1.1.1.1.(1)	Discussion/Interpretation
It is not intended that the NBC be used to enforce the retrospective application of new requirements to existing buildings	The Code is for new construction and there should be a clear reason for why it is applied to an existing building
Depending on the construction of the building and the changes in load, structural modifications may be required	Structural modifications should consider structural system, known deficiencies, and if load changes are occurring. Knowledge of historic buildings techniques and why industry stopped using them is required. Some practices changed because of experienced deficiencies, others for constructive practicalities. The former is a concern, the later is not
Code application to existing or relocated buildings requires careful consideration of the level of safety needed for that building. This consideration involves an analytical process similar to that required to assess alternative design proposals for new construction	Existing buildings may require a greater understanding and depth of evaluation than used for the equivalent new construction. Alternative evaluation and design processes are important. These two sentences suggest that in some cases application of NBCC Division B (Acceptable Solutions) may not be the best way to meet the Code Objectives
In developing Code requirements for new buildings, consideration has been given to the cost they impose on a design in relation to the perceived benefits in terms of safety. The former is definable; the latter difficult to establish on a quantitative basis. In applying the Code requirements to an existing building, the benefits derived are the same as in new buildings. On the other hand, the increased cost of implementing in an existing building a design solution that would normally be intended for a new building may be prohibitive	Application of the Code to existing buildings requires some balancing of priorities
…successful application of Code requirements to existing construction becomes a matter of balancing the cost of implementing a requirement with the relative importance of that requirement to the overall Code objectives. The degree to which any particular requirement can be relaxed without affective the intended level of safety of the Code requires considerable judgment on the part of both the designer and the authority having jurisdiction	Specialized knowledge and experience are valuable to support decisions regarding Code application to existing buildings. The involvement of both the designer and authority having jurisdiction (AHJ) in discussion is important

The code notes quoted in Table 1 provide the intent of the code when applied to existing buildings. The notes provide high level principles but there is much room for interpretation when confronted with the details of a given project. The application of the code to existing buildings currently recognizes prescriptive and alternative design measures (NBCC Division A Clause 1.2.1.1.). The referenced clause has two parts.

Table 2 JTG-AEB overarching principles

Number	Principle	Goal of principle
1	Closing the performance gap between the current code and the existing building stock	Recognise that requiring extensive interventions in the existing buildings is not realistic and expensive, and the focus is in reducing the performance gap more so than matching existing performance
2	Maintaining or increasing the life safety and overall building performance level. (An alteration cannot make the building worse)	Interventions must avoid making a building less safe through application that lacks consideration or understanding of the function of existing technology
3	Avoiding negative unintended consequences or unrealistic expectations	Highlights that an understanding of existing systems is required to avoid cases where repair with new techniques may cause damages. The most common structural implications are removal of 'non-load bearing' systems that have become load bearing (potentially unintended), or through repair with modern materials that damage the structure they intend to repair (seen commonly in masonry)
4	Ensuring that when a repair, maintenance or alteration is in progress, the building cannot be left in an unsafe state	Recognise that existing buildings construction sites must be safe
5	All regulatory measures should be reasonable, pragmatic and effective (applying Smart Regulation principles)	Address the need for solutions to be practical. The requirements should not create a situation where the best solution is demolition of the building
6	Allowing a degree of flexibility so as to encourage alterations to existing buildings rather than placing an undue burden on owners, which could inspire them to avoid alterations altogether	Recognise that existing building projects are unique and strict guidelines are not always possible. Flexibility will be important in meeting objectives
7	Allowing a degree of flexibility so as to preserve officially recognized (designated/registered) heritage elements	The value that historic buildings must be recognised as unique, and additional consideration must be given to their preservation. Accordingly, greater flexibility in application of requirements is needed
8	Regulatory measures and voluntary programs should complement each other	Encourage greater coordination between the tools available for both requiring changes and making it appealing for owners to undertake changes

The clause states "Compliance with this Code shall be achieved by (a) complying with the applicable acceptable solutions in Division B (see Note A-1.2.1.1.(1)(a)), or (b) using alternative solutions that will achieve at least the minimum level of performance required by Division B in the areas defined by the objectives and functional statements attributed to the application of acceptable solutions (see Note A-1.2.1.1.(1)(b))." Therefore, Division B, titled Acceptable Solutions, can be used as a (generally) prescriptive approach to meet minimum performance levels. Alternative solutions are acceptable so long as the evaluation demonstrates they meet the minimum performance levels of the equivalent Division B requirement.

Division A acknowledges that existing buildings should not be viewed in the same lens as new construction, and that alternatives are possible. This places a greater reliance on the designer and authority having jurisdiction (AHJ) possessing a greater depth of understanding of historic construction, building performance and the application of the code to existing buildings.

3 JTG-AEB Report

In 2016 the Canadian Commission on Building and Fire Codes established the Joint Task Group on Alterations to Existing Buildings [JTG-AEB]. The JTG-AEB was created to address the absence of clear requirements for existing buildings, as this void was resulting in confusion and could potentially result in unsafe construction practices. The JTG-AEB started with a look at the energy efficiency of existing buildings. As the work of the task group progressed it was realized that the focus on energy efficiency was a technique more suited to new construction. For many existing buildings, the contribution of diverse building features could contribute to energy efficiency and overall embodied carbon. This made it less clear than with new construction what building technologies were contributing to meeting code objectives. This presented challenges in how to move forward with code changes that would address the different technologies and construction methods found in existing buildings.

In August 2019, the joint task group report was released. This report documented the background of the issue, terms of reference for the task group and made recommendations for improvement of the NBCC. The report was issued to the executive committee of the NBCC as well as the various standing committees involved with code development [6].

The JTG-AEB recommended that additional code requirements applicable to existing buildings was preferable to creating a set of guidelines. It further recommended that a new Part of the Code cover the issue. In creating the recommendations, eight principles were established to guide the Standing Committees. These principles are outlined in Table 2.

The overarching principles contained in the JTG-AEB report provide an excellent foundation on which to direct future development work and to structure detailed code requirements. Much work is required to cover the range of existing buildings in the

scope of the code. In Canada there are buildings from the 1700s still in use. It will be a difficult task to cover the range of construction methods from this time to the present. As stated previously under the current NBCC requirements, it is evident that a greater reliance will be placed on the designer and authority having jurisdiction (AHJ) possessing a depth of understanding of historic construction and of building performance evaluation.

Although the principles contained in the JTG-AEB report provide a good basis for future code improvements, limited mention was made of the condition of an existing building when renovations are proposed. The discussions regarding application of the code appear to assume that there are no deficiencies in the structure. This is frequently not the case. Therefore, any discussion of projects involving existing buildings must first address the question of what is the condition of the existing building? This question is generally answered by a condition assessment. A condition assessment identifies deterioration or structural deficiencies that need to be addressed for the continued use and safety of the building.

4 NBCC Structural Commentaries

The NBCC is supported by technical documentation clarifying intent and summarizing experience in application of the code. The primary reference for structural issues is the Structural Commentaries: User's Guide for NBCC Part 4 of Division B [8]. Many of the commentaries provide context to better understand structural issues related to existing building. The user of this document is cautioned (Division B Sentence 4.1.1.5.(2)) that existing buildings often require applying structural alternatives. These alternatives are intended for use by persons qualified in the methods applied as the demonstration of safety may include evaluation of a full-scale structure, prototype with load tests, or through studies of model analogues.

The User's Guide provides detail on use of Limited Sates Design in Commentary A. The commentary provides background on loads that can provide value in determining the structural capacity of an existing system. Professionals can assume that prior professionals met minimum conditions of design at the time of construction. In making this assumption the professionals must know differences in code requirements at different times. For example:

1965 – prior to this date the design may not have considered the potential for snow drifts, and
1970 – prior to this date the code may not have considered blocked drains for rain load.

If it is known that the structure is in good condition, and that there are no known problems with the past construction approach, it is possible to use the historic evaluation technique to set a baseline.

To demonstrate this approach, consider a 1920's warehouse building. A current project proposes to add a storey to the building and convert its use for offices. With

sufficient information on past designs, the original design loads for the foundation can be calculated. Since the building is changed from warehouse loads to office loads the design can now consider load reduction factors (which were not allowed in the 1920's). With this change it is possible that the load capacity under the current code for offices is less than the minimum 1920's case for a warehouse. The combined knowledge of the 1920's structural system, vulnerability, and existing condition, may support the conclusion that an additional storey can be added to the building without requiring intervention to the foundation.

In Commentary L of the User's Guide is a summary of the fundamental considerations that guide design for new buildings. These considerations include: life safety; comfort of occupants; function of the building for its intended use; durability; and economics. For existing buildings the balance between these variables is different than for a new structure. When working with an existing building it becomes more important that there is good documentation. This documentation should cover what is known of the structure, findings of recent inspections, assumptions used in evaluations and provide a demonstration that the structural evaluation is appropriate. This documentation should be available for third party review.

Existing building projects frequently require assessment to demonstrate structural adequacy. Selection of the appropriate methodology or model is essential. One concern regarding the application of appropriate evaluation techniques relates to the proliferation of finite elements models (FEM) in analysis of unreinforced masonry (URM) structures. Some FEM software is based upon beam theory, and a URM structure functions in pure compression. This results in a model that defaults to consider some tensile response that does not exist for the actual structural mechanics. Pure compressive structures are no longer built. Many of the FEM software packages can manage URM without difficulty, but designers must be aware of the software's base assumptions.

An additional challenge arises in selecting the appropriate analysis method for an existing building. This challenge relates to defining what is a structure. Current design approaches take measures to separate different components in the building, some of these decisions help ensure that the structural system will be the stiffest elements and take the applied load. However, an existing building may not have these details. The designer must understand how the building is currently functioning as it has been found that the stiffest elements will take load until a failure point is reached. For example, plaster and lath systems may increase a 'partition' walls stiffness to the point that it becomes load bearing. There are instances where past changes to a building unintentionally increased the structural load on a 'non-load bearing wall'. In determining what is a structure, it is important to exercise caution.

Professionals working with existing buildings continues to learn more about how these buildings function and distribute loads. Past performance of the building does provide a measure of its structural capacity. A building is a full-scale model of itself. Therefore, if there is no damage, distress or deterioration; if load paths are in good condition; if there are no changes to use or loading conditions; and if these conditions have been stable for 30 years, we can assume it will continue to be stable. This approach should be supported by a condition assessment and a building history

that confirms loading conditions are not changing. A simple building change such as adding roof insulation can result in changes in the snow load. Where this has occurred the past performance may not continue and assumptions on stability are no longer reliable.

5 Other Provincial Code Considerations

Building codes are adopted provincially, and some provinces have different approaches to how existing structures are addressed. Ontario and Quebec have created a separate part of their codes on existing buildings, while other provinces include information in their legislation when adopting the NBCC that pertains to existing buildings. Most of this information relates to energy efficiency, accessibility, fire and life safety. The most common structural requirements are in line with the discussions in the previous sections of this paper.

6 International Design References

The Canadian Codes stress that existing buildings must be viewed differently than new construction. The NBCC provides guidance for design with existing structures, and provides an option for alternative solutions to accommodate unique conditions. This approach requires knowledgeable professionals and the exercise of engineering judgement. Internationally there are similar challenges with how to address existing buildings. The International Existing Building Code produced in the United States is one example of a code specific to existing buildings [12], as are various ASCE standards such as ASCE 11 *Guideline for Structural Condition Assessment of Existing Buildings* [3] or ASCE 41 *Seismic Evaluation and Retrofit of Existing Buildings* [4]. These documents provide good prescriptive based information and provide greater technical depth on the subject than is available in the NBCC. The *ICOMOS Charter – Principles for the Analysis Conservation and Structural Restoration of Architectural Heritage* (commonly referred to as the ISCARSAH Principles) [11], and the International Standard ISO 13822 – *Bases for design of structures – Assessment of existing structures* [13] provide clear guidance on special cases. The former, provides high level thoughts and process, while the later provides greater detail and evaluation information.

The ISCARSAH Principles were developed for structural work on internationally important historic sites. The principles were designed to be practical, think long term, and avoid causing future problems. Although developed for historic sites, these general principles are similar to the JTG-AEB principles and can be readily applied to all existing structures. Some of the ISCARSAH principles worth highlighting include:

- Use a multi-disciplinary approach. It is important that all those involved with design can participate in discussion early, it is easier to reduce the extent of interventions required and save resources.
- Use of a medical approach instead of a design approach. The importance of spending additional time to understand the structure, both the history and current state, in trying to determine the root causes for any deterioration (diagnosis). Ensuring the diagnosis of the problem is clearly defined, and that multiple potential treatments (remediation measures) are considered. Determine if continued monitoring of the building health is appropriate.
- Understand the benefits and harms before taking action. Where a building exists, any change will have impacts both positive and negative.
- Process information to first establish a general plan, then make the evaluations more detailed as a design progress.
- Ensure that diagnoses and evaluations are based on quantitative, qualitative, and historic approaches. If the information sets do not align, the building is not adequately understood. For example, if quantitative analysis finds that a structure could not carry its own dead loads, yet the past winter saw considerable snow load on the building for an extended period, there is a disagreement (misalignment) between quantitative and historic data.
- A full understanding of structural and material characteristics is required.
- Alternative measures should be documented in a report. This is important both for future professionals as well as to ensure that quality oversight is occurring.
- Greater emphasis should be placed on evaluation/design than with projects for new construction. This will help minimise the required construction interventions, save resources and reduce the last minutes changes for unforeseen issues.
- Ensure all interventions are compatible with the existing structure and materials.

The ISO 13822 standard contains valuable technical information. This standard looks at four situations where structural assessment would be necessary for an existing building: where the use or design life changes; where greater reliability is required (seismic being the most common); where deterioration to the structure has occurred and needs to be addressed; and where there is structural damage due to accidental actions. The standard provides a progressive procedure, including additional early-stage steps, to determine the scenarios and preliminary data requirements. It also provides discussion regarding the importance of a verification process and plausibility checks as a formal part of the design process. ISO 13822 references various other ISO standards as sources for more details, however the process can easily be applied to any limit states concept. The appendices provide a wealth of information, such as: an outline of the steps in an evaluation; information on how a structure's probability density function can change over its service life; and details on how the probability density function should be calculated. The steps laid out in this document are clear and progressive.

7 Recommended Process for Existing Buildings

The international references discussed previously support the need for a defined process for engineering projects with existing buildings. Any engineering process should have defined steps with a clearly stated purpose for each step. This paper outlines a suggested process in Table 3. The process is intended for the initial steps of a project before detailed assessment begins. The third column of the table provides examples to explain why each step is important. Each example was intended to be illustrative of the step and is only one of many that could be provided.

Table 3 Additional early existing building intervention steps

Step*	Purpose	Example
Define objective	Ensure that the objective of the project is clear to all participants to avoid potential confusion	The request to 'bring a building up to code' is common among the public and used interchangeable by some to mean a building is safe for continued use. Assumptions and errors here quickly propagate into larger problems
Determine potential scenarios and what is changing	Conceptual review of what is changing. Consideration of the changing scenarios, and how that will impact evaluation. This step is not required for new construction. Take time to understand how the building resists global forces, and how load paths function holistically should fit into the scenario review	In one past project new damages were occurring after a recent intervention. Evaluation eventually found that in the intervention the designer had judged a wall system to function as a stud wall, where the actual system functioned as a series of posts. This led to repairs that compromised the lateral force resisting system
Review of background and prior documentation	Understanding the building past provides clues for further inspection and analysis. Period of construction, techniques and technologies used are important knowledge for future steps. Prior documentation may provide a record of specific problems or demonstrate that a past issue has been addressed	A past project had a cantilevered stone masonry spiral stairwell with an open centre. Two sets of background information influenced evaluation significantly: first, design guides from the 1890's that showed how such a stair functions and is constructed; and second, a record of a prior load test when concerns arose previously. This research changed evaluation needs at relatively low cost

(continued)

Table 3 (continued)

Step*	Purpose	Example
Visually based condition assessment	Identify changes, deterioration, and stress locations in the building. Most existing building problems relate to inadequate past maintenance. With training, structural stresses and deficiencies can be identified in a visual review of a building. This visual review must be detailed and will direct where further information is required	Crack patterns in a building can be used to 'see' movement. Crack patterns in plaster can be used to identify regions where greater than acceptable movements are occurring. In one project this raised concerns in a portion of the building thought to be stable, and eventually revealed foundation problems
Preliminary evaluation checks	Before detailed information is available it is possible to undertake preliminary checks to understand where stress concentrations may be occurring, or use bounding to determine if more detail is necessary	Many pre 1920 vernacular structures include wood frame roof systems that do not lend themselves to easy structural analysis. Preliminary evaluation is an opportunity to make assumptions and gain an understanding of where stress could be concentrated and where additional focus provides the most benefit
Recommend-ations for next steps	Document recommendations as well as if any immediate actions. The initial steps will help focus the detailed assessment and future construction intervention thereby reducing costs	Some past projects had the global plan change due to findings during the initial stages In one project the original project was focused on the roofing system and structure, until the preliminary data revealed greater deterioration in in the upper masonry walls of the building. These walls had not been considered previously, as they were recently repaired. The past repairs were with incompatible materials In a separate project the initial recommendations found that by grading the wood structure in service (allowing knots in the compressive regions of a joist) and focusing on a broader material investigation would reduce the structural intervention needs

* These steps are outlined as a starting point for discussion.

Current design practice allows each specialty to proceed independently from others. In most existing buildings this is not possible. The number of exceptions at a detailed level makes it difficult to approach the codification in the same way the Division B of the NBCC approaches new design, future codes requiring either a new part or a portion of each Part dedicated to the topic.

8 Conclusions

There is evidence that a significant portion (44%) of construction activity involves existing buildings. Given the impact of construction on the environment, it is likely that there will be increased construction activity with existing buildings as a solution to observed negative impacts. Design and construction professionals need to prepare for this increased activity by improving their knowledge base and design processes.

Codes, standards, and technical guidelines for projects involving existing buildings acknowledge that they should not be treated the same as new construction. Technical literature highlights the importance of specialized knowledge for those responsible for this work. Specialized knowledge is needed on historic construction methods and materials; structural issues related to building function over its service life; and the selection of structural assessment methods appropriate to the building being evaluated. Currently in Canada there are limited resources and education materials available dedicated to structural engineering for existing buildings although this information is available internationally.

International standards for existing buildings also highlight the importance of a clear design process. This process should account for the history of the building, include a condition assessment, and utilize appropriate evaluation methods. Because of the unknowns and specialized nature of these buildings all work steps need to be clearly documented. Existing building projects conducted under the responsibility of knowledgeable professionals and following a defined process should result in reduced costs for the owner while helping professionals meet their obligations to the public, the environment, and the workplace.

References

1. AEPGNB (2020) By-Laws under the Engineering and Geoscience Professions Act. Fredericton, NB: Association of Professional Engineers and Geoscientists of New Brunswick
2. American Institute of Architecture (2020) The business of architecture 2020 - firm survey report. American Institute of Architecture
3. ASCE (1999) ASCE 11 - guideline for structural condition assessment of existing buildings. American Society of Civil Engineers, Reston
4. ASCE (2013) ASCE 41 - seismic evaluation and retrofit of existing buildings. American Society of Civil Engineers, Reston
5. Bergeron D (2004) Canada's objective-based codes. In: 5th International conference on performance-based codes and fire safety design methods. Luxembourg

6. Canadian Commission on Building and Fire Codes (2019) Final report - alternations to existing buildings: joint CCBFC/PTPACC task group on alterations to existing buildings. National Research Council Canada
7. Canadian Commission on Building and Fire Codes (2015) National building code of Canada. Natinoal Research Council Canada
8. Canadian Commission on Building and Fire Codes (2017) Structural Commentaries. National Research Council Canada, Ottawa
9. Department of Defence - ESTCP (2013) Demonstrating the environmental & economic cost-benefits of reusing DoD's pre-world war II buildings. ESTCP project SI-0931. US Department of Defence
10. Hansen AT (1984) Applying building codes to existing buildings.“ canadian building digest - division of building research. National Research Council Canada, January 230-1-230-4
11. ICOMOS (2003) ICOMOS charter - principles for the analysis conservation and structural restoration of architectural heritage. Charter. International Council on Monuments and Sites, Paris
12. International Code Council (2003) International existing building code. International Code Council
13. ISO (2010) ISO 13822: Bases for design of structures - assessment of existing structures. International Standards Organization, Standard
14. Resch E, Lausselet C, Brattebo H, Andresen I (2020) An analytical method for evaluating and visualizing embodied carbon emissinos of buildings. Build Environ168:106476

Input Motion Scaling for Seismic Evaluation of Rocking Components in Canadian Nuclear Power Plants

Amitabh Dar, Dimitrios Konstantinidis, and Wael W. El-Dakhakhni

1 Introduction

The seismic response of a damped oscillator depends on its natural period, which is independent of the vibration amplitude, and damping ratio. Attempts to represent a rigid block by a damped oscillator have been evaluated and found to be fundamentally flawed and numerically inaccurate [4, 12]. The period of a freestanding rigid block depends on its amplitude that is governed by two parameters: the size and slenderness of the rigid block. These two parameters are complimentary to each other in the sense that, to prevent overturning for a given excitation, the right combination of slenderness and size is required [5]. Therefore, scaling a block's size would alter its response unless the excitation is also scaled. The purpose of this study is to determine the appropriate scaling of the input motion that would result in the same response in the reference and candidate components. If the dimensionless responses of the reference and the candidate block (with respect to dimensionless time subject to their respective excitations) are the same, the block responses are said to be 'self-similar' [6]. The dimensionless rotation is the spatially normalized rotation (actual rotation θ divided by the slenderness angle α of a block; see Fig. 1), referred to as *normalized rotation* (or response) hereinafter. Similarly, the dimensionless time is the real time multiplied by the *frequency parameter* of the block, $p = \sqrt{3g/4R}$ (also known as the *size parameter*, the term used in this paper), and is referred to as *normalized time*

A. Dar (✉)
McMaster University, Hamilton, Canada
e-mail: dara@mcmaster.ca

Bruce Power Canada, Tiverton, Canada

D. Konstantinidis
Department of Civil and Environmental Engineering, University of California, Berkeley, USA

W. W. El-Dakhakhni
Department of Civil Engineering, School of Computational Science and Engineering, McMaster University, Hamilton, Canada

S. Walbridge et al. (eds.), *Proceedings of the Canadian Society of Civil Engineering Annual Conference 2021*, Lecture Notes in Civil Engineering 244,
https://doi.org/10.1007/978-981-19-0656-5_40

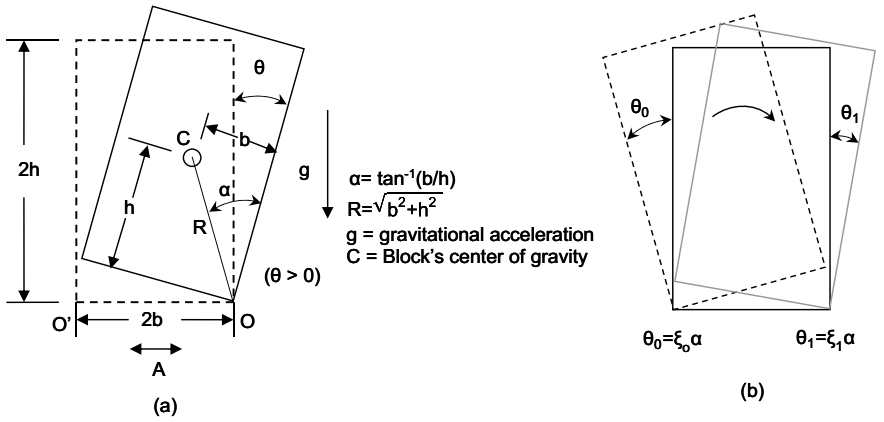

Fig. 1 **a** Schematic of a rocking block. **b** Pre and post impact rotations

hereinafter. R is the radius of the block (see Fig. 1). Dimitrakopoulos and DeJong [6] investigated the self-similarity in the responses of rocking blocks subjected to pulse excitations. Several other authors (e.g., [1, 7, 9, 11, 13, 14]) have used dimensional analysis in an effort to uncover self-similar responses. This study focuses on utilizing the concept of self-similarity for scaling the excitation to obtain the normalized response against normalized time of a scaled candidate block (the model) that would be equal to that of the full-size reference block (the prototype) subject to the unscaled excitation. The focus here is on obtaining the normalized response by varying the size and not the slenderness of the candidate block. Overturning is assumed to occur when normalized response is equal to or exceeds unity.

The simplest form of excitation is a rectangular pulse. For a block to uplift, the minimum amplitude of a rectangular pulse excitation is required to be tan(α)g. However, to sustain the response, the pulse must continue up to the time required to overturn the block. A rectangular pulse magnitude which is just above tan(α)g would require longer duration to overturn a large block but smaller duration to overturn a small block. Thus, slenderness governs the magnitude and size governs the time of the excitation required to overturn the block. This study utilizes this concept in determining the *spread* of spatially normalized excitation amplitudes over normalized and real time scales. The adjective "real" is used herein only to highlight its difference from normalized time. Sufficient friction is assumed at contact points, and sliding is not considered. The reader interested in the dynamics of a sliding-rocking block, including the effects of impact with and adjacent wall, is referred to Bao and Konstantinidis [2]. In nuclear power plants, the common range of the slenderness angle based on unanchored components that required seismic qualification (such as slender unreinforced masonry to stocky rigid scaffolds) varies from 0.2 to 0.6.

2 Review of Rocking Block

Figure 1(a) shows the schematic of a rocking block, experiencing positive rotation, subject to base acceleration, Yim et al. [15] presented the equations of motion of the rocking block as,

$$\ddot{\theta} = -p^2\left[\sin\{\alpha\ \mathrm{sgn}(\theta) - \theta\} + \frac{A}{g}\cos\{\alpha\ \mathrm{sgn}(\theta) - \theta\}\right] \tag{1}$$

sgn(.) denotes the signum function. Other parameters are as defined in Fig. 1. Damping due to impact is accounted for by modifying the post-impact velocity $\dot{\theta}_2$ by multiplying the pre-impact velocity $\dot{\theta}_1$ by the coefficient of restitution given by Housner [8]

$$e = 1 - \frac{3}{2}\sin^2\alpha \tag{2}$$

Figure 1(b) shows a rigid block under free vibration with initial rotation, $\theta_0 = \xi_0\alpha$, and the maximum rotation after the first impact, $\theta_1 = \xi_1\alpha$. The maximum rotation after the n^{th} impact was given by [8] as

$$\xi_n = 1 - \sqrt{1 - e^{2n}\left[1 - (1 - \xi_0)^2\right]} \tag{3}$$

It is noted that Housner [8] used the ratio of angular velocities squared to define a parameter r, which is equal to e^2. Therefore, the expression for obtaining the angular amplitude after the n^{th} impact in Housner [8] contains r^n and not r^{2n}. The period of free vibration was given by Housner [8] as

$$T_H = \frac{4}{p}\cosh^{-1}\left[\frac{1}{1 - \left(\frac{\theta_0}{\alpha}\right)}\right] \tag{4}$$

Overturning is defined when normalized rotation $\theta/\alpha = 1$, although it is known that the block may survive rotation beyond this limit [10, 16]. The numerical solution of Eq. 1, together with the constraint described by Eq. 2, is obtained by state space formulation, and referred to as *numerical* hereinafter.

3 Rocking Block Dynamics

3.1 Rocking Response of a Slender Block

Rewriting Eq. (1) for small α gives the following second order differential equation.

$$\ddot{\theta} = -p^2\left[\alpha\ \mathrm{sgn}(\theta) - \theta + \frac{A}{g}\right] \tag{5}$$

Dividing Eq. 5 by α gives

$$\ddot{\theta}_n = -p^2\left[\mathrm{sgn}(\theta_n) - \theta_n + \frac{A_n}{g}\right] \tag{6}$$

where, $\theta_n = \theta/\alpha$ is the normalized rotation of the block with respect to α, and $A_n = A/\alpha$ is the normalized excitation, A, as a function of real time.

3.1.1 Normalized Equation of Motion with Respect to Normalized Time

Considering the normalized time, t_N, as p t, the normalized rotation as a function of normalized time is expressed as $\theta_N = \theta_n(t_N)$. Differentiating θ_n with respect to t leads to, $\dot{\theta}_n = d\theta_n/dt = (d\theta_n/dt_N)(dt_N/dt)$. The derivative of θ_n with respective to t_N, is expressed as θ'_N. Hence, $\dot{\theta}_n = p\theta'_N$ and $\ddot{\theta}_n = p^2\theta''_N$. A_n with respect to t_N is A_N, meaning, A_N consists of the amplitudes of A_n plotted against normalized time which would appear to be stretched or compressed against real time. Rewriting Eq. 6 in terms of θ_N and A_N gives the size and slenderness normalized equation of motion as

$$\theta''_N = -\mathrm{sgn}(\theta_N) + \theta_N - \frac{A_N}{g} \tag{7}$$

The appearance of Eq. 7 can be misleading that it is independent of size and slenderness which it is not. As observed in the sequel, the spread of A_N would be on its original duration times the value of p being considered (Table 3).

Table 1 Example blocks considered in this study

Example number	Slenderness (α) (rad)	Size (p)* (1/s)	Radius (R) (mm)	Excitation
1	0.2	1/2	29420	Free vibration
2	0.2	1	7355	Free vibration
3	0.2	2	1839	Free vibration
4	0.2	3	817	Sine pulse
5	0.2	4	460	Sine pulse

*Sizes p = 1/2 and 1 are used for simplicity of numbers. Such sizes are not common to nuclear power plants but to other applications such as a bridge pier

Table 2 Sine pulse excitation

Pulse number	Frequency (ω_g) (rad)	Amplitude ($a_g/\alpha g$)
1	3	1.2
2	2	1.2

Table 3 Scaling of excitation frequencies

p (1/s)	Frequency (ω_g) (rad/s)	Scaled frequencies ω_{gsi}			Normalized frequency ($\omega_N = \omega_{gsi}/psi$)
		$p_{s1} = p/2$	$p_{s2} = p$	$p_{s3} = 2p$	
		$\omega_{gs1} = \omega_g/2$	$\omega_{gs2} = \omega_g$	$\omega_{gs3} = 2\omega_g$	
2	3	1.5	3	6	1.5
2	2	1	2	4	1

Table 4 Excitation scaling

Earthquake record	PGA (g)	Time interval Δt (s)	Scaled interval (Δt)		
			Reference p = 2/s	Candidate p = 1/s	Candidate p = 4/s
			$\Delta ts1 = \Delta t$ (s)	$\Delta ts1 = 2\Delta t$ (s)	$\Delta ts1 = \Delta t/2$ (s)
El Centro 1940 Array # 5	0.313	0.01	0.01	0.02	0.005
Northridge 1994 station 24,278	0.568	0.01	0.01	0.02	0.005
San Fernando PCD 164 station 279	1.226	0.01	0.01	0.02	0.005

3.2 Free-Vibration Response of Rocking Block

For free vibration, the block is lifted to an initial angle θ_0 and released. Defining, $\xi_0 = \theta(0)/\alpha$ and considering positive rotation ($sgn(\theta) = 1$) with respect to normalized time, $t_N = pt$, the solution of Eq. 7 is given as

$$\theta_N = -\xi_0 \cosh(t_N) + [1 - \cosh(t_N)] \tag{8}$$

Figure 2 shows the free vibration response for the first three slender block examples (Table 1) with $\alpha = 0.2$ and $p = 1/2$, 1 and 2 with the initial normalized rotation $\xi_0 = 0.99$. Here, $p = 1/s$ belongs to the reference block and the rest represent the candidate blocks. This initial normalized rotation leads to the subsequent maximum normalized rotations after the first and the second impact as $\xi_1 = 0.661$ and $\xi_2 = 0.535$ obtained from Eq. 3 [3]. Figure 2(a) shows the numerically obtained normalized response, θ_n, for a slender reference block with $p = 1$, for three initial normalized rotations: $\xi_0 = 0.99$, $\xi_1 = 0.661$ and $\xi_2 = 0.535$ against the time scale that is normalized by the period of the block given by Eq. 4. It is obvious that for every initial rotation, the block would attain zero rotation at the time equal to quarter of its period leading to $t/T_H = 0.25$ on the horizontal axis. The three curves in Fig. 2(a) represent the block's rotation before impact and after the first and the second impact. A combination of these in various orientations fits the curve in

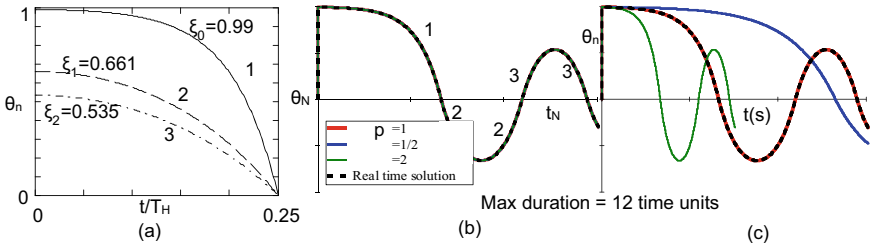

Fig. 2 Free vibration response of the first three blocks listed in Table 1 with p = 1/s representing the reference block: **a** Quarter-cycle response against real time normalized by Housner's period. **b** Normalized responses against normalized time $t_N = pt$ for three values of p **c** Responses against real time for three values of p for 12 s, and, the real time solution for = 1/s from Eq. 1

Fig. 2(b) which shows normalized rotation for the three values of p, against normalized time, t_N. Figure 2(c) depicts the same against real time, t. All responses coincide with each other, or *collapse* [6] to one curve in Fig. 2(b). As shown in Fig. 2(c), the reference block (p = 1/s) response remains the same whereas the other responses are either stretched or compressed on the time scale. Since $\alpha = 0.2$ for all cases, the coefficient of restitution (Eq. 2) remains the same for all cases. Also shown in Fig. 2(c) is the real time solution for p = 1/s, matching with the solution of Eq. 6 (for p = 1/s) plotted against real time.

3.2.1 Peak Normalized Rotation vs Normalized Time

The peaks and valleys of all response curves in Fig. 2(b) and (c) are equal in magnitude irrespective of their differences in p. Thus, the amplitudes of the candidate blocks (p = 1/2 and 2) are equal to those of the reference block despite being stretched or compressed on time scale. Nevertheless, the focus here is on normalized response amplitudes rather than their timing of occurrence and hence no information is lost or distorted.

3.3 Sine Pulse Excitation Response

Figure 3(a) presents the defining characteristics of a sine pulse excitation,

$$A(t) = -a_g \sin\left(\omega_g t + \Psi\right) \tag{9}$$

and Fig. 3(b) shows the two sine pulses from Table 2 and their summation Excitation scaling for two candidate blocks is presented below on the basis of the reference block. For scaling the half-sine pulse excitation, the reference block is chosen as

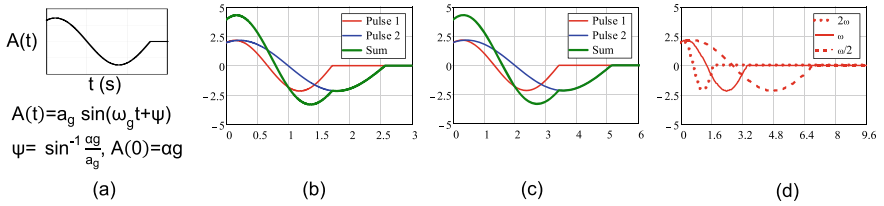

Fig. 3 Sine pulse details: **a** typical sine pulse parameters, **b** two sine pulses and their summation from Table 2 on real time, **c** on normalized time pt for p = 2/s, **d** Pulse 1 at three frequencies in proportion with the three values of p

example number 3 block in Table 1 with p = 2/s and α = 0.2. The response amplitudes of the candidate block are required to be the same as of the reference block by scaling the excitation. Thus, there are three size parameters p1 = ½ p, p2 = p and p3 = 2p. The ground excitation frequency ω_g, corresponding to the block with the size parameter, p, is scaled in the same proportion as p_i/p for the ith p. Table 2 shows the scaled ground frequencies corresponding ω_{gsi} to p_i. The normalized frequency $\omega_N = \omega_{gsi}/p_i$ is the same for all three cases.

Three responses are shown in each chart in Fig. 4 for p/2, p and 2p. The top and bottom rows show responses for the sine pulse excitations number 1 and 2 respectively from Table 2. The first column shows normalized response over real time and the

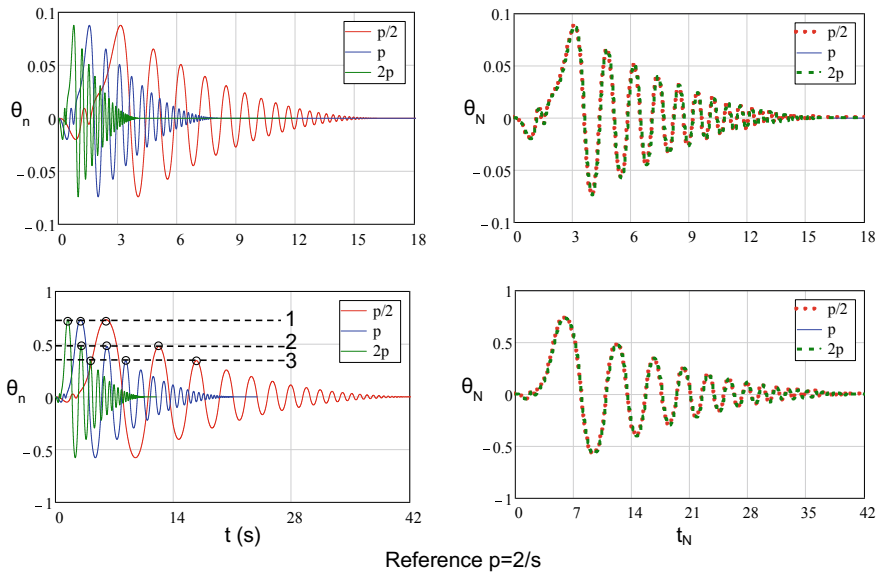

Fig. 4 Response to half sine-pulses from Table 2 for p/2, p and 2p with the reference p = 2/s. Top and bottom rows for sine pulse 1 sine pulse 2 (Table 2) respectively. Left and right columns: normalized response over normalized time on left and over real time on right

second column shows normalized response over normalized time. Similar to the observations in Fig. 2, the response amplitudes in each row are equal. A block's real response time gets stretched or compressed over the time axis, but its amplitudes remain the same as illustrated in the bottom row and first column of Fig. 2 where line 1 joins the first, line 2 the second and line 3 the third peaks of the individual response curves. This example demonstrates that the excitation frequency can be scaled in the same proportion as the candidate p and reference p in order to get the same normalized response that would be obtained for the reference block of size p.

3.4 Summation of Sine Pulses

Figure 3(c) shows that considering the normalized frequencies, $\omega_{Ni} = \omega_{gi}/p$, over normalized time, pt, of the two pulses would turn their summation into a function of normalized time, stretching or compressing for different values of p as the individual pulses. This means that stretching or compressing the time axis, the frequencies are automatically scaled. An earthquake record can be expressed in terms of the summation of orthogonal continuous harmonic functions. For scaling, all individual sine and cosine frequencies would be scaled in the same proportion, by the same value of p. Hence the entire record would be stretched or compressed on normalized time scale. This principle is applied in the next section to deal with earthquake records.

3.5 Scaling of Earthquake Records

Extending the observations for pulse excitation to earthquake excitation, the time interval of the earthquake record for the candidate component can be scaled by a factor given by the ratio of the reference component p value and the candidate component p value. The time interval will be decreased if the candidate p is larger (i.e., smaller block) than that of the reference p, and vice versa. This concept is demonstrated with the help of Fig. 5 and Table 4.

Time interval of the three earthquake records considered in the analysis, El Centro 1940 (Array #9, 180) Northridge 1994 (090 CDMG station 24,278), and San Fernando 1971 PCD 164 is 0.01 s. The reference block's size parameter, $p = 2/s$. It is desired to scale the records for the candidate blocks with size parameters, p/2 and 2p. For the candidate size p/2, the time interval is doubled to 0.02 s, stretching the entire record to twice its duration. Similarly, for the candidate size 2p, the time interval is reduced to 0.005 s, reducing its duration to half. Table 4 lists these details along with the peak ground accelerations (PGA) of all records. Again, appropriate scaling of the time interval causes the responses to collapse to a single response history.

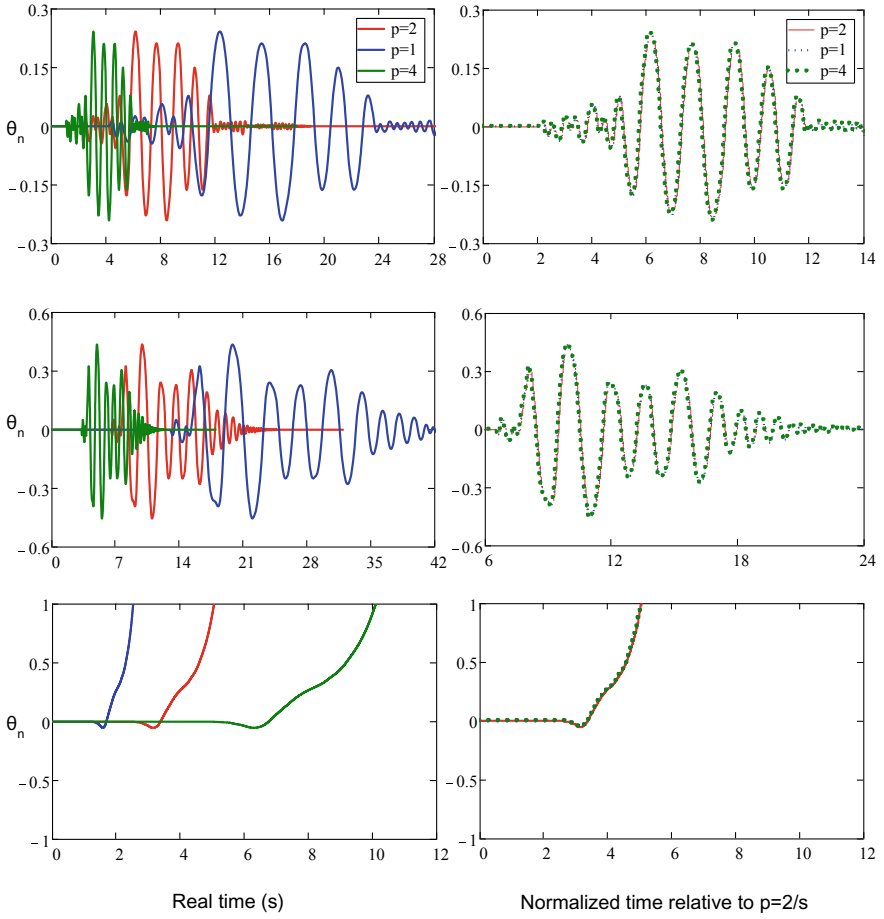

Fig. 5 Scaled earthquake records responses of the reference block (p = 2/s) and the candidate blocks with size parameters p/2 and 2p. Top row: El Centro Array #9, 180. Middle Row: Northridge 1994 090 CDMG station 24,278. Bottom row: San Fernando PCD 164

4 Conclusions

From this study, it is concluded that the excitation time history resulting in the same response of the candidate block as of the reference block to the real time history can be obtained by scaling the excitation time history of the reference block by stretching or compressing the time axis in proportion to the ratio of the size parameters of the two blocks. For an earthquake record, the time interval or the time step can be scaled depending on the ratio of the size parameters of the reference and the candidate block and numerical solution can be obtained over the normalized time. In simple words, for two blocks with the same slenderness, slower excitation of a large block would

produce the same normalized response (θ/α) as of a smaller block subjected to faster excitation.

The normalized response amplitudes of two blocks having same slenderness but different sizes remain the same over real time but their timing of occurrence becomes different. Nevertheless, the focus is on the normalized response amplitudes of a block rather than their timing of occurrence. In other words, the focus of the study is to know if a block would overturn when subjected to a particular excitation rather than its timing of overturning. This concept can be used to appropriately scale the time axis in shake table evaluations of scaled-down models of prototype (reference) components. Suitability of such time histories in accordance with the applicable standards is a subject of further research and is beyond the scope of this study.

References

1. Bachmann JA, Vassiliou MF, Stojadinović B (2017) Dynamics of rocking podium structures. Earthq Eng Struct Dyn https://doi.org/10.1002/eqe.2915
2. Bao Y, Konstantinidis D (2020) Dynamics of a sliding-rocking block considering impact with an adjacent wall. Earthq Eng Struct Dyn 5:498–523
3. Dar A, Konstantinidis D, El-Dakhakhni WW (2015) Shortcomings of the ASCE 43-05 approximate method for estimating the seismic demands on rocking objects in Canadian nuclear power plants. In: The 11th Canadian conference on earthquake engineering. Canadian Association for Earthquake Engineering, Victoria
4. Dar A, Konstantinidis D, El-Dakhakhni WW (2016) Evaluation of ASCE 43-05 seismic design criteria for rocking objects in nuclear facilities. J Struct Eng https://doi.org/10.1061/(ASCE)ST.1943-541X.0001581
5. Dar A, Konstantinidis D, El-Dakhakhni WW (2018) Seismic response of rocking frames with top support eccentricity. Earthq Eng Struct Dyn 47(12):2496–2518. https://doi.org/10.1002/eqe.3096
6. Dimitrakopoulos EG, DeJong MJ (2012) Revisiting the rocking block: closed-form solutions and similarity laws. The Royal Society Publishing. http://rspa.royalsocietypublishing.org/content/468/2144/2294. Accessed 8 May 2018
7. Dimitrakopoulos E, Paraskeva TS (2015) Dimensionless fragility curves for rocking response to near-fault excitations. Earthq Eng Struct Dyn 44(12):2015–2033
8. Housner GW (1963) The behavior of inverted pendulum structures during earthquakes. Bull Seismol Soc Am 53(2):403–417
9. Konstantinidis D, Makris N (2009) Experimental and analytical studies on the response of freestanding laboratory equipment to earthquake shaking. Earthq Eng Struct Dyn 38(6):827–848
10. Linde SA, Konstantinidis D, Tait MJ (2020) Rocking response of unanchored building contents considering horizontal and vertical excitation. J Struct Eng 146(9):04020175
11. Makris N, Kampas G (2016) Size versus slenderness: two competing parameters in the seismic stability of free-standing rocking columns. Bull Seismol Soc Am 106(1):104–122
12. Makris N, Konstantinidis D (2003) The rocking spectrum and the limitations of practical design methodologies. Earthq Eng Struct Dyn 32(2):265–289
13. Makris N, Vassiliou M (2012) Sizing the slenderness of free-standing rocking columns to withstand earthquake shaking. Arch Appl Mech 82(10):1497–1511
14. Voyagaki E, Psycharis IN, Mylonakis G (2013) Rocking response and overturning criteria for free standing rigid blocks. Soil Dyn Earthq Eng 46:85–95

15. Yim CK, Chopra A, Penzien J (1980) Rocking response of rigid blocks to earthquakes. Earthq Eng Struct Dyn 8(6):565–587
16. Zhang J, Makris N (2001) Rocking response of free-standing blocks under cycloidal pulses. J Eng Mech (ASCE) 127(5):473–483

Improving Wind Performance of Structural Systems of Tall Buildings Using Topology Modifications

Magdy Alanani and Ahmed Elshaer

1 Introduction

Nowadays, about 60% of the consumption of worldwide resources is related to the Construction industry [21]. According to the Organization for Economic Co-operation and Development (OCED), an intergovernmental economic organization, increasing world's demand for construction materials coupled with an increase in the world's population imposes a risk that providing the required amount of construction materials per capita will be impossible using the current design and construction methodologies. Moreover, the Construction industry is responsible for 28% of operational carbon emissions and 11% related to the materials and construction process with an overall 39% of global energy-related carbon emissions [25]. These facts are an alert to reduce carbon emissions to avoid exceeding the earth's remaining carbon budget. Consequently, it becomes a crucial objective for structural designers to provide more optimized and cost-effective structures while maintaining the balance between aesthetics, serviceability, and safety of structures [2]. While the world's urban cities are growing up with the aid of the latest technologies, these technologies push tall buildings to their limits. Tall buildings mainly depend on lateral load resisting systems (LLRS) (i.e. shear walls, cores, and bracing systems) to withstand earthquakes and wind loadings. Whilst a minor change in their layout, size, or shape will affect the cost tremendously.

Originally, a methodology was developed to get frames with the minimum amount of materials to resist certain elementary systems of forces using Maxwell's Theorem of virtual work [16]. This methodology got developed in a more rational way to include a discrete finite number of bars taking into consideration the structural weight of bars and joints [19].

M. Alanani · A. Elshaer (✉)
Civil Engineering Department, Lakehead University, Thunder Bay, ON, Canada
e-mail: aelshaer@lakeheadu.ca

S. Walbridge et al. (eds.), *Proceedings of the Canadian Society of Civil Engineering Annual Conference 2021*, Lecture Notes in Civil Engineering 244,
https://doi.org/10.1007/978-981-19-0656-5_41

Structural wind optimization can generally be categorized into (i) outer shape optimization and (ii) structural system optimization. As for outer shape modifications**,** it aims to increase the aerodynamic performance of structures against wind. Besides the architectural perspective of the outer shape of buildings, changing the outer shape has a significant impact on the attracted wind loads through the aerodynamic behaviour of the building [3, 4, 8, 9, 12]. On the other hand, structural system optimization is to find the optimal structural system layout within a group of constraints. In the last decades, there are many research work has been done on the topology optimization of the LLRS. Most of the literature tackled the optimization either from an architectural perspective or from a structural one. Architectural optimization focuses on spaces and accessibility of floors and rooms [13, 20]. While most of the previous structural optimization research focuses on the vertical layout of the LLRS. For example, topology and element size optimization was applied on the braced systems using hybrid algorithms of optimality criteria and genetic algorithms [5]. [11] used a new metaheuristic algorithm named "Center of masses" to apply topology optimization on steel bracing systems. [14] tried to allocate outriggers within tall buildings using topology optimization. [15] developed a mathematical gradient approach that allocates optimal bracing systems on a pre-existed frames. Unlike the latter discrete approach, a continuous topology optimization approach was applied to find the optimal placement of bracing systems. [22] experimented pattern gradation with topology optimization, and it achieved a good balance between aesthetics and structural requirements. Moreover, various applications of structural topology optimization on tall structures have been introduced using the solid isotropic material with penalization (SIMP) [18, 24].

Not only altering the vertical layout of LLRS is the only way to optimize tall structures against various lateral loading conditions, but also changing the location of the LLRS within the structure domain can affect the overall structural performance. For instance, a group of predefined shapes (e.g. T, Z, and L) have been investigated to find the optimal placement for reinforced concrete shear walls within an asymmetric plan against seismic loading [1]. These predefined shapes will yield a better-performing solution to a certain limit bounded by these shapes. [26] developed a computational method to find the optimal shear wall location within an architectural layout with more flexible shape formations. However, Complex architectural consideration can be a barrier against reaching the targeted solutions. [23] proposed applying a new metaheuristic algorithm to satisfy a group of structural requirements within the design process (e.g. structural behaviour: flexural and shear resistance) and a group of architectural requirements (e.g. openings). The accessibility constraints within this algorithm still face problems with the complex architecture plans. It also did not consider the changes of the shear wall cross-section along the building's height, besides assessing the shear wall performance using sectional analysis.

In the current study, a 20-stories building's wind performance is assessed against the shear walls' location alteration within architectural constraints using the Finite Element Method. Four different scenarios are proposed in order to check the efficiency of altering the LLRS location within the building's layout while using the same amount of materials and the same LLRS's orientation. This assessment is

trying to enhance the applicability and the practicality of choosing the LLRS location according to the best structural performance.

2 Case Study

A multistory residential building of 20 floors, each of 3.5 m height, is adopted in this study. A single symmetric benchmark layout of rectangular-shaped flat slabs with dimensions of 24.75 × 18.75 m is used. A superimposed dead load of 5 kN/m^2 and a live load of 1.9 kN/m^2 are applied to all slabs. The layout is designed according to the Canadian Standards Association CSA 23.3-14 [6] using concrete of $f_c' =$ 35 MPa and steel reinforcement ASTM992 of grade 50. The ultimate limit state and serviceability limit load combinations are used for designing structural elements. The selected building is designed to resist a mean-hourly wind velocity pressure, q, of 0.39 kPa, importance factor, I, of 1, and topographic factor, C_g of 1. The terrain is considered open terrain with no topology effect. As shown in Fig. 1, twelve shear walls are arranged through the plan with equal distribution of stiffness in both X and Y directions. The center of mass and center of rigidity are chosen to coincide through the arrangement of the shear walls to minimize induced torsion. Six shear walls are oriented vertically while the remaining six shear walls are oriented horizontally. Each shear wall segment is of 3000 mm length and 300 mm thickness as illustrated in Fig. 2 (a). Each floor is supported by 14 columns of 750 × 750 mm cross-section dimensions and 2.5% steel reinforcement, as shown in Fig. 2(b). The finite element method analysis is performed using ETABS [7].

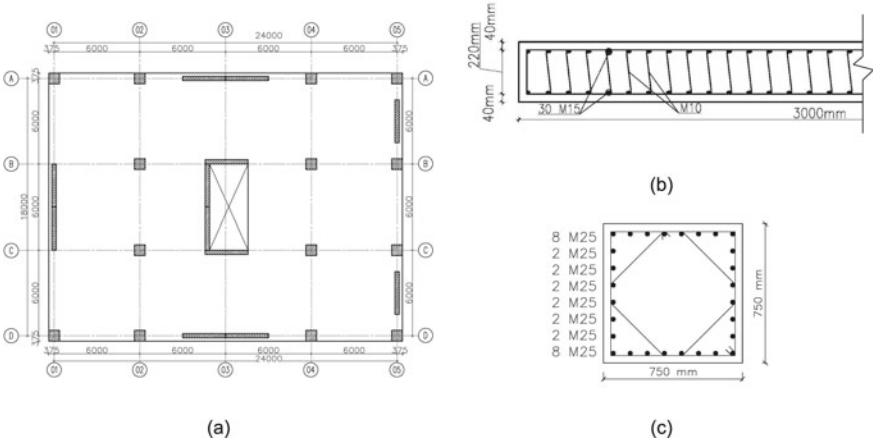

Fig. 1 **a** Benchmark plan layout, Concrete dimensions, and reinforcement detailing for cross-sections of **b** Shear wall segment and **c** Column

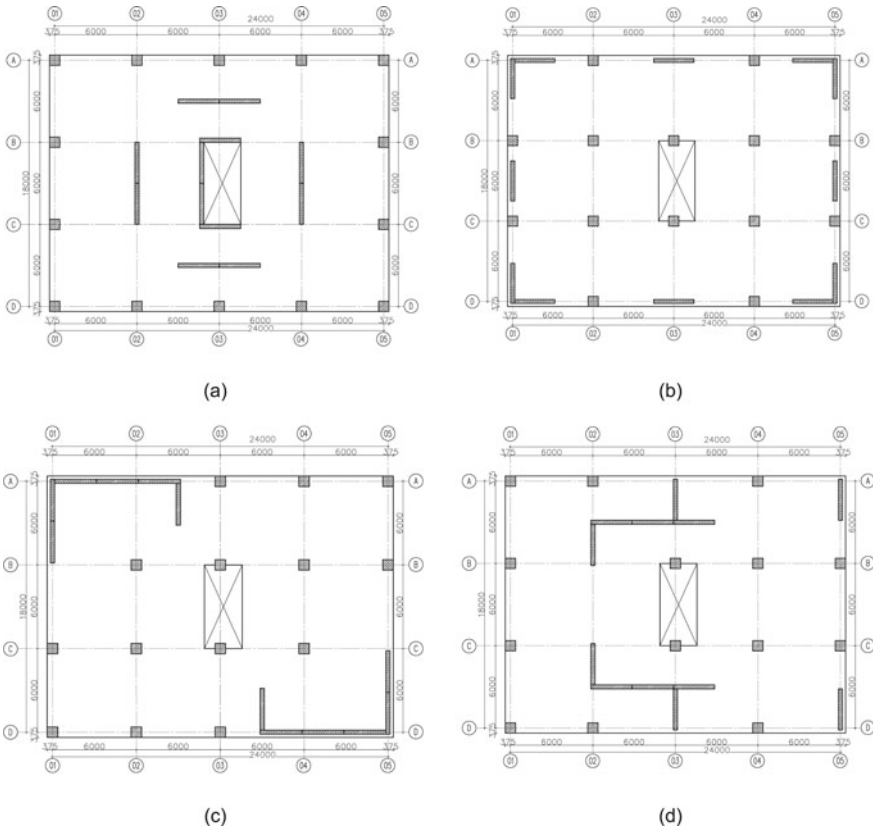

Fig. 2 Structural plan view of **a** Scenario 1, **b** Scenario 2, **c** Scenario 3, and **d** Scenario 4

In order to assess the effect of shear walls' location alteration around the plan, 4 different scenarios of the predesigned benchmark structure are proposed with various layout scenarios of the LLRS as shown in Fig. 2. All scenarios have the same amount of materials used in the first benchmark structure by maintaining the predefined reinforced concrete dimensions and steel reinforcement ratios. Also, the same number of columns, shear walls, reinforcement bars, and slabs are maintained.

3 Results and Discussion

In this section, inter-story drift, base moment, base shear, and torsional effect will be assessed for the 4 scenarios along with the benchmark to examine the effect of alteration in the shear wall distribution.

3.1 Inter-story Drift and Top Deflection

The inter-story drift and top deflection displacement are considered effective parameters that affect the design process to ensure the serviceability of the building through various lateral loading cases. According to the NBCC, the total allowable drift per story against wind and gravity loading shall not exceed 1/500 [17]. Although the benchmark building is designed to satisfy that limit, the four proposed scenarios show different behaviors either by exceeding this limit or by being conservatively safe. Figure 3 and Fig. 4 show the maximum story drift and displacement in X-direction and Y-direction, respectively. It can be noticed that Scenario 3 shows great efficiency in resisting the wind effect in X-direction by reducing the maximum story drift by 83% compared to the benchmark. On the other hand, Scenario 2 increased the story drift by 43%, which exceeds the allowable drift according to the NBCC. While in Y-direction, Scenario 3 has failed to satisfy the maximum allowable drift in the Y-axis direction due to the reduced stiffness compared to the larger windward and leeward faces. Although Scenario 1 has the least reduction in story drift in the X-direction by 18%, compared to Scenario 3 and Scenario 4, it is the only scenario that satisfies the limit in the Y-direction.

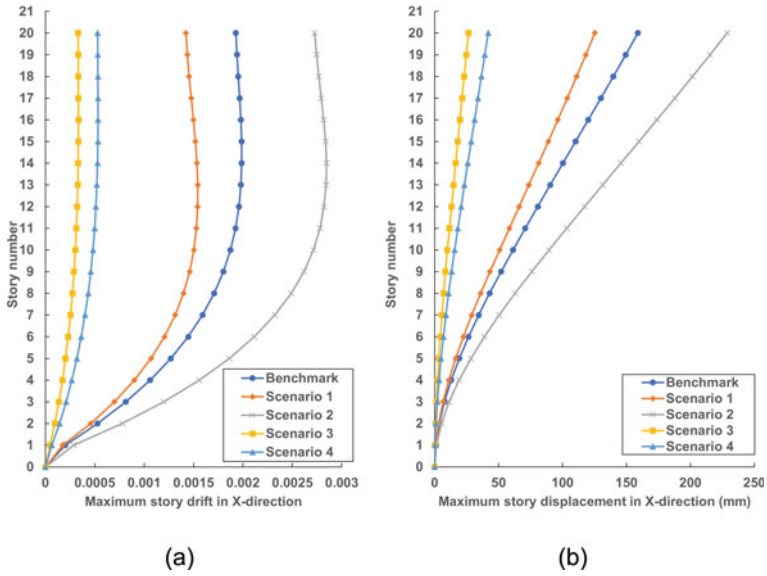

Fig. 3 **a** Maximum story drift, and **b** maximum story displacement in X-direction due to wind loading

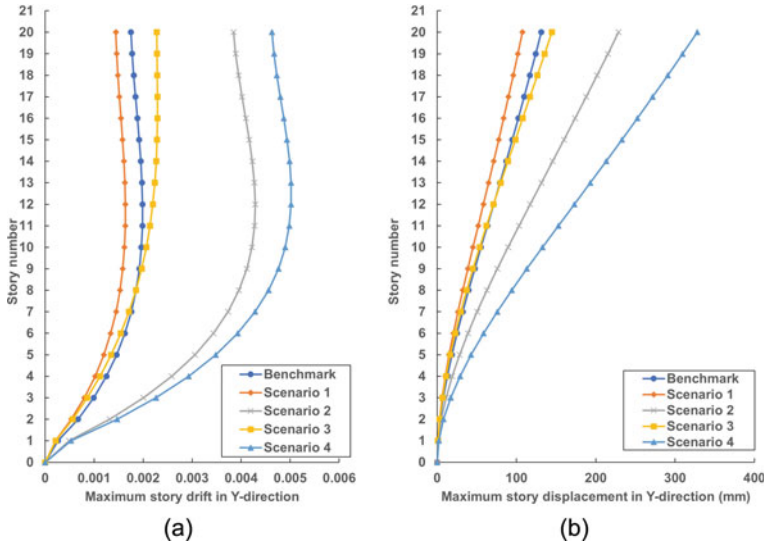

Fig. 4 **a** Maximum story drift, and **b** maximum story displacement in Y-direction due to wind loading

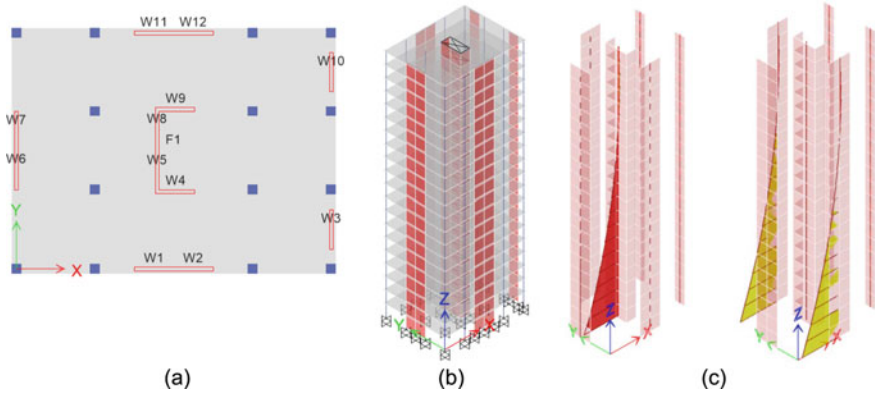

Fig. 5 **a** typical floor with shear wall labels, **b** 3D view of the structure, and **c** the bending moment diagram against wind loads in X-direction of the benchmark model

3.2 Base Moment and Shear

The total internal forces induced at the base level are all equal due to the consistency of the number of structural elements used. However, each shear wall segment (i.e., 3.0 × 0.3 m) sustained a different share of these straining actions based on their orientation and location within the building as shown in Fig. 5. Table 1 shows the bending moments' standard deviation at the base level, per each shear wall segment,

Table 1 Bending moment standard deviation values at the base level

Scenario	Bending moment mean values (KN.m)	Standard deviation (KN.m)	Maximum flexural demand/Capacity (D/C)
Benchmark	3855.95	3932.62	0.887
1	3371.98	3432.36	0.849
2	3711.34	1767.24	2.609
3	4832.35	0.73	0.816
4	4638.91	2161.98	1.278

in addition to the maximum demand-to-capacity (D/C) ratios for all scenarios. It can be noticed that Scenario 3 induced the highest mean for the bending moment per segment with the lowest standard deviation, which is attributed to the fact that all shear wall segments are connected to form a higher stiffness LLRS. This scenario has an almost equal distribution of bending moment all over the shear wall segments. The noticeable variabilities in the straining action for each shear wall segment indicated the possibility of decreasing the governing D/C for the LLRS by altering their location and orientation. The maximum D/C ratio of Scenario 3, lowest story drift in X-direction, is decreased by 9% compared to the benchmark scenario, which can result in a possible saving in the reinforcing steel if the structure is redesigned. Furthermore, Scenario 1, which satisfies drift limitations in X and Y directions, reduced the D/C ratio by 5%.

3.3 Torsional Effect

The distance between the center of rigidity (C_R) and the center of mass (C_M) for the floor is a function in the shear walls' layout, which indicates the expected torsional effect on the LLRS. Figure 6 displays the eccentricity in the X-direction (E_x) only, as C_R and C_M are coincide in the Y-direction due to symmetry. It has been taken into consideration to propose significant variations in the shear walls' layout to get different eccentricities. It can be noticed that, Scenario 4 has the largest E_x, while Scenario 2 has the smallest E_x, due to symmetric shear walls in both X and Y directions.

Table 2 shows the mass participation ratio for each scenario in X-direction (UX), Y-direction (UY), and the torsional rotation around Z-axis (RZ). Scenario 4, with the highest eccentricity, is the only scenario that showed torsional contribution in the first mode shape. A torsional mode shape is found to occur in the second mode of the benchmark, Scenario 1 and Scenario 4. As for the benchmark, E_x has a significant value of 1.7 m. For Scenario 1, the concentration of rigidity in the middle of the plan resulted in weaker peripherals, which induces a higher torsional mode, while in Scenario 4, the rigidity of the LLRS is shifted from the C_M of the structural causing a torsional mode in the second mode. On the third mode shape, Scenarios with smaller

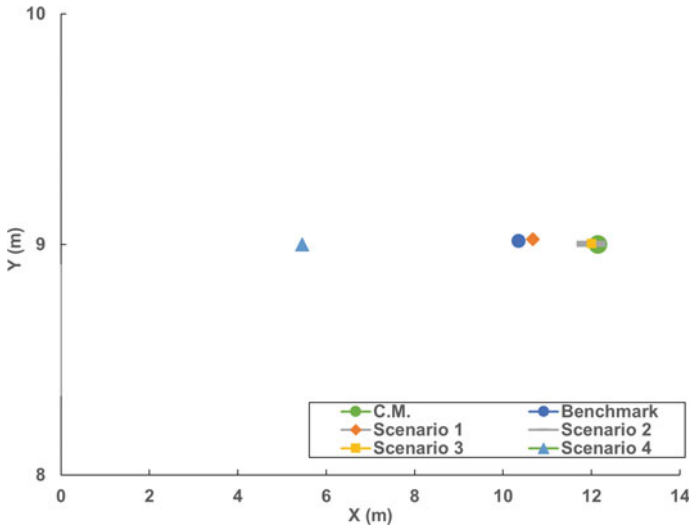

Fig. 6 Distance between the center of rigidity (C_R) and the center of mass (C_M)

Table 2 Mass participation ratio for all scenarios

	Benchmark			Scenario 1			Scenario 2			Scenario 3			Scenario 4		
Mode	UX	UY	RZ	UX	UY	RZ	UX	UY	RZ	UX	UY	RZ	UX	UY	RZ
1	0.65	0.00	0.00	0.65	0.00	0.00	0.65	0.00	0.00	0.02	0.62	0.00	0.00	0.59	0.07
2	0.00	0.34	0.32	0.00	0.05	0.63	0.00	0.66	0.00	0.62	0.02	0.00	0.00	0.06	0.59
3	0.00	0.31	0.34	0.00	0.61	0.05	0.00	0.00	0.65	0.00	0.00	0.65	0.64	0.00	0.00
4	0.18	0.00	0.00	0.00	0.01	0.15	0.00	0.17	0.00	0.01	0.19	0.00	0.00	0.15	0.02
5	0.00	0.07	0.09	0.17	0.00	0.00	0.18	0.00	0.00	0.20	0.01	0.00	0.00	0.02	0.17
6	0.00	0.11	0.08	0.00	0.17	0.01	0.00	0.00	0.17	0.00	0.07	0.00	0.20	0.00	0.00

eccentricities (i.e. Scenario 2 and Scenario 3) start to show mass participation in torsional rotation around Z.

4 Conclusion

A parametric study was performed using three-dimensional Finite Element Analysis to assess the efficiency of altering the location of shear walls across a multistory building. Four different scenarios are proposed for a typically designed benchmark tall building. Scenario 1 was found to be better performing compared to the other four scenarios, which satisfied all the design requirements and limitations without changing elements dimensions or reinforcement ratio reducing the maximum story

drift by 18% and the Demand-to-capacity ratio by 9%. Scenario 3 showed a noticeable potential to reduce the used amount of materials but it has to be redesigned and the dimensions should be changed. Through the design process, numerous iterations can be done to reach a satisfactory solution that complies with structural and architectural requirements. Experienced engineers are required to apply an effective trial and error that will converge to an optimum solution. Furthermore, these solutions cannot be guaranteed to fit the most optimum solution for the governing constraints and parameters. Consequently, a multi-objective optimization framework should be proposed to find the optimal location and orientation of shear wall segments within the building's layout. In order to get the most optimum configuration, an automated procedure should be used that can fit structural and architectural requirements.

References

1. Aminnia M, Hosseini M (2015) The effects of placement and cross-section shape of shear walls in multi-story RC buildings with plan irregularity on their seismic behavior by using nonlinear time history analyses. Int J Civ Environ Eng 9(10):1327–1334
2. Beghini LL, Beghini A, Katz N, Baker WF, Paulino GH (2014) Connecting architecture and engineering through structural topology optimization. Eng Struct 59:716–726
3. Bernardini E, Spence SMJ, Wei D, Kareem A (2015) Aerodynamic shape optimization of civil structures: a CFD-enabled kriging-based approach. J Wind Eng Ind Aerodyn 144:154–164
4. Bobby S, Spence SMJ, Bernardini E, Kareem A (2014) Performance-based topology optimization for wind-excited tall buildings: a framework. Eng Struct 74:242–255. https://doi.org/10.1016/j.engstruct.2014.05.043
5. Chan CM, Wong KM (2008) Structural topology and element sizing design optimisation of tall steel frameworks using a hybrid OC-GA method. Struct Multidiscip Optim 35(5):473–488
6. CSA (2014) Design of concrete structures. 23.3-14. CSA Group
7. CSI (2018) ETABS. CSI
8. Elshaer A, Bitsuamlak G, El Damatty A (2017) Enhancing wind performance of tall buildings using corner aerodynamic optimization. Eng Struct 136:133–148. https://doi.org/10.1016/j.engstruct.2017.01.019
9. Elshaer A, Bitsuamlak G (2018) Multiobjective aerodynamic optimization of tall building openings for wind-induced load reduction. J Struct Eng 144(10):04018198
10. Elshaer A, Bitsuamlak G, El-Damatty A (2014) Wind load reductions due to building corner modifications. In: 22nd Annual Conference of the CFD Society of Canada, pp 1–5
11. Gholizadeh S, Ebadijalal M (2018) Performance based discrete topology optimization of steel braced frames by a new metaheuristic. Adv Eng Softw 123:77–92. https://doi.org/10.1016/j.advengsoft.2018.06.002
12. Kareem A, Spence SMJ, Bernardini E, Bobby S, Wei D (2013) Using computational fluid dynamics to optimize tall building design. Council of Tall Buildings and Urban Habitat
13. Lai H-J (1988) Contractions and Hamiltonian line graphs. J Graph Theory 12(1):11–15. https://doi.org/10.1002/jgt.3190120103
14. Lee S, Tovar A (2014) Outrigger placement in tall buildings using topology optimization. Eng Struct 74:122–129. https://doi.org/10.1016/j.engstruct.2014.05.019
15. Lu H, Gilbert M, Tyas A (2018) Theoretically optimal bracing for pre-existing building frames. Struct Multidiscip Optim 58(2):677–686. https://doi.org/10.1007/s00158-018-1921-7
16. Michell AGM (1904) LVIII. The limits of economy of material in frame-structures. Lond Edinb Dublin Philos Mag J Sci 8(47):589–597. https://doi.org/10.1080/14786440409463229

17. National Building Code of Canada (2015) Canadian Commission on Building and Fire Codes National Research Council of Canada
18. Nicolaou A, Tsavdaridis KD (2017) Topology optimisation study for the design of lattice towers. In: 9th Hellenic National Conference of Steel Structures, October 2017
19. Prager W (1977) Optimal layout of cantilever trusses. J Optim Theory Appl 23(1):111–117. https://doi.org/10.1007/BF00932301
20. Shekhawat K (2014) Algorithm for constructing an optimally connected rectangular floor plan. Front Archit Res 3(3):324–330. https://doi.org/10.1016/j.foar.2013.12.003
21. Sobek W (2014) Gebäudehüllen - Wie Weiter?[Building envelopes – What now?]. Bautechnik 91(7):506–517. https://doi.org/10.1002/bate.201400038
22. Stromberg LL, Beghini A, Baker WF, Paulino GH (2011) Application of layout and topology optimization using pattern gradation for the conceptual design of buildings. Struct Multidiscip Optim 43(2):165–180
23. Talatahari S, Rabiei M (2020) Shear wall layout optimization of tall buildings using quantum charged system search. Front Struct Civ Eng 14(5):1131–1151. https://doi.org/10.1007/s11709-020-0660-1
24. Tsavdaridis KD (2015) Applications of topology optimization in structural engineering: high-rise buildings and steel components. Jordan J Civ Eng 9(3):335–357. https://doi.org/10.14525/jjce.9.3.3076
25. WGBC (2019) Embodied carbon call to action report|World Green Building Council
26. Zhang Yu, Mueller C (2017) Shear wall layout optimization for conceptual design of tall buildings. Eng Struct 140:225–240. https://doi.org/10.1016/j.engstruct.2017.02.059

Shear Buckling Testing of Wood Sheathing Panels

M. Niazi, A. A. El Damatty, and A. Hamada

1 Introduction

Oriented strand board (OSB) and Plywood wood sheathing panels have a significant contribution to the lateral stiffness of light-framed wood buildings. Light-framed shear walls consist of wood sheathing panels nailed to walls studs, chords, and top and bottom wall plates, where the wood sheathing panel is responsible for resisting shear force. The sheathing panel in Light-Framed Wood Shear walls is stiff in in-plane deformation. The typical size of the sheathing panels in the construction industry is 1220×2440 mm and panels are connected to studs, chords, top and bottom plates by nails. One of the typical failure modes of shear wall segments under lateral loads is the excessive out-of-plane deformation (shear buckling) of sheathing panels where the nail-based connections do not reach their ultimate capacity. The literature contains a lot of analytical and numerical research on the stability of rectangular isotropic and orthotropic plates with different boundary conditions [1, 2, 9, 15–18, 21]. However, the experimental research on this topic is limited. The early experimental research on buckling strength of orthotropic plates with simply and fix supported boundaries under compression loads was conducted to verify the usual buckling theories and made some design recommendations [6]. The authors concluded that the theoretical equation to estimate the linear buckling of the plywood in compression was conservative and adequate for design purposes and further proposed a similar equation with the same analogy to calculate the shear buckling strength of such plates. The shear buckling of plywood panel with 1220×1220 mm and 610×1220 mm dimensions subjected to diagonal compression force was also carried out to determine the shear resistance of a typical farm diaphragm segment [20]. The authors reported the shear buckling strength was a limiting factor in diaphragm design in many typical

M. Niazi · A. A. El Damatty (✉)
University of Western Ontario, London, Canada
e-mail: damatty@uwo.ca

A. Hamada
Intelligent Engineering Design (IE Design), London, Canada

S. Walbridge et al. (eds.), *Proceedings of the Canadian Society of Civil Engineering Annual Conference 2021*, Lecture Notes in Civil Engineering 244,
https://doi.org/10.1007/978-981-19-0656-5_42

farm buildings. Another experiment was conducted by [12] to identify shear stress distribution and shear characteristics of wooden glued thin square shape of plywood panels (<5.5 mm).

The current Canadian wood design standard [4] presents an equation based on design recommendations was done by [6] to determine the critical shear force per unit length for a sheathing panel with simply supported boundaries along all edges with the assumption that the sheathing panel experiences uniform shear stress along all edges. The shear buckling strength of any panel depends on its boundary conditions. As discussed above, the sheathing panels in the wood shear walls are connected through spaced nails (nonlinear springs) to the frame and may not reflect simply supported boundary conditions. The objective of the research is to design a frame to conduct the experimental research on shear buckling of sheathing panels with real boundary conditions and to verify that the sheathing panels with intermittent nail supports subjected to pure shear follow the usual buckling theories. In this paper, a brief shear buckling equation background is described, followed by presenting the real boundary conditions of wood sheathing panels and a description of the test setup to evaluate the shear buckling strength of such panels. A discussion of test results and calculated code equation values is then presented.

2 CSA O86 Wood Sheathing Buckling Equation

The wooden sheathing panels, such as Oriented Strand Board (OSB) or plywood, are thin plates that are subjected to stability failure (buckling) under applied shear loads. The Engineering design in wood standard [4] assumes sheathing panels to behave like an orthotropic linear elastic material. The plate-bending theory as the basis of elastic plate stability has been discussed by many researchers. The general differential equation form for an orthotropic plate based on Saint [13] and [19] is as follows:

$$N_x \frac{\partial^4 w}{\partial x^4} + 2N_{xy} \frac{2\partial^4 w}{\partial x^2 \partial y^2} + N_y \frac{\partial^4 w}{\partial y^4} = q - t\sigma_x \frac{\partial^2 w}{\partial x^2} - t\sigma_y \frac{\partial^2 w}{\partial y^2} + 2t\tau_{xy} \frac{\partial^2 w}{\partial x \partial y} \quad (1)$$

Where w is the out-of-plane deflection of the plate, t is the plate thickness, $N_x = \frac{E_x t^3}{12(1-v_x v_y)}$ is the flexural stiffness for bending about the Y-axis, $N_y = \frac{E_y t^3}{12(1-v_x v_y)}$ is the flexural stiffness for bending about the X-axis, $N_{xy} = \frac{1}{2}\left(v_x N_y + v_y N_x\right) + 2\frac{Gt^3}{12}$ is the torsional rigidity, q is the uniform distributed out-of-plane load of intensity, σ_x and σ_y are the uniform normal stresses in two directions and along the edges, and τ_{xy} is the uniform shear stress along the edges.

The out-of-plane deflections normally occur due to out-of-plane loadings. When edge loads (compression and shear forces) act on a plate, it can be shown that the effect of such edge loads is to increase the out-of-plane deflections and by increasing the edge loads until the plate reaches instabilities. The lowest value of edge forces that

lead to instabilities is the elastic critical load (critical buckling load). Boundary conditions of plate edges significantly affect the value of this critical buckling load. Such critical load can be evaluated using different methods such as integration of differential equation, energy solutions, Galerkin's methods, and Lagrangian multiplier methods to solve for the equilibrium of the differential equation 1 [3].

[14] first derived the exact solution for long orthotropic plates with simply supported edges, loaded with uniform shear stress in the form of Eq. 2:

$$\tau_{cr} = K\frac{4\pi^2}{b^2 t}\sqrt[4]{N_x N_y^3} \tag{2}$$

And it can be found with $v_x = v_y = 0$ this becomes:

$$\tau_{cr} = K\frac{\pi^2 t^2}{3b^2}\sqrt[4]{E_x E_y^3} \tag{3}$$

Values of K can be obtained from the graph called "wrinkles" curves (provided by [6]–Fig. 29) based on the plate dimension ratio $\alpha_v = \frac{a}{b}\sqrt[4]{\frac{E_y}{E_x}}$ and stiffness coefficient $\eta = \frac{2G}{\sqrt{E_x E_y}}$.

[4] presents Eq. 4 based on [14] equation derivation to calculate the critical buckling shear force per unit length:

$$v_{pb} = k_{pb}\frac{\pi^2 t^2}{3000b}\sqrt[4]{B_{a,0} B_{a,90}^3} \tag{4}$$

Where k_{pb} = panel buckling factor and is a function of panel dimensions and material properties of the panel, which can be calculated as follows:

$$k_{pb} = 1.7(\eta + 1)\exp\left(\frac{-\alpha}{0.05\eta + 0.75}\right) + (0.5\eta + 0.8) \tag{5}$$

Where

$$\alpha = \frac{a}{b}\sqrt[4]{\frac{B_{a,90}}{B_{a,0}}}$$

$$\eta = \frac{2B_v}{\sqrt{B_{a,0} B_{a,90}}}$$

Where t is the sheathing thickness, mm, a is the larger dimension of the panel, mm, b is the smaller dimension of the panel, mm, B_a is the axial stiffness of panel 0 and 90 orientation, N/mm, and B_v is the shear through-thickness rigidity, N/mm.

3 Description of Test Setup

Figure 1 shows the real boundary conditions of a wood shear wall segment which includes a typical sheathing panel (1220 × 2440 mm) connected to the studs and chords using common nails at all edges. The frame consists of a number of vertical studs and two horizontal studs and those are connected through nail base connections. Based on literature and code equations, nail slippage at connection sheathing and studs behaves nonlinearly. In this study, the effect of intermediate studs is neglected. As it is shown in Fig. 1, the boundary condition of the frame can be described as fixed connections at the top and bottom plates (horizontal studs) and pinned at two ends of vertical studs which are free to move along their heights in out-of-plane directions. Thus, another spring (bending stiffness of lumbar studs) is added to the boundary conditions of sheathing panels in the long directions. Most of the research on the evaluation of the lateral performance of shear walls was carried out based on requirements of ASTM (E564 and E2126) standards for static and cyclic lateral loading protocols [11, 22]. According to those standards, the bottom of the assembly shall be attached to the test base and the lateral loads applied to the top plate which is laterally supported to prevent any out-of-plane motions. It can be found that this type of assembly resembles the actual building construction of wood shear walls, where the floor diaphragms provide the lateral support of the walls. However, the sheathing panel itself is subjected to the combination of shear force and bending force due to the deformation of the frame [10].

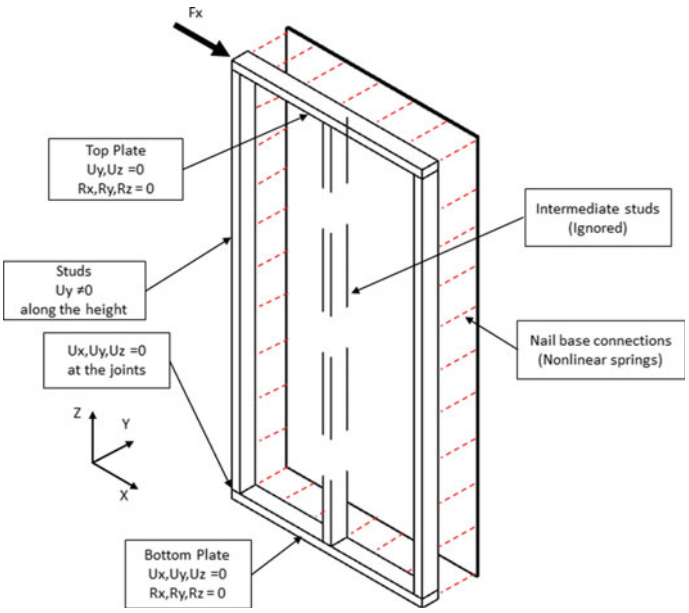

Fig. 1 Boundary conditions of a typical shear wall segment

The purpose of this study is to design a test set up to evaluate the stability of the sheathing panel with the real boundary conditions described above under the pure shear force. To achieve this, the assembly is adapted in a way that the shear edge loads are applied to all edges, and simultaneously through the studs. Studs are laterally supported to minimize their bending deformations. As shown in Fig. 2, a rigid platform consists of six double C-section beams supported by four w-section columns is designed to provide a flat surface with a minimum 800 mm clearance. A total of eight linear motion systems are mounted on top of the platform where the edge loads apply (two systems per edge) to the specimen. The linear motion system as the roller support allows each side of the specimen to move in the desired direction to create an equal simultaneous shear force on the four sides. Each linear motion system supports a stiffened rectangular steel tube which is welded to the upper frame. The upper frame, at the short sides, is built from two side steel plates, a bottom strip, and two rectangular tubes, and, at the long sides, two side steel plates welded to a bottom channel beam. Each wood stud is enclosed inside of the upper frame using multiple transverse ¼" bolts. The slutted holes are considered for the interior transverse bolts at the long sides to allow the out-of-plane movement of studs. As shown in Fig. 2, the studs are trimmed the maximum of 150 mm on each side which each edge can be loaded during the test.

In the test setup, a cable-pulley system is designed to apply the shear force to each edge by one actuator. A total of 16 pulleys are used which can support up to

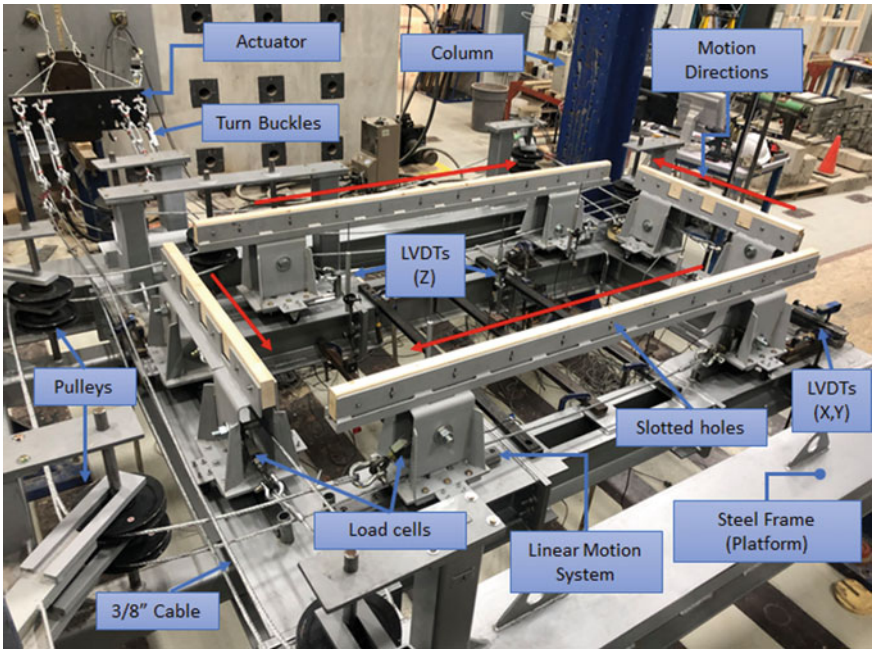

Fig. 2 Shear buckling test setup

3/8″ wire ropes. Each side stud is loaded by using two staggered 3/8″ wire ropes which are connected to the front and back steel tubes. On the other side of all wire ropes, turnbuckles are used to connect to one rigid plate at the actuator head and the actuator is supported by the reaction wall. To minimize the loading loss difference in cables at each side, the location of the actuator and pulleys are precisely determined to provide an average length of 5000 mm for two cables at each side.

The results of the testing are collected by Data Acquisition System. The out-of-plane displacement of the sheathing panel is measured using five LVDTs located beneath the specimen to cover multiple locations. Also, the movement of each side stud is identified using linear sensors (LVDTs) and the amount of force applied by each cable is recorded during the testing using eight mini-load cells located at the endpoint of cables (connection to steel tubes).

According to the ASTM standard (E564), the loading protocol is calibrated at a constant rate of 7 mm/min displacement control to reach the target limit in no less than 5 min. Before starting the first increment, the approximate preload of 0.5 kN is applied to each cable and specimen by tightening the turnbuckles for 5 min to seat all connections and to eliminate the cable sagging. Accordingly, all the readings are zeroed and the loading continues until the ultimate load is reached or any cable is experienced the maximum 11 kN axial force (the design limit load).

4 Results and Discussion

The shear buckling testing of sheathing panels with different nail spacing including 25, 50, and 100 mm along all edges is performed. The typical 8d (63.5 × 3.4 mm dia.) common framing nails and OSB panels (6.4 mm thickness) are used in this study (Fig. 3). In this case, the slenderness ratio of the plate ($\beta \geq 190$). Literature showed that such a plate with simply supported and clamped boundary conditions under shear force experiences elastic buckling and the tensile and compressive principal stresses are equal at 45° in the pre-buckling stage [1]. As shown in Fig. 4, the results are presented in the form of shear force per length (related to the short side) versus the out-of-plane displacement of the middle of the sheathing panel curves. It is observed that by using 25 and 50 mm nail spacing, the failure of nails is eliminated, and the specimens experience elastic buckling of wood sheathing as shown in Fig. 4. At the initial stage of loading, a small negative out-of-plane displacement due to the initial imperfection is detected before the sheathing panel reaches the instability. Those plates buckle due to compressive stresses when shear force per length reaches approximately 6 and 4.1 N/mm, respectively. The sheathing panels enter into the post-bucking stage by taking more loads and large out-of-plane deformations in the diagonal direction appeared due to the creation of the diagonal yield zone until their ultimate capacities at 10.6 and 8.9 N/mm, respectively. The softening stage follows the ultimate capacity and then a sudden shear failure of the sheathing panel at one of the compressive corners occurs (Fig. 5a). Where 100 mm nail spacing is used, the buckling of the sheathing panel coincides with the slippage of nails

Fig. 3 Test setup for 6.4 mm OSB sheathing panel with 63.5 mm nail @ 50 mm

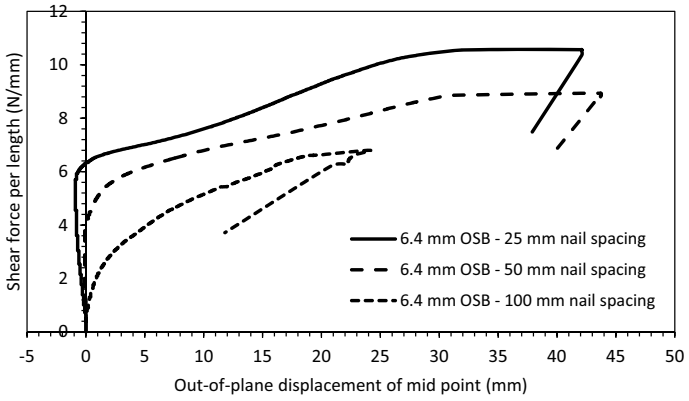

Fig. 4 Shear load versus out-of-plane deflection curve

beyond 1 N/mm loading rate. In other words, the material nonlinearity of nail base connections affects the buckling behavior of sheathing panels, and ultimately nail joints fail due to splitting OSB sheathing from the notch and/or nail punching at approximately 6.8 N/mm as shown in Fig. 5b.

To calculate the critical shear buckling capacity of OSB sheathing panel with 6.4 mm thickness, the material property of the panel is assumed as $B_{a,0} =$ 35,000 N/mm, $B_{a,90} =$ 27,000 N/mm, and $B_v =$ 9,000 N/mm. Thus, the critical shear per length can be determined as 4.25 N/mm using Eq. 4 which can be varied based upon the measured material properties. In this case, the ratio of the critical shear per length test results and calculated using Eq. 4 is 1.41 and 0.96 for panels

a) shear failure of OSB sheathing at the compressive corner

b) splitting OSB sheathing from the nail base connection and nail punching

Fig. 5 Typical failure modes of specimens

with 25 mm and 50 mm nail spacing, respectfully. The design values of Eq. 4 may not lead to conservative values for determining the shear buckling strength of wood sheathing panels with real boundary conditions.

5 Conclusions

A unique experimental setup is developed to investigate the buckling of typical wood sheathing OSB panels with 6.4 mm thickness under the pure in-plane shear. The real boundary conditions of sheathing panels including the nonlinear behavior of nail slippage and bending stiffness of studs are included in the experiments and the influence on the shear buckling of the OSB sheathing panel is presented. The following conclusions can be drawn based on the experimental results:

- Panels experience elastic buckling with large out-of-plane deformations.
- With the increase of nail spacing, the shear buckling capacity of the sheathing panel decreases due to the influence of boundary conditions, and the large deformation of the panel concurrently occurs with the nonlinearity of nail slip.
- The calculated shear buckling capacity of the sheathing panel with simply supported boundary conditions is almost 40% lower and 6% higher than the shear bucking capacity of the same panel with 25 and 50 mm nail spacing boundary conditions, respectively.
- Further investigation is required to understand the failure mechanism and the difference between the current buckling equation and the experiment concluded.

Acknowledgements Financial Support from Ontario Center of Excellence, Strik Baldinelli Moniz Ltd. (SBM) Engineering Consultant, London, Canada, and Ontario Graduate Scholarship (OGS) is gratefully acknowledged.

References

1. Alinia MM, Gheitasi A, Erfani S (2009) Plastic shear buckling of unstiffened stocky plates. J Constr Steel Res 65:1631–1643
2. Bank LC, Yin J (1996) Buckling of orthotropic plates with free and rotationally restrained unloaded edges. Thin Walled Struct 24:83–96
3. Bulson PS (1969) The Stability of Flat Plates. American Elsevier Publishing Company Inc., New York
4. CSA-O86 (2014) Engineering design in wood. CSA Group Mississauga, ON, Canada
5. Das YC (1963) Buckling of rectangular orthotropic plates. Appl Sci Res Sect A 11:97–103
6. Dekker J, Kuipers J, van Amstel HP (1978) Buckling strength of plywood – results of tests and design recommendations. Heron 23(4):1–59
7. E564-06 (2018) Standard practice for static load test for shear resistance of framed walls for buildings, ASTM standards. https://doi.org/10.1520/E0564-06R18
8. E2126-19 (2019) Standard test methods for cyclic (reversed) load test for shear resistance of vertical elements of the lateral force resisting systems for buildings. ASTM standards.https://doi.org/10.1520/E2126-19
9. Hwang I, Lee JS (2006) Buckling of orthotropic plates under various in-plane loads. KSCE J Civ Eng 10(5):349–356
10. Kallsner B, Girhammar UA (2009) Analysis of fully anchored light-frame timber shear walls – elastic model. Eng Struct 42:301–320
11. Kirkham W, Gupta R, Miller T (2014) State of the art: seismic behavior of wood-frame residential structures. J Struct Eng ASCE 140(4):04013097. https://doi.org/10.1061/(ASCE)ST.1943-541X.0000861
12. Noguchi H, Kajikawa H, Mitsuhashi A, Ogawa H (2006) Plywood buckling behavior and stress distribution of small-scale wooden panel bearing walls under in-plane shear force part1. In: Summaries of technical papers of annual meeting architectural institute of Japan, pp 205–206
13. Venant S (1883) Discussion in Theorie de l'elasticite des cors solides, by clebsch, p 704
14. Seydel EZ (1933) fur Flugtechnik u. Motorluftsch 24(3):37 (Translated: The critical shear load of rectangular plates. NACA, TN. 705, USA)
15. Stein M, Neff J (1947) Buckling stresses of simply supported rectangular flat plates in shear. NACA. TN. 1222, USA
16. Stowell EZ (1948) A unified theory of plastic buckling of columns and plates. NACA TN. 1556, USA
17. Stowell EZ (1949) Critical shear stress of infinitely long plates in the plastic region. NACA TN. 1681, USA
18. Timoshenko S, Gere SS (1961) Theory of Elastic Stability, 2nd edn. McGraw Hill, New York
19. Timoshenko SP, Woinowsky-Krieger S (1959) Theory of Plates and Shells. McGraw Hill, New York
20. Turnbull JE, Guertin SM (1975) Shear and buckling resistance of cladding materials used as structural diaphragms in farm buildings. Canadian Agric Eng 17(1):7–11
21. Wang CM, Xiang Y, Chakrabarty J (2001) Elastic/plastic buckling of thick plates. Int J Solids Struct 38:8617–8640
22. Winkel MH, Smith I (2010) Structural behavior of wood light-frame wall segments subjected to in-plane and out-of-plane forces. J Struct Eng ASCE 136(7):826–836

Bending Performance of Timber-Timber Composite Floors

Md Shahnewaz, Carla Dickof, and Thomas Tannert

1 Introduction

With an increase in pollution and climate change, the global demand is increasingly moving towards sustainable construction. Therefore, the construction industry has begun to utilize sustainable materials such as timber that has a low-carbon footprint in their life cycle. Cross-laminated timber (CLT) and Glue-laminated Timber (glulam) have become the most well-known engineered mass timber products, are gaining popularity, and taking over from steel and concrete as the wonder material of the twenty-first century due to the availability of innovative materials, connections, components, and composite systems [3]. CLT is a mass timber product, consisting of sawn lumbers laid-up on-flat in alternating directions and glued together; creating panels that have high in-plane strength and stiffness [4, 6, 7]. Timber construction is advancing in North America and the 2020 version of the National Building Code of Canada [5] allowed mass timber structures up to 12 storeys tall.

This paper investigates Timber-Timber Composite (TTC) floor systems made with CLT and glulam under quasi-static monotonic tests including various shear connections for the TTC floors are also investigated. The Vancouver School Board [9] commissioned two new buildings to replace the existing Begbie and Bayview elementary schools. The two-storey school buildings include learning spaces with exposed CLT walls, floors, and roofs. Both projects include long span systems in either the roof or the floor, with varying spans.

Timber Concrete Composite (TCC) systems have been extensively studied in recent years using mechanical connectors, adhesive bonds, or a combination [8]. Fewer studies have reported experimental, numerical, and analytical investigations on TTC systems, particularly with mechanical fasteners. The objective of the research

M. Shahnewaz (✉) · C. Dickof
Fast + Epp, Vancouver, Canada
e-mail: mshahnewaz@fastepp.com

T. Tannert
University of Northern British Columbia, Prince George, Canada

S. Walbridge et al. (eds.), *Proceedings of the Canadian Society of Civil Engineering Annual Conference 2021*, Lecture Notes in Civil Engineering 244,
https://doi.org/10.1007/978-981-19-0656-5_43

presented herein is to investigate the flexural performance of double-T shaped TTC floor systems using various connections.

2 Specimens Description

The CLT panels and glulam beams were fabricated by Structurlam in accordance with ANSI/APA/PRG 320 [1] and CSA O122 [2], some relevant material properties are provided in Table 1.

A total of six (double T cross-section) specimens composed of a CLT panel and two glulam beams were assembled and tested in the Wood Innovation Research Lab at the University of Northern British. The CLT panels were 105 mm thick [35/35/35], 9,144 mm long and 1,162 mm wide with an average density of 441 kg/m^3 at a moisture content of 11%. The 8,944 mm long glulam beams had a cross-section of 215 mm × 380 mm. Their average density and moisture content were 545 kg/m^3 and 12%, respectively. Two types of self-tapping screws (STS): i) 10Ø × 200 mm ASSY SK partially threaded washer head screws; and i) 8Ø × 300 mm ASSY VG cylinder head fully threaded screws, and one-component polyurethane adhesive (Lepage Premium PL) were used to connect the CLT panel to the glulam beams. The cross-section of the test specimens is illustrated in Fig. 1.

Three connections between CLT and Glulam were investigated:

a) Type A: 2 rows of 10Ø × 200 mm ASSY SK STS at 75 mm on centre installed at 90°, c.f. Fig. 2a.
b) Type B: 2 rows of 8Ø × 300 mm ASSY VG CYL STS at 150 mm on centre installed at 45°, c.f. Fig. 2b.
c) Type C: 2 rows of 10Ø × 200 mm ASSY SK STS at 300 mm on centre installed at 90°, in combination with an adhesive bond (one-component polyurethane adhesive - Lepage Premium PL), c.f. Fig. 2c.

Table 1 Material properties

	CLT	Glulam
Species	S-P-F	Douglas-Fir
Grade	105 V, grade V2M1.1	Grade 24f-E
Size	1.162 m × 105 mm	215 mm × 380 mm
Length	9.144 m	8.944 m
Avg. density	441 kg/m^3	545 kg/m^3
Avg. moisture content	11%	12%

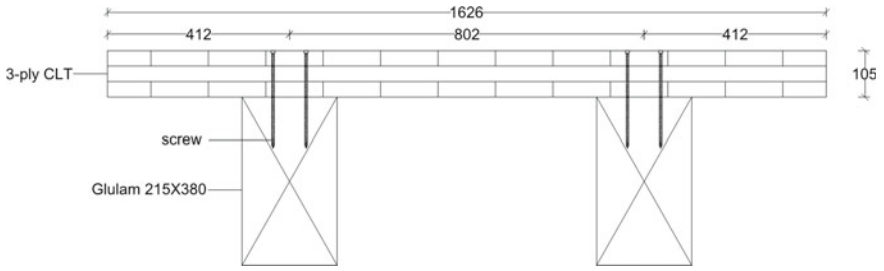

Fig. 1 Cross-section of test specimens [mm]

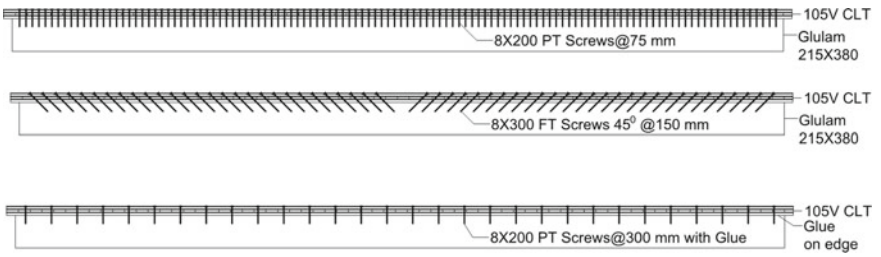

Fig. 2 Connections: **a** Type A; **b** Type B; **c** Type C

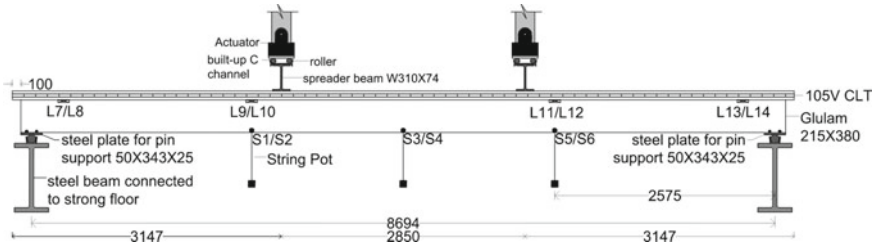

Fig. 3 Schematic of 4-point bending setup and location of sensors

3 Methods

Destructive 4-point bending tests were conducted. The test set-up consisted of two 500 kN actuators positioned as shown in Fig. 3. Six string pots, labelled S1 to S6 and eight linear variable differential transducers (LVDTs) labelled L7 to L14 were installed to measure the vertical deflections and the relative horizontal displacements between CLT and Glulam, respectively, c.f. Fig. 4. The floors were subjected to quasi-static monotonic loading with equal load applied to each actuator. The load was applied at a constant rate of 10 mm/min with an initial pre-load cycle to 40% of the anticipated ultimate load-carrying capacity, unloaded, and re-loaded to failure, where failure is defined as a drop in the applied load by more than 20%. The maximum

Fig. 4 Photo of a 4-point bending test

Table 2 Test results

Test ID	Connector Type	F_{max} [kN]	$d_{m,Fmax}$ [mm]	k_{dm} [kN/mm]
DT-1	Type A	310	84	4.3
DT-2		431	123	4.3
DT-3	Type B	403	92	4.6
DT-4		473	102	4.7
DT-5	Type C	391	83	5.6
DT-6		462	95	5.5

force, F_{max}, and its corresponding mid-span deflection, $d_{m,Fmax}$, were determined based on the actuator load, and the average of string pots S3 and S4 respectively. The elastic stiffness, k_{dm}, was determined for the range of 10–40% of F_{max}.

4 Results and Discussion

4.1 Load–Deflection Curves

The test results are listed in Table 2 and the load–deflection curves are illustrated in Fig. 5. The observed initial stiffness (0–10% F_{max}) observed for each specimen showed little variation regardless of connection type. Comparatively, variation in the load-carrying capacities was observed across all specimens, and variation in elastic

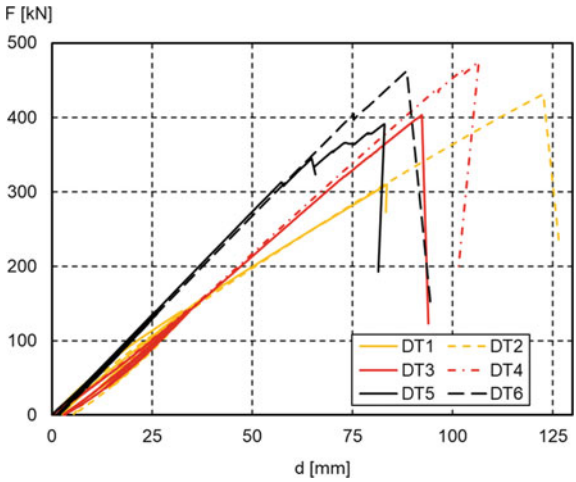

Fig. 5 Load-deflection curves from full-scale bending tests at mid-span

stiffnesses was observed between specimen types. The average capacity of composite floors with Type B connectors was the highest (438 kN), 15% higher compared to the average capacity of floors with Type A connectors. However, the floors with Type C connectors had a similar capacity like floors with Type B connectors. The applications glue in the composite floors with Type C connectors transformed into a very stiff system. The average stiffness of floors with Type C connectors was found 23% and 16% higher compared to floors with Type A and B, respectively.

4.2 Failure Modes

All 6 specimens failed in brittle tension failure of one of the two glulam beams at a location close to the mid-span of the specimen. A typical failure is shown in Fig. 6 for a Type A specimen. The right glulam in specimen DT1 (specimen type A) initiated earlier failure than other specimens; the glulam beam on the right side of the specimen had a finger joint near mid-span which experienced a sudden tension failure, resulting in earlier failure of DT1 compared to DT2 (e.g., DT1 shows at 28% lower ultimate load compared to DT2) and all other specimens. In addition to typical tension failure of one glulam, some CLT rolling shear failure was observed at the left CLT-glulam interface in specimen DT6. No special failure mechanisms, and joint failures were observed in any of the other specimens.

Fig. 6 Typical failure in Type A floor specimen

5 Conclusions

Six glulam and CLT double-T shaped full-scale timber-timber composite floors were tested for flexural performance. The composite systems were constructed using 3-ply CLT slabs with two glulam beams (double-T formation) connected by Type A-partially threaded screws installed at 90°, Type B- fully threaded screws at 45°, and Type C-partially threaded screws with glue at 90°. The load-deformation behaviour observed in the full-scale testing was linear up to failure. Type B and C connectors had the strongest capacity and stiffness compared to both Type A. The deformation capacity and ductility of Type A connector were found the highest among three types. The failure mechanism in all specimens was observed brittle tension failure at mid-span initiated at one of the two glulam beams.

Acknowledgements The project was supported by Natural Resources Canada (NRCAN) through the Green Construction through Wood (GCWood) Program.

References

1. ANSI/APA PRG 320 (2018) Standard for performance-rated cross-laminated timber. American National Standards Institute, New York
2. CSA O122 (2016) Structural glued-laminated timber. Canadian Standards Association, Rexdale
3. Dias AMPG, Skinner J, Crews K, Tannert T (2016) Timber-concrete-composites increasing the use of timber in construction. Eur J Wood Wood Prod 74(3):443–451
4. Gagnon S, Pirvu C (2020) Cross laminated timber (CLT) handbook. FPInnovations, Vancouver
5. NBCC (2020) National building code of Canada, Canadian commission on building and fire codes. National Research Council of Canada, Ottawa
6. Shahnewaz M, Tannert T, Alam MS, Popovski M (2017) In-plane stiffness of cross-laminated timber panels with openings. Struct Eng Int 27(2):217–223

7. Shahnewaz M, Alam MS, Tannert T (2018) In-plane strength and stiffness of cross-laminated timber shear walls. Buildings 8(8):100
8. Tannert T, Gerber A, Vallee T (2019) Hybrid adhesively bonded timber-concrete-composite floors. Int J Adhes Adhesiv 97:102490
9. Vancouver School Board (VSB). https://www.vsb.bc.ca. Accessed Sept 2020
10. Yeoh D, Fragiacomo M, De Franceschi M, Heng BK (2011) State of the art on timber-concrete composite structures: Literature review. J Struct Eng 137(10):1085–1095

Covid-19 Modular Construction

M. Suleiman, A. Elshaer, and M. Billah

1 Introduction

Coronaviruses are a family of viruses that are considered contagious and cause respiratory illnesses. In late 2019 and early 2020 an identified coronavirus, SARS-CoV-2, has caused a pandemic globally. The virus transfers through the patients' mouth-generated aerosols (i.e., coughing and sneezing). While the symptoms of coronavirus disease may appear up to 14 days after exposure, which is referred to as the incubation period, symptoms such as cough, fever, or shortness of breath may appear after the incubation period. It is important to be able to provide the medical care required to provide those in need (WHO, 2020). This pandemic highlighted the importance of having a strong and ready healthcare system in place to combat this crisis. While the government of Canada has been working endlessly to limit the spread of the virus by implementing and enforcing new laws and rules such as face mask requirements in public places, a social distancing of 2 m as the number of cases keep on rising, the hospitals are facing the challenge of the shortage in care beds, which in turn increasing the number of mortalities, especially for people who suffer from other health conditions. The health care system can be branched into three different categories: equipment, personnel, and space. Equipment involves different devices needed in an ICU room, and this can be overcome by purchasing more equipment. While for personnel retired doctors and nurses can be asked to provide their service in such a pandemic [1–8]. While for the space problem, modular construction can be the solution but needs an appropriate assessment of its performance, which this research will be able to explore solutions to this problem as shown in Fig. 1.

As of March 2021, the total number of cases in Canada has reached a maximum of 899,757 cases as shown in Fig. 2, which raises the importance of having an appropriate backup system in place. Building more hospitals can be a solution to this problem, although it is not viable, due to the complexity involved in the design,

M. Suleiman (✉) · A. Elshaer · M. Billah
Department of Civil Engineering, Lakehead University, Thunder Bay, Canada
e-mail: masuleim@lakeheadu.ca

S. Walbridge et al. (eds.), *Proceedings of the Canadian Society of Civil Engineering Annual Conference 2021*, Lecture Notes in Civil Engineering 244,
https://doi.org/10.1007/978-981-19-0656-5_44

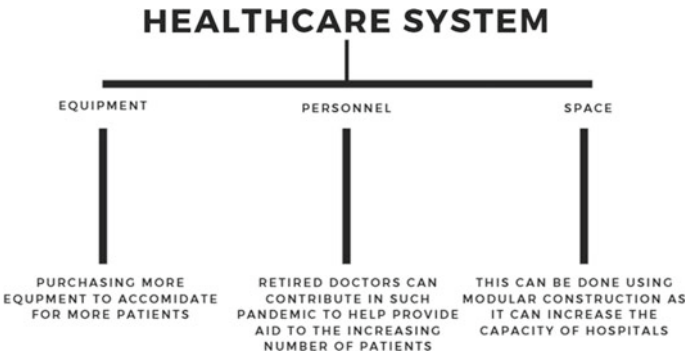

Fig. 1 Healthcare system problems and proposed solutions

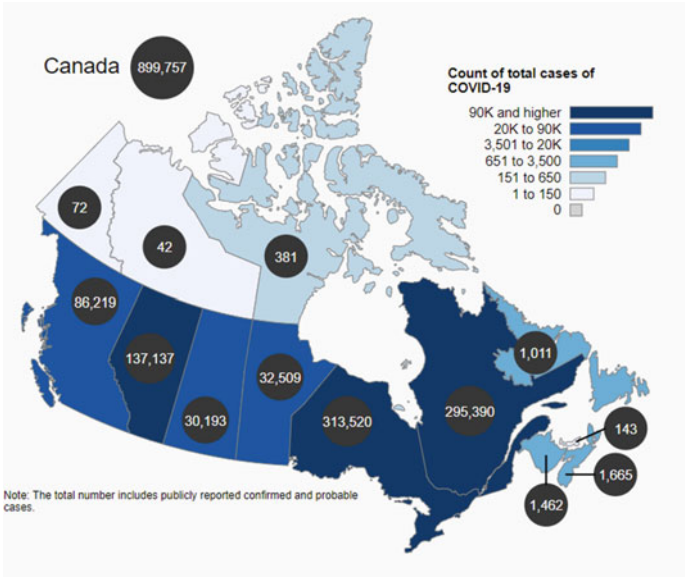

Fig. 2 COVID-19 Total number of cases across Canada (Government of Canada, March 2021)

and construction. Modular Construction (MC) on the other hand can be used in this situation, due to having the speed of delivery, physical separation of contaminants, security, and isolation. These important parameters dictate the spread of the virus within healthcare facilities. Otherwise, other patients and health workers may experience the risk of being infected by contagious patients. Modular construction can be deployed in fields, such as arenas, stadiums, and parking lots. This will also allow the hospital to operate normally for regular stream patients while being able to control the spread of the infection. Modular construction is an efficient method that uses pre-engineered building units, that can be assembled to rapidly form a

structure for different purposes. It is suitable for temporary structures and storage areas due to its simplicity and repetitive nature, especially when the pandemic has put pressure on the healthcare design and construction community to get rooms designed, approved, built, and operational quickly while maintaining the essential infection control requirements. MC provides less labour-intensive modern construction techniques while maintaining the social distancing that site workers require [9–14].

The current project aims to numerically simulate the airflow and respiratory droplet transfer mechanisms inside an MC field hospital room using computational fluid dynamics (CFD)-based numerical modelling. After validating the developed model, the efficiency of implemented controls can be accurately addressed. The high-fidelity numerical simulation will enable the track and visualization of the mouth-generated aerosols in the room, thus assessing the infection control abilities in the system in place. The project aims to examine different levels of air changes and their effect on the spread of aerosols. The outcome of this research is very important, as it can be used in different situations from pandemics to natural disasters, it will be an available asset to our emergency control system that can be rapidly and easily be deployed across Canada.

2 Validation Model

To validate the numerical model used to simulate the propagation of mouth-generated particle in a modular construction room, a study conducted by [15] involving a comprehensive comparison between a full-scale experimental system against CFD simulations of an air-conditioned chamber is used to assess the transport and the trajectory of cough-induced aerosol. The chamber geometry of 2.9 m long by 2.3 m wide by 2 m high was modelled including four chairs and four manikins, to simulate a gathering, as shown in Fig. 3.

The study was conducted under different air changes per hour (ACH) rates of 10, 20 and 40, which reflects the quality of air filtration across the room. The simulation included two scenarios where mouth-generated aerosols were assumed to be initiated by either manikin 1or manikin 3 under the same ACH rates. This has been designed to examine the impact of the boundary conditions on the aerosol and how being near the inlet or the outlet will change the destination of the aerosols. Six models were constructed using CFD, three involving manikin 1 coughing under different ACH rates, while the other three involved manikin 3 coughing under different ACH rates. It was determined as the ACH increases, the stronger air movement would prevent direct aerosol inhalation under various coughing conditions. It was apparent that the mouth-generated aerosols from manikin 1 caused more aerosols inhalation under 10, 20, and 40 ACH as it is located near the inlet, with percentages inhaled of 1.96, 0.36, and 0.2%, respectively. While the mouth-generated aerosols from manikin 3 caused aerosols inhalation of 0.86, 0.76, and 0.69%, respectively. It was also observed that as the ACH rate increases, more aerosols got carried back into the recirculation system.

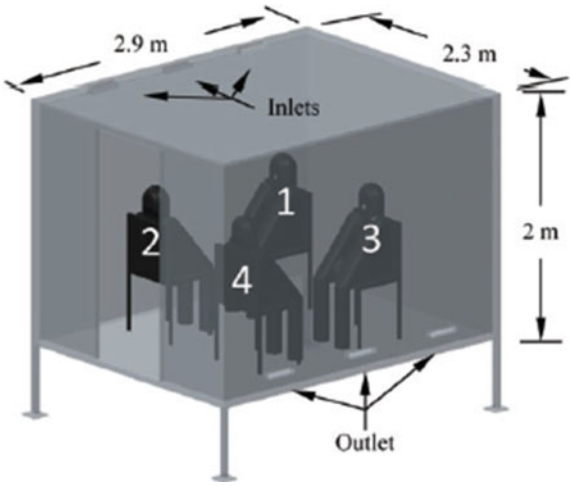

Fig. 3 The geometry of the validation model [15]

For instance, mouth-generated aerosols from manikin 1 caused fewer aerosols to be carried out of the outlet back into the AC recirculation with percentages of 4.5, 5.8, and 22.9%. While mouth-generated aerosols from manikin 3 were significantly more at 8.5, 10.3, and 32.7% respectively, due to it being closer to the outlet. Figure 4 demonstrates the differences between aerosol percentages at different rates for both mouth-generated aerosols from manikin 1 and 3.

CFD models were developed with a similar room geometry and physical description, as shown in Fig. 5. A hexahedral mesh discretization was generated with a size of 25 mm, and finer meshes in the middle where particle translation is mainly happening with a cell size of 12.5 mm, as shown in Fig. 6. The total number of cells in the computation domain was 2.5 M, while the simulation met the Courant-Friedrichs-Lewy (CFL) criterion of being less than 1.0 by setting the time-step to be 0.005 s with a total physical duration of 1 min. The first 200 steps were set to run at 0.1 s time-step interval, to establish flow stabilization, while the mouth-generated aerosols started after 1 s.

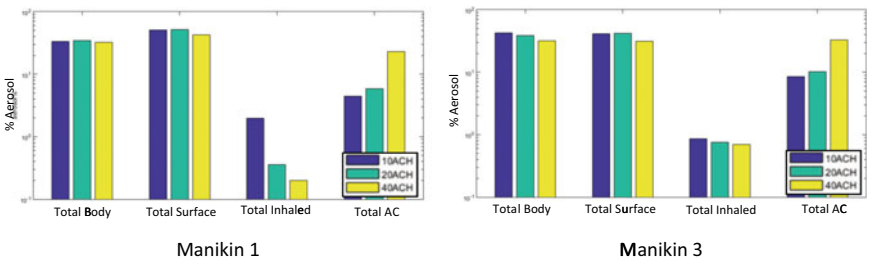

Fig. 4 Summary of aerosol destination of manikin 1 and manikin 3 [15]

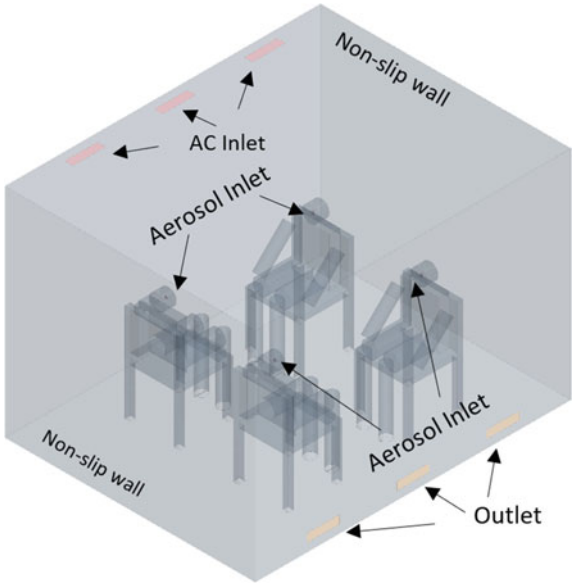

Fig. 5 Boundary conditions of the validation model

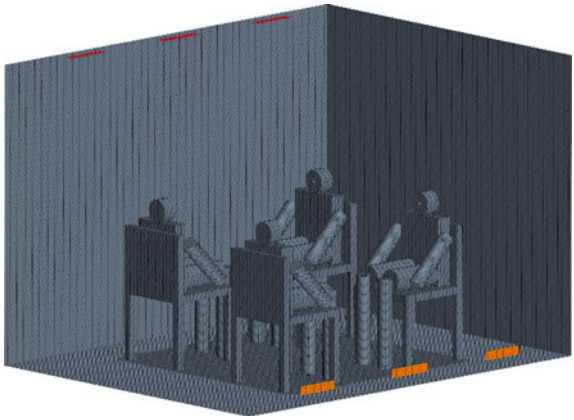

Fig. 6 Mesh grid resolution of validation model

After running the case study models, it was observed that, as the ACH rate increases, a similar trend was observed as fewer particles are being inhaled, due to the influence of AC. Under 10, 20, and 40 ACH, the percent inhaled for the mouth-generated aerosols from manikin 1 was 3.13, 2.01, and 1.9%, respectively, while the cough from manikin 3 was 2.84, 2.9, and 2.34%, respectively. The fluctuation in results is caused due to the difference in the manikin model. While aerosol percent going through the outlet increased as the ACH rate increases, less was observed in the case of manikin 3 under 10, and 20 ACH, due to having less direct influence from the AC at 0.129%, and 0.925%, respectively, more was observed at 40 ACH with 5.16% due to the higher influence of the outlet. While manikin 1 results showed a similar

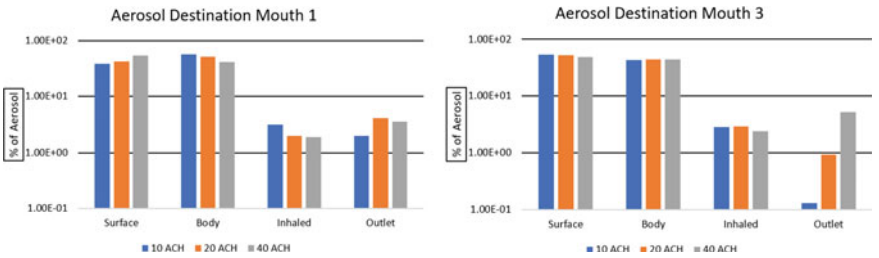

Fig. 7 Aerosol Destination percentage

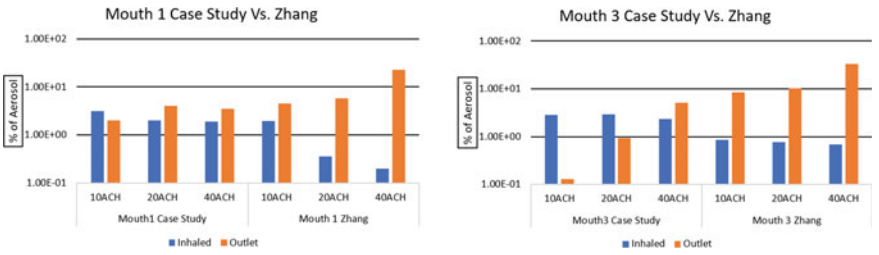

Fig. 8 Aerosol percent inhaled and recirculated through the outlet validation

trend, the impact of being near the inlet increased the percent aerosol going through the outlet by 2, 4.08, and 3.55%, respectively. Figure 7 shows the aerosol destination percentage, which is calculated as the ratio between the mass of the particles passing through a boundary to the mass of the summation of total particles going through all other boundaries.

The validation model result comparison is concerned with observing a similar trend in particle movement in the computational domain. The comparison involves comparing the aerosol percentage inhaled, and exited through the outlet, and was observed that as the rate of ACH increases, the more aerosols leave the computational domain as observed in Fig. 8. Figure 9 illustrates particle distribution in the domain under 10 ACH coming from manikin 1.

3 Case Study and Discussion

The geometry of the room in MC is a governing aspect as it dictates the required inlet ventilation system parameters (i.e., ventilation system inlet and outlet parameters). After designing the MS room, the dimensions were set to be 6.1 m long by 2.5 m wide, and 3 m high. The room will represent the computational domain in the simulation, as the droplet transfer will take place inside the room. Figure 10 describes the room dimensions and their components.

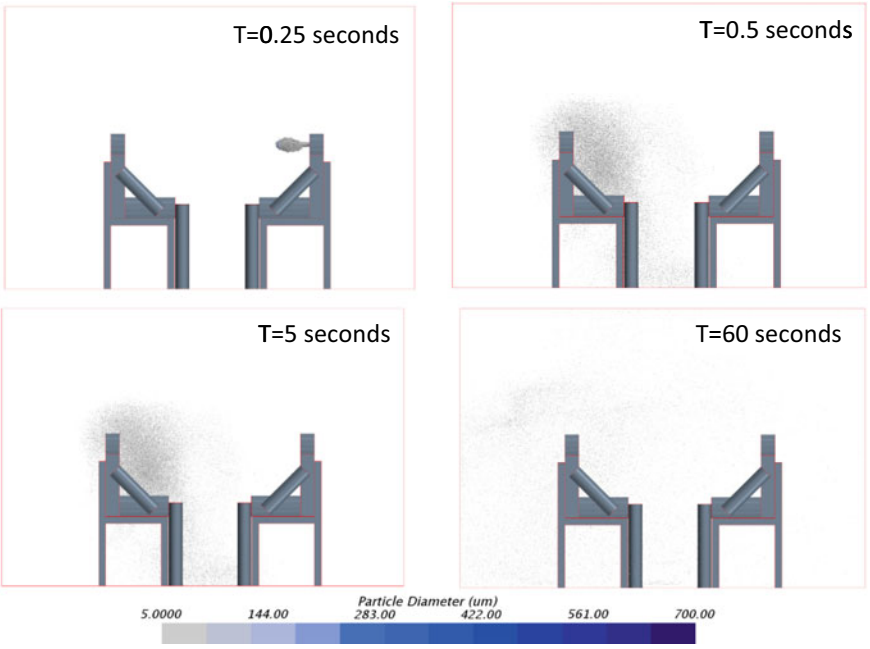

Fig. 9 Aerosol distribution in the computational domain

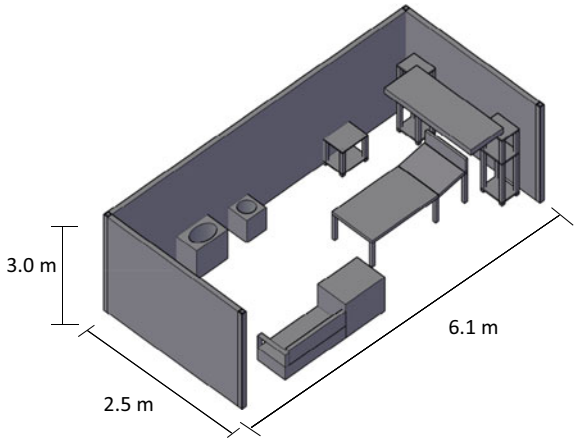

Fig. 10 A proposed design for the modular construction room

The computational domain was discretized to a hexahedral mesh with a base size of 75 mm while having finer mesh near the subject with sizes of 30 mm and 10 mm, which yielded 2 M cells. The time step was chosen to be 0.005 s based on the Courant-Friederichs-Lewy (CFL) number to be maintained below 1.0, to avoid divergence of the numerical modelling. The simulation was conducted for a total

of 12,200 time-steps, while allowing the first 200 steps to run at 0.1 s time-step interval, to establish flow stabilization, while the mouth-generated aerosol starts after the flow stabilization. Figure 11 demonstrates the mesh discretization across the computational domain.

There are three main boundary conditions of concern in this simulation, which are: the mouth, the system inlet, and the system outlet. The remaining boundary conditions are set to non-slip wall conditions, as demonstrated in Fig. 12. The mouth

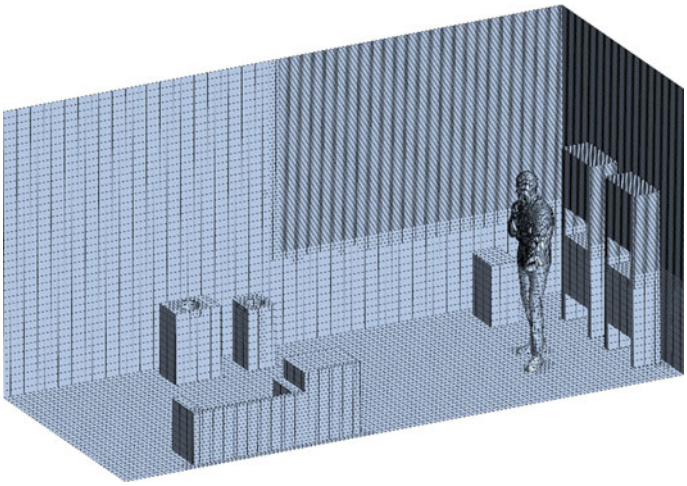

Fig. 11 Mesh grid resolution

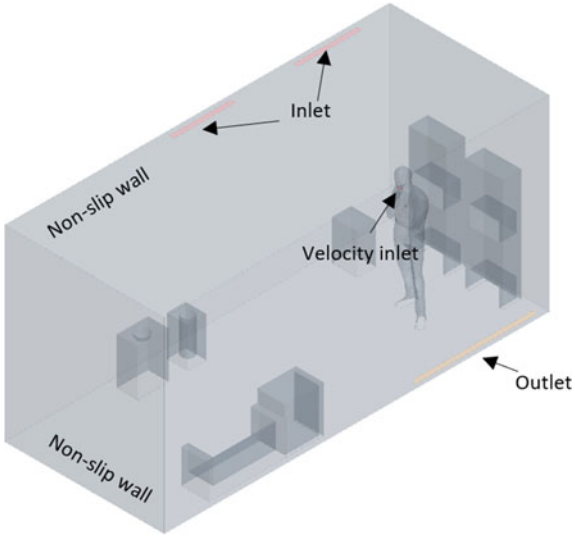

Fig. 12 Boundary conditions of case study

was assigned to be an opening of the area of 2000 mm^2. Aside from the coughing, the mouth boundary condition followed a sine wave function to simulate human breathing (inhale and exhale) as a function of time as shown in Eq. 1, while it will have a velocity of 10 m/s for the duration of the cough. The ventilation system inlet is located at the roof of the room with two openings near the subject with dimensions of 1.0 m × 0.064 m located 0.08 m away from the left wall and 0.61 m away from the back wall. Openings are placed 1 m apart from the edge to edge. The velocity of the system inlet was calculated based on the ACH rate. In this case, 10, 20, and 40 ACH required velocities of 1.02, 2.04, and 4.08 m/s, respectively. The inlet was adjusted to be inclined at an angle of 30 degrees from the roof normal towards the outlet. The ventilation system outlet is located on the right wall with dimensions of 2.0 m × 0.064 m and placed 0.08 m away from the floor and 0.19 m away from the back wall. The outlet was set as a pressure outlet with negative pressure calculated using the same flow rate as the inlet with an air density of 1.18 kg/m^3.

$$v(m/s) = 2.9\sin(1.28t) \tag{1}$$

The simulations involved different types of physics models mainly implicit unsteady, k-epsilon, segregated flow, and the two-layer all Y+ treatment low −Y+ and high −Y+ wall treatment, and the Lagrangian multiphase. The Lagrangian model focuses on the multiphase flow where a thermodynamic phase (solid, liquid, gas) in this case the droplets are liquid reacts with another distinct phase (air) gas. To simulate cough aerosols (saliva), a mixture of water, glycerin, and sodium chloride with a mass ratio of 1000:76:12. The weighted density of the liquid injected as the saliva was 1028.89 kg/m^3 [15, 16]. This simulation does not take into consideration the evaporation of particles, or the temperature of the surface, as it is concerned with particle translation within the computational domain. Injectors with a circular surface area of 5 cm^2 were placed in front of the mouth opening with a mass flow rate of 5 mg/s for 1 s to simulate a human cough. Since break-up models of particles are not considered two injectors were used to inject fine and coarse particles into the computational domain. Fine particles are represented as 5 μm, while the coarse particles followed Rosin–Rammler distribution with a minimum particle size of 77 μm and a maximum of 737 μm with an average of 170 μm. While the aerosol distribution scene was observed at intervals of 0.5 s. Figure 13 illustrates the distribution of the particles under 40 ACH (Aerosols are enlarged for visualization purposes).

After running the models, it was apparent that the trend of higher particles exiting the outlet as the ACH rate increases. The rate at which particles were exiting through the outlet increased by 41% by increasing the ACH from 10 to 20. While increasing the rate to 40 ACH yielded a 137% increase in particles leaving the outlet. While particles landing on equipment decreased by 19% by increasing the ACH rate from 10 to 20, while it decreased by 25% when the rate was increased to 40 ACH. Figure 14 illustrates the impact of the ACH rate on the destination of aerosols within the computational domain.

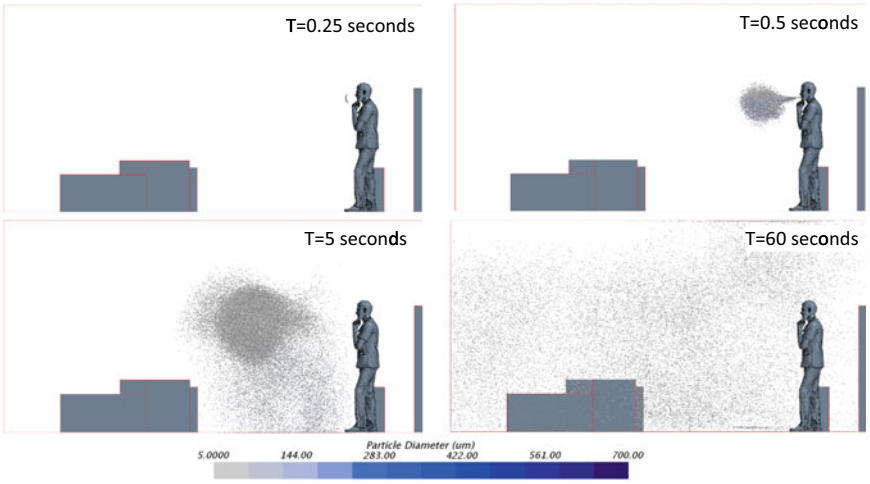

Fig. 13 Aerosol distribution in the computational domain

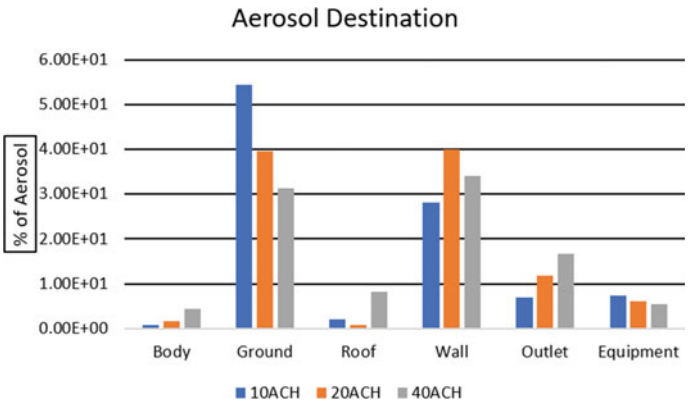

Fig. 14 Aerosol distribution across the hospital room

4 Conclusion

The current study examines the effect of different ventilation levels (i.e., 10, 20 and 40 ACH) in a modularly constructed hospital room by tracking the mouth-generated aerosol. It was found that as ACH increases, the ability of the ventilation system to eliminate more suspended aerosol will increase, which will result in less viral load inhaled by other patients and health workers. It was also found that the majority of the aerosol will get accumulated over wall and ground surfaces, which emphasizes the importance of continuous disinfection of these surfaces.

Acknowledgements The authors would like to acknowledge the financial support from the National Science and Engineering Research Center (NSERC). The authors would like also to thank Siemens, SHARCNET and their excellent techanical staff for facilitating the access to the numerical simlulation software and high performance computing platform.

References

1. Shoukat A, Wells CR, Langley JM, Singer BH, Galvani AP, Moghadas SM (2020) Projecting demand for critical care beds during COVID-19 outbreaks in Canada. CMAJ 192(19):E489–E496
2. Beggs CB, Kerr KG, Noakes CJ, Hathway EA, Sleigh PA (2008) The ventilation of multiple-bed hospital wards: review and analysis. Am J Infect Control 36(4):250–259
3. Blocken B, Malizia F, Van Druenen T, Marchal T (2020) Towards aerodynamically equivalent COVID19 1.5 m social distancing for walking and running. Preprint
4. Cho J, Woo K, Kim BS (2019) Removal of airborne contamination in airborne infectious isolation rooms. ASHRAE J 61(2):8–21
5. Gupta JK, Lin CH, Chen Q (2009) Flow dynamics and characterization of a cough. Indoor Air 19(6):517–525
6. Dudalski N (2018) Experimental measurements of human cough airflows from healthy subjects and those infected with respiratory viruses
7. Khankari K (2016) Patient room HVAC. ASHRAE J 58(6):16
8. Hyttinen M, Rautio A, Pasanen P, Reponen T, Earnest GS, Streifel A, Kalliokoski P (2011) Airborne infection isolation rooms–a review of experimental studies. Indoor Built Environ 20(6):584–594
9. Lindsley WG et al (2012) Quantity and size distribution of cough-generated aerosol particles produced by influenza patients during and after illness. J Occup Environ Hyg 9(7):443–449
10. Paul Ninomura PE, Richard Hermans PE (2008) Ventilation standard for health care facilities. ASHRAE J 50(10):52–57
11. Peoples M (2014) Canadian Tuberculosis Standards. Public Health Agency of Canada, Winnipeg, Canada
12. Seminara G, Carli B, Forni G, Fuzzi S, Mazzino A, Rinaldo A, dei Lincei AN (2020) Biological fluid dynamics of airborne COVID-19 infection: a review
13. Aliabadi AA (2013) Dispersion of expiratory airborne droplets in a model single patient hospital recovery room with stratified ventilation. PhD dissertation, University of British Columbia
14. World Health Organization (2020) Coronavirus disease (COVID-19)
15. Zhang Bo, Guo G, Zhu C, Ji Z, Lin C-H (2020) Transport and trajectory of cough-induced bimodal aerosol in an air-conditioned space. Indoor Built Environ 30(9):1546–1567. https://doi.org/10.1177/1420326X20941166
16. Zhu S, Kato S, Yang J-H (2006) Study on transport characteristics of saliva droplets produced by coughing in a calm indoor environment. Build Environ 41(12):1691–1702

Aerodynamic Mitigation of Low-Rise Building Roofs

Raghdah Al-Chalabi and Ahmed Elshaer

1 Introduction

Controlling wind-induced load is crucial for low-rise building designs to achieve optimal resilience. Low-rise buildings have relatively light dead loads on their roofs, thus more susceptible to uplift due to wind load [9]. Despite the improvements in building codes over the last few decades, damage surveys following wind events in Canada have shown a consistent pattern of wind damages to roof structures and connections between roofs and supporting walls [11]. These damages mainly result from system failures, especially to roofing components such as sheathing and tiles [2, 8]. Low-rise buildings experience an increase in damages, especially in wind-prone areas such as coastlines. The insurance Bureau of Canada (IBC) has attributed 62% of all the natural catastrophic damages to be partially or fully caused by wind events. The latter damages are probably because the design of buildings' external shape and orientation is mainly driven by architectural considerations, functional requirements, and site limitations rather than by aerodynamic considerations [10]. The rise of the damage-related losses can also be attributed to the ageing infrastructure and rising cost of residential buildings. Fortunately, modifications techniques added to the roof edge/corner shape can alter the wind flow and reduce the risk for potential losses. These features can mitigate the wind uplift forces on roofs and, consequently, protect buildings from damages.

Based on the fact that wind loads on bluff bodies are dominantly governed by their geometry, among other factors, many studies investigated modifying the roof edges using architectural aerodynamic elements. These architectural elements include wall extensions, roof edge extensions, pergolas and ridgeline extensions. They can be installed as permanent architectural features or used for rehabilitation purposes.

R. Al-Chalabi (✉) · A. Elshaer
Department of Civil Engineering, Lakehead University, Thunder Bay, Canada
e-mail: ralchal@lakeheadu.ca

S. Walbridge et al. (eds.), *Proceedings of the Canadian Society of Civil Engineering Annual Conference 2021*, Lecture Notes in Civil Engineering 244,
https://doi.org/10.1007/978-981-19-0656-5_45

Several mitigation techniques have been investigated in terms of effectiveness on the pressure variation on the low-rise building roof. [13] examined varieties of roof modification features, including adding semi-cylindrical projections and Rooftop radial splitters, among other techniques, to the gable roof of a low-rise building. The study concluded a 60% reduction in the peak pressure magnitude over the roof near the corner. [8] investigated the effectiveness of eight soffits (i.e., gutters) configurations for mitigating wind pressure on the roof surface using wind tunnel testing. The results illustrate that soffits can reduce the peak suction at the windward edges by up to 30%, while these elements did not impact wind pressure on downwind roof slopes. [4] investigated architectural elements' efficiency, including gable end and ridgeline extensions and wall extension to reduce roof and wall corner suction. The study found that the 200 mm in height ridgeline extension reduced peak suction close to the roof ridge by 60%, while the gable-end extensions reduced peak suction close to the roof's gable-end zone by 65%. A study by Aly et al. (2016) examined the effectiveness of barriers to reduce the wind-induced uplift loads on flat roofs. The latter study discussed the ability of these aerodynamic features in reducing the flat roof uplift forces up to 36%.

Parapets have been used as a standard architectural feature for decades, where they can be retrofitted to an existing building structure. They are often mounted on edge and corner areas where their height is a crucial factor in their aerodynamic impact on the building [8]. The parapet mechanism works by lifting the separated wind shear layers of the roof surface and dissipating the high local corner or edge suctions over a larger area [10]. The parapets are the most popular type of configuration, mainly due to their large architectural appeal [9]. One of the early studies to examine the aerodynamic impact of solid parapets on low-rise buildings was [3]. Their results show that tall parapets reduce the high suction on roofs, while short parapets were found to aggravate the edge and corner suction.

The current study aims to examine the effectiveness of using different architectural features to reduce the wind impact on low-rise building roofs. These objectives will be achieved by comparing (i) the variation of wind pressure on the roof surfaces and (ii) wind-induced lift forces on the roof. A total of 7 configurations will be investigated using computational fluid dynamics (CFD) simulations. Section 1 (this section) presents an introduction and a review of the state of art literature examining the impact of adding different aerodynamic modifications to the roof. In Sect. 2, a description of the study building's geometry and the utilized modifications techniques along with the adopted CFD model used in assessing the different models are illustrated. Section 3 examines the impact of introducing the ridgeline extension, edge extension, combined edge and ridgeline extension, and solid discontinuous corner parapets on the model's roof pressure. Section 4 summarizes the conclusion and the main finding of this study.

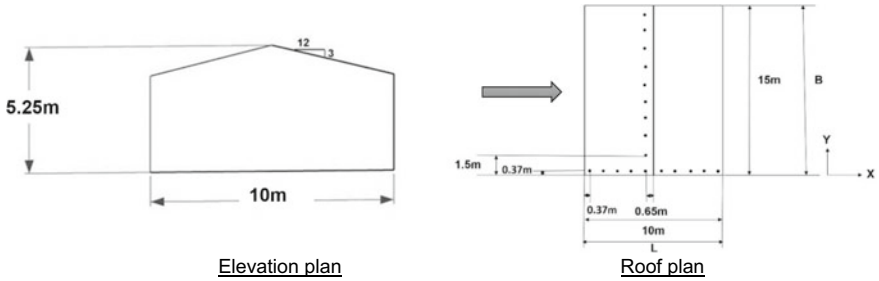

Fig. 1 Overall model dimensions and pressure probs layout on the roof surface

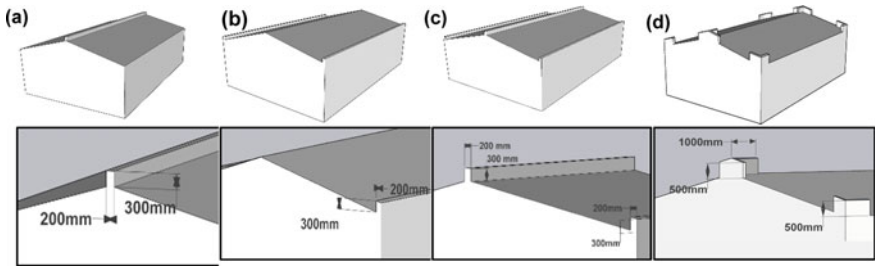

Fig. 2 Aerodynamic mitigation techniques (a) Full ridge extension (b) Full edge extension (c) Full ridge and edge extension and (d) Discontinues solid parapets

2 Numerical Modelling Details

2.1 Building Geometry and Test Models

The generic low-rise building model utilized in this study has a gable roof with a slope of 3:12, which occupies a footprint of 10 × 15 m and a total of 5.25 m. The overall model dimensions and pressure probs layout is illustrated in Fig. 1. The dimensions of the parapets and the architectural elements chosen for the aerodynamic mitigations are shown in Fig. 2.

2.2 Numerical Modelling

A Full-scale Large Eddy Simulation (LES) was performed to the computational domain dimensions and the boundary conditions shown in Fig. 3 using Star CCM + (14.04.013 version). The computational domain dimensions (150 × 100 m × 15 m) are inline with [6]. The conditions at the surface (top and sides faces) of the computational study domain were set as symmetry plane boundary conditions. At

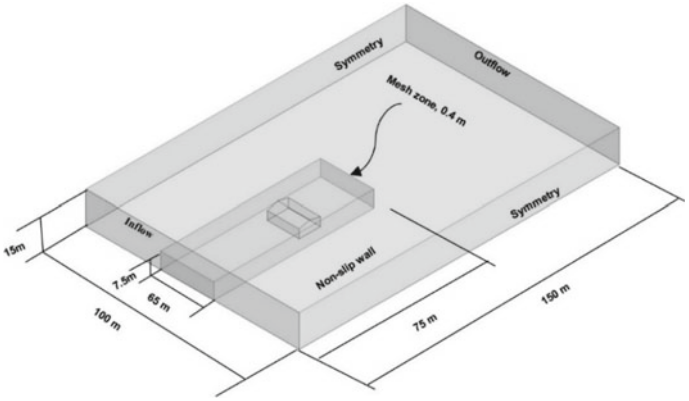

Fig. 3 The computational domain dimensions and the boundary conditions

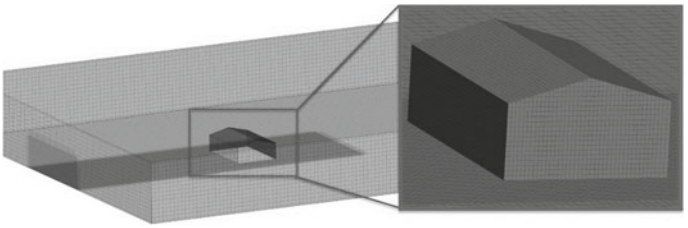

Fig. 4 Mesh grid resolution utilized in the CFD simulations

the same time, the ground was a non-slip wall boundary condition. The outlet surface was defined as an outflow. The inlet wall was defined as a time-varying inlet velocity boundary condition using the consistent discrete random flow generator described in [1].

The computational domain was discretized to a hexahedral mesh of 1.0 m and further refined near the building to a mesh sizes of 0.4 m to capture smaller scale turbulence near the building of interest, which yields a total number of mesh of 1.25 M cells. To ensure particles move from one cell to another within the one-time step, it essential to maintain the Courant-Friedrichs-Lewy (CFL) to be below 1.0 to avoid numerical divergence [5]. Accordingly, the time step was chosen to be equals to 0.02 s. The numerical simulations are conducted for 1500 time-steps, representing a total of 30 s since the flow statistics were found to converge beyond this duration. Figure 4 shows the discretized computational domain for this study.

To validate the adopted CFD model in the current study, an additional simulation was conducted for a low-rise building experimentally tested by [12] for a similar gable roof. The validation model has a dimension of 9.75 $\times$ 14.65 m and a roof reference height of 4.6 m. All the aerodynamic and geometrical details are set to match the wind tunnel setup, including geometry and inflow characteristics. The mean velocity and turbulence intensity profile is generated to match an open terrain

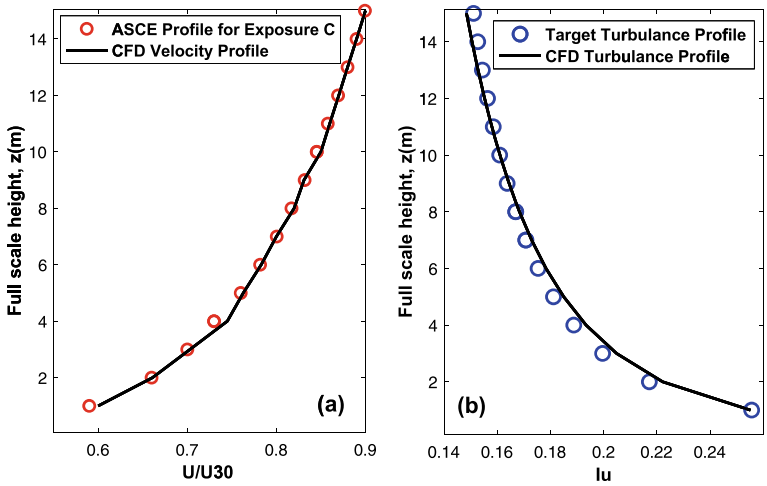

Fig. 5 Comparison of CFD and target profiles (a) Mean velocity profile and (b) Turbulence intensity profile

exposure, ASCE profiles exposure C, as demonstrated in Fig. 5, which was later used in the current study. The equivalent wind tunnel peak pressure coefficient (GCp) was extracted from a tap located at the gable roof corner, which was found to have a good agreement with the numerical model with an error of 1.7%.

3 Results and Discussion

In this section, the impact of introducing the ridgeline extension, edge extension and solid corner parapets on the roof pressure was studied for the benchmark model. Their mechanism works by displacing the vortex from the roof region. Therefore, these mitigation techniques' height can play a crucial role in modifying the local suction pressure [3]. The pressure coefficient values at 0° wind azimuth (perpendicular to the ridgeline) were extracted for probs located along the gable end and ridgeline. The location for critical issues was chosen where wind damage was repeatedly reported from past post damage assessments [4].

3.1 Full Ridgeline Extension

To understand how ridgeline extension of 300 mm in height modifies the roof suction and wind flow around the structure, the study comparatively displays the mean and rms of roof pressure along the line X/L and Y/B in .

Figure 6 and Fig. 7, while the mean velocity magnitude contour is shown in Fig. 8. The worst localized suction pressure on the gable roof occurred at the leading corner. This is visible when examining both mean and rms of pressure in Fig. 7. It can be noted that the rms and the mean Cp along the ridgeline were significantly reduced due to the adopted aerodynamic mitigation. The mean suction decreased by a maximum of 79% and an overall of 90% within the region next to the ridgeline. This observation agrees with what was reported by [4] using a ridge extension of

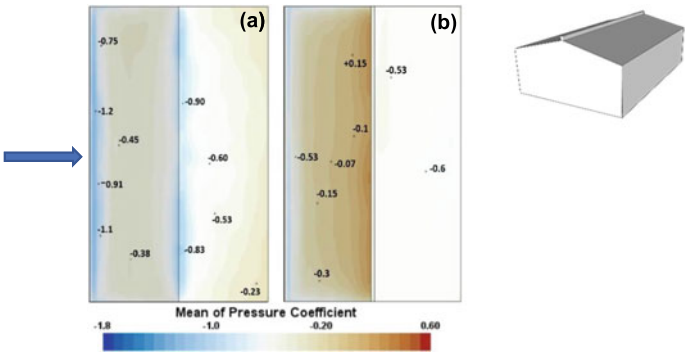

Fig. 6 The distribution of pressure coefficients on the roof surface (a) Benchmark model (b) model with 300 mm ridgeline extension

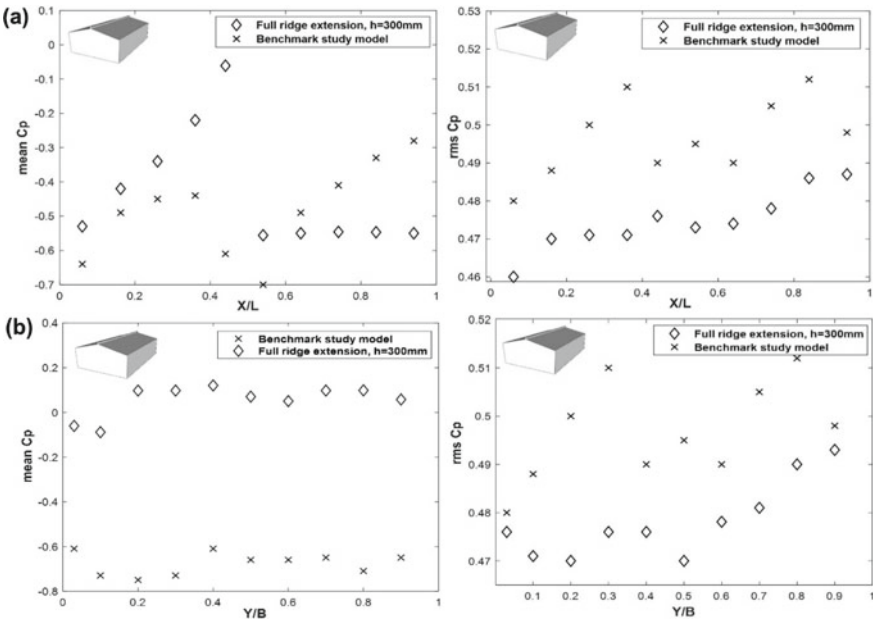

Fig. 7 Variation of mean and rms pressure coefficients along (a) the gable end and (b) the ridgeline

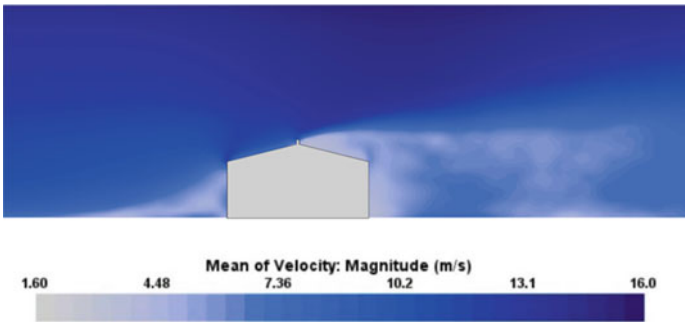

Fig. 8 Mean velocity contours and wind flow streamlines for the model with ridgeline extension

200 mm height on a gable roof, which reduced the peak suction along the ridgeline by 60%. Simultaneously, a maximum of 50% and an overall 10% suction reduction was observed on the leading gable end. It was noticed by comparing the pressure readings' plot between the benchmark and the modified model that the intense negative pressure is shifted from the leading gable edge. The latter flow behaviour indicates that the ridge extension successfully mitigated flow separation at the sharp edges within the separation zones, which led to a reduction in the roof suction, as shown in the mean velocity contour Fig. 8.

3.2 Full Edge Extension

According to the previous studies, the extension is located at the building's edge can displace the vortex formed at the roof windward eave and hence reduce the critical pressure in the same mitigating mechanism exhibited by the ridge extension. However, previous studies indicated edge extensions/plates with low height could aggravate the roof's suction. The edge extensions have been fitted at both sides of the roof edges (longer direction) with 300 mm in height and a thickness of 200 mm. Figure 9 shows a comparison between the benchmark study model and that with the mitigation technique. Figure 10 comparatively displays the rms and mean pressure coefficient (a) along the gable end and (b) in the zone next to the ridgeline. It was noted that the roof corner suction on the leading edge increased by 65% after adding the edge extension to the benchmark model while decreased on the overall gable end (i.e., 14%). The mean and rms values were reduced at the zone next to the ridgeline when the edge extension was introduced to the benchmark study model. The apparent impact of extending the edge on the windward eave where the pressure in the edge regions was increased is found to be in a similar manner when billboards used on commercial buildings, as indicated by Stathopoulous and Baskaran [3]. The latter observation is caused as the higher edges were added, the separation from the vertical edges of the extension altered the vortical structure of the flow over the roof. This

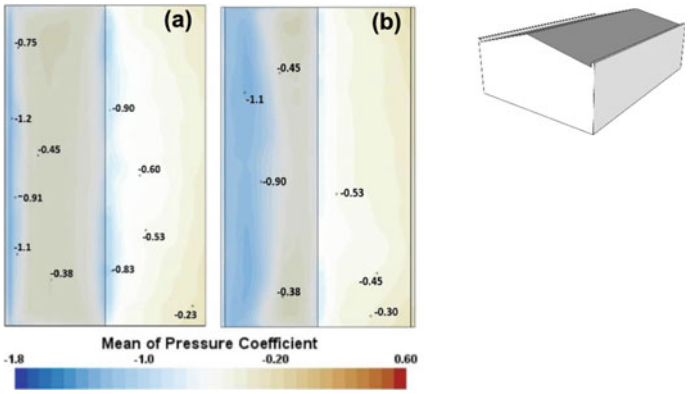

Fig. 9 The distribution of pressure coefficients on the roof surface (a) Benchmark study model (b) model with 300 mm height full edge extension

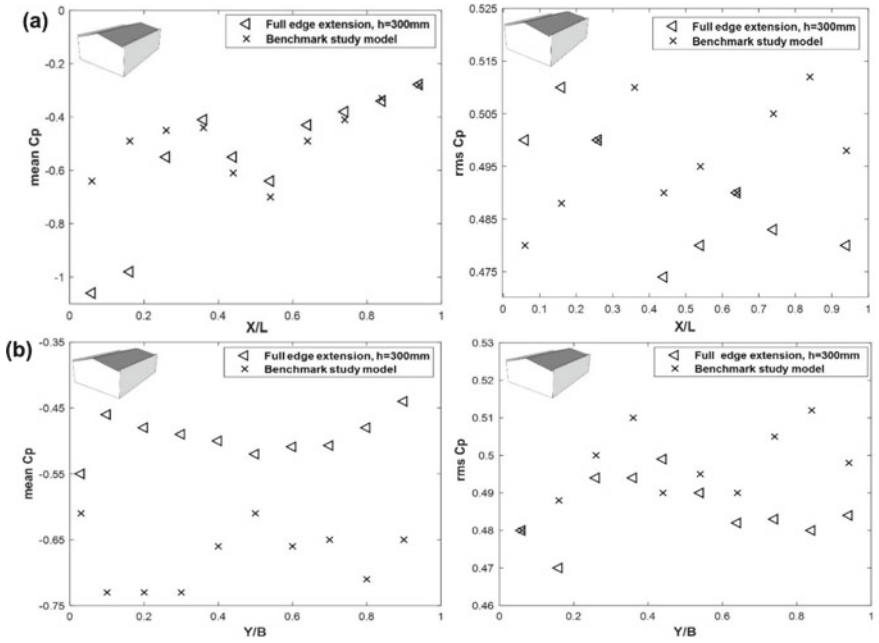

Fig. 10 Variation of mean and rms pressure coefficients along (a) the gable end and (b) the ridgeline

was also detected by Kopp et al. [9] when an isolated low-height full-length parapet was added to the windward eave. The total lift force acting on the entire roof was slightly increased (i.e., less than 2%) when the modification technique was applied to the benchmark study model.

3.3 Full Ridge and Edge Extension

The impact of adding a full edge and ridge extensions on the roof uplift forces was investigated by adding extensions to the edge of the windward and leeward eaves and on the roof rib. Two configurations were examined with heights of 300 and 500 mm and a thickness of 200 mm. Figure 11 displays the variation in the mean pressure distribution for the benchmark and modified models, and Fig. 12 reports the mean and rms of the pressure coefficients along the gable end and in zones next to the ridgeline (i.e., along X/L and Y/B). It can be noticed that adding a full edge and ridge extension led to a shift in the intense negative pressure to the surfaces behind the ridgeline. The latter is evident in the mean and rms pressure values along X/L for both mitigation geometries compared to the benchmark study model. This is probably attributed to the fact that the low height ridgeline extension failed to displace the wind flow, thus preventing separation at the roof rib in which caused greater streamline curvature. Hence, this technique's height plays a crucial role in their aerodynamic mitigation effectiveness. It can be observed from Fig. 12 that the worst suction pressure occurs close to the leading corner and decreases in magnitude away from the corner for the three model configurations. The latter behaviour is due to the fluctuating manners at which the flow separates at sharp edges and re-attaches again within the separation zones. It was also observed that the lower extension and the corner vortices at the leading edge are much evidence. In addition, increasing the extension height on both the ridgeline and edges (i.e., 500 mm) led to reducing the mean pressure in zones next to the ridgeline on the leading roof surface; however, it was still a lower reduction compared to the other modified model (i.e., 300 mm). The latter finding is caused by the fact that the higher ridgeline displaced the flow away from the roof while the lower ridgeline altered the wind flow to downward-acting on a low-rise building's leading roof.

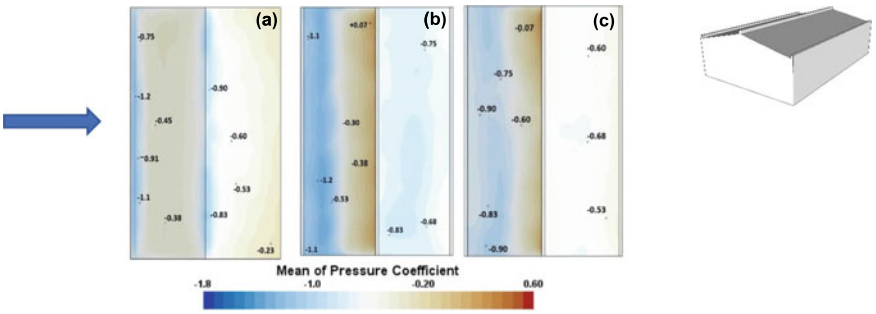

Fig. 11 The distribution of pressure coefficients on the roof surface (a) benchmark study model (b) model with full edge and ridge extensions of 300 mm height and (c) model with full edge and ridge extensions of 500 mm height

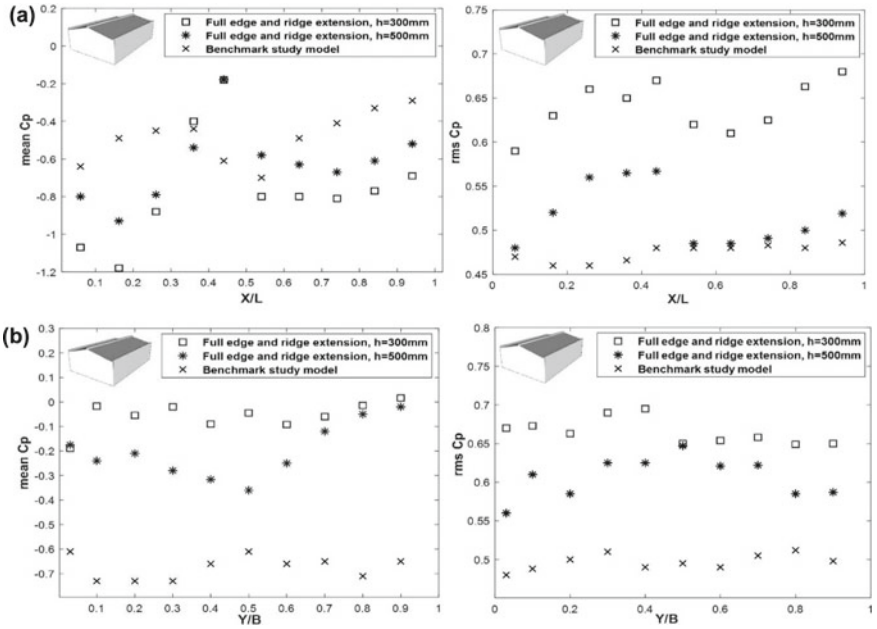

Fig. 12 Variation of mean and rms pressure coefficients along (a) the gable end and (b) the ridgeline

3.4 Discontinuous Solid Parapets

In addition to modifying the negative coefficients next to the ridgeline and at the windward eave, discontinuous parapets were introduced to alter the corner uplift forces. They were placed at four corners and at the gable end ridge intersection, regions where high peak suctions were expected, as demonstrated by Azzi et al. [2]. Pressure readings were recorded on roof surfaces with a slope of 3:12 and with parapets heights of h = 500 and 750 mm, the length is 1000 mm (10% of the building's shorter dimension), and the thickness is 200 mm. Figure 13 presents a variation in the mean pressure distribution for the benchmark study model and the models with discontinues solid parapets, while Fig. 14 illustrates the mean and rms of pressure coefficient at the gable end and in the zone next to the ridgeline. It was noted that the uplift on the leading-edge zone was aggravated after adding both of the parapet's configurations, while the mean and rms were reduced in the leading edge by the presence of the parapets. This finding is in agreement with Kopp et al. [9], where it was concluded that discontinuous parapets could lead to suction increase with $h_{parapet}/(H_{eave} + h_{parapet}) < 0.17$ at the leading corner/edge. The latter finding can be improvised by using porous parapets as it will disrupt wind flow and therefore weakens the conical vortices. [12] reported a drop of 60% in corner suction pressures while using a 33% porous corner/ ridge intersection parapet designed with the same length of 10% of the model's shortest dimension and height of 200 mm. In contrast,

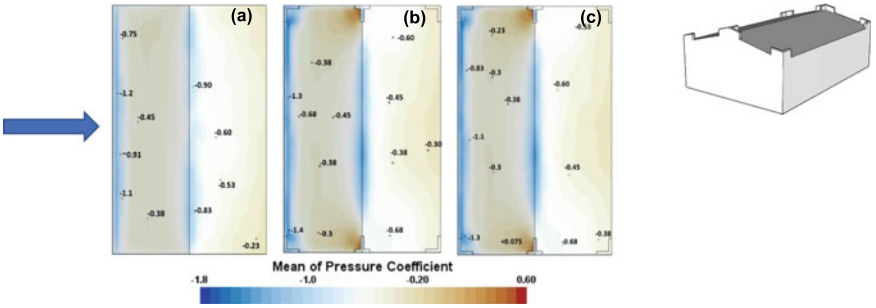

Fig. 13 The distribution of pressure coefficient on the roof surface (a) Benchmark study model, (b) Model with discontinuous solid parapets of 50 mm height and (c) model with discontinuous solid parapets of 750 mm height

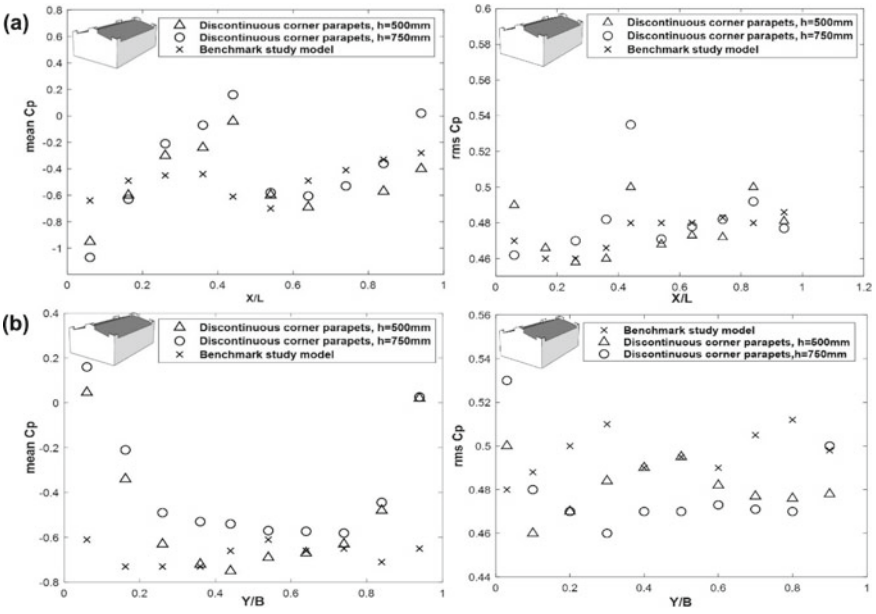

Fig. 14 Variation of mean and rms pressure coefficients along the (a) gable end and (b) the ridgeline

roof interior zones did not experience a change in the pressure magnitudes while using the parapets. 750 mm height corner parapet reduced the suction next to the ridgeline and gable end by an overall of 28% and 45%, respectively. Figure 15 shows the total uplift forces acting on the roof surface for the wind azimuth of 0° (i.e., perpendicular to the ridgeline). The latter figure indicates adding corner parapets led to a reduction in the total uplift forces on the roof surfaces by up to 8%.

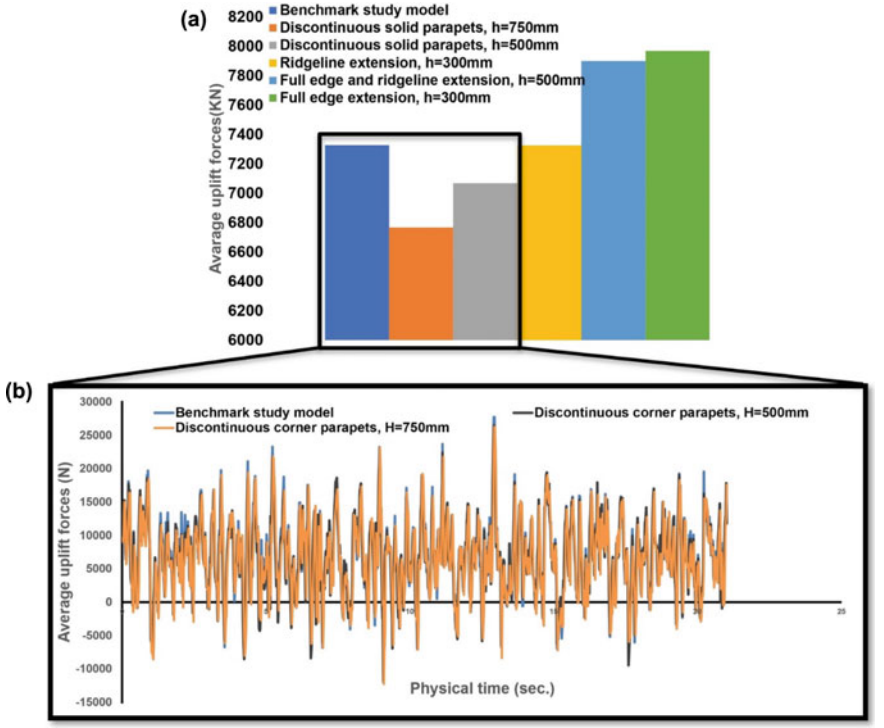

Fig. 15 (a) The avarage uplift forces for the all the modification techniques and (b) The uplift forces time historues on the roof building

4 Conclusion

This paper investigated the effectiveness of various aerodynamic modifications applied to a typical single-story building to reduce extreme suctions on the roof. These modification techniques were (i) ridgeline extension, (ii) edge extension, (iii) Full edge and ridgeline extension and (iv) discontinuous corner parapets. The performance of each modification technique was assessed by comparing the mean and rms values of the pressure on the gable end and zones next to the ridgeline and the average of the total uplift forces. All the modification techniques investigated led to an overall reduction in the pressure in regions next to the ridgeline ranging from 27 to 90%. For instance, extending the windward eave and leeward eave by 300 mm (i.e., edge extension) led to an overall decrease of 27% in the mean pressure along the ridgeline. In comparison, ridgeline extension led to a 90% overall reduction in mean pressure along the ridgeline. However, only the latter techniques reduced the leading corner's suction (i.e., 17%) among all the other modification techniques examined in this study. In contrast, 750 mm height parapets led to an 18% reduction in the corner's

suction attached to the leeward eave. The latter modification configuration also led to a reduction in the overall uplift force by 8%.

This study demonstrated that simple architectural modifications to the building roof edges can reduce the wind-induced suction on the building envelope. These modifications can be easily installed as permanent architectural features or temporarily used for rehabilitation purposes, making them an attractive solution to reduce sharp edges and corners in low-rise buildings.

References

1. Aboshosha H, Ahmed Elshaer GT, Bitsuamlak GT, El Damatty A (2015) Consistent inflow turbulence generator for les evaluation of wind-induced responses for tall buildings. J Wind Eng Ind Aerodyn 142:198–216
2. Azzi,Z, Habte F, Elawady A, Gan Chowdhury A, Moravej M (2020) Aerodynamic mitigation of wind uplift on low-rise building roof using large-scale testing. Front Built Environ
3. Baskaran A, Stathopoulos T (1988) Roof corner wind loads and parapet configurations. J Wind Eng Ind Aerodyn 29(1–3):79–88
4. Bitsuamlak GT, Asce M, Warsido W, Ledesma E, Chowdhury AG (2013) Aerodynamic mitigation of roof and wall corner suctions using simple architectural elements. Ascelibrary. Org 139(3):396–408
5. Courant R, Friedrichs K, Lewy H (1928) Über die partiellen differenzengleichungen der mathematischen physik. Math Ann 100(1):32–74
6. Franke J, Antti Hellsten K, Schlünzen H, Carissimo B (2011) The COST 732 best practice guideline for CFD simulation of flows in the urban environment: a summary. Int J Environ Pollut 44(1–4):419–427
7. Huang P, Peng X, Ming G (2014) Aerodynamic devices to mitigate rooftop suctions on a gable roof building. J Wind Eng Ind Aerodyn 135:90–104
8. Huang SH, Li QS, Wu JR (2010) A general inflow turbulence generator for large eddy simulation. J Wind Eng Ind Aerodyn 98(10–11):600–617
9. Kopp, GA, Surry, D (2005) Wind effects of parapets on low buildings: part 1. Basic aerodynamics and local loads. Elsevier
10. Mooneghi MA, Kargarmoakhar R (2016) Aerodynamic Mitigation and Shape Optimization of Buildings. Elsevier
11. Sandink D, Kopp GA, Stevenson SA, Dale N (2019) increasing high wind safety for canadian homes: a foundational document for low-rise residential and small buildings institute for catastrophic loss reduction building resilient communities
12. Suaris W, Irwin P (2010) Effect of roof-edge parapets on mitigating extreme roof suctions. J Wind Eng Ind Aerodyn 98(10–11):483–491
13. Surry D, Lin JX (1995) The effect of surroundings and roof corner geometric modifications on roof pressures on low-rise buildings. J Wind Eng Ind Aerodyn 58(1–2):113–138

Characterization of the Lateral Response of Base Rocking Steel Bridge Piers

A. Rahmzadeh, M. S. Alam, and R. Tremblay

1 Introduction

In the recent decades, the concept of controlled rocking has attracted a lot of attention. Systems built incorporating such a concept are capable of oscillating along the earthquake and reverting to their original position afterward. More recently, a research project was started by researchers at The University of British Columbia (UBC) and Polytechnique Montréal to investigate post-tensioned rocking steel piers as a cost-effective alternative to concrete piers [1]. The proposed pier comprises a circular tubular steel column, a post-tensioned tendon, and supplemental energy dissipaters (EDs). Instead of material nonlinearity, gap opening as a result of the rocking mechanism at the connection interface, provides substantial deformation capacity under lateral loading. Moreover, the pier exhibits a flag-shaped hysteresis response during a strong earthquake motion with limited or no residual displacements. The columns are prefabricated and can be easily erected on site, which makes the system suitable for accelerated bridge construction (ABC). This paper summarizes the findings of an experimental program on the rocking steel bridge pier. A description of the finite element (FE) validation procedure of the tested columns is also presented. Finally, a parametric study is conducted to identify important parameters that affect the lateral cyclic response of the system.

A. Rahmzadeh (✉) · M. S. Alam
The University of British Columbia, Kelowna, BC, Canada
e-mail: a.rahmzadeh@ubc.ca

R. Tremblay
Department of Civil, Geological and Mining Engineering, Polytechnique Montreal, Montreal, QC, Canada

S. Walbridge et al. (eds.), *Proceedings of the Canadian Society of Civil Engineering Annual Conference 2021*, Lecture Notes in Civil Engineering 244,
https://doi.org/10.1007/978-981-19-0656-5_46

2 Experimental Program

Table 1 lists the properties of the 1/3-scale specimens which were designed to rock at the interface with the foundation. The design procedure involved assuming a major bridge with two 32.4 m long spans located in Vancouver British Columbia Canada, performing time history analyses under three suites of ground motions representative of the site location, identifying the target drift, conducting continuum FE pushover analysis, and checking the performance at the target drift as per CSA S6-14 standard [3]. Then, the prototype was scaled down by a length factor of 3 (Specimen RP4-DT43-PT47-BP20-ED45). The test setup of this specimen is shown in Fig. 1. The specimen was equipped with four buckling-restrained energy dissipating steel bars.

Other variations of the pier include the pier without a base plate and EDs (Specimen RP1-DT43-PT45), the pier without a base plate and EDs having a higher diameter-to-thickness ratio (Specimen RP2-DT64-PT37), and the pier without EDs (Specimen RP3-DT43-PT44-BP20). These variations were designed to experimentally evaluate the findings of a previous analytical-FE investigation wherein it was found out that: (1) local buckling results in the loss of re-centering property of the system, (2) the presence of a base plate can have beneficiary effects on the local behaviour of the column at the highly stressed region of rocking plane [4].

Figure 2 plots the lateral force-drift response for the specimens. As shown in Fig. 2(a), a base plate resulted in having a higher post-uplifting stiffness which led to a higher lateral load capacity. An examination of the specimens following the tests confirmed that the base plate prevented local distortion of column at the rocking plane. The detrimental effects of local buckling are demonstrated in Fig. 2(b). The evolution of excessive out-of-plane deformation of the tube near the rocking interface throughout the lateral displacement cycles yielded in progressive stiffness and strength degradations and eventually led to the loss of self-centering ability. Figure 2(c) compares the specimens with and without ED devices. As expected, having EDs resulted in higher energy dissipation for the system.

Table 1 Details of specimens

Specimen	$d_c \times t_c$ (mm)	$d_{bp} \times t_{bp}$ (mm)	$f_{PT,0}/f_{PT,u}$
RP1-DT43-PT45	406 × 9.53	–	0.45
RP2-DT64-PT37	406 × 6.35	–	0.37
RP3-DT43-PT44-BP20	406 × 9.53	508 × 25.4	0.44
RP4-DT43-PT47-BP20-ED45*	406 × 9.53	508 × 25.4	0.47

* Four EDs added at an angle of 45° w.r.t the loading direction

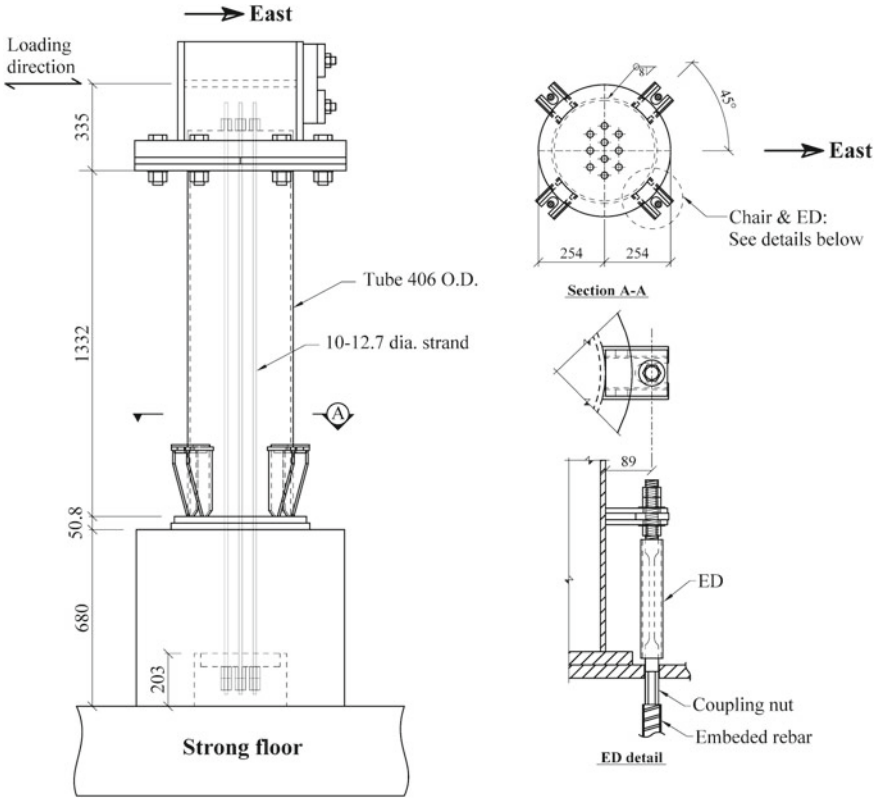

Fig. 1 Details of Specimen RP4-DT43-PT47-BP20-ED45 (dimensions in mm)

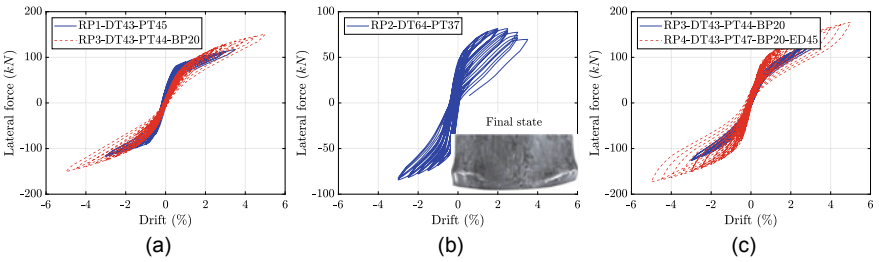

Fig. 2 Experimental lateral force vs. drift response of specimens

3 Validation of FE Modeling Procedure

3D continuum FE models of the specimens (e.g. Fig. 3) were constructed using [2]. 8-noded solid elements were used to mesh the volumes. Surface elements covering

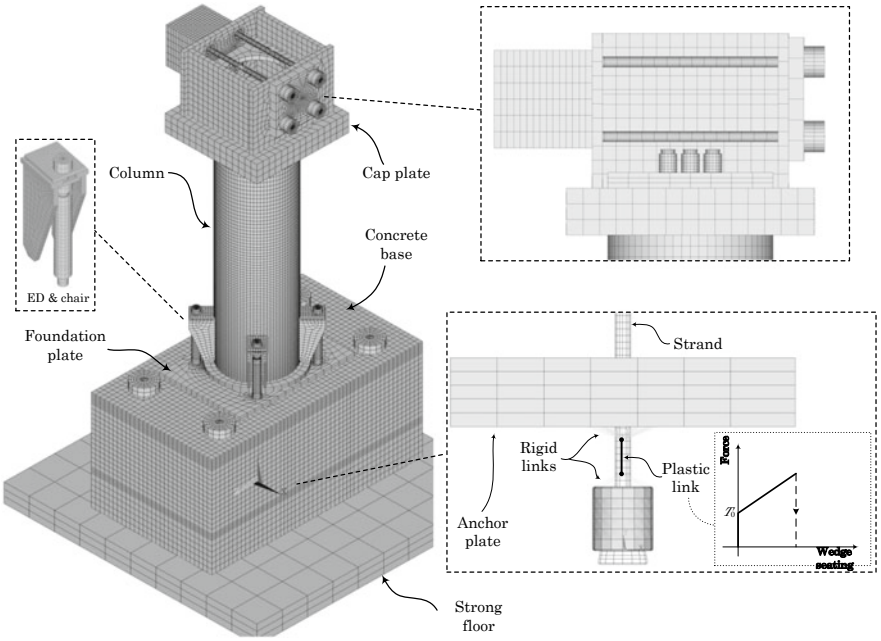

Fig. 3 FE model of Specimen RP4-DT43-PT47-BP20-ED4

underlying solid elements were utilized to model contacts between various components. Depending on the expected behaviour, contacts were set to be either bonded (tied) or standard (frictional). Reinforcing bars were modeled using link elements which share mutual nodes with the solid elements of the concrete base. Cyclic tests on dogbone specimens were conducted to obtain the kinematic and isotropic material responses which used in the calibration of nonlinear material model (Chaboche). A plastic link element was placed in the load path of the strands to indirectly model the cyclic wedge seating and corresponding loss of prestressing force. Eigen value analyses of the tube and fuse length of ED devices were performed, then they were perturbed from their perfect shapes using a combination of their mode shapes. The sequence of loading including prestressing the strands and base rods, and lateral displacement application was the same as the tests. Figure 4(a) displays the comparison between the experimentally recorded lateral force-displacement behaviour of Specimen RP4-DT43-PT47-BP20-ED4 and simulated FE response as well as the deformed shape of the FE model at the largest drift. Good correlation of experiment and FE responses indicates that the FE procedure is able to accurately predict the lateral cyclic behaviour of this system.

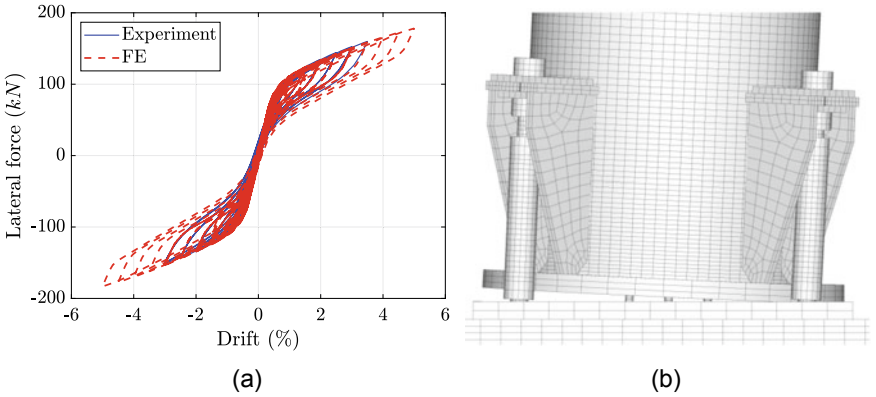

Fig. 4 **a** FE-experiment lateral force-drift comparison, **b** deformation at largest drift

4 Parametric Study

In order to perform a parametric study, a simplified 3D continuum FE model of the rocking steel pier was generated (Fig. 5a). The foundation and base plates and tube were modeled by solid elements. Surface elements were used to model gap opening/closing at the rocking interface. Frame elements were utilized to model the tendon. The tendon was fixed to the top of the column using rigid links. It was

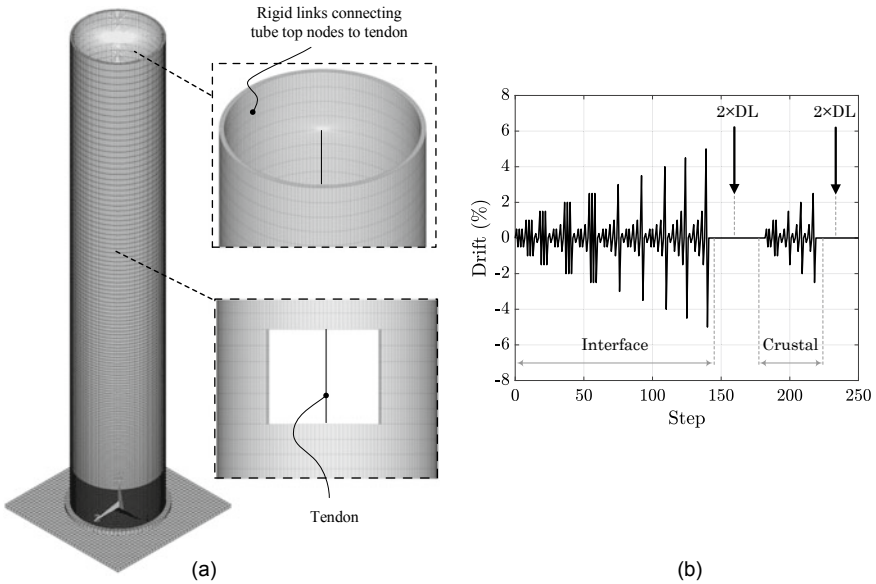

Fig. 5 **a** Simplified FE model of a rocking steel pier, **b** two-stage cyclic loading protocol

assumed that the ED devices did not have significant impact on the lateral stiffness and strength of the system, hence, no ED elements were considered. As shown in Fig. 5(b), the loading protocol consists of two stages illustrative of a scenario where the rocking pier experiences two earthquakes in its lifetime. These stages are representatives of interface and crustal earthquakes, each followed by analyzing the pier under increased dead load by 100% as a rather conservative consideration of the code required performance [3] following an earthquake, i.e. the pier should be able to resist dead load plus 50% live load. The simulations were conducted using [5] and Compute Canada clusters.

In the first set of analyses, height to thickness ratio (h_c/d_c) of the pier, diameter-to-thickness (d_c/t_c) of the tube, initial axial force ratio due to superstructure load, cross-sectional area of the tendon, and the amount of posttensioning force were varied. The initial axial force ratio is obtained by dividing the force from the superstructure load and tendon initial posttensioning by the tube axial yield strength. Residual drift after each analysis was calculated as an indication of the pier performance. The base plate diameter and thickness were kept constant.

An analysis of main effects and their interactions showed the cross-sectional area of the tendon and initial PT, initial axial force ratio due to superstructure load and diameter-to-thickness of the tube are the most influential parameters on the residual drift. Initial axial force ratio can partly embed the effect of tendon-related and dead load factors, however, it neglects the effect of increase in the PT force due to uplift which can play an important role in the buckling behaviour of moderately thin tubes. Figure 6 displays the generally increasing trend of residual drift with increasing initial axial force ratio and diameter-to-thickness ratio of the tube. Also, it suggests that these influential parameters can be adjusted such that the required performance is met. In the next set of analyses, diameter ($d_{bp} = d_c + 2e_{bp}$) and thickness (t_{bp}) of the base plate were added to the varied parameters. The effect of these variables for the tube diameter-to-thickness ratio of 68.5 and three tube aspect ratios is shown in Fig. 7. L_{bp} is the largest dimension of the base plate cross section at the edge of the tube. This figure indicates that the base properties can affect the residual drift for initial axial force ratios above 20%. These effects are less severe for smaller values of d_{bp}/t_c. However, the effects of the base plate properties are less pronounced than those of the d_c/t_c ratio.

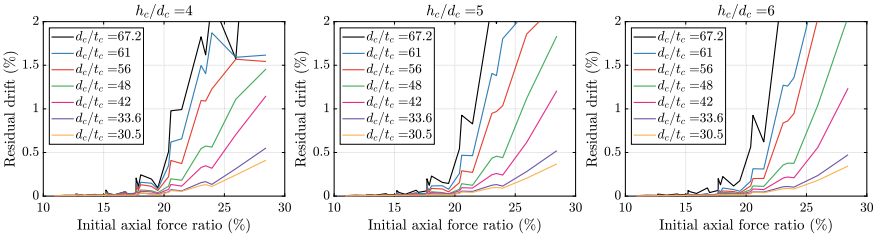

Fig. 6 Effect of axial force and diameter-to-thickness ratio of tube on residual drift

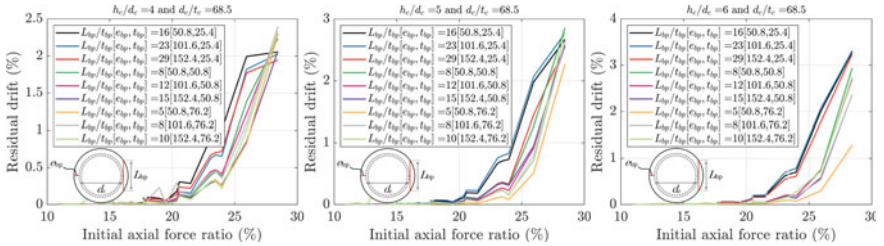

Fig. 7 Effect of base plate dimensions and initial axial force ratio on residual drift for $d_c/t_c = 68.5$

5 Conclusions

This paper presents experimental and numerical investigations on the lateral cyclic behaviour of rocking steel bridge piers. The results of four cyclic tests were summarized. It was shown that a pre-compressed hollow tube can return to its plumb position after being subjected to limited lateral displacements if local buckling is prevented. The addition of a base plate can improve the local and global behaviours of the system by protecting the tube at the rocking interface and increasing the post-uplifting stiffness. It was demonstrated that the continuum FE approach is able to capture the complex contact nonlinearity that occurs while the column uplifts, hence, it results in an accurate prediction of the lateral cyclic response of the system. The validated FE procedure was used to develop a simplified model of the system for a parametric study. Various parameters including tube and base plate dimensions, axial forces due to bridge dead load and initial posttensioning force, and tendon sectional area were considered as independent variables. Each variation of the system was analyzed under a two-stage cyclic loading and the resulting residual drift was recorded as the dependent variable. Tendon area, initial PT force, axial force due to dead load and diameter-to-thickness ratio of the tube were found to be the most influential factors on the pier residual drift. Base plate dimensions may affect the residual drift for high initial axial force ratios of the column. The residual drift can be reduced limited by limiting the proper selection of diameter-to-thickness ratio of tube and the initial axial force ratio.

Acknowledgements The research reported herein was funded by Natural Sciences and Engineering Research Council (NSERC) of Canada under the Collaborative Research and Development (CRD) grant program, and several industrial partners including the Canadian Institute of Steel Construction, Rapid Span Structures Ltd., S-FRAME Software Inc., Emil Anderson Construction Inc., and Klohn Crippen Berger Ltd. The support provided by Compute Canada is also gratefully acknowledged.

References

1. Alam MS, Tremblay R, Islam K, Rahmzadeh A, Hossain F, King P (2020) "Use of Rocking Steel Piers for Enhanced Bridge Seismic Performance." In: 17th World Conference on Earthquake Engineering, Sendai, Japan
2. ANSYS Multiphysics v19.2. ANSYS Inc., Canonsburg, PA
3. CSA (2014) CSA S6–14, Canadian Highway Bridge Design Code (CHBDC). Mississauga, ON: Canadian Standards Association (CSA)
4. Rahmzadeh A, Alam MS, Tremblay R (2018) Analytical prediction and finite-element simulation of the lateral response of rocking steel bridge piers with energy-dissipating steel bars. J Struct Eng 144(11):04018210. https://doi.org/10.1061/(ASCE)ST.1943-541X.0002216
5. UBC Advanced Research Computing (2019) "UBC ARC Sockeye." UBC Advanced Research Computing. https://doi.org/10.14288/SOCKEYE

Shape Factor Influence of Fibre Reinforced Elastomeric Isolators on the Seismic Response of a Bridge Pier

Miah Mohammed Riyadh, Jhordy Rodriguez, and M. Shahria Alam

1 Introduction

Bridge infrastructures play a key role in the transportation network of any country or region. Significant challenges underly to keep the bridges safe during such catastrophic events [22]. The concept of base isolation using elastomeric bearings is a well understood concept and widely utilized for alleviating the consequences following a seismic event. Large movements can be mitigated by placing a flexible damping system between the substructure and superstructure. Common examples of such flexible damping devices are lead core rubber isolators or traditional elastomeric isolators [12, 17, 30]. Fibre reinforced elastomeric isolators (FREIs), when compared to traditional elastomeric isolators, have the steel reinforcement layers substituted with an appropriate fibre material. As a result, FREIs are much lighter, cheaper as it does not require a labor-intensive bonding process, and can be mass produced with the help of precision cutters to shape them into required sizes from larger dimensions [9, 14].

[13] proposed a simplified theory to address issues with stability in elastomeric bearings. The theory relates the critical load capacity of elastomeric bearings being a function of the shape factors. The shape factor (S_F) is a measure of the local geometry of an elastomeric bearing that quantifies the inverse of each elastomeric layer's slenderness. The secondary shape factor (S_{F2}) is a measure of the inverse of the global slenderness which describes the bearing's tendency to remain stable under

M. M. Riyadh (✉) · J. Rodriguez · M. S. Alam
School of Engineering, University of British Columbia, Kelowna, Canada
e-mail: riyadmd@mail.ubc.ca

J. Rodriguez
e-mail: jirb96@mail.ubc.ca

M. S. Alam
e-mail: shahria.alam@ubc.ca

S. Walbridge et al. (eds.), *Proceedings of the Canadian Society of Civil Engineering Annual Conference 2021*, Lecture Notes in Civil Engineering 244,
https://doi.org/10.1007/978-981-19-0656-5_47

lateral displacements. Values $S_F > 5$ of and $S_F > 3$ are recommended to maintain good performance in both vertical and horizontal directions [21].

In this study, the seismic response of a prototype bridge pier is explored when isolated with carbon fibre reinforced elastomeric isolators (C-FREIs). By considering four different shape factors for the C-FREIs, the seismic response of the isolated pier models was compared to the non-isolated pier model. The material model for the high damping elastomer in the C-FREIs was first introduced and compared with reference experimental data. From the validated material model, four full-scale C-FREIs were designed having different shape factors. From the hysteresis behavior of the isolators, bilinear models were developed for each C-FREI which were incorporated into a suitable bridge pier numerical model. Three different ground motion sets (crustal, intraplate, subduction) were considered with each set having 11 ground motion records. Finally, non-linear time history analyses were carried out to obtain the dynamic response of the bridge piers and compare their seismic performance.

2 Modelling of Carbon-Fiber Reinforced Elastomeric Isolators

2.1 Validation of the High Damping Elastomer (HDE) Material

High damping elastomers (HDEs) have higher damping capacity and can withstand higher magnitudes of strain when compared to synthetic elastomers. HDEs are fabricated using vulcanized rubber synthesized with explicit materials such as extra-fine carbon black, oil, plasticizer, and other exclusive fillers [29]. It is difficult to accurately capture the rheological response of HDE due to its complex and non-linear behavior experienced at large deformations (often referred to as scragging behavior). Many analytical and theoretical modelling techniques have been applied to accurately capture the hysteresis behavior of high damping elastomers which is a function of strain amplitude combined with Mullins' effect [2, 20].

The modelling of HDE in this study was done in a finite element software ANSYS (2019 R3). The mechanical response of HDE subjected to combined compression-shear loadings is often captured by a hyper-elastic or a hyper-viscous material. Hyper-viscosity refers to a hybrid material model constituting the elastic behavior being denoted with a hyper-elastic material while the rate-dependent damping characteristic under pure shear load is denoted with a viscoelastic model. A combination of higher order Mooney-Rivlin hyper-elastic material and Prony viscoelasticity has been integrated to simulate the strain hardening behavior at large strains in several studies, providing excellent accuracy [1, 10]. Therefore, a 9 parameter Mooney-Rivlin is used to simulate the hyper-elastic behavior, and a Prony material model is selected to simulate its viscoelastic shear response.

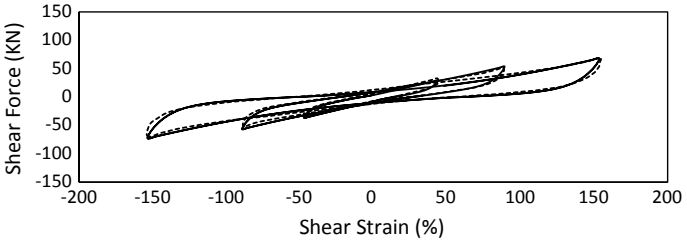

Fig. 1 Validation of the high damping rubber model with experimental results [6] adapted from

The accuracy of the material model chosen for HDE is proven by comparing it to an experimental investigation conducted on a high damping elastomeric bearing as demonstrated in Fig. 1 [6]. The dotted lines represent the experimental data while the solid lines represent the numerical data. As observed, the proposed material model is capable to capture the behavior of HDE to an acceptable degree of accuracy. The highest variations between the results are in the negative shear strain region due to the challenges associated with applying perfect symmetry conditions in real-time experiments with an absolute error lower than 10%.

2.2 Design of Carbon-Fiber Reinforced Elastomeric Isolators (C-FREIs)

Full-scale C-FREIs are designed in this section to be used as an isolation system for a bridge. To this end, four C-FREIs are modelled in bonded applications which have variable shape factors. The shape factor (S_F) and the secondary shape factor (S_{F2}) are calculated according to Eqs. 1 and 2.

$$S_F = (L \times W)/(2t_eL + 2t_eW) \tag{1}$$

$$S_{F2} = \frac{W}{n_e t_e} \tag{2}$$

Where, L and W are the length and width of the bearings, respectively, t_e is the thickness of individual elastomer layers, n_e is the number of elastomer layers.

This study is conducted on square shaped bearings to maintain consistency in both longitudinal and transverse directions. According to Eqs. 1 and 2, variations in the shape factor can be obtained either by varying the loading area of the bearings or the thickness of each elastomer layer while the secondary shape factor can be varied by either changing the thickness of each elastomer layer, the number of elastomer layers, as well as the loading area. In this study, changes in the shape factors were achieved by changing each elastomer layer thickness (t_e) whilst keeping the loading

Table 1 Physical dimensions and shape factors of the designed C-FREIs

Bearing	L × W (mm^2)	n_e	t_e (mm)	n_f	t_f (mm)	H_e (mm)	S_F	S_{F2}
C-FREI-1	400 × 400	7	12.50	6	4	111.5	8	4.6
C-FREI-2	400 × 400	7	10.00	6	4	94.0	10	5.7
C-FREI-3	400 × 400	7	8.30	6	4	82.1	12	6.9
C-FREI-4	400 × 400	7	7.15	6	4	74.1	14	8.0

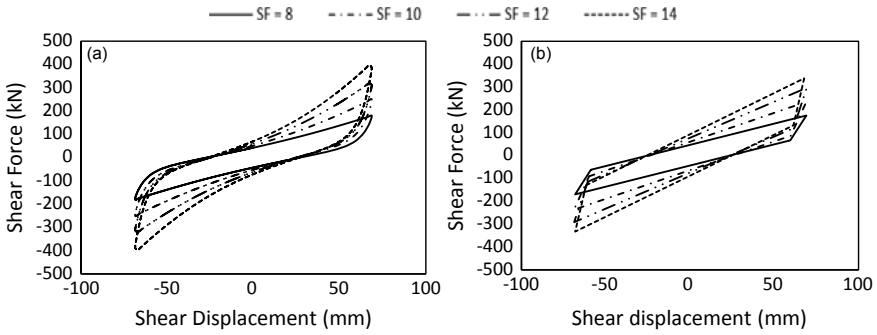

Fig. 2 **(a)** Shear force vs. Shear displacement hysteresis curves for C-FREIs with variable shape factors **(b)** Idealized bilinear models of C-FREIs with variable shape factors

area and the number of elastomer layers constant. Table 1 displays the geometric dimensions of the four C-FREIs. H_e is defined as the total height of the bearing as given in Eq. (3).

$$H_e = (n_e \times t_e) + (n_f \times t_f) \tag{3}$$

Where, n_f and t_f are the number of carbon-fiber reinforcement layers and the thickness of each reinforcement layer, respectively.

Values of S_F and S_{F2} are chosen accordingly to have superior performance in both vertical and horizontal directions [21, 28]. To model the C-FREIs in ANSYS, the validated 9 parameters Mooney Rivlin-Prony material model is chosen for the elastomer layers. Carbon fiber reinforcement layers are modelled with orthotropic elasticity with the parameters adapted from [7]. Each C-FREI is bonded to thick steel end plates which are modelled as an elastic isotropic model with Young's modulus of 200 GPa and Poisson's ratio of 0.3.

The C-FREIs are subjected to compressive-shear loadings to obtain the hysteresis functions. The numerical testing method is done according to as described in ISO 22762 [11]. The bearings are subjected to constant vertical pressure of 7.5 MPa followed by 3 cyclic shear displacements with a frequency of 0.5 Hz and an amplitude of 70 mm. The loading is applied to the bearing's top end steel plate where the bottom end plate is fixed in all directions. Figure 2a shows the hysteresis loops obtained from the finite element results for the four C-FREIs. It is observed that C-FREI with a

Table 2 Bilinear model properties of the designed C-FREIs

C-FREI	S_F	K_o (kN/mm)	F_Y (kN)	r
C-FREI-1	8	1.86	46.6	0.162
C-FREI-2	10	2.53	60.2	0.156
C-FREI-3	12	3.16	77.6	0.143
C-FREI-4	14	3.61	93.7	0.114

higher shape factor has higher horizontal stiffness and equivalent damping ratio when compared to a lower shape factor.

2.3 Bilinear Modelling of Carbon-Fiber reinforced Elastomeric Isolators (C-FREIs)

To characterize the behavior of an elastomeric bearing under cyclic loads, a bi-linear model is often preferred due to its simplicity when compared to other high damping elastomer material models [16]. A bilinear force–displacement relationship is represented with two linear slopes where each slope represents a particular stiffness magnitude. The stiffness of high damping isolators reduces at higher strains causing two different linear branches referred to as pre-yield and post-yield stiffnesses. Moreover, the bilinear model is the most suitable and readily available model in the software SeismoStruct (SeismoSoft 2021), which is used for modelling the bridge pier. Figure 2b shows the idealized bilinear models for the C-FREIs. The bilinear model properties are listed in Table 2. The model properties are determined by taking the stiffness, residual deformation, and the energy dissipated per cycle.

3 Modelling of Bridge Pier

3.1 Description of the Prototype Bridge Pier

To evaluate the seismic response of the bridge pier isolated with C-FREIs, a suitable bridge prototype needs to be selected. For this study, a single bridge pier system utilized in several shake-table tests at the University of California, Berkley, was considered [26]. The specimen was subjected to uniaxial shake table excitation to evaluate the nonlinear response (seismic performance) under such specifications. The test was carried out considering only the transverse direction of the bridge, allowing it to have fixed at the base and free at the top boundary conditions.

The specimen consisted of a 1.22 m-diameter (D) circular column of 7.32 m-height (L) above the footing, resulting in a height-to-diameter ratio (L/D) of 6

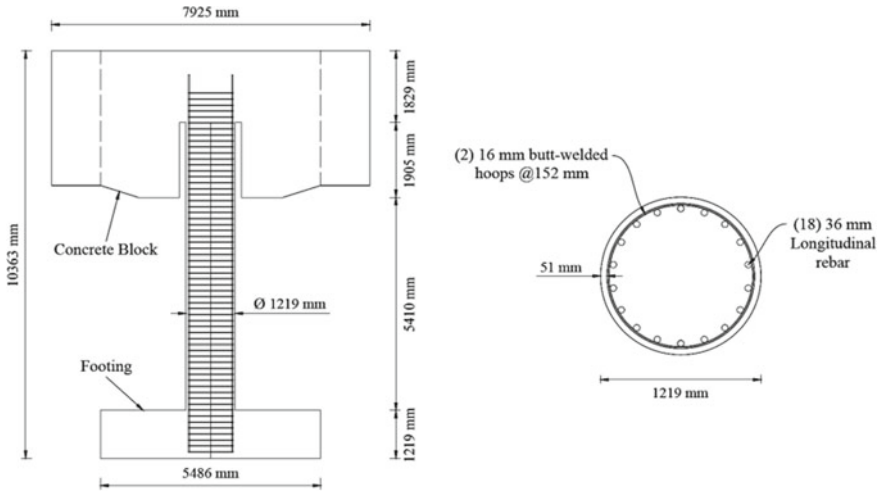

Fig. 3 Bridge Bent configuration and geometry and cross-section of the column

(predominant flexural behaviour). The column was provided with a longitudinal reinforcement ratio (ρ_o) of 1.55%, and a transverse volumetric configuration ratio (ρ_s) of 0.95%. The superstructure mass of the bridge was represented by a concrete block weighing 2.32 MN cast on top of the column. The bridge configuration is shown in Fig. 3. For more information, the reader can refer to the complete research report available on the PEER website [24].

3.2 Numerical Modelling and Validation of the Prototype Bridge Pier

The software SeismoStruct (SeismoSoft 2021) was utilized to create a suitable numerical model using force-based fiber-elements. The transverse response of the structure was represented by a single-degree-of-freedom (SDOF) model [25]. Likewise, the mass of the superstructure (two adjacent half spans) was lumped at the effective height from the foundation level to the centroid of the superstructure. A three-dimensional inelastic force-based element with five Gauss–Lobatto quadrature integration points was implemented to model the bridge pier. The constitutive laws of materials (nonlinearity) were defined as per the [18] and Menegotto and Pinto (1973) models, for the concrete and reinforcement steel, respectively. To connect the top of the column to the centroid of the superstructure a rigid link element was utilized. Similarly, an elastic rotational spring was added at the bottom end of the column to simulate bar-slip rotations. The effective stiffness (K_{SE}) and the effective strain penetration length (l_{sp}) are included and calculated using the expressions proposed by [8] and [23], respectively.

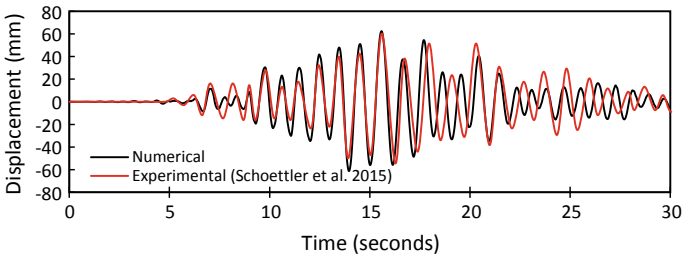

Fig. 4 Comparison of the experimental and numerical time-history displacement response

Before utilizing the numerical model, validation of the model with the experimental data reported is a critical step. The displacement time-history response generated numerically was compared against that measured experimentally by [26], as shown in Fig. 4.

From the figure, it is evident that the model can accurately predict the dynamic response of the bridge pier in the transverse direction under seismic loads. To model the bridge pier isolated with C-FREIs, an elastic bilinear link element was added connecting the top of the column to the centroid of the superstructure. The bilinear link element was modelled using the parameters reported in Table 2.

3.3 Selection of Ground Motions

The Cascadia subduction zone was considered to select the seismic hazards. This region is a high seismic region delimited from Northern California in the United States to Northern Vancouver Island in Canada. Here, three different sets of earthquake types have been identified: crustal earthquakes, subcrustal earthquakes, and subduction earthquakes [4], with each set having 11 records. The ground motion records were obtained from the Pacific Earthquake Engineering Research Center [24], Consortium of Organizations for Strong Motion Observation Systems (COSMOS), and Kyoshin Network (K-Net) databases, for crustal, intraplate, and subduction earthquakes, respectively. For each recording station, only the transverse horizontal ground motion components were considered. All ground motions were spectrally matched to the target design spectrum of Vancouver soil class C (2% in 50 years seismic hazard). Details of the selected ground motion sets are given in Table 3 and their mean response spectrum is shown in Fig. 5. In the next section, displacement time history analyses are carried out to obtain the relative displacements for each ground motion record.

Table 3 Details of the ground motions sets

Ground motion set	Number of records	Moment magnitude range	R^a (km)	PGA range (g)
Crustal	11	6.61–7.40	13–51	0.109–0.568
Intraplate	11	6.80–7.60	59–93	0.187–0.489
Subduction	11	9	152–166	0.800–1.246

R^a = Range of the closet distance to the rupture surface

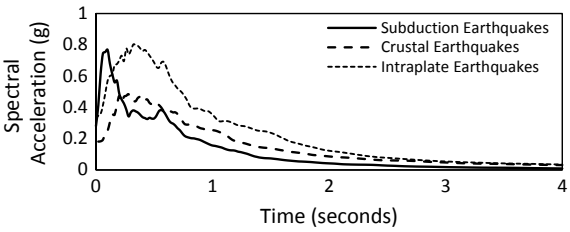

Fig. 5 Mean response spectrum of the selected seismic hazards

4 Results and Discussion

The superstructure mass was isolated from the pier by placing the C-FREIs between them. As a result, the forces which are transferred to the pier are considerably reduced. In this regard, the maximum relative displacements (δ_{max}) (displacement of the top of the pier with respect to the base) for the isolated pier will decrease compared to those from the non-isolated pier. Figure 6 shows the variations of the relative displacements of the pier subjected to various types of seismic hazards. An example of one record from each seismic hazard is included in Fig. 6 for visualization purposes.

Implementing the elastomeric bearings to isolate the bridge pier from the superstructure mass causes a significant reduction in the relative displacement of the pier as observed in Fig. 6. For all three different seismic hazards, the C-FREIs were successfully able to reduce the peak displacements experienced by the pier. A non-comprehensive visualization of the results shows that C-FREIs with different values of shape factors almost have similar performance to reduce the relative displacements incurred by the bridge pier. For instance, when comparing Fig. 6(a) and (b), for a specific record of crustal and sub-crustal seismic hazards respectively, C-FREIs with higher shape factors had a slightly superior performance in reducing the displacements incurred by the bridge pier. This behavior is expected as C-FREIs with a higher shape factor correspond to higher lateral stiffness and energy dissipating capability as depicted in Sect. 2.2.

Comparing Fig. 6(c) for the subduction hazard, a clear consensus cannot be made between the performance variation of the different C-FREIs due to their very similar performance levels. It is also noteworthy to mention that subduction records give higher peak displacements when compared to the other types of ground motion. However, in this study, the records were scaled to Vancouver site class C

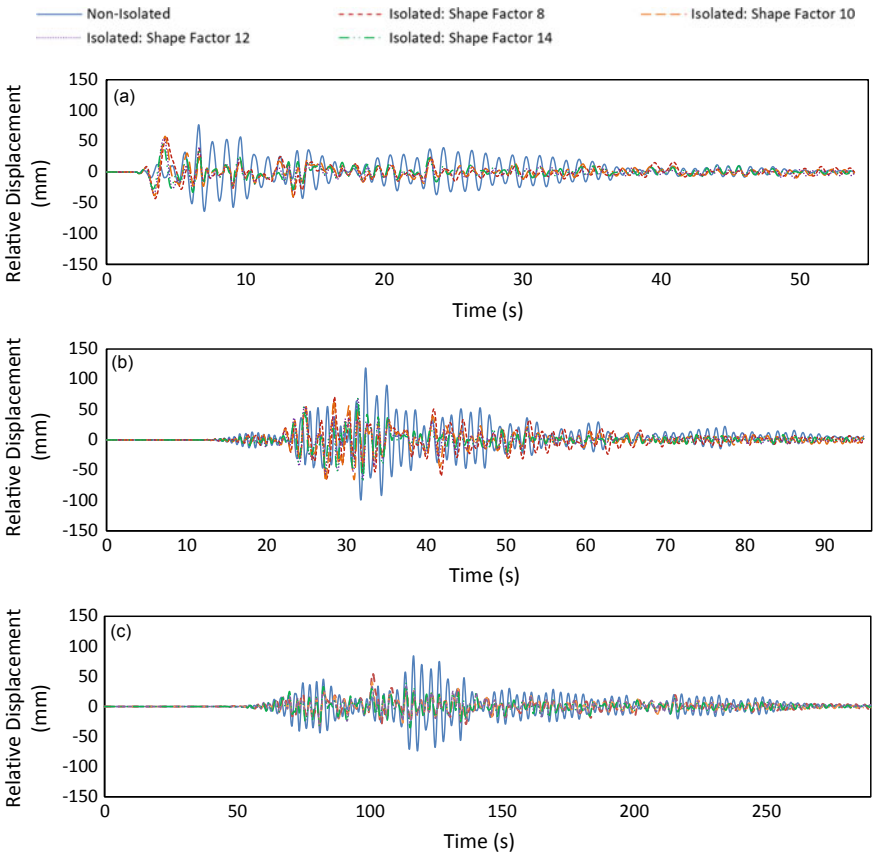

Fig. 6 Displacement time history response for **(a)** crustal hazard record **(b)** subcrustal hazard record **(c)** subduction hazard record

(2% in 50 years seismic hazard), which resulted in the subduction records giving lower displacements. The maximum relative displacements (δ_{max}) experienced by the bridge pier subjected to each ground motion is an excellent indicator to determine its state of damage. The damage limit states are defined according to Canadian Highway Bridge Design Code CSA S6-19 Table 4.16 [5] as minimal damage, repairable damage, extensive damage, and probable replacement. It is important to note that for the non-isolated pier, δ_{max} for crustal and subduction hazards (for all ground motion records) did not exceed minimal damage. However, for subcrustal hazard, the δ_{max} experienced by the pier exceeded the minimal damage state for the majority of the ground motion records but did not exceed the repairable damage state.

Figure 7 shows the box and whisker plots for the isolated and the non-isolated pier for all ground motions belonging to specific hazard level. Figure 7(a), (b), and (c) correspond to crustal, subcrustal, and subduction hazards, respectively. For crustal

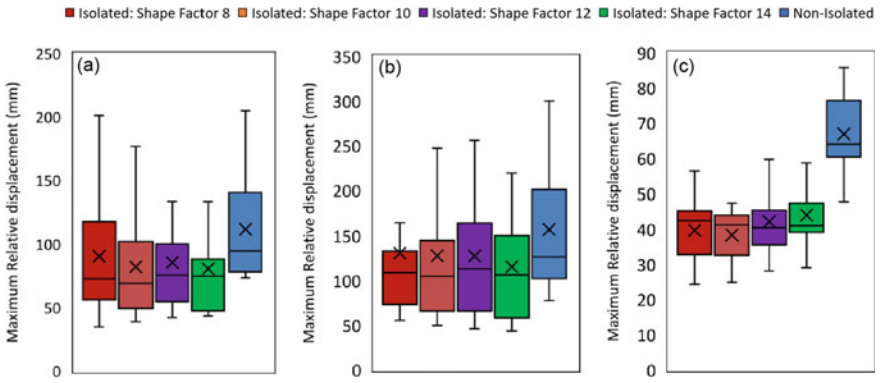

Fig. 7 Box and whisker plots for the maximum relative displacements for the pier **(a)** crustal hazard records **(b)** subcrustal hazard records **(c)** subduction hazard records

ground motions (see Fig. 7a), the mean maximum displacement (δ_{mean}) of the non-isolated pier is 24%, 36%, 31%, 38% higher than the pier isolated with C-FREIs having a shape factor of 8, 10, 12, and 14, respectively. Similarly, for subcrustal ground motions (see Fig. 7b), δ_{mean} for the non-isolated pier is 20%, 23%, 23%, and 36% higher than the pier isolated with C-FREIs having a shape factor of 8,10,12, and 14, respectively. For the subduction ground motions (see Fig. 7c), the pier isolated with C-FREIs having shape factors of 8, 10, 12, and 14 reduce the δ_{mean} values by 69%, 74%, 58%, 59%, and 52%, respectively compared to the non-isolated pier. These values imply that isolating the pier with C-FREIs are successfully able to dampen the forces transmitted to the pier thereby reducing the peak displacements incurred by the pier. However, it is worth noting that the damping offered by the C-FREIs are more pronounced for subduction type hazards. Moreover, different values of shape factors of the C-FREIs are observed to have very minimal variation for subduction type hazards, while for crustal and subcrustal type hazards, C-FREIs with higher shape factor are observed to have a slightly enhanced performance in damping the forces transmitted to the pier.

The damage states of the C-FREIs under respective ground motions are of concern due to their highly non-linear behavior under strong ground motions. The damage limit states of elastomeric bearings are determined based on available literature adapted from Zhang and Huo (2009). The damage states are based on the shear strains of the elastomeric bearings labelled as slight, moderate, extensive, and collapse, corresponding to 100%, 150%, 200%, and 250%, respectively. According to the strains calculated, for crustal type hazard, C-FREIs with the highest shape factor experienced extensive damage for only one ground motion. For subcrustal type hazard, C-FREI with the highest shape factor experienced collapse under three ground motion records. For subduction type hazard, the C-FREIs did not exceed the minimal damage. This imply that C-FREIs with a lower shape factor will often be preferred due to their ability to experience larger strain levels, and similar performance to C-FREIs with higher shape factors.

5 Conclusion

The performance of carbon-fiber reinforced elastomeric isolators (C-FREIs) with variable shape factors are studied by isolating a bridge pier in the transverse direction. Initially a numerical material model for high damping elastomer material is validated for designing the C-FREIs. Bilinear models are developed from the hysteretic behavior of the designed C-FREIs obtained from numerical simulations. The bilinear models were implemented along with the bridge pier numerical model to represent an isolated system subjected to three different hazards (crustal, subcrustal, and subduction). Displacement time history analyses were carried out to measure the seismic performance of the isolators and investigate their effectiveness. According to the results obtained, the C-FREIs were able to significantly reduce the peak displacements experienced by the pier system, thereby limiting their structural damage. C-FREIs with higher shape factors are observed to have a slightly superior performance for crustal and subcrustal type hazards. Whereas, for subduction type hazards, variable shape factor values are seen to have similar seismic performance. Moreover, isolating the pier system with C-FREIs are the most effective in subduction type hazards. Furthermore, larger strain levels are obtained for C-FREIs with a higher shape factor which are more prone to damage for strong ground motion records.

References

1. Ahmadipour M, Shahria Alam M (2017) Sensitivity analysis on mechanical characteristics of lead-core steel-reinforced elastomeric bearings under cyclic loading. Eng Struct 140:39–50
2. Amin AFMS, Lion A, Sekita S, Okui Y (2006) Nonlinear dependence of viscosity in modeling the rate-dependent response of natural and high damping rubbers in compression and shear: experimental identification and numerical verification. Int J Plast 22(9):1610–1657
3. COSMOS (Consortium of Organizations for Strong Motion Observation Systems). Strong-motion virtual data center. http://www.cosmos-eq.org/i
4. CREW (Cascadia Region Earthquake Workgroup) (2009) Cascadia deep earthquakes. Washington division of Geology and Earth Resources, Washington
5. CSA (Canadian Standards Association) (2019) Canadian Highway Bridge Design Code. CSA S6–19. Canadian Standards Association. Rexdale, Canada, CSA
6. Dall'Asta A, Ragni L (2006) Experimental tests and analytical model of high damping rubber dissipating devices. Eng Struct 28(13): 1874–1884
7. Das, A., Dutta, A., Deb, S.K.(2012) Modeling of fiber-reinforced elastomeric base isolators. In: 15th World Conference on Earthquake Engineering, Lisbon, Portugal
8. Elwood KJ, Eberhard MO (2009) Effective stiffness of reinforced concrete columns. ACI Struct J 106(4):476–484
9. Van Engelen NC, Osgooei PM, Tait MJ, Konstantinidis D (2014) Experimental and finite element study on the compression properties of modified rectangular fiber-reinforced elastomeric isolators (MR-FREIs). Eng Struct 74:52–64
10. Hedayati Dezfuli F, Shahria Alam M (2013) Multi-criteria optimization and seismic performance assessment of carbon FRP-based elastomeric isolator. Eng Struct 49:525–540
11. International Organization for Standardization (2018) Elastomeric Seismic-Protection Isolators, ISO 22762. International Organization for Standardization, Geneva

12. Ishii K, Kikuchi M (2019) Improved numerical analysis for ultimate behavior of elastomeric seismic isolation bearings. Earthq Eng Struct Dynam 48(1):65–77
13. Kelly JM (1993) Earthquake-Resistant Design with Rubber. Springer-Verlag, London
14. Kelly JM (1999) Analysis of fiber-reinforced elastomeric isolators. J Struct Earthquake Eng 2:19–34
15. K-Net (Kyoshin Network Database). Strong-motion data http://www.kyoshin.bosai.go.jpi
16. Liu T, Zordan T, Briseghella B, Zhang Q (2014) An improved equivalent linear model of seismic isolation system with bilinear behavior. Eng Struct 61:113–126
17. Lu X, Wang D, Wang S (2016) Investigation of the seismic response of high-rise buildings supported on tension-resistant elastomeric isolation bearings. Earthq Eng Struct Dynam 45(13):2207–2228
18. Mander JB, Priestley MJN, Park R (1988) Theoretical stress strain model for confined concrete. J Struct Eng 114:1804–1826
19. Menegotto M, Pinto PE (1973) Method of Analysis for Cyclically Loaded R.C. Plane Frames including Changes in Geometry and Nonelastic Behaviour of Elements under Combined Normal Force and Bending. In: Symposium on the Resistance and Ultimate Deformability of Structures, pp. 15–22
20. Miehe C, Keck J (2000) Superimposed finite elastic-viscoelastic-plastoelastic stress response with damage in filled rubbery polymers experiments, modelling and algorithmic implementation. J Mech Phys Solids 48(2):323–365
21. Montuori GM, Mele E, Marrazzo G, Brandonisio G, De Luca A (2016) Stability issues and pressure-shear interaction in elastomeric bearings: the primary role of the secondary shape factor. Bull Earthq Eng 14(2):569–597
22. Muntasir Billah AHM, Shahria Alam M (2015) Seismic fragility assessment of concrete bridge pier reinforced with superelastic shape memory alloy. Earthq Spectra 31(3):1515–1541
23. Panagiotakos TB, Fardis MN (2001) Deformations of reinforced concrete members at yielding and ultimate. ACI Struct J 98(2):135–148
24. PEER (Pacific Earthquake Engineering Research Center) (2011) "PEER ground motion database" (http://peer.berkeley.edu/nga/). Accessed 1 Sept 2020
25. Priestley MN, Seible F, Calvi GM (1996) Seismic Design and Retrofit of Bridges. John Wiley & Sons
26. Schoettler MJ, Restrepo JI., Guerrini G, Duck DE, Carrea F (2015) A full-scale, single-column bridge bent tested by shake-table excitation. In: PEER report 2015/02, Pacific Earthquake Engineering Research Center (PEER). University of California, Berkeley, CA
27. SeismoStruct [Computer software] (2021) Earthquake Engineering Software Solutions, Pavia, Italy
28. Shakeri H, Ali M (2013) Effect of shape factor and rubber stiffness of fiber-reinforced elastomeric bearings on the vertical stiffness of isolators. Trends in Applied Sciences Research 8(1):14–25
29. Vanngo T, Dutta A, Deb S (2017) Evaluation of horizontal stiffness of fibre-reinforced elastomeric isolators. Earthquake Eng Struct Dynam 46:1747–1767
30. Weisman J, Warn GP (2012) Stability of elastomeric and lead-rubber seismic isolation bearings. J Struct Eng 138(2):215–223
31. Zhang LW, Zhao Hui L, Chen C (2020) Seismic fragility analysis of bridge piers using methods of moment. Soil Dyn Earthq Eng 134:1–11

Effect of Slenderness Ratio on HSC Columns Reinforced with GFRP Bars and Spirals

M. Almomani, K. Mahmoud, and E. El-Salakawy

1 Introduction

Many attempts have been made to eliminate corrosion in reinforced concrete structures, but different treatments of existing steel reinforcement only seem to delay the inevitable corrosion [2]. The industry has turned to alternatives such as fiber-reinforced polymers (FRP) reinforcement. Many research studies have been carried out in recent years to investigate the behaviour of such materials, which were successful in proving the viability of FRP reinforcements. The use of glass FRP (GFRP) has been found to be more viable than other types due to its relatively cheap cost and its higher deformability [12]. The major differences between steel and GFRP reinforcement is the lack of yielding behaviour in GFRP and its low modulus of elasticity and compressive strength. GFRP bars showed effective contribution to column capacity as verified by multiple studies [1, 4, 8, 9, 13], however, codes are still very conservative about their use in such structural elements. Codes, such as the Canadian code for FRP-RC building structures, CSA S806-12 [7] and the ACI 440.1R-15 [3] design guideline do not consider any compressive capacity of FRP longitudinal reinforcement. However, the Canadian code for bridges, CSA S6-19 [6] has very recently allowed for considering of compression in bars, while limiting the strains in the FRP bars to 0.002.

The current literature provides evidence of the viability of GFRP reinforcement in columns with normal-strength concrete (NSC) [4, 12, 13]. However, high-strength

M. Almomani (✉) · K. Mahmoud · E. El-Salakawy
University of Manitoba, Winnipeg, Canada
e-mail: almomanm@myumanitoba.ca

K. Mahmoud
e-mail: karam.mahmoud@umanitoba.ca

E. El-Salakawy
e-mail: ehab.El-Salakawy@umanitoba.ca

S. Walbridge et al. (eds.), *Proceedings of the Canadian Society of Civil Engineering Annual Conference 2021*, Lecture Notes in Civil Engineering 244,
https://doi.org/10.1007/978-981-19-0656-5_48

concrete (HSC) has not been deeply investigated. The behaviour of HSC is very different from that of NSC, where it is more brittle and has different cracking behaviour. This makes it necessary to investigate the behaviour of HSC reinforced with GFRP reinforcement to provide enough data and make it possible to understand the behaviour of such combination. Studies, such as [9, 10], and [11], have investigated the GFRP-HSC short columns. It was found that GFRP reinforced columns behaved very similarly to steel-RC columns but were generally not as efficient in sustaining loads. Furthermore, replacing steel with GFRP resulted in a decrease in axial capacity of the columns. However, the ductility in GFRP-HSC columns was still higher than that of steel-RC columns.

Recently, [1] tested slender HSC columns reinforced with GFRP bars and spirals. The results for the HSC members showed material type failures as opposed to stability type failures. The study also provides evidence to the capability of GFRP bars to contribute to the axial capacity as well as lateral confinement and lateral resistance. Current data still needs to be verified to due to its scarcity, and thus, more research is required to make a meaningful impact on design codes and guidelines.

2 Experimental Program

2.1 Code Provisions and Specimen Design

The columns presented in this study were designed in accordance with the Canadian Standards for FRP-RC structures and bridges [5–7] where appropriate. The specimens were constructed with a diameter of 350 mm, which satisfying the dimensional limitation as per CSA A23.3-19 [5]. Furthermore, the CSA S6-19 [6] dictated that compression members must have a minimum height-to-diameter ratio of 2.5, this was satisfied for all specimens. In addition to dimensions of the columns, the reinforcement ratio used satisfies the minimum reinforcement ratio of 1.0% as required by CSA S806-12 [7], Clause 8.4.3.7. The longitudinal reinforcement consisted of six bars as required by Clause 8.4.3.8. Moreover, the spiral reinforcement satisfies Clause 8.4.3.13 of the CSA S806-12 [7] resulting in No. 10 bars spirals with a 75 mm pitch (clear spacing). The spiral pitch used is also more than the minimum requirement for the volumetric ratio of spiral reinforcement, where the minimum is provided by the following equation:

$$\rho_{Fs} = \frac{f_c^{'}}{f_{Fh}}\left(\frac{A_g}{A_c} - 1\right)\left(\frac{P}{P_0}\right) \tag{1}$$

$$\frac{p}{p_0} \geq 0.2 \text{ and } \frac{A_g}{A_c} \geq 0.3 \tag{2}$$

where A_g is the gross area of the section, A_c is the area of the concrete core f_{Fh} is the design stress level of the transverse confinement reinforcement.

2.2 Specimen Details

Six large-scale columns reinforced internally with GFRP bars and spirals were constructed and tested to failure. The diameter of the specimens was 350-mm and the heights were 1250, 1750 and 2450 mm, representing slenderness ratios (λ) of 14, 20 and 28, respectively. All columns were reinforced with No.15 and No.10 GFRP bars and spirals according to the requirements of CSA S806-12 [7]. A 25-mm clear concrete cover to the spiral was provided. The dimensions and details of columns are shown in Fig. 1.

The reinforcement consisted of sand-coated bars and spirals. The columns were reinforced with 6 longitudinal bars and had a spiral pitch of 85 mm. The properties of GFRP bars and spirals are summarised in Table 1. The columns were cast with a target 28-day concrete compressive strength of 60 MPa. The cylinders were tested on the day of testing of the corresponding specimen. The average concrete strength of the specimens was 61.3 MPa.

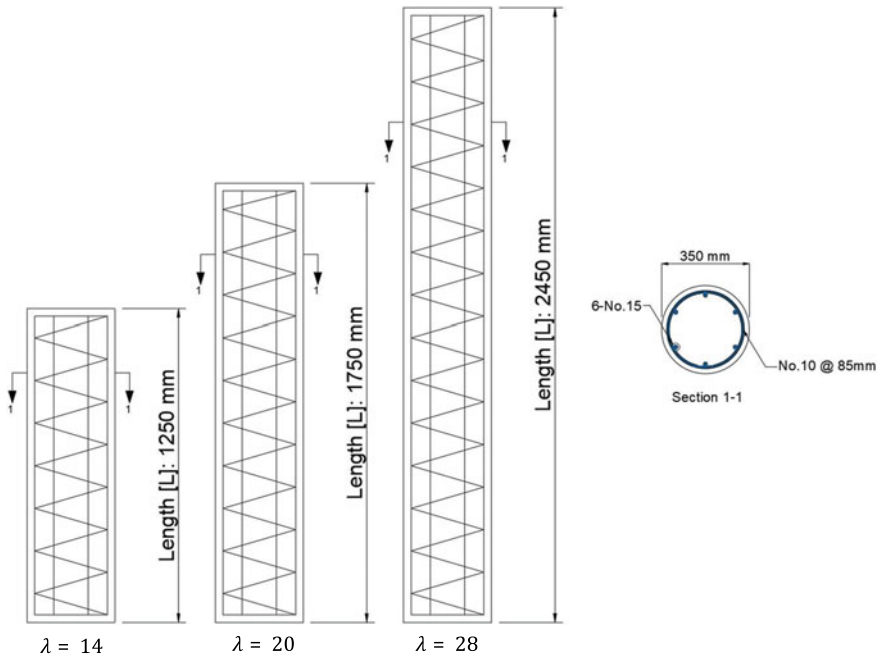

Fig. 1 Reinforcement detailing and specimen dimensions

Table 1 Mechanical properties of GFRP reinforcement

Bar No.	Diameter (mm)	Area of bar (mm^2)	Modulus of elasticity (GPa)	Tensile strength (MPa)
No. 10 (Spirals)	9.5	71	50	1,022
No. 15 (Straight bars)	15.9	199	62	1,184

Table 2 Test matrix and failure loads

Specimen name	Long reinforcement ratio (%)	Spiral reinforcement ratio (%)	Concrete strength (MPa)	$P_u{}^*$ (kN)
S-14-17	1.21	1.11	57.1	3,926
S-14-34	1.21	1.11	56.0	1,819
I-20-17	1.21	1.11	60.3	3,599
I-20-34	1.21	1.11	65.0	1,671
L-28-17	1.21	1.11	64.0	3,125
L-28-34	1.21	1.11	65.4	1,415

*Normalised using the average concrete strength with ratio $61.3/f_c{}'$

The test matrix is provided in Table 2. The two main variables are the slenderness ratio ($\lambda = k\ell/r$) and the *e/D* ratio; where "*e*" is the eccentricity at which the load was applied and "*D*" is the diameter of the specimen (350 mm). The specimen names consist of three parts reflecting the test parameters. The first indicates whether the column is short or slender (S for Short, I for Intermediate and L for Long/Slender). The second number refers to the slenderness ratio (14, 20 and 28). The last number represents the *e/D* ratio (17 and 34 for 0.17 and 0.34, respectively).

2.3 Test Setup and Instrumentation

The columns were tested under a displacement controlled monotonic load using a 5000-kN capacity hydraulic machine. The boundary conditions for the test were a pin-pin condition and were ensured using two specially fabricated steel collars. Each set of a specific slenderness ratio was tested under two eccentricities of magnitude 60 and 120 mm. The specimen and test setup are shown in Fig. 2. The column was instrumented with horizontal linear variable displacement transducers (LVDTs) to measure the lateral displacement. Electrical strain gauges, installed at critical locations, were used to monitor the developed strains in the reinforcement and concrete.

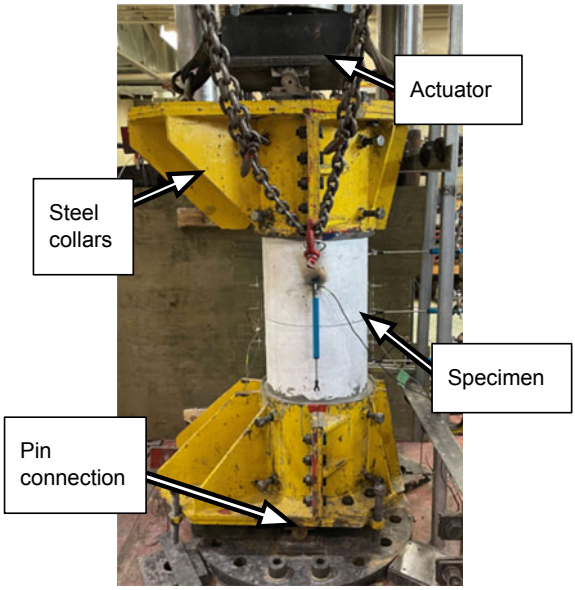

Fig. 2 A specimen in the test setup

3 Experimental Results and Discussion

3.1 General Behaviour and Failure Modes

Figure 3 shows the test specimens at failure. All specimens failed by crushing of concrete. In specimens with *e/D* ratio of 0.34, concrete crushing was preceded by cracks on the tension side. On the other hand, the specimens with *e/D* ratio of 0.17 showed tension cracks simultaneously with the crushing of concrete near failure. In all specimens, the failure was followed by a sharp drop in axial load. Specimen S-14-17 failure occurred by crushing of the concrete, followed by crushing of the outermost compression bar and the rupture or the spiral at the same location. In the remaining columns, reinforcement showed no signs of crushing/rupture failure even after the loss of 25% of the load capacity.

3.2 Effect of Test Parameters on Column Axial Capacity

The maximum capacities varied greatly with both test parameters. Specimen S-14-17 reached 3,926 kN while columns I-20-17 and L-28-17 achieved reduced capacities of 3,599 and 3,125 kN, respectively. The difference in those values represent a decrease of 8.3 and 13.2% when increasing the slenderness ratio from 14 to 20 and from 20 to 28, respectively. Similarly, increasing the *e/D* ratio resulted in a reduction in the column capacity. Column S-14-34 had a maximum axial capacity of 1,819 kN,

Fig. 3 Mode of failure of tested specimens

which represents a 53.7% decrease in axial capacity as compared to its counterpart S-14-17. Furthermore, specimen I-20-34 and L-28-34 had a maximum capacity of 1,671 and 1,415 kN, which represents a decrease of 53.6 and 54.7% compared to that of columns I-20-17 and L-28-17, respectively. The change in eccentricity had a pronounced effect on the axial capacity than the change in slenderness ratio. The change in *e/D* ratio caused a very consistent loss of load over the different slenderness ratio with an average of 54%.

3.3 Lateral Displacement

In general, as the slenderness ratio increases, the lateral displacement of the columns at mid-height increased (Fig. 4). For columns with *e/D* of 0.17 at peak load, the lateral displacement for columns S-14-17, I-20-17 and L-28-17 was 2.36, 5.82 and 8.87 mm, respectively. This represents an increase in the lateral displacement of 146 and 275% when the slenderness ratio increased from 14 to 20 and further to 28, respectively. Similarly, a decreasing trend is observed for columns with *e/D* ratio of 0.34. The shortest column, S-14-34 showed a mid-span lateral displacement of 4.1 mm. When the slenderness ratio is increased to 20 and then further to 28, the lateral displacement reached 8.6 and 15.56 mm, respectively, which translate into an increase of 110 and 280%, respectively. Furthermore, lateral deflections increased

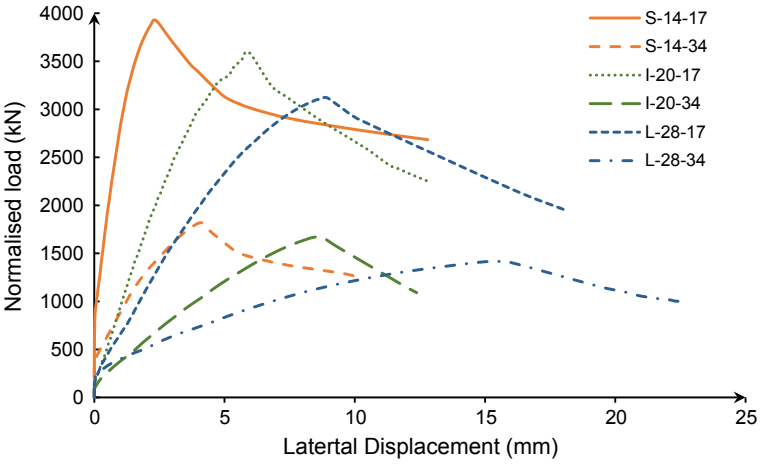

Fig. 4 Axial load-lateral displacement relationship for all test specimens

by 74, 48 and 75.4% when the *e/D* ratio increased from 0.17 to 0.34 in columns with slenderness ratios 17, 20 and 28, respectively.

4 Conclusion

This paper presents the experimental results of six large-scale high-strength concrete columns reinforced internally with GFRP bars and spirals. The following conclusions can be drawn.

1. All columns were able to resist the applied eccentric axial load and did not show stability type failures. All columns experienced material type failure characterised by crushing of the concrete cover.
2. The increase in slenderness ratio from 14 to 20 and from 20 to 28 showed a decrease in axial load capacity by 8.3 and 13.2%, respectively.
3. Increasing the *e/D* ratio had a more significant effect on the axial load capacity than the change in slenderness ratio. Doubling the *e/D* ratio, from 0.17 to 0.34 showed a decrease in the axial capacity of 53.7, 53.6 and 54.7% for columns with slenderness ratio 14, 20 and 28, respectively.
4. Increasing the slenderness ratio from 14 to 20 and further to 28 increased the lateral deflections by 146 and 52.4%, respectively, at the peak load for specimens tested under *e/D* of 0.17. For the same increase in the slenderness ratio, the lateral displacement at the peak load increased by 110 and 81%, respectively, for columns tested under *e/D* of 0.34.

Acknowledgements The authors would like to thank the Natural Sciences and Engineering Research Council of Canada (NSERC) for the financial support. The GFRP material was generously provided by Pultrall Inc. The authors would also like to thank the technical staff at the W.R. McQuade Heavy Structures Laboratory at the University of Manitoba for their assistance.

References

1. Abdelazim W, Mohamed HM, Benmokrane B, Nolan S (2020) Strength of bridge high-strength concrete slender compression members reinforced with GFRP bars and spirals: experiments and second-order analysis. ASCE, J. Bridge Eng. 25(9):04020066
2. ACI Committee 222 (2019). "Guide to Protection of Metalsin Concrete Against Corrosion" ACI 222R-19. American Concrete Institute (ACI): Farmington Hills, Detroit, MI
3. ACI Committee 440 (2015). "Guide for the Design and Construction of Structural Concrete Reinforced with Fiber-Reinforced Polymer (FRP) Bars". ACI 440.1R-15. American Concrete Institute (ACI): Farmington Hills, Detroit, MI
4. Barua S, El-Salakawy E (2020) Performance of GFRP-reinforced concrete circular short columns under concentric, eccentric, and flexural loads. ASCE, J. Composites Constr. 24(5):04020044
5. CSA (2019a). "Design of Concrete Structures", CSA A23.3–19, Canadian Standard Association (CSA): Toronto, Ontario, Canada
6. CSA (2019b). "Canadian Highway Bridge Design Code" CSA S6–19. Canadian Standard Association (CSA): Toronto, Ontario, Canada
7. CSA (2017). "Design and construction of building structures with fibre-reinforced polymers" CSA S806-12. Canadian Standard Association (CSA): Toronto, Ontario, Canada
8. De Luca A, Matta F, Nanni A (2010) Behavior of full-scale glass fiber-reinforced polymer reinforced concrete columns under axial load. ACI Struct J 107(5):589–596
9. Hadhood A, Mohamed HM, Benmokrane B (2016) Experimental study of circular high-strength concrete columns reinforced with GFRP bars and spirals under concentric and eccentric loading. ASCE J Composites Constr 21(2):04016078
10. Hadi MNS, Hasan HA, Sheikh MN (2017) Experimental investigation of circular high-strength concrete columns reinforced with glass fiber-reinforced polymer bars and helices under different loading conditions. ASCE J Composites Constr 21(4):04017005
11. Hales TA, Pantelides CP, Reaveley LD (2016) Experimental evaluation of slender high-strength concrete columns with GFRP and hybrid reinforcement. ASCE J Composites Constr 20(6):04016050
12. ISIS Canada (2007). "Reinforcing Concrete Structures with Fibre Reinforced Polymers." Design Manual No.3. ISIS Canada corporation: University of Manitoba, p 103, Winnipeg, Canada
13. Khorramian K, Sadeghian P (2017) Experimental and analytical behavior of short concrete columns reinforced with GFRP bars under eccentric loading. Eng Struct 151:761–773
14. Tavassoli A, Sheikh SA (2017) Seismic resistance of circular columns reinforced with steel and GFRP. ASCE J Composites Constr 21(4):04017002

Reinforcing Bar Connection of Hollow-Core Slabs to Steel Beam Supports

S. Hernandez Brito, K. Mahmoud, K. Truderung, and E. F. El-Salakawy

1 Introduction

Precast/Prestressed hollow-core slabs are commonly used to cover large spans in industrial and residential buildings. Designers prefer such slabs because of their cross-section efficiency and relatively lightweight, which leads to smaller section heights and deflections as well as longer spans. Other practical advantages include the convenience of the voids for mechanical, wiring and plumbing runs to save floor height and the noise isolation capabilities.

When HCS are supported on steel beams, a size 10 M "Z-shaped" steel reinforcing bar is commonly inserted between adjacent HCS and welded to the top flange of the steel beam. This type of connection is called "End Bearing Connection." Similar connection detailing is placed along the side of slabs, which is known as "Side Bearing Connection." According to construction practice in Eastern Canada, the connection bar has a minimum embedment length of 450-mm in regular-strength grout. The Z-steel bar is welded to the flange of the beam, leaving the external portion unrestrained, which is typically around 70-mm in length. Figure 1 shows the geometry of the bar for end and side bearing connections. However, different connection detailing is employed across Canada to tie the slabs to the supports. For instance, in Manitoba, it is common to weld stud-headed connectors on top of the flange of the beam and place hooks around this stud-headed connector. The hooks are then extended up to the shear key of the slab. Later, grout is poured in the connection to integrate the hooks to the slab. In addition, steel plates or angles can be welded to the top flange of the beam, and an expansion bolt is used to connect the plate to the slab. On the other hand, the [4] Manual for the Design of Hollow Core Slabs and

S. Hernandez Brito (✉) · K. Mahmoud · E. F. El-Salakawy
Department of Civil Engineering, University of Manitoba, Winnipeg, Canada
e-mail: hernan31@myumanitoba.ca

K. Truderung
Tower Engineering Group, Winnipeg, Canada

S. Walbridge et al. (eds.), *Proceedings of the Canadian Society of Civil Engineering Annual Conference 2021*, Lecture Notes in Civil Engineering 244,
https://doi.org/10.1007/978-981-19-0656-5_49

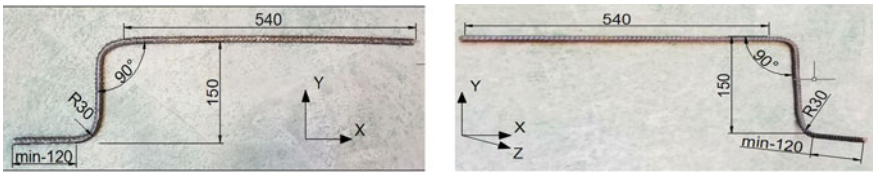

(a) 10M Connection bar for end bearing HCS (b) 10M Connection bar for side bearing HCS

Fig. 1 Typical connection detailing

Walls lists a series of connection detailing schemes that could be employed to avoid slab displacements. Nevertheless, the connection reinforcing bar shown in Fig. 1 is particularly widespread in North America because of its low cost, convenience and fast installation.

This steel reinforcement is used to tie the slab to the supports at the construction stage. Moreover, these bars maintain the overall structural integrity of the building. This connection prevents slab displacements that could result in loss of alignment of the units while erecting the floor or losing their bearing on the steel beam completely, leading to catastrophic accidents. In addition, the connection steel bar provides lateral bracing to the top flange of the steel beam. Moreover, HCS floors are designed to act as horizontal diaphragms, which transfer lateral loads (wind or seismic) to the steel structure throughout the steel connection bar.

Despite the importance of tie detailing in maintaining the structural integrity of buildings during the construction and at service, there are no provisions for their design in the North American codes. For instance, the Canadian Precast Concrete Institute Design Manual [1] and the CSA-A23.3-19 Design Standards [3] recommend using the shear-friction theory to quantify the reinforcement ratio required for placing ties in HCS floors. However, this concept is more applicable to monolithic or continuous connections, which is not the case for this specific type of connection.

In addition, the CSA A23.3-19 [3], the Prestressed Concrete Institute [4] Design Manual and ACI 318-19 Design Code [2] stated that longitudinal and transverse ties should be placed to preserve the structural integrity of buildings with floor diaphragm. Moreover, the ACI 318–19 [2] and the CSA A23.3–19 [3] specify that the minimum capacity expected for the connection of precast floors or roofs to their supports, formed by the integrity ties, should have a minimum nominal tensile capacity of 4.4 and 5.0 kN/m, respectively. Yet, these codes do not offer a methodology to design the detailing of such integrity ties nor calculate their capacity. Given the lack of information in the design codes and research regarding the tie bar connection, this study aims to investigate the behaviour and capacity of such connections while simulating the current construction practice.

2 Specimens, Test Setup and Instrumentation

Four full-scale specimens were tested under monotonic in-plane forces until failure. The HCS were pushed or pulled out to generate compression or tension stresses, respectively, in the connection rebar. The 203-mm thickness HCSs were cut to segments of 1,220-mm length. A minimum slab seating length of 75-mm was provided to satisfy Canadian Code requirements CSA A23.3-19 [3] and the CPCI design manual [1]. The connection bar illustrated in Fig. 1 was welded to a W250 × 67 steel beam following the construction practice. The grout used to fill in the joint was of regular strength (20–25 MPa). The properties of mixes typically used in the industry were taken as reference since no applicable provision was found in the North American Codes. This grout was mixed, poured, and cured in the laboratory following manufacturer guidelines.

Test variables in this study are the type of bearing of the slabs (EB for End Bearing connections and SB for Side Bearing connections) and the direction of loading (TN or CN for specimens with connection bar tested under tension or compression, respectively). Table 1 lists the details of the test specimens.

The test setup comprised: a) clamping beams to distribute the forces along the slabs uniformly; b) pinned-pinned supports, which carry half of the self-weight of the slab while allowing free displacement towards the end that is being pulled or pushed; and c) the supporting steel beam where the connection bar is welded. Figure 2 shows a schematic drawing of the test setup and specimen details. Electrical strain gauges were attached to the steel bar at the bends to determine the yielding load The applied load was measured using a load cell. The readings of instrumentation were processed through a Data Acquisition System. Cracking or spalling of the grout, if any, was carefully monitored and recorded during the test.

Table 1 Test matrix

Code	Type of bearing	Force applied	Force in connection rebar	Bend angle of connection rebar (degrees)
EB-CN-90	End Bearing	Pushing	Compression	90
EB-TN-90	End Bearing	Pulling	Tension	90
SB-CN-90	Side Bearing	Pushing	Compression	90
SB-TN-90	Side Bearing	Pulling	Tension	90

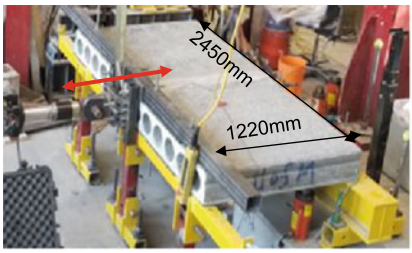

(a) End Bearing Specimens

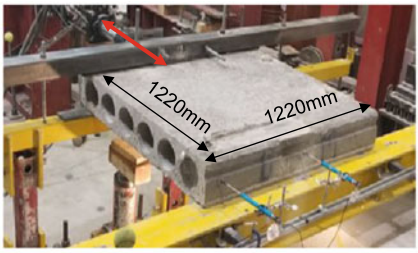

(b) Side Bearing Specimens

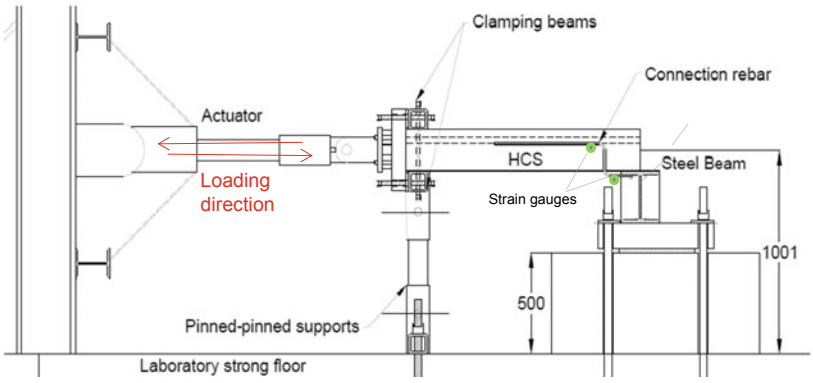

(c) Test Setup Scheme

Fig. 2 Details of specimens, test setup and instrumentation

3 Discussion of Test Results

3.1 Failure Modes

Different modes of failure were observed in the specimens based on the direction of the applied force on the connection bars (in-plane tension or compression). The failure mode observed in the specimens under tension was governed by yielding at the unrestrained portion of the rebar followed by grout cracking. As the load applied to the slabs acted on the connection rebar, the bend straightened, forming a nearly flat shape, as shown in Fig. 3. Afterwards, a single crack formed in the grout. The crack grew longitudinally along the shear-key in the end-bearing specimen (EB-TN-90) while it extended across the core filled with grout for the side-bearing specimen (SB-TN-90). Unexpectedly, the end bearing connection (EB-TN-90) experienced a bond failure at the onset of bar yielding. Therefore, the capacity of the connection was limited to the contribution of steel alone until the yielding point.

On the other hand, specimens subjected to compression forces did not experience any cracking during the test. The mode of failure observed in these specimens was bar bending and buckling. As the pushing force applied to, the free portion of the connection bar bent in the direction of the force. At the onset of buckling, the connection bar

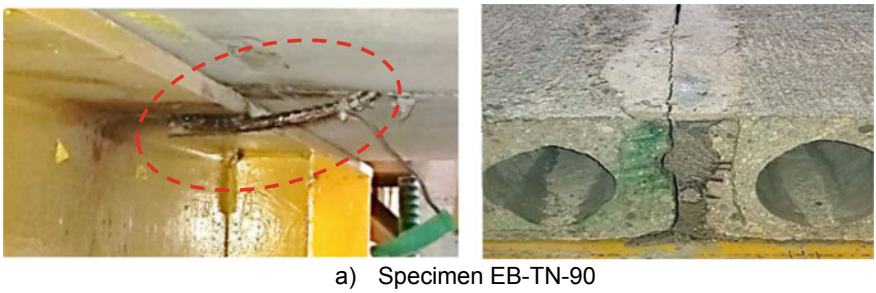

Fig. 3 Failure modes of specimens tested under tension. Bar flattening (yielding) followed by grout splitting

Fig. 4 Mode of failure of specimens tested under compression

reached its maximum capacity. After the peak load, the slabs pulled the unrestrained portion of the 10 M bar as the load dropped gradually. The connection bar experienced further deformation until it eventually formed a 180-degree shape, as shown in Fig. 4a and b. Finally, bar rupture occurred as a result of excessive deformation and buckling.

3.2 Capacity of Test Specimens

The connection bar tested in this research (size 10 M, Grade 400 W) has a minimum expected capacity of 40 kN under tension, which corresponds to the capacity at yielding. Therefore, the connection bar spaced at 1,220 mm according to the width of the HCS, complies with the minimum limits recommended by the ACI 318-19 [2] and CSA A23.3-19 [3].

Specimens tested under tension forces exhibited approximately double the capacity of their counterparts subjected to compression forces, as shown in Fig. 5. Whereas the specimens EB-TN-90 failed at a load of 30 kN, due to a bonding failure between the grout and the slabs (still reaching yielding), the side bearing specimen (SB-TN-90) reached a load of 45 kN. For the end-supported specimen, the connection bar reached 2,300 micro-strain at the peak load. In contrast, the side-bearing connection attained 13,000 micro strains when grout crashing occurred. The side-bearing connection was able to accumulate more deformation at the connection bar, leading to a larger capacity, compared to the end-bearing connection. Despite the unexpected bond failure of the end-bearing connection, both types of connections satisfied the minimum requirements of the CSA A23.3-19 [3] and ACI 318-19 [2] for the tensile strength of ties in HCS floors.

However, there is no specification in the above-mentioned design codes about the capacity of integrity ties when experiencing compression forces. Yet, specimens tested under compression forces showed a reduced capacity at the initiation of bar buckling. The maximum capacity of specimens EB-CN-90 and SB-CN-90 was 12.6 and 11.4 kN, respectively. The connection bar in these two specimens exhibited smaller values of deformation (900–1100 micro strains approximately) compared to their counterparts in tension. In these two specimens, the connection bar demonstrated little resistance to pushing forces after the peak load.

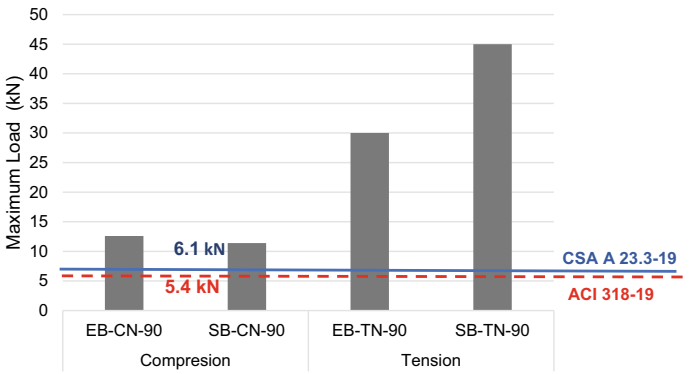

Fig. 5 Capacity of test specimens

4 Conclusions and Recommendations

Four full-scale connection rebar specimens under tension/compression forces were tested until failure. The following conclusions can be outlined:

- The connection reinforcing bar exhibited more capacity when tested under tension forces than when subjected to compression. The size 10 M bar experienced close-to-yielding or yielding stresses when subjected to tension forces. The specimens tested under tension forces failed due to bar yielding followed by grout cracking or slab splitting.
- The connection rebar in specimens tested under compression did not reach yielding at the peak load. The mode of failure was governed by bar bending or bar buckling. After the onset of bar buckling, load degradation occurred at a regular rate.
- The end supported specimens behaved similarly to the side supported specimens in terms of the failure mode, slab displacement and strain in the connection bar when tested under compression or tension forces.

Size 10 M, Z-shaped steel bar employed as reinforcement for HCS bearing connections to steel beams met the tensile strength specified in the codes for integrity ties. However, the relatively low capacity and lack of ductility under compression forces demonstrated that this connection detailing is unsuitable for HCS bearing connections. A compression failure might not result directly in the loss of bearing of the slabs. However, it could provoke a progressive collapse after overloading other bearing connections, floor movements, instability, and floor misalignments. Based on the results of this experimental study, the steel reinforcement of this bearing connection could be enhanced in two ways. First, the free portion of the connection bar could be eliminated or reduced by displacing the connection bar closer to the beam web. Second, the shorter end of the connection rebar could be welded to the top face of the flange of the beam to reduce eccentricities and embed the connection bar completely in the grout.

Acknowledgements The authors wish to express their gratitude for the financial support received from the Canadian Precast/Prestressed Concrete Institute (CPCI) and the Natural Sciences and Engineering Research Council of Canada (NSERC). The in-kind contributions received from Armtec Precast (Infrastructure Solutions) and Tower Engineering Group are greatly appreciated. In addition, the assistance received from the technical staff of the W. R. McQuade Structures Laboratory at the University of Manitoba is acknowledged.

References

1. CPCI (2017) CPCI design manual. 5th edn, Canadian Precast/Prestressed Concrete Institute, Ottawa, Ontario
2. ACI (2019) Building code requirements for structural concrete. ACI 318-19, American Concrete Institute, Detroitr, MI

3. CSA (2019) Design of concrete structures. CSA A23.3-19, Canadian Standards Association, Toronto, Ontario
4. PCI (2015) PCI manual for the design of hollow core slabs. Precast/Prestressed Concrete Institute, Hollow Core Slab Producers Committee, Chicago, Illinois

Rehabilitation Study of an Old Metallic Orthotropic Deck Bridge

M. M. Hassan and Abbas M. H. Hussein

1 Introduction

In 1969, the French Ministry of Equipment launched a competition for a standardized design of dismountable steel viaducts. The aim of the ministry was to avoid at grade traffic crossings particularly in the city of Paris. In March 1970, the jury declared the successful company. This company suggested standard design of road bridges of spans from 9 to 30 m, which are the most common spans used inside the cities for such viaducts. The proposed viaducts represented simple or continuous spans and could accommodate one, two or more traffic lanes. The system consisted of orthotropic deck plates fabricated entirely and painted in the shops and rapidly assembled on sites by mean of rivets/bolts. It was clear that the proposed orthotropic design fulfilled two essential conditions for economy in steel bridge design which are: efficient utilization of steel and maximum reduction of material dead weight.

Egypt in the beginning of last century was in crucial need for such standard design to avoid firstly the congested intersections and the traffic jams and secondly to avoid the interference with the construction of the first Cairo underground metro line. Many of these bridges were imported and assembled, enabling thus the fluid flow of traffic in the congested city of Cairo, a city of twelve million inhabitants at that time. It was necessary to adapt these standard designs to suit the alignments of the roads in Cairo and tailor it to cope with the country's practice and applicable procedures. Upon several designs, the structure shown in Fig. 1 was imported from France and constructed in Cairo. It is to be noticed that in France most of these bridges

M. M. Hassan—On leave from Cairo University.

M. M. Hassan (✉)
Structural Engineering Department, Cairo University, Giza, Egypt
e-mail: mahamoddather@eng.cu.edu.eg

Architectural Engineering Department, University of Prince Mugrin, Medina, Saudi Arabia

A. M. H. Hussein
Structural Engineering Department, Al Azhar University, Cairo, Egypt

S. Walbridge et al. (eds.), *Proceedings of the Canadian Society of Civil Engineering Annual Conference 2021*, Lecture Notes in Civil Engineering 244,
https://doi.org/10.1007/978-981-19-0656-5_50

Fig. 1 General view of curved part bridge

were considered temporary then removed and replaced by permanent more aesthetic bridges, while in Egypt most of these bridges are still in use in both governorates Cairo and Giza.

Many roadway bridges worldwide employ metallic orthotropic steel deck system due to its main advantage: reduced weights. The roadway network in Egypt includes many orthotropic metallic bridges that has been in service for a long time. Assessment and rehabilitation efforts of these bridges is a pressing issue in order to ensure a satisfactory level of performance under the increasing traffic loads. Inspection and repair of metallic orthotropic steel deck system have been investigated by several researchers. Most available research focus on the repair of fatigue cracks which is one of the most critical issues in metallic bridges [15–18].

The current paper lists the assessment and repair efforts for one of the major bridges in Cairo: Sayeda Eisha Bridge. This work is part of the performed efforts during the last years in order to assess the condition of the different railway and roadway bridges across the country [1, 2, 10, 12]. Assessment and rehabilitation procedure followed the recommendations by different researchers in other countries [3, 8, 9]. The next sections of the paper include description of the studied bridge, the observed defects, the analytical study in addition to the applied repair procedures.

2 Historical Background and Description of Bridge

Sayeda Eisha Bridge is a roadway bridge constructed in a vital traffic axis in 1970 in old Cairo district. It is located on Salah Salem Street, one of the busiest streets in Cairo. It connects Giza governorate to the Eastern district of the capital, the residential quarters of Abbassia, Nasr City, Heliopolis passing through Al-Gamaliya, Al-Ghoreya and Al Hussein, the historical districts of Cairo. The considered bridge represents two adjacent bridges with a total length of approximately 300 m divided on 13 successive bays serving traffic flow in both directions. The span of each bay ranges between 22.9 to 24.9 m. Each bridge consists of two traffic lanes following a

straight configuration at the approaches and a curved middle part. Bridge deck is an orthotropic floor system consisting of main longitudinal beams spaced at 1.75 m and transverse beams spaced at 3 m. In addition, bridge deck has welded longitudinal ribs spaced at approximately 400 mm. Steel moment frames supports the different adjacent bridge bays. Pipes were used at selective frames to support the forces resulting from braking forces. Figures 1, 2, 3, 4, 5 and 6 show the general view and different structural components of the studied bridge.

Fig. 2 Main beams of bridge

Fig. 3 Orthotropic deck system

Fig. 4 Supporting steel moment resisting frame

Fig. 5 Pipes added at selective frames

Fig. 6 Fixation of Guardrail

The bridge was built as a temporary traffic solution during Metro Line construction works. However, the bridge has been in service for around 50 years. During this period, many accidents were reported leading to damage to many structural members. The bridge has a sharp curved part while it lacks the required super elevation or friction to counterbalance the centrifugal force. This resulted in many accidents including vehicles falling from the bridge. Figures 7 and 8 show examples of accidents resulting in deformations and damage to some parts of the bridge.

Fig. 7 Truck on fire at the middle part of bridge

Fig. 8 Permanent deformations in bridge deck

3 Inspection and Observed Defects

Inspection campaign of the bridge started in December 2016 upon a request of Cairo Governorate as part of the efforts to elevate the quality of transportation network in Egypt. It was part of the study for assessing the condition of different bridges and tunnels at Cairo province. The study started by several visits to the bridge. During these visits, the different elements of the bridge were extensively investigated to pinpoint defects. Inspection focused on critical positions and fatigue prone positions. Unfortunately, existing documents of the bridge did not include all the required structural details. Hence, inspection teams measured missing dimensions of some elements and prepared sketching details at connections including number of rivets, bolts, spacing…etc. Accordingly, the structural system of the bridge was fully understood. Upon inspection, several defects were observed including loss of expansion joints, cracks at the lower parts of the supporting beams, corrosion and erosion of steel section, and loss of asphaltic layer for the different traffic lanes. Figures 9, 10, 11, 12, 13, 14 and 15 show the different observed defects (Figs. 16 and 17).

Fig. 9 Large observed distance

Fig. 10 Deformations of steel elements

Fig. 11 Corrosion at bottom of bridge columns

Fig. 12 Loss of asphaltic layer

Fig. 13 Accumulation of garbage

Fig. 14 Missing bolts at many connections

Fig. 15 Observed deformations in steel moment frame columns

4 FE Modeling

SAP2000 software was employed to build 3-D grillage models for the studied bridge. Figure 18 shows the general layout of the model. The model was built considering the sectional properties measured during the visual inspection phase. Frame elements

Fig. 16 Lack of speed limit signs

Fig. 17 Bad condition of guardrail

were used to simulate the different bridge components. Rigid joints were used to simulate the connection of the moment resisting frames while pinned joints were used to simulate the connection between main beams and supporting frames. The grillage modelling technique was used to capture bridge deck properties. Figures 19 and 20 shows the different sections included in the modeling of the bridge. The model was analyzed considering traffic loads imposed by latest edition of design codes considered in Egypt [7]. It is worth mentioning that these loads are higher than the ones the bridge was originally designed for.

Based on the built model, the different members and connections were checked under the resulting straining actions. It was found that the stresses on some members and connections exceed the allowable stress values set by Egyptian Code for Design of Steel Structures [6]. For example, the cross section of the main beam was found to be under increased tensile and shear stresses at middle and edge of beam, respectively. Moreover, beams and columns of the different supporting frames were checked, and it was found that column section at some locations are subjected to straining actions exceeding their supporting capacity. Upon checking the connection between main girder and moment resisting frames shown in Fig. 21, it was found that the existing bolts and decreased section properties are not sufficient to resist the applied

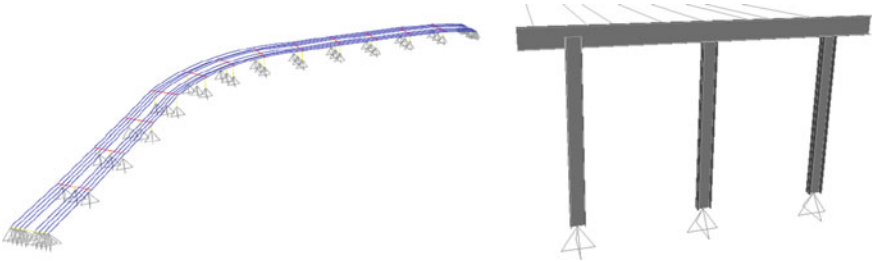

Fig. 18 General view of FE model and supporting moment resisting frame

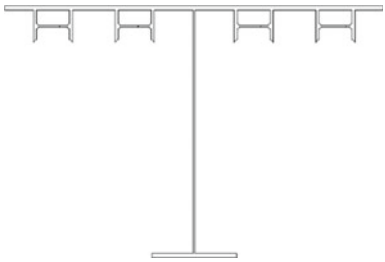

Fig. 19 Stress distribution for the longitudinal supporting beam

shear. Induced stresses in most bolts exceeded the allowable values. This resulted in repetitive loss of these bolts as seen in Fig. 14.

Strengthening alternatives were studied considering anticipated costs and ease of application. Moreover, it was considered crucial by authorities that any repair procedures should not hinder the traffic flow as the bridge is located in one of the busiest areas in Cairo. In addition, restriction over added weight was imposed by the condition and capacity of bridge foundation as seen in the following section.

5 Bridge Foundation

Imam and Chryssanthopoulos [14] reported that loss of pier or foundations represent 16% of most frequently causes of failure of metallic bridges. This stresses upon the importance of checking the condition of foundations of the considered bridge. Accordingly, excavation works were performed in order to explore type of foundations under Sayeda Eisha Bridge. The maximum depth of foundations was found equal to 5.5 m. Foundations composed of two reinforced concrete footings connected by a wide reinforced concrete girder and supported on two circular plain concrete footings as shown in Fig. 22. The middle column of the steel frame is only supported on the ground beam linking the two edge footings. Check on existing foundations indicated that stresses on soil approximately reach the allowable bearing capacity under the currently applied loads. Hence, any increase in bridge weight may result

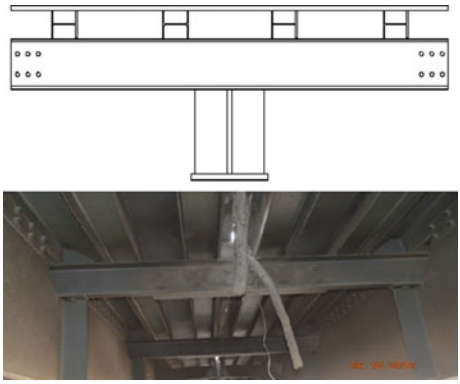

Fig. 20 Relation between cross beams and metallic deck

in needed strengthening applications for the foundation works. Accordingly, repair alternatives were compared based on their impact on the total weight of bridge.

6 Repair Works

Based upon the observed defects during the visual inspection phase and the structural analysis following the finite element modeling, the following defects were mainly considered, and repair procedures were suggested accordingly:

- Lack of proper super-elevation resulting in accidents involving vehicles dropping off bridge.
- Increased stresses in main beam, cross beams and supporting moment resisting frame columns when considering increased traffic loads.
- Insufficient number of bolts at main beam shear connection.
- Corrosion and loss of parts of the steel section for some members.
- Lack of expansion joints.
- Loss of top asphaltic layer and exposure of the steel plates.
- Lack of road signs.

Several alternatives were considered and studied to solve the above defects. For the main beams, it was decided to add bottom plates, Fig. 23, to decrease the resulting tensile stresses. The additional plates had a width larger than the width of the existing bottom flange of beams and were connected using two lines of fillet welding. One of the studied alternatives included adding concrete slab and introducing composite action between steel main beams and the slab and accommodate the needed superelevation. However, this solution resulted in increasing the dead weight of the bridge to an extent that will require strengthening of foundation. Increasing section depth at main beam connection was also adopted instead of adding cover plates to beam web due to faced construction difficulties and critical clear height below bridge. For steel

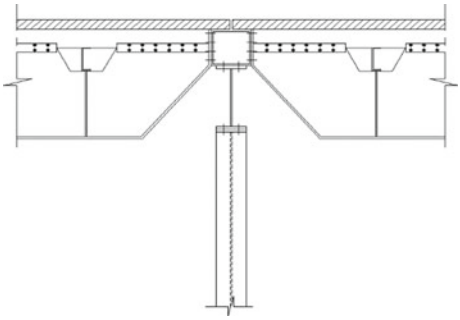

Fig. 21 Connection of main beam at supporting moment resisting frame

cross girders, structural calculations showed that its section is unsafe upon considering wheel load at its edge. Hence, diagonal box braces were added to distribute and support the applied loading, Fig. 24. Corrosion at all observed spots was removed by sand blasting and steel plates were added to make up for the lost thickness and decrease induced stresses in columns, Figs. 25 and 26. At some locations bracing members were added to redistribute the resulting stresses as shown in Fig. 27. Missing bolts were added and strengthening of the main beam connections was applied as listed in Fig. 28.

Other applied repair procedures included:

- Adding proper traffic signs indicating bridge curvature and limiting velocity on bridge.
- Replacing of asphaltic wearing surface for the whole bridge.
- Repairing of damaged parts of guardrail.

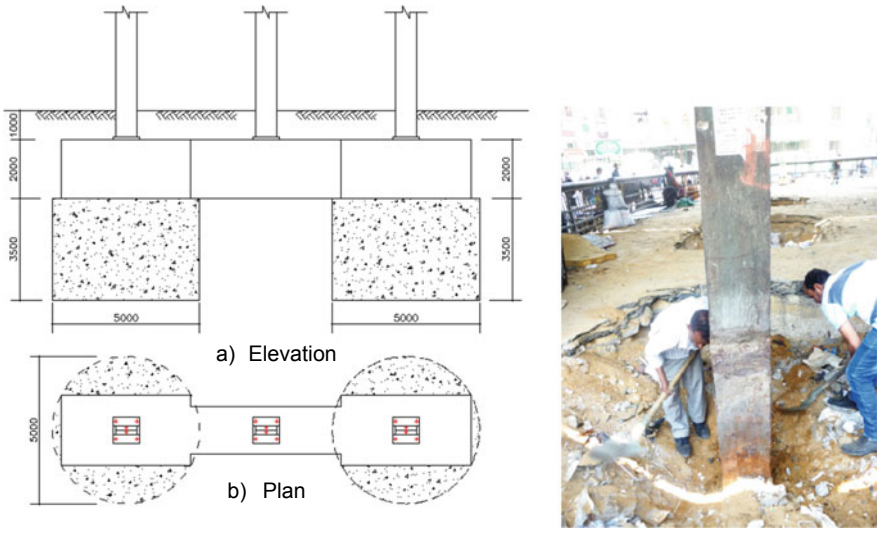

Fig. 22 Excavation works and foundation type

Fig. 23 Strengthening of main beams by adding bottom plates

Fig. 24 Adding diagonal bracing to cross beams

Fig. 25 Strengthening of columns

For the inadequate superelevation, several alternatives were checked including using concrete overlays and shear studs [4], adding a new steel plate to the existing deck to create a sandwich structure, use of open grid deck, or use of fiber reinforced polymer deck. However, to economic constraints, it was decided to limit speed over the bridge instead.

Fig. 26 Strengthening of base connection

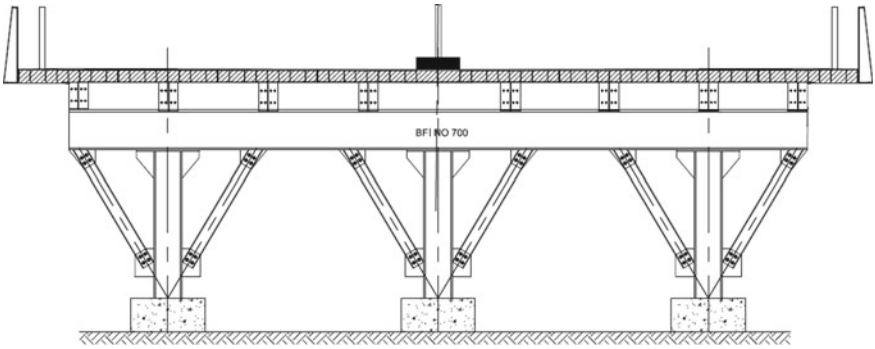

Fig. 27 Strengthening of moment resisting frame

These repair procedures were applied were applied to prolong the service life of the bridge till an alternative is present considering the Cairo governorate plan for developing the area.

7 Concluding Remarks

This paper explored the applied repair procedures for an old steel orthotropic bridge located in Cairo: Sayeda Eisha Bridge. Description of the bridge and its components was listed. Observations during the visual inspection phase were exhibited. Afterwards, the built finite element model was investigated. Several alternatives were

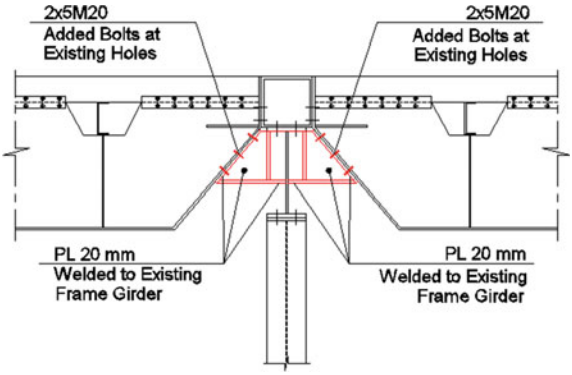

Fig. 28 Strengthening proposal of main beam end connection

studied, and detailed structural analysis calculations were performed for each alternative in addition to a cost analysis study focusing on anticipated direct costs in addition to costs related to traffic interruptions and ease of repair applications. Accordingly, repair methodologies were proposed, and examples of applied repairs were shared.

This paper represents part of the performed efforts to investigate and increase the service life of existing old bridges in Egypt. The following main conclusions can be categorized:

- The study showed that the inspected bridge had many defects including corrosion, increased stresses in members and connections, inadequate super-elevation, loss of expansion joints and loss of asphalt layer.
- No records were found regarding the design drawings of the studied bridge. Hence, measuring of different members dimensions had to be performed. In addition, excavation works had to be performed to explore type and dimensions of foundations.
- Corrective actions and repair methodologies were studied. The chosen procedures depended on several economic factors in addition to the sensitivity of bridge location.

The applied repair procedures do not preclude the importance of periodic maintenance in order to maintain a satisfactory level of behavior and extend the service life of bridge.

Acknowledgements The authors wish to express their sincere appreciation to the structural team at EHAF Consulting Office for the technical support.

References

1. Abbas HH, Hassan MM (2016a) Evaluation of strengthening applications for old railway bridges in Egypt. 19th IABSE Congress, Stockholm, Sweden

2. Abbas H, Hassan MM (2016b). Gestion des ouvrages d'art ferroviaires en Égypte/management of railway bridges of Egypt. Annales du Bâtiment et des Travaux Publics 68(3):40. Editions ESKA
3. Bancila R, Petzek E, Silvia R, Ionita O (2009) Assessment of failure and malfunction in steel bridges. In: Joint workshop of COST action TU0601 and E55, Ljubljana, Slovenia
4. Battista RC, Pfeil MS, Carvalho EM (2008) Fatigue life estimates for a slender orthotropic steel deck. J Constr Steel Res 64(1):134–143
5. CSI (2003) SAP2000 software: integrated software for structural analysis and design. Computers and Structures, Inc., Berkeley
6. ECP (2007) The Egyptian code of practice for steel construction – load and resistance factor design, ECP 205-2007. Research Center for Housing, Building and Physical Planning, Giza, Egypt
7. ECP (2012) Egyptian code of practice for loads and forces in structural works and buildings, ECP 201-2011. Research Center for Housing, Building and Physical Planning, Giza, Egypt
8. Ermopoulos J, Spyrakos CC (2006) Validated analysis and strengthening of a 19th century railway bridge. J Struct Eng 28:783–792
9. Frangopol, D.M., Strauss, A., Kim, S.: Bridge reliability assessment based on monitoring. J. Bridge Eng. **13**(3), 258–270 (2008)
10. Hassan MM, Saleh MM, Abbas HH (2015) Assessment of existing steel combined railway and roadway bridges over waterways. In: 2nd international conference on bridge testing, monitoring & assessment
11. Hassan MM, Abbas HH (2017) Dynamic characteristics of old railway steel bridges in Egypt. In: International conference on advances in sustainable construction materials & civil engineering systems, ASCMCES 2017. In MATEC Web of Conferences, 120: 01005
12. Hassan MM, Elsawaf SA, Abbas HH (2017) Existing metallic bridges in Egypt: current conditions and problems. J Civ Struct Heal Monit 7(5):669–687
13. IABSE reports of the working commissions (1971) Rapports des commissions de travail AIPC = IVBH Berichte der Arbeitskommissionen
14. Imam BM, Chryssanthopoulos MK (2009) Failure statistics for metallic bridges
15. Liu Y, Xinhui X, Naiwei L, Yang D (2016) Fatigue reliability assessment of orthotropic bridge decks under stochastic truck loading. J Shock Vibr
16. Mizokami Y, Masafumi K, Yuki K, Masahiro S (2017) A study on repair method using TRS for fatigue cracks in orthotropic steel deck. CE/Papers 1(2–3):4570–4578
17. Suzuki H (2015) Experimental study on strength of joints connected with thread forming screw. J Struct Eng 61 A:614–626
18. Wu W, Henk K, Milan V, Richard P, Jos V (2017) Fatigue behaviour of the closed rib to deck and crossbeam joint in a newly designed orthotropic bridge deck. CE/papers 1(2–3):2378–2387